申报	系列：教师系列教学科研并重型
	专业：管理科学与工程
	职称：教授

业绩成果材料

（申报人的业绩成果材料包括论文、科研项目、获奖以及其他成果等）

单　位（二级单位）　数学与信息学院

姓　名　张建桃

材料核对人：　　单位盖章：

核对时间：

华南农业大学

目 录

一、教学研究业绩.....1

1.教学研究项目：广东省高等教育教学改革项目《大数据背景下基于文本挖掘的新农科人才需求分析与人才培养模式改革研究》立项通知及有关佐证材料.....1

2.教学研究项目：广东省教育厅研究生教改项目《大数据视角下专业学位研究生实践能力需求与培养研究—以计算机技术领域为例》立项通知及有关佐证材料7

3.教学研究项目：中国高等教育学会高等教育科学研究项目《招聘大数据分析视角下论新农科人才学科交叉融合培养》立项通知及有关佐证材料.....11

4. 教学研究项目：全国农业教指委研究课题《新农科背景下基于大数据分析的农业专业学位研究生培养要素优化研究》立项通知及有关佐证材料.....14

5. 教学研究项目：高等农林院校课程思政联盟2025年教学改革研究项目《农林特色课程思政案例智能生成与应用研究》立项通知及有关佐证材料.....19

6. 教学研究项目：广东省高等学校教学管理学会2021 年度课程思政建设项目《课程思政建设项目：应用统计学》立项通知及有关佐证材料.....22

7.教学研究项目：中国农学会教育教学类第八批课题《基于文本挖掘的新农科人才跨学科能力需求分析与培养探索》立项通知及有关佐证材料.....27

8. 教学研究项目：关于《CDIO理念的工业工程专业人才培养模式探索与研究——基于美国佛罗里达大学实地调研》项目的有关佐证材料.....33

9.教学质量工程项目：关于《线下示范课程：设施规划》项目的立项通知及有关佐证材料.....34

10. 教学质量工程项目：关于《华南农业大学金蝶精一实践教学基地》项目的有关佐证材料.....38

11. 教学质量工程项目：关于《课程思政示范课程：应用统计学》项目的有关佐证材料.....39

12. 教学质量工程项目：关于《在线开放课程：应用统计学》项目的立项通知及有关佐证材料.....44

13.教学研究项目：关于《基于文本挖掘课程思政元素挖掘研究—以应用统计学为例》项目的有关佐证材料.....48

14.教改论文：《基于市场需求的工业工程专业课程设置》论文及其检索证明.52

15. 华南农业大学研究教学成果奖一等奖（排第二）：《真场景，实应用:面向农业数智化转型的信息管理类硕士培养模式创新与实践》有关佐证材料.....61

二、科研项目.....62
1.主持《松材线虫病疫点镇拔除技术指导示范》项目的立项通知及有关佐证材料.....62
2.主持广东省哲学社会科学项目：《基于大数据分析的广东省乡村振兴人才需求和培养研究》立项通知及有关佐证材料.....68
3. 主持《梅州兴宁市农用无人机高效丝苗种植县级农技推广服务驿站技术服务》项目的立项通知及有关佐证材料.....72
4. 主持广东省自然科学基金《禽流感空气消毒多振子超声雾化气溶胶喷雾器的研制》立项通知及有关佐证材料.....75
5. 主持广州市科技计划重点研发项目《稻田农药减施与污染治理技术的研究与示范》立项通知及有关佐证材料.....80
6. 主持《簕菜叶面肥无人机喷施参数优化与推广应用》项目的立项通知及有关佐证材料.....84
7. 主持《基于高频超声雾化的农药超低量喷雾器关键技术研究》项目的立项通知及有关佐证材料.....88
8. 主持广东省普通高校“人工智能”重点领域专项：关于《基于人工智能和触觉感知的植保无人机纳米农药减施关键技术研究》项目的立项通知及有关佐证材料.....91
9. 主持广东省教育科学规划课题(高等教育专项):《人工智能背景下课程思政元素智能挖掘与覆盖程度评价研究》立项通知及有关佐证材料.....95
10.主持《植物精油微孔压电超声雾化机理研究》项目的立项通知及有关佐证材料.....98
11.主持《“无人机及其在农业领域的应用”华农社区科普行活动》项目的立项通知及有关佐证材料.....102
12.主持《珠海湿地公园环保科普基地建设》项目的立项通知及有关佐证材料.....106
13.主持《检疫处理无人机超低容量喷雾装置研究试验》项目的立项通知及有关佐证材料.....107
14.主持华农温氏科技创新中心项目：《不确定需求下的生猪屠宰冷链配送路径优化研究》立项通知及有关佐证材料.....110
15.主参《精准农业中无人机作业关键装置研究及应用》项目的立项通知及有关佐证材料.....113
16.主参国家自然科学基金《触觉感知遥操控无人机精准变量施药》立项通知及有关佐证材料.....118
17.主参国家自然科学基金《基于棉花冠层特征与沉积量预测模型的无人机精确喷施控制研究》项目的立项通知及有关佐证材料.....122

三、论文、著作等.....126
1. 检索证明.....126
2. 以第一作者发表本专业论文情况.....132
2.1 长春花感染柑橘黄龙病菌微波热处理防控效果.....132
2.2 农药液滴在水稻叶面的动态润湿铺展行为.....144
2.3 柑橘黄龙病热空气快速处理温度场分布特性试验研究.....163
2.4 农用超声雾化换能器参数优化设计与试验.....178
2.5 柑橘黄龙病远红外热处理温度场分布特性试验研究.....190
2.6 Application of artificial neural network (ANN) and response surface methodology (RSM) for modeling and optimization of the contact angle of rice leaf surfaces.....208
2.7 Effects of temperature and humidity on the contact angle of pesticide droplets on rice leaf surfaces 227
3. 以通讯作者发表本专业论文情况.....241
3.1 A Human Finger-Inspired Shape-Locking Pneumatic Gripper Enabled by Folding Laminar Jamming Structure.....241
3.2 Single-rotor UAV flow field simulation using generative adversarial networks 257
3.3 农用无人机超低容量旋流喷嘴的雾化特性分析与试验.....281
3.4 农药液滴在玉米叶片表面铺展面积的影响因素.....294
3.5 Origami Improved Dielectric Elastomer Actuation for Tunable Lens 306
3.6 Fluid-Solid Coupling and Experimental Realization of a Piezoelectric Atomizer under Standing-Wave Resonance 319
3.7 基于共振声学放大原理的涡激振动自发电装置设计与试验.....337
3.8 技术机会发现领域专利挖掘方法研究述评.....352
3.9 基于CiteSpace可视化分析的柑橘黄龙病研究进展 369
3.10 An improved YOLO model for detecting trees suffering from pine wilt disease at different stages of infection 390
四、科研成果.....404
1. 知识产权.....404
1.1 专利授权证书：一种柑橘黄龙病的热空气处理装置及其使用方法.....404
1.2 专利授权证书：一种柑橘幼苗微波加热杀菌装置.....406
1.3 专利授权证书：基于胜任力的招聘文本专业知识点分类方法及装置.....408
1.4 专利授权证书：一种基于改进Yolo v3网络模型的松材线虫病疫木检测方法 410

1.5 专利授权证书：一种微孔压电超声雾化器.....412
1.6 软著授权证书：植保无人机喷雾雾滴在水稻叶片表面润湿展布性能预测系统.....414
五、其他业绩.....416
1. 指导学生学科竞赛.....416
1.1 第五届广东省暨粤港澳大湾区工业工程创新大赛三等奖“基于线性回归模型的气象预测系统”.....416
1.2 第三届广东省暨粤港澳大湾区工业工程创新大赛三等奖“基于SLP的胶粘剂生产车间布置优化”.....418
1.3 第五届广东省暨粤港澳大湾区工业工程创新大赛二等奖“Amazon kindle保护壳精密注塑成型仿真及工艺参数多目标优化”.....420
1.4 第六届广东省暨粤港澳大湾区工业工程创新大赛三等奖“基于IE的现代办公家具设计研究”.....422
1.5 第六届广东省暨粤港澳大湾区工业工程创新大赛三等奖“基于Anylogic的H医院急诊中心仿真与优化”.....424
1.6 第七届广东省暨粤港澳大湾区工业工程创新大赛二等奖“无人机蝶旋桨注塑参数优化”.....426
1.7 第七届广东省暨粤港澳大湾区工业工程创新大赛三等奖“基于供应商交付的物料齐套方法研究”.....427
2. 个人荣誉.....428
2.1 华南农业大学十佳创新创业导师证书.....429
2.2 广州市科普名师.....432
2.3 华南农业大学首届课程思政教学大赛三等奖.....433
2.4 华南农业大学 “教书育人、管理育人、服务育人” 校级先进个人.....434
2.5 华南农业大学 研究生教学成果奖一等奖（排第二）：真场景，实应用:面向农业数智化转型的信息管理类硕士培养模式创新与实践.....435
3. 社会服务.....437
3.1 2022年社会服务工作量：58.....437
3.2 2023年社会服务工作量：114.....438
3.3 2024年社会服务工作量：133.....439
3.4 2025年社会服务工作量：94.....440

一、教学研究业绩

1.教学研究项目：广东省高等教育教学改革项目《大数据背景下基于文本挖掘的新农科人才需求分析与人才培养模式改革研究》立项通知及有关佐证材料

广 东 省 教 育 厅

粤教高函〔2020〕20号

广东省教育厅关于公布2020年广东省高等教育教学改革项目立项名单的通知

各本科高校：

按照《广东省教育厅关于开展2020年度省高等教育教学改革项目推荐工作的通知》安排，省教育厅组织各本科高校开展了2020年度省高等教育教学改革项目（以下简称“教改项目”）推荐工作。经学校遴选推荐及省教育厅审核、公示，现将本年度省教改项目立项名单予以公布，并就有关事项通知如下：

一、立项情况

确定立项建设2020年度省高等教育教学改革项目共756项（详细名单见附件）。

二、项目经费

项目由各校统筹省“冲补强”提升计划资金及自有资金，根据立项项目研究内容、性质和特点，综合确定资助额度，保障项目顺利开展研究和实践。

省教改项目的立项建设是申报省高等教育教学成果奖的重

要基础，项目建设成效同时列入学校“冲补强”提升计划绩效考核因素，并直接影响下一年度学校教改项目立项限额。

三、项目管理

（一）日常管理

省高等教育教学改革项目要求立足学校教学改革实际，突出问题导向、实践导向和应用导向，项目最终要为推动学校教学改革服务。项目所在高校要加强对项目的日常管理、指导和检查，为项目研究并切实应用于教学实践提供必要条件。

（二）中期检查和结题验收

项目建设周期一般不超过3年，请学校管理部门按期做好项目中期检查和校内结题验收等工作。校内结题时，邀请校外评审专家人数不得少于专家总人数的三分之二。

满足以下条件的项目，经学校正式申请，可以参与省教育厅统一组织的项目验收：

1.项目已完成立项时设定的主要建设目标，且项目建设成果已在教学实践中有效应用；

2.已按照要求完成项目校内结题；

3.符合当年度省统一验收规定的其他条件。

（三）项目变更和调整

为保证项目建设的延续性和成果的一致性，原则上，项目研究过程中不得更换项目负责人；不得大幅变更研究内容或研究方向；不得拖延项目建设进程。

如遇特殊情况需要进行项目变更或延期的，须由项目负责人在项目结题前至少6个月向学校提出书面申请，学校审核同意后，以正式函件形式（并附相关材料）报省教育厅。

对擅自做出变更决定或临时延长建设期限的项目，将视情况予以撤销或终止项目研究，取消相应负责人3年内省教改项目的申报资格，并核减项目所在学校下一轮次教改项目推荐数额。

四、其他事项

（一）2020年度各校向省教育厅推荐并获得立项的项目，学校须将相关项目校内评审推荐及立项材料妥善保存，留底备查。

（二）项目立项后，学校应组织专家对项目进行开题论证，进一步优化项目建设目标和实施计划。

（三）省高等教育教学改革项目优秀成果将以适当方式在省级平台上向广大高校推介。

联系人：陈丽云、李成军， 联系电话：020-37627703、37629463。

附件：2020年广东省高等教育教学改革项目立项名单

广东省教育厅

2020年12月24日

公开方式：主动公开

校对人：陈丽云

93	华南农业大学	基于学生工程能力培养的 机械基础实验课程改革与实践	甄文斌
94	华南农业大学	大数据背景下基于文本挖掘的新农科人才需求分析与人才培养模式改革研究	张建桃
95	华南农业大学	大规模远程在线考核关键技术研究	陈湘骥
96	华南农业大学	“三全育人” 背景下《无机功能材料》课程思政的建设与实践	倪春林
97	华南农业大学	基于创新能力培养的《养兔学》教学模式 改革研究与实践	孙宝丽
98	华南农业大学	数学类课程线上线下混合教学的探究与实践	江雪萍
99	华南农业大学	以新工科人才培养为导向的发酵工程实践教学模式探索	徐学锋
100	华南农业大学	课程思政教育在《禽病学》教学中的应用与实践	贾伟新
101	华南农业大学	基于高阶性、创新性和挑战度“三位一体”的“金课”改革研究与实践——以《中国文学批评史》为例	孙素美
102	华南农业大学	中国民族音乐课程中的思政教学探索	朱虹
103	华南农业大学	高等农林院校工程类专业“普通化学”线上线下课程建设与应用	刘海峰
104	华南农业大学	基于移动平台的自然地理野外实习虚拟仿真系统建设与研究	钟晓兰
105	华南农业大学	新工科背景下工程类人才培养中课程思政育人模式研究	李高扬
106	华南农业大学	以传承中华优秀传统文化为特色的应用型音乐人才培养模式改革研究	郑颜文
107	华南农业大学	风景园林专业美术类课程群模块构建与教学创新	李静
108	华南农业大学	基于TPC模式的温氏班《养牛学实训》课程改革与实践	邓铭
109	华南农业大学	基于“新农科”建设的农林经济管理专业人才培养模式探索与实践	陈有华
110	华南农业大学	工程基础实践课在高校“冲一流”背景下的改革与实践	徐相华
111	华南农业大学	基于教育数据挖掘的高校学习评价方法研究	倪妙珊
112	南方医科大学	基于教学绩效评价的高校教学质量保障体系优化与实践	蔡谱
113	南方医科大学	基于形成性评价的整合课程考核体系的构建与实践	陈宏
114	南方医科大学	生本视角下高校教师教学发展体系构建的研究与实践	陈曦
115	南方医科大学	医科院校一流课程建设管理机制改革与实践	陈昕昀
116	南方医科大学	《精神心理照护学》混合式教学改革优化与实践	陈瑜
117	南方医科大学	校企协同创新育人模式下智慧医疗卓越工程师人才培养研究与实践	傅蓉
118	南方医科大学	医学影像诊断课程混合式教学改革设计及应用	何子龙
119	南方医科大学	基于3D打印解剖形态学模具与传统 实验教学结合的新型课堂模式研究	黄文华
120	南方医科大学	药学综合性实验教学改革的设计与实践	李琳
121	南方医科大学	《病理学》在线课程考核评价机制的探索与实践	林洁
122	南方医科大学	基于执业医师资格考试数据分析的通过率提升的改革与实践	林锦娜
123	南方医科大学	八年制卓越医师科研创新能力提升路径研究与实践	刘杰
124	南方医科大学	“新医科”下基于OBE的生物药剂学与药物动力学课程思政体系建设与实践	刘孟华

2.教学研究项目：广东省教育厅研究生教改项目《大数据视角下专业学位研究生实践能力需求与培养研究—以计算机技术领域为例》立项通知及有关佐证材料

广 东 省 教 育 厅

粤教研函〔2022〕1号

广东省教育厅关于公布2022年广东省研究生教育创新计划项目的通知

各研究生培养单位:

为加强创新人才培养体系建设,进一步改革人才培养机制和创新人才培养模式,形成有利于高层次、高质量、创造性人才培养的研究生培养体系,提升研究生创新能力,提高研究生培养质量,今年我厅继续实施广东省研究生教育创新计划项目。经学校推荐并组织专家评审,现认定“中山大学第七届‘海纳百川’模拟国际学术论坛”等76个项目立项为2022年广东省研究生学术论坛,“2023年中山大学天琴中心引力波暑期学校”等27个项目立项为2022年广东省研究生暑期学校,“面向高质量发展的地理学研究生培养体系改革研究”等155个项目立项为2022年广东省学位与研究生教育改革研究项目,“国际中文教育研究方法”等95项课程立项为2022年广东省研究生示范课程建设项目,“《财务报表分析》课程教学案例库建设”等82个项目立项为2022年广东省研究生案例库建设项目,中山大学与佛山市顺德

区旺海饲料实业有限公司联合共建的研究生联合培养基地等83个基地为2022年广东省联合培养研究生示范基地。具体名单附后。

请各有关高校根据相关规定要求，切实履行管理职责，进一步完善管理制度，规范项目管理，为项目实施提供支持保障，确保实施进度，达到预期目标。

附件：1. 2022年广东省研究生教育创新计划项目一览表（分发）

2. 2022年广东省联合培养研究生示范基地一览表（分发）

广东省教育厅

2022年6月18日

公开方式：依申请公开

校对人：阮念

附件1

2022年广东省研究生教育创新计划项目一览表（分发）

单位	序号	项目名称	立项类别	负责人姓名	项目批准号
华南农业大学	1	高校研究生“导学思政”模式建构路径研究	学位与研究生教育改革研究	孔晓娟	2022JGXM019
华南农业大学	2	农业专业学位研究生“专项制”培养模式改革研究	学位与研究生教育改革研究	邓诣群	2022JGXM020
华南农业大学	3	科技小院“五协同”创新型乡村振兴人才培养模式研究	学位与研究生教育改革研究	杨慧荣	2022JGXM021
华南农业大学	4	国际视野下研究生课程建设研究—以科学技术史学科为例	学位与研究生教育改革研究	陈志国	2022JGXM022
华南农业大学	5	基于校企协同育人的风景园林专业学位研究生实践能力培养模式创新研究	学位与研究生教育改革研究	刘小蓓	2022JGXM023
华南农业大学	6	大数据视角下专业学位研究生实践能力需求与培养研究—以计算机技术领域为例	学位与研究生教育改革研究	张建桃	2022JGXM024
华南农业大学	7	数智时代艺工农交叉融合的艺术硕士专业实践环节创新与探索	学位与研究生教育改革研究	邹岚	2022JGXM025
华南农业大学	8	基因工程原理与方法	研究生示范课程建设项目	周海	2022SFKC017
华南农业大学	9	舞台正音与表演	研究生示范课程建设项目	郑颜文	2022SFKC018
华南农业大学	10	园艺植物基因工程原理与技术	研究生示范课程建设项目	陈长明	2022SFKC019
华南农业大学	11	科学技术史	研究生示范课程建设项目	赵艳萍	2022SFKC020
华南农业大学	12	分子数量遗传学	研究生示范课程建设项目	刘桂富	2022SFKC021
华南农业大学	13	蚕桑资源利用课程教学案例库	专业学位研究生教学案例库建设项目	刘吉平	2022ANLK014
华南农业大学	14	网络食品犯罪案例库建设	专业学位研究生教学案例库建设项目	杜国明	2022ANLK015
华南农业大学	15	新工科典型工程教学仿真案例库建设	专业学位研究生教学案例库建设项目	丛沛桐	2022ANLK016
华南农业大学	16	专业学位研究生高级植物学课程教学案例库的建设与应用	专业学位研究生教学案例库建设项目	白玫	2022ANLK017
华南农业大学	17	涉农企业管理教学案例库	专业学位研究生教学案例库建设项目	郭萍	2022ANLK018
华南农业大学	18	农业产业振兴社会调查研究——《社会调查研究方法》课程教学案例库建设	专业学位研究生教学案例库建设项目	齐文娥	2022ANLK019
华南农业大学	19	《现代翻译技术》涉农翻译教学案例库建设	专业学位研究生教学案例库建设项目	吕靖	2022ANLK020

3.教学研究项目：中国高等教育学会高等教育科学研究项目《招聘大数据分析视角下论新农科人才学科交叉融合培养》立项通知及有关佐证材料

中国高等教育学会

高学会〔2024〕39号

中国高等教育学会关于公布“2024年度高等教育科学研究规划课题”立项名单的通知

相关会员高校、课题申请人：

中国高等教育学会于2024年5月启动了“2024年度高等教育科学研究规划课题”申报工作，经资格审查、匿名评审、公示后，现予以正式公布。

附件：中国高等教育学会“2024年度高等教育科学研究规划课题”立项名单

中国高等教育学会

2024年9月6日

中国高等教育学会“2024年度高等教育科学研究规划课题”立项名单

第二类

七十三、高等农林教育实践研究

序号	课题编号	课题名称	课题负责人	所在单位	立项类别
1	24NL0301	新农科背景下基于“三元要素”和指向“扎根精神”的地方高校农林人才培养模式改革与案例实践	孙翠萍	潍坊科技学院	重点课题
2	24NL0302	服务生态文明建设的风景园林专业硕博培养体系改革研究	郑曦	北京林业大学	重点课题
3	24NL0303	涉农高校农林人才培养与和美乡村建设耦合发展指标体系研究	袁媛	山东科技大学	重点课题
4	24NL0304	基于内涵建设的涉农传统专业改造提升途径研究	陈丹	河海大学	重点课题
5	24NL0401	农林类高校生成式人工智能赋能下的教学评价模型构建研究与探索	王瑞	浙江海洋大学	一般课题
6	24NL0402	新时代农林高校生命教育的实施与课程体系建设研究	李侃侃	西北农林科技大学	一般课题
7	24NL0403	招聘大数据分析视角下论新农科人才学科交叉融合培养	张建桃	华南农业大学	一般课题
8	24NL0404	乡村振兴视域下涉农高职院校工科专创融合课程创新改革研究与实践	高帅	江苏农林职业技术学院	一般课题
9	24NL0405	面向四新的地方涉农高校动物类专业实践课程体系构建与实践	刘静波	西南科技大学	一般课题
10	24NL0406	知行合一，学农为农——《农业经济学》全课堂耕读育人模式创新与实践	李修平	青岛滨海学院	一般课题
11	24NL0407	“思政引领、问题导向、科研驱动”协同构建本科专业课程教育教学新路径	周志强	东北林业大学	一般课题
12	24NL0408	涉农高校基层教学组织制度建设创新研究	王广深	华南农业大学	一般课题
13	24NL0409	新工科与新农科融合的农业智能装备专业课程体系与教材建设研究	张祥彩	山东理工大学	一般课题
14	24NL0410	新农科背景下涉农高校工科类专业双创人才培养多元保障机制研究	肖茂华	南京农业大学	一般课题
15	24NL0411	“理实融通、厚基强能”：新农科背景下以数据素养提升为导向的《生物统计学》课程教学改革研究	高丽	烟台大学	一般课题
16	24NL0412	新农科背景下食品微生物检验技术课程教学创新改革与实践研究	丁新丽	山东商业职业技术学院	一般课题
17	24NL0413	数字化背景下“蔬菜栽培学”慕课的教学重构	缪旻珉	扬州大学	一般课题
18	24NL0414	一懂两爱、一专多能——“定向农科生”人才培养课程体系构建的研究与实践	郭建忠	浙江农林大学	一般课题
19	24NL0415	北大荒精神引领下农林类院校创新创业应用型本科人才培育模式创新与实践	殷大伟	黑龙江八一农垦大学	一般课题
20	24NL0416	基于OBE理念的涉农高校专业教育、耕读教育与课程思政一体化协同研究	季洪亮	潍坊学院	一般课题

4. 教学研究项目：全国农业教指委研究课题《新农科背景下基于大数据分析的农业专业学位研究生培养要素优化研究》立项通知及有关佐证材料

全国农业专业学位研究生教育指导委员会
2025 年研究生教育研究课题 · 立项通知书

张建桃：

经专家组评审推荐，全国农业专业学位研究生教育指导委员会（以下简称“全国农业教指委”）审批，您申报的课题 新农科背景下基于大数据分析的农业专业 ，已获准立项列入全国农业教指委 2025 年研究生教育研究 面上项目 ，课题编号为： 2025-NYYB-36 ，承担单位及实施保障部门： 华南农业大学。

现将有关事项通知如下：

1. 请接此通知后，尽快确定实施方案并按照《全国农业专业学位研究生教育指导委员会研究课题管理办法》组织实施。

2. 课题研究时间设定为 2 年，即 2025 年 6 月至 2027 年 6 月，全国农业教指委秘书处将于 2026 年 6 月开展中期检查。

3. 提请各项目承担单位及实施保障部门为课题研究提供必要的人力、时间和经费支持，重点课题为 4 万元，一般课题为 2 万元。

全国农业专业学位研究生教育指导委员会

2025 年 6 月 10 日

全国农业专业学位研究生教育指导委员会

农业教指委〔2025〕2号

关于全国农业教指委2025年研究课题立项的通知

各培养单位：

为促进农业专业学位研究生教育的科学研究和改革发展，全国农业专业学位研究生教育指导委员会（以下简称“教指委”）启动了2025年研究课题申报评审工作。根据评审办法，各培养单位限额推荐共183项课题，通过教指委秘书处形式审查有效材料177项。经初审推荐、会议审议及教指委委员表决等程序，共93项课题获准立项，其中重点课题10项，一般课题83项（详见附件）。现将有关事项通知如下：

1. 请各课题负责人接此通知后，按照《全国农业专业学位研究生教育指导委员会研究课题管理办法》（附件2）组织实施。

2. 课题研究时间为2年，农业教指委秘书处将于2026年6月开展项目中期检查。

3. 请各项目依托单位为课题研究提供必要的人力、物力和经费支持，建议重点课题每项支持4万元，一般课题每项支持2万元。

联系人：王老师，010-62732630，mae@cau.edu.cn

附件：1.全国农业教指委2025年研究课题立项名单

2.全国农业专业学位研究生教育指导委员会研究课题管理办法

全国农业专业学位研究生教育指导委员会

2025年5月29日

序号	课题类型	课题名称	负责人	申请单位	评审结果	课题编号
24	思政导学类	农业专业学位研究生“党建+思政+实践”三融三促育人机制研究	荆立群	山西农业大学	一般项目	2025-NYYB-24
25	思政导学类	基于导学关系建设的新时代农业专业学位研究生教育管理模式研究	段文昌	内蒙古农业大学	一般项目	2025-NYYB-25
26	思政导学类	基于党教协同育人的多维思政案例教学法在专业学位研究生培养中的探索与实践	周浩宇	河南科技学院	一般项目	2025-NYYB-26
27	思政导学类	塔里木大学农业硕士研究生党建思政与实践育人路径的融合创新研究	汪　慧	塔里木大学	一般项目	2025-NYYB-27
28	课程教学研究类	人工智能在智慧农业研究生教育中的应用	马福韬	中国农业大学	一般项目	2025-NYYB-28
29	课程教学研究类	服务攀西地区特色农业发展的农业硕士课程建设研究	李　静	西昌学院	一般项目	2025-NYYB-29
30	课程教学研究类	农业专业学位研究生案例教学的智能技术融合路径研究：动态生成、精准适配与评价反馈	沈　璐	大连海洋大学	一般项目	2025-NYYB-30
31	课程教学研究类	基于“一体六翼”的农业专业学位研究生第二课堂体系建设研究	李砚忠	河北农业大学	一般项目	2025-NYYB-31
32	课程教学研究类	《农村社会学》研究生课程思政资源库建设	张　雯	沈阳农业大学	一般项目	2025-NYYB-32
33	课程教学研究类	农业工程专业学位研究生课程体系与教学资源建设研究	王　洋	吉林农业大学	一般项目	2025-NYYB-33
34	课程教学研究类	“推理型 AI”赋能农业专业学位研究生生态伦理决策能力提升研究	邓德强	南京林业大学	一般项目	2025-NYYB-34
35	课程教学研究类	基于“互联网十”背景下边远地区高校畜牧专业学位研究生校企课程教学模式的构建研究	耿春银	延边大学	一般项目	2025-NYYB-35
36	课程教学研究类	新农科背景下基于大数据分析的农业专业	张建桃	华南农业大学	一般项目	2025-NYYB-36

5. 教学研究项目：高等农林院校课程思政联盟 2025 年教学改革研究项目《农林特色课程思政案例智能生成与应用研究》立项通知及有关佐证材料

高等农林院校课程思政联盟

关于公布高等农林院校2025年课程思政教学改革研究项目的通知

各相关单位：

为深入推进课程思政研究，加强全国农林高校间交流，根据《高等农林院校课程思政联盟关于2025年教学改革研究项目申报工作的通知》要求，经学校遴选推荐、专家评审，决定立项72项教学改革研究项目，具体名单见附件。

希望各高校加强组织领导，广大教师认真开展教学研究与实践，及时固化课程思政教学案例及成果，形成具有农林高校特色的可推广、可复制的课程思政教育教学新模式，切实提高课程思政教学能力和育人质效。

全国高等农林院校课程思政联盟

（华中农业大学代章）

2025年11月14日

	的构建与实践		
nllm202566	新文科背景下农林院校国际经济学课程思政的探索与实践	长江大学	王伶
nllm202567	乡土情怀与绿色匠心—城乡规划全程漫润式思政教学团队	四川农业大学	曹迎
nllm202568	立德树人强农兴农引领下的农林院校课程思政数字资源库建设与应用研究	沈阳农业大学	江红霞
nllm202569	基于 OBE 与案例教学双驱动的《植被生态学》课程思政教学模式构建与实践	山西农业大学	宋厚娟
nllm202570	《羊生产学》课程思政元素的系统性挖掘与分类体系构建研究	中国农业大学	张微
nllm202571	高等农林院校课程思政建设成效的多维度评价指标体系研究	天津农学院	张洪霞
nllm202572	农林特色课程思政案例智能生成与应用研究	华南农业大学	张建桃

6. 教学研究项目：广东省高等学校教学管理学会 2021 年度课程思政建设项目《课程思政建设项目：应用统计学》立项通知及有关佐证材料

广东省高等学校教学管理学会

广东省高等学校教学管理学会关于公布2021年度课程思政建设项目立项名单的通知

各会员单位:

根据《广东省高等学校教学管理学会关于开展2021年度课程思政建设项目申报的通知》，学会组织开展了2021年度课程思政建设项目的推荐与遴选工作。经专家评审，学会常务理事会审议，共遴选出《生命科学研讨课》等296个项目立项为2021年度课程思政建设项目。现将名单（见附件）予以公布，并就有关事项通知如下:

一、立项建设项目由项目的牵头高校和共建高校共同开展建设与研究。

二、牵头高校要做好项目的监督与管理工作，保障项目的建设进度与成效。

三、项目负责人要积极整合团队力量，按照要求开展项目建设，确保项目目标任务如期完成。

四、项目建设期为2年，结题时需提供以下材料:

1.一门或多门课程融入课程思政完整的教案（包含每章节的课程思政目标、课程思政元素、课程思政融入策略、课程思政考核要素）;

2.一门或多门课程的思政案例集(每门课程至少10个)。

五、学会将按学科门类选出有示范、推广借鉴价值的优秀案例编制成册，并资助出版。

附件：

1. 广东省高等学校教学管理学会2021年度课程思政建设项目立项名单（本科）

2. 广东省高等学校教学管理学会2021年度课程思政建设项目立项名单（高职）

广东省高等学校教学管理学会

2022年1月25日

附件 1

广东省高等学校教学管理学会 2021 年度课程思政建设项目

立项名单（本科）

序号	项目编号	牵头单位	支持类别	课程名称	课程负责人	建设经费/元
1	X-KCSZ2021001	中山大学	重点	生命科学研讨课	张雁	10000
2	X-KCSZ2021002	华南理工大学	重点	电工与电子技术	邓红雷	10000
3	X-KCSZ2021003	暨南大学	重点	生理学	王跃春	10000
4	X-KCSZ2021004	华南农业大学	重点	消费者行为学	贾莉	10000
5	X-KCSZ2021005	华南农业大学	重点	概率论	肖莉	10000
6	X-KCSZ2021006	华南农业大学	重点	饲料生物技术	孙加节	10000
7	X-KCSZ2021007	南方医科大学	重点	护士人文修养	翟惠敏	10000
8	X-KCSZ2021008	南方医科大学	重点	医学寄生虫学	彭鸿娟	10000
9	X-KCSZ2021009	华南师范大学	重点	微观经济学	瞿华	10000
10	X-KCSZ2021010	华南师范大学	重点	学习理论与学习心理研究	莫雷	10000
11	X-KCSZ2021011	广东外语外贸大学	重点	中级财务会计	王艳	10000
12	X-KCSZ2021012	广东外语外贸大学	重点	国际经济与贸易专业课程群	张建武	10000
13	X-KCSZ2021013	广州大学	重点	电路/电路实验	邹涛	10000
14	X-KCSZ2021014	广州大学	重点	环境监测实验	宋刚	10000
15	X-KCSZ2021015	广州大学	重点	结构力学	汪大洋	10000
16	X-KCSZ2021016	广州大学	重点	环境学概论	吴卓	10000
17	X-KCSZ2021017	广州大学	重点	民族乐舞欣赏与美学分析	何艳珊	10000
18	X-KCSZ2021018	广东石油化工学院	重点	审计学	张芹秀	10000
19	X-KCSZ2021019	广东石油化工学院	重点	高级财务会计	姚翠红	10000
20	X-KCSZ2021020	惠州学院	重点	新媒体概论	周海英	10000
21	X-KCSZ2021021	嘉应学院	重点	高级英语	张宏武	10000
22	X-KCSZ2021022	广东科技学院	重点	网络营销	王金良	10000
23	X-KCSZ2021023	广东东软学院	重点	综合商务英语 I-II	陈若静	10000
24	X-KCSZ2021024	北京理工大学珠海学院	重点	工业机器人	曹少泳	10000
25	X-KCSZ2021025	华南理工大学	一般	调查统计与分析	付佳	2000
26	X-KCSZ2021026	华南农业大学	一般	数字图像处理	薛月菊	2000

27	X-KCSZ2021027	华南农业大学	一般	应用统计学	张建桃	2000
28	X-KCSZ2021028	南方医科大学	一般	传染病学	樊蓉	2000
29	X-KCSZ2021029	广州中医药大学	一般	公共事业管理（健康养老）专业核心课程群的课程思政建设探索	许星莹	2000
30	X-KCSZ2021030	华南师范大学	一般	中国古代文学	张巍	2000
31	X-KCSZ2021031	华南师范大学	一般	社会调查研究方法	刘劲宇	2000
32	X-KCSZ2021032	华南师范大学	一般	大学生职业生涯规划与管理	余晓玲	2000
33	X-KCSZ2021033	华南师范大学	一般	物理化学实验	马国正	2000
34	X-KCSZ2021034	广东工业大学	一般	机械设计基础	唐文艳	2000
35	X-KCSZ2021035	广东工业大学	一般	半导体材料	李娜	2000
36	X-KCSZ2021036	广东工业大学	一般	化工原理	郑育英	2000
37	X-KCSZ2021037	广东工业大学	一般	建筑钢结构设计	何嘉年	2000
38	X-KCSZ2021038	广东外语外贸大学	一般	基础日语	张志刚	2000
39	X-KCSZ2021039	汕头大学	一般	动物学	马洪雨	2000
40	X-KCSZ2021040	广东财经大学	一般	明清小说导读	张琼	2000
41	X-KCSZ2021041	广东财经大学	一般	政府预算管理	邝艳华	2000
42	X-KCSZ2021042	广东财经大学	一般	证券投资学	邓学斌	2000
43	X-KCSZ2021043	广东医科大学	一般	环境卫生学	刘小山	2000
44	X-KCSZ2021044	广东海洋大学	一般	海水贝类增养殖学	栗志民	2000
45	X-KCSZ2021045	仲恺农业工程学院	一般	广告创意	黄丽燕	2000
46	X-KCSZ2021046	广东技术师范大学	一般	智能控制技术	杨舰	2000
47	X-KCSZ2021047	韩山师范学院	一般	中国现当代文学作品选读	曹亚明	2000
48	X-KCSZ2021048	韩山师范学院	一般	品牌设计与传播	蔡梦虹	2000
49	X-KCSZ2021049	广东第二师范学院	一般	钢琴	赵昕	2000
50	X-KCSZ2021050	广州大学	一般	建筑设备自动化	廖云丹	2000
51	X-KCSZ2021051	广州大学	一般	空间分析	李颉	2000
52	X-KCSZ2021052	广州大学	一般	旅游投资与财务管理	李惠娟	2000
53	X-KCSZ2021053	广州医科大学	一般	组织学与胚胎学	杜宝玲	2000
54	X-KCSZ2021054	广州医科大学	一般	护理心理学	高云	2000
55	X-KCSZ2021055	深圳大学	一般	环境影响评价	肖轲	2000
56	X-KCSZ2021056	韶关学院	一般	基础化学课程群	郭会时	2000
57	X-KCSZ2021057	广东科技学院	一般	商务谈判	卢玲	2000
58	X-KCSZ2021058	广州工商学院	一般	金融学	曾素梅	2000

7.教学研究项目：中国农学会教育教学类第八批课题《基于文本挖掘的新农科人才跨学科能力需求分析与培养探索》立项通知及有关佐证材料

中国农学会

中国农学会教育教学类第八批科研课题立项通知书

_____ 同志：

经专家评审和中国农学会审批，您申报的_____已获准立项为_____课题，批准号为：_____。

中国农学会教育教学类第八批科研课题申请一经批准，其《申报书》即成为有约束力的协议，课题主持人须严格按照《申报书》中填写的相关内容，认真开展研究工作，取得预期研究成果。为规范课题管理，课题主持人及其所在单位须了解以下规定：

一、资助课题经费一万元一次性划拨至课题主持人所在单位，建议相关单位给予本单位资助课题主持人不低于二万元的配套经费支持，给予本单位立项课题主持人不低于一万元的经费支持。

二、课题完成时间为2024年12月31日前，成果形式为研究论文，论文必须公开发表在中国农学会教育专业委员会指定的期刊上（目录见附件），并标注本项目资助（名称和编号）。

三、若变更课题主持人、课题完成时间等，须由课题立项时主持人所在单位提出书面申请，报中国农学会教育专业委员会批准。

四、目前部分课题经费暂未到位，课题主持人可先行开展研究工作，待经费到位后即刻拨付。

附件：1.中国农学会教育教学类第八批教育教学类课题立项名单

2.中国农学会教育专业委员指定期刊目录

中国农学会

2022 年 12 月 20 日

附件 1

中国农学会教育教学类第八批教育教学类课题立项名单

一、立项资助课题（11 项）

课题编号	单位	姓名	课题名称
PCE2201	华南农业大学	彭思喜	乡村振兴战略下农林院校教育发展人才培养战略研究
PCE2202	东北林业大学	笔玉友	面向“三新”的农林高校新农科建设绩效提升路径研究
PCE2203	中国农业大学	吴嘉琦	高等教育经费配置对农林人才培养质量的影响研究
PCE2204	西北农林科技大学	豆书龙	嵌合性视角下涉农高校服务乡村振兴的长效机制研究
PCE2205	东北农业大学	孙楠	农林类院校创新创业教育生态系统构建
PCE2206	中央农广校	姚亚萍	农民田间学校线上线下教育培训融合路径研究
PCE2207	吉林农业科技学院	王帅	新农科背景下应用型人才产教融合培养模式研究
PCE2208	河北农业大学	祝丽云	新农科视角下农业院校教学质量评价及提升路径研究
PCE2208	山西农业大学	张丽	有效性视角下农科高校教师职称制度改革路径优化研究
PCE2210	华中农业大学	金安江	基于生命健康链的跨学科人才培养的探索与实践
PCE2211	南京农业大学	李二斌	学术期刊服务学会高质量发展的路径探索与思考

二、立项课题（23 项）

课题编号	单位	姓名	课题名称
PCE2212	四川农业大学	吴德	产教融合背景下地方农业大学新农科人才培养模式研究
PCE2213	西北农林科技大学	王倩	农林院校创新创业教育生态系统建构及评价研究
PCE2214	华南农业大学	张建桃	基于文本挖掘的新农科人才跨学科能力需求分析与培养探索
PCE2215	华南农业大学	李楠	基于科教融合的研究型实验教学模式探索与实践

PCE2216	西北农林科技大学	宋瑜龙	种业产教融合人才培养模式的探索与实践
PCE2217	东北林业大学	高玉娟	乡村振兴战略背景下创新创业型农业硕士培养模式优化研究
PCE2218	东北农业大学	崔嵩	产学研协同优化新农科研究生培养模式与评价体系构建
PCE2219	中国农业大学	史博	农林高校“双方位+四平台”全链条导学关系新模式构建研究
PCE2220	东北林业大学	曲发义	农林类高校学科建设动态监测及自评估机制的探索与实践
PCE2221	南京农业大学	章棋	农林高校人工智能专业人才培养模式创新的实现路径研究
PCE2222	华中农业大学	刘广乐	农业高校创业教育历史、现状与对策研究
PCE2223	山东畜牧兽医职业学院	李鑫	乡村振兴背景下农林类高职学生劳动教育实施路径研究
PCE2224	扬州大学	张荣天	面向乡村振兴的农林院校农业硕士人才培养路径建构
PCE2225	福建农林大学	坚瑞	农林院校高质量“五育并举”教师培训体系研究
PCE2226	江苏农牧科技职业学院	陈熔	“一带一路”背景下农业职业院校国际学生跨文化能力培养与研究
PCE2227	湖南生物机电职院	曹敏志	教育 4.0 背景下校企协同多元管理顶岗实习评价机制研究
PCE2228	苏州农业职业技术学院	秦昌友	产学深度融合下农业类高职院校应用型人才培养模式探究
PCE2229	河北农业大学	勾俊芳	农业院校工科 PBL 下《工程结构》TJA 增值性评价探索
PCE2230	南京农业大学	葛焱	依托产教融合创新平台的专业硕士联合培养模式研究
PCE2231	仲恺农业工程学院	王正梅	教育评价改革背景下农林本科院校思政理论课教学质量评价体系研究
PCE2232	安徽农业大学	宋有洪	麦玉周年栽培技术智慧化升级培养双创人才
PCE2233	浙江农林大学	钱晓虎	地方农林高校助力乡村振兴实施路径与策略研究
PCE2234	华南农业大学	刘洋	双链融合的农业知识产权创新人才培养模式构建

附件 2

中国农学会教育专业委员会指定期刊目录

第一类刊物

教育研究	高等教育研究	中国高教研究	中国高等教育	北京大学教育评论
比较教育研究	清华大学教育研究	教育发展研究	教育与经济	

第二类刊物

教师教育研究	高等工程教育研究	教育科学	教育学报	学位与研究生教育
中国电化教育	电化教育研究	教育研究与实验	开放教育研究	复旦教育论坛
中国大学教学	江苏高教	高教探索	国家教育行政学院学报	现代大学教育
华东师大学报（教育科学版）	北京大学学报(哲学社会科学版)	北京师范大学学报（社会科学版）	河北大学学报(哲学社会科学版)	河南大学学报(社会科学版)
湖南科技大学学报(社会科学版)	复旦学报（社会科学版）	南京大学学报（哲学·人文科学·社会科学）	南开学报（哲学社会科学版）	吉林大学社会科学学报
中山大学学报（社会科学版）	厦门大学学报（哲学社会科学版）	清华大学学报（哲学社会科学版）	华中师范大学学报（人文社会科学版）	西安交通大学学报（社会科学版）
南京农业大学学报(社会科学版)	浙江大学学报（人文社会科学版）	南京师范大学报（社会科学版）	西北师大学报（社会科学版）	四川大学学报（哲学社会科学版）
东北师大学报（哲学社会科学版）	华东师范大学学报（哲学社会科学版）	陕西师范大学学报（哲学社会科学版）	西南大学学报（社会科学版）	上海交通大学学报（哲学社会科学版）
上海大学学报(社科版)	上海师范大学学报(哲社版)	天津师范大学学报（社会科学版）	武汉大学学报（哲学社会科学版）	湘潭大学学报(哲学社会科学版)
云南师范大学学报(哲社版)	中国地质大学学报(社会科学版)	中国农业大学学报(社科版)	中山大学学报(社会科学版)	重庆大学学报(社会科学版)
湖南师范大学社会科学学报	山东大学学报（哲学社会科学版）			

第三类刊物

中国农业教育	中国教育学刊	课程·教材·教法	现代教育技术	外国教育研究
全球教育展望	远程教育杂志	思想理论教育导刊	研究生教育研究	中国特殊教育
现代远距离教育	现代远程教育研究	大学教育科学	安徽大学学报(哲学社会科学版)	安徽师范大学学报(人文社科版)
北京工商大学学报(社会科学版)	北京理工大学学报(社科版)	大连理工大学学报(社会科学版)	福建师范大学学报(哲社版)	海南大学学报(人文社会科学版)
河南师范大学学报(哲社版)	湖北大学学报(哲社版)	华东理工大学学报(社科版)	华南师范大学学报(社科版)	暨南学报(哲学社会科学版)
山西大学学报(哲学社会科学版)	深圳大学学报(人文社会科学版)	首都师范大学学报(社科版)	四川师范大学学报(社会科学版)	西藏大学学报(社会科学版)
新疆大学学报(哲学人文社科版)	新疆师范大学学报(哲社版)	烟台大学学报(哲社版)	郑州大学学报(哲社版)	中国海洋大学学报(社科版)
湖南大学学报（社会科学版）	西北大学学报（哲学社会科学版）	兰州大学学报（社会科学版）	天津大学学报（社会科学版）	华中科技大学学报（社会科学版）
东南大学学报（哲学社会科学版）	同济大学学报（社会科学版）	东北大学学报（社会科学版）	教育探索	教育导刊
教学与研究	教育评论	教育科学研究	高教发展与评估	思想教育研究
教育理论与实践	高校理论战线	学校党建与思想教育	思想理论教育	现代教育管理
人民教育	中国成人教育	当代教育科学	教育学术月刊	高校教育管理
黑龙江高教研究	上海教育科研	上海教育评估研究	外语电化教学	高等农业教育
实验室研究与探索	实验技术与管理	高校实验室工作研究		

8. 教学研究项目：关于《CDIO 理念的工业工程专业人才培养模式探索与研究——基于美国佛罗里达大学实地调研》项目的有关佐证材料



9.教学质量工程项目：关于《线下示范课程：设施规划》项目的立项通知及有关佐证材料

华南农业大学文件

华南农教〔2019〕58号

关于公布华南农业大学2019年度校级质量工程立项项目的通知

各学院、部处、各单位:

根据《教育部关于加快建设高水平本科教育全面提高人才培养能力的意见》(教高〔2018〕2号)和《广东省普通本科高校“十三五”教学质量与教学改革工程建设实施方案》(粤教高函〔2016〕128号)精神，以及《关于申报华南农业大学2019年度校级“质量工程”建设项目的通知》要求，学校组织开展了本年度质量工程项目遴选工作。经项目负责人申请、单位推荐、学校组织专家评审、校内公示无异议等程序，确定“海洋学院实验教学示范中心”等124个项目为2019年度校级质量工程项目，现予以公布(详见附件)。

请各项目负责人按照项目任务书及时开展各项工作，推进学

校人才培养改革。各单位要切实加强对项目建设的督促、指导，以确保项目如期完成。

特此通知。

附件：华南农业大学2019年校级质量工程立项名单

华南农业大学

2019年9月16日

公开方式：主动公开

华南农业大学校长办公室　　2019年9月19日印发

zlgc19047	线下示范课程	水生生物学	杨慧荣	海洋学院
zlgc19048	线下示范课程	C++程序设计	徐 兴	电子工程学院
zlgc19049	线下示范课程	模拟电子技术	殷惠莉	电子工程学院
zlgc19050	线下示范课程	旅游生态学	叶延琼	资源环境学院
zlgc19051	线下示范课程	植物生理学 B	刘太波	生命科学学院
zlgc19052	线下示范课程	硬笔书法鉴赏	张机	林学与风景园林学院
zlgc19053	线下示范课程	设施规划	张建桃	数学与信息学院
zlgc19054	线下示范课程	大学英语 IV（阅读模块）	林桂珊	外国语学院
zlgc19055	线下示范课程	旅游心理学	刘小蓓	林学与风景园林学院
zlgc19056	线下示范课程	饲料学	朱勇文	动物科学学院
zlgc19057	在线开放课程	动物生物化学	张永亮	动物科学学院
zlgc19058	在线开放课程	食品营养学	王弘	食品学院
zlgc19059	在线开放课程	精准农业航空技术及应用	兰玉彬	工程学院
zlgc19060	在线开放课程	林木育种学	陈晓阳	林学与风景园林学院
zlgc19061	在线开放课程	遗传学	刘向东	农学院
zlgc19062	在线开放课程	禽病学	廖明	兽医学院
zlgc19063	在线开放课程	普通昆虫学	王敏	农学院
zlgc19064	在线开放课程	植物化学保护	徐汉虹	农学院
zlgc19065	在线开放课程	兽医药理学	曾振灵	兽医学院
zlgc19066	在线开放课程	汽车构造	王海林	工程学院
zlgc19067	精品实践课程	包装印刷工艺实验	范小平	食品学院
zlgc19068	精品实践课程	水生生物学实验	杨慧荣	海洋学院
zlgc19069	精品实践课程	历史建筑调查与测绘	吴运江	水利与土木工程学院
zlgc19070	精品实践课程	风景园林植物应用（树木、花卉）实训	翁殊斐	林学与风景园林学院
zlgc19071	精品实践课程	通识管理能力训练	库夭梅	公共基础课实验教学中心
zlgc19072	精品实践课程	生态种田综合训练	黎华寿	资源环境学院
zlgc19073	精品实践课程	制药工程综合设计研究性实验	周武艺	材料与能源学院
zlgc19074	精品实践课程	电子设计自动化实验	刘勇	电子工程学院

10. 教学质量工程项目：关于《华南农业大学金蝶精一实践教学基地》项目的有关佐证材料



11. 教学质量工程项目：关于《课程思政示范课程：应用统计学》项目的有关佐证材料

华南农业大学文件

华南农教〔2024〕7号

关于公布华南农业大学2023年度课程思政示范项目建设名单的通知

各学院、部处、各单位：

根据《华南农业大学课程思政实施方案》（华农党发〔2022〕26号）精神和《关于开展2023年度校级课程思政示范建设项目申报工作的通知》要求，学校组织开展了2023年度课程思政示范项目评选工作。

经项目负责人申请、所在单位遴选推荐、学校组织专家评审、校内公示等程序，决定立项建设华南农业大学2023年度课程思政示范项目125项，其中包括工程学院等课程思政试点学院3个、农学专业课程思政教学示范团队等课程思政示范团队7个、《电机学》等课程思政示范课程24门、《“数值分析”第四章第一节拉格朗日插值法》等课程思政示范课堂31个、《现实主义电影：

从意大利“新现实主义”到当下华语电影中的“温暖现实主义”》等课程思政典型案例60个（名单详见附件），现予以公布。

本次立项的示范项目建设期至2025年12月，建设期内示范项目原则上不允许更换负责人或变更项目团队成员。各项目团队要严格按照项目建设任务及要求及时开展工作，加快推进课程思政改革，确保高质量完成建设目标。

请各学院充分认识课程思政改革的重要意义，认真贯彻《华南农业大学课程思政实施方案》，加强对教师的相关培训、指导、引领和支持，带动教师全员积极参与课程思政教学改革，持续深入抓典型、树标杆、推经验，全面提升本科人才培养质量。

附件：华南农业大学2023年度课程思政示范项目建设名单

华南农业大学

2024年1月21日

公开方式：主动公开

华南农业大学党政办公室　　2024年1月23日印发

附件

华南农业大学2023年度课程思政示范项目建设名单

序号	类别	项目名称	单位	项目负责人	团队成员（不含负责人）
kcsz2023001	试点学院	课程思政试点学院	工程学院	李　君	
kcsz2023002	试点学院	课程思政试点学院	植物保护学院	闫笑久	
kcsz2023003	试点学院	课程思政试点学院	食品学院	魏剑波	
kcsz2023004	示范团队	农学专业课程思政教学示范团队	农学院	刘自强	马启彬、王少奎、周玉亮、王小龙、王兰、冯发强、吴锦文、汪文毅
kcsz2023005	示范团队	集成电路课程群课程思政示范团队	电子工程学院（人工智能学院）	刘洪山	谢家兴、梁亨茂、代秋芳、罗霞、王建、张宇、赵懿琨
kcsz2023006	示范团队	以农史教育为特色的中国史课程思政教学团队	人文与法学学院	刘玲娣	杨品优、赵艳萍、衷海燕、王福昌、翟麦玲、周晴、余格格、陈志国
kcsz2023007	示范团队	《大学数学》课程思政示范团队	数学与信息学院、软件学院	杨德贵	肖莉、何婧、付银莲、李凤、周燕、杨志程、丁仕虹、夏英俊、李朗

kcsz2023008	示范团队	茶学专业核心课程思政教学团队	园艺学院	张凌云	黄亚辉、陈文品、张灵枝、孙彬妹、郑鹏、马红彦、李丹、晏嫦妤、谭新东
kcsz2023009	示范团队	机械设计制造及自动化专业课程思政教学团队	工程学院	王红军	王慰祖、刘天湖、段洁利、夏红梅、金莫辉、甄文斌
kcsz2023010	示范团队	《理论力学》课程思政教学示范团队	水利与土木工程学院	胡圣荣	卢玉华、许静静、刘新红、张秀丽
kcsz2023011	示范课程	电机学	工程学院	孙振刚	闫国琦、陆永超、孔莲芳、梅慧兰、莫嘉嗣、周锡恩
kcsz2023012	示范课程	电子工艺实习（电类）	电子工程学院（人工智能学院）	薛秀云	殷惠莉、李震、宋淑然、孙道宗、吕石磊
kcsz2023013	示范课程	遗传学实验	基础实验与实践训练中心	郭海滨	刘向东、库夭梅、刘自强、李亚娟、李楠、吴锦文
kcsz2023014	示范课程	应用统计学	数学与信息学院、软件学院	张建桃	宋世领、黄丽清、刘伟章、朱梅阶
kcsz2023015	示范课程	耕作学	农学院	王小龙	祁剑英、潘圣刚、陈健文、王媛媛
kcsz2023016	示范课程	民族服饰传承与传播	艺术学院	陈金怡	金惠、赵英姿 杨翠钰、马宏林

12. 教学质量工程项目：关于《在线开放课程：应用统计学》项目的立项通知及有关佐证材料

华南农业大学文件

华南农教〔2024〕4 号

关于公布 2023 年度校级在线开放课程建设立项项目的通知

各学院、部处、各单位:

根据《华南农业大学在线开放课程建设与管理办法》(华南农办〔2022〕35 号)和《关于开展 2023 年度校级在线开放课程建设工作的通知》,学校组织开展了 2023 年度在线开放课程建设项目评选工作。

经课程负责人申报、所在单位推荐、学校组织专家评审和校内公示等环节,确定《跨文化交际》等 20 门课程为华南农业大学 2023 年度在线开放课程立项项目,现予以公布。

请各课程团队严格按照相关文件和通知要求,及时开展课程建设工作,确保如期高质量完成建设目标。

附件:华南农业大学 2023 年度在线开放课程建设立项项目

名单

华南农业大学

2024 年 1 月 17 日

（联系人：冯安伟，电　话：85288020 ）

公开方式：主动公开

华南农业大学党政办公室　　2024 年 1 月 18 日印发

附件

华南农业大学2023年度在线开放课程建设立项项目名单

编　号	课程名称	负责人	所属单位
zxkc202301	跨文化交际	刘傲冬	外国语学院
zxkc202302	情商训练	吴　琪	人文与法学学院
zxkc202303	动物组织学与胚胎学	梁晓欢	兽医学院
zxkc202304	应用统计学	张建桃	数学与信息学院、软件学院
zxkc202305	理论力学	胡圣荣	水利与土木工程学院
zxkc202306	瑜伽——身心疗愈，共创美好	何灵捷	体育教学研究部
zxkc202307	会计学原理	陈晓敏	经济管理学院
zxkc202308	森林培育学	邱　权	林学与风景园林学院
zxkc202309	民族服饰传承与传播	陈金怡	艺术学院
zxkc202310	动物营养学	张世海	动物科学学院
zxkc202311	社会调查理论与方法	廖　杨	公共管理学院
zxkc202312	树木学	秦新生	林学与风景园林学院
zxkc202313	《红楼梦》里的哲学	李　飞	人文与法学学院
zxkc202314	工程热力学与传热学	张　烨	工程学院
zxkc202315	园艺产品营养与功能	王惠聪	园艺学院
zxkc202316	媒介概论	赵　娜	艺术学院
zxkc202317	复变函数	刘　丹	数学与信息学院、软件学院
zxkc202318	统计学原理	谭　莹	经济管理学院
zxkc202319	种子加工与贮藏学	张亚锋	农学院
zxkc202320	新能源材料	胡　航	材料与能源学院

13.教学研究项目：关于《基于文本挖掘课程思政元素挖掘研究—以应用统计学为例》项目的有关佐证材料

华南农业大学文件

华南农教〔2023〕68号

关于公布华南农业大学2023年度校级教改项目和质量工程项目立项的通知

各学院、部处、各单位：

根据《广东省教育厅关于开展2023年度广东省本科高校教学质量与教学改革工程项目申报推荐工作的通知》和学校《关于开展2023年度本科教学质量与教学改革工程项目申报工作的通知》要求，为进一步推进学校教学改革，建设一流本科教育，提升人才培养质量，学校组织开展了2023年度校级本科教学质量与教学改革工程项目遴选工作。

经项目负责人申请、所在单位遴选推荐、学校组织专家评审和公示无异议等程序，确定“高阶思维视域下《种子生物学》‘四维融合’混合式教学模式改革与实践”等122个项目立项为2023年度校级教学改革项目，具体名单见附件1；确定“绿色与智能

精准纳米农药实验室”等47个项目立项为2023年度校级质量工程项目，具体名单见附件2。

请各项目负责人按照项目建设任务及要求，及时开展各项工作，加快推进学校人才培养改革，并力争取得高水平的教学成果。各单位要切实履行项目建设主体责任，加强对项目建设的督促、指导，以确保项目能如期高质量完成建设任务。

特此通知。

附件：1. 华南农业大学2023年校级教改项目立项名单

2. 华南农业大学2023年校级质量工程项目立项名单

华南农业大学

2023年12月13日

（联系人：孙齐胜、孙　航，电　话：85288020、85280052）

公开方式：主动公开

华南农业大学党政办公室　　2023年12月25日印发

30	JG2023030	招标项目	面向乡村振兴的农业高校传媒类新文科人才培养研究	胡辉	艺术学院
31	JG2023031	重点项目	以教育数字化转型为契机的《林木遗传育种 学》混合式教学创新研究	李培	林学与风景园林学院
32	JG2023032	重点项目	国际合作办学背景下建成环境历史课的中外融合与创新	李晓雪	林学与风景园林学院
33	JG2023033	重点项目	“双碳”背景下《包装材料学》课程教学改革与实践	刘涛	食品学院
34	JG2023034	重点项目	构建《遗传学》课程思政教学体系的探索与实践	刘自强	农学院
35	JG2023035	重点项目	基于数据挖掘的土木工程专业人才培养方案优化研究	张巍	水利与土木工程学院
36	JG2023036	重点项目	以培养创新人才为导向的《分析化学实验》教学改革与实践	熊亚红	材料与能源学院
37	JG2023037	重点项目	课程思政引领的《药剂学实验》 线上线下混合式教学探究与实践	胡洋	材料与能源学院
38	JG2023038	重点项目	课程链模式下农林院校学生用外语讲中国农耕文化故事能力的培养	秦建华	外国语学院
39	JG2023039	重点项目	基于人工智能技术的大学物理课程思政教学研究与实践	徐初东	电子工程学院 (人工智能学院)
40	JG2023040	重点项目	“大思政课”视域下高校思政课实践教学 协同育人创新模式研究与实践	林晓燕	马克思主义学院
41	JG2023041	重点项目	基于文本挖掘的课程思政元素挖掘研究--以应用统计学为例	张建桃	数学与信息学院、软件学院
42	JG2023042	重点项目	新农科背景下《动物解剖与组织胚胎学》课程思政改革创新	马勇江	兽医学院
43	JG2023043	重点项目	学科交叉融合的植物检疫学线上线下一体化教学实践	何晓芳	植物保护学院
44	JG2023044	重点项目	测绘地理信息类专业“学赛研”三位一体实践教学改革研究	刘惠明	资源环境学院
45	JG2023045	重点项目	新农科建设背景下高校图书馆开展中华优秀传统文化教育的探索与实践	黎小妮	图书馆

14.教改论文:《基于市场需求的工业工程专业课程设置》论文及其检索证明

[illegible]

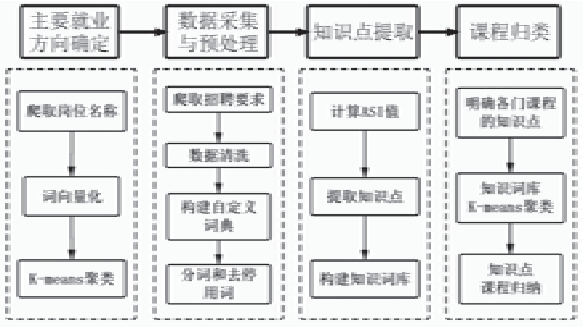
[illegible]

[illegible]

[illegible]

[

。


主要就业方向确定
数据采集与预处理
知识点提取
课程归类
爬取岗位名称
词向量化
K-means聚类
爬取招聘要求
数据清洗
构建自定义词典
分词删去停用词
计算BSI值
提取知识点
构建知识词库
明确各门课程的知识点
知识词库K-means聚类
知识点课程归纳

、、。

、、、。

、、、、。

、、、。

。

A、、。

。A。A。

。A。

。

A、、。

、、、。

、、、、。

、、、。

。

、、、。

、、、。

、、、

[illegible]、[illegible]、[illegible]。

[illegible]

[illegible]、[illegible]、[illegible]、[illegible]。[illegible]。[illegible]。[illegible]。[illegible]。[illegible]。[illegible]。[illegible]。[illegible]。[illegible]。

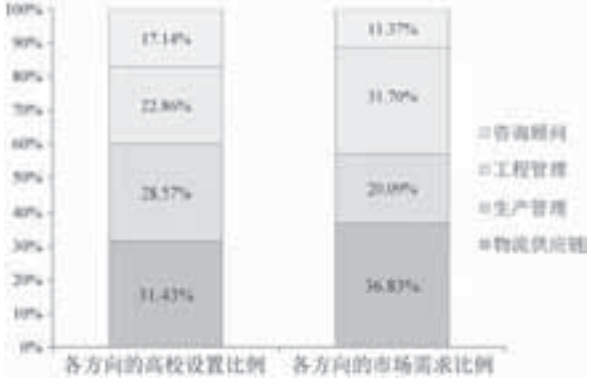
[illegible]

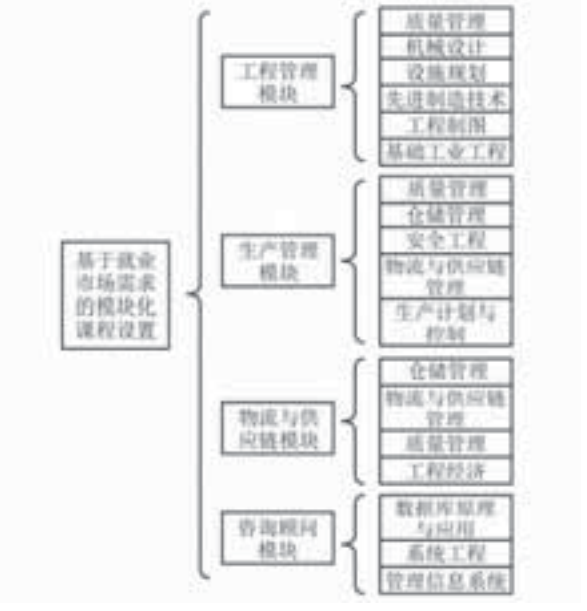
[illegible]	[illegible]	[illegible]	[illegible]
[illegible]	[illegible]	[illegible]	[illegible]
	[illegible]	[illegible]	[illegible]
	[illegible]	[illegible]	[illegible]
	[illegible]	[illegible]	[illegible]
[illegible]	[illegible]	[illegible]	[illegible]

[illegible]

[illegible]。[illegible]A[illegible]。[illegible]、[illegible]、[illegible]、

■ ■ ■


100%
90%
80%
70%
60%
50%
40%
30%
20%
10%
0%
17.14%
22.86%
28.57%
31.43%
11.37%
31.70%
20.09%
36.83%
□咨询顾问
□工程管理
□生产管理
■物流供应链
各方向的高校设置比例
各方向的市场需求比例


基于就业市场需求的模块化课程设置
工程管理模块
质量管理
机械设计
设施规划
先进制造技术
工程制图
基础工业工程
生产管理模块
质量管理
仓储管理
安全工程
物流与供应链管理
生产计划与控制
物流与供应链模块
仓储管理
物流与供应链管理
质量管理
工程经济
咨询顾问模块
数据库原理与应用
系统工程
管理信息系统

[redacted]

[redacted]

[redacted]

[redacted]

[redacted]

SCAULIB202405803

检索证明

根据委托人提供的论文材料，委托人华南农业大学数学与信息学院 张建桃 1 篇论文收录情况如下表。

序号	论文名称	发表刊物及发表的年月卷期/页码等	作者排名	论文等级	作者文中单位	收录情况	影响因子	中科院大类分区
1	基于市场需求的工业工程专业课程设置	高等工程教育研究 出版年：2022 卷期： 3 页码：- 文献号： 文献类型：	第一	B 类	华南农业大学	北大核心	无	无

说明：论文等级和中科院大类分区按《华南农业大学学术论文评价方案（试行）》划分。

报告免责声明:如未盖章,报告无效

检索员：尹银怀

华南农业大学图书馆

2024-03-19

华南农业大学图书馆SCAULIB202405803

15. 华南农业大学研究教学成果奖一等奖（排第二）:《真场景，实应用:面向农业数智化转型的信息管理类硕士培养模式创新与实践》有关佐证材料


华南农业大学

研究生教学成果奖

获奖证书

获奖成果：

获 奖 者：

获奖等级：一等奖

证书编号：YJSJXC025016

二、科研项目

1.主持《松材线虫病疫点镇拔除技术指导示范》项目的立项通知及有关佐证材料

广东省林业局文件

粤林财〔2022〕8号

广东省林业局关于下达2023年度省级财政事业发展性支出项目计划的通知

局机关有关处（室），局直属有关单位，有关项目单位：

根据《广东省林业局林业项目全过程绩效管理办法（试行）》《广东省林业局关于进一步规范项目绩效管理的通知》要求，为进一步夯实项目前期准备，提高项目成熟度，确保做到预算一经批复即可执行，现将2023年度省级财政事业发展性支出项目计划下达给你们，并将有关事项通知如下：

一、严格论证评估重大项目

立项总额超过500万元的项目，项目单位须按照《广东省财政厅关于印发<广东省省级财政绩效评估指南>的通知》（粤财绩

〔2020〕3 号）要求，组织编制绩效评估报告并于 11 月 25 日前报送归口处室。归口处室审核汇总后，连同自身使用的相关重大项目绩效评估报告，于 11 月 30 日前书面报规划财务处。

本次绩效评估报告是在下达项目计划后补充报送，但以后年度将在项目入库阶段报送，并将作为项目纳入规划财务处项目库和部门项目库的必要条件。

二、科学编制项目实施方案（作业设计、合同）

审批或备案的实施方案、作业设计以及签订的科研项目合同，是项目执行、检查、评价、验收的最重要依据。项单位目须按照《广东省林业局关于进一步规范项目绩效管理的通知》要求及参考格式，及时编制项目实施方案。其中，造林抚育类项目编制的作业设计、科研类项目签订的科研项目合同，视同项目实施方案。以上请于 11 月 25 日前报归口业务处室审批或备案，其中业务处室自身使用项目需报请局领导批准。（该项工作不用报规划财务处）。

三、规范制定项目资金支出计划和项目实施计划

请各项目单位认真填报《项目实施工作计划统计表》《项目资金支出计划统计表（时间）》《项目资金支出计划统计表（支出内容）》，并于**11 月 10 日前**报送归口处室，归口处室审核汇总并连同自身使用的项目计划情况，于**11 月 15 日前**书面报规划财务处。

根据省财政厅提高年初预算到位率的要求，本次项目相关计划自2023年1月起分月填报,其中资金支出计划每月填累计额度，原则上6月底不低于50%，10月底不低于95%，全年支付完毕。项目资金支出计划和项目实施计划将嵌入预算系统和“双监控”系统，并据此监测和通报各单位支出进度。

四、其他注意事项

(一)项目计划是年度省级财政事业发展性支出项目立项依据。

（二）本次同步将各二级项目的绩效目标一并下达，项目单位要做好绩效运行监控，确保年度绩效目标如期实现。

（三）涉及土地（房屋）、投审、消防、节能、环保等的项目，要及时开展相关工作，确保项目具备相关要素。

（四）涉及政府采购的项目，要尽快明确采购需求、采购方式、代理的选定，并及时开展政府采购意向公开等工作。

附件：1.2023年度自然资源事务专项资金—生态林业建设及

自然保护地体系建设（第一批）项目计划

2.2023年度海洋事业费及海洋赔偿款项目计划

3.2023年度省级以上公益林效益补偿省统筹项目计划

4.各二级项目绩效目标

5.项目实施工作计划统计表及资金支出计划统计表格式

6.广东省林业局关于进一步规范项目绩效管理的通知

广东省林业局

2022年10月24日

（联系人：梁海燕；电话：020-81825078）

公开方式：不公开

校稿：梁海燕

广东省林业局办公室　　2022年10月24日印

序号	归口处室	一级名称	单位	名称	建设内容	申请财政资金额度（万元）	拟纳入部门库额度（万元）	2023年建议安排资金额度（万元）	备注
5	防治检疫处	自然资源事务管理—生态林业建设（省级组织实施）—森林资源管护	1555003-华南农业大学	松材线虫病疫点镇拔除技术指导示范	1. 根据广东省松材线虫病疫情防控五年攻坚行动要求，利用无人机低空遥感，结合人工智能算法，对松材线虫病重点感染地区的高速公路边第一重山进行无人机的暗访拍摄，对暗访区域内的松材线虫病疫木进行自动识别、定位、危害等级分类和计数，检验松材线虫病疫情防控五年攻坚行动年度任务完成情况。 2. 松材线虫病疫点镇拔除工作跟踪指导：对重点防控区域松材线虫病疫点拔除工作进行	115.00	100	100	
6	防治检疫处	自然资源事务管理—生态林业建设（省级组织实施）—森林资源管护	403013-广东省农业科学院动物卫生研究所	松材线虫病防治质量核验（珠三角）	（1）珠三角片区松材线虫病防效质量核验 根据相关技术要求及全省核验统一部署，在珠三角片区7市25个县级行政区核验，覆盖林地面积50万亩次。对珠三角林地松材线虫病的防治效果进行监测，追踪该地区疫情监测、疫情防治、疫情管理等情况，进行分析、评估，掌握跟踪松材线虫病疫情控制效果，完成防止质量核验中期报告、最终评估报告。	120.00	120	120	
7	防治检疫处	自然资源事务管理—生态林业建设（省级组织实施）—森林资源管护	1555085-广东生态工程职业学院	林业有害生物检测鉴定及排查	1. 林业有害生物检测鉴定：对全省林业有害生物监测、防治和检疫过程中各地林业主管部门、森防检疫部门送检的松材线虫病等林业有害生物样品的检测鉴定。 2. 松材线虫病新发疫情排查：对去发生区松材	50.00	50	50	
8	防治检疫处	自然资源事务管理—生态林业建设（省级组织实施）—森林资源管护	199001-广东省林业局	林业外来入侵物种普查（植物部分）（中国林业科学研究院热带林业研究所）	承担森林草原生态系统外来入侵物种（植物部分）的普查及风险性评估等工作。在47个重点区域完成2次全面调查，同时指导审核7个市40多个县的普查情况，收集汇总全省森林草原生态系统外来入侵物种（植物部分）。摸清我省森林草原生态系统外来入侵植物的种类数量、	475.00	475	475	
9	防治检疫处	自然资源事务管理—生态林业建设（省级组织实施）—森林资源管护	199001-广东省林业局	鼎湖山国家级自然保护区松材线虫病、薇甘菊的监测和防控（中国科学院华南植物园-鼎湖山国家级自然保护区管理局）	松材线虫病的监测和防控； 薇甘菊的监测和防控。	400.00	100	100	
10	防治检疫处	自然资源事务管理—生态林业建设（省级组织实施）—森林资源管护	199087-广东省乐昌林场（广东后洞森林公园管理处）	松材线虫病防治	一、疫情普查：乐昌林场行政区辖内的松树的林班总面积约0.5万亩，开展春秋两次松材线虫病疫情普查工作。 二、疫木除治：选择磷化铝熏蒸松材线虫和松褐天牛 1、伐桩处理：疫木伐除后，塑料薄膜覆盖； 2、疫木处理：对3000株（估算）疫木采伐下来的所有树干（木材）、枝条就地实施熏蒸除害处理； 3、药剂防治：使用机动喷粉机喷洒1%噻虫啉微囊粉剂防治0.2万亩（已发生面积） 三、宣传普及防治知识。	200.00	80	80	
11	防治检疫处	自然资源事务管理—生态林业建设（省级组织实施）—森林资源管护	199084-广东省龙眠洞林场（广东莲花顶森林公园管理处）	林业有害生物防治	2023年对林场松材线虫病、薇甘菊、红火蚁等重大林业有害生物进行监测调查，除治消杀等工作	100.00	80	80	
12	防治检疫处	自然资源事务管理—生态林业建设（省级组织实施）—森林资源管护	199089-广东省东江林场（广东东江森林公园管理处）	松材线虫病防治	1、松材线虫普查： 采用踏查和样地调查相结合的方法，全面掌握虫情动态。 2、固定监测点监测： 对4个工区的4个固定样地进行跟踪监测，观测松树有无枯死树现象、发生发展趋势、防治效果等。对疑似枯死树木取样进行室内分析，并送省、市站分析鉴定。 3、疑似疫木处理： 对病死的松树全部进行砍伐。 4、做好检疫封锁工作，严禁松木输入运出，对疫木严格就近指定地点处理。	400.00	80	80	
13	防治检疫处		199082-广东省乳阳林场（广东南岭国家森林公园管理处）	松材线虫病综合防治	1. 松材线虫病防控宣传 做好与全场辖区涉及的5个乡镇、14个行政村、20个自然村的沟通联系，加强联防联治，印发松材线虫病防治宣传通告，建设范围为20个自然村。范围是林场辖区、周边乡镇、村庄。 2. 开展日常监测和专项普查 从签订合同至2023年底，做好每月的日常监测工作，做好春、秋两季的普查工作。范围是乳阳林场辖区。 3. 综合防治和疫木清除 通过可疑木取样鉴定、疫木伐除清理处理、打孔注药、其他防治措施等，对发现松材线虫病的区域实行综合防治。范围是乳阳林场全域。	100.00			
14	防治检疫处	自然资源事务管理—生态林业建设（省级组织实施）—森林资源管护	199090-广东省九连山林场（广东九连山森林公园管理处）	松材线虫病防治	1. 2023年对林场管辖范围内2215.8亩松林进行2次全面普查，春季、秋季普查各1次； 2. 2023年5月-12月，每月1-2次进行定期巡查； 3. 全面清理林区内的松树枯死、濒死木，并进行消杀。	100.00	80	80	
15	防治检疫处	自然资源事务管理—生态林业建设（省级组织实施）—森林资源管护	199094-广东省云浮林场	林业有害生物薇甘菊防控	根据广东省林业局文件《广东省林业局办公室关于做好2023年自然资源事务（生态林业建设）专项资金（省级组织实施）入库申报工作的通知》。建设内容为林业有害生物薇甘菊的防治，防治方法主要有人工清除和化学防治。	30.00	30	30	
16	防治检疫处	自然资源事务管理—生态林业建设（省级组织实施）—森林资源管护	199024-广东车八岭国家级自然保护区管理局	松材线虫病防治	车八岭松材线虫病防治项目主要建设内容包括：1、松材线虫检测、紧急处置和消杀；2、松材线虫智能监测预警与网格化普查；3、防治效果跟踪检查与评估。	80.00	80	80	
17	防治检疫处		199088-广东省连山林场（广东鹰扬关森林公园管理处）	林业有害生物防治和森林外来入侵物种普查与风险评估	1、2023年开展松材线虫病春季和秋季普查，全面清理林区内的松树枯死、濒死木和防治消杀，防治面积5000亩； 2、红火蚁综合防治，防治面积500亩（包含林地和生活区）； 3、森林外来入侵物种普查与风险评估，普查面积11.92万亩。	142.00			
18	防治检疫处	自然资源事务管理—生态林业建设（省级组织实施）—森林资源管护	199092-广东省德庆林场	林业有害生物（薇甘菊、红火蚁）防控	建设内容为林业有害生物薇甘菊和红火蚁的防治，薇甘菊防治主要采用人工持续清除和薇甘菊专用除草剂化学防治；红火蚁防治主要采用以毒饵诱杀法为主。	15.00	15	15	
19	防治检疫处		199085-广东省樟木头林场（广东宝山森林公园管理处、广东九洞森林公园管理处）	薇甘菊有害生物防治	2023年完成薇甘菊有害生物防治面积1000亩的防治任务	24.40	0	0	

2.主持广东省哲学社会科学项目:《基于大数据分析的广东省乡村振兴人才需求和培养研究》立项通知及有关佐证材料

广东省哲学社会科学规划专项小组

粤社科规专通〔2023〕47号

广东省哲学社会科学规划2023年度学科共建项目立项通知书

张建桃同志：

经省哲学社会科学工作领导小组审批，您申报的广东省哲学社会科学规划2023年度学科共建项目《基于大数据分析的广东省乡村振兴人才需求和培养研究》获准立项，批准号：GD23XJY49。学科共建项目单项经费2万元，由项目负责人所在单位自筹并分期划拨给项目负责人，第一次拨款1.4万元，预留经费0.6万元在项目鉴定结项后拨付。请于9月15日前在广东省哲学社会科学规划项目管理平台认真填写预算。

项目负责人填写预算后，本通知即成为具有约束效力的立项协议。项目负责人所在单位须承担保证责任。项目负责人及所在单位须了解和执行以下规定：

1.课题组须学习并遵守《广东省哲学社会科学规划项目管理办法》。对于出现违规行为的，省哲学社会科学规划专项小组依据《广东省哲学社会科学规划项目管理办法》的相关规定进行处理。

2.立项项目经费不再追加。课题组如不接受，省哲学社会科学规划专项小组将撤销该项目立项。而立项经费一经接受，课题组将不得以资助经费不足为由，擅自变更原设计的最终成果形式和内容。

3.项目研究过程中，如有变更项目负责人、延长完成时间、改变成果内容或形式、变更项目管理单位、变更或增补课题组成员、终止项目或撤销项目等重要事项，项目负责人或所在单位必须按要求填写《广东省哲学社会科学规划项目重要事项变更审批表》，并及时报省哲学社会科学规划专项小组审批。

4.项目研究的阶段性成果发表时，必须注明“广东省哲学社会科学规划项目”字样。

5.项目成果的鉴定结项由省哲学社会科学规划专项小组组织，实行匿名鉴定制度。项目鉴定结项所需材料及装印要求，详见“广东社科规划”网站。

6.成果鉴定等级分为优秀、良好、合格和不合格四个

等次。不合格者即未能通过结项，不予拨付预留经费。项目成果的最终鉴定等级均通过“广东社科规划”网站予以公布，并通知项目负责人所在单位。

7.为提高成果质量，项目的最终成果（专著、研究报告）必须经鉴定结项后方能出版。对于违反规定擅自出版的，视为项目负责人自行终止立项协议，该项目即时终止，省哲学社会科学规划专项小组将不再受理该项目的结项鉴定申请，并通知项目负责人所在单位不再拨付预留经费。

以上规定，项目负责人及所在单位应严格遵守。如有异议，可不接受资助（逾时未在广东省哲学社会科学规划项目管理平台填报预算视为放弃立项），立项协议自行废止。

地址：广州市天河北路618号广东社科中心B座928室

电话：(020)83825078

邮编：510635

广东省哲学社会科学规划专项小组

2023年9月5日

3. 主持《梅州兴宁市农用无人机高效丝苗种植县级农技推广服务驿站技术服务》项目的立项通知及有关佐证材料

新农村发展研究院2021年度农业科技合作共建项目拟立项公示名单

序号	项目名称	申报人	单位	专题类别	项目类别
1	茂名罗非鱼加工服务	钟南	工程学院	科特派团队服务专题	高校服务乡村振兴共同体技术服务项目
2	怀集丝苗米产业园协同服务	肖武明	国家植物航天育种工程技术研究中心	科特派团队服务专题	高校服务乡村振兴共同体技术服务项目
3	湛江市特色优质杂交稻育繁推服务	郭涛	国家植物航天育种工程技术研究中心	科特派团队服务专题	高校服务乡村振兴共同体技术服务项目
4	肇庆市高要区南药种植与资源利用协同服务	唐光大	林学与风景园林学院	科特派团队服务专题	高校服务乡村振兴共同体技术服务项目
5	基于高光谱技术的高州桂圆品质快速检测服务	谌国莲	食品学院	科特派团队服务专题	高校服务乡村振兴共同体技术服务项目
6	河源东瑞生猪现代农业产业园猪只智能估重技术服务	肖德琴	数信学院	科特派团队服务专题	高校服务乡村振兴共同体技术服务项目
7	大埔蜜柚提质增效服务	秦永华	园艺学院	科特派团队服务专题	高校服务乡村振兴共同体技术服务项目
8	河源蔬菜智能化种植服务	刘厚诚	园艺学院	科特派团队服务专题	高校服务乡村振兴共同体技术服务项目
9	信宜三华李产业园种植技术服务	何业华	园艺学院	科特派团队服务专题	高校服务乡村振兴共同体技术服务项目
10	华南农业大学—嘉应学院高校服务乡村振兴共同体花生产业绿色	钟国华	植物保护学院	科特派团队服务专题	高校服务乡村振兴共同体技术服务项目
11	生猪重要疫病快速诊断技术研究和应用示范	封柯宇	动物科学学院	科特派团队服务专题	高校服务乡村振兴共同体技术服务项目
12	惠州胡须鸡养殖服务	蔺文成	动物科学学院	科特派团队服务专题	高校服务乡村振兴共同体技术服务项目
13	肉用黑山羊优势杂交方案及高效养殖技术示范推广	柳广斌	动物科学学院	科特派团队服务专题	高校服务乡村振兴共同体技术服务项目

30	广东从化荔枝科技小院技术服务	王惠聪	园艺学院	科特派团队服务专题	科技小院技术服务项目
31	广东惠东叶菜科技小院技术服务	翁群芳	植物保护学院	科特派团队服务专题	科技小院技术服务项目
32	阳西县荔枝园智慧果园服务	谢家兴	电子工程学院	科特派团队服务专题	县级农技推广服务驿站技术服务项目
33	食用百合的种质资源收集、引种栽培与生产加工产业化研究	郁书君	林学与风景园林学院	科特派团队服务专题	县级农技推广服务驿站技术服务项目
34	梅州兴宁市农用无人机高效丝苗种植县级农技推广服务驿站技术	张建桃	数学与信息学院	科特派团队服务专题	县级农技推广服务驿站技术服务项目
35	阳山县丝苗米现代农业产业园——水稻精准施肥技术服务	周志艳	工程学院	科特派团队服务专题	现代农业产业园服务项目
36	清新区鳜鱼高效养殖服务	严慕婷	海洋学院	科特派团队服务专题	现代农业产业园服务项目
37	阳江市深海网箱养殖产业园技术服务	李远友	海洋学院	科特派团队服务专题	现代农业产业园服务项目
38	东源县无人机病虫害智能检测及防控技术	岳学军	电子工程学院	科特派团队服务专题	驻镇帮镇扶村帮扶项目
39	丘陵山区林果茶园运输机械化技术示范和推广	吴伟斌	工程学院	科特派团队服务专题	驻镇帮镇扶村帮扶项目
40	化州市新安镇化橘红智能烘干设备研发服务	孙振刚	工程学院	科特派团队服务专题	驻镇帮镇扶村帮扶项目
41	东源县优质水产品养殖与病害防控技术服务	赵会宏	海洋学院	科特派团队服务专题	驻镇帮镇扶村帮扶项目
42	汕尾市海丰县赤坑镇鱼类无抗养殖服务	魏京广	海洋学院	科特派团队服务专题	驻镇帮镇扶村帮扶项目
43	海水水产健康养殖技术示范与推广	周胜	海洋学院	科特派团队服务专题	驻镇帮镇扶村帮扶项目
44	东源县高品质淡水水产工厂化养殖技术推广应用与培训服务	郑丁科	基础实验与实践训练中心	科特派团队服务专题	驻镇帮镇扶村帮扶项目

4. 主持广东省自然科学基金《禽流感空气消毒多振子超声雾化气溶胶喷雾器的研制》立项通知及有关佐证材料

2016年科技发展专项资金（公益研究与能力建设方向）
拟安排项目及资金分配方案表（不含科技装备动员项目）

序号	项目名称	申报单位	负责人	当期拨付金额（万元）
合计：1265项				55,792
一、农业和社会民生、工业、科技服务业领域研究攻关				26,153
1、产业技术融合创新				560
1	物联网微型天线技术研究与制备	中山大学	Terry Ye	80
2	定制家居制造物联技术及其制造执行系统研发	广东华中科技大学工业技术研究院	朱海平	80
3	考虑制造约束的智能下料排样优化服务平台	广东工业大学	刘强	80
4	大数据环境下广东LED产业安全动态智能监测预警系统的开发与应用	广东省半导体光源产业协会	李文玉	80
5	数字化电梯门板机器人生产线	广东省工业技术研究院（广州有色金属研究院）机电工程研究所	段先云	80
6	制造业企业信息化数据分析及应用技术研究	广东省科技基础条件平台中心	陈阳	80
7	海洋输油立管的振动迭代学习控制研究	广东第二师范学院	邬依林	80
2、创新医疗器械研发与示范				1,080
1	数字化脑血管介入手术规划与手术模拟系统研发	中国科学院深圳先进技术研究院	吴剑煌	50
2	基于物联网的家用智能止鼾背垫研发	中山大学附属口腔医院	陶谦	50
3	检测易损斑块的光声光谱/超声双模血管内成像系统	中山大学附属第一医院	廖新学	50
4	多感觉交互效应下的可穿戴康复设备研发与应用	中山大学附属第一医院	黄东锋	50
5	围产期抑郁症筛查系统的研发与临床研究	中山大学附属第一医院	徐敏	30
6	新型自主研发微创膝关节置换手术器械的研发与改良	中山大学附属第一医院	徐栋梁	50
7	基于麻醉机呼吸回路的术中雾化给药系统研究开发	中山大学附属第三医院	黑子清	50
8	眼睛光学生物多参数测量仪	佛山科学技术学院	曾亚光	50
9	全自动肝癌消融精准机器人穿刺系统研制	华南理工大学	杨荣骞	50
10	高性能低骨损伤新型微创钻（磨）削刀头的研发及产业化	华南理工大学	刘允中	50
11	利用高斯模型结合多光子技术创建移植肾间质纤维化精确分级系统的研究	南方医科大学珠江医院	赵明	50
12	数字化高仿真肝癌手术训练系统的构建研究	南方医科大学珠江医院	杨剑	50
13	创新型高灵敏荧光纳米微球侧向层析联检试纸及集成仪器平台的研发与示范	广东医学院	潘庆军	50
14	牙齿树脂修复透视测量仪的研发与推广应用	广东工业大学	周延周	50
15	脑损伤上肢智能康复机器人的整机研发及示范应用评价	广东省医疗器械质量监督检验所	李伟松	50
16	基于心音识别技术的冠心病便携式辅助诊断仪器的研发	广东顺德西安交通大学研究院	吴贺勇	50
17	基于半规管成像信息的智能型前庭功能诊治系统关键技术研究	广州医科大学附属第一医院	张明	50
18	个性化唇侧矫治器3D打印技术研究与产业化	暨南大学	孔卫东	50

序号	项目名称	申报单位	负责人	当期拨付金额（万元）
38	基于菌根真菌的蓝莓专用生物有机肥的研发与应用示范	华南农业大学	姚青	15
39	草鱼营养性脂肪肝防治研究	华南农业大学	甘炼	15
40	稻壳热解气化学链循环制纯H2协同CO2捕集关键技术研究	华南农业大学	许细薇	15
41	高效种猪体细胞克隆扩繁技术研究与应用示范	华南农业大学	李紫聪	15
42	重要药材紫锥菊高倍非整倍体种质的创制与评价	华南农业大学	杨跃生	15
43	菠萝黑心病防控关键技术研究与示范	华南农业大学	朱世江	15
44	串果类水果振动采收关键技术研究	华南农业大学	李君	15
45	广东省羊口疮疫苗候选毒株的筛选及评估	华南农业大学	宁章勇	15
46	基于RNAi技术的真菌杀虫剂的研制与示范	华南农业大学	金丰良	15
47	基于WSN自主调整航线的无人机防雾滴飘移控制技术	华南农业大学	胡洁	15
48	小菜蛾钠离子通道双功能阻断剂设计合成与生物活性评价	华南农业大学	江定心	15
49	辣木对荷斯坦奶牛生产性能和牛奶品质的影响研究	华南农业大学	孙宝丽	15
50	利用多基因代谢工程创制胚乳特异合成虾青素的新型功能营养型水稻	华南农业大学	祝钦泷	15
51	功能化生物炭研制及其阻控畜禽养殖废水中典型抗生素和重金属复合污染技术研究	华南农业大学	林云琴	15
52	基于多信息融合深度学习模型的发情家畜自动识别研究	华南农业大学	高月芳	15
53	基于计算机视觉的蛹虫草长势监测技术研究与应用	华南农业大学	万华	15
54	基于混合智能计算的农业航空作业规划关键技术研究	华南农业大学	吕石磊	15
55	基于农产品交易、休闲农业和特色文化旅游三位一体环境设计的陈皮村模式研究与应用	华南农业大学	吴宗建	15
56	利用CRISPR-cas9系统开发害虫嗅觉行为调控遗传防治技术	华南农业大学	易欣	15
57	南方山地果园轻型自走式风送仿形高效喷雾机研制	华南农业大学	徐兴	15
58	禽流感空气消毒多振子超声雾化气溶胶喷雾器的研制	华南农业大学	张建桃	15
59	山地果园单轨循环式运送系统关键技术研究与示范	华南农业大学	李震	15
60	水生花卉与水稻间作修复稻田土壤镉污染的关键技术研究与示范	华南农业大学	章家恩	15
61	甜味剂对红火蚁的生物活性及其饵剂开发	华南农业大学	许益镌	15
62	晚熟抗寒优质龙眼荔枝属间杂交种质的创制及评价利用	华南农业大学	傅嘉欣	15
63	香蕉枯萎病菌重要致病因子筛选平台的建立与应用研究	华南农业大学	聂燕芳	15
64	一种新型作物保护剂—稻瘟菌激发子的制备与应用研究	华南农业大学	李云锋	15
65	蔗段机械化种植机关键技术研究与示范	华南农业大学	文晟	15
66	杂交稻机械化种植方式对比试验研究及应用示范	华南农业大学	李泽华	15
67	食品中孕酮类激素的电化学免疫传感器技术研究及应用	华南农业大学	刘毅新	15
68	虚拟现实技术在南方特色水果柔性加工线设计中的应用研究	华南农业大学	刘昌余	15
69	运用体外程序化定向酶解改造大麦营养价值的关键技术开发与应用	华南农业大学	左建军	15

受理编号：c1630550100264

项目编号：2016A020210092

文件编号：粤科规财字〔2016〕47号



广东省省级科技计划项目

合同书

项目名称：禽流感空气消毒多振子超声雾化气溶胶喷雾器的研制

计划类别：农村科技领域

项目起止时间：2016-01-01　至　2018-12-31

管理单位(甲方)：广东省科学技术厅

承担单位(乙方)：华南农业大学

乙方主管部门(丙方)：华南农业大学

通讯地址：广东省广州市天河区五山路483号

邮政编码：510642　　单位电话：020-38632819

项目负责人：张建桃　　联系电话：020-85285396

项目联系人：张建桃　　联系电话：020-85285396

2016A020210092

广东省科学技术厅

二〇一四年制

九、本合同签约各方

管理单位（甲方）： 广东省科学技术厅 （盖章）

单位地址： 广东省广州市连新路171号

法定代表人（或授权代表）： 黄宁生 （签章）

联系人（经办人）姓名： 刘世伟 （签章）

Email： liusw@gdstc.gov.cn

电话： 020-83163909

2016年 9月 1日

承担单位（乙方）： 华南农业大学 （盖章）

二级部门： 华南农业大学数学与信息（软件）学院

单位地址： 广东省广州市天河区五山路483号

法定代表人（或法人代理）： 陈晓阳 （签章）

联系人（项目主管）姓名： 石睿 （签章）

Email： 77909213@qq.com

电话： 020-85283435

开户单位名称： 华南农业大学

开户银行及帐号： 广东广州工行五山支行 3602002609000310520

2016年 9月 1日

乙方主管部门（丙方）： 华南农业大学 （盖章）

单位地址： 广东省广州市天河区五山路483号

法定代表人（或法人代理）： 陈晓阳 （签章）

联系人（项目主管）姓名： 石睿 （签章）

Email： 77909213@qq.com

电话： 020-85283435

开户单位名称： 华南农业大学

开户银行及帐号： 广东广州工行五山支行 3602002609000310520

2016年 9月 1日

5. 主持广州市科技计划重点研发项目《稻田农药减施与污染治理技术的研究与示范》立项通知及有关佐证材料

任务书编号：2023B03J1362

广州市科技计划项目

任务书

项目名称：	稻田农药减施与污染治理技术的研究与示范
承担单位：	华南农业大学
项目负责人：	张建桃
计划类别：	重点研发计划
专题名称：	2023年度农业和社会发展科技专题
方向名称：	（五）绿色低碳循环技术
组织单位：	华南农业大学
起止时间：	2023-04-01 至 2026-03-31
主管处室：	农村和社会发展科技处

广州市科学技术局制

二〇二三年

广州市科技项目任务书2023-03-30

一、项目基本信息

项目名称	稻田农药减施与污染治理技术的研究与示范			
计划类别	重点研发计划		专题名称	2023年度农业和社会发展科技专题
方向名称	（五）绿色低碳循环技术			
支持子方向	43.基于生产生活的面源污染防控与绿色治理技术研究			
指南发布日期	2022-04-15			
项目开始时间	2023-04-01		项目结束时间	2026-03-31
资助方式	竞争性前资助		市财政科技经费(万元)	50
广东省技术领域	农业技术农业装备(农业机械、设备及材料等)；			
承担单位	华南农业大学			
合作单位	仲恺农业工程学院；			
组织单位	华南农业大学			
	姓名	办公电话	手机号码	电子邮箱
项目负责人	张建桃	13076759646	13076759646	zhangjiantao@yeah.net
项目联系人	张建桃	020-85285396	13076759646	zhangjiantao@yeah.net
科研财务助理	周腾媛	020-85285396	15813380483	923770133@qq.com
项目摘要	农业面源污染已成为我国水体污染的重要来源，其中农药面源污染问题十分严峻，农药的高毒性和高残留性对水生态系统和人类健康造成极大威胁。针对稻田农药污染问题，提出采用“源头减量+末端治理”的方法。首先，在“源头减量”方面，基于农用无人机搭建水稻病虫害低空遥感监测平台，实现水稻病虫害防治处方图自动生成，优化纳米农药无人机喷施参数，筛选典型的具有防飘移、附着性能优良的高工效纳米农药制剂和助剂，研制稻田纳米农药无人机变量喷施系统，从源头提高农药的利用率，减少农药的施用量；其次，在“末端治理”方面，筛选高富集农药的水生植物、人工湿地填料，构建生态沟渠-生态拦截坝-人工湿地组合系统，对稻田湿地排水中农药污染进行处理，去除稻田湿地排水中残留的农药污染，保证整个农业生产的可持续发展及临近水环境的安全；最后，将研究成果在广州市增城丝苗种植基地进行应用示范。项目的实施将实现农业工程、作物学、植物保护、生态学等多个学科与人工智能技术的深度融合，实现农田面源污染全链条控制，有望将稻田农药施用量减少10%，利用率提高5%，稻田退水农药去除率达50%以上，为稻田生态环境的农药污染控制提供技术支撑。			

广州市科技项目任务书 2023-03-30

任务书签署

甲乙丙三方根据《广州市科技计划项目管理办法》《广州市科技计划项目经费管理办法》《广州市科技计划科技报告管理办法》等有关文件规定，以及有关法律、政策和管理要求，签署本任务书。

签订地点：广州市越秀区

广州市科学技术局（甲方）：广州市科学技术局
局项目经办人：夏万志　　联系电话：83124147
责任处室负责人：赵晓曦

2023年03月30日

项目承担单位（乙方）：华南农业大学
二级部门：华南农业大学数学与信息学院
项目负责人：张建桃
项目经费汇入账号
账户名：华南农业大学　　账号：3602002609009310520
开户银行：广东广州工行五山支行
财务负责人：肖斐

2023年03月22日

组织单位（丙方）：华南农业大学
项目经办人：倪慧群

2023年03月22日

广州市科技项目任务书2023-03-30

6. 主持《簕菜叶面肥无人机喷施参数优化与推广应用》项目的立项通知及有关佐证材料

恩平市科技服务中心

关于2022年度恩平市农村科技特派员项目立项的通知

各有关单位:

现将2022年度恩平市农村科技特派员项目立项计划下达给你们（详见附件）,请各项目承担单位尽快与恩平市科技服务中心签订《恩平市农村科技特派员项目合同书》(合同书一式四份，请在2023年1月31日前报送到恩平市科技服务中心）。

各项目承担单位必须严格按照有关专项规定和项目合同要求使用专项资金，认真组织实施。在项目实施期间如遇到问题，请及时与市科技服务中心联系。

附件：2022 年度恩平市农村科技特派员项目立项项目明细表

恩平市科技服务中心

2023 年 1 月 15 日

（联系人：黎肇源、袁梓荃，联系电话：0750-7814477、0750-7815742）

附件

2022年度恩平市农村科技特派员项目立项项目明细表

序号	项目类型	项目名称	项目申报单位	特派员姓名	派出单位	拟安排扶持资金（万元）
1	高校派驻农村科技特派员项目（推荐单位：华南农业大学）	夏季高温黄羽肉鸡高效低排饲料配制技术与示范	恩平基龙实业有限公司	朱勇文	华南农业大学	5
2		作物绿色栽培与清洁生产	恩平供销农业科技服务有限公司	蔡昆争	华南农业大学	5
3		辣椒新品种推广及高效绿色栽培技术集成示范	恩平市良民良田农产品专业合作社	程蛟文	华南农业大学	5
4		陈皮果渣及提取物在猪养殖中的应用	广东大广生物科技有限公司	张庆	华南农业大学	5
5		鹅菜叶面肥无人机喷施参数优化与推广应用	恩平市雪莊农业科技有限公司	张建桃	华南农业大学	5
6	江门市农村科技特派员项目（推荐单位：恩平市农业农村局）	恩平市农业机械化智能驾驶项目	恩平市穗丰农业机械装备有限公司	郑健林	恩平市农机推广服务中心	5
7		香水柠檬高产栽培技术应用	恩平市星浩农业科技有限公司	谭卫娜	恩平市农产品质量监督检验测试中心	5
8		皇帝柑水肥一体化技术应用	恩平市大田镇橙一橙水果种植场	冯健超	恩平市农业技术推广服务中心	5
9		水稻生态有机种植	恩平市川爸农业专业合作社	梁玩广	恩城街道农业综合服务中心	5
10		恩平市火龙果光补种植技术应用	恩平市金富水果种植专业合作社	岑越彪	恩平市农业技术推广服务中心	5
	小计					**50**

7. 主持《基于高频超声雾化的农药超低量喷雾器关键技术研究》项目的立项通知及有关佐证材料

项目编号：S2013010013747
资助类别：自由申请
文件编号：粤科基办字〔2013〕3号

广东省自然科学基金 自由申请 重点项目 博士启动

合同书

2013年广东省自然科学基金项目合同书

课题名称：	基于高频超声雾化的农药超低量喷雾器关键技术研究
下达单位（甲方）：	广东省自然科学基金管理委员会
课题负责人：	张建桃　　资助经费：　5（万元）
通信地址：	华南农业大学信息学院409
邮政编码：	510642　　联系电话：　13076759646
电子邮件：	zhangjiantao@yeah.net
依托单位（乙方）：	华南农业大学
联 系 人：	苏弟华　　联系电话：　020-85280070
执行年限：	2013年10月至 2015年10月
填表日期：	2013年10月01日

广东省自然科学基金管理委员会

二〇一〇年 制

本合同签约各方

下达单位（甲方）：广东省自然科学基金管理委员会　　（盖章）

法定代表人（或法人代理）：　　（签章）

2013年11月4日

依托单位（乙方）：　　（盖章）

法定代表人（或法人代理）：　　（签章）

联系人（项目主管）姓名：　　（签章）

电话：020-85280070　　乙方开户银行名称：广东广州工行五山支行

乙方开户单位名称：华南农业大学

乙方开户银行帐号：3602002609000310520

年　月　日

联系人（课题负责人）姓名：　　（签章）

电话：13076759646　　E-mail：zhangjiantao@yeah.net

2013年10月1日

2013年广东省自然科学基金项目合同书

8. 主持广东省普通高校“人工智能”重点领域专项：关于《基于人工智能和触觉感知的植保无人机纳米农药减施关键技术研究》项目的立项通知及有关佐证材料

广 东 省 教 育 厅

广东省教育厅关于公布普通高校人工智能和服务乡村振兴重点领域专项立项名单的通知

各有关高校:

为贯彻落实《新一代人工智能发展规划》和《乡村振兴战略规划（2018－2022年）》，切实推进我省新一代人工智能技术在各领域深度融合应用和乡村振兴战略的实施，着力提升全省高校科技创新能力，经学校推荐、省教育厅组织专家评审，现将批准立项的2019年度普通高校人工智能和服务乡村振兴重点领域科研项目（见附件）下达各高校。

请各高校按照《广东省高等教育“创新强校工程”专项资金管理办法》（粤财教〔2014〕130号）及相关科研项目管理办法，统筹安排项目资金，加强资金管理，督促项目承担人按照项目申请书开展建设工作，跟进并协助解决项目实施过程中遇到的问题和困难。

附件: 1.2019年度广东省普通高校人工智能重点领域专项立项名单

2.2019年度广东省普通高校服务乡村振兴重点领域专

项立项名单

广东省教育厅

2020年3月18日

（联系人及电话：赖欣，020-37628271；陈阿丽，020-37627742。）

公开方式：主动公开

校对人：陈阿丽

附件1

2019年度广东省普通高校“人工智能”重点领域专项立项名单

序号	项目编号	项目名称	负责人	所属学校
1	2019KZDZX1001	面向区块链技术的家禽供应链溯源关键技术研究	韩宇星	华南农业大学
2	2019KZDZX1002	基于人工智能和触觉感知的植保无人机纳米农药减施关键技术研究	张建桃	华南农业大学
3	2019KZDZX1003	丘陵山区智能水稻直播机器人关键技术与应用研究	杨文武	华南农业大学
4	2019KZDZX1004	基于人工智能的智慧建筑设备集成关键技术研究及应用	岑健	广东技术师范大学
5	2019KZDZX1005	基于多水平演化的群体智能优化算法	刘群锋	东莞理工学院
6	2019KZDZX1006	基于深度学习和PBPK模型的医学急救模拟人开发及其在智能教育中的应用	何新	广东药科大学
7	2019KZDZX1007	基于自动化深度学习的计算机视觉关键技术研究	鲁坚	深圳大学
8	2019KZDZX1008	录音取证智能对抗研究	罗达	东莞理工学院
9	2019KZDZX1009	太阳能智能精准灌溉装备关键技术及应用研究	梁忠伟	广州大学
10	2019KZDZX1010	具有类脑神经突触功能的超低功耗智能器件研究	陈心满	华南师范大学
11	2019KZDZX1011	群体智能算法的改进机制研究及其在QoS组播路由问题中的应用	魏文红	东莞理工学院
12	2019KZDZX1012	无人农场的边缘智能化关键技术研究	邓小玲	华南农业大学
13	2019KZDZX1013	基于人工智能的乳腺肿瘤超声影像智能分析与研究	庄哲民	汕头大学
14	2019KZDZX1014	机器学习驱动的互联网金融平台系统性风险挖掘	胡大宁	南方科技大学
15	2019KZDZX1015	基于纵向深度特征学习的帕金森病早期诊断与预测关键技术研究	雷海军	深圳大学

9. 主持广东省教育科学规划课题(高等教育专项):《人工智能背景下课程思政元素智能挖掘与覆盖程度评价研究》立项通知及有关佐证材料

广东省教育科学规划领导小组办公室

广东省教育科学规划领导小组办公室关于公布2024年度教育科学规划课题（高等教育专项）立项名单的通知

各有关高校：

为深入贯彻党的二十大精神、二十届三中全会精神和习近平总书记视察广东重要讲话、重要指示批示精神，聚焦落实省委“1310”具体部署，加强哲学社会科学学科建设，提升高等教育内涵发展水平，为我省在推进中国式现代化建设中走在前列提供有力人才保障和智力支撑，省教育科学规划领导小组办公室组织开展了教育科学规划课题（高等教育专项）的遴选工作。经学校推荐、省教育科学规划办组织专家评审，现将批准立项的2024年度教育科学规划课题（高等教育专项）（见附件）下达各高校。

请各高校按照国家和省相关科研平台和项目的管理办法，统筹安排项目资金，并督促项目承担人按照项目申请书开展研究工作，协助解决项目实施过程中遇到的困难和问题，加强项目管理和经费使用管理，确保研究项目如期完成目标任务。省教育科学规划办将适时组织抽查工作。

372	2024GXJK372	面向本科生就业能力提升的新文科建设路径研究——以公共管理学科为例	华南农业大学	朱庆莹
373	2024GXJK373	AI赋能数字公共管理人才培养的实现路径研究	华南农业大学	方敏
374	2024GXJK374	新工科背景下智能农业机器人工业设计人才培养模式研究	华南农业大学	郭涵
375	2024GXJK375	人工智能背景下课程思政元素智能挖掘与覆盖程度评价研究	华南农业大学	张建桃
376	2024GXJK376	数智时代大学生奋斗观演变与培育研究	华南农业大学	李若衡
377	2024GXJK377	体育强国建设背景下广东省高校体育社团发展路径研究	华南农业大学	宋明伟
378	2024GXJK378	数字美育视角下汉服艺术高质量发展研究	华南农业大学	邹岚
379	2024GXJK379	短视频传播背景下大学生社会主义核心价值观培养的优化路径研究——以“抖音”APP为例	华南农业大学	梁健晟
380	2024GXJK380	基于多模态话语分析的课程思政教学创新能力研究	华南农业大学	林绿
381	2024GXJK381	新文科视域下高校新闻传播教育课程思政创新路径研究——以《品牌设计与传播》为例	韩山师范学院	蔡梦虹
382	2024GXJK382	语文教材的认同思想构建与实现路径研究	韩山师范学院	苑青松
383	2024GXJK383	高校重大突发事件危机学习影响机理及优化策略研究	韩山师范学院	鲍江东
384	2024GXJK384	基于生成式人工智能提升大学生中华文化国际传播能力的路径研究	韩山师范学院	陈慕侨
385	2024GXJK385	广东省公费师范生数字素养现状调查与提升策略研究	韩山师范学院	刘茂军
386	2024GXJK386	公费师范生乡村地方感及其培养路径研究	韩山师范学院	徐学
387	2024GXJK387	新质生产力视角下虚拟设计工作室教学模式研究	韩山师范学院	黄兵
388	2024GXJK388	高质量发展背景下学前教育师范生家庭教育指导胜任力研究	韩山师范学院	徐青
389	2024GXJK389	基于扎根粤东西北理念的数智赋能循证体育教师教育实践研究	韩山师范学院	温搏
390	2024GXJK390	从南泥湾到高精尖——新质生产力背景下材料类专业学生立体化、循环化劳动教育的研究	韩山师范学院	李洪亮

10.主持《植物精油微孔压电超声雾化机理研究》项目的立项通知及有关佐证材料

项目编号: 2018KTSCX019

广东省普通高校省级重大科研项目（青年创新人才、特色创新）合同书（自然科学类）

项目类别：特色创新项目(自然科学)

项目名称：植物精油微孔压电超声雾化机理研究

项目负责人：张建桃

承担单位（学院）：数学与信息学院

项目起止时间：2019 年 5 月至 2021 年 4 月

填表日期：2019 年 5 月 29 日

华南农业大学科技处

二 O 一八年制

七、本合同签约各方

本合同各项内容真实、数据准确，不涉密，没有知识产权争议。承诺以本合同为有约束力协议，遵守有关规定，按计划认真开展研究工作，取得预期成果，并按时报送有关材料。若填报失实和违反规定，本人将承担全部责任。

项目负责人（签名）：张建利

2019 年5 月30日

乙方：学院（公章）

负责人（签名）：

2019 年 5 月 31 日

甲方：华南农业大学（公章）

代表人（签名）：

2019 年6 月11 日

附件7：

广东省普通高校特色创新类项目

自然科学类				
序号	项目编号	项目名称	负责人姓名	所属学校
1	2018KTSCX001	紫外/氯高级氧化技术对船舶压舱水污染物去除技术研究	张欣然	中山大学
2	2018KTSCX002	增强湿热地区绿墙耐候性的关键技术研究	萧蕾	华南理工大学
3	2018KTSCX003	环保无卤阻燃硬质聚氨酯泡沫塑料的结构、性能与阻燃机理研究	陈勇军	华南理工大学
4	2018KTSCX004	结构风致振动的现场实测及动力参数识别研究	余先锋	华南理工大学
5	2018KTSCX005	具有微层结构的聚甲基乙撑碳酸酯/纳米纤维素复合材料的结构与性能调控	蒋果	华南理工大学
6	2018KTSCX006	多参数的无芯片传感器研究	赖晓铮	华南理工大学
7	2018KTSCX007	双侧人工耳蜗植入者的空间听觉能力提升研究	孟庆林	华南理工大学
8	2018KTSCX008	耦合三维石墨烯/纳米零价铁与三维石墨烯/δ-MnO2复合材料对地下水中砷的吸附与氧化还原的协同去除机理	罗汉金	华南理工大学
9	2018KTSCX009	“水热-成型”RDF燃烧与酸性气体污染物调控的多尺度研究	唐玉婷	华南理工大学
10	2018KTSCX010	中药木荷中抗真菌活性成分的发现、作用机制及构效关系研究	刘百联	暨南大学
11	2018KTSCX011	低成本大面积有机太阳电池稳定阴极的研究	蔡婉珠	暨南大学
12	2018KTSCX012	血清近红外光谱判别分析用于乳腺癌的快速筛查	姚立军	暨南大学
13	2018KTSCX013	低维稳定型钙钛矿材料的理论计算与潜在应用	时婷婷	暨南大学
14	2018KTSCX014	新型TRK抑制剂的设计合成和构效关系研究	张章	暨南大学
15	2018KTSCX015	新型α1D-AR拮抗剂的发现、构效关系和抗良性前列腺增生活性研究	徐未	暨南大学
16	2018KTSCX016	互联网的移动恶意软件安全智能检测研究	官全龙	暨南大学
17	2018KTSCX017	应用黄芩苷保护妊娠糖尿病胚胎心脏发育的机制研究	王广	暨南大学
18	2018KTSCX018	辣木营养成分快速测定体系建立及高蛋白低抗营养新品种选育	骈瑞琪	华南农业大学
19	2018KTSCX019	植物精油微孔压电超声雾化机理研究	张建桃	华南农业大学
20	2018KTSCX020	柑橘容器育苗基质自动装填技术与装备研究	薛秀云	华南农业大学
21	2018KTSCX021	霉菌毒素压力下猪细胞蛋白质稳态研究	孙峪	华南农业大学

11.主持《“无人机及其在农业领域的应用”华农社区科普行活动》项目的立项通知及有关佐证材料

(4)

合同编号：K2019010201039

广州市科学技术协会

项目合同书

（科普经费类）

项目名称：城镇劳动者科学素质提升工程--和谐幸福社区科普行

子项目名称："无人机及其在农业领域的应用"华农社区科普行活动

项目类别：1.一次性专项经费项目☑

2.经常性专项业务费项目□

经办部门（处室）：广州市科学技术协会科学普及部

项目承担单位：华南农业大学

起止年限：2019 年 1 月到 2019 年 12 月

一、项目单位基本情况			
项目承担单位	华南农业大学	单位性质	国有
项目参加单位	无		
承担单位地址	广州市天河区五山路483号	邮政编码	510642
单位负责人	董梅	职称/职务	主任科员
联系电话	85285390	手机	13602414573
电子邮件	xswyh@scau.edu.cn	传真	020-85281885
项目负责人	张建桃	职称/职务	副教授/系副主任
联系电话	020-85285396	手机	13076759646
电子邮件	zhangjiantao@yeah.net	传真	020-85285393

二、项目团队主要参加人员情况			
姓名	工作单位	职务和职称	此项目的分工职责
文晟	华南农业大学	国家精准农业航空施药中心副主任/副教授	植保无人机技术科普
尹选春	华南农业大学	精准农业航空人工智能实验室主任/讲师	无人机智能控制技术科普
卢玉华	华南农业大学	讲师	无人机飞行动力学科普
曾家俊	华南农业大学	硕士研究生	无人机科普资源收集和整理

六、共同条款

（一）项目承担单位必须按要求编报项目执行情况和有关统计报表，及时上报项目归口管理部门，并配合市财政局、市科协对项目进行支出进度统计、绩效跟踪和评价等工作；项目归口管理部门按规定做好项目绩效跟踪和评价。

（二）任务执行过程中，如项目承担单位提出需调整任务内容或绩效目标，必须按照规定程序报市科协、市财政局审批。

（三）项目承担单位因某种原因（如：与可行性研究内容有出入、挪用经费、技术措施或某些条件不落实）不能按计划执行而主动要求中止任务时，应视不同情况，部分或全部退还所拨经费；项目承担单位未按财经法规列支且未主动提出中止任务的要求，市科协有权提出中止任务。

（四）项目承担单位承担任务所需经费应按本合同书中规定的经费支出范围开支，市科协有权监督项目经费使用情况或委托第三方对项目经费支出情况、项目绩效完成情况进行审计。

（五）合同书签订各方均负有相应的责任。若有争议或纠纷时，按有关法规和管理办法处理。

（六）由市科协专项经费全额支持的项目研究成果及其形成的知识产权归市科协所有，部分支持项目列明市科协权限。

（七）本合同书一式四份，广州市科协三份，项目承担单位一份。

七、合同签署各方

项目承担单位名称：华南农业大学　　开户名称：华南农业大学

开户银行：广州工行五山支行　　银行账号：3602 0026 0900 0310 520

法定代表人/委托代理人（签字）：

（单位公章）

2019 年 4 月 4 日

经办部门（处室）：

法定代表人/委托代理人（签字）：

（公章）

2019 年 4 月 19 日

12.主持《珠海湿地公园环保科普基地建设》项目的立项通知及有关佐证材料



13.主持《检疫处理无人机超低容量喷雾装置研究试验》项目的立项通知及有关佐证材料

HXKJHT2020[illegible]

项目编号：2019HK033

科研项目合作合同书

项目名称：检疫处理无人机超低容量喷雾装置研究试验

甲方：广州阿佩斯康生物科技有限公司

项目负责人：张九美

统一社会信用代码： 914440101MA59MX178M

乙方： 华南农业大学

项目负责人： 张建桃

统一社会信用代码：124400004554165634

乙方三份。

（本页无正文，为《科研项目合作合同书》之签署页）

甲方（盖章）：广州阿佩斯康生物科技有限公司

法定代表人／委托代理人：

项目负责人：（签名）

2020年5月8日

乙方（服务单位）（盖章）：华南农业大学

法定代表人／委托代理人：（签名）

项目负责人：（签名）

2020年1月8日

14. 主持华农温氏科技创新中心项目:《不确定需求下的生猪屠宰冷链配送路径优化研究》立项通知及有关佐证材料

合同编号: WS-2025-WSCX-JS-000129

技术开发（合作）合同

项目名称：不确定需求下的生猪屠宰冷链配送路径优化研究

项目类型：华农温氏科创中心人才项目

甲　　方：温氏食品集团股份有限公司

乙　　方：华南农业大学

丙　　方：温氏食品集团股份有限公司研究院

签订时间：2025 年 9 月 30 日

签订地点：广东省云浮市新兴县

有效期限：2025 年 5 月 1 日至 2027 年 4 月 30 日

人，丙方指定 郭红娟 为丙方项目联系人。项目联系人承担以下责任：

一方变更项目联系人的，应当及时以书面形式通知其他各方。未及时通知并影响本合同履行或造成损失的，应承担相应的责任。

第十八条 合作各方确定，出现下列情形，致使本合同的履行成为不必要或不可能的，可以解除本合同：

1. 因发生不可抗力和技术风险；

第十九条 合作各方因履行本合同而发生的争议，应协商、调解解决。协商、调解不成的，确定按以下第 2 种方式处理：

1. 提交云浮仲裁委员会仲裁；
2. 依法向新兴县人民法院起诉。

第二十条 本合同一式 四 份，具有同等法律效力。

第二十一条 本合同经合作各方签字盖章后生效。

甲方：温氏食品集团股份有限公司（盖章）

法定代表人/委托代理人：陈 [illegible]（签名）

2025 年 9 月 30 日

乙方：华南农业大学（技术合同专用章）

法定代表人/委托代理人：薛 [illegible]（签名）

2025 年 9 月 30 日

项目负责人：张建 [illegible]（签字）

丙方：温氏食品集团股份有限公司研究院（盖章）

法定代表人/委托代理人：[illegible]（签名）

2025 年 9 月 30 日

项目负责人：郭红娟（签字）

15.主参《精准农业中无人机作业关键装置研究及应用》项目的立项通知及有关佐证材料

编　　号:		专题编号:	20170117
技术领域:	农业装备(农业机械、设备及材料等)	专题名称:	无人机关键技术与应用

（广东科技微信公众号）（受理纸质材料二维码）

广东省科技计划项目
申报书

(技术开发及产业化类别)

1021752155

项目名称:	精准农业中无人机作业关键装置研究及应用				
专项资金类别:	前沿与关键技术创新				
业务类型:	无人智能技术				
申请单位:	华南农业大学				
通讯地址:	广东省-广州市-天河区 五山路483号				
邮政编码:	510642	单位电话:	020-38632819	传真:	020-85281885
项目负责人:	兰玉彬	联系电话:	020-85281421	手机:	13922707507
项目联系人:	尹选春	联系电话:	020-85281421	手机:	17817886297
电子邮箱:	xc_yin@scau.edu.cn				
县(区)主管:					
推荐单位:	华南农业大学				
申报日期:	2017 年 02 月 17 日				

广东省科学技术厅
二零一四年一月制

一、项目基本情况表

项目名称	精准农业中无人机作业关键装置研究及应用		
项目起止时间	2017 年 04 月 01 日 - 2020 年 03 月 31 日		
项目总经费预算	300.00 万元	申请经费资助	300.00 万元
课题研究方向	精准农业中无人机作业关键装置研究及应用		
社会经济目标	农作物种植及培育		

项目内容摘要:

项目针对我国精准农业航空中作业装备和核心技术研发不足的问题，研究无人机作业环境参数实时获取、多源信息实时融合等关键技术，研制无人机环境感知作业装备和机载智能喷洒系统，制定航空智能喷洒作业规程。无人机环境感知作业装备根据作物长势及病虫害信息生成精准变量施药处方图；智能喷洒系统根据变量施药处方图实现无人机精准变量施药。项目研究成果可为航空施药精准调控提供理论依据，为减少农药使用量提供技术支撑。

关键字(用；隔开):	植保无人机 ； 遥感与农情信息获取 ； 变量喷施 ； 实时融合技术 ； 农业智能装备

项目技术信息:

项目研究阶段	前期研究	技术来源	省内高校	技术领域	农业装备(农业机械、设备及材料等)
研究活动类型	应用研究	学科	机器人机械学		

预期成果形式:

新产品，新工艺，新装置，技术标准(国际标准、国家标准、行业标准、企业标准)，专利，计算机软件 ，论文论著，研究报告

项目已受财政资金资助情况:

无

简要说明：（限100字）	无

其它需要说明的问题（限100字）:

无

本项目是否涉及实验动物：□是 ■否

7081759 2155

六、项目组人员情况

项目负责人

序号	姓名	职称	职务	最高学位	现从事专业	所在单位	身份证号码	在本项目中承担的工作任务	签名
1	兰玉彬	教授	“千人计划”国家特聘专家	博士	精准农业航空	华南农业大学	479002889	总体项目设计、关键技术研究	

主要参与人员

序号	姓名	职称	职务	学位	现从事专业	所在单位	身份证号码	在本项目中承担的工作任务	签名
1	尹选春	讲师	无	博士	农业电气化与自动化	华南农业大学	511223197904047812	基于触觉反馈的无人机控制技术研究与部件开发	
2	杨秀丽	讲师	无	博士	农业电气化与自动化	华南农业大学	142331197105171048	遥感信息获取及解析关键技术研究	
3	张建桃	副教授	系副主任	博士	农业电气化与自动化	华南农业大学	44010619781223189X	变量控制理论研究，变量施药控制系统的研发	
4	卢玉华	讲师	无	博士	计算流体力学、农业航空药液喷施效果研究	华南农业大学	440105197812290033	旋翼风场下雾滴飘移沉积规律研究	
5	朱秋阳	工程师	总经理	其他	无人机设计与开发	广州天翔航空科技有限公司	420103198708173732	协助项目申报单位进行关键部件及系统的产业化生产、销售，撰写相关技术规程	
						深圳高科新		协助项目申报单位进行关键部件及系	

7021759215

6	付维	工程师	董事 副总经理	学士	无人机研发	农技术有限公司	210102197711223016	统的产业化生产、销售及推广示范，并撰写相关技术规程	
7	王先菊	副教授	无	博士	凝聚态物理	华南农业大学	430703196911241660	雾滴在作物冠层的润湿铺展理论研究	
8	邓继忠	教授	无	博士	农业航空遥感	华南农业大学	650103196312103230X	基于处方图生成技术的作业感知关键装备的研发	
9	文晟	副教授	无	博士	计算流体力学、精准航空喷雾技术	华南农业大学	430102197405160513	多源信息融合技术研究，智能化喷洒系统的研发	
10	邓小玲	副教授	无	博士	电子信息工程	华南农业大学	445122197807180420	遥感信息获取技术研究，作业感知装备的研发	
11	漆海霞	副教授	系副主任	博士	自动化	华南农业大学	610103196903213708	多源遥感信息获取及融合技术研究	
12	张建瓠	副教授	无	博士	农业工程	华南农业大学	320502196507203010	航空专用喷嘴子系统的设计与优化	
13	王国宾	未取得	无	硕士	农业机械化工程	华南农业大学	371202199101044512	航空施药效果检测技术的研究	
14	张海艳	未取得	无	学士	农业机械化工程	华南农业大学	150430199205260767	航空专用雾化喷嘴的设计与试验	
15	姚伟祥	未取得	无	学士	农业机械化工程	华南农业大学	130732199309251836	药效及施药装备的田间试验与测试	
16	汤镇安	未取得	无	学士	农业电气化与自动化	华南农业大学	440184199404136314	变量喷施系统的试验测试	

7021759225

16.主参国家自然科学基金《触觉感知遥操控无人机精准变量施药》立项通知及有关佐证材料

关于国家自然科学基金资助项目批准及有关事项的通知

尹选春　先生/女士：

根据《国家自然科学基金条例》的规定和专家评审意见，国家自然科学基金委员会（以下简称自然科学基金委）决定批准资助您的申请项目。项目批准号：61773171，项目名称：触觉感知遥操控无人机精准变量施药，直接费用：64.00万元，项目起止年月：2018年01月至2021年12月，有关项目的评审意见及修改意见附后。

请尽早登录科学基金网络信息系统（https://isisn.nsfc.gov.cn），获取《国家自然科学基金资助项目计划书》（以下简称计划书）并按要求填写。对于有修改意见的项目，请按修改意见及时调整计划书相关内容；如对修改意见有异议，须在计划书电子版报送截止日期前提出。**注意：请严格按照《国家自然科学基金资助项目资金管理办法》填写计划书的资金预算表，其中，劳务费、专家咨询费科目所列金额与申请书相比不得调增。**

计划书电子版通过科学基金网络信息系统（https://isisn.nsfc.gov.cn）上传，由依托单位审核后提交至自然科学基金委进行审核。审核未通过者，返回修改后再行提交；审核通过者，打印为计划书纸质版（一式两份，双面打印），由依托单位审核并加盖单位公章后报送至自然科学基金委项目材料接收工作组。计划书电子版和纸质版内容应当保证一致。

向自然科学基金委提交和报送计划书截止时间节点如下：

1、提交计划书电子版截止时间为**2017年9月11日16点**（视为计划书正式提交时间）；

2、提交计划书电子修改版截止时间为**2017年9月18日16点**；

3、报送计划书纸质版截止时间为**2017年9月26日16点**。

请按照以上规定及时提交计划书电子版，并报送计划书纸质版，未说明理由且逾期不报计划书者，视为自动放弃接受资助。

附件：项目评审意见及修改意见表

国家自然科学基金委员会

信息科学部

2017年8月17日

申请代码	F030601
受理部门	
收件日期	
受理编号	6177020045



国家自然科学基金

申 请 书

（2 0 1 7 版）

NSFC 2017

资助类别： 面上项目

亚类说明：

附注说明： 常规面上项目

项目名称： 触觉感知遥操控无人机精准变量施药

申 请 人： 尹选春 **电 话：** 17817886297

依托单位： 华南农业大学

通讯地址： 广东省广州市天河区 五山路483号

邮政编码： 510642 **单位电话：** 020-85280070

电子邮箱： xc_yin@scau.edu.cn

申报日期： 2017年02月07日

国家自然科学基金委员会

项目组主要参与者（注：项目组主要参与者不包括项目申请人）

编号	姓名	出生年月	性别	职 称	学 位	单位名称	电话	电子邮箱	证件号码	每年工作时间（月）
1	张建桃	1978-12-23	男	副教授	博士	华南农业大学	02085285396	zhangjiantao@yeah.net	44010619781223189X	6
2	韩宇星	1983-08-15	女	教授	博士	华南农业大学	02085281421	yuxinghan@scau.edu.cn	230103198308157324	6
3	欧阳帆	1986-03-24	男	助理研究员	博士	华南农业大学	02085288421	151229643@qq.com	440106198603241818	6
4	卢玉华	1978-12-29	男	讲师	博士	华南农业大学	02085286120	luyuhua@scau.edu.cn	440105197812290033	6
5	黎志宏	1989-10-24	男	助理实验师	硕士	华南农业大学	02082581241	lizhihong@scau.edu	44010219891024065X	6
6	陈盛德	1989-12-04	男	博士生	硕士	华南农业大学	18819492958	163145190@qq.com	421126198912047210	10
7	杨汶泊	1990-09-02	男	硕士生	学士	华南农业大学	17761660862	ywb3572@163.com	412723199009022516	10
8	黄晓宇	1996-03-18	男	硕士生	学士	华南农业大学	18320728665	824029495@qq.com	411421199603180031	10

总人数	高级	中级	初级	博士后	博士生	硕士生
9	2	3	1	0	1	2

NSFC 2017

17.主参国家自然科学基金《基于棉花冠层特征与沉积量预测模型的无人机精确喷施控制研究》项目的立项通知及有关佐证材料

国家自然科学基金资助项目批准通知

（预算制项目）

文晟　先生/女士：

根据《国家自然科学基金条例》、相关项目管理办法规定和专家评审意见，国家自然科学基金委员会（以下简称自然科学基金委）决定资助您申请的项目。项目批准号：32271985，项目名称：基于棉花冠层特征与沉积量预测模型的无人机精确喷施控制研究，直接费用：54.00万元，项目起止年月：2023年01月至 2026年 12月，有关项目的评审意见及修改意见附后。

请您尽快登录科学基金网络信息系统（https://isisn.nsfc.gov.cn），**认真阅读《国家自然科学基金资助项目计划书填报说明》并按要求填写《国家自然科学基金资助项目计划书》（以下简称计划书）**。对于有修改意见的项目，请您按修改意见及时调整计划书相关内容；如您对修改意见有异议，须在电子版计划书报送截止日期前向相关科学处提出。

请您将电子版计划书通过科学基金网络信息系统（https://isisn.nsfc.gov.cn）提交，由依托单位审核后提交至自然科学基金委。自然科学基金委审核未通过者，将退回的电子版计划书修改后再行提交；审核通过者，打印纸质版计划书（一式两份，双面打印）并在项目负责人承诺栏签字，由依托单位科研、财务管理等部门审核、签章并在承诺栏加盖依托单位公章，且将申请书纸质签字盖章页订在其中一份计划书之后，一并报送至自然科学基金委项目材料接收工作组。纸质版计划书应当保证与审核通过的电子版计划书内容一致。**自然科学基金委将对申请书纸质签字盖章页进行审核，对存在问题的，允许依托单位进行一次修改或补齐。**

向自然科学基金委提交电子版计划书、报送纸质版计划书并补交申请书纸质签字盖章页截止时间节点如下：

1. **2022年10月8日16点：**提交电子版计划书的截止时间；

2. **2022年10月14日16点：**提交修改后电子版计划书的截止时间；

3. **2022年10月19日：**报送纸质版计划书（一式两份，其中一份包含申请书纸质签字盖章页）的截止时间。

4. **2022年10月28日：**报送修改后的申请书纸质签字盖章页的截止时间。

申请代码	C1301
接收部门	
收件日期	
接收编号	3227150400

3227150400

国家自然科学基金

申 请 书

（2 0 2 2 版）

NSFC 2022

资助类别： 面上项目

亚类说明：

附注说明：

项目名称： 基于棉花冠层特征与沉积量预测模型的无人机精确喷施控制研究

申 请 人： 文晟 **电 话：** 020-85572761

依托单位： 华南农业大学

通讯地址： 广东省广州市五山路华南农业大学工程学院

邮政编码： 510642 **单位电话：** 020-85280070

电子邮箱： vincen@scau.edu.cn

填写日期： 2022年02月06日

国家自然科学基金委员会

主要参与者（注：主要参与者不包括项目申请人）

编号	姓名	出生年月	性别	职 称	学 位	工作单位	项目分工	电话	证件号码
1	张建桃	1978-12-23	男	副教授	博士	华南农业大学	深度神经网络算法研究	02085285396	4**********X
2	卢玉华	1978-12-29	男	讲师	博士	华南农业大学	旋翼风场流体力学研究		4**********3
3	黎志宏	1989-10-24	男	实验师	硕士	华南农业大学	无人机实验与数据分析		4**********X

总人数	高级	中级	初级	博士后	博士生	硕士生
9	2	2	0	0	1	4

NSFC 2022

三、论文、著作等

1. 检索证明

SCAULIB202405422

检索证明

根据委托人提供的论文材料，委托人**华南农业大学数学与信息学院 张建桃** 2 篇论文收录情况如下表。

序号	论文名称	发表刊物及发表的年月卷期/页码等	作者排名	论文等级	作者文中单位	收录情况	影响因子	中科院大类分区
1	Effects of temperature and humidity on the contact angle of pesticide droplets on rice leaf surfaces	JOURNAL OF PESTICIDE SCIENCE 出版年：2022 卷期：47 2 页码：59-68 文献号： 文献类型：Article	第一作者	B 类	华南农业大学	SCI	IF2-year=2.4 IF5-year=2.3 （2022）	农林科学 4 区 Top 期刊：否 （2022）
2	Application of artificial neural network (ANN) and response surface methodology (RSM) for modeling and optimization of the contact angle of rice leaf surfaces	ACTA PHYSIOLOGIAE PLANTARUM 出版年：2020 卷期：42 4 页码：- 文献号：51 文献类型：Article	第一作者	B 类	华南农业大学	SCI	IF2-year=2.354 IF5-year=2.711 （2020）	生物学 4 区 Top 期刊：否 （2020）

说明：论文等级和中科院大类分区按《华南农业大学学术论文评价方案（试行）》划分。

报告免责声明:如未盖章,报告无效

检索员：张进

华南农业大学图书馆

华南农业大学图书馆SCAULIB202405422
华南农业大学图书馆 信息检索专用章

SCAULIB202519397

检索证明

根据委托人提供的论文材料，委托人**华南农业大学数学与信息学院 张建桃** 1 篇论文收录情况如下表。

序号	论文名称	发表刊物及发表的年月卷期/页码等	作者排名	论文等级	作者文中单位	收录情况	影响因子	中科院大类分区
1	A Human Finger-Inspired Shape-Locking Pneumatic Gripper Enabled by Folding Laminar Jamming Structure	IEEE-ASME TRANSACTIONS ON MECHATRONICS 出版年：2024 出版日期：OCT 卷期：29 5 页码：3626-3637 文献类型：Article	共同通讯作者（倒数第一）	T2类	College of Mathematics and Informatics, South China Agricultural University	SCI	IF2-year=7.3 IF5-year=7.1 （2024）	工程技术 1区 Top 期刊：是（2025）

说明：论文等级和中科院大类分区按《华南农业大学学术论文评价方案（试行）》划分。

报告免责声明:如未盖章,报告无效

检索员：张洪

华南农业大学图书馆

2025-07-17

华南农业大学图书馆SCAULIB202519397

SCAULIB202405438

检索证明

根据委托人提供的论文材料，委托人**华南农业大学数学与信息学院 张建桃** 3 篇论文收录情况如下表。

序号	论文名称	发表刊物及发表的年月卷期/页码等	作者排名	论文等级	作者文中单位	收录情况	影响因子	中科院大类分区
1	Origami Improved Dielectric Elastomer Actuation for Tunable Lens	IEEE TRANSACTIONS ON INSTRUMENTATION AND MEASUREMENT 出版年：2022 卷期：71 页码：- 文献号：7502709 文献类型：Article	共同通讯作者（倒数第一）	A 类	华南农业大学	SCI	IF2-year=5.6 IF5-year=5.4 （2022）	工程技术 2 区 Top 期刊：否 （2022）
2	Single-rotor UAV flow field simulation using generative adversarial networks	COMPUTERS AND ELECTRONICS IN AGRICULTURE 出版年：2019 卷期：167 页码：- 文献号：105004 文献类型：Article	通讯作者	A 类	华南农业大学	SCI	IF2-year=3.858 IF5-year=4.008 （2019）	农林科学 2 区 Top 期刊：是 （2019）
3	FLUID-SOLID COUPLING AND EXPERIMENTAL REALIZATION OF A PIEZOELECTRIC ATOMIZER UNDER STANDING-WAVE RESONANCE	APPLIED ENGINEERING IN AGRICULTURE 出版年：2016 卷期：32 3 页码：327-340 文献号： 文献类型：Article	通讯作者	B 类	华南农业大学	SCI	IF2-year=0.505 IF5-year=0.667 （2016）	农林科学 4 区 Top 期刊：否 （2016）

华南农业大学图书馆SCAULIB202405438
华南农业大学图书馆 信息检索专用章

说明：论文等级和中科院大类分区按《华南农业大学学术论文评价方案（试行）》划分。

报告免责声明:如未盖章,报告无效

检索员：卢炳卫

华南农业大学图书馆

2024-03-04

华南农业大学图书馆SCAULIB20240438

SCAULIB202405679

检索证明

根据委托人提供的论文材料，委托人**华南农业大学数学与信息学院 张建桃** 1 篇论文收录情况如下表。

序号	论文名称	发表刊物及发表的年月卷期/页码等	作者排名	论文等级	作者文中单位	收录情况	影响因子	中科院大类分区
1	An improved YOLO model for detecting trees suffering from pine wilt disease at different stages of infection	REMOTE SENSING LETTERS 出版年：2023 卷期：14 2 页码：114-123 文献号： 文献类型：Article	通讯作者	B 类	华南农业大学	SCI	IF2-year=2.3 IF5-year=2.4 （2022）	地球科学 4 区 Top 期刊：否 （2023）

说明：论文等级和中科院大类分区按《华南农业大学学术论文评价方案（试行）》划分。

报告免责声明:如未盖章,报告无效

检索员：张进

华南农业大学图书馆

2024-03-13

华南农业大学图书馆SCAULIB202405679

2. 以第一作者发表本专业论文情况

2.1 长春花感染柑橘黄龙病菌微波热处理防控效果

《中文核心期刊要目总览》收录
Ei Compendex(核心版)收录
百种中国杰出学术期刊
RCCSE中国权威学术期刊

ISSN 1002-6819
CN 11-2047/S
CODEN NGOXEO
www.tcsae.org

农业工程学报

NONGYE GONGCHENG XUEBAO | TRANSACTIONS OF THE CHINESE SOCIETY OF AGRICULTURAL ENGINEERING

2024年 第40卷 Vol. 40 03



农 业 工 程 学 报

2024 年 2 月第 3 期 （总第 476 期） 第 40 卷

目 次

· 专论与综述 ·

根区土壤氧气检测技术与方法研究进展 …… 周海洋，孙卿峰，夏鹏凯，关 鹏，赵燕东，郑一力（1）
微藻在农业可持续发展中的应用研究进展 …… 赵 江，侯 琤，沈 峥，张亚雷（14）

· 农业装备工程与机械化 ·

2BP-2000 型水稻育秧播种机分盘装置研制 …… 谢方平，杨 靖，符志勇，刘大为，龚 明，程乐根（26）
油菜高速直播机开畦沟装置刀组优化与试验 …… 王立宗，廖庆喜，张子龙，李蒙良，张青松，王 磊，廖宜涛（37）
顶钵-夹茎组合式取苗装置设计与试验 …… 张 妮，张国忠，付建伟，刘婉茹，陈立明，唐楠锐（50）
偏移剪叉式油茶果收集装置设计与试验 …… 李正超，唐乐为，吴明亮，张诗怡，张慧宇（62）
旋转剪切式青花椒采摘装置设计与试验
…… 杨 玲，张 原，何志远，李守太，蒲应俊，陈维汉，杨 仕，杨明金（72）

· 农业水土工程 ·

多因素耦合的光伏水泵提水系统配置优化方法 …… 赵 航，朱德兰，张 锐，纳扎罗夫·胡代贝尔迪，柳昌新（84）
不同类型重构土壤水分运移特征 …… 郭拿拿，黄明斌（94）
黑土长缓坡地形与横垄对土壤有机碳空间分异的交互作用
…… 李雪亮，张晴雯，李孟妮，石玉龙，于博威，荆雪锴，蒋嫘可，刘国成（103）
松嫩平原不同耕作模式与秸秆还田量对土壤磷组分及大豆产量的影响
…… 王 蒙，付 强，侯仁杰，李天霄，薛 平（114）
碎石含量对三峡库区坡耕地土壤氮磷流失特征的影响
…… 赵冰琴，胡鑫凯，高儒章，施伟豪，张兴凤，朱万庆，夏振尧，许文年（127）
大规模灌溉对海河流域气候影响模拟研究 …… 桂云鹏，赵 勇，杨明祥，王庆明，翟家齐（138）
乌兰布和荒漠绿洲过渡带白刺灌丛沙堆防风效应风洞模拟 …… 智 丹，王京学，肖辉杰，辛智鸣，李俊然（147）

· 农业信息与电气技术 ·

基于目标检测仔猪乳头计数及乳房形态评估方法 …… 李熙雅，尹 令，黄文杰，吴珍芳，蔡更元，田绪红（156）
基于改进 ConvNeXt 模型的黄羽鸡表皮层黑色素智能分级方法 …… 肖德琴，陈芳玲，刘又夫，谢青梅，张新珩（165）
构建 VED-SegNet 分割模型提取鱼类表型比例 …… 李健源，柳春娜，卢晓春，王鲁海，刘 轶，卢 佳（175）
基于迁移学习的苹果落叶病识别与应用 …… 郭惠萍，曹亚州，王晨思，荣麟瑞，李 怡，王霆伟，杨福增（184）
基于改进 HRNet 的遥感影像冬小麦语义分割方法 …… 李旭青，吴冬雪，王玉博，陈文博，顾会涛（193）

面向葡萄知识图谱构建的多特征融合命名实体识别 …… 聂啸林，张礼麟，牛当当，吴华瑞，朱华吉，张宏鸣（201）
长春花感染柑橘黄龙病菌微波热处理防控效果 …… 张建桃，刘杰帆，梁家茵，刘广彬，郑永钦，许美容（211）
基于分焦平面偏振成像的冬青卫矛含水率快速无损检测
…… 徐　翔，姬业钦，陈志坚，刘增辉，孙　博，华灯鑫（219）

·农业生物环境与能源工程·

基于 LIO-SAM 建图和激光视觉融合定位的温室自主行走系统 …… 孙国祥，黄银锋，汪小旦，袁云鹏，陈光宇（227）
Venlo 型温室柱脚螺栓节点力学性能 …… 李雄彦，徐　航，徐开亮，闫冬梅，张秋生，曹　楠（240）
肉鸡平养鸡舍自走式粪污清收装袋一体机研制
…… 李许杰，闫锋欣，胡　凯，何　鑫，马泽峰，袁青妍，MIRZOEV Shamsullo Izatovich（251）
屋顶光伏—土壤源热泵系统在不同气候区分娩猪舍的应用 …… 张长兴，罗明仙，路希正，许　冲，彭冬根（262）
增氧条件下粉绿狐尾藻的氮磷吸收特征 …… 张文萍，蒋　易，张鑫全，文清柏，李汉常，谭　歆，王润贤（271）

·土地保障与生态安全·

规划管控约束下耕地细碎化评价与整治分区 …… 魏　鹏，余　敦，胡宜之，胡海洋，孙聪康（283）
基于反现实情景模拟的耕地“进出平衡”政策绩效预测 …… 章礼杰，邹镰钊，江舒静（294）

·农产品加工工程·

基于改进 YOLOv7-ByteTrack 的干制哈密大枣缺陷检测与计数系统
…… 刘　鑫，马本学，李玉洁，陈金成，喻国威（303）
运用多维视角融合视觉转换器的食品气调枕形包装漏气检测 …… 郭向东，刘天真，李聪聪，滕桂法（313）

·研究速报·

安徽矾矿土壤重金属污染源解析模型对比与优选
…… 周蓓蓓，李文倩，郭　江，陈晓鹏，干　彬，杨玉姣，杨　强，范东亮，杨　勰，杨泽昊，安凤秋（321）
1982—2020 年乌兰县植被 NPP 时空动态特征及驱动力量化分析
…… 刘　辉，宋孝玉，王荣荣，祝德名，何　希，刘斯琪（328）

期刊基本参数：CN 11-2047/S*1985*s*16*334*zh*P* ￥80.00*260*33*2024-02

✦✲✦✲✦✲✦✲✦✲✦✲✦✲✦✲✦✲✦✲✦✲✦✲✲

致谢：感谢农业农村部规划设计研究院设施农业研究所提供的封面图片“华发现代农业粤港澳示范基地智能温室内景实拍图”

长春花感染柑橘黄龙病菌微波热处理防控效果

张建桃[1]，刘杰帆[1]，梁家茵[2]，刘广彬[1]，郑永钦[2]，许美容[2※]
（1. 华南农业大学数学与信息学院，广州 510642；2. 华南农业大学柑桔黄龙病研究室，广州 510642）

摘 要：为探索黄龙病防治途径，开展微波热处理对黄龙病的防控效果研究。该研究搭建了微波热处理平台，对长春花微波热处理参数（转盘转速、单个磁控管的微波功率、磁控管数量）进行优化，并用优化后的参数组合对感病长春花进行热处理，处理后 90 d 内跟踪检测长春花叶片中黄龙病菌的浓度、淀粉和类黄酮的含量。结果表明，长春花微波热处理的最优参数组合为单个磁控管的微波功率 150 W、3 个磁控管、转速 15 r/min；热处理 90 d 后，感病长春花叶片中的黄龙病菌 C_t 值（阈值循环数，该值低于 32 时为阳性）由阳性 (17.01 ± 0.97) 转至近阴性（31.91 ± 2.35），病菌浓度下降了 99.98%，淀粉含量和类黄酮含量恢复至正常水平，植株的活性恢复较好。研究表明，微波热处理有效抑制植物体内的黄龙病菌，可为黄龙病的规模化防治提供新思路。

关键词：病害；微波；热处理；黄龙病；长春花；防治效果
doi：10.11975/j.issn.1002-6819.202307265
中图分类号：S432 **文献标志码：**A **文章编号：**1002-6819(2024)-03-0211-08

张建桃，刘杰帆，梁家茵，等. 长春花感染柑橘黄龙病菌微波热处理防控效果[J]. 农业工程学报，2024，40(3)：211-218. doi: 10.11975/j.issn.1002-6819.202307265 http://www.tcsae.org
ZHANG Jiantao, LIU Jiefan, LIANG Jiayin, et al. Effect of microwave heat treatment in eliminating "*Candidatus* Liberibacter asiaticus" on periwinkle infected with Citrus Huanglongbing[J]. Transactions of the Chinese Society of Agricultural Engineering (Transactions of the CSAE), 2024, 40(3): 211-218. (in Chinese with English abstract) doi: 10.11975/j.issn.1002-6819.202307265 http://www.tcsae.org

0 引 言

黄龙病（Huanglongbing，HLB）是柑橘生产中最具毁灭性的传染性病害，能够侵染几乎所有商业栽培品种，严重影响柑橘品质和产量，制约了中国乃至世界柑橘产业的可持续发展[1−2]。该病的病原体是一种寄生在韧皮部的革兰氏阴性细菌（“*Candidatus* Liberibacter spp.”），主要通过柑橘木虱和带病接穗嫁接进行传播[3]。黄龙病菌体外培养技术的缺乏，严重限制了黄龙病的防控和病原生物学研究[4]，而长春花（*Catharanthus roseus*）作为研究黄龙病的模式寄主，具有生长周期短、易栽培、感染黄龙病后发病时间短、症状明显等特点[5]，因此许多学者以感染黄龙病菌的长春花为研究对象。目前无特效药可治愈黄龙病，针对该病的防控仍基本沿用林孔湘于 1963 年提出的三项措施：灭杀柑橘木虱、使用无病繁殖材料、及时铲除病原（树）[6]。其中灭杀柑橘木虱是关键举措，主要采用化学药物进行防治[7]，但长期使用药物容易使柑橘木虱产生耐药性，也易造成环境污染。长远考虑人体健康和环境安全，应大力推广和发展黄龙病的物理防治技术。

黄龙病热处理防治的主要原理是利用外界的传热介质，如热水、湿热蒸汽、热空气等，向感染黄龙病的植株传递足够热量，在不显著影响其正常生长的前提下，使植株中的黄龙病菌钝化或者死亡，直到症状改善或者消失[8]。YANG 等[9] 结合 45 ℃ 温室热疗与磺胺类抗生素化疗的方式，对感染黄龙病的柑橘树进行处理，处理后病菌浓度下降了 64.43 %。贾志成等[10] 对染病柑橘树进行湿热蒸汽处理，能有效促进植物生命力的恢复，且明显降低黄龙病菌的浓度。张建桃等[11] 对感染黄龙病的柑橘树进行快速热空气处理，黄龙病菌的浓度平均降低了 80.28 %。DING 等[12] 研究了不同温度下热处理或四环素对黄龙病菌分子机制的影响，发现两种方式均可诱导长春花体内黄龙病菌基因组中的噬菌体转化，进而导致病菌裂解，减轻黄龙病的症状。

上述研究表明，热处理能一定程度防治黄龙病，但以水或空气作为传热介质存在传热效率低下、能耗高、局限于表皮加热等问题，难以实现大规模推广。微波加热具有时间短、可瞬时控制、节能、穿透性强等优势，已被广泛应用于植物和种子的脱毒中。ABDELRHIM 等[13] 通过试验证明微波处理可降低因黑曲霉和尖孢镰孢引起的洋葱幼苗猝倒病发病率，并显著提高洋葱种子的发芽率和活力指数。HILTON 等[14] 结合微波辐射和微波吸收剂，消杀山核桃接穗中的革兰氏阴性杆状细菌，能有效降低接穗中细菌的阳性率，同时不影响植物的生长。这

收稿日期：2023-07-27 修订日期：2024-01-15
基金项目：广州市科技计划重点研发计划项目（2023B03J1362）；广东省普通高校特色创新类项目（2019KZDZX1002）；华南农业大学新农村发展研究院农业科技合作共建项目（2021XNYNYKJHZGJ034）；恩平市农村科技特派员项目
作者简介：张建桃，博士，副教授，研究方向为精细农业。
E-mail：zhangjiantao@yeah.net
※通信作者：许美容，博士，副教授，研究方向为柑橘黄龙病的寄主–病原–介体互作、柑橘病原分子生物学及病原流行学等。
E-mail：meirongxu@scau.edu.cn

中国知网 https://www.cnki.net

些研究表明微波可用于植物病害的防治，但对黄龙病的抑制效果研究尚未见报道。

本研究旨在探究微波热处理对黄龙病的抑制效果。首先对长春花植株进行单因素试验和正交试验，确定微波热处理的最优参数组合，接着以该组合对感染黄龙病的长春花进行微波热处理，处理后使用实时荧光定量 PCR 定期检测植株叶片中的病菌浓度、淀粉与类黄酮两种代谢物的含量变化，以期为黄龙病的微波热处理提供依据。

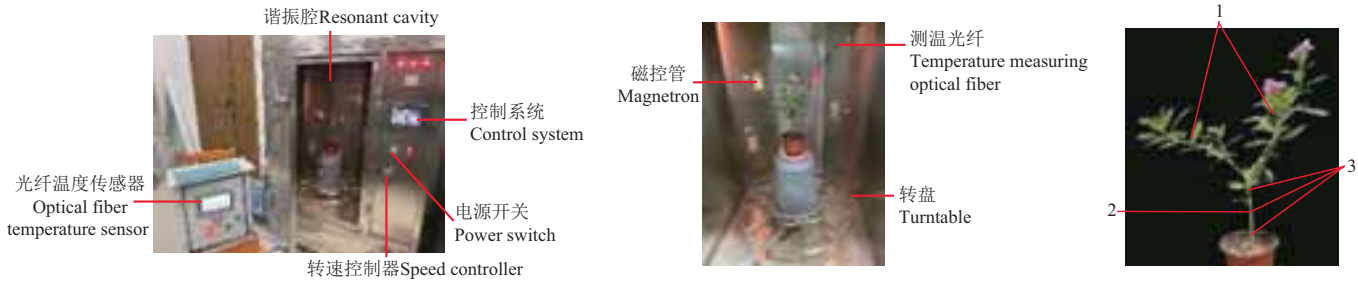
1 试验装置与方法

1.1 供试材料

试验所用的长春花种植于华南农业大学柑橘黄龙病研究室的防虫网室内，正常水肥管理。待植株长至 18～20 cm 时，选用生长状况一致的健康长春花进行微波热处理参数优化试验，以确定最优参数组合。另外，参照陈俊甫等[15]的方法，将感染黄龙病的长春花叶片以顶接的方式嫁接在健康长春花上，待植株出现斑驳黄化症状，并经实时荧光 PCR 检测出阈值循环数结果为阳性（C_t < 30）后[16]，开展微波热处理的防控效果试验。

1.2 微波热处理试验平台与热处理流程

微波热处理平台由工业微波炉和温度采集系统组成（图 1）。工业微波炉型号为 CNWB-4X（广州万程微波设备有限公司），箱体尺寸为 700 mm×700 mm×1 100 mm（长×宽×高），主要由控制面板、磁控管、转动系统、单元加热箱、带扼流装置微波门、时间控制系统、排湿排热系统、温控系统等部件组成。可调节的参数包括转盘转速、磁控管数量和单个磁控管的微波功率（后文简称微波功率），其中磁控管共有 4 个，每个磁控管的工作频率为 2.45 GHz，最大功率为 1 kW，总输出功率为 0～4 kW；转盘转速在 0～20 r/min 范围内可调。温度采集系统由 10 通道 YT-PZB 系列光纤温度传感器（西安固泰传感器有限公司）组成，其中温感探头的外形尺寸为 Φ2.1 mm×20 mm（宽×长），测温范围为−40～210 ℃，精度为 0.1 ℃，测量时间 t < 0.5 s。



a. 微波加热及测温系统
a. System of microwave heating and temperature measurement

b. 谐振腔内装置
b. Device of resonant cavity

c. 春花部位
c. Periwinkle position

1. 侧枝；2. 主干；3. 测温点。
1. Lateral branch; 2. Trunk; 3. Temperature measuring point.

图 1 微波热处理平台和长春花部位

Fig.1 Microwave heat treatment platform and periwinkle position

植株微波热处理流程：用散热性良好的胶带，将 3 个光纤温度传感器的探头分别固定在植株主干的顶、中、底 3 个部位，将植株放置于微波炉腔正中央，设置好参数组合后关闭柜门，参考张建桃等[17]处理健康柑橘芽条的方法，待植株温度上升到 48 ℃ 后停止加热。

1.3 微波热处理参数优化单因素试验

为初步确定微波热处理参数的取值范围，分别对转盘转速、微波功率、磁控管数量进行单因素试验。在转盘转速的单因素试验中，固定微波功率 150 W 和 3 个磁控管，转速取值 0、5、10、15、20 r/min；在微波功率的单因素试验中，固定 2 个磁控管和转速 15 r/min，微波功率取值 150、250、350、450 W；在磁控管数量的单因素试验中，固定微波功率 200 W 和转速 15 r/min，磁控管数量取值 1、2、3、4。每次试验取 3 个测温点中的最高值，重复 3 次，结果取平均值。

1.4 微波热处理参数优化正交试验

在单因素试验初步筛选的参数基础上，进行 3 因素 3 水平的正交试验（表 1），试验采用 3 个评价指标：植株过热程度、植株温度均匀度和植株活性。植株过热程度表示试验植株的最高温度减去 48 ℃，其数值越高说明植株过热越严重。

表 1 正交试验表及因素水平值

Table 1 Orthogonal experiment table and factor levels

试验编号 Test number	A 转盘 Turntable		B 微波 Microwave		C 磁控管 Magnetrons		D 空列 Blank column
	转速 Rotating speed/(r·min^{-1})	水平值 Horizontal value	功率 Power/W	水平值 Horizontal value	数量 Number	水平值 Horizontal value	
1	10	1	150	1	2	1	1
2	10	1	200	2	3	2	2
3	10	1	250	3	4	3	3
4	15	2	150	1	3	2	3
5	15	2	200	2	4	3	1
6	15	2	250	3	2	1	2
7	20	3	150	1	4	3	2
8	20	3	200	2	2	1	3
9	20	3	250	3	3	2	2

植株温度均匀度用 3 个测温点的温度极差衡量，其数值越低说明植株受热更均匀。植株活性评价见表 2：分别从植株的主干、侧枝及主干的新生叶片面积 3 个方面进行评分，植株活性评价得分为 3 个方面的分数之和，满分为 100 分；主干部分是植株能否快速生长新叶及侧

中国知网 https://www.cnki.net

枝的关键部位，该项评分最高为 80；侧枝部分容易因过热而损伤，但对植株活性不会造成太大影响，故该项评分最高为 6；主干的新生叶片面积反映植株的活性恢复程度，该项评分最高为 14；分别在热处理后的 5 d 和 20 d 对植株进行评分，计算两次评分的均值。每个处理试验重复 3 次，结果取均值。

表 2　长春花活性评价

Table 2　Activity evaluation of periwincle plants

主干 Trunk		侧枝 Collateral		主干新叶面积占比 Proportion of new leaf area on trunk	
受损比例 Damage ratio/%	分数 Score	受损比例 Damage ratio/%	分数 Score	比值 Ratio/%	分数 Score
＜30	80	＜20	6	＞80	14
30～50	60	20～40	5	＞60～80	12
＞50～70	40	＞40～60	4	＞40～60	8
＞70～80	20	＞60～80	3	20～40	4
＞80	0	＞80	2	＜20	2

注：主干满分 80，侧枝满分 6，主干新叶面积占比满分为 14。
Note:The full score of trunk is 80. The full score of lateral branches is 6. The full score of proportion of new leaf area on trunk is 14.

1.5　长春花叶片代谢物的提取与测定

采用文献 [18] 的方法，对植株的淀粉与类黄酮两种代谢物进行提取与测定。先用淀粉含量检测试剂盒（型号 BC0705，北京索莱宝科技有限公司）与植物类黄酮含量检测试剂盒（型号 BC1175，北京索莱宝科技有限公司）分别制作待测液与标准液，再使用酶标仪 BioTek Synergy H1（美国 BioTek 公司）分别测定待测液与标准液的吸光度，根据吸光度进行两种代谢物含量的换算。

1.6　长春花叶片的 DNA 提取

将长春花叶片的叶中脉切碎，并取 0.1 g 进行 DNA 的提取。选用植物 DNA 提取试剂盒 HP Plant DNA Kit（型号 2 485-02，OMEGA BIO-TEK 公司）提取植物总 DNA。使用超微量紫外-可见光分光光度计 NanoDrop one (Thermo Fisher Scientific 公司) 对所提取的 DNA 样品进行浓度和纯度的测定，确保 DNA 的浓度不低于 50 ng/μL，并保存于−20 ℃ 备用。

1.7　CLas（黄龙病菌亚洲种）的实时荧光 PCR 检测

采用 BAO 等[19] 测量方法，对 DNA 样品进行 SYBR 实时荧光 PCR 检测。RT-qPCR 反应体系（20 μL）包括：1.0 μL 上下游引物（10 μmol/L）、10 μL PerfectStart® Green qPCR SuperMix（TransGen Biotech Co.，北京）、8 μL 无核酸酶水（Nuclease-free Water）、1.0 μL DNA（50 ng/μL）模板。PCR 反应均在 Bio-Rad Real-Time PCR 仪（Bio-Rad Laboratories，Inc.，Hercules，CA，美国）上进行，扩增程序为：95 ℃ 5 min、95 ℃ 10 s、58 ℃、30 s、40 个循环，在每个 58 ℃ 步骤结束时捕获荧光信号，结果以 C_t 值显示。使用对照分别为：已知感染 CLas 的长春花 DNA 为阳性对照，健康长春花 DNA 为阴性对照，无核酸酶水为空白对照。

1.8　样品检测时间设定

为了对比热处理后植株活性的短期变化（30 d 内）和最终情况（90 d），分别在 0 、15 、30 和 90 d 提取并检测植株叶片淀粉和类黄酮的含量，同时检测 C_t 值，根据 C_t 值计算病菌浓度。病菌浓度（bacterica concentration，CN）为每 ng 植物总 DNA 中的 CLas 浓度，计算采用标准化方程[20]：

$$y = -3.363x + 41.431, R^2 = 0.9995 \quad (1)$$

式中 y 为样品 DNA 的 C_t 值；x 为样品中病菌 DNA 的拷贝数。

0 d 样品的提取时间为热处理后 30 min 内。考虑到热处理后植株的侧枝均已死亡，30 d 所采集的样品为主干部分同一水平面的叶片。另外，热处理后每隔 5 d 进行拍照观察，以追踪观测植株经过热处理后 30 d 内的恢复情况，并在 90 d 时拍摄植株最终的生长情况。

1.9　数据分析

基于 SPSS 26 软件，对正交试验数据进行极差分析和方差分析（ANOVA），结合综合平衡法确定微波热处理参数的最优组合，采用邓肯氏新复极差法（Duncan's multiple range test, DMRT），对所得的淀粉、类黄酮含量、C_t 值和病菌浓度 4 类数据进行多重比较。

2　结果与分析

2.1　单因素试验结果分析

根据单因素试验结果（表 3），当转盘转速为 0 时，植株过热程度较为严重，最高温度达到 58.8 ℃；当转速为 5 r/min 时，最高温度达到 52.6 ℃；而其他转速下的温度差异较小，最高不超过 51.8 ℃，由此确定转盘转速取值 10、15、20 r/min。当微波功率为 250、350 和 450 W 时，植株最高温度分别达到 60.9 、67.5 和 75.6 ℃，达到严重过热程度，因此微波功率不应超过 250W，取值 150、200、250 W。当分别开启 2、3、4 个磁控管时，植株最高温度达到 48 ℃，因此磁控管数量取值 2、3、4 个。

表 3　微波参数类型的单因素试验结果

Table 3　Single factor test results of microwave parameters

转盘转速 Rotating speed of turntable/(r·min^{-1})	最高温度 Maximum temperature /℃	微波功率 Microwave power /W	最高温度 Maximum temperature /℃	磁控管数量 Number of magnetrons	最高温度 Maximum temperature /℃
0	58.8	150	47.0	1	47.4
5	52.6	250	60.9	2	53.0
10	50.2	350	67.5	3	60.8
15	51.8	450	75.6	4	62.6
20	51.8				

2.2　正交试验结果分析

由正交试验结果可知（表 4），随着微波功率的增大或磁控管数量的增加，植株加热到 48 ℃ 的时间相继缩短。根据 3 个评价指标的极差分析结果（表 5），影响每个指标的主次因素排序均为 B（功率）、C（磁控管数量）、A（转盘转速），可见功率对植株热处理 3 个指标的影响最为显著。指标 1（植株过热程度）和指标 2（植株温度均匀度）的优选组合取 k_i（每个因素 i 个水平的平均值）中的最小值，因为指标 1 的 k_i 越大，植株过热越严重，指标 2 的 k_i 越大，3 个测温点的温度极差越大，说明植株受热越不均匀。指标 3（植株活性评价）的 k_i 则根据评分规则应取最大值，因为指标 3 的 k_i 越大，植

中国知网　https://www.cnki.net

株热处理后的活性越好。根据表 5，指标 1 和指标 2 的优选组合为 $A_3B_1C_1$(20-150-2) 和 $A_2B_1C_1$(15-150-2)，指标 3 的优选组合为 $A_3B_1C_2$(20-150-3)。从表 1 和表 4 中可知，组合 $A_3B_1C_1$(20-150-2) 和 $A_2B_1C_1$(15-150-2) 对应的植株受热温度未达到 48 ℃，故不采纳该组合。考虑到增加因素 B（微波功率）易造成过热，磁控管数量对加热影响偏小，因此优先考虑增加磁控管数量，即组合为 $A_3B_1C_2$（20-150-3），与指标 3 的优选组合一致。

表 4 长春花植株微波热处理正交试验结果

Table 4 Results of orthogonal experiment for microwave-based thermotherapy on periwinkle plants

试验编号 Test number	温度 Temperature /℃			加热到 48℃ 所需时间 Time required for heating to 48℃ / s	评价指标 Evaluating index		
	主干顶部 Top of trunk	主干中部 Middle of trunk	主干底部 Bottom of trunk		植株过热程度 Degree of plant overheating	植株温度均匀度 Degree of plant temperature uniformity	植株活性评价 Plant activity evaluation
1	46.6	39.0	32.6	/	−1.43	15.43	86.00
2	66.2	47.4	30.4	26	18.20	35.77	67.67
3	68.8	62.8	31.8	23	20.83	37.07	38.00
4	51.8	47.3	31.4	94	3.77	20.40	90.50
5	59.9	46.4	32.7	40	11.90	27.23	51.17
6	60.1	44.2	33.9	40	12.10	26.20	57.00
7	54.0	47.8	30.7	52	6.03	23.30	84.17
8	52.7	46.9	32.8	74	4.73	19.97	81.67
9	60.5	51.7	29.3	34	12.50	31.17	67.83

注：试验编号 1 的温度未达到 48 ℃ 的要求，因此加热时间未做计算。

Note: The temperature of test No.1 does not meet the requirement of 48 ℃, so the heating time is not calculated.

表 5 正交试验极差分析结果

Table 5 Results of range analysis of orthogonal test

评价指标 Evaluating index	分析角度 Analysis angle	因素 Factors			主次因素 Factor priority	最优组合 Optimal combination
		转盘转速 (A) Rotating speed of turntable/ ($r \cdot min^{-1}$)	微波功率 (B) Microwave power /W	磁控管数量 (C) Number of magnetrons		
植株过热程度 Degree of plant overheating	k1	12.53	2.79	5.13	B>C>A	$A_3B_1C_1$(20-150-2)
	k2	9.26	11.61	11.49		
	k3	7.76	15.14	12.92		
	极差 Extreme difference *R*	4.78	12.36	7.79		
植株温度均匀度 Degree of plant temperature uniformity	k1	29.42	19.71	20.53	B>C>A	$A_2B_1C_1$(15-150-2)
	k2	24.61	27.66	29.11		
	k3	24.81	31.48	29.20		
	极差 Extreme difference *R*	4.81	11.77	8.67		
植株活性评价 Plant activity evaluation	k1	63.89	86.89	74.89	B>C>A	$A_3B_1C_2$(20-150-3)
	k2	66.22	66.83	75.33		
	k3	77.89	54.28	57.78		
	极差 Extreme difference *R*	14.00	32.61	17.56		

由指标 1 和指标 2 的方差分析结果（表 6）可知，因素 B 和因素 C 对 2 个指标的影响极其显著（$P < 0.01$），而因素 A 不显著（$P > 0.05$），可见在 10～20 r/min 范围内调节因素 A 不会对加热造成显著影响。

表 6 正交试验方差分析结果

Table 6 Results of ANOVA of orthogonal test

评价指标 Evaluating indicator	方差来源 Source of variance	离差平方和 Sums of squared deviations	自由度 Freedom	均方 Mean square	*F*	*P* 值 *P* value
植株过热程度 Degree of plant overheating	模型 Model	1 235.134	8	154.392	9.233	< 0.01
	A	107.463	2	53.731	3.213	> 0.05
	B	728.927	2	364.464	21.796	< 0.01
	C	309.343	2	154.671	9.250	< 0.01
	误差 Error	89.401	2	44.700	/	/
植株温度均匀度 Degree of plant temperature uniformity	模型 Model	1 296.321	8	162.040	7.749	< 0.01
	A	133.347	2	66.674	3.188	> 0.05
	B	648.534	2	324.267	15.506	< 0.01
	C	446.092	2	223.046	10.666	< 0.01
	误差 Error	68.347	2	34.174	/	/

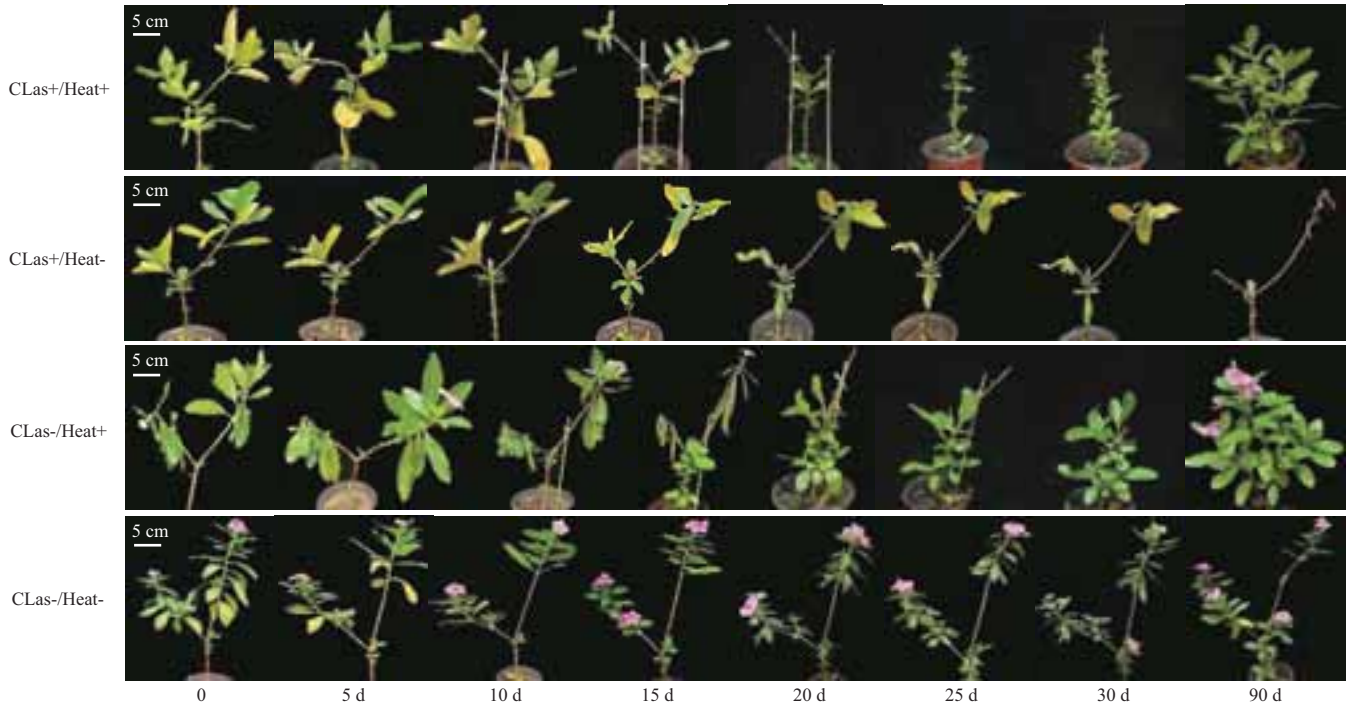
指标 3 是对植株的活性恢复情况进行评价，没有直接体现温度与微波参数之间的关系，故不作方差分析。结合极差分析结果，可确定最优组合为 B_1C_2（150-3），因素 A 取值范围为 10～20 r/min。

2.3 感病长春花的微波热处理结果分析

利用最优参数组合 $A_2B_1C_2$（转盘转速 15 r/min，

中国知网 https://www.cnki.net

150W，3 个磁控管）对感染黄龙病的长春花进行热处理，记录植株长势变化（图 2）及病菌含量（表 7）。



注：“CLas+”表示感病长春花。“CLas-”则表示健康长春花。“Heat+”为经过微波热处理。“Heat-”为未经热处理的对照。
Note: "CLas+" means periwinkle plants infected by CLas. "CLas-" means healthy periwinkle plants. "Heat+" indicates the plants are subjected to microwave heat treatment. "Heat-" means the control without heat treatment.

图 2　感病长春花与健康长春花经微波热处理后不同时间的表型
Fig.2　Phenotypes of diseased Periwincle plants and healthy Periwincle plants with and without microwave heat treatment

表 7　热处理后不同时间植株中黄龙病菌的实时荧光 PCR 定量结果
Table 7　Real-time quantitative PCR detection results of the "*Candidatus* Liberibacter asiaticus" on periwinkle samples at different time points after microwave heat treatment

处理	0 d		15 d		30 d		90 d	
Treatment	C_t	CN	C_t	CN	C_t	CN	C_t	CN
CLas+/Heat+	17.01 ± 0.97a	85 533.01 ± 68377.18a	18.72 ± 1.32a	41 464.22 ± 23304.68a	25.99 ± 1.20a	324.84 ± 251.64a	31.91 ± 2.35a	13.59 ± 20.16a
CLas+/Heat-	17.87 ± 2.63a	129 582.30 ± 105419.77b	16.29 ± 0.45b	156 041.63 ± 8079.33b	15.62 ± 0.71b	343 635.61 ± 159853.21b	死亡 Death	死亡 Death
CLas-/Heat+	32.20 ± 1.12b	N/A	33.21 ± 0.67c	N/A	34.29 ± 1.32c	N/A	34.06 ± 1.67a	N/A
CLas-/Heat-	32.75 ± 1.78b	N/A	32.78 ± 0.96c	N/A	32.15 ± 0.66 d	N/A	33.78 ± 0.66a	N/A

注：C_t，阈值循环数；CN，病菌浓度；同列之间不相同的字母，表示差异显著（$P < 0.05$）。“N/A”表示没有黄龙病菌。
Note: C_t, threshold number of cycles; CN, bacterica concentration; Different letters in the same column indicate significant differences ($P < 0.05$). "N/A" means no CLas was detected.

从图 2 可看出，热处理后 30 d 的感病植株的长势得到一定的恢复，90 d 时长势较好，有侧枝重新长出，但与健康植株相比有一定差距。感病对照的长势则持续衰退，未新增嫩叶，直至死亡。另外，热处理后健康植株的侧枝和叶片在 15 d 内不断萎靡，但主干部分不断地新生嫩叶和侧枝，90 d 时长势旺盛，说明了热处理虽对植株的活性造成一定损伤，但未对主干造成致命伤害，因此植株的活性能在短时间内迅速恢复。

从表 7 可看出，健康样品的 C_t 值在 32 以上。受热感病样品的 C_t 值由 0 d 的阳性 (17.01 ± 0.97) 转至 90 d 的近阴性 (31.91 ± 2.35)，病菌浓度下降了约 99.98 %，可见微波热处理消杀了绝大部分黄龙病菌。反观感病对照，其 C_t 值在 30 d 内不断加重阳性（由 17.87 ± 2.63 下降到 15.62 ± 0.71），病菌浓度是 0 d 的 2.65 倍，到 90 d 时植株已经死亡。

2.4　微波热处理对长春花的淀粉和类黄酮两种代谢物含量的影响

由淀粉含量测定结果可知（表 8），受热感病样品及受热健康样品在 0 d 的淀粉含量相较对照有明显提高，可见植株响应微波胁迫时会做出应激性反应。15 d 时，受热健康样品的淀粉含量已和健康对照基本一致。受热感病样品的淀粉含量到 15 d 时显著下降，明显低于感病对照。90 d 时，受热感病样品的淀粉含量与健康样品基本一致，而感病对照的淀粉不断累积，直至植株死亡。

由类黄酮含量测定结果可知（表 8），0 d 受热样品的类黄酮含量均比相应对照高，说明微波胁迫可能会在短期内促进植株体内类黄酮的增加。0 d 感病样品的类黄酮含量均比健康样品低，说明黄龙病菌可能会抑制类黄酮的增加。随着时间推移，感病对照的类黄酮含量在持续上升，而健康样品总体却没有显著变化，说明植株可能通过增加类黄酮含量的方式来抵御黄龙病菌。受热感病样品因黄龙病菌被大幅消杀，其类黄酮含量在 90 d 内逐渐恢复至正常水平，淀粉 42.44 mg/g，类黄酮 32.44 mg/g。

中国知网　https://www.cnki.net

表 8 热处理后长春花植株叶片中的淀粉和类黄酮含量变化

Table 8 Changes of starch and flavonoid content in leaf samples of periwinkle plants after heat treatment (mg·g^{-1})

处理 Treatment	淀粉 Starch				类黄酮 Flavonoid			
	0 d	15 d	30 d	90 d	0 d	15 d	30 d	90 d
CLas+/Heat+	254.67 ± 23.36a	104.84 ± 22.75b	74.06 ± 25.53bc	42.44 ± 10.04c	7.69 ± 2.00a	13.42 ± 1.20ab	23.23 ± 0.89bc	32.42 ± 12.11c
CLas+/Heat-	106.13 ± 14.56a	144.00 ± 39.07a	174.23 ± 64.32a	死亡 Death	7.26 ± 0.90a	15.76 ± 6.09a	19.87 ± 13.60a	死亡 Death
CLas-/Heat+	117.98 ± 29.65a	33.77 ± 11.52b	26.88 ± 3.74b	39.67 ± 25.23b	32.47 ± 2.31a	28.44 ± 17.13a	27.47 ± 0.44a	31.14 ± 5.95a
CLas-/Heat-	24.55 ± 1.12a	35.95 ± 18.61a	24.75 ± 3.12ab	46.65 ± 4.35b	27.50 ± 7.23a	35.40 ± 5.39a	37.03 ± 10.55a	26.86 ± 4.46a

注：同行之间不相同的字母，表示差异显著（$P < 0.05$）。

Note: Different letters between peers indicate significant differences. ($P < 0.05$).

3 讨 论

微波热处理在保障长春花存活的同时有效消杀了黄龙病菌。黄龙病菌亚洲种（“*Candidatus* Liberibacter asiaticus”，CLas）是中国黄龙病的唯一病原，属耐热型细菌，经 38 ℃ 处理后其病菌浓度极显著下降[2,21]。同时，受试对象过热致死的温度与黄龙病菌受抑制的温度之间存在明显差距，为热处理防治黄龙病提供有效依据[22]。本研究用微波将长春花加热至 48 ℃ 时停止加热，超过抑制黄龙病菌最低有效温度的同时不对植株产生致命影响。与对照相比，加热后植株的黄龙病症状明显缓解，抽生大量嫩叶与枝干，但 30 d 时检出阳性，可能与死亡的黄龙病菌 DNA 残留有关。另外，微波的高温热处理也可能诱导了黄龙病菌基因组中的噬菌体转化，导致处理组的黄龙病菌裂解，促进病菌浓度下降。

感染黄龙病的植株会出现异常生理生化代谢，其中淀粉和类黄酮是受黄龙病影响较大的两个主要基础代谢物。根据试验结果，感病对照的淀粉含量不断升高，症状持续加重，原因是黄龙病菌会促进淀粉合成并干扰其分解途径，导致淀粉在植株中大量累积，进而使叶绿体类囊体系统崩解，产生叶片斑驳黄化的典型黄龙病症状[23]。感病对照的类黄酮含量持续增加的原因是该化合物会参与到植株对黄龙病的防御机制，可能在限制黄龙病菌的增殖方面起到重要作用[24]。微波热处理后，受热样品的淀粉含量与类黄酮含量相比对照有所增加，但后续逐渐恢复至正常水平，可见植株会对热处理做出应激反应，也具有高度的恢复能力[25]。

相较以往热处理方式，微波热处理颇具应用前景。从加热程度来看，以往加热方式局限于植株表皮，难以深入病菌所在的韧皮部，而微波热处理的热量是通过植株体内的水极性分子在微波电磁场的剧烈运动之下产生的[26]，可穿透植株的韧皮部，实现植株内外同时加热，研究表明杀菌效果好。从成本来看，微波加热时间短，不需要中间传热介质，能量转化效率高，人工成本和能源成本较低。为进一步提高工作效率，可以考虑同时处理多棵植株，或采用流水线式的微波装置进行批量热处理[27]；另外针对柑橘成树，可设计适合田间作业的可移动式微波热处理装置。

虽然本研究证实了微波热处理对黄龙病的抑制效果较好，但也存在不足之处，如黄龙病菌会在根部繁殖，现有条件难以开展位于土壤深处的根部热处理；长春花与柑橘树相比，两者的微波加热效果会因植物体内的含水率不同而有差异，未来需用柑橘树进行长期验证；微波除了产生热效应，同时还产生非热效应。研究表明，频率为 2.45 GHz、功率为几微瓦、处理时间 1 s 的非热处理可促使拟南芥在 24 d 内显著生长[28]，而本研究的微波加热装置难以将微波功率调控至不生热的情况，无法开展黄龙病的非热处理试验，应改进设备来探究非热处理对黄龙病菌与寄主的影响。

4 结 论

本研究搭建微波热处理平台，对感病长春花进行微波热处理，并在试验后跟踪检测植株样品中的生理生化指标，初步证明了微波热处理防治黄龙病的可行性，主要研究结论如下：

1）根据微波参数优化试验结果，得出感病长春花的微波热处理最优参数组合为：150 W、3 个磁控管、转速 15 r/min。热处理后，感病植株的病菌浓度在 90 d 后下降了约 99.98 %，植株活性恢复较好，而感病对照的病菌浓度持续增加，活性不断衰弱，到 90 d 时已经死亡。

2）0 d 时受热感病样品的淀粉含量与类黄酮含量均比相应对照高，之后不断下降至健康水平（淀粉 42.44 mg/g，类黄酮 32.42 mg/g），可见植株经过微波胁迫后具有高度的恢复能力；感病对照的淀粉含量和类黄酮含量不断增加，前者是黄龙病菌干扰淀粉代谢活动的结果，后者则用于参与植株对黄龙病的防御机制。

综上所述，微波热处理可大幅消杀长春花植株体内的黄龙病菌，植株的活性也会在短期内快速恢复。从处理效率、杀菌效果、使用成本来看，微波热处理具备田间应用的前景。另外，由于长春花的含水率与柑橘树差异较大，两者的受热情况可能不一致，今后仍需使用柑橘树进行长期验证。

[参 考 文 献]

[1] 兰玉彬，王天伟，郭雅琦，等. 柑橘黄龙病光谱特征波段选择及光谱检测仪研制[J]. 农业工程学报，2022，38(20)：119-128.
LAN Yubin, WANG Tianwei, GUO Yaqi, et al. Selection of spectral characteristic bands of HLB disease of citrus and spectrum detector development[J]. Transactions of the Chinese Society of Agricultural Engineering(Transactions of the CSAE), 2022, 38(20): 119-128. (in Chinese with English abstract)

[2] 吕若亚，李云，郑永钦，等. 黄龙病菌在柑橘果实橘络中的分布[J]. 园艺学报，2023，50(5)：1110-1117.
LÜ Ruoya, LI Yun, ZHENG Yongqin, et al. The distribution pattern of *Candidatus* Liberibacter asiaticus in fruit pith[J]. Acta Horticulturae Sinica, 2023, 50(5): 1110-1117. (in Chinese

中国知网 https://www.cnki.net

with English abstract)

[3] 刘杰帆，林铭佳，张建桃，等. 基于 CiteSpace 可视化分析的柑橘黄龙病研究进展[J]. 果树学报，2023，40(4)：771-787.
LIU Jiefan, LIN Mingjia, ZHANG Jiantao, et al. Research progress in citrus Huanglongbing based on citespace visual analysis[J]. Journal of Fruit Science, 2023, 40(4): 771-787. (in Chinese with English abstract)

[4] 雷天刚. 柑橘黄龙病菌半离体培养系统的构建及其应用研究[D]. 重庆：西南大学，2022.
LEI Tiangang. Study on Establishment and Application of a Semi-Invitro Culture System for “*Candidatus* Liberibacter asiaticus” in Citrus[D]. Chongqing: Southwest University, 2022. (in Chinese with English abstract)

[5] 全达万，李栋，张金莲，等. 长春花接种丛枝菌根真菌对柑橘黄龙病菌的抑制效果[J]. 热带作物学报，2020，41(11)：2259-2266.
QUAN Dawan, LI Dong, ZHANG Jinlian, et al. Effects of inhibition citrus Huanglongbing on *Catharanthus roseus* with different arbuscular mycorrhizal fungi species[J]. Chinese Journal of Tropical Crops, 2020, 41(11): 2259-2266 . (in Chinese with English abstract)

[6] 范国成，刘波，吴如健，等. 中国柑橘黄龙病研究 30 年[J]. 福建农业学报，2009，24(2)：183-190.
FAN Guocheng, LIU Bo, WU Rujian, et al. Thirty years of research on citrus Huanglongbing in China[J]. Fujian Journal of Agricultural Sciences, 2009, 24(2): 183-190 . (in Chinese with English abstract)

[7] 胡双双，戴素明，张阳，等. 柑橘木虱防控药剂筛选及矿物油对其增效作用评价[J]. 植物保护，2022，48(2)：247-254.
HU Shuangshuang, DAI Suming, ZHANG Yang, et al. Screening of insecticides for controlling diaphorina citri andsynergism of mineral oil to insecticides[J]. Plant Protection, 2022, 48(2): 247-254. (in Chinese with English abstract)

[8] 贾志成，郑加强，黄雅杰，等. 柑橘黄龙病热处理防治技术研究进展[J]. 农业工程学报，2015，31(23)：1-9.
JIA Zhicheng, ZHENG Jiaqiang, HUANG Yajie, et al. Review and prospect of thermotherapy for citrus Huanglongbing[J]. Transactions of the Chinese Society of Agricultural Engineering(Transactions of the CSAE), 2015(23): 1-9 . (in Chinese with English abstract)

[9] YANG C, POWELL C A, DUAN Y, et al. Deciphering the bacterial microbiome in Huanglongbing-affected citrus treated with thermotherapy and sulfonamide antibiotics[J]. Plos One, 2016, 11(5): e155472.

[10] 贾志成，EHSANI R，郑加强，等. 柑橘黄龙病蒸汽快速热处理升温特性及田间防治效果[J]. 农业工程学报，2017，33(11)：219-225.
JIA Zhicheng, EHSANI R, ZHENG Jiaqiang, et al. Heating characteristics and field control effect of rapid citrus Huanglongbing steam heat treatment[J]. Transactions of the Chinese Society of Agricultural Engineering(Transactions of the CSAE), 2017, 33(11): 219-225 . (in Chinese with English abstract)

[11] 张建桃，陈鸿，文晟，等. 柑橘黄龙病热空气快速处理温度场分布特性试验研究[J]. 农业工程学报，2017，33(8)：267-277.
ZHANG Jiantao, CHEN Hong, WEN Sheng, et al. Experiment on temperature field distribution characteristics of citrus Huanglongbing hot air rapid treatment[J]. Transactions of the Chinese Society of Agricultural Engineering(Transactions of the CSAE), 2017, 33(8): 267-277 . (in Chinese with English abstract)

[12] DING F, ALLEN V, LUO W, et al. Molecular mechanisms underlying heat or tetracycline treatments for citrus HLB control[J]. Horticulture Research, 2018, 5(30): 1-11.

[13] ABDELRHIM A S, DAWOOD M F, GALAL A A. Hydrogen peroxide-mixed compounds and/or microwave radiation as alternative control means against onion seed associated pathogens, aspergillus niger and fusarium oxysporum[J]. Journal of Plant Pathology, 2021,104: 49-63.

[14] HILTON A, JEONG M, HSU J, et al. Thermal treatment using microwave irradiation for the phytosanitation of xylella fastidiosa in pecan graftwood[J]. Plos One, 2021, 16(1): e244758.

[15] 陈俊甫，郑正，邓晓玲. 黄龙病菌和植原体在长春花体内的移动、增殖以及相关症状研究[J]. 植物病理学报，2019，49(2)：160-166.
CHEN Junfu, ZHENG Zheng, DENG Xiaoling. Research on the movement and propagation of " *Candidatus* Liberibacter asiaticus " and " *Candidatus* Phytoplasma asteri " in periwinkle and their associated symptoms.[J]. Acta Phytopathologica Sinica, 2019, 49(2): 160-166. (in Chinese with English abstract)

[16] 罗小玲，郑永钦，李桃，等. 广佛手感染黄龙病叶果的症状及枝条的病原分布规律[J]. 中国南方果树，2023，52(1)：1-4.
LUO Xiaoling, ZHENG Yongqin, LI Tao, et al. Symptoms on leaf and branch of bergamot infected by citrus greening pathogen and the distribution of pathogen in branches[J]. South China Fruits, 2023, 52(1): 1-4. (in Chinese with English abstract)

[17] 张建桃，叶剑云，曾莉，等. 柑橘黄龙病苗木微波加热试验研究[J]. 江苏农业科学，2020，48(12)：75-79.
ZHANG Jiantao, YE Jianyun, ZENG Li, et al. Experimental study on microwave heating of citrus Huanglong disease seedlings[J]. Jiangsu Agricultural Sciences, 2020, 48(12): 75-79. (in Chinese with English abstract)

[18] 陈燕玲. 砂糖橘响应黄龙病菌及热处理胁迫的生理生化特征[D]. 广州：华南农业大学，2019.
CHEN Yanling. The Characteristics of Physiological and Biochemical in Shatangju Following Thermotherapy and Infection by “*Candidatus* Liberibacter Asiaticus” [D]. Guangzhou: South China Agricultural University, 2019. (in Chinese with English abstract)

[19] BAO M, ZHENG Z, SUN X, et al. Enhancing PCR capacity to detect‘*Candidatus* Liberibacter asiaticus’utilizing whole genome sequence information[J]. Plant Disease, 2020, 104(2): 527-532.

[20] ZHENG Y, ZHANG J, LI Y, et al. Pathogenicity and transcriptomic analyses of two "*Candidatus* Liberibacter asiaticus" strains harboring different types of phages[J]. Microbiology Spectrum, 2023 , 11(3): e00754-23 .

[21] LOPES S A, FRARE G F, BERTOLINI E, et al. Liberibacters associated with citrus Huanglongbing in Brazil: ‘*Candidatus* Liberibacter asiaticus’ is heat tolerant, ‘*Ca*. L. americanus’ is heat sensitive[J]. Plant Disease, 2009, 93(3): 257-262.

[22] 林孔湘，郑儒钰. 柑桔黄梢（龙）病毒和柑桔枝条组织耐

中国知网　https://www.cnki.net

热力的初步研究[J]. 植物病理学报，1964，7(1)：61-65.
LIN Kongxiang, ZHENG Ruyu. A preliminary study on the resis-tange of yellow shoot virus and citrus budwood tissue to heat[J]. Acta Phytopathologica Sinica, 1964, 7(1): 61-65. (in Chinese with English abstract)
[23] DUAN J, LI X, ZHANG J, et al. Cocktail therapy of fosthiazate and cupric-ammoniun complex for citrus Huanglongbing[J]. Frontiers in Plant Science, 2021, 12: 643971.
[24] RAO M J, DING F, WANG N, et al. Metabolic mechanisms of host species against citrus Huanglongbing (greening disease)[J]. Critical Reviews in Plant Sciences, 2018, 37(6): 496-511.
[25] DORADO J F, PINTO G, MONTEIRO P, et al. Heat stress and recovery effects on the physiology and biochemistry of castanea sativa Mill[J]. Frontiers in Forests and Global Change, 2023, 5: 1072661.
[26] KIPRIYANOV F A, SAVINYKH P A, ISUPOV A Y, et al. Prospects for the use of microwave energy in grain crop seeding[J]. Journal of Water and Land Development, 2021, 49 (4-6): 74-78.
[27] 张建桃，宋庆奎，周腾媛，等. 一种柑橘幼苗微波加热杀菌装置：202010778637.9 [P]. 2022-05-27.
[28] HORIKOSHI S. Improvement and effective growth of plants' environmental stress tolerance on exposure to microwave electromagnetic wave effects[J]. Agritech: Innovative Agriculture Using Microwaves and Plasmas: Thermal and Non-Thermal Processing, Sophia University, Japan: Springer Nature, 2022: 61-74.

Effect of microwave heat treatment in eliminating "*Candidatus* Liberibacter asiaticus" on periwinkle infected with Citrus Huanglongbing

ZHANG Jiantao[1], LIU Jiefan[1], LIANG Jiayin[2], LIU Guangbin[1], ZHENG Yongqin[2], XU Meirong[2※]

(1. *College of Mathematics and Informatics*, *South China Agricultural University*, *Guangzhou* 510642, *China*; 2. *Citrus Huanglongbing Research Laboratory*, *South China Agricultural University Guangzhou* 510642, *China*)

Abstract: Citrus Huanglongbing (HLB) is one of the most serious bacterial diseases in the citrus industry. Starch and flavonoids are two organic materials that are associated with HLB affection. Thermotherapy can be effective in eliminating the "*Candidatus Ldiberibacter asiaticus*" (CLas), the putative pathogen of HLB. However, the previous thermotherapy cannot fully meet the large-scale production, due to the low efficiency, high energy consumption, or with high cost. In this study, a microwave heat treatment was proposed to control the citrus HLB. A systematic investigation was implemented to explore the inhibitory effect of microwave heat treatment on the physiological materials of HLB-affected periwinkle plants. Firstly, a batch of 30-day-old periwinkles seedlings were cultivated and then graft-inoculated in an insect-proof screen house. Secondly, a microwave thermotherapy platform was built preliminarily. A single-factor test was conducted on three microwave parameters, including the rotating speed of the turntable (RST), microwave power (MP), and number of magnetrons (NM). The parameter levels were determined after the orthogonal test, according to the degree of overheating. Thirdly, the orthogonal test of L9(3^4) was carried out. Range and analysis of variance (ANOVA) were performed on the three indicators i.e., plant overheating degree, temperature range, and activity evaluation. The optimal combination of parameters was determined using the comprehensive balance. Finally, the optimized microwave treatment was used for thermotherapy on HLB-affected periwinkle plants. CLas titers were determined by real-time quantitative PCR. The starch and flavonoid concentrations of the leaves from the treated and untreated plants were detected within 90 days after heat treatment. The results show that: 1) The factor values for the L9(3^4) orthogonal test were obtained after single factor testing: RST of 10, 15, and 20 r/min, MP of 150, 200, and 250 W, and NM of 2, 3, and 4. The range analysis showed that the MP was the most important influencing factor on heating, followed by NMs, and finally RSP. 2) Combined with the ANOVA, the optimal combination was determined to be MP of 150 W with 3 magnetrons, where the value range of RST was from 15 r/min. The Ct value of infected samples increased from 17.01±0.97 before treatment to 31.91±2.35 at 90 days post-treatment, with the titers of CLas decreased by 99.98% after treatment with the optimized. 3) The previously CLas-infected plants were recovered after heat treatment, compared with the untreated plants, with more new leaves and lateral branches. The contents of starch and flavonoid were gradually recovered to the levels in the healthy control plants. Comparatively, the starch content of healthy samples increased significantly on the day of heating but gradually recovered to normal level. While there was no significant difference in the total flavonoid content. The flavonoid content in the untreated HLB-affected control was lower than that of the healthy control. The flavonoid content continued to increase until died, as time went by. In conclusion, 1) most CLas in periwinkle plants were eliminated to recover the growth conditions of plants into the healthy control level after microwave heat treatment. 2) Microwave heat treatment gradually restored the starch and flavonoid contents of infected samples, compared with the healthy control and the untreated diseased plants. 3) The platform of microwave heat treatment can be effective for pot-growing periwinkle seedlings. The microwave heat treatment is also required for long-term verification with the different conditions in citrus trees in the future. 4) Microwave heat treatment performed the better inhibitory effect on CLas, with the low cost, short treatment cycle, low consumption and high efficiency. It is also expected to achieve large-scale promotion in the field.

Keywords: disease; microwave; heat treatment; Huanglongbing; periwinkle; control efficiency

中国知网 https://www.cnki.net

2.2 农药液滴在水稻叶面的动态润湿铺展行为

ISSN 0578-1752
CODEN CKNYAR

中国农业科学

SCIENTIA AGRICULTURA SINICA

第 57 卷 第 13 期
Vol.57 No.13

2024

中国农业科学院
中国农学会 主办

中国农业科学
ZHONGGUO NONGYE KEXUE 2024年第57卷第13期

目 次

作物遗传育种·种质资源·分子遗传学

2497-2508 doi: 10.3864/j.issn.0578-1752.2024.13.001
宁夏引黄灌区春小麦品种（系）抗倒伏相关性状杂种优势及配合力分析
孙伟豪 刘亭 桑祎楠 杨政伟 张改生 宋瑜龙 张双喜

2509-2524 doi: 10.3864/j.issn.0578-1752.2024.13.002
玉米镰孢菌复合病原茎腐病抗性种质资源鉴定及抗性基因挖掘
桂翠林 马亮 王银莹 谢富贵 赵彩宏 王文森 李鑫 王青 高夕全

2525-2538 doi: 10.3864/j.issn.0578-1752.2024.13.003
茉莉酸调控马铃薯离体块茎发育的主要代谢物变化
梁丽娟 程李香 袁剑龙 撒刚 张峰

耕作栽培·生理生化·农业信息技术

2539-2548 doi: 10.3864/j.issn.0578-1752.2024.13.004
不同产量水平麦田植株氮素转运和籽粒氮素积累的差异
张振 石玉 于振文 张永丽

2549-2567 doi: 10.3864/j.issn.0578-1752.2024.13.005
绿肥部分替代化肥对玉米干物质积累与产量形成的影响
秦文利 智健飞 谢楠 张立锋 刘忠宽 刘振宇 冯伟 潘璇 代云霞

植物保护

2568-2582 doi: 10.3864/j.issn.0578-1752.2024.13.006
黑龙江省88份小麦品种（系）抗秆锈基因鉴定及抗性评价
高福 王睿 刘东军 孙会言 王子叶 宋维富 李天亚

2583-2598 doi: 10.3864/j.issn.0578-1752.2024.13.007
农药液滴在水稻叶面的动态润湿铺展行为
张建桃 黄路生 刘广彬 兰玉彬 文晟

土壤肥料·节水灌溉·农业生态环境

2599-2611 doi: 10.3864/j.issn.0578-1752.2024.13.008
长期施用化肥对南方稻田土壤酸化和盐基离子损失的影响
黄建华 吕真真 刘淑珍 侯红乾 刘益仁 刘秀梅 李絮花 蓝贤瑾

中国农业科学 2024,57(13):2583-2598
Scientia Agricultura Sinica
doi: 10.3864/j.issn.0578-1752.2024.13.007

开放科学（资源服务）标识码（OSID）：

农药液滴在水稻叶面的动态润湿铺展行为

张建桃[1,2,3]，黄路生[1,3]，刘广彬[1,3]，兰玉彬[3]，文晟[3,4]✉

[1]华南农业大学数学与信息学院，广州 510642；[2]农业农村部华南热带智慧农业技术重点实验室，广州 510642；[3]国家精准农业航空施药技术国际联合研究中心，广州 510642；[4]华南农业大学工程学院，广州 510642

摘要：【目的】探究表面张力、液滴粒径和叶片倾角对农药液滴在水稻叶片近轴面、远轴面动态润湿铺展行为的影响，为通过调控农药液滴在水稻叶面的动态润湿铺展行为实现水稻施药的“减施增效”提供依据。【方法】通过调节 Silwet-408 的浓度配制出表面张力为 21.4、33.2、43.7 mN·m^{-1}的 Silwet-408 溶液代替农药药液，利用液滴发生器生成 532、627、746、830、957 μm 的单液滴，对其在倾角为 40°、65°、85°水稻叶片近轴面、远轴面的动态润湿铺展行为进行全因子试验。【结果】表面张力、液滴粒径、叶片倾角均显著影响($P<0.05$)水稻叶面的液滴接触角变化率，且近轴面、远轴面所受影响的整体趋势基本相同，增大叶片倾角或减小液滴粒径或降低表面张力均能增大接触角变化率，促进液滴润湿铺展。其中，以降低表面张力的效果最显著，当表面张力从 33.2 mN·m^{-1}降至与水稻叶面临界表面张力接近的 21.4 mN·m^{-1}时，叶片近轴面的接触角(前进角和后退角)变化率分别增大 7.49、6.22 倍，远轴面的分别增大 11.13、7.61 倍，液滴的润湿性在 75 s 内从较差或差(80°≤接触角＜100°或接触角≥100°)转变成中等或好(60°≤接触角＜80°或接触角＜60°)；当表面张力比水稻叶面临界表面张力大得多时，接触角变化率随叶片倾角的增大而增大，随液滴粒径的减小而增大，但叶片倾角的影响小于液滴粒径的影响，经过 75 s 后，几乎所有粒径的液滴仍保持较差或差的润湿性(80°≤接触角＜100°或接触角≥100°)。液滴润湿滞后现象分析表明，水稻叶面的粗糙度相对较小，液滴润湿滞后现象并不严重。表面张力与水稻叶面临界表面张力接近的液滴在固-液-气三相体系动态表面张力的驱使下在叶面润湿铺展，接触角随时间的动态变化可使用模型$\theta=\theta_e+A\exp(-Kt)$进行拟合；表面张力比水稻叶面临界表面张力大得多的液滴虽能稳定地黏附在叶面上，没有出现滚落现象，但始终未突破叶面的钉扎效应和滞留阻力，无法实现润湿铺展。【结论】表面张力、液滴粒径、叶片倾角 3 个因素均显著影响农药液滴在水稻叶面的动态润湿铺展行为，在实际施药场景中，由于叶片倾角无法人为调节，因此可根据施药的目的调节药液的表面张力和液滴粒径进而调控液滴的动态润湿铺展行为。研究结果有助于理解农药液滴在水稻叶面动态润湿铺展的机理，并可为水稻施药场景中合理选择药液表面张力、液滴粒径提供理论支持与指导。

关键词：农药液滴；水稻叶面；动态润湿铺展；接触角；润湿滞后；表面张力

The Dynamic Wetting and Spreading Behavior of Pesticide Droplet on Rice Leaf Surface

ZHANG JianTao[1,2,3], HUANG LuSheng[1,3], LIU GuangBin[1,3], LAN YuBin[3], WEN Sheng[3,4]✉

[1]College of Mathematics and Informatics, South China Agricultural University, Guangzhou 510642; [2]Key Laboratory of Smart Agricultural Technology in Tropical South China, Ministry of Agriculture and Rural Affairs, Guangzhou 510642; [3]National Center for International Collaboration Research on Precision Agricultural Aviation Pesticides Spraying Technology, Guangzhou 510642; [4]College of Engineering, South China Agricultural University, Guangzhou 510642

收稿日期：2023-12-29；**接受日期：**2024-02-22
基金项目：广州市科技计划项目重点研发计划（2023B03J1362）、国家自然科学基金面上项目（32271985）、广东省普通高校特色创新类项目（2019KZDZX1002）、广东省自然科学基金（2022A1515011008）、高等学校学科创新引智计划（D18019）
联系方式：张建桃，E-mail：zhangjiantao@yeah.net。通信作者文晟，E-mail：vincen@scau.edu.cn

Abstract:【Objective】The objective of this study is to investigate the effects of surface tension, droplet size, and leaf angle on the dynamic wetting and spreading behavior of pesticide droplets on both adaxial and abaxial surfaces of rice leaf, and to provide a basis for realizing the "reduce application and increase efficiency" of rice spraying by regulating the dynamic wetting and spreading behavior of pesticide droplets on the rice leaf surface.【Method】A full factorial experiment was designed to investigate the dynamic wetting and spreading behavior of single droplet on both adaxial and abaxial surfaces of rice leaf in this study. The Silwet-408 solutions with surface tension of 21.4, 33.2, and 43.7 mN·m^{-1} were formulated by adjusting the concentration of Silwet-408 to replace the pesticide solutions. A droplet generator was used to produce the single droplets of 532, 627, 746, 830, and 957 μm. The leaf angles were set as 40°, 65°, and 85°.【Result】There were significant effects of surface tension, droplet size, and leaf angle on the rate of change of droplet contact angle on the rice leaf surface (P＜0.05), and the overall trend of the influences on the adaxial and abaxial surfaces was basically the same; increasing leaf angle or reducing droplet size or lowering surface tension could increase the rate of change of contact angle and promote the wetting and spreading of droplet. Among them, the effect of lowering surface tension was the most significant. When the surface tension was decreased from 33.2 to 21.4 mN·m^{-1}, which was close to the critical surface tension of rice leaf surface, the rate of change of the contact angle (advancing contact angle and receding contact angle) increased by 7.49 and 6.22 times for the adaxial surface, and 11.13 and 7.61 times for the abaxial surface, and the wettability of the droplets was changed from relatively poor or poor (80°≤contact angle＜100° or contact angle≥100°) to medium or positive (60°≤contact angle ＜80° or contact angle＜60°) within 75 s; when the surface tension was much larger than the critical surface tension of rice leaf surface, the rate of change of contact angle increased with the increase of leaf angle, and increased with the decrease of droplet size, but the effect of leaf angle was less than that of droplet size, and droplets of almost all particle sizes still maintained relatively poor or poor wettability (80°≤contact angle＜100° or contact angle≥100°) after 75 s. In addition, the analysis of droplet wetting hysteresis phenomenon showed that the roughness of the rice leaf surface was relatively small, and the droplet wetting hysteresis phenomenon was not serious. The droplet with surface tension close to the critical surface tension of rice leaf was driven by the dynamic surface tension of the solid-liquid-gas three-phase system to wet and spread on the leaf surface, and the dynamic change of the contact angle with time could be fitted by the model $\theta=\theta_e+A\exp(-Kt)$; although the droplet with a surface tension much higher than the critical surface tension of rice leaf could steadily adhere to the leaf surface without the phenomenon of roll-off, it was never able to break through the pinning effect and retention resistance of the leaf surface, and could not achieve wetting and spreading.【Conclusion】All three factors, surface tension, droplet size, and leaf angle, significantly affect the dynamic wetting and spreading behavior of pesticide droplets on the rice leaf surface. In the actual application scenarios, since the leaf angle cannot be adjusted artificially, the surface tension and droplet size of the pesticide solution can be adjusted according to the purpose of the application to regulate the dynamic wetting and spreading behavior of the droplet. The results of this study are helpful to understand the mechanism of dynamic wetting and spreading of pesticide droplet on the rice leaf surface, and can provide theoretical support and guidance for the rational selection of surface tension and droplet size in rice pesticide application scenarios.

Key words: pesticide droplet; rice leaf surface; dynamic wetting and spreading; contact angle; wetting hysteresis; surface tension

0 引言

【研究意义】喷施农药是农业生产中的一个重要环节，可以保障作物的产量和质量[1]。然而，过量使用农药也严重威胁着环境安全。全球每年的农药投入量已高达 460 万吨，其中 90%的农药流失到环境或残留在农产品中[2]。提高农药利用率、大幅降低农药用量并减轻对环境的影响是当前精准农业发展亟需解决的问题[3]。农药主要是通过喷施器械以液滴的形式沉积到靶标表面上发挥作用[4]。农药液滴沉积到靶标表面后会经历润湿铺展、渗透吸收和传输等一系列的动态过程[5-7]，如果农药液滴在靶标表面动态润湿铺展过慢，则容易导致其因相邻液滴聚并后滚动、外界环境因素扰动而脱靶[8-10]；若动态润湿铺展过快，则会加速其蒸发，进而降低叶面持留量，致使靶标对药液的吸收不足[11-14]。农药液滴着靶后的动态润湿铺展行为将直接影响施药效果，并决定药液在生态系统中的传递方向[14-15]。此外，研究表明农药药液从喷嘴喷出到作用于靶标的全过程中，存在着药液剂量传递逐级递减的现象；其中，在靶标表面的传递会造成约 35%的剂量损失[2,16]。因此，研究农药液滴在靶标表面润湿铺展的整个动态过程，明晰其润湿铺展机理，进而调控其在靶标表面的动态润湿铺展行为是提高农药防治效果、减少农药流失、降低环境污染的有效途径。【前

人研究进展】近年来，国内外学者围绕农药液滴在靶标表面的动态润湿铺展行为开展了部分研究，并取得了一定的研究成果。XU 等[17]研究了不同浓度条件下 4 种类型的助剂液滴在蜡质和毛状叶片上的润湿铺展过程，发现液滴的润湿铺展行为随助剂的种类、浓度以及叶面特性的不同而变化极大；在一定的浓度范围内，液滴润湿铺展的速度随浓度的增大而增加；根据叶面的特性，选择助剂的类型和浓度可调控液滴的润湿铺展行为，进而实现农药的“减施增效”。张红涛等[15]探究了 9 种质量百分数的烷基聚葡糖苷液滴在黄瓜叶面的动态润湿铺展行为，发现溶液的表面张力与其动态润湿铺展行为关联密切。ZHU 等[18]研究了生长期对水稻叶面液滴润湿铺展行为的影响，结果表明不同生长期水稻叶面的粗糙程度不同，Triton X-100 液滴在叶面的接触角随着生长期的增长逐渐增大，润湿性能逐渐下降。OLIVEIRA 等[13]在粒径对 2,4-D 除草剂液滴在杂草叶面润湿铺展影响的试验中观察到 800 和 950 μm 的超粗液滴可显著增加杂草表面的除草剂滞留量。段洁利等[19]将不同体积的液滴滴在不同倾角的蕉叶表面，并观察其润湿行为，发现叶片倾角和液滴体积会影响液滴在蕉叶表面的稳定黏附。【本研究切入点】以上研究充分说明液滴粒径、药液表面张力、叶面特性以及叶片倾角等因素会影响液滴在靶标表面的动态润湿铺展行为。在实际的农药喷施场景中，液滴的靶标表面动态润湿铺展行为会受到上述因素乃至环境因素的耦合影响，目前的研究还存在着一些不足。例如有关的研究多集中在平面上，而对在斜面上的液滴行为研究较少[20]；多数研究所采用的液滴粒径比实际施药中的粒径大得多，远超生物最佳粒径；此外，多数研究采用控制变量法进行单因素试验，无法明晰各因素的影响程度以及交互作用。【拟解决的关键问题】通过不同浓度的非离子表面活性剂杰效利配制出不同表面张力的水溶液代替农药药液，利用液滴发生器生成不同粒径的单液滴，对其在不同倾角的水稻叶片近轴面、远轴面的动态润湿铺展行为进行全因子试验，分析药液表面张力、液滴粒径以及叶片倾角等因素对动态接触角、接触角变化率、液滴润湿滞后的影响，以期明晰农药液滴在水稻叶面动态润湿铺展的机理，并为提高水稻喷施过程中的农药利用率提供理论依据和途径。

1　材料与方法

试验于 2023 年在华南农业大学国家精准农业航空施药技术国际联合研究中心农业航空喷施雾化研究实验室完成。

1.1　材料与仪器设备

非离子表面活性剂杰效利（Silwet-408），迈图高新材料南通有限公司；去离子水；新鲜水稻叶片（品种为黄华占，室外盆栽种植），取拔节期的叶片，为保持叶片新鲜不脱水，现场摘取叶片进行试验。

EZ-Pi Plus 便携式静态表面张力仪，芬兰 Kibron 公司；CAPST-2000At 全自动接触角测量仪，东莞市普赛特检测设备有限公司；DH-HV1351UM-ML 工业数字摄像机，中国大恒有限公司；液滴发生器由美国 EFD 公司的 Ultimus I-II 型高精度点胶机和上海捷豹压缩机制造有限公司的 OLF750AF 型气体压缩机组成；自制角度可调的斜板。

1.2　方法

1.2.1　不同浓度 Silwet-408 溶液表面张力及水稻叶面接触角测定　采用去离子水与 Silwet-408 配制不同浓度的 Silwet-408 溶液（配制好的溶液在 2 h 内使用），然后使用 EZ-Pi Plus 表面张力仪，通过 Wilhelmy 平板法测定表面张力，每种浓度重复测定 10 次，取平均值，测定时温度为（26±1）℃，相对湿度为（65±3）%。

取拔节期新鲜健康的水稻叶片，平整地粘贴固定在全自动接触角测量仪的水平载物台上，用微量注射器将不同浓度的 Silwet-408 溶液以 2 μL 液滴的形式点滴在水稻叶面上。待液滴稳定后，用全自动接触角测量仪测定各浓度 Silwet-408 液滴在水稻叶面的接触角 θ，每浓度重复测定 3 次，取平均值，叶片近轴面、远轴面的测定方法相同，测定时温度为（26±1）℃，相对湿度为（65±3）%。

1.2.2　液滴生成及粒径校准方法　液滴生成器可通过调节点胶时间、点胶气压以及真空度来调控液滴粒径，不受液体性质的影响，可生成 200—2 000 μm 的单个液滴[21]。液滴粒径 d 由 ZHU 等[22]提出的公式 $d=1.06A^{0.445}$，根据水敏纸上的液滴斑点面积 A 获得。先将水敏纸扫描成电子图片，使用 Image J 软件获得液滴斑点的图像像素点个数，再根据电子图片的像素点尺寸得到 A 值。在本试验中，电子图片的水平分辨率和垂直分辨率均为 1 200 dpi，像素点的尺寸为 21.17 μm×21.17 μm。前期多次测试得到粒径为 532、627、746、830、957 μm 的 5 种液滴。

1.2.3　液滴在水稻叶面动态润湿铺展行为　选择新鲜健康的水稻叶片进行液滴动态润湿铺展行为试验。

将水稻叶片裁剪成 1 cm×3 cm 的长条，并粘贴固定在角度可调的斜板上。QIU 等[23]通过对大量水稻植株的叶片进行角度测量后认为水稻顶部、中部、底部冠层的叶片倾角分别为 40°、65°、85°。为此，设置斜板与水平面的夹角分别为 40°、65°、85°，以不同表面张力的 Silwet-408 溶液为流体，通过液滴生成器生成 532、627、746、830、957 μm 的单个液滴，并让液滴以零速度点滴到水稻叶面上，待液滴到达叶面后，立刻启动工业数字摄像机以每 3 s 采集一张照片的速度记录下 75 s 内液滴在水稻叶面上的动态润湿铺展行为。液滴在水稻叶片近轴面、远轴面的试验方法相同。试验设计为三因素多水平的全因子试验，每组试验重复 3 次，相关试验数据取平均值。

1.2.4 数据统计分析 试验完成后，使用全自动接触角测量仪自带的图像分析软件测量不同时间点所对应接触角（前进角θ_a、后退角θ_r）的大小。参照徐广春等[20]的方法描述前进角θ_a和后退角θ_r，如图 1 所示。使用 IBM SPSS Statistics 26 软件进行方差分析确定接触角（前进角θ_a、后退角θ_r）变化率的主次影响因素，并使用Duncan新复极差法进行事后检验，分析接触角变化率在各影响因素不同水平之间的差异。随后使用 MATLAB 软件通过二维插值方法绘制交互效应曲面图分析各影响因素对接触角变化率的交互作用。最后使用 Origin Pro 2018 软件绘制润湿阻力系数$\Delta\cos\theta$随时间 t 变化的折线图分析液滴润湿滞后现象，并拟合接触角θ随时间 t 动态变化的函数。前进角θ_a变化率、后退角θ_r变化率、润湿阻力系数$\Delta\cos\theta$[24]公式：

$$\theta_a\text{变化率}=\frac{\theta_{a(t\to 0s)}-\theta_{a(t\to 75s)}}{75};$$

$$\theta_r\text{变化率}=\frac{\theta_{r(t\to 0s)}-\theta_{r(t\to 75s)}}{75};$$

$$\Delta\cos\theta=\cos\theta_r-\cos\theta_a。$$

式中，θ_a和θ_r的单位为°；75 为时间，单位为 s；θ_a变化率和θ_r变化率的单位均为°·s^{-1}。

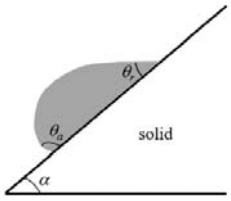


图 1 单个液滴在斜面上的形态图

Fig. 1 The shape of single droplet on the inclined plane

2 结果

2.1 不同浓度 Silwet-408 溶液表面张力及水稻叶面接触角

药液的表面张力不仅会影响液滴在靶标表面的接触角大小，同时还会影响液滴的动态润湿铺展行为[15,20]。测量了去离子水、不同浓度 Silwet-408 溶液的表面张力及其在水稻叶片近轴面和远轴面的接触角大小，结果表明这两个指标均随浓度的升高而降低（表 1）。去离子水和浓度为 0.002 mg·mL^{-1}的 Silwet-408 溶液的表面张力差别较大，分别为 72.8 和 43.7 mN·m^{-1}，而二者在水稻叶片近轴面和远轴面的接触角大小却分别只相差 4.6°和 2.7°，故推断表面张力介于 43.7—72.8 mN·m^{-1}的 Silwet-408 溶液的接触角大小应该与去离子水的十分接近。徐广春等[25]在常用农药表面张力的研究中发现，大部分农药在推荐浓度下表面张力的范围约为 27—62 mN·m^{-1}。结合上述推断，为了更全面地模拟常用农药液滴在水稻叶面的动态润湿铺展行为，选择表面张力为 21.4、33.2、43.7 mN·m^{-1}的 Silwet-408 溶液进行下一步试验。

表 1 不同浓度 Silwet-408 溶液的表面张力及其在水稻叶片近轴面、远轴面的接触角

Table 1 Surface tension of Silwet-408 solutions with different concentrations and their contact angles on the adaxial and abaxial surfaces of rice leaf

浓度 Concentration (mg·mL^{-1})	表面张力 Surface tension (mN·m^{-1})	接触角（近轴面） Contact angle (the adaxial surface) (°)	接触角（远轴面） Contact angle (the abaxial surface) (°)
0	72.8±0.07	132.0±0.51	118.4±0.90
0.002	43.7±0.10	127.4±0.19	115.7±0.68
0.01	33.2±0.10	108.5±0.68	83.6±0.88
0.1	21.4±0.03	24.1±1.24	20.9±1.90

2.2　水稻叶面动态接触角

在不同水平的表面张力、叶片倾角的试验组合下，不同粒径的液滴在水稻叶片近轴面的θ_a和θ_r于 75 s 内的动态变化如图 2 所示。横向排列，叶片倾角分别为 40°、65°、85°；纵向排列，表面张力分别为 21.4、33.2、43.7 mN·m^{-1}。由图 2 可见，液滴在水稻叶片近轴面的θ_a和θ_r均随着时间的推移而减小，但 21.4 mN·m^{-1}液滴的θ_a、θ_r（图 2-a、2-b、2-c）在变化的趋势、幅度方面均与 33.2 mN·m^{-1}（图 2-d、2-e、2-f）、43.7 mN·m^{-1}（图 2-g、2-h、2-i）所对应的存在明显差异，呈现出先快速减小，随后缓慢减小的趋势，在 75 s 内，液滴在叶片近轴面的润湿性从较差或差（80°≤θ<100°或θ≥100°）转变成中等或好（60°≤θ<80°或θ<60°）。有所区别的是，不同的叶片倾角，θ_a和θ_r从快速减小向缓慢减小转变的拐点出现时间不同。40°（图 2-a）、65°（图 2-b）、85°倾角（图 2-c），拐点出现的时间分别约在 30—33、27—30、9—12 s 处。此外，85°倾角，拐点出现后，θ_a和θ_r的减小速率仍比 40°、65°倾角的大。由此说明，对于表面张力为 21.4 mN·m^{-1}的液滴，更大的叶片倾角有助于加速θ_a和θ_r的减小，加快液滴的润湿铺展。33.2、43.7 mN·m^{-1}液滴的θ_a和θ_r均随时间推移而缓慢减小，减小幅度明显小于 21.4 mN·m^{-1}液滴的减小幅度，经过 75 s 后，几乎所有粒径的液滴在叶片近轴面仍保持较差或差的润湿性（80°≤θ<100°或θ≥100°）。另外，不同叶片倾角对θ_a和θ_r减小幅度的影响并不明显；而不同液滴粒径之间，532、627 μm 液滴θ_a和θ_r的减小幅度略大于 830、957 μm 液滴的减小幅度。

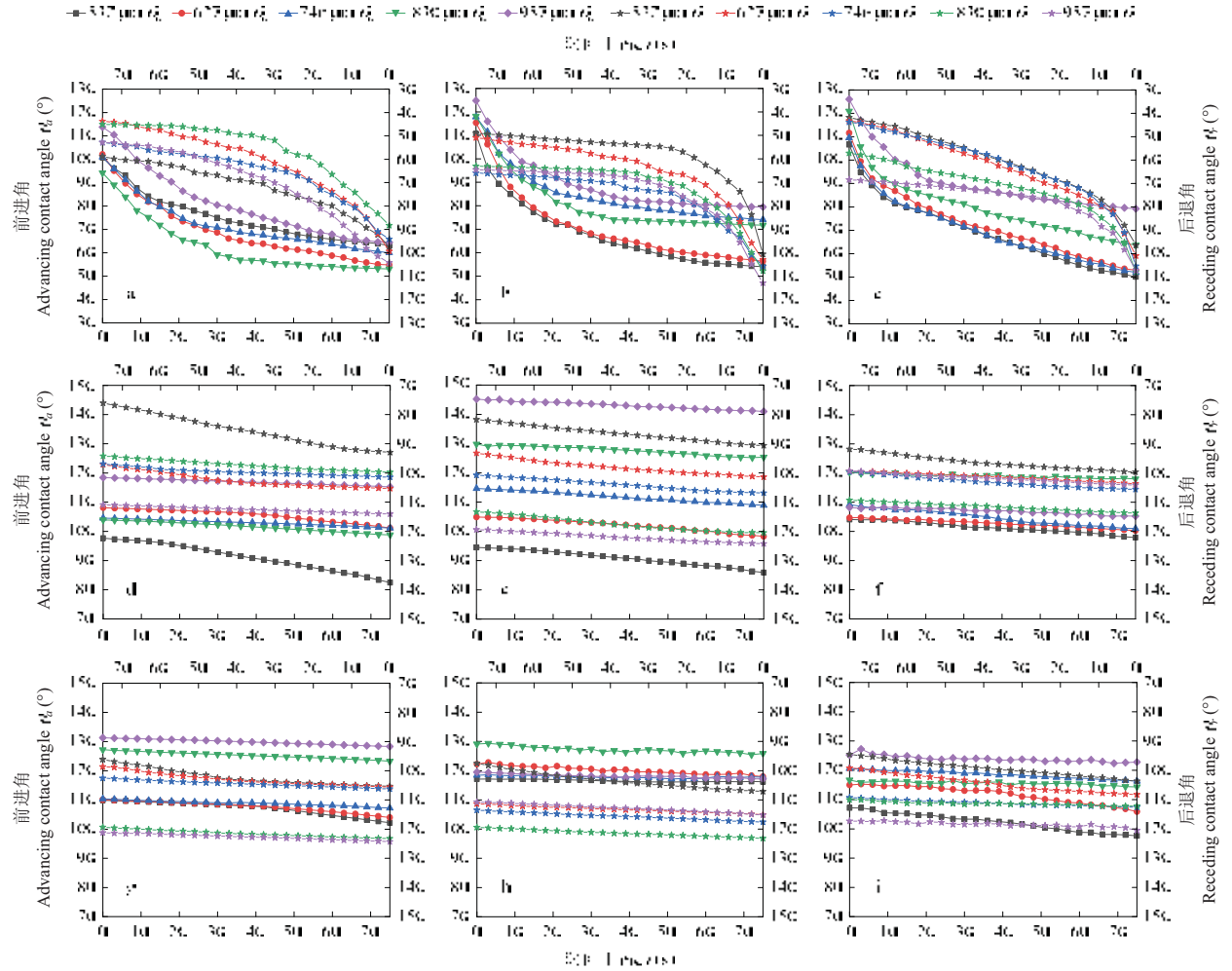


图 2　水稻叶片近轴面动态接触角

Fig. 2　Dynamic contact angle on the adaxial surface of rice leaf

在与水稻叶片近轴面相同的试验组合下，不同粒径的液滴在水稻叶片远轴面的θ_a和θ_r于 75 s 内的动态变化如图 3 所示。通过对比图 3 和图 2 可知，水稻叶片远轴面的θ_a、θ_r变化规律与叶片近轴面的基本相似。

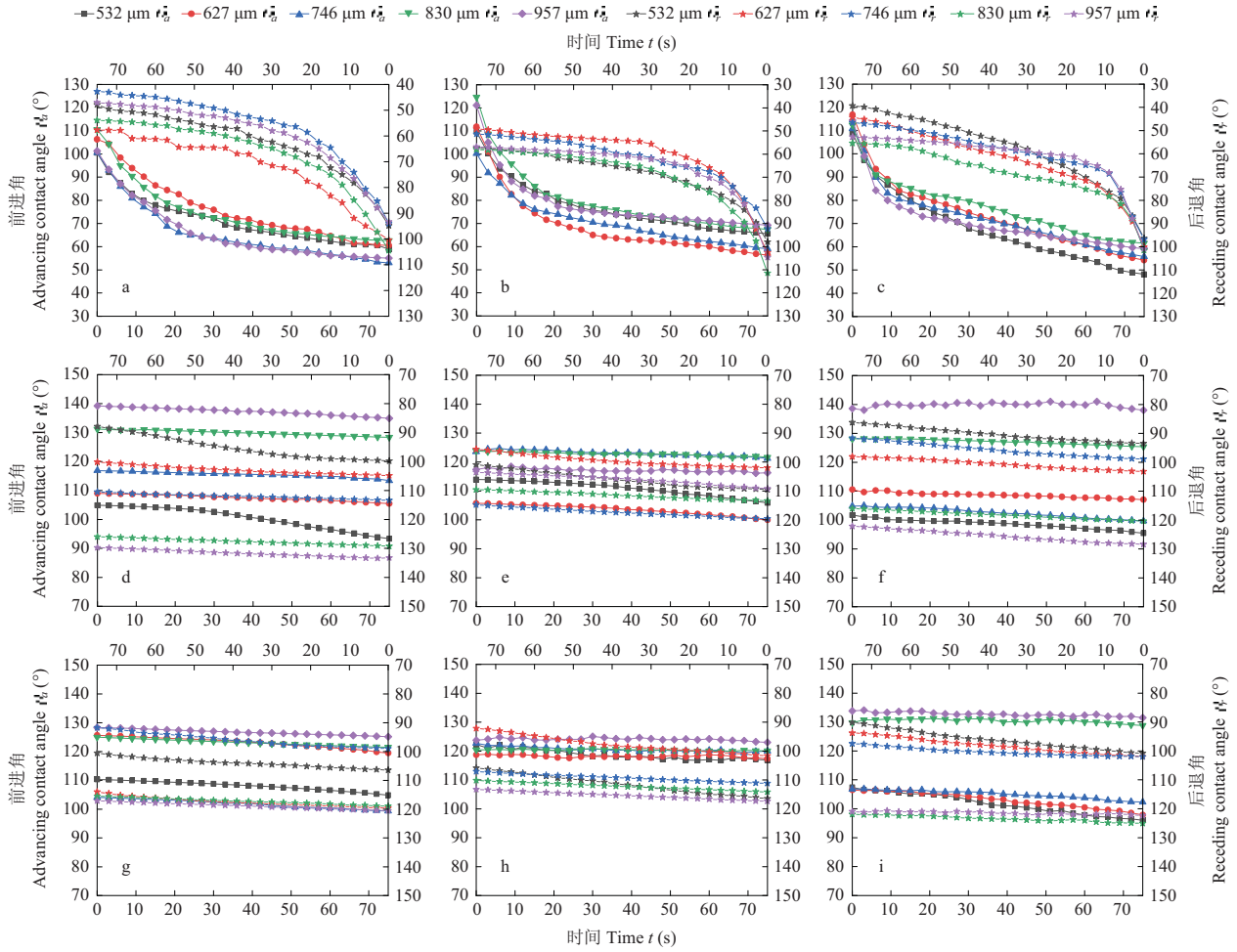


图 3 水稻叶片远轴面动态接触角

Fig. 3 Dynamic contact angle on the abaxial surface of rice leaf

2.3 水稻叶面接触角变化率方差分析

使用方差分析（ANOVA）确定各试验因素对水稻叶面上液滴接触角动态变化的影响程度，结果如表 2 所示。对于叶片近轴面或远轴面的θ_a和θ_r变化率，液滴粒径（A）、表面张力（B）以及叶片倾角（C）均产生显著影响（$P<0.05$），而且三者之间的交互作用同样显著（$P<0.01$）。方差整体模型对试验数据的拟合程度高（调整后 R^2=0.979—0.985），可以解释接触角变化率 97.9%—98.5%的变异原因。对于叶片近轴面的θ_a和θ_r变化率，在三因素及其交互作用所对应的效应量中，表面张力的效应量明显大于其他几个，分别为 0.985 和 0.989；对于叶片远轴面的θ_a和θ_r变化率，表面张力的效应量也分别达到 0.988 和 0.989。因此，可以认为表面张力对总体变异的贡献最大，是影响接触角变化率最为显著的一个因素。

方差分析结果表明，3 个试验因素均显著影响接触角变化率，为进一步明确各试验因素不同水平之间的差异，采用 Duncan 新复极差法进行事后检验。在对其中一个试验因素进行事后检验时，接触角变化率为其他两个试验因素所有水平的平均值。由表 3 可知，3 个试验因素对叶片近轴面、远轴面θ_a和θ_r变化率影响的整体趋势相同。当液滴粒径增大时，θ_a和θ_r变化率均随之而减小，532、627 μm 两种液滴的θ_a和θ_r变化率显著高于其他 3 种液滴（$P<0.05$），约为其他 3

表 2　试验因素对接触角变化率影响的方差分析

Table 2　ANOVA of the influence of experimental factors on the rate of change of contact angle

	变异来源 Source of variability	平方和 Sum of squares	自由度 Degree of freedom	均方 Mean square	*F*	*P*	效应量 Effect size
水稻叶片近轴面θ_a θ_a on the adaxial surface of rice leaf	修正模型 Correction model	11.178	44	0.254	142.562	＜0.001	0.986
	A	0.097	4	0.024	13.610	＜0.001	0.377
	B	10.637	2	5.318	2984.524	＜0.001	0.985
	C	0.054	2	0.027	15.061	＜0.001	0.251
	A×*B*	0.039	8	0.005	2.757	0.009	0.197
	A×*C*	0.041	8	0.005	2.863	0.007	0.203
	B×*C*	0.162	4	0.041	22.766	＜0.001	0.503
	A×*B*×*C*	0.148	16	0.009	5.194	＜0.001	0.480
水稻叶片近轴面θ_r θ_r on the adaxial surface of rice leaf	修正模型 Correction model	10.266	44	0.233	198.958	＜0.001	0.990
	A	0.114	4	0.029	24.385	＜0.001	0.520
	B	9.739	2	4.869	4152.493	＜0.001	0.989
	C	0.011	2	0.005	4.512	0.014	0.091
	A×*B*	0.062	8	0.008	6.648	＜0.001	0.371
	A×*C*	0.069	8	0.009	7.338	＜0.001	0.395
	B×*C*	0.061	4	0.015	13.070	＜0.001	0.367
	A×*B*×*C*	0.209	16	0.013	11.152	＜0.001	0.665
水稻叶片远轴面θ_a θ_a on the abaxial surface of rice leaf	修正模型 Correction model	12.127	44	0.276	182.035	＜0.001	0.989
	A	0.051	4	0.013	8.503	＜0.001	0.274
	B	11.661	2	5.831	3850.864	＜0.001	0.988
	C	0.063	2	0.032	20.901	＜0.001	0.317
	A×*B*	0.075	8	0.009	6.158	＜0.001	0.354
	A×*C*	0.056	8	0.007	4.593	＜0.001	0.290
	B×*C*	0.125	4	0.031	20.680	＜0.001	0.479
	A×*B*×*C*	0.096	16	0.006	3.954	＜0.001	0.413
水稻叶片远轴面θ_r θ_r on the abaxial surface of rice leaf	修正模型 Correction model	10.285	44	0.234	189.769	＜0.001	0.989
	A	0.054	4	0.013	10.871	＜0.001	0.326
	B	10.011	2	5.005	4063.746	＜0.001	0.989
	C	0.009	2	0.005	3.777	0.027	0.077
	A×*B*	0.044	8	0.006	4.488	＜0.001	0.285
	A×*C*	0.052	8	0.006	5.254	＜0.001	0.318
	B×*C*	0.019	4	0.005	3.824	0.006	0.145
	A×*B*×*C*	0.096	16	0.006	4.881	＜0.001	0.465

水稻叶片近轴面θa：R^2=0.986（调整后 R^2=0.979）、水稻叶片近轴面θr：R^2=0.990（调整后 R^2=0.985）；水稻叶片远轴面θa：R^2=0.989（调整后 R^2=0.983）、水稻叶片远轴面θr：R^2=0.989（调整后 R^2=0.984）θa on the adaxial surface of rice leaf: R^2=0.986 (adjusted R^2=0.979), θr on the adaxial surface of rice leaf: R^2=0.990 (adjusted R^2=0.985); θa on the abaxial surface of rice leaf: R^2=0.989 (adjusted R^2=0.983), θr on the abaxial surface of rice leaf: R^2=0.989 (adjusted R^2=0.984)

种液滴的 1.13—1.27 倍。叶片近轴面、远轴面θ_a和θ_r变化率随叶片倾角的增加而增大，85°倾角的θ_a 和θ_r变化率与 40°、65°所对应的存在显著差异（P＜0.05）。在 85°叶片近轴面，θ_a 变化率与 40°、65°的相比，分别增大 19.7%和 12.3%，θ_r 变化率分别增大 7.2%和 6.8%；在叶片远轴面，θ_a 变化率分别增大 19.0%和

18.1%，θ_r变化率分别增大 7.3%和 5.7%。而 40°和 65°叶片近轴面、远轴面所对应的θ_a和θ_r变化率差异并不显著（$P>0.05$）。如方差分析结果所示，表面张力是影响接触角变化率最为显著的因素。在叶片近轴面，表面张力从 33.2 降至 21.4 mN·m^{-1}时，θ_a和θ_r变化率分别增大 7.49 和 6.22 倍；而表面张力从 43.7 降至 33.2 mN·m^{-1}时，θ_a和θ_r变化率分别仅增大 39.3%和 28.6%。在叶片远轴面，表面张力从 33.2 降至 21.4 mN·m^{-1}时，θ_a和θ_r变化率分别增大 11.13 和 7.61 倍；而表面张力为 33.2、43.7 mN·m^{-1}两种液滴的θ_a和θ_r变化率均无显著差异。徐广春等[20]研究表明，只有表面张力小于叶面的临界表面张力且药液中表面活性剂的浓度达到临界胶束浓度才能使液滴迅速在叶面润湿铺展。从上述接触角变化率随表面张力变化的情况推测，21.4 mN·m^{-1}应该比较接近水稻叶面的临界表面张力值。

综上所述，液滴粒径、表面张力、叶片倾角均对水稻叶片近轴面、远轴面的液滴接触角变化率产生显著影响，且近轴面和远轴面所受影响的整体趋势基本相同。在本研究所设置的 3 个试验因素中，可以认为表面张力对接触角变化率的影响最大，其次是液滴粒径，叶片倾角的影响最小，而且三者之间存在一定的交互作用。

表 3 各试验因素不同水平之间接触角变化率的事后检验

Table 3 Post hoc tests on the rate of change of contact angle between different levels of various experimental factors

试验因素 Experimental factor			样本量 Sample number	接触角变化率 The rate of change of contact angle (°·s^{-1})	
				θ_a	θ_r
水稻叶片近轴面 The adaxial surface of rice leaf	液滴粒径 Droplet size (μm)	532	27	0.295a	0.306a
		627	27	0.301a	0.305a
		746	27	0.248b	0.252b
		830	27	0.246b	0.245b
		957	27	0.237b	0.241b
	叶片倾角 Leaf angle (°)	40	45	0.244b	0.263b
		65	45	0.260b	0.264b
		85	45	0.292a	0.282a
	表面张力 Surface tension (mN·m^{-1})	21.4	45	0.662a	0.650a
		33.2	45	0.078b	0.090b
		43.7	45	0.056c	0.070c
水稻叶片远轴面 The abaxial surface of rice leaf	液滴粒径 Droplet size (μm)	532	27	0.288a	0.295a
		627	27	0.286a	0.290a
		746	27	0.247b	0.257b
		830	27	0.250b	0.255b
		957	27	0.246b	0.247b
	叶片倾角 Leaf angle (°)	40	45	0.247b	0.261b
		65	45	0.249b	0.265b
		85	45	0.294a	0.280a
	表面张力 Surface tension (mN·m^{-1})	21.4	45	0.679a	0.654a
		33.2	45	0.056b	0.076b
		43.7	45	0.055b	0.076b

数据后不同小写字母表示在 0.05 水平下差异显著 Lowercases after the data indicate significant differences at the 0.05 level

2.4　液滴粒径、表面张力、叶片倾角的交互作用分析

为明晰液滴粒径、表面张力和叶片倾角对接触角变化率的交互影响，通过 MATLAB 软件使用二维插值方法绘制交互效应曲面图。由 2.3 节的分析可知，叶片近轴面或远轴面的θ_a和θ_r变化率均受到 3 个试验因素交互作用的极显著影响（$P<0.01$），且随 3 个试验因素水平值的变化展现出基本相同的变化趋势，由此推测 3 个试验因素的交互作用对叶片近轴面或远轴面θ_a和θ_r变化率的影响一致。因此，下一步仅以叶片近轴面的θ_a变化率为例，绘制交互效应曲面图进行 3 个试验因素的交互作用分析。

液滴粒径与表面张力的交互效应曲面图（图 4）显示，在所有角度下，θ_a变化率都呈现出随表面张力减小而增大的趋势，而在液滴粒径变化的方向上并没有呈现出明显的变化规律。倾角为 40°时，曲面整体的上升趋势相对较平缓，θ_a变化率的最大值和最小值分别为 0.658 和 0.040°·s^{-1}，均在液滴粒径为 957 μm 处取得，所对应的表面张力分别为 21.4 和 43.7 mN·m^{-1}。65°倾角所对应的曲面相较于 40°的更为陡峭，θ_a变化率在液滴粒径为 627 μm、表面张力为 21.4 mN·m^{-1}处取得最大值 0.796°·s^{-1}；在液滴粒径为 746 μm、表面张力为 43.7 mN·m^{-1}处取得最小值 0.009°·s^{-1}，最大值约为最小值的 88.44 倍。85°倾角所对应的曲面在表面张力为 33.2—21.4 mN·m^{-1}的区间内整体的上升趋势最为陡峭，证明表面张力变化所导致的θ_a大小变化更为明显；液滴粒径为 627 μm、表面张力为 21.4 mN·m^{-1}时，θ_a变化率具有最大值 0.782°·s^{-1}；液滴粒径为 830 μm、表面张力为 43.7 mN·m^{-1}时，θ_a变化率具有最小值 0.031°·s^{-1}，最大值约为最小值的 25.23 倍。对于不同的叶片倾角，降低药液表面张力均能增大θ_a的变化率，促进液滴在叶面上的润湿铺展，但在不同倾角下，促进液滴润湿铺展的能力有所不同，以 85°的最为显著；虽然在此交互作用中θ_a变化率随液滴粒径的变化未呈现出明显规律，但结合曲面图及试验数据可知，532 和 627 μm 的液滴在不同倾角的叶面上均展现出相对较大的接触角变化率，在叶面上的接触角减小得更快。

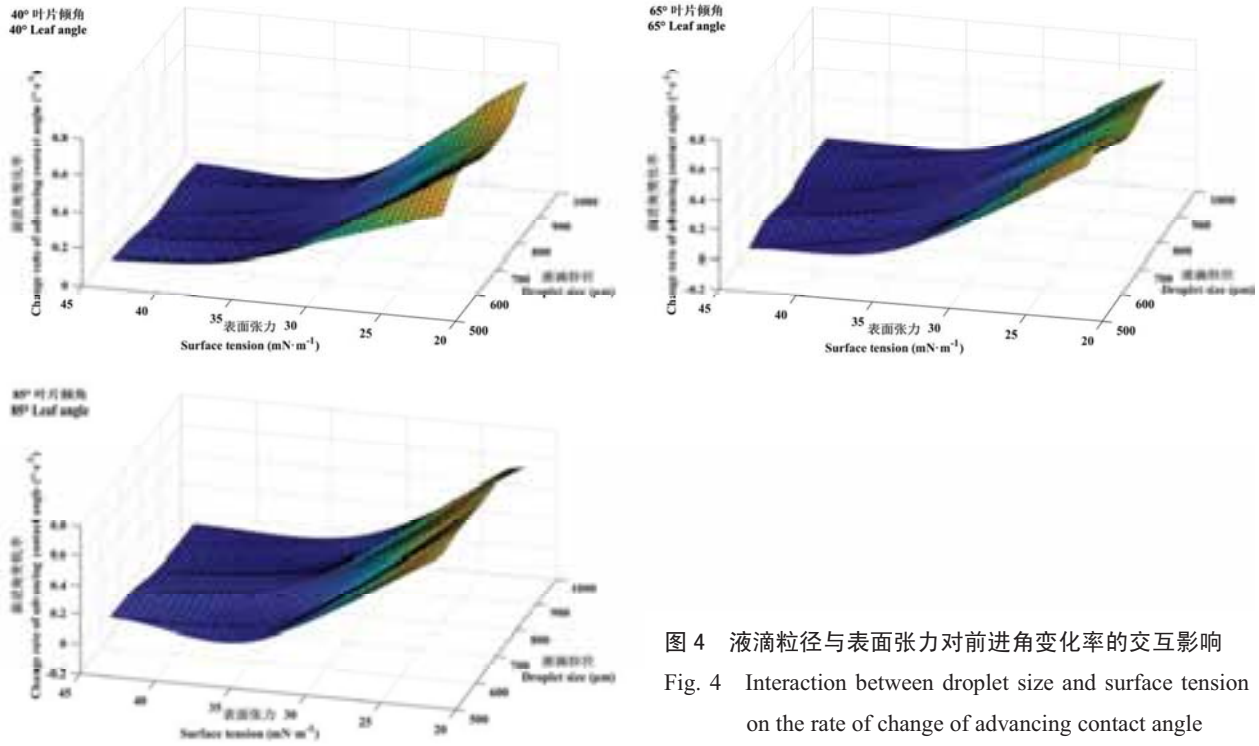


图 4　液滴粒径与表面张力对前进角变化率的交互影响

Fig. 4　Interaction between droplet size and surface tension on the rate of change of advancing contact angle

液滴粒径与叶片倾角的交互效应曲面图如图 5 所示。表面张力为 21.4 mN·m^{-1}时，曲面的整体趋势为θ_a变化率随叶片倾角的增加而增大，在液滴粒径的变化方向上呈现出波动状态。表面张力分别为 33.2 和 43.7 mN·m^{-1}时，液滴粒径和叶片倾角交互作用在整体上呈现出的趋势为θ_a变化率随叶片倾角的增大而增大，随液滴粒径的减小而增大，但叶片倾角对θ_a变化率的影响小于液滴粒径的影响。

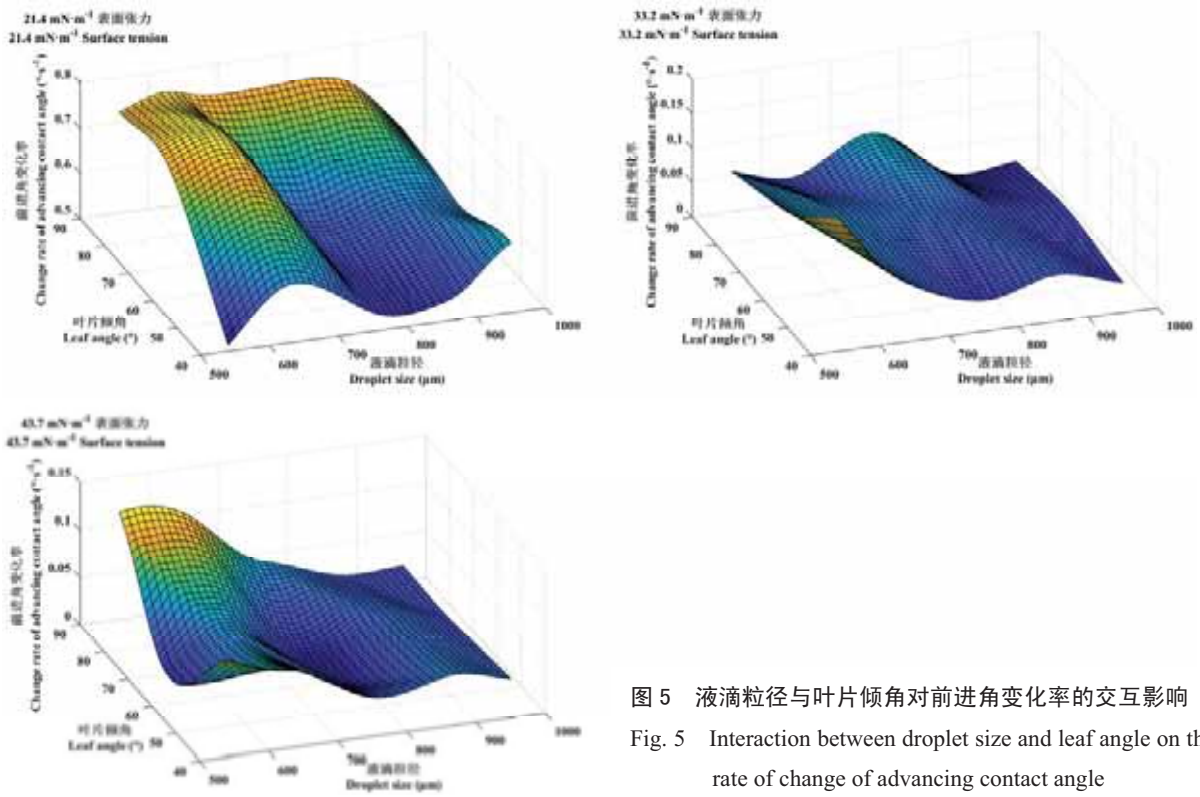


图 5　液滴粒径与叶片倾角对前进角变化率的交互影响

Fig. 5　Interaction between droplet size and leaf angle on the rate of change of advancing contact angle

根据 2.3 节叶片近轴面 θ_a 变化率在不同液滴粒径条件下的组间差异性事后检验结果，选择粒径为 532 和 957 μm 的液滴进行表面张力与叶片倾角的交互作用分析，θ_a 变化率交互效应曲面图如图 6 所示。532 μm 的液滴，表面张力较小时，θ_a 变化率随叶片倾角增大而增大；表面张力较大时，θ_a 变化率随叶片倾角增大呈现出先减小后增大的趋势，最小值在叶片角度为 65°、表面张力为 43.7 mN·m^{-1} 处取得，仅为 0.012°·s^{-1}。957 μm 的液滴，θ_a 变化率随表面张力增大而减小，叶片倾角对其影响不够明显；相较于 532 μm 的液滴，当表面张力增大时，θ_a 变化率以更快的速度减小至较低值，这表明在同等条件下 532 μm 液滴的润湿性能转变能力更好，能更稳定地附着在水稻叶面。

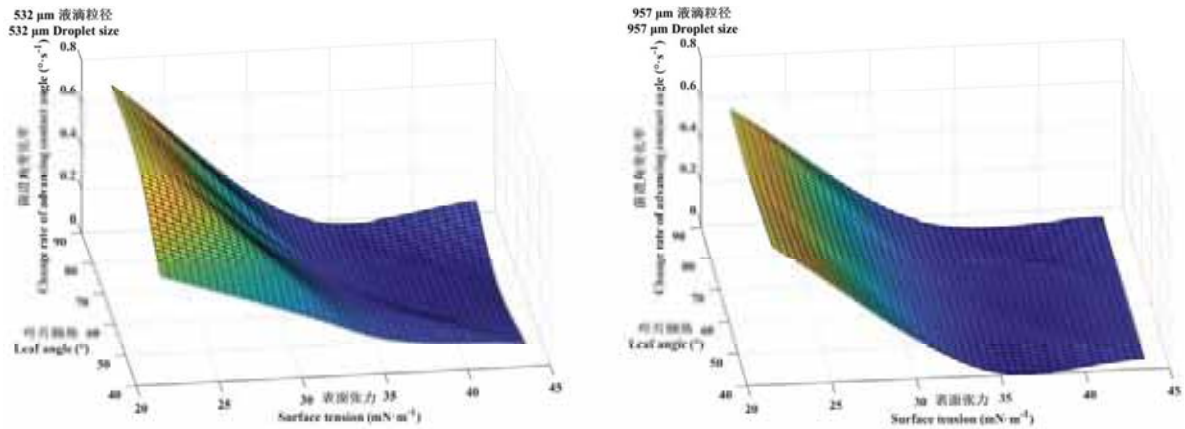


图 6　表面张力与叶片倾角对前进角变化率的交互影响

Fig. 6　Interaction between surface tension and leaf angle on the rate of change of advancing contact angle

从交互作用分析可知，当其中一个交互因子为表面张力时，接触角变化率会随表面张力的降低而增大，而在另一个交互因子变化的方向上则没有呈现出相对比较明显的变化规律，再一次证实了表面张力是影响农药液滴在水稻叶面润湿铺展最为显著的一个因素。在实际施药中，当药液的表面张力较大时，可采用雾化效果更好的器械喷施粒径更小的液滴，让液滴与靶标的接触角更快地减小，降低液滴因外界因素扰动而脱靶的风险。

2.5　液滴在水稻叶面的润湿滞后

以叶片近轴面为例，固定叶片倾角为 85°，分析不同表面张力条件下粒径为 532、957 μm 的液滴在水稻叶面上的润湿滞后，75 s 内润湿阻力系数Δcosθ的变化如图 7 所示。根据王晓东等[26-27]对粗糙表面液滴润湿滞后现象分析得到的结论以及本试验过程中θ_a、θ_r均同时减小且二者的差值Δθ较小的现象，结合图 7 的试验数据可以推断出水稻叶面的粗糙度相对较小，液滴润湿滞后现象并不严重。

表面张力为 21.4 mN·m^{-1}时，两种粒径的液滴所对应的Δcosθ在前 18 s 内都出现了波动起伏，18 s 后呈现缓慢减小的态势。如图 8-a、8-b 所示，两种液滴在润湿铺展过程中，三相接触线都发生了前移，在 0—3 s 内最为明显，在 18 s 内液滴前端的前移距离比后端的更大，整体上三相接触线都变得更长。0—3 s 时，532 μm 液滴（图 8-a）的前端比后端更迅速地向前铺展，而且可能是体积更小所受重力也更小的原因，液滴在前端的集聚并不如 957 μm 液滴（图 8-b）的显著，此过程中θ_a的减小幅度大于θ_r的减小幅度，使得Δcosθ迅速减小；3—18 s 内，液滴的后端几乎没有前移，而前端缓慢移动，液滴的形状被缓缓拉长，液滴可能因此而被引流，相对更集中在前端，此过程中θ_r的减小幅度大于θ_a的减小幅度，使得Δcosθ逐渐增大。0—6 s 时，957 μm 液滴的前、后端均向前移动，同样是前端的移动更为迅速，但可能是重力的作用，液滴更为集聚在前端，使得θ_a的减小幅度接近、甚至小于θ_r的减

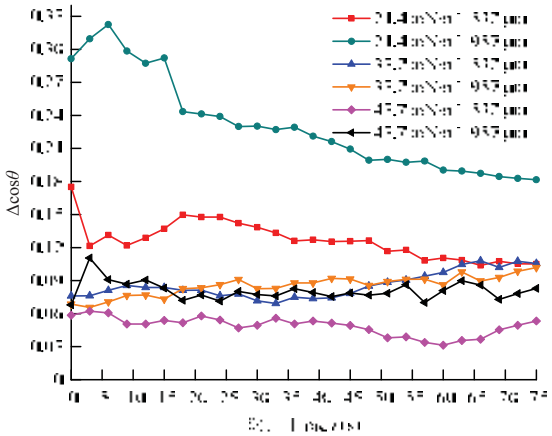


图 7　532、957 μm 液滴在 85°倾角叶片近轴面的润湿滞后变化

Fig. 7　Changes in wetting hysteresis of 532 and 957 μm droplets on the adaxial surface of 85° inclined leaf

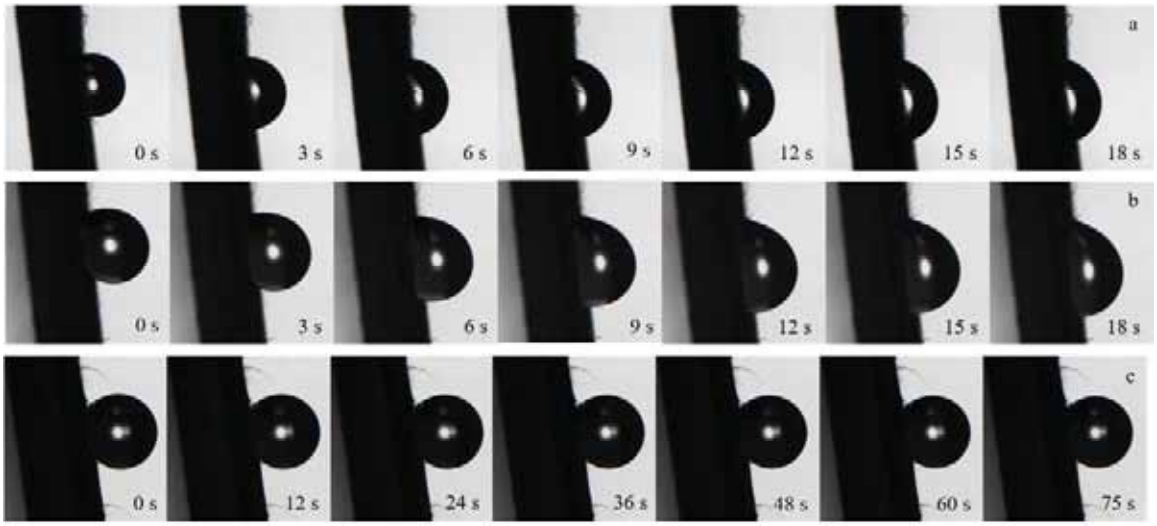


图 8　液滴在 85°倾角叶片近轴面的动态润湿铺展形貌

Fig. 8　Dynamic wetting and spreading morphology of droplets on the adaxial surface of 85° inclined leaf

小幅度，Δcosθ逐渐增大；6—18 s 内，液滴的后端缓慢前移，而前端依然较快移动，将液滴整体向前拉长，液滴也较快地向前润湿铺展，使得θ_a的减小幅度大于θ_r的减小幅度，Δcosθ迅速减小。在后续的时间里，两种液滴的后端均几乎没有前移，前端则缓慢移动，θ_a的减小幅度大于θ_r的减小幅度，Δθ的值越来越小，Δcosθ缓慢减小。

当表面张力分别为 33.2、43.7 mN·m^{-1}时，两种液滴所对应的Δcosθ在 75 s 内的变化情况大致相同，呈现平稳上升的态势。试验过程中观察到这两种液滴均能稳定附着在水稻叶面，未发生移动、滚落，如图 8-c（以 43.7 mN·m^{-1}、957 μm 液滴为例）所示。这与前人研究[20]得到“含较低浓度表面活性剂的液滴会从具有一定倾角的水稻叶面上滚落”的试验结果有所不同，推测原因是本试验所研究的液滴粒径比前人所研究的小得多，液滴所受的重力不足以克服固-液黏附力与水稻叶面微观结构产生的能量势垒，因此液滴无法在叶面上发生移动、滚落。此外，试验过程中还观察到 75 s 内液滴几乎没有发生形变，θ_a和θ_r仅在环境蒸发作用的影响下以几乎同等的微弱趋势减小，液滴始终以一种润湿性差的状态（θ＞100°）附着在水稻叶面。

2.6 水稻叶面接触角动态变化的拟合函数

根据液滴在水稻叶面接触角动态变化的试验数据，结合 2.3 节方差分析及事后检验的结果，选择以叶片近轴面，532、957 μm 的液滴为例，应用 Origin Pro 2018 软件拟合不同水平的表面张力、叶片倾角试验组合下θ_a随时间 t 动态变化的函数，结果如表 4 所示。从表 4 可以看出，表面张力为 33.2、43.7 mN·m^{-1}时，θ_a动态变化的拟合函数为一次函数，决定系数 R^2均大于 0.75，呈现出较高的拟合程度；所有一次函数斜率的绝对值都较小（≤0.207），说明θ_a在单位时间内减小的幅度较小。表面张力为 21.4 mN·m^{-1}时，θ_a动态变化拟合函数的形式与周兆兵等[28]建立的木材水平表面胶粘剂动态润湿模型$\theta=\theta_e+A\exp(-Kt)$相同，决定系数 R^2均大于 0.97，拟合的一致性非常好。周兆兵等[28]定义θ_e为平衡接触角，A 为积分常数，K 为单位时间内接触角的衰减速率常数（K 值越大，接触角达到平衡的时间就越快），负号表示接触角是减小的。相关拟合函数结合试验数据进行对比分析发现，在 65°倾角的叶面，957 μm 液滴的θ_a在 69—75 s 时的取值为 79.8°—79.4°且逐渐趋于稳定，与拟合函数中的 79.36°非常接近；而 532 μm 液滴的θ_a在 75 s 时的大小为 54.0°，根据试验过程中观察到θ_a在越往后的时间里越缓慢减小甚至趋于稳定的变化趋势推测拟合函数中的 53.69°应该出现在 75 s 后，符合 K 值越大，接触角达到平衡的时间就越快的描述。此外，在 40°、85°倾角的叶面也发现了同样规律，与周兆兵等[28]对θ_e和 K 值的定义描述一致。因此，当表面张力为 21.4 mN·m^{-1}时，不同倾角水稻叶面上液滴接触角的动态变化可使用模型$\theta=\theta_e+A\exp(-Kt)$进行拟合，根据拟合函数即可直观推断出平衡接触角的大小；同时，通过对比 K 值的大小，判断出在相同的试验组合下，何种粒径的液滴在水稻叶面上的接触角能更快达到平衡状态。

表 4 水稻叶片近轴面前进角动态变化拟合函数

Table 4 Fitting function for the dynamic change of advancing contact angle on the adaxial surface of rice leaf

表面张力/叶片倾角 Surface tension (mN·m^{-1})/Leaf angle (°)	液滴粒径 Droplet size (μm)	
	532	957
21.4/40	θ_a=61.50+38.03exp(-0.036t), R^2=0.9931	θ_a=59.47+54.52exp(-0.031t), R^2=0.9970
21.4/65	θ_a=53.69+51.56exp(-0.048t), R^2=0.9858	θ_a=79.36+44.49exp(-0.063t), R^2=0.9981
21.4/85	θ_a=40.25+58.90exp(-0.022t), R^2=0.9772	θ_a=80.68+43.88exp(-0.062t), R^2=0.9915
33.2/40	θ_a=98.81-0.207t, R^2=0.9917	θ_a=118.49-0.043t, R^2=0.9987
33.2/65	θ_a=95.13-0.115t, R^2=0.9909	θ_a=145.18-0.056t, R^2=0.9913
33.2/85	θ_a=104.46-0.084t, R^2=0.9857	θ_a=108.58-0.044t, R^2=0.9333
43.7/40	θ_a=110.84-0.100t, R^2=0.9265	θ_a=131.38-0.040t, R^2=0.9963
43.7/65	θ_a=117.17-0.016t, R^2=0.7900	θ_a=119.17-0.027t, R^2=0.8893
43.7/85	θ_a=107.24-0.132t, R^2=0.9912	θ_a=125.43-0.041t, R^2=0.7582

3　讨论

3.1　3 个试验因素对液滴动态润湿铺展的影响

含表面活性剂液滴的润湿铺展过程是表面活性剂单体从胶束等聚集体中分离，并扩散、吸附到新表面的过程[29]。当液滴附着到叶面后会形成液-固界面，同时液滴的曲率半径也会因此发生变化，进而形成新的气-液界面，原有气-液界面的表面活性剂分子密度平衡被打破，产生表面张力梯度，出现 Marangoni 效应，使液滴在叶面逐渐渗透[30-32]。在试验中，表面张力为 21.4 mN·m^{-1} 的液滴内部含有较多的表面活性剂分子，液滴黏附在叶面后这些表面活性剂分子开始向液-固界面和新形成的气-液界面转移并吸附，随着吸附量的增加，液-固界面张力降低，接触角减小，从而实现润湿铺展；当内部的表面活性剂分子都吸附到界面后，液滴的表面张力从动态变化趋于平衡，液滴停止润湿铺展，接触角在环境蒸发作用的影响下缓慢减小。表面张力为 33.2、43.7 mN·m^{-1} 的液滴所含的表面活性剂分子数量有限，液滴黏附在叶面形成新的界面后，没有足够多的表面活性剂分子转移、吸附在新界面，甚至原有界面的表面活性剂分子的分布密度被进一步稀释，液滴水分子之间的相互吸引力增大，表面张力也随之增大，再加上液滴粒径较小，所受重力较小，液滴始终没能突破水稻叶面的钉扎效应和滞留阻力，无法实现润湿铺展；此外，试验过程中观察到液滴与叶面的接触角、接触半径同时减小，该现象与 PICKNETT 等[33]提出的界面上液滴混合模式蒸发的现象相同，因此推测接触角变化主要是由于环境因素引起的蒸发作用所导致；而且 532、627 μm 液滴的接触角、接触半径同时减小的现象相较于 830、957 μm 液滴的更为明显，推测原因是粒径更小的液滴更容易受到环境因素影响而蒸发，相同时间内接触角、接触半径的减小幅度更大。

接触角变化率随叶片倾角变化呈现出的差异程度与高荣等[34]在研究叶片倾角对液滴铺展面积影响时所得到的结果相似，即 85°的大倾角相较于 40°、65°的小倾角更容易促进液滴润湿铺展，40°、65°的小倾角在促进液滴润湿铺展方面的差异不显著。曹军琳等[35]认为当叶片倾角增大时，液滴所受重力的作用也增大，能促使液滴更容易流动。徐德进等[36]认为叶片倾角小，沉积在叶面上的液滴发生滚动和流淌的机率也小。因此推断叶片倾角对接触角变化率的影响主要是由于重力的作用，而 40°和 65°倾角所对应的接触角变化率无差异的原因可能是这两种角度的倾斜度较小，重力的作用还无法对液滴实现引流的效果。

3.2　根据施药目的合理调控农药液滴的表面张力和粒径

农药液滴在靶标界面的动态润湿铺展行为影响施药效果并决定农药化学成分在生态系统中的传递方向，因此研究农药液滴动态润湿铺展的整个过程，比单纯地比较初始或平衡接触角更具实际意义。由本研究的结果可知，表面张力对农药液滴水稻叶面动态润湿铺展行为的影响最为显著，表面张力为 33.2、43.7 mN·m^{-1} 的液滴以润湿性较差或差的状态黏附在水稻叶面。这意味着市场上绝大多数水稻常用农药在推荐浓度下的药液经过喷施器械以液滴的形式到达水稻叶面后并不能润湿铺展，存在着因外界因素扰动而脱靶流失的风险。在实际的水稻喷施场景中，叶片倾角属于植物的固有属性，无法人为控制；而表面张力、液滴粒径则可分别通过添加助剂或表面活性剂、更换不同类型的喷头或调节喷施参数等进行调控[34]。施药时，应根据农药类型、病虫害发生的部位选择适宜的表面张力和液滴粒径。对于触杀型农药，要减小表面张力促进液滴润湿铺展，同时减小液滴粒径增大液滴的覆盖密度，提高药液与病虫害接触的概率；对于内吸型农药，则要通过适当地增大表面张力和液滴粒径以减缓液滴润湿铺展的速度，防止液滴因蒸发过快而使靶标对药液吸收不足。兰玉彬等[37]认为细小的液滴具有更好的穿透能力，能深入并沉积到靶标内部。对于稻纵卷叶螟、稻飞虱等位于水稻植株卷叶处、底部深处的害虫，小粒径的液滴更容易突破各种阻拦到达虫害发生部位并发挥药效。根据施药目的，合理调控农药液滴的表面张力和粒径有助于提高农药的防治效果和利用率。

3.3　水稻叶面临界表面张力对液滴动态润湿铺展的影响

靶标表面的临界表面张力是决定液滴能否在表面润湿铺展的关键因素。参照顾中言等[38]和 Zisman 图[39]的方法测得黄华占水稻叶片近轴面、远轴面的临界表面张力分别约为 18.2 和 19.8 mN·m^{-1}。从本研究中可以看出，添加极少量的 Silwet-408 即可将去离子水的表面张力降至 21.4 mN·m^{-1}，与水稻叶面的临界表面张力接近。当液滴的表面张力接近水稻叶面的临界表面张力时，液滴在水稻叶面上的润湿铺展行为与三相体系中气-液界面张力、液-固界面张力的动态变化有关；此外，接触角 θ 随时间 t 的动态变化可使用木材水平表面胶粘剂动态润湿模型 $\theta=\theta_e+A\exp(-Kt)$ 进行拟合，通过

θ_e 和 K 值分别判断平衡接触角大小以及比较相同条件下不同粒径的液滴达到平衡接触角所需时间快慢。但值得注意的是，在倾斜叶面上，液滴达到平衡接触角的时间越快，并不意味着平衡接触角越小，这可能与重力作用的引流效应以及三相体系中界面张力动态变化的规律有关，有待更多的试验来验证。当液滴的表面张力为 33.2、43.7 mN·m^{-1} 时，比水稻叶面的临界表面张力大得多，液滴会以润湿性较差或差的状态黏附在水稻叶面上，接触角、接触半径在蒸发作用的影响下极其缓慢地减小，容易脱靶流失。因此，在实际的水稻喷施场景中除了要考虑农药液滴的表面张力和喷施粒径，还需要了解水稻叶面的临界表面张力，科学合理地选择农药喷雾助剂的类型和剂量，提高农药液滴在水稻叶面的滞留能力。

4 结论

表面张力、液滴粒径、叶片倾角均显著影响农药液滴在水稻叶面的动态润湿铺展行为，近轴面、远轴面所受影响的整体趋势基本相同，影响大小依次为表面张力、液滴粒径、叶片倾角，且三者之间存在交互作用。水稻叶面的粗糙度相对较小，液滴润湿滞后现象并不严重。表面张力接近水稻叶面临界表面张力的液滴，其接触角随时间的动态变化符合模型 $\theta=\theta_e+A\exp(-Kt)$。综上，表面张力对水稻叶面农药液滴动态润湿铺展行为的影响机理在于其液滴内部所含的表面活性剂分子能否有效降低固-液-气三相体系中的界面张力；液滴粒径的影响机理主要在于环境因素所引起的混合模式蒸发使得接触角、接触半径同时减小，小粒径的液滴相对更容易受影响；而叶片倾角的影响机理则主要在于重力作用的引流效应。

参考文献 References

[1] CHEN H B, LAN Y B, K FRITZ B, HOFFMANN W C, LIU S B. Review of agricultural spraying technologies for plant protection using unmanned aerial vehicle (UAV). International Journal of Agricultural and Biological Engineering, 2021, 14(1): 38-49.

[2] ZHAO X, CUI H X, WANG Y, SUN C J, CUI B, ZENG Z H. Development strategies and prospects of nano-based smart pesticide formulation. Journal of Agricultural and Food Chemistry, 2018, 66(26): 6504-6512.

[3] 康峰, 吴潇逸, 王亚雄, 郑永军, 李守根, 陈冲冲. 农药雾滴沉积特性研究进展与展望. 农业工程学报, 2021, 37(20): 1-14.
KANG F, WU X Y, WANG Y X, ZHENG Y J, LI S G, CHEN C C. Research progress and prospect of pesticide droplet deposition characteristics. Transactions of the Chinese Society of Agricultural Engineering, 2021, 37(20): 1-14. (in Chinese)

[4] 宋玉莹, 曹冲, 徐博, 冉刚超, 曹立冬, 李凤敏, 赵鹏跃, 黄啟良. 农药雾滴在植物叶面的弹跳行为及调控技术研究进展. 农药学学报, 2019, 21(5/6): 895-907.
SONG Y Y, CAO C, XU B, RAN G C, CAO L D, LI F M, ZHAO P Y, HUANG Q L. Research progress on bouncing behavior and control technology of pesticide droplets at plant leaf surface. Chinese Journal of Pesticide Science, 2019, 21(5/6): 895-907. (in Chinese)

[5] ZWERTVAEGHER I K, VERHAEGHE M, BRUSSELMAN E, VERBOVEN P, LEBEAU F, MASSINON M, NICOLAÏ B M, NUYTTENS D. The impact and retention of spray droplets on a horizontal hydrophobic surface. Biosystems Engineering, 2014, 126: 82-91.

[6] 马英剑, 甄硕, 孙喆, 于萌, 赵锐, 郭鑫宇, 徐勇, 吴学民. 农药制剂研发的精细化、功能化与农业生产高效利用. 农药学学报, 2022, 24(5): 1080-1098.
MA Y J, ZHEN S, SUN Z, YU M, ZHAO R, GUO X Y, XU Y, WU X M. Refinement and functionalization of pesticide formulation research and development and efficient utilization in agricultural production. Chinese Journal of Pesticide Science, 2022, 24(5): 1080-1098. (in Chinese)

[7] 张海艳, 兰玉彬, 文晟, 陈春玲, 许童羽, 陈盛德. 无人机旋翼风场作用下雾滴在水稻植株上的黏附量模型构建. 农业工程学报, 2022, 38(18): 40-50.
ZHANG H Y, LAN Y B, WEN S, CHEN C L, XU T Y, CHEN S D. Modelling approach of spray retention on rice in plant protection using unmanned aerial vehicle. Transactions of the Chinese Society of Agricultural Engineering, 2022, 38(18): 40-50. (in Chinese)

[8] ZHOU Z L, CAO C, CAO L D, ZHENG L, XU J, LI F M, HUANG Q L. Evaporation kinetics of surfactant solution droplets on rice (*Oryza sativa*) leaves. PLoS ONE, 2017, 12(5): e0176870.

[9] ZHOU Z L, CAO C, CAO L D, ZHENG L, XU J, LI F M, HUANG Q L. Effect of surfactant concentration on the evaporation of droplets on cotton (*Gossypium hirsutum* L.) leaves. Colloids and Surfaces B: Biointerfaces, 2018, 167: 206-212.

[10] 王潇楠, 齐鹏, 于聪伟, 何雄奎. 农药雾滴雾化沉积飘失研究进展. 农药学学报, 2022, 24(5): 1065-1079.
WANG X N, QI P, YU C W, HE X K. Research and development of atomization, deposition and drift of pesticide droplets. Chinese Journal of Pesticide Science, 2022, 24(5): 1065-1079. (in Chinese)

[11] 王穗, 彭尔瑞, 吴国星, 张天顺, 时玲, 张川, 余杨. 植物叶面农药

雾滴蒸发时间研究在我国的应用. 广东农业科学, 2009(11): 104-107.

WANG S, PENG E R, WU G X, ZHANG T S, SHI L, ZHANG C, YU Y. Application of evaporation of pesticide droplets on plant leaves in China. Guangdong Agricultural Sciences, 2009(11): 104-107. (in Chinese)

[12] 周召路, 曹冲, 曹立冬, 郑丽, 马超, 李凤敏, 黄啟良. 不同类型界面液滴蒸发特性与农药利用效果研究进展. 农药学学报, 2017, 19(1): 9-17.

ZHOU Z L, CAO C, CAO L D, ZHENG L, MA C, LI F M, HUANG Q L. Research advances of droplet evaporation on different interfaces and the efficiency of pesticide utilization. Chinese Journal of Pesticide Science, 2017, 19(1): 9-17. (in Chinese)

[13] OLIVEIRA R B, BONADIO PRECIPITO L M, GANDOLFO M A, OLIVEIRA J V, LUCIO F R. Effect of droplet size and leaf surface on retention of 2,4-D formulations. Crop Protection, 2019, 119: 97-101.

[14] 郑丽, 程雪健, 黄桂珍, 赵鹏跃, 曹冲, 曹立冬, 吴进龙, 黄修柱, 黄啟良. 农药兑水茎叶喷施对靶沉积剂量传递与调控研究进展. 农药学学报, 2022, 24(5): 1034-1048.

ZHENG L, CHENG X J, HUANG G Z, ZHAO P Y, CAO C, CAO L D, WU J L, HUANG X Z, HUANG Q L. Research progress in target dose transfer and regulation of pesticides deposition by foliar spray diluted with water. Chinese Journal of Pesticide Science, 2022, 24(5): 1034-1048. (in Chinese)

[15] 张红涛, 陆军, 魏德云, 胡玉霞. 烷基聚葡糖苷液滴在黄瓜叶面的润湿状态及动态铺展行为. 农业工程学报, 2017, 33(3): 81-87.

ZHANG H T, LU J, WEI D Y, HU Y X. Wetting state and dynamic spreading behavior of alkyl polyglycoside drop on cucumber leaf surface. Transactions of the Chinese Society of Agricultural Engineering, 2017, 33(3): 81-87. (in Chinese)

[16] 马悦, 张晨辉, 杜风沛. 农药制剂发展趋势及前沿技术概况. 现代农药, 2022, 21(1): 1-8.

MA Y, ZHANG C H, DU F P. Development tendency and frontier technology of pesticide formulations. Modern Agrochemicals, 2022, 21(1): 1-8. (in Chinese)

[17] XU L Y, ZHU H P, OZKAN H E, BAGLEY W E, KRAUSE C R. Droplet evaporation and spread on waxy and hairy leaves associated with type and concentration of adjuvants. Pest Management Science, 2011, 67(7): 842-851.

[18] ZHU Y Q, GAO Y X, ZHANG C H, ZHAO X, MA Y, DU F P. Static and dynamic wetting behavior of TX-100 solution on super-hydrophobic rice (*Oryza sativa*) leaf surfaces. Colloids and Surfaces A: Physicochemical and Engineering Aspects, 2018, 547: 148-156.

[19] 段洁利, 蒋婷婷, 蒋寅龙, 杨洲. 香蕉叶表面特征及浸润性机理研究. 华南农业大学学报, 2023, 44(2): 314-323.

DUAN J L, JIANG T T, JIANG Y L, YANG Z. Study on the surface characteristics and infiltration mechanism of banana leaf. Journal of South China Agricultural University, 2023, 44(2): 314-323. (in Chinese)

[20] 徐广春, 顾中言, 徐德进, 许小龙. 稻叶表面特性及雾滴在倾角稻叶上的沉积行为. 中国农业科学, 2014, 47(21): 4280-4290. doi: 10.3864/j.issn.0578-1752.2014.21.013.

XU G C, GU Z Y, XU D J, XU X L. Characteristics of rice leaf surface and droplets deposition behavior on rice leaf surface with different inclination angles. Scientia Agricultura Sinica, 2014, 47(21): 4280-4290. doi: 10.3864/j.issn.0578-1752.2014.21.013. (in Chinese)

[21] ZHU H P, YU Y, OZKAN H E, DERKSEN R C, KRAUSE C R. Influence of spray additives on droplet evaporation and residual patterns on wax and wax-free surfaces//An ASABE Meeting Presentation Paper Number: 083752, 2008.

[22] ZHU H P, SALYANI M, FOX R D. A portable scanning system for evaluation of spray deposit distribution. Computers and Electronics in Agriculture, 2011, 76(1): 38-43.

[23] QIU W, GUO H B, ZHENG H, CAO Y B, LV X L, FANG J, ZHAI C Y, YU H F. CFD modelling to analyze the droplets deposition behavior on vibrating rice leaves. Computers and Electronics in Agriculture, 2022, 201: 107330.

[24] YARNOLD G D. The motion of a mercury index in a capillary tube. Proceedings of the Physical Society, 1938, 50(4): 540-552.

[25] 徐广春, 顾中言, 徐德进, 许小龙, 董玉轩. 常用农药在水稻叶片上的润湿能力分析. 中国农业科学, 2012, 45(9): 1731-1740. doi: 10.3864/j.issn.0578-1752.2012.09.008.

XU G C, GU Z Y, XU D J, XU X L, DONG Y X. Wettability analysis of pesticides on rice leaf. Scientia Agricultura Sinica, 2012, 45(9): 1731-1740. doi: 10.3864/j.issn.0578-1752.2012.09.008. (in Chinese)

[26] 王晓东, 彭晓峰, 陆建峰, 刘涛, 王补宣. 粗糙表面接触角滞后现象分析. 热科学与技术, 2003, 2(3): 230-234.

WANG X D, PENG X F, LU J F, LIU T, WANG B X. Analysis of contact angle hysteresis on rough surfaces. Journal of Thermal Science and Technology, 2003, 2(3): 230-234. (in Chinese)

[27] 肖易航, 郑军, 何勇明, 刘鸿博, 龚丁. 不同润湿性液体在粗糙表面的润湿滞后现象. 中国表面工程, 2019, 32(6): 150-156.

XIAO Y H, ZHENG J, HE Y M, LIU H B, GONG D. Contact angle hysteresis with different wetting-liquids on rough surfaces. China Surface Engineering, 2019, 32(6): 150-156. (in Chinese)

[28] 周兆兵, 张洋, 贾翀. 木质材料动态润湿性能的表征. 南京林业大

学学报(自然科学版), 2007, 31(5): 71-74.
ZHOU Z B, ZHANG Y, JIA C. Describing on dynamic wettability of wood and wood-based materials. Journal of Nanjing Forestry University (Natural Sciences Edition), 2007, 31(5): 71-74. (in Chinese)

[29] 张越, 张高勇, 韩富. 新型三硅氧烷表面活性剂在低能表面的铺展机理. 化学学报, 2007, 65(5): 465-469.
ZHANG Y, ZHANG G Y, HAN F. Spreading mechanism of new glucosamide-based trisiloxane surfactant on low-energy surface. Acta Chimica Sinica, 2007, 65(5): 465-469. (in Chinese)

[30] ZHANG Y, ZHANG G Y, HAN F. The spreading and superspeading behavior of new glucosamide-based trisiloxane surfactants on hydrophobic foliage. Colloids and Surfaces A: Physicochemical and Engineering Aspects, 2006, 276(1/3): 100-106.

[31] LIN J, ZHU M N, WU X, ZHENG C, LIU Z L, WANG Q Y, LU D D, HE Q Y, CHEN X Y. Microwave-assisted synthesis of trisiloxane superspreader and its superspreading behavior on plant leaves surfaces. Colloids and Surfaces A: Physicochemical and Engineering Aspects, 2016, 511: 190-200.

[32] 张晨辉, 赵欣, 雷津美, 马悦, 杜凤沛. 非离子表面活性剂 Triton X-100 溶液在不同生长期小麦叶片表面的润湿行为. 物理化学学报, 2017, 33(9): 1846-1854.
ZHANG C H, ZHAO X, LEI J M, MA Y, DU F P. Wettability of Triton X-100 on wheat (*Triticum aestivum*) leaf surfaces with respect to developmental changes. Acta Physico-Chimica Sinica, 2017, 33(9): 1846-1854. (in Chinese)

[33] PICKNETT R G, BEXON R. The evaporation of sessile or pendant drops in still air. Journal of Colloid and Interface Science, 1977, 61(2): 336-350.

[34] 高荣, 黄路生, 文晟, 尹选春, 张建桃. 农药液滴在玉米叶片表面铺展面积的影响因素. 农业工程学报, 2022, 38(20): 41-48.
GAO R, HUANG L S, WEN S, YIN X C, ZHANG J T. Factors influencing the spreading areas of pesticide droplets on the surface of maize leaves. Transactions of the Chinese Society of Agricultural Engineering, 2022, 38(20): 41-48. (in Chinese)

[35] 曹军琳, 祁力钧, 杨知伦, 葛鲁振, 吴亚垒, 程一帆. 基于图像处理的雾滴沉积分布试验研究. 中国农业大学学报, 2019, 24(1): 130-137.
CAO J L, QI L J, YANG Z L, GE L Z, WU Y L, CHENG Y F. Experimental study of droplet distribution based on image processing. Journal of China Agricultural University, 2019, 24(1): 130-137. (in Chinese)

[36] 徐德进, 徐广春, 许小龙, 顾中言. 施液量、雾滴大小、叶片倾角及助剂对农药在稻叶上沉积的影响. 西南农业学报, 2015, 28(5): 2056-2062.
XU D J, XU G C, XU X L, GU Z Y. Effect of application volume, droplet size, rice leaf incline angle and spray adjuvant on pesticide deposition. Southwest China Journal of Agricultural Sciences, 2015, 28(5): 2056-2062. (in Chinese)

[37] 兰玉彬, 彭瑾, 金济. 农药喷雾粒径的研究现状与发展. 华南农业大学学报, 2016, 37(6): 1-9.
LAN Y B, PENG J, JIN J. Research status and development of pesticide spraying droplet size. Journal of South China Agricultural University, 2016, 37(6): 1-9. (in Chinese)

[38] 顾中言, 许小龙, 韩丽娟. 几种植物临界表面张力值的估测. 现代农药, 2002, 1(2): 18-20.
GU Z Y, XU X L, HAN L J. Study on the measure of the critical surface tension of plants. Modern Agrochemicals, 2002, 1(2): 18-20. (in Chinese)

[39] 屠豫钦, 李秉礼. 农药应用工艺学导论. 北京: 化学工业出版社, 2006: 33-36.
TU Y Q, LI B L. Introduction to Application Technology of Pesticides. Beijing: Chemical Industry Press, 2006: 33-36. (in Chinese)

（责任编辑 岳梅）

2.3 柑橘黄龙病热空气快速处理温度场分布特性试验研究

《中文核心期刊要目总览》收录
Ei Compendex(核心版)收录
百种中国杰出学术期刊
RCCSE中国权威学术期刊

2017.8
第33卷 VOL. 33

ISSN 1002-6819
CN 11-2047/S
CODEN NGOXEO

农业工程学报

TRANSACTIONS OF THE CHINESE SOCIETY OF AGRICULTURAL ENGINEERING

NONGYE GONGCHENG XUEBAO



ISSN 1002-6819

中国农业工程学会 主办

·农业信息与电气技术·

传感器节点自主供电的环境混合能量收集系统设计 …… 徐雷钧，白　雪，潘炜雯，毛罕平（147）

多源卫星遥感秸秆焚烧过火面积动态监测 …… 武喜红，刘　婷，程永政，王来刚，郭　燕，张　彦，贺　佳（153）

基于 COSIM 模型的新疆棉花产量动态预报方法 …… 王雪姣，潘学标，王　森，胡莉婷，郭燕云，李新建（160）

·农业生物环境与能源工程·

日光温室番茄不同空间尺度蒸散量变化及主控因子分析 …… 龚雪文，刘　浩，孙景生，张　昊，马筱建，王万宁（166）

畜舍热交换芯体-风机热回收通风系统的热回收效果 …… 李　琴，刘　鹏，刘中英，王美芝，刘继军，吴中红（176）

分隔式循环水池塘养殖系统设计与试验 …… 田昌凤，刘兴国，车　轩，顾兆俊，曾宪磊，朱　浩，杨家朋（183）

鸡粪发酵液培养的小球藻水热液化制备生物原油及其特性

…… 朱张兵，王　猛，张源辉，李保明，张婷婷，董泰丽，刘志丹（191）

不同补水方式下砂壤土渗滤系统对硝态氮去除效果 …… 潘维艳，黄权中，张子元，普薇如，黄冠华（197）

酶法复合脱毒提高玉米秸秆水解液丁醇发酵效率 …… 王凤芹，谢媽媛，苏增平，杨　森，谢　慧，宋安东（204）

纳米 SiO_2/氨基淀粉黏合剂秸秆炭的结构及除磷特性

…… 孙恩惠，钱玉婷，靳红梅，黄　慧，武国峰，常志州，黄红英（211）

·土地整理工程·

基于土地适宜性的耕地规划 CA 模拟及验证 …… 房阿曼，陈伟强，董霁红（219）

珠三角丘陵区耕地质量综合评价及指标权重敏感性分析

…… 赵小娟，叶　云，周晋皓，刘　洛，戴文举，王秋香，胡月明（226）

基于复杂网络的辽宁省县域农村居民点空间结构变化分析 …… 危小建，肖晨春，侯贺平，陈竹安（236）

·农产品加工工程·

果蔬品质手持式近红外光谱检测系统设计与试验 …… 郭志明，陈全胜，张　彬，王庆超，欧阳琴，赵杰文（245）

吹扫式仿生嗅觉检测装置的设计与性能试验 …… 文　韬，郑立拿，龚中良，李立君，聂玉祥，董　帅（251）

支持分布环境的农产品协同追溯平台构建 …… 钱建平，范蓓蕾，李　洁，李小刚，赵　丽，王新令，史　策（259）

柑橘黄龙病热空气快速处理温度场分布特性试验研究 …… 张建锋，陈　晓，文　晟，李夏华，邱小玲，兰玉彬（267）

低压静电场下不同储藏结-解冻对牛肉品质的影响 …… 李　侠，魏书亮，杨方威，孙　丽，尚　珂，张春晖（278）

[illegible] …… [illegible]，刘关瑞（286）

[illegible] …… [illegible]，郭顺堂（293）

[illegible] …… [illegible]，韩永斌（301）

[illegible] …… [illegible]，周瑞香（309）

柑橘黄龙病热空气快速处理温度场分布特性试验研究

张建桃[1]，陈　鸿[1]，文　晟[2※]，李晟华[3]，邓小玲[4]，兰玉彬[3]

（1. 华南农业大学数学与信息学院，广州 510642；2. 华南农业大学工程基础教学与训练中心，广州 510642；
3. 华南农业大学工程学院，广州 510642；4. 华南农业大学电子工程学院，广州 510642）

摘　要：针对柑橘黄龙病自然热罩热处理存在的处理周期长、效率低、对自然条件依赖大、处理罩内温差过大等不足，提出了一种柑橘黄龙病热空气快速处理方法。为解决热空气快速处理时罩内温差过大的问题，搭建了柑橘黄龙病热空气快速处理温度场分布特性试验平台，研究了有无回风道、风速、热空气入口位置、热空气出口位置、入风口热空气温度对处理罩内温度场分布的影响。试验结果表明：风速、热空气入口位置、热空气出口位置、入风口热空气温度对处理罩内各截面温度场均有显著影响（P<0.05）；回风道不仅能使处理罩内温度场更均匀，而且能够降低能耗。通过试验得出柑橘黄龙病快速热空气处理的优选参数为：有回风道，风速 14.5 m/s，热空气入口位于处理罩下层，热空气出口位于处理罩上层，且与入口呈 90°，入风口热空气温度 90℃。在该优选参数下，处理罩内温度从 32 ℃上升到 48 ℃，耗时约为 9 min，处理罩内的温度极差为 3.9 ℃，比非优选参数下罩内的温度极差相比下降了 14.1 ℃。并在此参数下对柑橘黄龙病进行快速热空气处理田间试验，处理后病菌浓度平均降低 80.28%。研究结果为黄龙病热空气规模化处理设备的优化设计提供参考。

关键词：病害防治；热处理；温度；均匀性；黄龙病
doi：10.11975/j.issn.1002-6819.2017.08.036
中图分类号：S121　　**文献标志码**：A　　**文章编号**：1002-6819(2017)-08-0267-11

张建桃，陈　鸿，文　晟，李晟华，邓小玲，兰玉彬. 柑橘黄龙病热空气快速处理温度场分布特性试验研究[J]. 农业工程学报，2017，33(8)：267－277.　doi：10.11975/j.issn.1002-6819.2017.08.036　http://www.tcsae.org
Zhang Jiantao, Chen Hong, Wen Sheng, Li Shenghua, Deng Xiaoling, Lan Yubin. Experiment on temperature field distribution characteristics of citrus huanglongbing hot air rapid treatment[J]. Transactions of the Chinese Society of Agricultural Engineering (Transactions of the CSAE), 2017, 33(8): 267－277. (in Chinese with English abstract)
doi：10.11975/j.issn.1002-6819.2017.08.036　http://www.tcsae.org

0　引　言

1956 年，华南农业大学林孔湘教授根据中国广东潮汕地区农民对柑橘黄龙病的俗称，称其为黄龙病，1995 年“huanglongbing-HLB”被正式确定为该病的英文名称[1-2]。黄龙病(HLB)是由属于韧皮部杆菌属的病原菌引起的毁灭性疾病[3]，根据特点及发现地域的不同，分为 Candidatus Liberibacter asiaticus（CaLas）、Candidatus Liberibacter africanus（CaLaf）和 Candidatus Liberibacter americanus（CaLam）3 种类型[4-5]。其中，CaLaf 和 CaLam 为热敏感型[6]，仅在 30～32 ℃的凉爽地带传播，CaLas 为耐热型，耐热温度达到 30 ℃以上[7]。患有黄龙病的柑橘树表现为植株矮化，结果变少，果实变小畸形，且着色不均匀[8-10]。通常新树患病后 1～2 a 内死亡，老树患病后 3～5 a 内死亡或丧失结果能力，严重时可造成毁园[11]。目前，亚洲、非洲、大洋洲、北美洲和南美洲近 50 个国家和地区已经出现黄龙病，中国 19 个柑橘生产省（自治区、市）中有 11 个已受到该病危害。据估计柑橘黄龙病已经造成全世界上亿株柑橘树染病或死亡[12-14]，截至 2016 年，美国的佛罗里达州超过 80%的柑橘树已感染黄龙病[15]。由于黄龙病的存在，2011 年佛罗里达州的柑橘产量大约为 1.5 亿箱，预计 20 a 后将保持在该值；若没有黄龙病，20 a 后产量预计达到 2.25 亿箱[16]。如果黄龙病出现在巴西的巴伊亚州，那么未来 20 a 黄龙病将给该州造成巨大损失；如果不对该病进行控制，不对病树进行治疗，那么造成的损失将达 8.9 亿元[17]。

100 多年前，热治疗就已开始在植物上应用，后来用于除去柑橘等多年生植物体中通过嫁接传染的病原菌[18]。Fan 等[19]将感染黄龙病的柑橘树置于受控的温室环境中，让其在 45 和 48 ℃的环境下接受 4 h 处理，8 周之后黄龙病症状明显减轻。在温室环境中处理盆栽柑橘树幼苗可以消除黄龙病症状，并且至少可以维持 2 a[20]。Hoffman 等[21]将感染了 CaLas 病菌的柑橘树置于 40～42 ℃温度可控的温室环境中，连续处理 48 h，可有效减少或消除感染了黄龙病苗木中的 CaLas 病菌；该方法可以用于处理生长于苗圃或温室环境中，且受到 CaLas 病菌感染的柑橘幼苗。但用该种方法在田间处理带病柑橘树 3～10 d，结论却不相同，这可能与试验使用的便携式温室中温度波动和土壤温度低有关[22]。邓晓玲利用自然热罩，将染病柑橘树置于 45～52 ℃环境下持续处理 2～5 h，连续处理 3～4 周，能大大减少或消除病树中的病原菌含量[23-25]。范国成采用自然热罩方法，利用夏秋季强光照处理带病柑橘树 7 h（10:00-17:00），间歇处理 3 次，90 d 后田间

收稿日期：2016-06-24　修订日期：2017-03-29
基金项目：国家自然科学基金项目（61675003）；广东省科技计划项目（2016A020210092，2016A020210100）；教育部高等学校博士学科点专项科研基金（20134404120020）；广东省自然科学基金（2015A030310182）
作者简介：张建桃，男，湖南双峰人，博士，副教授，主要从事精细农业和压电器件方面的研究。广州　华南农业大学数学与信息学院，510642。
Email：zhangjiantao@yeah.net
※通信作者：文　晟，男，湖南长沙人，博士，副教授，主要从事植保机械和精准喷雾技术的研究。广州　华南农业大学工程基础教学与训练中心，510642。Email: vincen@scau.edu.cn

(C)1994-2023 China Academic Journal Electronic Publishing House. All rights reserved.　http://www.cnki.net

柑橘黄龙病树症状明显减轻，黄龙病菌浓度也显著降低[26-27]。利用自然热罩处理带病柑橘树时，树冠顶部温度处于 50～53 ℃范围内，而树冠底部仅有 36～43 ℃[28]，且树冠顶部容易因为处理罩内顶部温度过高而灼伤[29]。林孔湘教授通过利用 48 ℃湿热空气处理带病柑橘苗木可使其恢复健康，但空气温度不均匀会使电烘箱内植株实际所受的温度低于预设的处理温度，进而对处理结果产生影响[30]。

上述研究结果表明，热处理对于柑橘黄龙病的防治是有效的。虽然自然热罩处理对柑橘园地面情况要求不高，但是严重依赖天气条件，且处理罩内温差大，处理周期长，不利于推广应用。本文针对自然热罩处理周期长、效率低、对自然条件依赖大、处理罩内温差大等不足，提出了柑橘黄龙病热空气快速处理方法，并为解决热空气处理时罩内温差过大的问题，搭建了柑橘黄龙病热空气快速处理温度场分布特性试验平台。通过研究有无回风道、风速、热空气入口位置、出口位置、入风口热空气温度对热空气处理温度场分布的影响，为处理罩的结构优化设计提供可靠的依据。

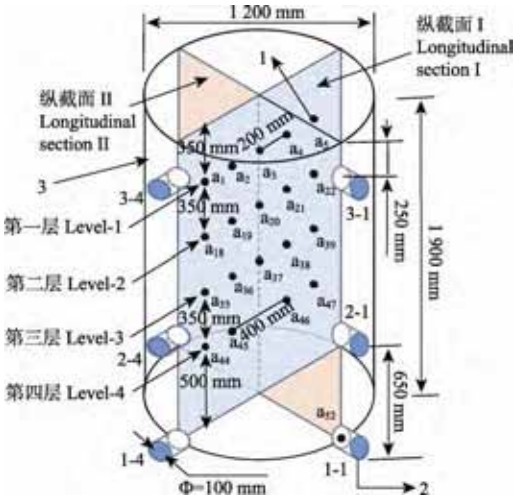
1 试验装置及方法

1.1 热空气快速处理方法

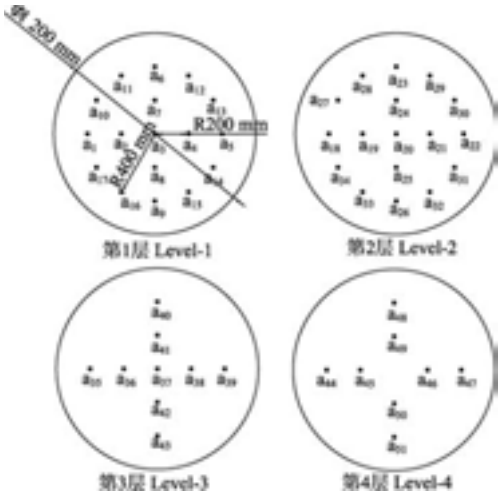
热空气快速处理方法，利用处理罩罩住染病柑橘树，并向其中通入热空气，使罩内温度快速达到均匀状态，各个位置快速达到处理所需温度，以缩短处理时间。该方法使用热处理杀死树体中的病原菌，无需使用农药、抗生素等化学物质，经济环保。与自然热罩相比，不受天气条件影响，即使是在秋冬低温季节，也可用该方法处理带病树体。

1.2 试验平台

柑橘黄龙病热空气处理温度场分布特性试验平台如图 1 所示。此试验平台配置有 HLJT-3380-TX20A 工业热风机（浙江嘉兴航林机电设备有限公司），温控方式为 PID/SSR，电热功率为 20 kW，风机功率为 0.75 kW，风机频率为 50 Hz，风压为 1 210 Pa，最大风量为 1 200 m^3/h。处理罩由 PVC 双面涂塑防水布制成，开口位置在图 1a 中标出，共 12 个，1 号位置对面为 3 号位置，4 号位置对面为 2 号位置。无纸记录仪（杭州盘古自动化系统有限公司），型号为 VX8140R，具有 40 路输入端口，连接 PT100 温度传感器，量程为–200～650 ℃。12 通道温度记录仪（台湾路昌电子企业股份有限公司），型号为 BTM-4208SD，K 型探头分辨率为 0.1 ℃，量程为–50.0～999.9 ℃，精度为±（0.4%+0.5） ℃。工作空间共布置 52 个温度测试点，其中第 52 个测试点测试入风口热空气温度，其余 51 个测试点分布在处理罩内部。树冠层树叶密度由上到下逐层降低，布置测温探头时数量由上到下逐渐减少。第 1 层和第 2 层各布置 17 个测试点，第 3 层布置 9 个测试点，第 4 层布置 8 个测试点，温度探头分布位置如图 1b 所示。试验装置见图 1c，工业热风机经处理罩上的通风口向其内部通入热风，由无纸记录仪和 12 通道温度记录仪同时记录各测点温度，本文试验时室内平均温度为 30 ℃。



a. 试验平台原理图
a. Schematic diagram of experimental platform



b. 测温探头分布
b. Temperature measuring probe distribution



c. 试验平台实物图
c. Physical diagram of experimental platform

1. 温度传感器（a_1～a_{52} 为测温探头） 2. 通风口（1–1～3–4 为各通风口标号） 3. 处理罩 4. 工业热风机 5. 12 通道温度记录仪 6. 无纸记录仪 7. 柑橘树 8. 处理罩
1. Temperature sensor (from a_1 to a_{52} are temperature measuring probes) 2. Air vent(1–1 to 3–4 for each vent label) 3. Heat treatment enclosure 4. Industrial hot air blower 5. 12 channels temperature recorder 6. Paperless recorder 7. Citrus tree 8. Heat treatment enclosure

图 1 温度场分布特性试验平台
Fig.1 Experimental platform of temperature field distribution characteristics

(C)1994-2023 China Academic Journal Electronic Publishing House. All rights reserved. http://www.cnki.net

1.3　试验方法

试验选取 1 棵 3 年生柑橘树（高 1.86 m，树冠最大直径 1.2 m），考虑柑橘树形状以及高度对试验结果的影响，并根据前期试验结果，选取有无回风道、风速、热空气入口位置、出口位置、入风口热空气温度 5 个影响因素，以及相应的水平，如表 1 所示。然后将柑橘树置于处理罩（直径 1.2 m，高度 1.9 m）内，通过对 5 个影响因素进行单因素试验研究，分析这些因素对柑橘黄龙病快速热空气处理温度场均匀性的影响，得出相应的较佳参数。

表 1　试验因素水平值

Table 1　Experimental factors and levels

试验因素 Experimental factors	水平值 Levels
回风道 Air return duct	有、无
风速 Wind speed/(m·s^{-1})	8.5、14.5、17、19.5
热空气入口位置 Hot air inlet position	1-1、2-1
热空气出口位置 Hot air outlet position	2-1、2-2、2-3、2-4、3-1、3-2、3-3、3-4
入风口热空气温度 Inlet hot air temperature/℃	75、90、105

回风道（长度为 4 m）为连接处理罩热空气出口和工业热风机进风口的耐高温管道（Φ=89 mm），作用在于将处理罩出口处温度较高的空气直接导入到工业热风机进风口。每次试验只设置一个热空气入口位置和一个热空气出口位置，其余的通风口用扎带封闭。在选取热空气入口、出口位置时，入口位置和出口位置不位于同一层。试验开始前，调节工业热风机的加热温度，使第 52 个温度探头测得的温度稳定在某一特定的值，然后在此加热温度下进行试验，每次试验进行 10 min，每组试验重复进行 3 次，进行重复试验时根据室温使处理罩内温度降至 32 ℃时开始下一次试验。

1.4　数据处理方法

温度场分布特性是指处理罩内温度分布的均衡性，以温度标准差和温度极差来表示。试验时，由无纸记录仪和 12 通道温度记录仪实时采集各测点的温度，每秒采集一次。分析计算每次试验时各测点的稳定温度值，即在 1 min 内温度波动小于 0.5 ℃时，该时间段内最高温度值与最低温度值的平均值，并计算每组试验重复 3 次后各测点稳定温度的平均值。计算不同参数下各截面的温度标准差，通过 SPSS 数据处理软件分析试验因素对第 1 层、第 2 层、第 3 层、第 4 层、纵截面Ⅰ和纵截面Ⅱ的温度场均匀性影响的显著性。分别计算处理罩内温度场达到稳定状态后，非优选参数和优选参数下各测试点之间的温度极差，分析试验效果。

2　结果与分析

2.1　非优选参数下处理罩内温度分布

选取无回风道、风速 17 m/s、热空气入口位置 2-1、出口位置 3-1、入风口热空气温度 90 ℃进行试验，分析处理罩内各测试点温度分布情况。试验重复进行 3 次，各测试点温度在 9 min 后趋于稳定，稳定温度值及试验分析结果如表 2 所示。从表 2 可知，第 1 层的温度极差为 4.8 ℃，第 2 层的温度极差为 14.6 ℃，第 3 层的温度极差为 9.2 ℃，第 4 层的温度极差为 6.5 ℃。根据表 2 中各测试点温度值，计算出纵截面Ⅰ的温度平均值为 58.8 ℃，温度极差为 18 ℃，纵截面Ⅱ的温度平均值为 57.4 ℃，温度极差为 13.5 ℃。

表 2　非优选参数下温度分布

Table 2　Temperature distribution under non-optimal parameter

℃

测温探头序号 Temperature measuring probe sequence number				测试点温度 Measuring points temperature/℃			
第 1 层 Level-1	第 2 层 Level-2	第 3 层 Level-3	第 4 层 Level-4	第 1 层 Level-1	第 2 层 Level-2	第 3 层 Level-3	第 4 层 Level-4
a_1	a_{18}	a_{35}	a_{44}	58.0	65.7	58.9	57.8
a_2	a_{19}	a_{36}	a_{45}	57.9	69.2	60.9	56.8
a_3	a_{20}	a_{37}	a_{46}	58.2	65.2	59.6	52.6
a_4	a_{21}	a_{38}	a_{47}	58.4	58.3	54.8	51.2
a_5	a_{22}	a_{39}	a_{48}	59.1	56.3	52.2	55.3
a_6	a_{23}	a_{40}	a_{49}	56.4	57.1	51.7	52.5
a_7	a_{24}	a_{41}	a_{50}	57.3	54.6	54.1	54.7
a_8	a_{25}	a_{42}	a_{51}	60.3	59.3	57.6	55.3
a_9	a_{26}	a_{43}		60.2	60.0	60.2	
a_{10}	a_{27}			58.9	68.7		
a_{11}	a_{28}			60.8	65.4		
a_{12}	a_{29}			56.2	57.6		
a_{13}	a_{30}			59.4	56.7		
a_{14}	a_{31}			60.4	56.7		
a_{15}	a_{32}			61.1	58.5		
a_{16}	a_{33}			57.5	59.5		
a_{17}	a_{34}			57.1	59.4		
各层温度平均值 Average temperature of each level/℃				58.7	60.5	56.7	54.5
各层温度极差 Temperature range of each level/℃				4.8	14.6	9.2	6.5
整体温度极差 Temperature range of whole/℃				18.0			

注：无回风道、风速 17 m·s^{-1}、热空气入口位置 2-1、热空气出口位置 3-1、入风口热空气温度 90 ℃。

Note: No air return duct, wind speed is 17 m·s^{-1}, hot air inlet position is 2-1, hot air outlet position is 3-1, and inlet hot air temperature is 90 ℃.

从以上计算结果可以看出，第 2 层的温度平均值最高，第 4 层的温度平均值最低，第 2 层的温度平均值比第 4 层高 6 ℃。整个处理罩内的温度极差为 18 ℃，各截面中，纵截面Ⅰ的温度极差最大，这与第 2 层温度值较高而第 4 层温度值较低有关。第 2 层的温度极差为 14.6 ℃，由于第 2 层所在位置分布着大量树叶，过大的温差容易导致一部分树叶因为过热而出现干枯的现象，另一部分树叶因为热不足出现治疗效果不佳的现象。针对温差过大问题，接下来将对各影响因素进行逐一优选，最后对优选参数进行组合试验，以期减小处理罩内温差，并将优选参数结果与该非优选参数结果进行比较。

2.2　回风道对处理罩内温度场的影响

由于在参数无回风道、风速 17 m/s、热空气入口位置 1-1、出口位置 3-1、入风口热空气温度 90 ℃下，处理罩

(C)1994-2023 China Academic Journal Electronic Publishing House. All rights reserved.　http://www.cnki.net

内温差较非优选参数下有所降低，为了得到更优的参数组合，接下来对该参数组合依次进行轮换，分析有回风道和无回风道对处理罩内第 1 层至第 4 层、纵截面Ⅰ和纵截面Ⅱ的温度场均匀性的影响。试验重复进行 3 次，各测点温度在 9 min 后趋于稳定，稳定温度平均值及第 1、2、3、4 层试验分析结果如表 3 所示。从表 3 可知，有回风道时，第 1、2、3、4 层的平均温度依次为 50.2、50.8、50.6、52.5 ℃；无回风道时，第 1、2、3、4 层的平均温度依次为 53.4、53.8、52.2、51.8 ℃。根据表 3 中各点温度值分析计算纵截面Ⅰ和纵截面Ⅱ在有、无回风道条件下的温度平均值、标准差和显著性。有、无回风道时，纵截面Ⅰ的温度平均值依次为 50.6、51.8 ℃，标准差依次为 1.8、1.8 ℃，显著性 P=0.05；纵截面Ⅱ的平均值依次为 50.8、52.6 ℃，标准差依次为 1.8、1.7 ℃，显著性 P=0.00。

表 3 回风道对处理罩内第 1、2、3、4 层温度场的影响

Table 3 Effect of return air duct on temperature field of level-1, level-2, level-3 and level-4 in heat treatment enclosure ℃

测温探头序号 Temperature measuring probe sequence number				第 1 层 Level-1		第 2 层 Level-2		第 3 层 Level-3		第 4 层 Level-4	
				回风道 Return air duct							
第 1 层 Level-1	第 2 层 Level-2	第 3 层 Level-3	第 4 层 Level-4	有 Yes	无 No	有 Yes	无 No	有 Yes	无 No	有 Yes	无 No
a_1	a_{18}	a_{35}	a_{44}	47.9	55.2	50.0	52.5	51.3	49.8	56.6	51.4
a_2	a_{19}	a_{36}	a_{45}	49.5	52.0	49.6	50.7	49.6	52.1	51.3	48.9
a_3	a_{20}	a_{37}	a_{46}	49.6	50.0	49.3	50.5	49.2	50.6	50.6	52.0
a_4	a_{21}	a_{38}	a_{47}	49.8	49.3	50.0	52.0	51.0	52.9	51.5	52.9
a_5	a_{22}	a_{39}	a_{48}	50.9	51.8	52.3	55.0	51.5	54.1	51.8	54.3
a_6	a_{23}	a_{40}	a_{49}	51.6	55.8	53.6	54.5	53.3	52.0	49.5	50.2
a_7	a_{24}	a_{41}	a_{50}	49.9	52.6	51.2	52.1	50.1	51.4	55.0	51.8
a_8	a_{25}	a_{42}	a_{51}	49.9	51.9	49.8	52.8	49.7	52.2	53.6	52.8
a_9	a_{26}	a_{43}		49.3	53.8	49.9	55.3	50.1	54.8		
a_{10}	a_{27}			49.7	54.6	51.5	53.9				
a_{11}	a_{28}			51.7	56.3	51.9	53.6				
a_{12}	a_{29}			52.2	54.9	52.6	57.0				
a_{13}	a_{30}			52.2	52.6	52.4	55.0				
a_{14}	a_{31}			51.2	53.0	50.1	55.0				
a_{15}	a_{32}			50.5	53.9	49.9	54.9				
a_{16}	a_{33}			50.2	54.6	49.9	55.8				
a_{17}	a_{34}			47.7	55.1	48.8	54.9				
平均值 Mean value/℃				50.2	53.4	50.8	53.8	50.6	52.2	52.5	51.8
标准差 Standard deviation/℃				1.3	2.0	1.4	1.8	1.3	1.6	2.4	1.7
显著性 Significance				P=0.00		P=0.00		P=0.03		P=0.51	

注：风速 17 m·s^{-1}、热空气入口位置 1-1、热空气出口位置 3-1、入风口热空气温度 90 ℃。

Note: wind speed is 17 m·s^{-1}, hot air inlet position is 1-1, hot air outlet position is 3-1, and inlet hot air temperature is 90 ℃.

从计算结果可以看出，在风速为 17 m/s、热空气入口位置为 1-1、热空气出口位置为 3-1、入风口热空气温度为 90 ℃的情况下，回风道对处理罩内 1、2、3 层及纵截面Ⅱ的温度场分布影响显著（P<0.05）。综合各截面温度标准差可知，有回风道时，第 1、2、3 层的温度标准差都明显小于无回风道时，纵截面Ⅰ和纵截面Ⅱ的温度标准差在有、无回风道时接近，即有回风道时，处理罩内温度场均匀性优于无回风道时。这是因为工业热风机通过回风道吸取处理罩内的空气，使处理罩内出风口处形成负压，处理罩内压差增大，内部空气运动加剧，有助于提高内部温度场均匀性。有回风道时，工业热风机吸入的是处理罩内经过加热的热空气，与无回风道时吸入温度为室温的空气相比，加热空气所消耗的能量有所降低。因此，试验结果表明，回风道不仅能使处理罩内的温度场更加均匀，而且能够降低加热空气所需的能耗。

2.3 风速对处理罩内温度场的影响

选取有回风道、热空气入口位置 1-1、热空气出口位置 3-1、入风口热空气温度 90 ℃，分析风速对处理罩内第 1 层至第 4 层、纵截面Ⅰ和纵截面Ⅱ的温度场均匀性的影响。风速分别为 8.5、14.5、17.0、19.5 m/s。试验重复进行 3 次，各测试点温度在 9 min 后趋于稳定，稳定温度平均值如图 2 所示。根据图 2 中各数据点的值，计算各截面在不同风速下的温度平均值、标准差和显著性。当风速为 8.5、14.5、17.0、19.5 m/s 时，第 1 层的温度平均值依次为 44.5、49.2、50.2、54.5 ℃，标准差依次为 1.4、0.9、1.3、1.6 ℃，显著性 P=0.00；第 2 层的温度平均值依次为 44.6、50.1、50.8、55.0 ℃，标准差依次为 1.4、0.9、1.4、1.9 ℃，显著性 P=0.00；第 3 层的温度平均值依次为 44.0、49.4、50.6、55.2 ℃，标准差依次为 1.4、0.7、1.3、2.5 ℃，显著性 P=0.00；第 4 层的温度平均值依次为 45.0、50.5、52.5、55.9 ℃，标准差依次为 2.0、0.6、2.4、1.9 ℃，显著性 P=0.00；纵截面Ⅰ的温度平均值依次为 43.8、49.6、50.6、54.8 ℃，标准差依次为 1.1、1.0、1.8、1.6 ℃，显著性 P=0.00；纵截面Ⅱ的温度平均值依次为 44.8、50.1、50.9、55.9 ℃，标准差依次为 1.5、0.8、1.8、2.2 ℃，显著性 P=0.00。

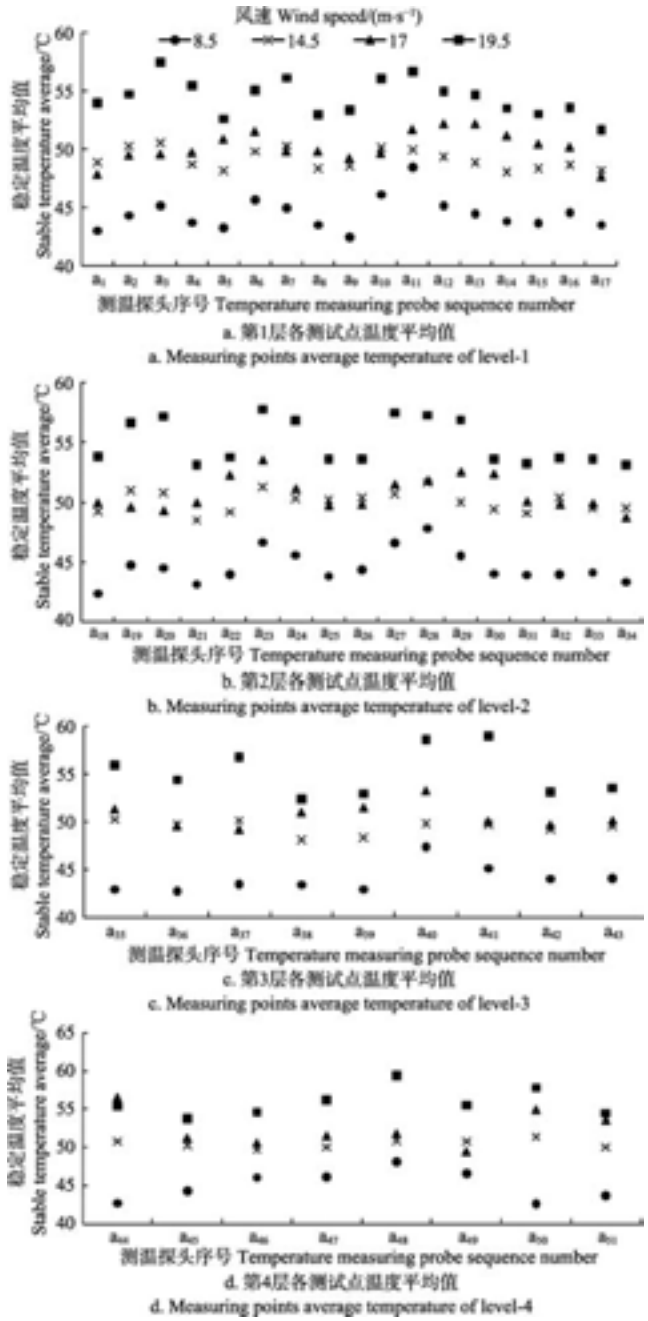
从计算结果可以看出，在有回风道、热空气入口位置为 1-1、热空气出口位置为 3-1、入风口热空气温度为 90 ℃的情况下，风速对处理罩内各截面温度场均匀性均有显著影响（P<0.05），且风速为 14.5 m/s 时，各截面温度标准差均小于其他风速时的温度标准差。风速为 8.5 m/s 时各截面温度平均值均低于其他风速下的温度平均值，风速为 19.5 m/s 时各截面温度平均值最高。试验结果表明，各截面温度平均值随着风速的增加而增加；当风速为 14.5 m/s 时，处理罩内各截面温度场均匀性优于其他风速。

2.4 热空气入口位置对处理罩内温度场的影响

选取有回风道、风速 14.5 m/s、热空气出口位置 3-1、入风口热空气温度 90 ℃，分析热空气入口位置对处理罩内第 1、2、3、4 层、纵截面Ⅰ和纵截面Ⅱ的温度场均匀性的影响。热空气入口位置分别为 1-1、2-1。试验重复进行 3 次，各测点温度在 8 min 后趋于稳定，稳定温度平均值及第 1、2、3、4 层试验分析结果如表 4 所示。从表 4 可知，热空气入口位置为 1-1 时，第 1、2、3、4 层的温度平均值依次为 49.2、50.1、49.4、50.5 ℃；热空气入口位置为 2-1 时，第 1、2、3、4 层的温度平均值依次为 49.8、51.2、52.2、51.9 ℃。根据表 4 中各点温度值分析计算纵截面Ⅰ和纵截面Ⅱ在不同热空气入口位置下的温度平均值、标准差和显著性。热空气入口位置分别为 1-1、2-1 时，

(C)1994-2023 China Academic Journal Electronic Publishing House. All rights reserved. http://www.cnki.net

纵截面Ⅰ的平均值依次为 49.6、50.9℃，标准差依次为 1.0、1.3 ℃，显著性 P=0.00；纵截面Ⅱ的平均值依次为 50.1、51.1 ℃，标准差依次为 0.8、1.3 ℃，显著性 P=0.01。



注：有回风道、热空气入口位置 1-1、热空气出口位置 3-1、入风口热空气温度 90 ℃。

Note: Air return duct, hot air inlet position is 1-1, hot air outlet position is 3-1, and inlet hot air temperature is 90 ℃.

图 2　不同风速下处理罩内各测试点温度分布

Fig.2　Temperature distribution of measuring points in enclosure under different wind speeds

从计算结果可以看出，在有回风道、风速为 14.5 m/s、热空气出口位置为 3-1、入风口热空气温度为 90℃的情况下，热空气入口位置对处理罩内各截面温度场均匀性影响显著（P<0.05）。当热空气入口位置为 1-1 时，各截面温度平均值接近；当热空气入口位置为 2-1 时，各截面温度平均值比热空气入口位置为 1-1 时高，同时各截面的温度标准差也相对较高。因此，综合各截面温度标准差可知，当热空气入口位置为 1-1 时，处理罩内的温度场分布相对均匀。试验结果表明，热空气入口位于处理罩下层时，处理罩内的温度场均匀性更优。

表 4　热空气入口位置对处理罩内第 1、2、3、4 层温度场的影响

Table 4　Effect of hot air inlet position on temperature field of level-1, level-2, level-3 and level-4 in heat treatment enclosure　℃

测温探头序号 Temperature measuring probe sequence number				第 1 层 Level-1		第 2 层 Level-2		第 3 层 Level-3		第 4 层 Level-4	
				热空气入口位置 Hot air inlet position							
第 1 层 Level-1	第 2 层 Level-2	第 3 层 Level-3	第 4 层 Level-4	1-1	2-1	1-1	2-1	1-1	2-1	1-1	2-1
a_1	a_{18}	a_{35}	a_{44}	48.9	51.0	49.3	52.2	50.2	52.6	50.8	52.4
a_2	a_{19}	a_{36}	a_{45}	50.3	49.0	51.0	51.8	49.7	51.9	50.3	49.8
a_3	a_{20}	a_{37}	a_{46}	50.6	49.7	50.8	51.2	50.1	52.2	49.7	52.0
a_4	a_{21}	a_{38}	a_{47}	48.7	49.1	48.5	49.7	48.1	51.5	50.0	52.1
a_5	a_{22}	a_{39}	a_{48}	48.2	48.9	49.2	50.1	48.3	50.2	50.9	53.2
a_6	a_{23}	a_{40}	a_{49}	49.8	48.3	51.3	52.3	49.8	52.4	50.8	52.0
a_7	a_{24}	a_{41}	a_{50}	50.3	49.2	50.3	51.6	49.7	53.0	51.4	50.8
a_8	a_{25}	a_{42}	a_{51}	48.4	49.7	50.2	51.1	49.2	50.0	50.0	50.4
a_9	a_{26}	a_{43}		48.6	51.6	50.4	51.3	49.5	50.6		
a_{10}	a_{27}			50.2	49.8	50.7	51.6				
a_{11}	a_{28}			50.0	49.6	51.6	51.9				
a_{12}	a_{29}			49.4	48.6	50.0	50.6				
a_{13}	a_{30}			48.9	49.4	49.4	49.2				
a_{14}	a_{31}			48.1	50.2	49.1	49.9				
a_{15}	a_{32}			48.4	50.4	50.4	50.5				
a_{16}	a_{33}			48.7	51.7	49.5	52.6				
a_{17}	a_{34}			48.2	51.0	49.5	52.5				
平均值 Mean value/℃				49.2	49.8	50.1	51.2	49.4	52.2	50.5	51.9
标准差 Standard deviation/℃				0.9	1.0	0.9	1.0	0.7	1.4	0.6	1.1
显著性 Significance				P=0.04		P=0.00		P=0.00		P=0.01	

注：有回风道、风速 14.5 m·s^{-1}、热空气出口位置 3-1、入风口热空气温度 90 ℃。

Note: Air return duct, wind speed is 14.5 m·s^{-1}, hot air outlet position is 3-1, and inlet hot air temperature is 90 ℃.

2.5　热空气出口位置对处理罩内温度场的影响

选取有回风道、风速 14.5 m/s、热空气入口位置 1-1、入风口热空气温度 90 ℃，分析热空气出口位置对处理罩内第 1、2、3、4 层、纵截面Ⅰ和纵截面Ⅱ的温度场均匀性的影响。热空气出口位置分别为 2-1、2-2、2-3、2-4、3-1、3-2、3-3、3-4。试验重复进行 3 次，各测点温度在 8 min 后趋于稳定，稳定温度平均值及试验分析结果如表 5 所示。从表 5 可知，热空气出口位置分别为 2-1、2-2、2-3、2-4、3-1、3-2、3-3、3-4 时，第 1 层的温度平均值依次为 49.4、49.1、49.0、49.1、49.2、50.9、48.3、47.2 ℃，第 2 层的温度平均值依次为 49.3、50.6、49.2、49.7、50.1、52.0、48.2、46.6 ℃，第 3 层的温度平均值依次为 48.4、49.9、48.3、48.9、49.4、50.5、47.4、45.9 ℃，第 4 层的温度平均值依次为 47.8、49.2、47.8、48.3、50.5、49.6、46.9、46.3 ℃。根据表 5 中各点温度值分析计算纵截面

(C)1994-2023 China Academic Journal Electronic Publishing House. All rights reserved.　http://www.cnki.net

Ⅰ和纵截面Ⅱ在不同出风口下的平均值、标准差和显著性。热空气出口位置分别为 2-1、2-2、2-3、2-4、3-1、3-2、3-3、3-4 时，纵截面Ⅰ的平均值依次为 48.6、49.2、48.3、48.7、49.6、50.7、47.3、46.3 ℃，标准差依次为 1.2、1.3、1.3、1.0、1.0、1.0、1.2、0.7 ℃，显著性 P=0.00；纵截面Ⅱ的平均值依次为 48.5、49.5、48.6、48.8、50.1、50.7、47.7、46.4 ℃，标准差依次为 0.9、1.5、1.0、0.8、0.8、1.4、1.0、1.0 ℃，显著性 P=0.00。

从表 5 可知，在有回风道、风速为 14.5 m/s、热空气入口位置为 1-1、入风口热空气温度为 90 ℃的情况下，热空气出口位置对处理罩内各截面的温度场均匀性影响显著（P<0.05）。对于第 1、2、3 层，当出风口位于 3-4 时，温度标准差最小。由于树冠层位于 1、2、3 层，故对于 1、2、3 层温度均匀度要求更高。综合各截面温度标准差，可知当热空气出口位于 3-4 时，处理罩内的温度场均匀性最好。出风口 3-2 与 3-4 处于相对位置，均与入风口 1-1 成 90°，故效果应一致，但由于柑橘树长势以及试验误差的影响，使其与 3-4 效果存在一定差异。因此，试验结果表明，热空气出口位于处理罩上层，且与热空气入口成 90°时，处理罩内温度场更均匀。且与一般的下方入风上方出风的设计不同，本设计则重点讨论了不同的出风角度对温度场的影响。

表 5 热空气出口位置对处理罩内第 1、2、3、4 层温度场的影响

Table 5 Effect of hot air outlet position on temperature field of level-1, level-2, level-3 and level-4 in heat treatment enclosure ℃

测温探头序号 Temperature measuring probe sequence number		热空气出口位置 Hot air outlet position															
第 1 层 Level-1	第 2 层 Level-2	2-1	2-2	2-3	2-4	3-1	3-2	3-3	3-4	2-1	2-2	2-3	2-4	3-1	3-2	3-3	3-4
a_1	a_{18}	51.5	50.8	50.2	50.8	48.9	52.5	49.9	48.1	51.0	51.3	50.9	51.1	49.3	52.2	49.2	46.8
a_2	a_{19}	48.5	47.3	49.1	48.3	50.3	50.7	48.0	46.0	48.0	48.5	49.1	48.5	51.0	51.1	47.4	45.9
a_3	a_{20}	48.5	47.1	49.0	48.2	50.6	51.3	48.0	47.2	48.6	48.1	48.5	48.4	50.8	50.5	47.0	46.0
a_4	a_{21}	48.5	47.5	47.8	47.9	48.7	50.3	46.6	46.5	49.2	49.6	48.2	49.0	48.5	50.8	47.0	46.1
a_5	a_{22}	47.9	48.9	47.1	48.0	48.2	49.7	46.2	46.0	48.9	51.0	48.6	49.5	49.2	52.0	48.2	47.0
a_6	a_{23}	49.2	48.5	49.0	48.9	49.8	49.3	48.9	47.8	50.5	51.4	50.5	50.8	51.3	54.5	49.7	46.7
a_7	a_{24}	48.6	46.8	48.1	47.8	50.3	49.9	47.8	47.2	48.2	49.7	48.8	48.9	50.3	51.6	48.2	45.1
a_8	a_{25}	48.6	49.5	48.8	49.0	48.4	51.4	47.7	46.8	48.2	49.5	48.4	48.7	50.2	51.2	47.5	46.3
a_9	a_{26}	47.8	51.1	49.1	49.3	48.6	51.7	48.5	47.3	48.2	51.5	48.8	49.5	50.4	52.4	47.5	46.8
a_{10}	a_{27}	51.2	49.5	49.6	50.1	50.2	51.8	48.8	47.9	51.1	51.5	50.3	51.0	50.7	52.0	48.9	47.8
a_{11}	a_{28}	52.0	50.7	50.4	51.0	50.0	52.3	49.8	48.9	50.3	51.3	49.9	50.5	51.6	52.7	48.5	46.7
a_{12}	a_{29}	48.9	48.0	48.2	48.4	49.4	48.4	48.2	47.9	49.6	50.8	50.0	50.1	50.0	53.4	50.1	47.2
a_{13}	a_{30}	49.4	49.3	48.5	49.1	48.9	49.3	47.7	47.7	48.7	49.3	47.8	48.6	49.4	50.5	47.2	47.9
a_{14}	a_{31}	49.4	50.2	48.9	49.5	48.1	51.5	48.0	46.7	49.3	50.9	48.6	49.6	49.1	51.8	47.7	46.7
a_{15}	a_{32}	49.5	49.9	48.6	49.3	48.4	51.1	47.7	47.2	49.6	51.6	48.8	50.0	50.4	52.2	48.0	47.0
a_{16}	a_{33}	49.5	50.3	49.8	49.9	48.7	52.1	49.4	46.8	48.4	51.7	48.9	49.7	49.5	52.5	48.3	46.4
a_{17}	a_{34}	50.0	50.0	50.1	50.0	48.2	51.5	49.5	46.1	49.6	52.1	49.7	50.5	49.5	52.6	49.6	46.5
平均值 Mean value/℃		49.4	49.1	49	49.1	49.2	50.9	48.3	47.2	49.3	50.6	49.2	49.7	50.1	52.0	48.2	46.6
标准差 Standard deviation/℃		1.2	1.4	0.9	1	0.9	1.2	1.0	0.8	1	1.2	0.9	0.9	0.9	1.0	1.0	0.7
显著性 Significance		P=0.00								P=0.00							
第 3 层 Level-3	第 4 层 Level-4	2-1	2-2	2-3	2-4	3-1	3-2	3-3	3-4	2-1	2-2	2-3	2-4	3-1	3-2	3-3	3-4
a_{35}	a_{44}	49.5	51.1	49.7	50.1	50.2	51.0	48.8	46.6	46.8	50.3	47.5	48.2	50.8	50.2	46.7	46.6
a_{36}	a_{45}	47.9	48.7	48.5	48.4	49.7	50.5	47.1	46.0	46.6	47.8	47.3	47.3	50.3	48.9	46.4	46.3
a_{37}	a_{46}	48.6	48.8	47.8	48.4	50.1	50.7	46.5	45.3	47.7	49.8	48.0	48.5	49.7	50.3	47.1	46.1
a_{38}	a_{47}	48.5	50.5	48.6	49.2	48.1	51.2	47.9	46.3	48.5	48.6	45.0	47.4	50.0	49.1	44.4	45.2
a_{39}	a_{48}	47.8	49.4	47.4	48.2	48.3	49.7	46.9	45.3	48.4	50.8	47.4	48.8	50.9	50.6	47.1	45.4
a_{40}	a_{49}	50.3	52.1	49.0	50.5	49.8	51.7	47.7	45.3	47.5	50.4	47.2	48.4	50.8	50.0	46.5	45.3
a_{41}	a_{50}	47.2	50.2	47.8	48.4	49.7	50.2	46.9	45.4	47.6	48.0	48.5	48.0	51.4	48.6	47.1	47.0
a_{42}	a_{51}	47.5	48.8	48.1	48.1	49.2	49.5	47.5	46.8	49.2	48.2	51.2	49.5	50.0	48.8	49.8	48.6
a_{43}		48.0	49.5	47.7	48.4	49.5	50.1	47.0	46.1								
平均值 Mean value/℃		48.4	49.9	48.3	48.9	49.4	50.5	47.4	45.9	47.8	49.2	47.8	48.3	50.5	49.6	46.9	46.3
标准差 Standard deviation/℃		1.0	1.2	0.7	0.9	0.7	0.7	0.7	0.6	0.9	1.2	1.7	0.7	0.6	0.8	1.5	1.1
显著性 Significance		P=0.00								P=0.00							

注：有回风道、风速 14.5 m·s^{-1}、热空气入口位置 1-1、入风口热空气温度 90 ℃。

Note: Air return duct, wind speed is 14.5 m·s^{-1}, hot air inlet position is 1-1, and inlet hot air temperature is 90 ℃.

(C)1994-2023 China Academic Journal Electronic Publishing House. All rights reserved. http://www.cnki.net

2.6　入风口热空气温度对处理罩内温度场的影响

选取有回风道、风速 14.5 m/s、热空气入口位置 1-1、出口位置 3-4，分析入风口热空气温度对处理罩内第 1、2、3、4 层、纵截面Ⅰ和纵截面Ⅱ的温度场均匀性的影响。入风口热空气温度分别为 75、90、105 ℃。试验重复进行 3 次，各测点温度在 8 min 后趋于稳定，稳定温度平均值及第 1、2、3、4 层试验分析结果如表 6 所示。从表 6 可知，入风口热空气温度为 75 ℃时，第 1、2、3、4 层的温度平均值分别为 45.3、46.0、46.3、47.3 ℃；入风口热空气温度为 90 ℃时，第 1、2、3、4 层的温度平均值分别为 47.2、46.6、45.9、46.3 ℃；入风口热空气温度为 105 ℃时，第 1、2、3、4 层的温度平均值分别为 54.7、55.4、55.8、57.4 ℃。根据表 6 中各点温度值分析计算纵截面Ⅰ和纵截面Ⅱ在不同入风口热空气温度下的温度平均值、标准差和显著性。入风口热空气温度为 75、90、105 ℃时，纵截面Ⅰ的温度平均值依次为 45.8、46.3、55.2 ℃，标准差依次为 1.1、0.7、1.4 ℃，显著性 P=0.00；纵截面Ⅱ的平均值依次为 46.4、46.4、56.0 ℃，标准差依次为 1.2、1.0、1.7 ℃，显著性 P=0.00。

从计算结果可以看出，在有回风道、风速为 14.5 m/s、热空气入口位置为 1-1、出口位置为 3-4 的情况下，入风口热空气温度对处理罩内各截面温度场均匀性影响显著（P<0.05）。各截面平均温度随着入风口热空气温度的升高而升高，综合各截面温度标准差可知，入风口热空气温度为 105 ℃时，处理罩内各截面标准差最大，且与 75、90 ℃相差较大，而入风口热空气温度为 75 ℃与 90 ℃时，各截面温度标准差相差较小。以第 1 层中心位置 a_3 点为例，绘制入风口热空气温度为 75、90 和 105 ℃时该点的温度上升曲线，如图 3 所示。从图 3 可知，当入风口热空气温度为 75 ℃时，a_3 点温度从 32 ℃上升到 45 ℃需要 8 min，前 2 min 温度升高 9 ℃，2 min 后温度上升幅度降低，从 41 ℃上升到 45 ℃用时高达 6 min，且未能达到 48 ℃；当入风口热空气温度为 90 ℃时，a_3 点温度从 32 ℃上升到 45 ℃，用时比 75 ℃时减少了一半，为 4 min，且 2 min 后温度上升速度变缓，从 41 ℃上升到 45 ℃用时为 2 min，上升到 48 ℃用时为 9 min；当入风口热空气温度为 105 ℃时，a_3 点从 32 ℃上升到 45 ℃仅需 2 min，上升到 48 ℃需 3 min，且该阶段为温度快速上升阶段，直到第 4 min 后该点温度上升速度才变缓。

表 6　入风口热空气温度对处理罩内第 1、2、3、4 层温度场的影响

Table 6　Effect of inlet hot air temperature on temperature field of level-1, level-2, level-3 and level-4 in heat treatment enclosure　℃

测温探头序号 Temperature measuring probe sequence number				第 1 层 Level-1			第 2 层 Level-2			第 3 层 Level-3			第 4 层 Level-4		
				入风口热空气温度 Inlet hot air temperature/℃											
第 1 层 Level-1	第 2 层 Level-2	第 3 层 Level-3	第 4 层 Level-4	75	90	105	75	90	105	75	90	105	75	90	105
a_1	a_{18}	a_{35}	a_{44}	44.5	48.1	54.0	45.4	46.8	54.5	45.8	46.6	55.3	48.1	46.6	57.4
a_2	a_{19}	a_{36}	a_{45}	44.7	46.0	53.9	45.1	45.9	54.0	46.1	46.0	54.8	48.3	46.3	59.5
a_3	a_{20}	a_{37}	a_{46}	45.2	47.2	54.8	45.3	46.0	53.8	45.4	45.3	54.7	46.2	46.1	55.7
a_4	a_{21}	a_{38}	a_{47}	44.4	46.5	54.1	45.4	46.1	54.3	45.7	46.3	54.6	46.8	45.2	55.1
a_5	a_{22}	a_{39}	a_{48}	45.2	46.0	55.0	46.3	47.0	56.6	46.5	45.3	56.5	47.1	45.4	56.9
a_6	a_{23}	a_{40}	a_{49}	46.3	47.8	54.5	49.0	46.7	57.7	48.1	45.3	57.0	46.1	45.3	55.6
a_7	a_{24}	a_{41}	a_{50}	45.0	47.2	54.1	47.7	45.1	55.5	45.9	45.4	55.0	47.1	47.0	59.9
a_8	a_{25}	a_{42}	a_{51}	44.7	46.8	54.5	45.9	46.3	55.6	46.6	46.8	57.5	48.3	48.6	59.2
a_9	a_{26}	a_{43}		45.7	47.3	55.5	45.5	46.8	55.6	46.2	46.1	57.1			
a_{10}	a_{27}			44.7	47.9	53.8	44.6	47.8	53.8						
a_{11}	a_{28}			44.9	48.9	54.3	45.7	46.7	53.8						
a_{12}	a_{29}			47.4	47.9	55.3	47.2	47.2	57.3						
a_{13}	a_{30}			46.8	47.7	56.0	46.4	47.9	56.7						
a_{14}	a_{31}			45.7	46.7	55.6	45.4	46.7	57.0						
a_{15}	a_{32}			45.3	47.2	55.4	45.9	47.0	55.8						
a_{16}	a_{33}			45.5	46.8	55.4	45.4	46.4	54.9						
a_{17}	a_{34}			44.9	46.1	54.0	45.4	46.5	54.6						
平均值 Mean value/℃				45.3	47.2	54.7	46.0	46.6	55.4	46.3	45.9	55.8	47.3	46.3	57.4
标准差 Standard deviation/℃				0.8	0.8	0.7	1.1	0.7	1.3	0.8	0.6	1.2	0.9	1.1	1.9
显著性 Significance					P=0.00			P=0.00			P=0.00			P=0.00	

注：有回风道、风速 14.5 m·s^{-1}、热空气入口位置 1-1、热空气出口位置 3-4。

Note: Air return duct, wind speed is 14.5 m·s^{-1}, hot air inlet position is 1-1, and hot air outlet position is 3-4.

综合计算结果和图 3 可知，入风口热空气温度为 75 ℃时，处理罩内各截面温度场均匀性较 105 ℃时好，但温度上升速度慢，耗时长；入风口热空气温度为 105 ℃时，温度上升速度比 75 ℃和 90 ℃时快，但各层温度场均匀性最差，容易出现某些位置过热和某些位置欠热的情况；入风口热空气温度为 90 ℃时，各层温度场均匀性最好，且温度上升速度居中。因此，试验结果表明，入风口热空气温度对处理罩内各层温度场的均匀性影响显著；入风口热空气温度越高，处理罩内温度上升越快；入风口热空气温度为 90 ℃时，处理罩内温度场均匀性最好，温度上升速度较快。

(C)1994-2023 China Academic Journal Electronic Publishing House. All rights reserved.　http://www.cnki.net

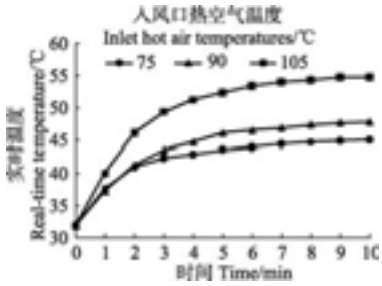


图 3 不同入风口热空气温度下 a_3 点温度上升曲线
Fig.3 Temperature rising curves of a_3 under different inlet hot air temperatures

2.7 优选参数下处理罩内温度分布

选取优选参数有回风道、风速 14.5 m/s、热空气入口位置 1-1、热空气出口位置 3-4、入风口热空气温度 90 ℃，进行 3 次重复试验，分析处理罩内各测试点温度分布情况。试验重复进行 3 次，将 48 ℃视为参考温度[30]，罩内温度从 32 ℃上升到 48 ℃耗时约 9 min，未出现大量落叶情况。各测试点稳定温度值及试验分析结果如表 7 所示。从表 7 可知，第 1 层的温度极差为 2.9 ℃，第 2 层的温度极差为 2.9 ℃，第 3 层的温度极差为 1.6 ℃，第 4 层的温度极差为 3.5 ℃。根据表 7 中各测试点温度值，计算出纵截面Ⅰ的温度平均值为 46.3 ℃，温度极差为 3.0 ℃，纵截面Ⅱ的温度平均值为 46.4 ℃，温度极差为 3.6 ℃。

表 7 优选参数下温度分布
Table 7 Temperature distribution under optimal parameter

测温探头序号 Temperature measuring probe sequence number				测试点温度 Measuring points temperature/℃			
第 1 层 Level-1	第 2 层 Level-2	第 3 层 Level-3	第 4 层 Level-4	第 1 层 Level-1	第 2 层 Level-2	第 3 层 Level-3	第 4 层 Level-4
a_1	a_{18}	a_{35}	a_{44}	48.1	46.8	46.6	46.6
a_2	a_{19}	a_{36}	a_{45}	46.0	45.9	46.0	46.3
a_3	a_{20}	a_{37}	a_{46}	47.2	46.0	45.3	46.1
a_4	a_{21}	a_{38}	a_{47}	46.5	46.1	46.3	45.2
a_5	a_{22}	a_{39}	a_{48}	46.0	47.0	45.3	45.4
a_6	a_{23}	a_{40}	a_{49}	47.8	46.7	45.3	45.3
a_7	a_{24}	a_{41}	a_{50}	47.2	45.1	45.4	47.0
a_8	a_{25}	a_{42}	a_{51}	46.8	46.3	46.8	48.6
a_9	a_{26}	a_{43}		47.3	46.8	46.1	
a_{10}	a_{27}			47.9	47.8		
a_{11}	a_{28}			48.9	46.7		
a_{12}	a_{29}			47.9	47.2		
a_{13}	a_{30}			47.7	47.9		
a_{14}	a_{31}			46.7	46.7		
a_{15}	a_{32}			47.2	47.0		
a_{16}	a_{33}			46.8	46.4		
a_{17}	a_{34}			46.1	46.5		
各层温度平均值 Average temperature of each level/℃				47.2	46.6	45.9	46.3
各层温度极差 Temperature range of each level/℃				2.9	2.9	1.6	3.5
整体温度极差 Temperature range of the whole/℃				3.9			

注：有回风道、风速 14.5 m·s^{-1}、热空气入口位置 1-1、热空气出口位置 3-4、入风口热空气温度 90 ℃。
Note: Air return duct, wind speed is 14.5 m·s^{-1}s, hot air inlet position is 1-1, hot air outlet position is 3-4, and inlet hot air temperature is 90 ℃.

从计算结果可以看出，第 1 层与第 3 层的温度平均值相差最大，为 1.3 ℃。整个处理罩内的温度极差为 3.9 ℃，与非优选参数下整个处理罩内的温度极差（18 ℃）相比下降了 14.1 ℃。各截面的温度极差与 2.1 节中非优选参数下各截面的温度极差相比，第 1 层下降了 1.9 ℃，第 2 层下降了 11.7 ℃，第 3 层下降了 7.6 ℃，第 4 层下降了 3 ℃，纵截面Ⅰ下降了 15 ℃，纵截面Ⅱ下降了 9.9 ℃。因此，试验结果表明，优选参数组合下处理罩内温度场分布与非优选参数下相比更加均匀，优选参数下罩内各点温度从 32 ℃上升到 48 ℃耗时约 9 min。

3 处理效果检测

根据以上试验结果，处理田间带病柑橘树，对处理前后柑橘树叶进行实时荧光定量聚合酶链反应（polymerase chain reaction，PCR）检测，以研究柑橘黄龙病快速热空气处理效果。

试验在华南农业大学柑橘黄龙病研究室的柑橘实验园进行，选取 6 棵带病柑橘树，分为 2 组，每组 3 棵。第一组（hot-1，hot-2，hot-3）采用热空气快速处理方法进行处理，所用参数根据本研究得出的最优参数进行设置，为有回风道，风速 14.5 m/s，热空气入口位于处理罩下层，热空气出口位于处理罩上层，且与入口成 90°。由于进行该试验时外界温度（20 ℃）较低，根据已有的试验经验以及柑橘树的耐热性[31]，调节入风口热空气温度至 100 ℃，加热 9 min 处理罩内平均温度升至 48℃，保持 6 min 后，关闭加热，自然降温 10 min 至 30 ℃时结束，试验装置布置如图 4 所示，该试验每周进行一次，连续进行四周。第二组（hot-CK-1，hot-CK-2，hot-CK-3）作为对照组，不进行处理。在第一次试验前，采集来自试验组以及对照组共 6 棵树的树叶样本，在东西南北 4 个方位各采集一片，进行实时荧光定量 PCR 检测，第 4 次试验结束一个月后，再次采集树叶样本进行检测，检测结果如表 8 所示。



1. 处理罩 2. 工业热风机 3. 入风道 4. 回风道
1. Heat treatment enclosure 2. Industrial hot air blower 3. Air inlet duct 4. Air return duct

图 4 田间效果试验装置图
Fig.4 Experiment device of field effect

(C)1994-2023 China Academic Journal Electronic Publishing House. All rights reserved. http://www.cnki.net

表 8　样本实时荧光定量 PCR 检测结果

Table 8　Sample real-time fluorescence quantitative PCR detection results

样本 Sample	*Ct* 值 *Ct* Value		病菌浓度 Bacteria concentration		浓度降低率 Concentration reduction rate/%
	处理前 Before treatment	处理后 After treatment	处理前 Before treatment	处理后 After treatment	
hot-1	23.46	25.78	1.73×10^{8}	3.20×10^{7}	81.47
hot-2	19.85	21.98	2.38×10^{9}	5.07×10^{8}	78.72
hot-3	20.13	22.39	1.94×10^{9}	3.76×10^{8}	80.64
hot-CK-1	18.70	17.86	5.49×10^{9}	1.01×10^{10}	–84.10
hot-CK-2	20.79	19.81	1.20×10^{9}	2.45×10^{9}	–103.81
hot-CK-3	21.18	21.54	9.06×10^{8}	6.97×10^{8}	23.01

注：*Ct* 值为 4 片树叶检测结果的平均值；处理后表示第 4 次处理结束一个月后；病菌浓度(*CN*)为每 ng 总 DNA 中黄龙病菌拷贝数[26]，计算公式为 $CN=35.50\times10^{8}\times10^{(Ct-19.3)/-3.1692}$。

Note: *Ct* value is the average of four leaves test results; After treatment means one month after the end of the fourth treatment; Bacterial concentration (*CN*) is the copy number of huanglongbing bacteria in the total DNA of each nanogram, the formula is $CN=35.50\times10^{8}\times10^{(Ct-19.3)/-3.1692}$.

Ct 值表示在 PCR 扩增过程中，扩增产物（荧光信号）到达阈值时（进入指数增长期）所经过的扩增循环次数，当 *Ct* 值低于 30 时，则可认为样本感染了黄龙病[32]。从表 8 可以看出，所选试验树均感染了黄龙病，处理前实验组的平均 *Ct* 值为 21.15，病菌平均浓度（*CN*）为 1.50×10^{9}，经过 4 次处理后，试验组 *Ct* 值增加，平均 *Ct* 值为 23.38，病菌平均浓度变为 3.05×10^{8}，病菌浓度平均降低率为 80.28%。处理前对照组的平均 *Ct* 值为 20.22，病菌平均浓度为 2.53×10^{9}，一个月后，对照组平均 *Ct* 值降低，为 19.74，病菌平均浓度变为 4.42×10^{9}，一个月后对照组病菌平均浓度比处理前升高了 75%。因此，可以认为热空气快速处理对于柑橘黄龙病防治具有一定效果。

4　结　论

研究结果表明：1）回风道对处理罩内第 1、2、3 层和纵截面Ⅱ有显著影响（$P<0.05$），对第 4 层和纵截面Ⅰ无显著影响（$P>0.05$）。回风道不仅能使处理罩内的温度场更加均匀，而且能够降低能耗。2）风速对处理罩内各截面的温度场均有显著影响（$P<0.05$）。各截面温度平均值随着风速的增加而增加，当风速为 14.5 m/s 时，处理罩内各截面温度场均匀性优于其他风速。3）热空气入口位置对处理罩内各截面温度场均有显著影响（$P<0.05$）。热空气入口位于处理罩下层时，处理罩内的温度更均匀。4）热空气出口位置对处理罩内各截面温度场均有显著影响（$P<0.05$）。热空气出口位于处理罩上层，且与热空气入口位置成 90°时，处理罩内温度更均匀。5）入风口热空气温度对处理罩内各截面温度场均有显著影响($P<0.05$)；入风口热空气温度越高，处理罩内温度上升越快；从处理罩内温度场均匀性和温度上升速度两方面考虑，入风口热空气温度为 90 ℃时，处理罩内各截面温度场均匀性较其他温度好。6）热空气快速处理方法对于柑橘黄龙病的防治具有一定效果。

通过试验得出柑橘黄龙病快速热空气处理的优选参数为：有回风道，风速为 14.5 m/s，热空气入口位于处理罩下层，热空气出口位于处理罩上层，且与入口成 90°，入风口热空气温度为 90 ℃。在优选参数下，罩内温度从 32 ℃上升至 48 ℃，加热时间约为 9 min，且罩内温度场分布较均匀。处理罩内温度场达到稳定状态后，优选参数下整个处理罩内的温度极差为 3.9 ℃，非优选参数下处理罩内的温度极差为 18 ℃，与非优选参数相比，优选参数下处理罩内的温度极差下降了 14.1 ℃。各截面的温度极差与非优选参数下各截面的温度极差相比，第 1 层下降了 1.9 ℃，第 2 层下降了 11.7 ℃，第 3 层下降了 7.6 ℃，第 4 层下降了 3 ℃，纵截面Ⅰ下降了 15 ℃，纵截面Ⅱ下降了 9.9 ℃。经过热空气处理后患病柑橘树的病菌浓度下降，平均降低率为 80.28%

此次试验虽然说明了热空气处理对柑橘黄龙病的防治具有一定的效果，但是未能考虑各影响因素之间的交互作用，除此之外，利用热空气处理方式防治柑橘黄龙病需要对病树进行处理的次数、相邻两次处理的时间间隔、每次处理的时间以及处理温度等对柑橘黄龙病处理效果的影响，以及如何提高处理效果，还需进行进一步的研究。

[参　考　文　献]

[1] Bové J M. Half a century on huanglongbing learning about the disease, trying to control it[J]. Journal of Citrus Pathology, 2015, 2(1): 1－4.

[2] Bové J M. Huanglongbing or yellow shoot, a disease of Gondwanan origin: Will it destroy citrus worldwide?[J]. Phytoparasitica, 2014, 42(5): 579－583.

[3] Wang N, Trivedi P. Citrus huanglongbing: A newly relevant disease presents unprecedented challenges[J]. Phytopathology, 2013, 103(7): 652－665.

[4] 程春振，曾继吾，钟云，等. 柑橘黄龙病研究进展[J]. 园艺学报，2013，40(9)：1656－1668.
Cheng Chunzhen, Zeng Jiwu, Zhong Yun, et al. Research progress on citrus huanglongbing disease[J]. Acta Horticulturae Sinica, 2013, 40(9): 1656－1668. (in Chinese with English abstract)

[5] Trivedi P, He Z, Van Nostrand J D, et al. Huanglongbing alters the structure and functional diversity of microbial communities associated with citrus rhizosphere[J]. Isme J, 2012, 6(2): 363－383.

[6] Gasparoto M, Coletta H, Bassanezi R, et al. Influence of temperature on infection and establishment of 'Candidatus Liberibacter americanus' and 'Candidatus Liberibacter asiaticus' in citrus plants[J]. Plant Pathology, 2012, 61(4): 658－664.

[7] 贾志成，郑加强，黄雅杰，等. 柑橘黄龙病热处理防治技术研究进展[J]. 农业工程学报，2015，31(23)：1－9.
Jia Zhicheng, Zheng Jiaqiang, Huang Yajie, et al. Review and prospect of thermotherapy for citrus huanglongbing[J]. Transactions of the Chinese Society of Agricultural Engineering (Transactions of the CSAE), 2015, 31(23): 1－9. (in Chinese with English abstract)

(C)1994-2023 China Academic Journal Electronic Publishing House. All rights reserved.　http://www.cnki.net

[8] 陈凯男，李充璧. 柑橘黄龙病研究概况[J]. 浙江农业科学，2015，56(7)：1048－1050.
Chen Kainan, Li Chongbi. Research overview on citrus huanglongbing disease[J]. Journal of Zhejiang Agricultural Sciences, 2015, 56(7): 1048－1050. (in Chinese with English abstract)

[9] 梅慧兰，邓小玲，洪添胜，等. 柑橘黄龙病高光谱早期鉴别及病情分级[J]. 农业工程学报，2014，30(9)：140－147.
Mei Huilan, Deng Xiaoling, Hong Tiansheng, et al. Early detection and grading of citrus huanglongbing using hyperspectral imaging technique[J]. Transactions of the Chinese Society of Agricultural Engineering (Transactions of the CSAE), 2014, 30(9): 140－147. (in Chinese with English abstract)

[10] Lee J A, Halbert S E, Dawson W O, et al. Asymptomatic spread of huanglongbing and implications for disease control[J]. Proceedings of the National Academy of Sciences, 2015, 112(24): 7605－7610.

[11] 陈国庆，鹿连明，杜丹超，等. 柑橘黄龙病防控技术研究进展[J]. 浙江柑橘，2012，29(3)：20－27.
Chen Guoqing, Lu Lianming, Du Danchao, et al. Research progress on citrus huanglongbing disease prevention and control technology[J]. Zhejiang Citrus, 2012, 29(3): 20－27.(in Chinese with English abstract)

[12] 许美容，戴泽翰，孔维文，等. 基于分子技术的柑橘黄龙病研究进展[J]. 果树学报，2015，32(2)：322－334.
Xu Meirong, Dai Zehan, Kong Weiwen, et al. Citrus Huanglongbing research based on molecular biology techniques[J]. Journal of Fruit Science, 2015, 32(2): 322－334. (in Chinese with English abstract)

[13] 张娟，王宁，张以民，等. 基于 Web of Science 的国际柑橘黄龙病文献计量分析[J]. 果树学报，2014，31(6)：1139－1146.
Zhang Juan, Wang Ning, Zhang Yiming, et al. Bibliometric analisis of the research on Citrus Huanblongbing based on Web of Science[J]. Journal of Fruit Science, 2014, 31(6): 1139－1146. (in Chinese with English abstract)

[14] 刘蕊，杜小珍，钟进良，等. 梅州市柑橘黄龙病的发生与防治[J]. 现代农业科技，2012(4)：209－213.
Liu Rui, Du Xiaozhen, Zhong Jinliang, et al. Occurrence and control of citrus yellow shoot disease in meizhou city[J]. Modern Agricultural Science and Technology, 2012(4): 209－213. (in Chinese with English abstract)

[15] Stover E, Inch S, Richardson M L, et al. Conventional citrus of some Scion/Rootstock combinations show field tolerance under high huanglongbing disease pressure[J]. HortScience, 2016, 51(2): 127－132.

[16] Spreen T H, Baldwin J. The impact of huanglongbing (HLB) on citrus tree planting in Florida[C]// Annual Meeting of the Southern Agricultural Economics Association, 2013.

[17] de Oliveira J, Do Nascimento A, de Miranda S, et al. Estimating the economic impact of an eventual introduction of huanglongbing (HLB) in the state of Bahia, Brazil[J]. Revista Brasileira De Fruticultura, 2013, 35(3): 755－762.

[18] 林雄杰，范国成，胡菡青，等. 湿度对田间自然热罩防治柑橘黄龙病的影响[J]. 福建农业学报，2014，29(5)：475－482.
Lin Xiongjie, Fan Guocheng, Hu Hanqing, et al. The effect of humidity on citrus huanglongbing thermotherapy in the field[J]. Fujian Journal of Agricultural Sciences, 2014, 29(5): 475－482. (in Chinese with English abstract)

[19] Fan G, Xia Y, Lin X, et al. Evaluation of thermotherapy against Huanglongbing (citrus greening) in the greenhouse[J]. Journal of Integrative Agriculture, 2016, 15(1): 111－119.

[20] Brien D O, Duan Y. Prescription for curing citrus greening[J]. Agricultural Research, 2013, 61(7): 4-6.

[21] Hoffman M T, Doud M S, Williams L, et al. Heat treatment eliminates' Candidatus Liberibacter Asiaticus' from infected citrus trees under controlled conditions[J]. Phytopathology, 2013, 103(1): 15－22.

[22] Doud M, Hoffman M, Zhang M, et al. Thermal treatments eliminate or suppress the bacterial pathogen in huanglongbing-affected citrus[C]// Annual Meeting of the American-Phytopathological-Society (APS), Providence, RI, 2012. Amer Phytopathological Soc, 3340 Pilot Knob Road, St Paul, Mn 55121 Usa, Aug 04-08, 2012.

[23] 邓晓玲，许美容，关磊，等. 一种利用热处理防治柑橘黄龙病的方法：103404397 A[P]，2013-11-27.

[24] Deng X L, Guan L, Liang M D, et al. Heat treatment of huanglongbing-affected citrus trees in field for reduction of “ Candidatus Liberibacter asiaticus” [C]// International Citrus Congress Proceedings, 2012.

[25] 关磊，梁美丹，仇绮琪，等. 利用热处理技术降低柑橘黄龙病菌的浓度[C]// 中国植物病理学会 2012 年学术年会，青岛，2012.
Guan Lei, Liang Meidan, Chou Qiqi, et al. Reducing the concentration of citrus huanglongbing virus by heat treatment technology[C]// Academic annual meeting of the Chinese Society for plant pathology 2012. Qingdao, China, 2012. (in Chinese with English abstract)

[26] 范国成，林雄杰，王贤达，等. 田间自然热罩治疗柑橘黄龙病的效果分析[J]. 果树学报，2016：1－12.
Fan Guocheng, Lin Xiongjie, Wang Xianda, et al. Field study of the efficacy of PVC film cover against Huanglongbing[J]. Journal of Fruit Science, 2016: 1－12.(in Chinese with English abstract)

[27] Fan G, Liu B, Lie X, et al. Study of thermotherapy against citrus huanglongbing in fujian province, china[J]. Journal of Citrus Pathology, 2014, 1(1): 216.

[28] Khot L R, Jones S E, Trivedi P, et al. In-field thermal treatment of Huanglongbing (HLB) infected trees [J]. Journal of Citrus Pathology, 2014, 1(1): 212.

[29] Ehsani R, De Corcuera J I R, Khot L. The potential of thermotherapy in combating HLB[J]. Resource Magazine, 2013, 20(6): 18－19.

[30] 林孔湘, 骆学海. 柑桔黄稍（黄龙）病热治疗的初步研究[J]. 植物保护学报, 1965, 4(2): 169－175.
Lin Kongxiang, Luo Xuehai. A preliminary study on thermotherapy of Yellow shoot disease of citrus[J]. Acta

(C)1994-2023 China Academic Journal Electronic Publishing House. All rights reserved. http://www.cnki.net

Phytophylacica Sinica, 1965, 4(2): 169－175. (in Chinese with English abstract)

[31] Lopes S A, Frare G F, Bertolini E, et al. Liberibacters associated with citrus huanglongbing in Brazil:‘Candidatus Liberibacter asiaticus’ is heat tolerant,‘Ca. L. americanus’ is heat sensitive[J]. Plant Disease, 2009, 93(3): 257－262.

[32] 张贺，李波，周虚，等. 实时荧光定量 pcr 技术研究进展及应用[J]. 动物医学进展，2006，27（增刊 1）：5－12. Zhang He, Li Bo, Zhou Xu, et al. Progress and application of real-time fluorescent quantitative polymerase chain reaction [J]. Progress in Veterinary Medicine, 2006, 27(Supp.1): 5－12. (in Chinese with English abstract)

Experiment on temperature field distribution characteristics of citrus huanglongbing hot air rapid treatment

Zhang Jiantao[1], Chen Hong[1], Wen Sheng[2※], Li Shenghua[3], Deng Xiaoling[4], Lan Yubin[3]

(1. *College of Mathematics and Informatics, South China Agricultural University, Guangzhou* 510642, *China*;
2. *Engineering Fundamental Teaching and Training Center, South China Agricultural University, Guangzhou* 510642, *China*;
3. *Engineering College, South China Agricultural University, Guangzhou* 510642, *China*;
4. College of Electronic Engineering, South China Agricultural University, Guangzhou 510642, *China*)

Abstract: For the weak points of citrus huanglongbing (HLB) heat treatment by sunlight, such as long treatment period, low efficiency, serious dependence on natural condition, and large temperature difference in treatment enclosure, one citrus HLB hot air rapid treatment method was proposed. To solve the problem of large temperature difference in the heat treatment enclosure, an experimental platform was set up for analyzing the temperature field distribution characteristics of HLB hot air rapid treatment, which consisted of heat treatment enclosure, industrial hot air blower, paperless recorder and 12-channel temperature recorder. And the influence of air return duct existence or not, wind speed, hot air inlet position, outlet position, and inlet hot air temperature on the temperature field distribution of hot air treatment were investigated. The results showed that: (a) Return air duct had a significant impact on the cross section of middle and upper layer and the longitudinal section where the hot air inlet position existed in the enclosure, but had no significant effect on the cross section of lower layer and the longitudinal section where the hot air outlet position existed. When there was a air return duct, not only the uniformity was better in the enclosure, but also the energy consumption was lower than the condition without it. (b) Wind speed had a significant impact on each section in the heat treatment enclosure, and the average temperature of each section increased with the increase of wind speed. When the wind speed was 14.5 m/s, the uniformity of each section was better. (c) Hot air inlet position had a significant impact on each section in the heat treatment enclosure, and the uniformity of each section was better when the hot air inlet position was located at the lower layer of the enclosure. (d) Hot air outlet position had a significant impact on each section in the heat treatment enclosure, and the uniformity of each section was better when the hot air outlet position was located at the upper layer of the enclosure, which had a 90° angle with the inlet position. (e) Inlet hot air temperature had a significant impact on each section in the heat treatment enclosure, and the higher the inlet temperature, the faster the temperature rising in the heat treatment enclosure. When the uniformity and the rising speed of temperature in the enclosure were taken into consideration, 90 ℃ was the best temperature of inlet hot air. (f) The optimal parameters were that there was a return air duct, the wind speed was 14.5 m/s, the hot air inlet position was located at the lower layer of the enclosure, the hot air outlet position was located at the upper layer of the enclosure, which had a 90° angle with the inlet position, and the inlet hot air temperature was 90℃. Under the optimal parameters, the temperature in the treatment enclosure rising from 32 to 48 ℃ took about 9 min, and the temperature range of the whole enclosure was 3.9 ℃, which dropped by 14.1 ℃ compared to that under non-optimal parameters; and the temperature range of each section under the optimal parameters was also decreased. Under the optimal parameters, the effectiveness of rapid hot air treatment on the control of citrus HLB was proved, and the average reduction rate of bacteria concentration after treatment was 80.28%. The results provide a reference for the optimization design of large-scale HLB hot air treatment equipment.

Keywords: disease control; heat treatment; temperature; uniformity; Huanglongbing

(C)1994-2023 China Academic Journal Electronic Publishing House. All rights reserved.　http://www.cnki.net

房阿曼，等. 基于土地适宜性的耕地规划 CA 模拟及验证（图3）

Fang Aman, et al. CA simulation and verification of cultivated land planning based on land suitability (Figure 3)

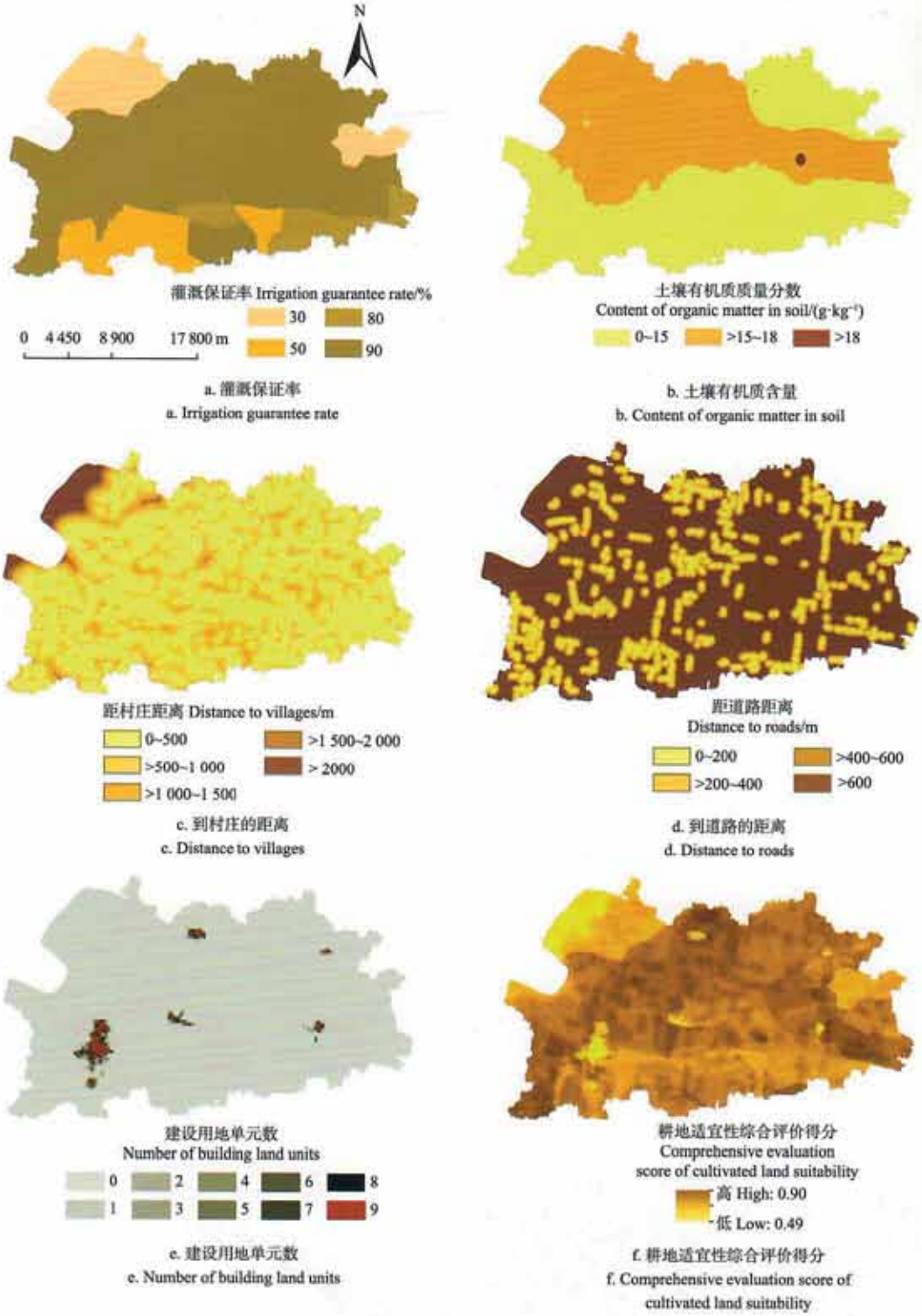


图 3 部分评价因子及综合评价结果图

Fig.3 Part of evaluation factors and comprehensive evaluation result

中国标准连续出版物号：ISSN 1002-6819 CN11-2047/S　　国内邮发代号：18-57　　国内定价：50 元

2.4 农用超声雾化换能器参数优化设计与试验

《中文核心期刊要目总览》收录
Ei Compendex(核心版)收录
百种中国杰出学术期刊
RCCSE中国权威学术期刊

2015. 12
第31卷 VOL. 31

ISSN 1002-6819
CN 11-2047/S
CODEN NGOXEO

农业工程学报

TRANSACTIONS OF THE CHINESE SOCIETY OF AGRICULTURAL ENGINEERING

NONGYE GONGCHENG XUEBAO



ISSN 1002-6819

中国农业工程学会 主办

农业工程学报
二〇一五年六月
第三十一卷
第十二期
中国农业工程学会

农 业 工 程 学 报

2015 年 6 月　第 12 期　总第 263 期（第 31 卷）

目　次

·综合研究·关键技术·

基于激光诱导击穿光谱的土壤类型判别分析……余克强，何　勇，刘　飞（1）

·农业装备工程与机械化·

农用超声雾化换能器参数优化设计与试验 ……张建桃，李晟华，文　晟，等（8）

4LZ-0.8 型水稻联合收割机清选装置气固两相分离作业机理…… 任述光，谢方平，王修善，等（16）

水稻气力式排种器投种轨迹试验与分析 …… 邢　赫，臧　英，曹晓曼，等（23）

4LZG-3.0 型谷子联合收割机的设计与试验 ……梁苏宁，金诚谦，张奋飞,等（31）

4U1Z 型振动式马铃薯挖掘机的设计与试验…… 吕金庆，田忠恩，吴金娥，等（39）

刀齿排布旋向对免耕覆秸精播机清秸单体性能的影响 …… 顿国强，陈海涛，李　昂，等（48）

轮式拖拉机线控液压转向系统路感特性与评价 …… 鲁植雄，刁秀永，龚佳慧，等（57）

轻载荷条件下轻型车辆车轮牵引通过性模型的建立与验证 …… 黄　晗，李建桥，吴宝广，等（64）

柴油机喷油脉宽和喷油压力变化对喷油器流量系数的影响 …… 杜慧勇，张紫微，刘建新，等（71）

基于非奇异终端滑模的物料提升机位置控制 ……姚来鹏，侯保林（77）

自动变速器换挡控制参数自整定策略应用 …… 鲁　曦，郭　伟，王书翰，等（83）

基于粒子图像测速技术的液力变矩器涡轮内流场测试与分析 …… 柴博森，王玉建，刘春宝，等（92）

·农业水土工程·

气候变化背景下中国北方干湿区降水资源变化特征分析 …… 高继卿，杨晓光，董朝阳，等（99）

基于节水高产优质目标的冬小麦适宜水分亏缺模式 ……王书吉，康绍忠，李　涛（111）

生物质炭对冬小麦产量、水分利用效率及根系形态的影响 ……李中阳，齐学斌，樊向阳，等（119）

水稻控制灌溉对稻麦轮作农田 N_2O 排放的调控效应……侯会静，陈　慧，杨士红，等（125）

递推关系概化前期产流条件改进 SCS 模型 ……焦平金，许　迪，于颖多，等（132）

不同水分胁迫条件下 DSSAT-CERES-Wheat 模型的调参与验证 ……姚　宁，周元刚，宋利兵，等（138）

基于动水法的流量过程线推移法在渠道渗漏计算中的应用 ……柴春岭，高惠嫣，杨路华，等（151）

基于探地雷达波振幅包络平均值确定土壤含水率 ……吴志远，彭苏萍，杜文凤，等（158）

深沟造林条件下秸秆覆盖对土壤养分和盐分变化的影响 ……鲁天平，史　征，刘永萍，等（165）

·农业信息与电气技术·

基于 GIS 和 RS 的大理河流域植被格局分形维数时空变化特征 ……李斌斌，李占斌，李　鹏（173）

·农业装备工程与机械化·

农用超声雾化换能器参数优化设计与试验

张建桃[1]，李晟华[2]，文　晟[2]，兰玉彬[2]，廖贻泳[2]，张铁民[2※]
（1. 华南农业大学数学与信息学院，广州 510642；　2. 华南农业大学工程学院，广州 510642）

摘　要：为解决超声雾化换能器用于超低量喷雾时雾化量少、换能器结构复杂等问题，根据超声雾化换能器的工作原理和农药喷施对换能器提出的雾化要求，设计了一种农用超声雾化换能器。首先利用 ANSYS 参数化设计语言建立换能器超声振子的参数化模型；然后对其进行尺寸参数优化，在设定的雾滴体积中径 3～5 μm 范围内，使雾化量达到最大；最后根据优化结果制作样机，进行相关试验测试。试验结果表明，当施加峰-峰值为 100 V 的交流正弦电压时，超声雾化换能器最大雾化量从 1.20 提高到 1.29 g/min，相比优化前提高了 7.5%，93%的雾滴颗粒直径分布在设定的 3～5 μm 范围内，并且实测的换能器谐振频率与仿真结果的误差为 5.9%。研究结果为农用超声雾化换能器结构优化设计和雾化量的提高提供参考。

关键词：喷雾；有限元法；优化；结构设计；超低量喷雾
doi：10.11975/j.issn.1002-6819.2015.12.002
中图分类号：S224.3　　**文献标志码**：A　　**文章编号**：1002-6819(2015)-12-008-08

张建桃，李晟华，文　晟，等. 农用超声雾化换能器参数优化设计与试验[J]. 农业工程学报，2015，31(12)：8－15.
doi：10.11975/j.issn.1002-6819.2015.12.002　http://www.tcsae.org
Zhang Jiantao, Li Shenghua, Wen Sheng, et al. Parameter optimization design and experiment of agricultural ultrasonic atomization transducer[J]. Transactions of the Chinese Society of Agricultural Engineering (Transactions of the CSAE), 2015, 31(12): 8－15. (in Chinese with English abstract)　doi：10.11975/j.issn.1002-6819.2015.12.002　http://www.tcsae.org

0　引　言

化学防治具有工效高、防治及时等特点，在农作物保护上发挥了巨大的作用。据统计，中国病虫害化学防治年均挽回粮食产量损失 750 亿 kg 以上，约占中国粮食年产量的 15%，化学防治是减少农作物病虫草害频发、保障粮食稳产增产和农产品品质安全的有效措施[1]。

目前，中国农业上常用结构简单的手动喷雾器进行大喷量、盲目、不对称的施药，普遍存在着较为严重的“跑、冒、滴、漏”等现象[2]，而且农药的喷施量大，产生的雾滴粒径粗，在作物上的附着率低，农药利用率只有 30%左右，导致防治效果下降和用药量增加。此外，常规喷雾的大部分农药都沉降到土地和飘移到周围环境中，严重污染和破坏农业生态环境，导致农产品出现质量安全问题，甚至造成人畜中毒。

近年来，超低量喷雾是植保行业大力推广的一种施药技术[3]。研究结果表明，超低量喷雾与常规喷雾相比，可节约农药 10%～30%[4-5]。为满足超低量喷雾和生物最佳粒径的要求，现有的超低量喷雾器主要采用压力雾化、离心雾化、静电雾化等一种或多种雾化方式相结合的方法，存在喷雾器结构较复杂，成本较高等缺点[2]。超声雾化换能器具有结构紧凑、响应迅速，且具有雾化颗粒直径较小、粒径均匀等特点，已广泛应用于空气加湿、油雾润滑、雾化治疗、超声喷墨和药品喷雾干燥等诸多领域[6-11]。文献[2]对超声雾化应用于农药超低量喷雾的前景进行了分析，得出超声雾化具有省时、省力、节水和雾滴便于管道输送等优点。

目前市面上现有超声雾化换能器的结构没有专门针对农药喷施进行设计，结构较复杂，雾化量有待进一步提高。本文根据超声雾化换能器的工作原理和农药喷施对换能器提出的雾化要求，研制一种农用超声雾化换能器，利用 ANSYS 参数化设计语言（ANSYS parametric design language，APDL）建立了换能器超声振子的参数化模型，进行尺寸参数优化，最后根据优化结果制作样机，并进行相关试验测试，以期达到增大雾化量的目的。

1　农用超声雾化换能器结构及其超声振子有限元模型

1.1　超声雾化工作原理

在超声振子上加载高频正弦交流电压，压电材料的逆压电效应使其产生高频机械振动，即超声波，超声波按照正弦曲线规律在液体介质中纵向传播，强弱相间，依次传递，当较弱的声波信号作用于液体介质时，液体介质产生负压，介质内部出现大量微小的气泡，当较强的声波信号作用于液体介质时，则会对液体产生一定的正压，介质中的微小气泡随之长大和崩溃，同时释放能量巨大的冲击波，相当于瞬间产生几百度高温和上百兆

收稿日期：2015-05-16　修订日期：2015-06-04
基金项目：广东省自然科学基金（S2013010013747）；教育部高等学校博士学科点专项科研基金（20134404120020）
作者简介：张建桃，男，湖南双峰人，博士，副教授，硕士生导师，主要从事压电器件和精细农业方面的研究。广州　华南农业大学数学与信息学院，510642。Email：zhangjiantao@yeah.net
※通信作者：张铁民，男，黑龙江人，博士、双博士后，教授，博士生导师，主要从事智能控制、微机电系统控制及自动化研究。广州　华南农业大学工程学院，510642。Email：tm-zhang@163.com

帕的大气压，使液体分子间的作用力遭到破坏，从液体表面脱出形成直径达微米级的气雾，在空气泵的作用下得到持续的气雾[12]。

1.2　农用超声雾化换能器的结构及尺寸参数

本文设计的农用超声雾化换能器结构分解图如图 1 所示，由文氏管 1、容腔 2、橡胶垫圈 3、超声振子 4、法兰盖 5、平垫圈 6 和螺栓 7 等零件组成。其中，超声振子 4 由压电陶瓷（piezoelectric transducer，PZT）圆片和不锈钢薄片组成。不锈钢薄片粘在压电陶瓷片上，厚度约为 0.1 mm，其作用是防止压电陶瓷的银电极因超声波的空化作用造成空化腐蚀，导致银电极成片脱落 [13]。超声振子嵌在橡胶垫圈 3 里，橡胶垫圈 3 起到减震、密封和定位的作用，然后把它们共同放置在容腔 2 底部定位环内，通过法兰盖 5、螺栓 7 和平垫圈 6 进行紧固。此外，容腔 2 壁上均匀地焊接有 4 个中空的小圆柱管道作为入风口，通过塑料管道与外接的空气泵连接。



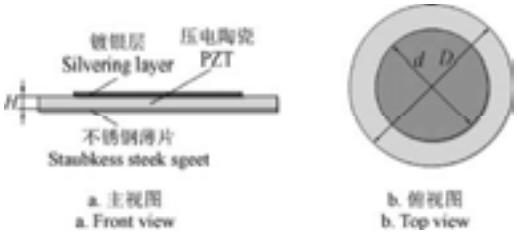
1. 文氏管　2. 容腔　3. 橡胶垫圈　4. 超声振子　5. 法兰盖　6. 平垫圈　7. 螺栓
1.Venturitube　2. Square-cavity　3. Rubber washer　4. Ultrasonic vibrator　5.Flange cover　6. Flat washer　7. Bolt

图 1　农用超声雾化换能器结构分解图

Fig.1　Structure exploded view of agricultural ultrasonic atomization transducer

换能器工作时，先启动空气泵使空气在容腔 2 内形成旋流，然后对超声振子施加高频交变电压使液体雾化。空气旋流带动雾滴旋转并向上运动，避免雾滴因无序扩散而黏附在容腔 2 内壁。气雾通过大口径文氏管 1 时，根据伯努利原理[14]，管口附近的低压空气会进一步将气雾快速拉升，尽可能减少雾滴停留在容腔 2 和文氏管 1 内的时间，减少雾滴在内壁上的吸附，降低雾化量耗损。此外，空气泵还能给雾滴提供较大的初速度，使雾滴在气流输送下，尽快达到靶标，减少蒸发。

超声振子结构示意图如图 2 所示，压电陶瓷沿轴向方向极化，D 为压电陶瓷的直径，H 为压电陶瓷厚度，d 为镀银层区域直径，即电极覆盖区域的直径。市面上常见的换能器超声振子尺寸如下：直径 D 为 25 mm，厚度 H 为 1.2 mm，镀银层直径 d 为 14 mm，本研究将其作为优化前的初始尺寸。由于不锈钢薄片厚度远小于压电陶瓷的厚度，在高频振动时对超声振子的谐振频率影响较小，故不考虑其对换能器雾化效果的影响[15]。



注：D 为压电陶瓷直径，25 mm；d 为镀银层直径，14 mm；H 为压电陶瓷厚度，1.2 mm.
Note: D is the diameter of the PZT, 25 mm. d is the diameter of the silvering layer, 14 mm. H is the thickness of the PZT, 1.2 mm.

图 2　超声振子结构示意图

Fig.2　Structure schematic diagram of ultrasonic vibrator

1.3　超声振子的有限元模型

超声振子具有电能和机械能相互转换的特性，极化后具有各向异性，难以用精确的数学模型模拟实际耦合场转换。有限元法可处理高度复杂的耦合场问题，获得定量化的分析结果，且求解精度高，可用于压电振子的优化设计[16]。本文利用有限元法建立超声振子的三维模型，通过仿真分析超声振子沿轴向振动的模态振型及其对应的谐振频率，并以此为基础做优化设计。压电单元的机电耦合作用采用线性压电本构方程描述，其动力学微分方程为[17]：

$$\begin{bmatrix} \boldsymbol{M} & 0 \\ 0 & 0 \end{bmatrix}\begin{bmatrix} \ddot{\boldsymbol{u}} \\ \ddot{\boldsymbol{v}} \end{bmatrix}+\begin{bmatrix} \boldsymbol{C}_m & 0 \\ 0 & 0 \end{bmatrix}\begin{bmatrix} \dot{\boldsymbol{u}} \\ \dot{\boldsymbol{v}} \end{bmatrix}+\begin{bmatrix} \boldsymbol{K}_m & \boldsymbol{K}_{me} \\ \boldsymbol{K}_{me}^T & \boldsymbol{K}_e \end{bmatrix}\begin{bmatrix} \boldsymbol{u} \\ \boldsymbol{v} \end{bmatrix}=\begin{bmatrix} \boldsymbol{F}_c \\ Q_e \end{bmatrix} \tag{1}$$

式中：$\boldsymbol{M}$ 为质量矩阵，kg；$\boldsymbol{C}_m$ 为阻尼矩阵；$\boldsymbol{K}_m$ 为刚度矩阵，Pa；$\boldsymbol{K}_e$ 为介电常数矩阵，F/m；$\boldsymbol{K}_{me}$ 为压电耦合矩阵；$\boldsymbol{u}$ 为节点位移向量，m；$\boldsymbol{v}$ 为电自由度向量；$\boldsymbol{F}_c$ 为分布式接触力所对应的等效节点力，N；Q_e 为压电陶瓷表面电极上的电荷量，C。

选用三维的八节点六面体单元 SOLID5 建立超声振子有限元模型。为使建立的有限元模型能准确反映实际情况，将超声振子分为两部分，电极覆盖区域内的圆柱部分赋予压电材料的全部属性，包括材料密度、压电常数、刚度矩阵和相对介电常数，而其余部分则设定压电材料的相对介电常数为 0，并赋予上述前 3 个材料参数。压电材料选用 PZT-4，其材料属性如表 1 所示。

表 1　压电材料的材料属性表

Table 1　Material properties table of piezoelectric materials

项目 Items	数值 Values
密度 Density/(kg·m^{-3})	7 500
压电常数 Piezoelectric constant/(C·m^{-2})	e_{31}=5.6 e_{33}=11.3 e_{15}=7.6
刚度矩阵 Stiffness matrix/GPa	C_{11}=119.0 C_{12}=57.9 C_{13}=56.0 C_{33}=110.0 C_{44}=30.5 C_{66}=30.4
相对介电常数 Dielectric constant	ε_{33}=100

2 基于 ANSYS 的超声振子尺寸参数优化设计

2.1 目标函数与约束条件

对于农用超声雾化换能器，最主要的评价因素是雾滴直径分布和雾化量。要提高换能器的雾化量，除了减少雾滴在形成过程中的耗损，更重要的是增大超声振子的振幅。因此，需对超声振子进行结构优化设计。优化过程如下：首先确定超声振子的基本结构和初始尺寸，然后利用 APDL 建立其有限元模型，选择尺寸参数作为优化设计变量，其有效振动量为优化目标变量，同时确定这些变量的变化范围和优化方法，用 ANSYS 自身一系列的优化迭代计算过程优化各变量，直到各变量趋于收敛，最终输出最优尺寸参数组合和最优解。

超声雾化所生成雾滴直径与换能器激励频率有关，雾化对象为水时，其关系如式（2）所示[18]：

$$D = 0.34\left(\frac{8\pi\sigma}{\rho f^2}\right)^{1/3} \tag{2}$$

式中：D 为雾化液滴的直径（本文用体积中径表示），m；σ为水的表面张力，N/m；ρ为水的密度，kg/m^3；f 为超声激励频率，Hz。

在常温下（20℃），水的表面张力σ为 7.28×10^{-2} N/m，密度ρ为 1.0×10^3 kg/m^3。在喷雾量相同的情况下，雾滴直径越小，雾滴数量就越多，所能覆盖的面积就越大[19]，而且雾滴直径越小，其分布就越均匀。在农业喷药领域，微小的雾滴更容易渗入微细空隙粘附在植株和昆虫上，减少药液向周围环境的散失，既提高药液利用率，又减少环境污染[20]。本文将超声雾化换能器的雾滴体积中径预设为 3～5 μm。由式（2）可计算出换能器超声激励频率的范围为 0.76～1.63 MHz。而雾化量的计算实质上是超声波声压的计算，可由下式近似计算[21]：

$$P = 0.5\rho c\omega A^2 = \rho c\pi f A^2 \tag{3}$$

式中：P 为声压，Pa；c 为声波在水中的传播速度，m/s；ω为相位角，rad，ω=2πf；A 为振动质点的最大振幅，m。

由式（3）得，压电陶瓷沿轴向振动的振幅越大，则其产生的超声波声压越大，雾化量也越大[22-24]。

因此，本文优化的目标在于使农用超声雾化换能器雾化量达到最大，即压电陶瓷沿轴向振动的振幅达到最大，同时所产生的雾滴体积中径在 3～5 μm 范围内，即外界所施加的超声激励频率范围在 0.76～1.63 MHz。故换能器优化设计的数学模型可表述为：

$$\begin{cases} \max\ A(x_i) \\ s.t.\ 0.76\times10^6 \leqslant P_j \leqslant 1.63\times10^6 \end{cases} \tag{4}$$

式中：x_i 为设计变量；P_j 为超声激励频率，Hz。

由于 ANSYS 程序总是最小化目标函数[25]，所以可将问题转化为如下形式：

$$\min F = M - A \tag{5}$$

式中：M 是大于振幅 A 的常数，此处取为 0，同时 F 被设为优化目标函数。

2.2 设计变量

压电材料的加工工艺较为复杂，因而换能器所用压电陶瓷的结构参数 D 保持不变，其余的结构参数 d 和 H 定为设计变量。

此外，文献[26]的试验表明，压电陶瓷直径 D 和镀银层直径 d 之比一般取 1.2≤D/d≤2.5，若超过这个比值，雾化量大幅度下降。

因此，尺寸参数 d 的取值范围如下：

$$\begin{cases} 1.2 \leqslant D/d \leqslant 2.5 \\ 0 \leqslant d \leqslant D \end{cases} \tag{6}$$

式中：D 为压电陶瓷直径，mm；d 为镀银层直径，mm，即 10 mm≤d≤20.83 mm.

对于尺寸参数 H，基于已有的设计经验[27]，取 H/6 作为上下限变化范围，由此设定尺寸参数 H 的取值范围为[1.0 mm，1.4 mm]，其中，优化的收敛误差取 1×10^{-6} mm。

2.3 罚函数求解不等式约束优化问题

带不等式约束的最优化问题，数学上常用罚函数法来解决。其中，增广乘子法是求解罚函数的一种重要方法。在参数优化设计中，压电振子的设计变量为其结构参数 x，目标函数为 min $f(x)$，其约束条件为 $g_i \leqslant 0$，i=1，2，…，m，引入附加变量 y=(y_1，y_2，…，y_m)$^{\mathrm{T}}$，将该模型转换为式（7）。

$$\begin{cases} \min\ f(x) \\ \text{s.t.}\ g_i(x) + y_i^2 = 0, i = 1,2,...,m \end{cases} \tag{7}$$

即可写出对应的乘子罚函数为：

$$\bar{L}(x,y,\gamma_k,\lambda_k) = f(x) + \sum_{i=1}^{m}\left\{\frac{\gamma_k}{2}\left[y_i^2 - \frac{1}{\gamma_k}\left(\gamma_k g_i(x) - \lambda_i^k\right)\right]^2 - \frac{\left(\lambda_i^k\right)^2}{2\gamma_k}\right\} \tag{8}$$

式中：γ_k（k=1,2….n）为罚因子；λ_i^k（k=1,2….n）为乘子；g_i（x）为约束条件；y_i 为附加变量。

为了定义与 y_i 无关的乘子罚函数，需将式（8）对 y 求极小值，最终得到：

$$L(x,\gamma_k,\lambda_k) = f(x) + \frac{1}{2\gamma_k} \sum_{i=1}^{m}\left\{\left[\max\left(0,\lambda_i^{(k)} + \gamma_k g_i(x)\right)\right]^2 - \left(\lambda_i^{(k)}\right)^2\right\} \tag{9}$$

通过变换，就把求带不等式约束的最优化问题转化成求解式（9）最小值的无约束问题。

2.4 模态振型的智能识别

在有限元优化计算迭代过程中，需对超声振子进行多次的设计变量修改和模态分析。在每次的模态分析结果中（计算中设定提取前 200 阶模态，频率范围 0.76～1.63 MHz），除了包含所需的工作模态外，还有许多其他模态的存在，而且所需的工作模态随定子结构参数的变化，其顺序与阶次在结果中也会发生改变。因此需要用一种方法来使 ANSYS 智能识别出所要求的工作模态。本文利用模态置信准则方法（modal assurance criteria，MAC）对所需的工作模态进行识别。MAC 值可以表示为[28]：

$$(MAC)_{ij} = \frac{\left(\phi_{ai}^{\mathrm{T}}\phi_{bj}\right)^2}{\left(\phi_{ai}^{\mathrm{T}}\phi_{ai}\right)\left(\phi_{bj}^{\mathrm{T}}\phi_{bj}\right)} \tag{10}$$

式中：ϕ_{ai}（i=1,2,...,200）表示用有限元方法计算所得的待辨识的超声振子振型；ϕ_{bj}（i=132）为选定的初始结构下第 132 阶振动的振型即参考振型（图 3）。MAC 值的范围是 $0 \leqslant MAC \leqslant 1$，其大小反映了待辨识振型与参考振型的相似程度，值越大则相似程度越高，据此可以实现在优化设计中对所需的振动模态的识别。

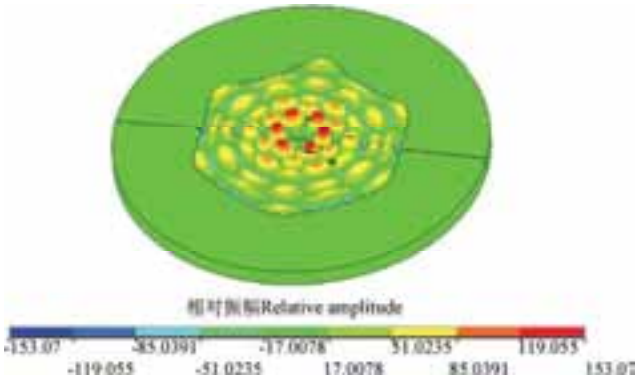


图 3　超声振子沿轴向方向振动的变形

Fig.3　Vibration deformation of ultrasonic vibrator along axial direction

2.5　参数优化过程及结果

参数优化过程是利用 ANSYS 的参数化语言 APDL 编程实现的，它采用的优化设计方法为 ANSYS 优化设计模块中的子问题近似法，即罚函数法。

为使压电陶瓷的雾化量达到最大，其有效振动的面积和轴向振动的振幅都应为最大值，通过模态分析选取的参考振型如图 3 所示。该振型主要特征为在压电振子有效振动面积内轴向振动分布较均匀，且与其他振型相比它的振动范围和轴向振幅最大[29]。

为模拟压电陶瓷在电压激励下的实际变形，以便获取轴向变形的振幅值，对其施加与参考振型的谐振频率一致的电压幅值为 100 V 的正弦交变电压，在 ANSYS 中继续对有限元模型进行瞬态分析后，提取轴向振动位移最大值所对应的节点（坐标值为 1.5088×10^{-4} m，1.5088×10^{-4} m，0 m），其响应曲线如图 4 所示，在响应的时间内最大的位移值为 4.75×10^{-5} mm。

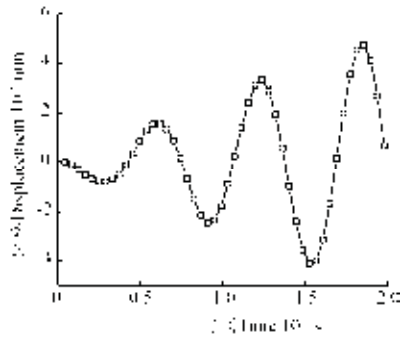


图 4　轴向振动位移最大节点的响应曲线

Fig.4　Response curve of node with maximum displacement along axial direction

在优化模块中，设计变量不断摄动并组合形成新的结构参数。在此优化过程中，状态变量 P_j 的值都在设定的频率范围内正常变动。从第 15 次迭代开始，设计变量 d、H 和目标函数 F 的值趋于稳定，并且前后 2 次迭代之间的差值逐渐收敛。经过 25 次迭代后，目标函数和设计变量同时达到收敛误差范围内，即稳定状态，优化设计过程终止。优化结果显示，当优化过程进行到第 10 次迭代时，目标函数 F 为最小值，即振幅 A 为最大值。表 2 为各项目优化前后的数值对比，在外部超声激励下，超声振子上的节点（坐标值为 -7.4134×10^{-3} m，1.6824×10^{-4} m，0 ）最大能产生 5.06×10^{-5} mm 的沿轴向方向振动的振幅，与优化前相比提高了 6.7%。由式（3）可得，优化之后超声波声压比优化之前提高了 13.8%。

表 2　优化前后各参数对比

Table 2　Comparison of parameters before and after optimization

名称 Name	变量名 Variable name	初始值 Initial value	优化值 Optimal value
设计变量 Design variable	镀银层直径 d/mm	14.00	20.40
	压电陶瓷厚度 H/mm	1.20	1.16
状态变量 State variable	谐振频率 P_j/Hz	1.63×10^{6}	1.62×10^{6}
优化目标 Objective function	振幅 A/mm	4.75×10^{-5}	5.06×10^{-5}

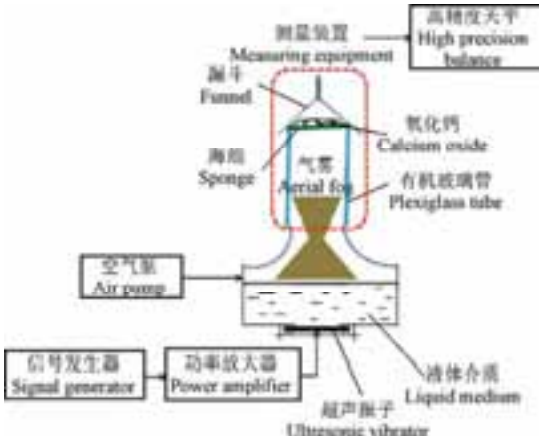
3　试验分析

按照优化计算结果（表 2）得出的尺寸值，采用相同的材料和加工工艺，分别加工 2 组压电陶瓷和试验样机，分别测量农用超声雾化换能器实际的雾化量和雾滴体积中径，试验主要设备如下：信号发生器（WF1946A，日本 NF 公司），功率放大器（HAS4014，日本 NF 公司），喷雾激光粒度分析仪（Winner318B，济南微纳颗粒仪器公司），计算机（LenovoM4360，联想公司），空气泵（ACO-002，森森集团股份有限公司）和高精度天平（YP-B5002 500g/0.01g，上海光正医疗仪器公司）。

信号发生器产生高频正弦信号，功率放大器将信号放大，通过换能器将其转换为超声机械振动（即超声波），超声波通过空化作用而使液体雾化，在空气泵的作用下气雾螺旋状喷出。在激励频率为 1.53 MHz，峰-峰值为 100 V 的正弦电压作用下，雾滴旋转上升运动轨迹和预期一致。

3.1　雾化量测量试验

雾化量测量试验原理如图 5a 所示，将足量的粉状氧化钙平铺在厚度为 0.3 mm 的海绵上，然后把两者置于内壁光滑的有机玻璃管的端面上，同时将一个漏斗倒扣在氧化钙上，防止空气中的水分干扰试验结果的准确度。将这套测量装置平稳地放在文氏管端面上，当空气旋流带动雾滴从文氏管出来后继续旋转上升并通过氧化钙，最终空气从漏斗颈尖端排出。因为氧化钙具有强烈的吸水性，在试验过程中测量装置会发生质量变化，用精度为 0.01 g 的电子天平测出试验前后测量装置的质量，即可计算出单位时间内换能器产生的雾化量。雾化量测量实物装置如图 5b 所示。



a. 原理图
a. Schematic diagram



1. 信号发生器 2. 功率放大器 3. 漏斗 4. 氧化钙 5. 海绵 6. 有机玻璃管 7. 空气泵 8. 农用超声雾化换能器
1.Signal generator 2.Power amplifier 3.Funnel 4.Calcium oxide 5.Sponge 6.Plexiglass tube 7.Air pump 8.Agricultural ultrasonic atomization transducer

b. 实物图
b. Physical map

图 5 雾化量测量试验
Fig.5 Atomization amount measurement experiment

从预试验中可知，换能器在 1.50～1.63 MHz 范围内产生的雾化量较大。为了准确测出雾化量最大时压电陶瓷的谐振频率和优化前后实际的雾化量，在图 5b 所示的试验装置上对换能器在不同的电压激励频率下产生的雾滴进行雾化量测量，测量 3 次，取平均值作为该频率下的雾化量。由于换能器开始喷雾到稳定喷雾需要一定的时间，经过反复测量，此时间约为 2 s。当测试时间取 60 s 时，远大于稳定时间 2 s，可忽略稳定时间对雾化量的影响。当施加电压的峰-峰值为 100 V，测试时间为 60 s，对优化前后的超声雾化换能器的雾化量进行测量，结果如表 3 所示。

对于表 3 中所有的激励频率，优化后的平均雾化量之和为 10.87 g/min，而优化前的平均雾化量之和为 10.15 g/min，相较而言，优化后换能器的平均雾化量比优化前提高了 7.1%。优化后换能器在激励电压频率为 1.53 MHz 时，雾化量达到最大，为 1.29 g/min；优化前的换能器在激励电压频率为 1.56 MHz 时，雾化量达到最大，为 1.20 g/min，优化后换能器的最大雾化量相比优化前提高了 7.5%，说明本文使用 ANSYS 对超声雾化换能器进行参数优化设计可行。

表 3 优化前后压电陶瓷的雾化量测量结果对比
Table 3 Result comparison of atomization flow measurement before and after optimization

试验号 Test number	激励频率 Excitation frequency f/MHz	优化后的雾化量 Flow of measurement device after optimization P_1/g	优化前的雾化量 Flow of measurement device before optimization P_2/g
1	1.50	0.69	0.22
2	1.51	0.94	0.37
3	1.52	1.20	0.45
4	1.53	1.29	0.67
5	1.54	1.19	0.77
6	1.55	1.12	1.15
7	1.56	1.06	1.20
8	1.57	1.00	1.17
9	1.58	0.67	1.01
10	1.59	0.55	0.93
11	1.60	0.53	0.71
12	1.61	0.32	0.61
13	1.62	0.19	0.55
14	1.63	0.12	0.34

注：施加电压的峰-峰值为 100 V，测试时间为 60 s。
Note: Peak-peak value of the applied voltage is 100 V and the test time is 60 s.

由于压电陶瓷在高频振动下产生的是微位移，受试验条件所限，难以直接测量。但雾化量测量试验可以间接地反映位移值大小，在频率一定的条件下，位移值越大，雾化量越大[22-24]，因此可视作对仿真结果的间接试验验证。

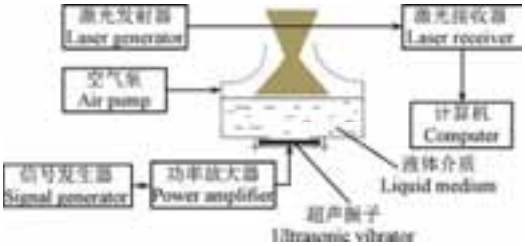
3.2 换能器谐振频率对比分析

由表 3 可知，当作用在优化后换能器的激励频率小于 1.53 MHz 时，雾化量随着激励频率的提高而增加，超过该频率后随着激励频率的提高而减少。优化前换能器的雾化量在 1.56 MHz 附近也呈现相同规律。由此可见，1.53 和 1.56 MHz 分别为优化后和优化前换能器产生参考振型（图 3）时的谐振频率，当外界的激励频率与谐振频率一致时，超声振子的振动量达到最大，相应地雾化量也达到最大。这也说明了要使超声雾化换能器产生较大的雾化量，应尽可能使其工作在谐振频率。

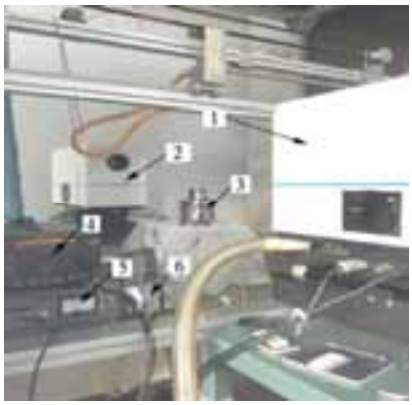
此外，优化后换能器的谐振频率为 1.53 MHz，仿真得出的谐振频率为 1.62 MHz，两者的误差为 5.9%，证明了本文通过有限元软件所建立的参数化模型是正确的。产生误差的原因主要是以下 2 个：一是利用 ANSYS 软件计算时未能非常准确模拟压电陶瓷的边界条件，二是压电陶瓷存在材料的均匀性和加工误差问题。

3.3 雾滴体积中径测量试验

雾滴体积中径测量试验原理如图 6a 所示，采用济南微纳颗粒仪器公司生产的 Winner318B 型分体式喷雾激光粒度仪测量雾滴颗粒的体积中径。激光发射器发射激光，雾滴进入激光时，产生衍射现象，衍射的光线被激光接收器后转换成电信号，送到计算机分析处理，由此可获得雾滴直径的分布情况[30]。雾滴体积中径测量实物装置如图 6b 所示。

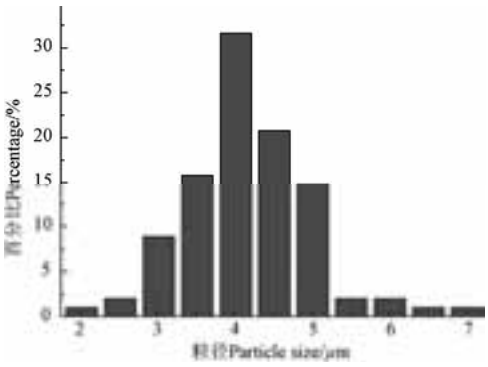


a. 雾滴体积中径测量试验原理图
a. Schematic diagram of volume median diameter of droplet measurement experiment



1. 激光接收器　2. 激光发生器　3. 农用超声雾化换能器　4. 信号发生器　5. 功率放大器　6. 空气泵
1. Laser receiver　2. Laser generator　3. Agricultural ultrasonic atomization transducer　4. Signal generator　5. Power amplifier　6. Air pump

b. 雾滴体积中径测量试验图
b. Figure of volume median diameter of droplet measurement experiment



注：激励电压峰-峰值为 100 V，频率为 1.53 MHz。
Note: Peak-peak value of applied voltage is 100 V and frequency is 1.53 MHz.

c. 雾滴粒径分布直方图
c. Histogram of droplet size distribution

图 6　雾滴体积中径测量试验

Fig.6　Volume median diameter of droplet measurement experiment

当激励电压峰-峰值为 100 V，频率为 1.53 MHz 时，测量出的雾滴粒径分布范围直方图如图 6c 所示，93%的雾滴颗粒直径分布在设定的范围 3～5 μm 内，其中，直径为 4 μm 的雾滴占比最多，为 32%，试验结果与优化设计时预设的雾滴体积中径相吻合。

4　结　论

根据超声雾化换能器的工作原理和农药喷施雾化要求，采用 ANSYS 参数化设计语言建立了换能器超声振子的参数化模型，并进行尺寸参数优化，设计了一种农用超声雾化换能器，相关研究表明：

1）实测的农用超声雾化换能器谐振频率为 1.53 MHz，仿真计算得出的频率为 1.62 MHz，两者的误差为 5.9%，证明了本文通过有限元软件所建立的参数化模型是正确的。

2）通过优化设计，农用超声雾化换能器产生的雾化量得到了较大提高。试验结果显示，当施加峰-峰值为 100 V 交流正弦电压时，换能器的最大平均雾化量从 1.20 提高到 1.29 g/min，比优化前提高了 7.5%，由此可证明本文使用的优化方法是可行的。

3）在考虑工程实用性的情况下，在仿真计算过程中对超声振子模型进行了简化，不考虑不锈钢薄片对超声振子谐振频率的影响，试验证明，采用简化模型对农用超声雾化换能器进行优化设计是可行的。

本研究在结构优化过程中将雾滴体积中径预设为 3～5 μm，该雾滴粒径是否为最佳生物粒径，应根据应用领域与不同病虫害防治对象进行研究。因此本课题组将根据植保专家对雾滴体积中径的要求，进一步研制相应雾滴粒径的农用超声雾化换能器。

［参　考　文　献］

[1] 周海燕，杨炳南，严荷荣，等. 我国高效植保机械应用现状及发展展望[J]. 农业工程，2014，4(6)：4－6.
Zhou Haiyan, Yang Bingnan, Yan Herong, et al. Application status and development prospects of effective plant protection machinery[J]. Agricultural Engineering, 2014, 4(6): 4－6. (in Chinese with English abstract)

[2] 张建桃，文晟，江定心，等. 超声雾化在超低量喷雾中的应用前景[J]. 中国植保导刊，2014(10)：67－70.
Zhang Jiantao, Wen sheng, Jiang Dingxin, et al. Application of ultrasonic atomization to plant protection machinery[J]. China Plant Protection, 2014(10): 67－70. (in Chinese with English abstract)

[3] 郑文钟，应霞芳. 我国植保机械和施药技术的现状、问题及对策[J]. 农机化研究，2008(5)：219－221.
Zhen Wenzhong, Ying Xiafang. Study on actuality and problems with measure of plant protection machinery and spray techniques of agricultural chemicals in China. 2008(5): 219－221. (in Chinese with English abstract)

[4] Ferguson J C, Gaussoin R E, Eastin J A, et al. Effect of application carrier volume on a conventional sprayer system and an ultra-low volume sprayer[J]. Pesticide Formulation and Delivery Systems, 2014, 23: 13－22.

[5] Ferguson J C, Gaussoin R E, Eastin J A, et al. Comparison of herbicide efficacy and adjuvants using a conventional sprayer and an ultra-low volume sprayer[J]. Pesticide Formulation and Delivery Systems, 2014, 33: 23－25.

[6] Huang Yaoxin, Ye Mu, Chen Haiqiang. Efficacy of washing with hydrogen peroxide followed by aerosolized antimicrobials as a novel sanitizing process to inactivate Escherichia coli O157:H7 on baby spinach[J]. International Journal of Food Microbiology, 2012, 153(3): 306－313.

[7] Kirpalani D M, Suzuki K. Ethanol enrichment from ethanol-water mixtures using high frequency ultrasonic

atomization[J]. Ultrasonics Sonochemistry, 2011, 18(5): 1012－1017.

[8] 梁泽钦，邱红喜，杨明丰，等. 超声雾化加湿系统研究与设计[J]. 武汉工业学院学报，2006，25(3)：24－26.
Liang Zeqin, QiuHongxi, Yang Mingfeng, et al. Study and design on the ultrasonic atomization watering system[J]. Journal of Wuhan Polytechnic University, 2006, 25(3): 24－26. (in Chinese with English abstract)

[9] 林书玉，杨月花. 医学超声治疗技术研究及其应用[J]. 陕西师范大学学报，2004，32(2)：117－122.
Lin Shuyu, Yang Yuehua. Medical ultrasonic therapy and its applications[J]. Journal of Shaanxi Normal University, 2004, 32(2): 117－122. (in Chinese with English abstract)

[10] Jeng Yeauren, Su Chienchan, Feng Guohua. A pzt-driven atomizer based on a vibrating flexible membrane and a micro-machined trumpet-shaped nozzle array[J]. Microsystem Technologies, 2009, 15(6): 865－873.

[11] 黄卫星，高建民，陈翠英. 超声雾化的研究现状及在农业工程中的应用[J]. 农机化研究，2007(3)：154－158.
Huang Weixing, Gao Jianmin, Chen Cuiying. Present situations and prospects of ultrasonic atomization application[J]. Journal of Agricultural Mechanization Research, 2007(3): 154－158. (in Chinese with English abstract)

[12] 黄卫星. 超声雾化试验研究[D]. 镇江：江苏大学，2007.
Huang Weixing. Experimental Study on Ultrasonic Atomization[D]. Zhenjiang: Jiangsu University, 2007. (in Chinese with English abstract)

[13] 姜德星. 超声波雾化换能器的研究[J]. 江苏陶瓷，1998(1)：13－14.
Jiang Dexing. Ultrasonic atomization transducer[J]. Jiangsu Ceramics, 1998(1): 13－14. (in Chinese with English abstract)

[14] Kester F E. Another demonstration of the bernoulli principle[J]. American Journal of Physics, 1945, 13(5): 349－349.

[15] 许龙. 基于有限元法的耦合振动夹心换能器的特性和设计研究[D]. 西安：陕西师范大学，2008.
Xu Long. Characteristics and Design Research of Coupled Oscillation Sandwich Transducer Based on Finite Element Method[D]. Xi'an: Shaanxi Normal University, 2008. (in Chinese with English abstract)

[16] 文晟，张铁民，张建桃，等. 钹型阵列式压电俘能器的参数优化设计与实验[J]. 中国机械工程，2013，24(11)：1431－1436.
Wen Sheng, Zhang Tiemin, Zhang Jiantao, et al. Parametric optimum design and experiment of a cymbal stack piezoelectric harvester[J]. China Mechanical Engineering, 2013, 24(11): 1431 － 1436. (in Chinese with English abstract)

[17] Allik H, Hughes T J R. Finite element method for piezoelectric vibration[J]. International Journal for Numerical Methods in Engineering, 1970, 2(2): 151－157.

[18] 黄晖，姚熹，汪敏强，等. 超声雾化系统的雾化性能测试[J]. 压电与声光，2004，26(1)：62－64.
Huang Hui, Yao Xi, Wang Minqiang, et al. The measurements of atomizing properties of ultrasonic atomizing system[J]. Piezoelectrics & Acoustooptics, 2004, 26(1): 62－64. (in Chinese with English abstract)

[19] 刘秀娟，周宏平，郑加强. 农药雾滴漂移控制技术研究发展[J]. 农业工程学报，2005，21(1)：186－190.
Liu Xiujuan, Zhou Hongping, ZhengJiaqiang. Research advances of the technologies for spray drift control of pesticide application[J]. Transactions of the Chinese Society of Agricultural Engineering (Transactions of the CSAE), 2005, 21(1): 186－190. (in Chinese with English abstract)

[20] 耿爱军，李法德，李陆星. 国内外植保机械及植保技术研究现状[J]. 农机化研究，2007(4)：189－191.
Geng Aijun, Li Fade, Li Lunxing. The plant protection machinery and technology at home and abroad[J]. Journal of Agricultural Mechanization Research, 2007(4): 189－191. (in Chinese with English abstract)

[21] 易启伟，王旺平. 大功率超声雾化器在粮食着水中的应用[J]. 粮食加工，2010，35(4)：66－68.
Yi Qiwei, Wang Wangping. Application of high-power ultrasonic atomizerin grain with water[J]. Grain Processing, 2010, 35(4): 66－68. (in Chinese with English abstract)

[22] Balasubrahmanyam A, Mohan N P, Parag R G, et al. Ultrasonic atomization: Effect of liquid phase properties[J]. Ultrasonics, 2006, 44(2): 146－158.

[23] 王世长，林辉. 超声加湿器用压电元件的检测研究[C]//94' 全国结构陶瓷、功能陶瓷、金属/陶瓷封接学术会议论文集，1994：52－54.
Wang Shichang, Lin Hui. Study on detection of ultrasonic humidifier piezoelectric component[C]//94' National Structural Ceramics, Functional Ceramics, Metal/Ceramic Sealing Academic Conference Proceedings, 1994: 52－54. (in Chinese with English abstract)

[24] Keiji Y, Hiroyuki H, Yoshiyuki A, et al. Effect of frequency on ultrasonic atomization[C]// Mami M. The 31st Symposium on Ultrasonic Electronics. Tokyo: Meijin University, 2010: 363－364.

[25] 曾攀，雷丽萍，方刚. 基于 ANSYS 平台有限元分析手册：结构的建模与分析[M]. 北京：机械工业出版社，2010：270－272.

[26] 蔡晓峰，何维庚，姜德星，等. 压电陶瓷超声雾化换能器的研制[J]. 佛山陶瓷，1994(3)：18－20.
Cai Xiaofeng, He Weigeng, Jiang Dexing, et al. Development of piezoelectric ultrasonic atomizing transducer[J]. Foshan Ceramics, 1994(3): 18 － 20. (in Chinese with English abstract)

[27] Silva E C N, Kikuchi N. Design of piezoelectric transducers using topology optimization[J]. Smart Materials and Structures, 1999, 8(3): 350.

[28] 赵淳生. 超声电机技术与应用[M]. 北京：科学出版社，2007：215－219.

[29] 胡方军. 微泵型压电超声波雾化器研究[D]. 南京：南京航空航天大学，2013.
Hu Fangjun. Research on Micro Pump Piezoelectric Ultrasonic Atomizer[D]. Nanjing: Nanjing University of Aeronautics and Astronautics, 2013. (in Chinese with English abstract)

[30] 高建民，陆岱鹏，刘昌鑑，等. 微型指数振子低频超声雾化喷头的研制及喷雾试验[J]. 农业工程学报，2014，30(4)：40－46.
Gao Jianmin, Lu Daipeng, Liu Changjian, et al. Development and spray test of micro index low-frequency ultrasonic nozzle[J]. Transactions of the Chinese Society of Agricultural Engineering (Transactions of the CSAE), 2014, 30(4): 40－46. (in Chinese with English abstract)

Parameter optimization design and experiment of agricultural ultrasonic atomization transducer

Zhang Jiantao[1], Li Shenghua[2], Wen Sheng[2], Lan Yubin[2], Liao Yiyong[2], Zhang Tiemin[2※]
(1. *College of Mathematics and Informatics of South China Agricultural University, Guangzhou* 510642*, China*;
2. *Engineering College of South China Agricultural University, Guangzhou* 510642*, China*)

Abstract: In order to solve the problems when ultrasonic atomization transducer was used for ultra-low-volume spraying pesticides, i.e. the atomization flow was little and the transducer's structure was complex, this paper presented a new structure of agricultural ultrasonic atomization transducer based on the atomization requirements proposed by the working principle of ultrasonic atomization transducer and agricultural pesticide spraying. The transducer mainly consisted of a venturi tube, a cylindrical square-cavity, an ultrasonic vibrator, a rubber washer and a flange cover. When the high-frequency alternating current (AC) voltage was applied on the ultrasonic vibrator, liquid was atomized. In the meantime, the circumscribed air pump formed the air vortex in the square-cavity, which would drive the droplet to rotate and move upward, prevent the spread of droplet and avoid attaching on the inner wall of the vessel. Firstly, the parametric model of the ultrasonic vibrator was established and then optimized with ANSYS parametric design language (APDL) to control the droplet diameter of the transducer within the setting range and maximize the atomization flow. In the atomization process, we chose the electrode diameter and the thickness of the ultrasonic vibrator as the design variables, the vibration amplitude of the ultrasonic vibrator as the objective function, and the driving frequency as the constraint condition. Secondly, penalty function was used to solve the optimization problem with inequality constraints. Meanwhile, the modal assurance criteria (MAC) were adopted to recognize the target modals intelligently by ANSYS finite element software. If the value of MAC was closed to 1, the target model was similar to the reference model. This indicated that the vibration along the axial direction was concentrated on the surface of the ultrasonic vibrator and the vibration amplitude was larger than other models. Thirdly, a prototype built based on the optimization results was manufactured to conduct the atomization flow measurement experiment and the droplet diameter measurement experiment. The measured resonant frequency of the optimized transducer was 1.53 MHz, which was very close to the simulated value of ANSYS finite element software (1.62 MHz) and the error was 5.9%. The measured resonant frequencies of the transducer before and after optimization were 1.56 and 1.53 MHz respectively. When the excitation frequency was at the resonant frequency 1.53 MHz, the atomization flow rate of the optimized agricultural ultrasonic atomization transducer reached the maximum. If the excitation frequency of the ultrasonic atomization transducer was lower or higher than the resonant frequency, the atomization flow rate would be reduced, which illustrated that the ultrasonic vibrator should work in the resonant frequency to make the transducer produce the largest amount of aerial fog. The maximal atomization flow rate of the agricultural ultrasonic atomization transducer increased from 1.20 to 1.29 g/min when applying an AC sine-wave voltage whose peak-peak value was 100 V, that was, it was raised by 7.5% compared with the flow before optimization. At the same time, the VMD (volume median diameter) of droplet measured by a laser particle size analyzer (Winner318B) was consistent with the design requirement. Research results provide a scientific reference for optimum structural design of agricultural ultrasonic atomization transducer and the increase of the atomization flow.

Key words: spraying; finite element method; optimization; physical design; ultra-low-volume spraying

庆祝《农业工程学报》创刊三十周年

荣誉









2014年《农业工程学报》h5指数位列
google学术搜索高被引期刊第10位





昨日荣誉　今日起点

中国标准连续出版物号：ISSN 1002-6819 / CN11-2047/S　　邮发代号：18-57　　国内定价：50元

2.5 柑橘黄龙病远红外热处理温度场分布特性试验研究

QK1946070

美国《工程索引》（Ei）收录期刊
美国《化学文摘》（CA）收录期刊
Scopus数据库收录期刊
中文核心期刊　中国科技核心期刊
中国科学引文数据库来源期刊
RCCSE中国权威学术期刊

ISSN 1000-1298
CODEN NUYCA3

农业机械学报

NONGYE JIXIE XUEBAO

Transactions of the Chinese Society for Agricultural Machinery

第50卷

2019 10

中国农业机械学会主办

ISSN 1000-1298

万方数据

胁迫下玉米叶片光谱谐波振幅特征与胁迫程度判别 …… 郭 辉 杨可明 张 超(153)
基于地基 LiDAR 高度指标的小麦生物量监测研究
…… 邱小雷 方 圆 郭 泰 程 涛 朱 艳 姚 霞(159)
基于视觉里程计的森林样地调查系统研究 …… 陈盼盼 冯仲科 范永祥 高 祥 申朝永(167)
柑橘黄龙病远红外热处理温度场分布特性试验研究
…… 张建桃 林耿纯 陈 鸿 文 晟 尹选春 邓小玲(175)
基于颜色取样的苹果树枝干点云数据提取方法 …… 郭彩玲 刘 刚(189)
基于光学相机的植物表型测量系统与时序生长模型研究
…… 张慧春 王国苏 边黎明 郑加强 周宏平(197)
基于微分 L-系统的水稻根系三维生长模型研究 …… 杨 乐 彭 军 杨红云 易文龙(208)
基于被动水声信号的淡水鱼混合比例识别 … 黄汉英 杨咏文 李 路 赵思明 熊善柏 涂群资(215)
基于红外热成像的白羽肉鸡体温检测方法 … 沈明霞 陆鹏宇 刘龙申 孙玉文 许 毅 秦伏亮(222)
基于改进 CoSaMP 的农田信息异常事件检测算法 …… 肖利平 全腊珍 余 波 霍览宇(230)
农田信息采集车设计与试验 …… 姚照胜 刘 涛 刘升平 邓国强 武 威 孙成明(236)
基于改进樽海鞘群算法的四旋翼飞行器姿态优化控制 …… 丁 力 高振奇 龚 青(243)

农业水土工程

深松处理对豫北农田土壤水分与作物耗水的影响
…… 张 凯 刘战东 强小嫚 米兆荣 冯荣成 孙景生(251)
东北旱作区土壤碳氮磷生态化学计量特征及其影响因素
…… 卓志清 李 勇 兴 安 曹 梦 黄元仿 赵云泽(259)
黑土区坡耕地连年施加生物炭的最佳模式研究 …… 魏永霞 冯 超 石国新 吴 昱 刘 慧(269)
施用沼液对设施番茄生长与土壤生态环境的影响
…… 郑 健 殷李高 朱传远 马 静 张平安(278)
基于 DSSAT 模型的冬小麦最优灌溉制度研究 …… 邵光成 王志宇 王小军 汤树海 姚怀柱(289)
生物炭对北方寒区农田土壤热性能参数的影响
…… 马效松 付 强 徐淑琴 李天霄 侯仁杰 于鑫彤(298)
稻田总磷迁移规律与最佳灌排模式研究 …… 郝树荣 王子欣 潘永春 吴蕴玉 郑成鑫 陈文猛(306)

农业生物环境与能源工程

白云石基多孔陶瓷负载 Al_2O_3 催化生物质热解试验 … 毕冬梅 张凯真 易维明 柳善建 李泊铮(315)
基于连续灰分区间定标模型的生物炭金属含量 LIBS 检测…… 段宏伟 韩鲁佳 黄光群(323)

农产品加工工程

基于均匀板加热法的饲料糊化参数试验研究 …… 金 楠 方 鹏 王红英 段恩泽(329)
异硫氰酸苄酯纳米乳液射流空化制备与冻融稳定性研究
…… 田 甜 周 艳 高 悦 李 杨 王中江 李 良(337)

万方数据

doi:10.6041/j.issn.1000-4298.2019.10.020

柑橘黄龙病远红外热处理温度场分布特性试验研究

张建桃[1,2]　林耿纯[1,2]　陈　鸿[1]　文　晟[2,3]　尹选春[2,4]　邓小玲[2,5]

(1. 华南农业大学数学与信息学院，广州 510642；2. 国家精准农业航空施药技术国际联合研究中心，广州 510642；
3. 华南农业大学工程基础教学与训练中心，广州 510642；4. 华南农业大学工程学院，广州 510642；
5. 华南农业大学电子工程学院，广州 510642)

摘要：针对柑橘黄龙病热空气处理存在能耗高、加热设备笨重、传热较慢等问题，提出了柑橘黄龙病远红外热处理方法。为解决远红外加热时柑橘树温差过大的问题，搭建了柑橘黄龙病热空气快速处理温度场分布特性试验平台，研究了远红外灯管组数量、单根灯管功率、加热时间、远红外灯与支架顶部距离对柑橘树温度场分布的影响，并对远红外加热影响因素进行优化，研究结果表明：远红外灯管组数量、单根灯管功率以及加热时间对柑橘树叶和枝干的温度场分布均有显著影响，远红外灯与支架顶部距离对树叶的温度场分布影响显著，试验优化后的参数为：远红外灯管组数量为 3，单根灯管功率为 1 kW，加热时间为 3 min，远红外灯与支架顶部距离为 10 cm。在此条件下，树叶温度平均值为 58.1℃，枝干温度平均值为 43.1℃，整体温度平均值为 52.3℃。在此参数下对柑橘黄龙病进行远红外热处理田间试验，病菌浓度平均降低 34.4%。研究结果可为柑橘黄龙病规模化远红外热处理设备的优化设计提供参考。

关键词：柑橘；黄龙病；远红外热处理；温度场；防治效果

中图分类号：S436.6；S129　　**文献标识码**：A　　**文章编号**：1000-4298(2019)10-0175-14

Experiment on Temperature Field Distribution Characteristics of Citrus HLB Far Infrared Heat Treatment

ZHANG Jiantao[1,2]　LIN Gengchun[1,2]　CHEN Hong[1]　WEN Sheng[2,3]　YIN Xuanchun[2,4]　DENG Xiaoling[2,5]

(1. *College of Mathematics and Informatics, South China Agricultural University, Guangzhou* 510642, *China*
2. *National Center for International Collaboration Research on Precision Agricultural Aviation Pesticides Spraying Technology, Guangzhou* 510642, *China*
3. *Engineering Fundamental Teaching and Training Center, South China Agricultural University, Guangzhou* 510642, *China*
4. *College of Engineering, South China Agricultural University, Guangzhou* 510642, *China*
5. *College of Electronic Engineering, South China Agricultural University, Guangzhou* 510642, *China*)

Abstract: For the weak points of citrus Huanglongbing (HLB) heat treatment by hot air, such as high energy consumption, slow heat transfer, and heavy heating equipment, far infrared heat treatment method for citrus HLB was put forward. An experimental platform of HLB far infrared heat treatment was set up, which consisted of heat treatment enclosure, far infrared lamp groups, a paperless recorder, a 12 channels temperature recorder and some temperature sensors, to study the influence of the far infrared lamp groups quantity, the power of far infrared lamp, the heating time, position of the far infrared lamps on the temperature field distribution of far infrared heat treatment. The results showed that the quantity of far infrared lamp groups, the power of single far infrared lamp and the heating time had significant effect on the temperature field distribution of leaves and branches, the distance between the far infrared lamp groups and the top of the stent had significant effect on the temperature field distribution of leaves. The factors that affecting the temperature field distribution were optimized. The optimum parameters were as follows: the quantity of far infrared lamp groups was 3, the power of single far infrared lamp was 1 kW,

收稿日期：2018-12-24　修回日期：2019-06-02

基金项目：国家重点研发计划项目(2017YFD0701001)、国家自然科学基金项目(61773171、61675003)、广东省科技计划项目(2016A020210092、2017B010117010)、广东省教育厅平台建设项目(2015KGJH2007)和大学生创新创业项目(201710564193)

作者简介：张建桃(1978—)，男，副教授，博士，主要从事精细农业研究，E-mail：zhangjiantao@ yeah.net

通信作者：邓小玲(1978—)，女，副教授，博士，主要从事柑橘黄龙病智能无损检测技术研究，E-mail：dengxl@ scau.edu.cn

the heating time was 3 min, and the distance between far infrared light and the top of the bracket was 10 cm. Under the optimal parameters, the average temperature of leaves was 58.1℃, the average temperature of branches was 43.1℃, and the average temperature of the whole treatment enclosure was 52.3℃. Under the parameters the effectiveness of infrared heat treatment on the control of citrus HLB was proved by experiments, the average reduction rate of bacteria concentration after treatment was 34.4%. The results provided a reference for the optimization design of large-scale HLB infrared heat treatment equipment.

Key words: citrus; Huanglongbing; far infrared heat treatment; temperature field; control effectiveness

0 引言

柑橘黄龙病(HLB)是由韧皮部杆菌属的病原菌引起的毁灭性疾病[1],除了采取预防措施,如移除受感染的植株、种植无疾病的幼苗和管理昆虫媒介之外,没有其他有效管理办法[2]。根据发病特点及发现地域的不同,柑橘黄龙病分为 *Candidatus Liberibacter asiaticus*(CaLas)、*Candidatus Liberibacter africanus*(CaLaf)和 *Candidatus Liberibacter americanus*(CaLam)3 种类型[3-4]。其中,CaLas 和 CaLam 侵染植株后,在 22~24℃和 27~32℃均可引起症状,属于耐热型;CaLaf 侵染植株后,在 22~24℃可使植株表现严重症状,在 30℃以上症状减轻或消失,属于热敏感型[3-4]。患有黄龙病的柑橘树表现为植株矮化、结果变少、果实变小、畸形,且着色不均匀[7-9]。柑橘黄龙病传播途径除了嫁接、月病树接穗繁殖以及接穗和染病苗木的远距离传播之外,柑橘木虱是重要的传播媒介[10]。目前,针对柑橘黄龙病的防控仍以防为主,尚无特效药及抗病品种[11]。化学防治主要作为一种间接防治方法,它是利用化学药品杀死柑橘黄龙病传播媒介柑橘木虱等,阻止黄龙病的传播,进而对柑橘黄龙病进行防治。但化学药品的使用容易使柑橘木虱产生抗药性,且会造成环境污染。砍除病树对于防治黄龙病具有一定的效果,但是大量砍除病树将对以柑橘为经济来源的果农造成巨大损失。针对柑橘木虱进行生物防治,对抑制柑橘黄龙病的传播具有一定的作用,但成本过高,见效慢。除此之外,热处理方法是抑制黄龙病传播的有效物理防治方法,该方法利用黄龙病菌对温度的敏感性,直接抑制黄龙病菌的传播[12]。

热处理也称热疗,是应用较早的一种脱毒技术[13-16]。柑橘黄龙病热处理技术的主要原理就是利用外界的传热介质,如光照、湿热空气、热水或蒸汽等,向感染黄龙病的柑橘植株传递足够热量,在不影响其正常生长的前提下,使黄龙病病菌钝化甚至死亡,黄龙病症状消失[17-28]。文献[17-28]研究证明,热处理对于柑橘黄龙病的防治是有效的,但自然热罩热处理存在处理周期长、效率低、对自然条件依赖大、处理罩内温差过大等问题;热空气快速热处理以空气作为传热介质,存在加热设备笨重、传热慢、能耗高等问题。

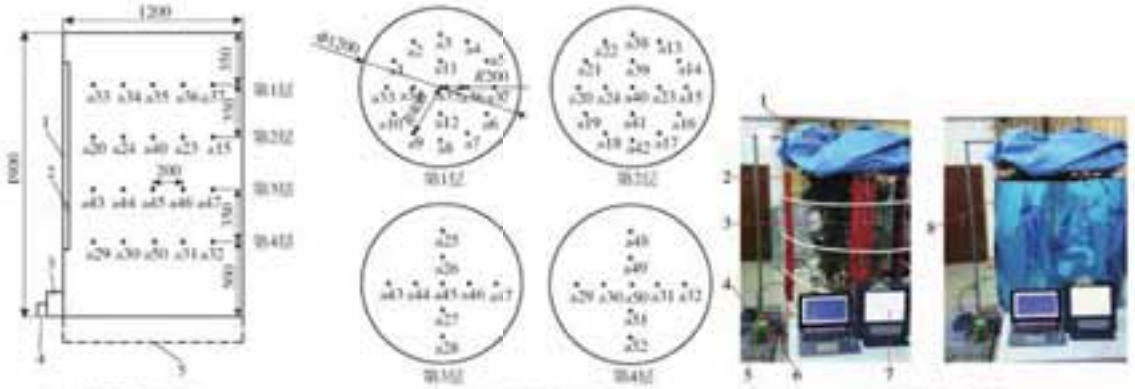
远红外线具有除菌杀毒的作用,利用远红外线加热细菌内毒素时,180℃温度下加热 120 min,或 250℃下加热 30 min,内毒素均转阴性[29]。文献[30]利用远红外加热技术处理桑椹菌核病,当远红外灯管与菌核间距离为 45 mm,加热 60 s,温度为 120℃时,可有效杀死病原菌。文献[31]采用远红外基质消毒机处理蔬菜育苗基质,能够杀死基质中的病菌、虫卵、害虫以及杂草种子。远红外热处理具有加热快、能耗低、无污染等特点,已在植物除菌杀毒等方面得到了成功的应用。

本文提出采用远红外对柑橘黄龙病进行热处理,搭建柑橘黄龙病远红外热处理温度场分布特性试验平台,通过研究远红外灯管组数量、灯管功率、加热时间等对温度场分布的影响,为柑橘黄龙病远红外热处理设备的优化设计提供依据。

1 材料与方法

1.1 柑橘黄龙病远红外热处理试验平台

搭建的柑橘黄龙病远红外快速热处理温度场分布特性试验平台如图 1 所示。此试验平台配置有远红外灯,其灯管为碳纤维石英加热管,额定电压 220 V,额定功率 1 000 W,长度 600 mm,灯罩尺寸为 620 mm×180 mm×46 mm;功率调节器(衡鑫电热电器制造厂),额定电压 220 V,最大调节功率 9 kW;功率表型号为 PZEM-061(V2.0),量程 0~22 kW;无纸记录仪(杭州盘古自动化系统有限公司)型号为 VX8140R,具有 40 路输入端口,连接 PT100 型温度传感器,量程为 -200~650℃,精度为 0.1℃;12 通道温度记录仪(台湾路昌电子企业股份有限公司),型号为 BTM-4208SD,K 型探头,分辨率为 0.1℃,量程为 -50.0~999.9℃,精度为 ±0.4% FS +0.5℃;在线式红外测温仪(南京隆顺仪表有限公司),型号 LSCI-SJG/300A,量程 -50~300℃,精度为 2% FS,可以测量物体的最小尺寸为 22.5 mm,最大尺寸为



(a) 试验平台示意图　　(b) 测温探头分布图　　(c) 试验平台实物图

图 1　柑橘黄龙病远红外快速热处理试验平台

Fig. 1　Citrus HLB far infrared rapid heat treatment test platform

1. 处理罩　2. 远红外灯管组　3. 柑橘树　4. 功率表　5. 功率调节器　6. 12 通道温度记录仪　7. 无纸记录仪　8. 铝板

50 mm，测量的最佳距离为 360 mm，最远测量距离为 700 mm；处理罩由 PVC 双面涂塑防水布制成，防水布厚度 0.45 mm；镜面反射铝板，厚度为 0.3 mm。

两盏远红外灯竖直拼接在一起，各连接一根灯管（每盏远红外灯内可平行安装两根管式红外加热灯管），并以此作为一个整体，即一组远红外灯管。远红外灯管组垂直布置在处理罩内侧。在红外灯辐射区域内，辐射能不需要任何中介物质，直接辐射或经反射涂层反射到柑橘树表面，柑橘树吸收辐射转换为内部的蓄热能[26]，柑橘树叶和树枝温度升高。灯管功率由功率调节器调节，功率用功率表测量。柑橘树叶、枝干的温度通过 PT100 型温度传感器、K 型温度传感器和在线式红外测温仪测量。由于柑橘树的树叶比较稀疏，部分红外灯辐射会透过柑橘树空隙，照射到对面的处理罩上。为了充分利用这部分能量，处理罩内侧布置镜面铝板，透过柑橘树的红外辐射就会被反射到柑橘树，从而提高热辐射效率。

处理罩内共布置 52 个温度测试点，如图 1a 所示，温度传感器分布位置如图 1b 所示。其中 a1 – a32 号温度传感器测量树叶温度，a33 – a52 号温度传感器测量枝干温度。树冠层树叶密度由上到下逐层降低，测温探头数量由上到下逐渐减少。第 1 层和第 2 层各布置 17 个测试点，其中 12 个用于测量树叶温度，另外 5 个用于测量枝干温度；第 3 层和第 4 层各布置 9 个测试点，每层 4 个用于测量树叶温度，5 个用于测量枝干温度。试验装置实物如图 1c 所示，远红外灯管组用于加热柑橘树，外侧铝板用于反射远红外辐射，由无纸记录仪和通道温度记录仪同时记录各测点温度，试验时室内平均温度为 18℃。树叶、枝干温度利用绝缘胶布将 PT100 和 K 型温度传感器固定在树叶或枝干表面上进行测量。

1.2　柑橘树温度测量方法

为了明确柑橘黄龙病远红外热处理时柑橘树的温度场分布，需测量树叶和枝干的温度。在线式红外测温仪能够直接测量物体表面温度，但只能用于环境温度为 0 – 50℃的场合。试验过程中处理罩内温度会超过这个范围。PT100 型温度传感器和 K 型温度传感器可以测量固体表面温度，以及气体、液体等的温度[32]。本研究采用 PT100 型温度传感器和 K 型温度传感器测量树叶和枝干温度。测量时要将传感器固定在树叶或树干上，为了测定试验中采用的固定方法是否能真实反映被测物的温度，需要用红外测温仪对 PT100 型温度传感器和 K 型温度传感器进行标定。

1.2.1　树叶温度测量

测量树叶温度的传感器布置方法如图 2 所示，用 2 kW 的远红外灯在距离为 50 cm 的地方对树叶进行加热，加热 5 min，记录各传感器测量的温度变化。其中位置 1 用在线式红外测温仪直接测量树叶温度；位置 2、3 分别用绝缘胶布将 K 型温度传感器和 PT100 型温度传感器固定在树叶上；位置 4 用在线式红外测温仪测量绝缘胶布外表面的温度；位置 5、6 分别将 PT100 型温度传感器和 K 型温度传感器直接暴露在空气中，用于测量远红外加热对 PT100 型温度传感器和 K 型温度传感器金属探头的加热效果。

用远红外加热柑橘树 5 min，各传感器的温度变化如图 3 所示，从图 3 可以看出，位置 1、2、3 在前 2 min 内温度上升了 20℃，2.5 – 5 min 时测量的温度相近；位置 4 的温度明显高于其他位置，高出位置 1、2、3 约 6℃；位置 6 测得的温度最低，为 26.4℃，在



图 2 柯叶温度测量试验

Fig. 2 Leaf temperature measurement test

2 ~ 5 min 时几乎没有变化；位置 5 测得的温度随着远红外加热时间的延长而升高，5 min 内温度低于位置 1、2、3 传感器测得的温度。试验结果表明：绝缘胶布外表面温度明显高于柯叶温度；柯叶温度高于传感器金属探头直接暴露在空气中的温度；利用绝缘胶布固定 PT100 和 K 型温度传感器测量的柯叶温度，与用在线式红外测温仪直接测量的柯叶表面温度接近，故可用此方法测量柯叶温度。

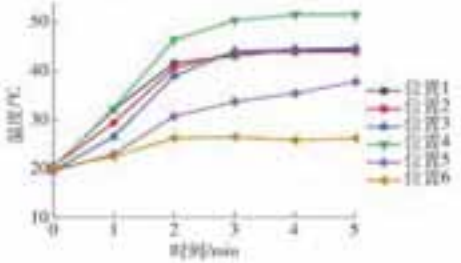


图 3 柯叶温度测量试验结果

Fig. 3 Temperature measurement results of citrus leaves

1.2.2 枝干温度测量

测量枝干温度的传感器布置方法如图 4 所示，用 2 kW 的远红外灯在距离为 50 cm 的地方对枝干进行加热，记录各传感器测量的温度变化，加热时间为 5 min。其中位置 1 用在线式红外测温仪直接测量枝干温度，位置 2、3 分别用绝缘胶布将 K 型温度传感器和 PT100 型温度传感器固定在枝干上，测量枝干表皮温度；位置 4 用在线式红外测温仪测量绝缘胶布外表面温度，验证位置 2、3 的传感器测量的是枝干表皮温度还是绝缘胶布的温度；位置 5、6 的 PT100 温度传感器和 K 型温度传感器直接暴露在空气中，用于测量远红外加热对 PT100 型温度传感器和 K 型温度传感器金属探头的加热效果。

用远红外加热柑橘树 5 min，各位置的温度变化如图 5 所示。从图 5 可以看出，位置 1、2、3 在前 2 min 内温度均上升了 12℃左右，并在 2 ~ 4 min 内测量的温度相近，差值在 1℃以内；3 min 后位置 4 传感器测出的绝缘胶布温度与位置 1、2、3 测得的温



图 4 枝干温度测量

Fig. 4 Temperature measurement of citrus branch

度相比略高；位置 5 传感器测量的温度随着远红外加热时间的延长而升高，但低于位置 1、2、3、4 测得的温度；位置 6 传感器测得的温度最低，为 29.45℃，在 1 ~ 5 min 内几乎没有上升。试验结果表明，利用绝缘胶布固定 PT100 和 K 型温度传感器测量的枝干温度与用在线式红外测温仪测量的枝干表皮温度在 2 ~ 4 min 内接近，绝缘胶布外表面经远红外加热后的温度在 3 min 后高于枝干温度，同时 5 min 内测得的枝干温度高于传感器金属探头受远红外加热后测得的自身温度。故使用绝缘胶布固定 PT100 和 K 型温度传感器测量枝干表皮温度是可行的。

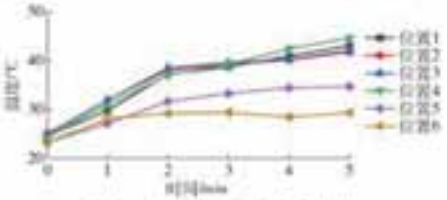


图 5 枝干温度测量试验结果

Fig. 5 Temperature measurement results of citrus branch

1.3 试验方法

将 5 年生柑橘树（高 1.87 m，树冠最大直径 1.0 m）置于处理罩内，首先通过对远红外灯管组数量、单根远红外灯管功率、加热时间、远红外灯管组与支架顶部距离 4 个影响因素进行单因素试验研究，分析这些因素对柑橘黄龙病远红外热处理温度场分布的影响；然后在确定因素水平对其影响的基础上，利用正交试验确定较优的试验参数组合。

选取的各因素和实际取值如表 1 所示，将两盏远红外灯竖直拼接在一起，各连接 1 根灯管，并以此作为一个整体，组成远红外灯管组。改变远红外灯管组数量时，各远红外灯管均匀布置在处理罩内四周，如图 1c 所示，当灯管组数为 1 时，布置在左侧；当灯管组数为 2 时，左右各布置 1 个；当灯管组数为 3 时，以左侧为基准，均匀布置；当灯管组数为 4 时，前后左右 4 个方位各布置 1 个。试验时处理罩封

闭，起到保温作用。首先进行单因素试验，研究远红外灯管组数量、单根远红外灯管功率、加热时间、远红外灯顶端与支架顶部距离等因素对温度场分布的影响；然后进行正交试验，优选出能使柑橘树均匀加热的参数；最后利用优选的参数，对柑橘黄龙病进行远红外热处理田间试验，检测处理效果。

表 1　试验因素与取值

Tab. 1　Experiment factors and values

试验因素	取值
远红外灯管组数量/个	1,2,3,4
单根远红外灯管功率/kW	0.7,0.8,0.9,1.0
加热时间/min	2.0,2.5,3.0,3.5
远红外灯与支架顶部距离/cm	10,15,20,25

2　结果与分析

2.1　单因素试验结果与分析

2.1.1　远红外灯管组数量对温度场的影响

试验条件：单根远红外灯管功率固定为 0.8 kW，加热时间 3 min，远红外灯与支架顶部距离 10 cm，通过改变远红外灯管组数量来改变加热功率，其他试验条件不改变，远红外灯管组数量分别选取为 1、2、3、4，试验重复 3 次，试验结果如表 2、3 所示。根据表 2 中不同远红外灯管组数量下树叶温度，利用 Matlab 分别进行曲面插值，插值结果如图 6 所示。图 6 中坐标原点位于处理罩中心，边缘位置与远红外灯的最近距离为 20 cm。从理论分析，图 6b～6d 中温度应为对称分布，但从图 6 中可以看出，实际测得的温度分布并不对称，其主要原因应该是柑橘树叶和枝干分布不均匀，导致柑橘树吸收红外辐射量不一致，造成温度不对称。

表 2　远红外灯管组数量对树叶温度场的影响

Tab. 2　Citrus leaves temperature under different far infrared lamp groups quantity　℃

传感器序号		远红外灯管组数量/个							
		1		2		3		4	
a1	a17	28.6	23.3	36.1	34.0	53.7	63.4	54.8	66.9
a2	a18	27.6	23.9	34.2	33.5	54.1	50.2	63.6	58.1
a3	a19	26.8	33.8	36.5	38.3	55.6	57.3	67.0	62.1
a4	a20	23.3	51.6	40.8	54.1	60.1	65.4	62.6	69.9
a5	a21	24.4	40.6	48.7	39.1	58.2	50.5	66.5	58.7
a6	a22	25.5	30.4	48.3	37.1	59.8	57.5	67.7	68.8
a7	a23	24.7	23.7	36.6	38.5	64.9	50.9	59.7	55.9
a8	a24	25.7	26.3	34.9	32.5	59.8	43.2	67.7	50.3
a9	a25	23.8	26.2	31.8	34.9	50.3	51.7	58.7	71.6
a10	a26	28.4	26.3	34.6	34.4	53.6	52.4	57.5	52.1
a11	a27	25.0	21.6	35.2	28.0	48.2	40.5	63.4	48.7
a12	a28	23.1	22.3	32.2	29.2	48.8	54.3	49.9	56.4
a13	a29	25.2	36.5	37.0	48.2	65.5	51.5	71.0	53.9
a14	a30	25.6	28.9	46.1	34.8	54.4	41.6	67.1	44.7
a15	a31	23.2	23.2	51.2	31.0	46.4	43.0	62.5	47.1
a16	a32	22.0	23.4	41.5	53.8	55.3	53.8	56.1	66.8
平均值/℃		27.0		38.3		53.6		60.0	
极差/℃		30.0		37.5		30.5		26.9	
显著性		$P<0.01$							

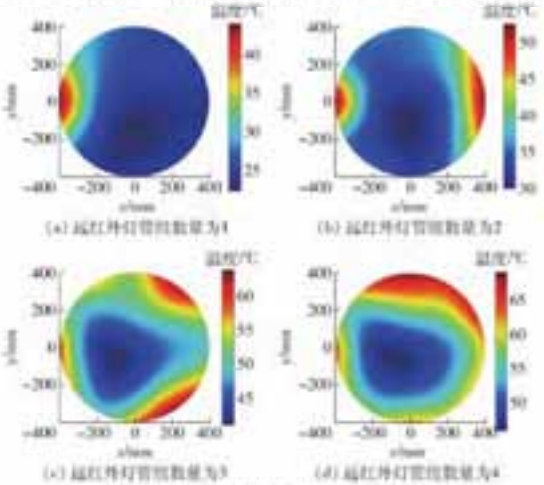
表 3　远红外灯管组数量对枝干温度场的影响

Tab. 3　Citrus branches temperature under different far infrared lamp groups quantity　℃

传感器序号		远红外灯管组数量/个							
		1		2		3		4	
a33	a43	40.3	39.5	41.4	40.4	61.2	53.6	66.8	62.4
a34	a44	25.5	24.9	31.3	27.7	41.9	34.6	45.4	38.0
a35	a45	21.9	24.7	25.8	27.2	37.3	33.4	40.7	40.2
a36	a46	21.7	20.3	31.5	29.5	42.7	37.3	44.5	38.9
a37	a47	23.8	20.6	41.0	41.9	49.7	44.9	68.9	48.8
a38	a48	24.2	24.0	29.7	29.1	50.0	47.9	63.7	60.8
a39	a49	21.9	19.6	26.5	22.0	39.4	29.8	42.4	31.9
a40	a50	20.2	19.4	25.0	20.2	31.4	25.9	33.8	27.7
a41	a51	21.9	20.1	28.0	22.6	40.3	29.1	43.6	30.9
a42	a52	20.2	21.4	24.3	25.1	35.5	32.3	38.1	35.9
平均值/℃		25.8		29.5		39.9		45.2	
极差/℃		20.9		21.7		35.3		41.2	
显著性		$P<0.01$							

从表 2 和表 3 可以得出，远红外灯管组数量对树叶（表 2）和枝干（表 3）的温度场分布均有极显著影响（$P<0.01$）。随着远红外灯管组数量的增加，树叶以及枝干的平均温度均增加，且树叶温度高于枝干温度。结合图 6 可以得出，当远红外灯管组数量为 1 或 2 时，处理罩内树叶温度场非常不均匀。

当远红外灯管组数量为 3 和 4 时，树叶平均温度分别为 53.6、60.0℃，树叶温度极差分别为 30.5、26.9℃；枝干平均温度分别为 39.9、45.2℃，枝干温



(a) 远红外灯管组数量为1　(b) 远红外灯管组数量为2

(c) 远红外灯管组数量为3　(d) 远红外灯管组数量为4

图 6　不同远红外灯管组数量树叶温度分布图

Fig. 6　Leaf temperature distribution maps under different far infrared lamp groups quantity

度极差分别为35.3、41.2℃。说明采用4组灯管组与3组灯管组加热相比，前者树叶温度场更均匀，而后者枝干温度场更均匀。

从以上试验结果及分析可以看出，远红外灯管组数量对树叶以及枝干温度场分布影响显著。随着远红外灯管组数量的增加，树叶以及枝干的平均温度值增加，且树叶温度高于枝干温度。灯管组数量为4时，树叶温度均匀，灯管组数量为3时，枝干温度较均匀。当远红外灯管组数量为3时，树叶平均温度为53.6℃，枝干为39.9℃。

2.1.2 单根远红外灯管功率对温度场的影响

试验条件：固定远红外灯管组数量为3，加热时间2 min，远红外灯与支架顶部距离10 cm，其他试验条件不变，改变远红外灯功率来加热柑橘树，远红外灯功率取0.7、0.8、0.9、1.0 kW，试验重复3次，试验结果如表4和表5所示。

表4 单根远红外灯管功率对树叶温度场的影响

Tab.4 Citrus leaves temperature under different far infrared lamp power ℃

传感器序号		单根远红外灯管功率/kW							
		0.7		0.8		0.9		1.0	
a1	a17	45.2	53.7	37.9	51.8	52.4	63.2	51.1	62.1
a2	a18	41.1	44.2	39.0	37.9	46.4	50.9	44.7	45.5
a3	a19	45.4	41.8	46.9	42.5	52.1	46.5	50.4	45.0
a4	a20	45.4	47.0	51.8	52.8	52.2	52.7	49.9	51.3
a5	a21	42.3	44.9	44.4	40.2	48.4	52.0	47.5	51.3
a6	a22	41.1	43.3	46.9	43.7	48.4	49.1	46.6	47.7
a7	a23	58.9	41.3	59.1	38.2	71.2	46.9	70.4	45.4
a8	a24	46.9	37.9	48.1	41.8	52.8	42.9	50.7	41.8
a9	a25	40.5	40.9	37.1	42.7	47.5	47.8	45.8	46.4
a10	a26	44.4	38.9	39.2	41.4	50.8	43.3	48.7	43.1
a11	a27	38.1	35.8	35.2	33.1	42.7	39.4	41.4	38.5
a12	a28	42.2	43.8	35.0	43.8	47.5	48.7	46.3	48.7
a13	a29	54.9	41.4	52.7	44.7	63.9	46.8	59.9	45.3
a14	a30	40.4	34.1	43.7	35.8	46.1	37.6	45.9	36.7
a15	a31	35.6	34.0	35.8	39.1	40.5	37.0	39.4	32.5
a16	a32	39.1	35.3	50.2	45.2	43.2	38.6	42.3	38.2
平均值/℃		42.5		43.0		48.4		47.2	
标准差/℃		5.7		6.3		7.4		7.1	
显著性		$P<0.01$							

从表4和表5可以看出，当远红外灯管组数量为3，加热时间为2 min，远红外灯与支架顶部距离为10 cm时，单根远红外灯管功率对树叶（表4）和枝干（表5）温度场分布均影响显著（$P<0.05$）。树叶的平均温度均达到40℃以上，当单根远红外灯管功率为0.9 kW和1.0 kW时，树叶、枝干温度平均值接近，当单根远红外灯管功率为0.7 kW和0.8 kW时，树叶、枝干的温度平均值也接近，但与0.9 kW和1.0 kW相比时，温度更低，同时温度标准差也稍低。

表5 单根远红外灯管功率对枝干温度场的影响

Tab.5 Citrus branches temperature under different far infrared lamp power ℃

传感器序号		单根远红外灯管功率/kW							
枝干		0.7		0.8		0.9		1.0	
a33	a43	39.2	44.2	46.2	43.3	45.1	50.2	44.7	48.6
a34	a44	35.9	29.3	32.4	31.2	40.5	31.7	38.9	31.1
a35	a45	30.6	32.3	30.4	28.9	33.5	34.9	32.6	34.5
a36	a46	33.6	30.0	32.7	31.5	37.3	32.2	36.1	32.0
a37	a47	39.0	26.1	36.9	39.3	45.7	27.4	44.1	27.2
a38	a48	36.9	40.3	37.4	40.7	41.2	44.2	39.3	42.5
a39	a49	33.2	27.3	33.2	28.1	36.0	28.7	35.6	28.7
a40	a50	26.4	24.6	28.6	25.3	27.7	24.8	28.0	25.4
a41	a51	35.8	26.8	33.2	26.8	38.9	28.3	38.3	28.3
a42	a52	31.4	28.7	29.8	28.7	33.9	30.8	33.2	30.0
平均值/℃		32.6		31.2		35.7		35.0	
标准差/℃		5.4		5.7		7.1		6.5	
显著性		$P<0.01$							

不同功率下树叶平均温度的变化如图7所示，从图7可以看出，不同功率下树叶平均温度上升趋势相似：加热功率为0.9、1.0 kW时，树叶温度明显高于0.7、0.8 kW；功率为0.9、1.0 kW时，树叶温度上升速度基本接近，但前者温度高于后者。当单根远红外灯管的功率为1.0 kW时，树叶温度平均值在1.5 min时上升到38.5℃，2 min时上升为47.2℃，0.5 min内上升8.7℃，上升速度与0.9 kW时接近。当单根远红外灯管的功率为0.7 kW时，树叶温度平均值在1.5 min时上升为35.2℃，2 min时上升为42.5℃，0.5 min内上升7.3℃，上升速度与0.8 kW时接近。

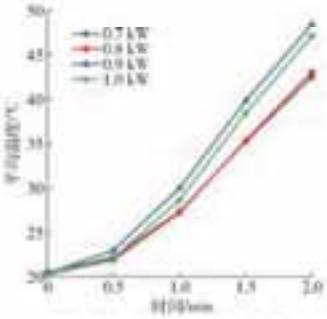


图7 不同功率下树叶平均温度变化曲线

Fig.7 Average temperature curves of leaves under different far infrared lamp powers

试验结果表明，增加单根远红外灯管功率可在一定程度上增加树叶以及枝干的温度平均值，且相同条件下树叶温度高于枝干温度。相同加热时间，功率越高树叶平均温度上升幅度越大。0.7、0.8 kW以及0.9、1.0 kW时测得的树叶以及枝干温度相近。

2.1.3　加热时间对温度场的影响

试验条件：远红外灯管组数量固定为 3 个，单根远红外灯管功率 0.8 kW，远红外灯与支架顶部距离 10 cm，其他试验条件不变，探究不同加热时间对温度场分布的影响，加热时间取 2.0、2.5、3.0、3.5 min，试验重复 3 次。树叶以及枝干的温度平均值、标准差、显著性分析结果如表 6 所示。

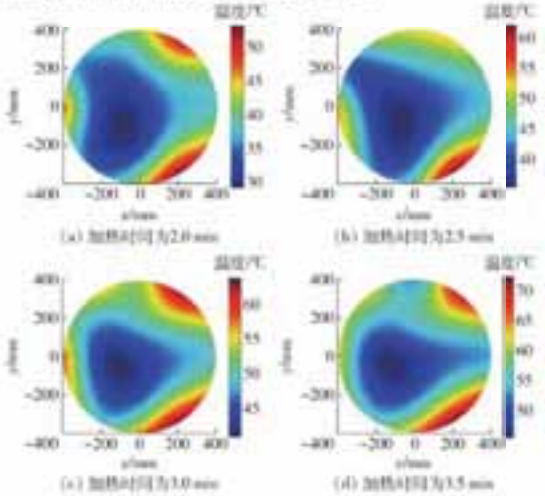
表 6　加热时间对温度场的影响

Tab.6　Effects of heating time on temperature field

类别	评价指标	加热时间/min			
		2.0	2.5	3.0	3.5
树叶	平均值/℃	41.0	48.3	53.6	59.6
	标准差/℃	6.3	7.7	6.7	7.7
	显著性	$P<0.01$			
枝干	平均值/℃	31.2	36.2	39.9	43.6
	标准差/℃	5.7	8.6	9.1	10.2
	显著性	$P<0.01$			

从表 6 可以看出，加热时间对树叶以及枝干的温度场分布均有显著影响（$P<0.01$）。随着加热时间的增加，树叶以及枝干的温度平均值均增加，当加热时间为 3.5 min 时，树叶温度达到 59.6℃，枝干温度平均值达 43.6℃；当加热时间为 2.0 min 时，树叶温度平均值为 41.0℃，枝干温度平均值为 31.2℃，温度上升幅度随着时间推移逐步降低。

由于树叶与枝干不能单独加热，且相同加热条件下树叶温度高于枝干温度，因此应该重点考虑树叶温度，根据表 6 中不同远红外灯管组数量下树叶温度，利用 Matlab 分别进行曲面插值，插值结果如图 8 所示。图中坐标原点位于处理罩中心，边缘位置与远红外灯的最近距离为 20 cm。



(a) 加热时间为2.0 min　(b) 加热时间为2.5 min

(c) 加热时间为3.0 min　(d) 加热时间为3.5 min

图 8　不同加热时间树叶温度分布图

Fig.8　Leaf temperature distribution maps under different heating time

对于树叶而言，加热时间为 2.0、2.5、3.0、3.5 min 时，在灯的正前方距离灯 20 cm 处，平均温度分别为 50.2、56.2、61.8、67.7℃，最高温度分别为 53.5、62.4、64.2、72.7℃。在灯的正前方距离灯 40 cm 处，平均温度分别为 31.8、37.7、42.4、46.6℃。随着加热时间的增加，虽然距离远红外灯 20 cm 以及 40 cm 处的树叶温度平均值均增加，但从 20 cm 至 40 cm 的温度降低的幅度没有变化。

试验结果表明，在 2 – 3.5 min 内，加热时间增加 0.5 min，树叶温度平均值升高 6℃左右。在远红外灯正前方，距离从 20 cm 增加到 40 cm 时，树叶温度平均值下降幅度不随加热时间的变化而变化。相同条件下树叶温度高于枝干温度。

2.1.4　远红外灯顶端与支架顶部距离对温度场的影响

试验条件：远红外灯管组数量固定为 3 个，单根远红外灯管功率 0.8 kW，加热时间 3 min，其他试验条件不变，改变远红外灯与支架顶部距离来加热柑橘树，选取水平为 10、15、20、25 cm，试验重复 3 次。不同远红外灯与支架顶部距离下，树叶以及枝干的温度平均值、标准差、显著性计算结果如表 7 所示。

表 7　远红外灯与支架顶部距离对温度场的影响

Tab.7　Influence of distance between far infrared lamp and top of bracket on temperature field

类别	评价指标	远红外灯与支架顶部距离/cm			
		10	15	20	25
树叶	平均值/℃	53.6	55.3	55.3	54.8
	标准差/℃	6.7	7.9	4.9	6.8
	显著性	$P=0.01$			
枝干	平均值/℃	39.9	40.7	40.9	41.0
	标准差/℃	9.1	9.5	9.0	9.9
	显著性	$P=0.07$			

从表 7 可以看出，当固定远红外灯管组数量为 3，单根远红外灯管功率为 0.8 kW，加热时间为 3 min 时，远红外灯与支架顶部距离对树叶的温度场分布影响显著（$P<0.05$），对枝干的温度场分布无显著影响（$P>0.05$）。树叶以及枝干各水平下的温度平均值接近，树叶温度平均值达到 50℃以上，枝干温度平均值在 40℃左右。当远红外灯与支架顶部距离为 20 cm 时，树叶以及枝干的温度标准差较其他水平时更小，且树叶温度标准差低于枝干温度标准差。

2.2　正交试验结果与分析

2.2.1　正交试验方案

根据单因素试验结果，正交试验考虑远红外灯管组数量（A）、单根远红外灯管功率（B）、加热时间（C）、远红外灯与支架顶部距离（D）4 个因素，选用 L64(421) 正交表，正交试验因素水平如表 8 所示。

根据 L64(421) 正交表安排正交试验，试验测量指标分为两类：温度平均值和温度标准差，包含树叶、枝干、整体(即所有测试点)温度平均值和树叶、枝干、整体温度标准差共 6 个具体评价指标，试验结果如表 9 所示。

表 8 正交试验因素水平

Tab. 8 Factors and levels of orthogonal test

因素水平	A/个	B/kW	C/min	D/m
1	1	0.7	2.0	10
2	2	0.8	2.5	15
3	3	0.9	3.0	20
4	4	1.0	3.5	25

表 9 正交试验结果

Tab. 9 Orthogonal test results ℃

序号	温度平均值			温度标准差			序号	温度平均值			温度标准差		
	树叶	树干	整体	树叶	树干	整体		树叶	树干	整体	树叶	树干	整体
1	25.6	23.3	24.7	3.8	4.1	4.0	33	39.6	30.1	35.9	6.6	4.5	7.4
2	26.7	23.4	25.4	4.2	3.9	4.3	34	44.8	34.4	40.8	4.9	6.8	7.6
3	28.9	24.1	27.1	4.4	5.3	5.3	35	53.9	39.9	48.5	6.5	8.9	10.1
4	30.1	25.6	28.4	4.8	4.6	5.2	36	56.6	42.6	51.2	6.8	10.9	11.0
5	25.9	23.1	24.8	4.6	4.4	4.7	37	42.8	32.9	39.0	5.2	5.3	7.1
6	29.0	24.9	27.5	4.6	4.8	5.0	38	50.1	37.1	45.1	7.9	8.6	10.3
7	30.4	25.5	28.5	5.2	4.8	5.6	39	56.5	42.5	51.1	7.1	11.0	11.1
8	32.9	26.6	30.5	6.7	6.9	7.4	40	61.0	46.7	55.5	6.9	11.8	11.4
9	27.8	24.3	26.4	4.7	3.9	4.7	41	47.8	35.7	43.1	6.2	7.1	8.8
10	29.7	25.1	27.9	5.4	4.7	5.6	42	54.9	40.0	49.1	6.7	8.9	10.5
11	33.0	27.6	30.9	6.1	7.1	7.0	43	59.3	43.1	53.1	8.3	10.1	12.0
12	34.3	28.5	32.1	5.7	7.3	6.9	44	65.9	48.1	59.1	7.0	11.1	12.3
13	27.2	23.8	25.9	5.0	4.2	5.0	45	49.9	36.5	44.7	7.0	7.2	9.6
14	31.4	25.8	29.3	6.8	6.2	7.1	46	54.4	39.4	48.7	7.3	8.6	10.7
15	33.5	27.8	31.3	6.6	7.4	7.4	47	62.0	45.2	55.6	6.0	10.4	11.4
16	36.1	29.2	33.4	7.6	9.2	8.8	48	67.7	50.0	60.9	8.3	14.0	13.8
17	33.6	28.8	31.7	4.6	6.0	5.6	49	47.7	36.7	43.5	6.6	7.1	8.7
18	37.5	31.2	35.0	5.2	8.4	7.3	50	54.9	43.2	50.4	5.9	11.2	10.0
19	41.8	32.6	38.3	7.0	8.0	8.6	51	64.5	48.7	58.5	9.2	13.4	13.3
20	45.4	35.9	41.7	5.9	8.9	8.5	52	71.4	54.3	65.4	9.5	14.5	15.1
21	35.9	30.4	33.8	5.3	8.0	6.9	53	57.0	42.3	51.3	6.9	8.4	10.3
22	41.2	34.5	38.7	5.7	9.9	8.2	54	63.2	47.4	57.3	4.8	10.1	10.8
23	46.2	36.1	42.3	6.5	9.2	9.0	55	71.1	52.0	64.1	9.9	12.1	14.6
24	47.5	36.5	43.3	6.1	8.7	8.9	56	68.8	51.5	62.5	10.5	13.6	14.9
25	38.0	30.1	34.9	6.5	6.8	7.6	57	56.2	41.9	51.1	6.3	8.3	10.4
26	44.8	34.9	41.0	7.1	9.1	9.2	58	69.3	51.2	62.3	9.7	14.6	14.7
27	50.5	39.0	46.1	7.9	10.9	10.7	59	73.1	53.8	65.7	7.6	13.3	13.9
28	51.8	41.1	47.7	6.8	13.3	11.0	60	81.1	60.2	73.0	9.3	15.2	15.6
29	38.6	31.4	35.9	6.2	7.2	7.4	61	59.5	45.6	54.4	8.7	10.6	12.0
30	45.0	34.8	41.1	8.2	9.2	9.8	62	66.2	48.0	59.6	9.4	11.1	13.9
31	48.7	39.3	45.1	6.2	12.7	10.2	63	77.8	57.2	70.2	10.5	14.9	16.1
32	53.0	42.4	48.9	7.0	13.1	11.0	64	81.0	58.9	72.8	8.9	13.4	15.4

2.2.2 正交试验直观分析

正交试验直观分析是利用极差衡量各因素对各指标影响情况，极差越大则说明对该指标的影响越大，为重要影响因素，相反极差小则为次要因素[33]，直观分析结果如表 10 所示，图 9 则表示了各因素水平与各指标均值、标准差之间的关系。

由表 10 可知，因素 A、B、C 对树叶、枝干、整体的温度平均值以及温度标准差这 6 个指标均有影响，除树叶温度标准差指标外，对其他指标的影响大小一致，从大到小的顺序为 A、C、B。D 对 6 个评价指标也均有影响。对于树叶、枝干和整体温度平均值指标，各因素对其影响大小顺序为 A、C、B、D，最优组合为 $A_4B_4C_4D_1$。对于树叶、枝干和整体温度标准差指标，各因素对其影响大小顺序为 A、C、B、D(其中树叶温度标准差为 A、C 与 B、D 相同)，最优组合为 $A_1B_1C_1D_4$。从表 10 还可以看出，对于温度

表 10　直观分析结果

Tab. 10　Visual analysis result

指标		因素	各水平均值/℃				极差	优水平
			水平 1	水平 2	水平 3	水平 4	R/℃	
温度平均值	树叶	A	30.2	43.7	54.2	66.4	36.3	4
		B	43.9	47.5	51.1	52.0	8.1	4
		C	40.8	46.5	52.0	55.3	14.5	4
		D	49.1	48.3	49.0	48.1	1.0	
		误差列	48.7	48.7	48.6	48.5	0.8	
	枝干	A	25.5	34.9	40.3	49.5	24.0	4
		B	34.7	36.9	39.0	39.7	5.0	4
		C	32.3	35.9	39.7	42.4	10.1	4
		D	38.2	37.4	37.6	37.0	1.3	
		误差列	37.6	37.6	37.5	37.6	0.6	
	整体	A	28.4	40.3	46.8	60.1	31.8	4
		B	40.4	43.5	46.5	47.4	6.9	4
		C	37.6	42.4	47.3	50.4	12.8	4
		D	45.0	44.2	44.6	43.9	1.1	
		误差列	44.5	44.5	44.4	44.4	0.7	
温度标准差	树叶	A	5.4	6.4	6.8	8.4	3.0	
		B	6.0	6.5	7.0	7.5	1.5	
		C	5.9	6.5	7.2	7.4	1.5	
		D	6.9	6.8	7.0	6.2	0.8	4
		误差列	6.7	6.8	6.6	6.7	0.5	
	枝干	A	5.6	9.3	9.1	12.0	6.4	
		B	7.9	8.6	9.5	10.0	2.0	
		C	6.4	8.5	10.0	11.0	4.6	
		D	9.7	9.2	9.0	8.0	1.7	4
		误差列	9.0	8.9	9.0	9.0	0.4	
	整体	A	5.9	8.8	10.3	13.1	7.2	
		B	8.3	9.1	10.1	10.6	2.3	
		C	7.5	9.1	10.4	11.1	3.6	
		D	9.9	9.6	9.6	9.0	0.9	4
		误差列	9.5	9.6	9.5	9.5	0.3	

平均值类指标，各因素的最优水平一致，因素 *A*、*B*、*C* 的最优水平为 4，因素 *D* 的最优水平为 1。对于温度标准差类指标，各因素的最优水平也一致，且与温度平均值类指标均不同，因素 *A*、*B*、*C* 的最优水平为 1，因素 *D* 的最优水平为 4。

由图 9 可知，从温度平均值类指标来看，因素 *A* 可以明显提高树叶、枝干、整体的温度平均值。因素 *B* 以及因素 *C* 对树叶、枝干、整体的温度平均值的提高具有一定的促进作用，且因素 *C* 的促进作用比因素 *B* 明显。因素 *D* 对树叶、枝干、整体的温度平均值的提高无明显作用。从温度标准差类指标来看，因素 *A* 对整体温度标准差的影响随着 *A* 的增加而逐渐增大，当因素 *A* 水平为 3 时，枝干温度标准差与水平 2、4 相比有所降低，树叶温度标准差随着 *A* 的增加变化较缓慢。因素 *B* 水平变化时树叶、枝干、整体的温度标准差无明显改变。因素 *C* 对枝干、整体的温度标准差的影响随着 *C* 的增加也逐步加大，但对树叶温度标准差无明显作用。随着因素 *D* 的加大，树叶、枝干以及整体的温度标准差在一定程度上有所降低。

2.2.3　正交试验方差分析

直观分析虽然能够将各因素对评价指标的影响按照极差大小进行排序，但是各因素对指标的影响是否显著却不清楚。对于评价指标有显著影响的因素应进行严格控制，而对于评价指标影响不显著的因素则不用考虑。选取显著性水平 $\alpha \leqslant 0.05$，对试验结果进行方差分析，分析结果如表 11 所示，其中贡献率为因素平方和与总平方和的比值，贡献率越大则该因素对评价指标的影响越大。

从表 11 可知，因素 *A*、*B* 以及 *C* 对温度平均值都是显著影响因素。因素 *A*、*C* 对温度平均值类指标的贡献率最高，对树叶温度平均值的贡献率分别为 78%、14%，对于枝干温度平均值的贡献率分别为 77%、15%，对于整体温度平均值的贡献率分别为 78%、14%。而因素 *D* 对温度平均值影响不显

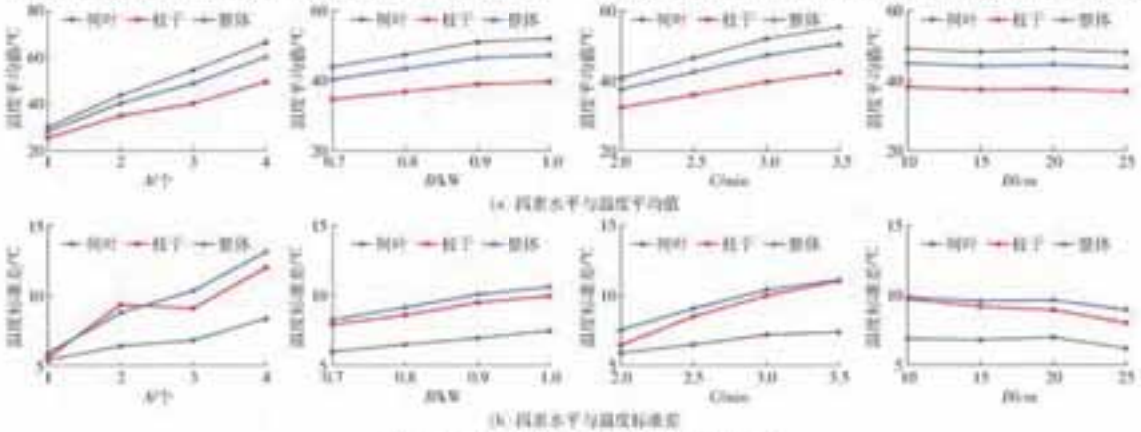


图 9　因素水平与各指标均值、标准差的关系

Fig. 9　Diagrams of relationship between factor level and mean value, standard deviation of each index

表 11 方差分析结果

Tab. 11 Variance analysis results

指标		变异来源	平方和	自由度	均方	F	P	贡献率/%
温度平均值	树叶	A	11 721.15	3	3 907.05	397.44	<0.01	78
		B	668.42	3	222.81	22.67	<0.01	4
		C	2 056.46	3	685.49	69.73	<0.01	14
		D	17.34	3	5.78	0.59	0.63	0
		误差	501.35	51	9.83			3
		合计	14 964.72	63				
	枝干	A	5 048.64	3	1 682.88	340.40	<0.01	77
		B	252.84	3	84.28	17.05	<0.01	4
		C	946.47	3	315.49	63.82	<0.01	15
		D	15.45	3	5.15	1.04	0.38	0
		误差	252.13	51	4.94			4
		合计	6 515.53	63				
	整体	A	8 812.06	3	2 937.35	386.11	<0.01	78
		B	484.90	3	161.63	21.25	<0.01	4
		C	1 578.57	3	526.19	69.17	<0.01	14
		D	15.18	3	5.06	0.67	0.58	0
		误差	387.99	51	7.61			3
		合计	11 278.70	63				
温度标准差	树叶	A	130.89	3	43.63	73.43	<0.01	56
		B	26.13	3	8.71	14.66	<0.01	11
		C	43.40	3	14.47	24.35	<0.01	18
		D	4.77	3	1.59	2.67	0.06	2
		误差	30.30	51	0.59			13
		合计	235.49	63				
	枝干	A	448.44	3	149.48	176.49	<0.01	58
		B	45.50	3	15.17	17.91	<0.01	6
		C	201.82	3	67.27	79.43	<0.01	26
		D	33.52	3	11.17	13.19	<0.01	4
		误差	43.20	51	0.85			6
		合计	772.48	63				
	整体	A	506.47	3	168.82	302.43	<0.01	68
		B	56.75	3	18.92	33.89	<0.01	8
		C	144.31	3	48.10	86.17	<0.01	19
		D	7.69	3	2.56	4.59	0.01	1
		误差	28.47	51	0.56			4
		合计	743.69	63				

著。因素 A、B、C 对温度标准差类指标均有极显著影响。因素 A 对温度标准差指标的贡献率最高，对树叶、枝干、整体温度标准差的贡献率分别为 56%、58%、68%。因素 C 对树叶、枝干、整体温度标准差的贡献率分别为 18%、26%、19%。因素 B 对树叶、枝干、整体温度标准差的贡献率为 11%、6%、8%。因素 D 对枝干、整体温度标准差有极显著影响，但对树叶温度标准差没有显著影响。表 11 还表明，对于各评价指标，因素 A 的贡献率是最大的，因素 C 次之，说明远红外灯管组数量对评价指标的影响能力最大，其次是加热时间。因素 D 仅对枝干和整体温度标准差指标有显著影响。

2.2.4 同一因素不同水平差异显著性检验

采用邓肯式新复极差检验法（Shortest significant ranges，SSR）对同一因素不同水平均值间的差异进行显著性检验，检验结果如表 12 所示。

由表 12 可知，对于树叶温度平均值，因素 A、C 的 4 个水平均达到极显著差异，因素 B 的第 3 水平和第 4 水平均与第 1、2 水平达到极显著差异。对于枝干温度平均值，因素 A、C 的 4 个水平均达到极显著差异，因素 B 的第 3 水平和第 4 水平均与第 1、2 水平达到极显著差异，因素 D 的第 1 水平与第 4 水平达到极显著差异。对于整体温度平均值，因素 A、C 的 4 个水平均达到极显著差异，因素 B 的第 3 水

表 12　同一因素各水平间差异显著性 SSR 检验

Tab. 12　Significant SSR test for differences between levels of the same factor

指标		温度平均值			温度标准差		
		树叶	枝干	整体	树叶	枝干	整体
A	水平 1	a	a	a	a	a	a
	水平 2	b	b	b	b	b	b
	水平 3	c	c	c	b	b	c
	水平 4	d	d	d	c	c	d
B	水平 1	a	a	a	a	a	a
	水平 2	b	b	b	ab	b	b
	水平 3	c	c	c	bc	c	c
	水平 4	c	c	c	c	c	d
C	水平 1	a	a	a	a	a	a
	水平 2	b	b	b	a	b	b
	水平 3	c	c	c	b	c	c
	水平 4	d	d	d	b	d	d
D	水平 1	a	b	b	ab	c	b
	水平 2	a	ab	ab	ab	bc	b
	水平 3	a	ab	ab	b	b	b
	水平 4	a	a	a	a	a	a

平和第 4 水平均与第 1、2 水平达到极显著差异，因素 D 的第 1 个水平与第 4 个水平达到极显著差异。对于树叶温度标准差，因素 A 的第 2 水平和第 3 水平均与第 1、4 水平达到极显著差异，因素 B 的第 1 水平和第 4 水平达到极显著差异，因素 C 的第 3 水平和第 4 水平均与第 1 水平和第 2 水平达到极显著差异，因素 D 的第 3 个水平与第 4 个水平达到极显著差异。对于枝干温度标准差，因素 A 的第 2 水平和第 3 水平均与第 1、4 水平达到极显著差异，因素 B 的第 3 水平和第 4 水平均与第 1、2 水平达到极显著差异，因素 C 的 4 个水平均达到极显著差异，因素 D 的第 1、3、4 水平达到显著差异。对于整体温度标准差，因素 A、B、C 的 4 个水平均达到极显著差异，因素 D 的第 1、2、3 水平与第 4 水平达到极显著差异。除此之外，其他因素不同水平均值间的差异均不显著。同一因素不同水平差异显著性检验，为确定多指标正交试验的最优水平提供了帮助。

2.2.5　正交试验结果验证

对于多指标正交试验，不同的评价指标受不同因素以及因素水平的影响也存在一定的差异，若仅注重优化某一评价指标，则其他评价指标对应的结果可能较差，因此，应综合考虑各评价指标的试验效果，综合选择各参数的最优水平。在采用直观分析、方差分析、SSR 检验的基础上利用综合平衡法确定最优参数水平组合。

评价指标不同，各因素的最优水平存在差异，根据表 11 和表 12 的方差分析、贡献率以及同一因素各水平间差异显著性 SSR 检验可知，在确定最优参数水平时，优先考虑整体温度平均值，然后考虑树叶温度平均值、整体温度标准差，再考虑枝干温度平均值、枝干温度标准差，最后考虑树叶温度标准差。

对于整体温度平均值，各显著性影响因素贡献率由大到小依次为：A、C、B，首先分析因素 A、C，考虑病菌、树叶的耐热性，剔除温度在 40℃以下、60℃以上的搭配，整体温度平均值在 40℃以上、60℃以下，A、C 搭配按温度由高到低进行排列的结果为：A_4C_2、A_3C_4、A_3C_3、A_4C_1、A_3C_2、A_2C_4、A_2C_3、A_3C_1、A_2C_2、A_2C_1、A_1C_4、A_1C_3、A_1C_2、A_1C_1。A、B 搭配的排列顺序为：A_4B_2、A_4B_1、A_3B_4、A_3B_3、A_3B_2、A_3B_1、A_2B_4。在以上排列的基础上对树叶温度平均值试验结果进行排序，剔除温度在 40℃以下、60℃以上的搭配，A、C 搭配按温度由高到低进行排列顺序为：A_3C_1、A_4C_1、A_3C_2、A_2C_4、A_4C_2、A_3C_3、A_3C_4、A_2C_3、A_2C_2、A_2C_1、A_1C_4、A_1C_3、A_1C_2、A_1C_1。A、B 搭配的排列顺序为：A_4B_1、A_3B_4、A_3B_3、A_3B_2、A_3B_1、A_2B_4。在以上排列的基础上对整体温度标准差按照从小到大的顺序排列为：A_3C_3、A_2C_3、A_3C_2、A_2C_4、A_4C_1、A_3C_1。在以上排列的基础上对枝干温度平均值按照从高到低的顺序排列为：A_3C_3、A_4C_1。在以上排列的基础上对枝干温度标准差试验结果平均值按照从小到大的顺序排列为：A_4C_1、A_3C_1。

考虑整体以及树叶温度平均值指标时，在 40～60℃内，在因素 A 与因素 C 的搭配中，A_3C_3 温度平均值最高，A_4C_1 次之，A_3C_1 比 A_4C_1 高出 2℃左右；在因素 A 与因素 B 的搭配中，A_4B_1 最高，A_3B_4 次之，且二者之间相差也为 2℃。枝干温度平均值在 40～60℃内的搭配为 A_3C_1、A_4C_1。因素 A 的贡献率最大，然后是因素 C 和因素 B，综合考虑各指标试验结果、因素以及显著性交互作用搭配，对于 A、B、C 3 个因素考虑选取 $A_3B_4C_3$，对于因素 D，选择其在整体温度平均值指标下对应的最优水平 1，因此得到优化的参数组合为 $A_3B_4C_3D_1$。

按照优化后的参数组合进行试验，远红外灯管组数量为 3，单根远红外灯管功率为 1.0 kW，加热时间为 3 min，远红外灯与支架顶部距离为 10 cm，各测点温度以及各指标结果如表 13 所示。树叶温度平均值为 58.1℃，枝干温度平均值为 43.1℃，整体温度平均值为 52.3℃。

2.3　处理效果检测

根据以上试验结果，处理田间带病柑橘树，对处理前后柑橘树叶进行实时荧光定量聚合酶链反应（Polymerase chain reaction，PCR）检测[34]，以研究柑橘黄龙病远红外处理效果。

试验在华南农业大学柑橘黄龙病研究室的柑橘实验园进行，试验选取 4 棵柑橘树，分为两组，每组

表 13 优化参数组合下的温度分布

Tab. 13 Temperature distribution under optimal parameter combination

树叶		枝干	
测试点	温度/℃	测试点	温度/℃
a1	63.5	a33	61.3
a2	60.0	a34	45.8
a3	60.5	a35	39.8
a4	62.7	a36	45.9
a5	59.7	a37	54.7
a6	61.3	a38	56.3
a7	63.8	a39	41.9
a8	61.5	a40	33.2
a9	53.5	a41	43.7
a10	57.2	a42	38.3
a11	54.5	a43	56.6
a12	52.9	a44	38.4
a13	65.4	a45	36.0
a14	60.5	a46	40.2
a15	53.0	a47	50.8
a16	61.9	a48	57.1
a17	67.2	a49	30.4
a18	51.7	a50	27.4
a19	58.4	a51	31.0
a20	66.7	a52	33.9
a21	65.2		
a22	60.5		
a23	56.0		
a24	54.0		
a25	58.8		
a26	51.6		
a27	44.6		
a28	59.7		
a29	58.1		
a30	50.3		
a31	48.1		
a32	56.1		
平均值/℃	58.1		43.1
整体平均值/℃		52.3	
标准差/℃	5.5		10.1
整体标准差/℃		10.5	

2 棵，一组作为对照组，不进行处理，另一组作为试验组，进行远红外处理。根据本研究得出的最优参数进行设置，远红外灯管组数量为 3，单根远红外灯管功率为 1.0 kW，加热时间为 3.0 min，远红外灯与支架顶部距离为 10 cm。外界温度为 20℃，加热 3.0 min 后，树叶平均温度达到 58℃，关闭加热，自然降温 9 min 至 30℃时结束，试验装置如图 10 所示，该试验每 7 d 进行一次，连续进行 28 d。



图 10 远红外田间效果试验装置

Fig. 10 Far-infrared field test equipment diagram

1. 处理架 2. 通道温度记录仪 3. 功率调节器

试验开始前，采集对照组（R-CK-1，R-CK-2）以及试验组（R-1，R-2）4 棵树症状明显的树叶样本，每棵树东西南北方各采集一片，然后提取叶中脉 DNA 进行实时荧光定量 PCR 检测。第 4 次试验结束 1 个月后，用同样方法采集对照组以及试验组的树叶样本进行检测。试验前后检测以及计算结果如表 14 所示。T 表示在 PCR 扩增过程中，扩增产物（荧光信号）到达阈值时（进入指数增长期）所经过的扩增循环次数，当 T 小于 30 时，则可认为样本感染了黄龙病。从表 14 可以看出，所选试验树均感染了黄龙病。根据检测结果计算处理前后试验组以及对照组的 T 平均值和病菌平均浓度（N）值。处理前试验组的 T 平均值为 19.84，N 平均值为 1.64×10^{6}，经过 4 次处理后，试验组 T 值增加，T 平均值为 20.54，N 平均值为 1.01×10^{6}，平均降低率为 34.4%。处理前对照组的 T 平均值为 19.73，N 平

表 14 样本实时荧光定量 PCR 检测结果

Tab. 14 Sample real-time fluorescent quantitative PCR detection results

类别	样本	T		病菌浓度（N）		浓度降低率/%
		处理前	处理后	处理前	处理后	
试验组	R-1	20.07	20.26	1.38×10^{6}	1.20×10^{6}	12.5
	R-2	19.60	20.81	1.89×10^{6}	8.26×10^{5}	56.3
对照组	R-CK-1	19.00	19.74	2.84×10^{6}	1.72×10^{6}	39.4
	R-CK-2	20.46	19.73	1.05×10^{6}	1.73×10^{6}	-64.5

注：T 为 4 片树叶检测结果的平均值；处理后指 4 次热处理完 1 个月后的测量值。病菌浓度（N）为每 ng 总 DNA 中黄龙病菌拷贝数[28]，计算公式为：$N=35.50\times10^{6}\times10^{(T-19.51)/(-3.369)}$。

均值为 1.95×10^6，处理后，对照组 T 平均值仍为 19.74，N 平均值为 1.73×10^6，病菌平均浓度降低了 11%。因此，可以认为远红外处理对于柑橘黄龙病防治具有一定效果。

3　讨论

通过试验得出柑橘黄龙病远红外处理的较佳参数为：远红外灯管组数量为 3，单根远红外灯管功率为 1.0 kW，加热时间为 3 min，远红外灯与支架顶部距离为 10 cm。在此条件下，树叶温度平均值为 58.1℃，枝干温度平均值为 43.1℃，整体温度平均值为 52.3℃。

远红外灯管组数量为 4 时，加热源更均匀，温度场应该比灯管组数量为 3 更均匀，但研究结果并非如此。因为当红外灯管组数量为 4（偶数）时，每组灯管的对面是另一组红外灯，而红外灯管组数量为 3（奇数）时，每组灯管对面没有其他红外灯，对面是镜面反射铝板，因柑橘树枝叶比较稀疏，透过柑橘树的红外辐射会被反射到柑橘树上，枝干的温度会比较均匀一些。因此红外灯管组数量为 3（奇数）时，柑橘树温度差小。

远红外热处理方法对柑橘黄龙病的防治具有一定效果，在优化的参数下，远红外方式处理后病菌浓度平均降低 34.4%。而热空气快速处理病菌浓度平均降低率为 66.2%[16]，对比热空气快速处理方法，热空气处理方式的处理效果更佳。热空气加热方式使处理罩内温度从 32℃上升到 48℃，耗时约为 9 min，热风机功率 20 kW，能耗约为 3 kW·h；但采用红外加热方式时，只需加热 3 min，树叶温度平均值可从 18℃上升为 58.1℃，3 组灯管组（6 根，每根功率约为 1.0 kW）能耗约为 0.3 kW·h，仅为热空气加热能耗的 1/10 左右。热空气加热风机质量达 70 kg，而3 组灯管总质量约为 3 kg，不及热风机质量的 1/20。因此远红外快速热处理方法具有加热快、质量轻、能耗低等优势，处理成本将更低，但病菌浓度去除率还有待提高。

利用远红外处理方式防治柑橘黄龙病，对病树进行红外热处理所需要的最佳温度、处理时间、处理的次数、相邻两次处理的时间间隔等因素对柑橘黄龙病处理效果的影响，以及如何提高处理效果，还需进行进一步研究。另外，远红外加热对柑橘树木的长势、挂果率、柑橘品质等的影响未知，还有待进一步研究。

4　结论

（1）提出采用远红外对柑橘黄龙病进行热处理，研究了远红外灯管组数量、单根远红外灯管功率、加热时间、远红外灯与支架顶部距离对处理罩内温度场分布的影响，并通过田间试验验证了柑橘黄龙病进行热处理方法的有效性。

（2）远红外灯管组数量对树叶以及枝干温度场分布均影响显著。随着远红外灯管组数量的增加，树叶以及枝干的平均温度均升高，树叶温度高于枝干温度。

（3）单根远红外灯管功率对树叶以及枝干温度场分布均影响显著。相同加热时间，功率越高树叶平均温度上升幅度越大。

（4）加热时间对树叶以及枝干的温度场分布均有显著影响。在 2 ~ 3.5 min 内，加热时间每增加 0.5 min，树叶温度平均值升高 6℃左右。在远红外灯正前方，距离从 20 cm 增加到 40 cm 时，树叶温度平均值下降幅度不随加热时间的变化而变化。

（5）远红外灯与支架顶部距离对树叶的温度场分布影响显著。

参 考 文 献

[1] WANG N, TRIVEDI P. Citrus Huanglongbing: a newly relevant disease presents unprecedented challenges [J]. Phytopathology, 2013, 103(7): 652 - 665.

[2] FAN G, XIA Y, LIN X, et al. Evaluation of thermotherapy against Huanglongbing (citrus greening) in the greenhouse [J]. Journal of Integrative Agriculture, 2016, 15(1): 111 - 119.

[3] TRIVEDI P, HE Z, VAN NOSTRAND J D, et al. Huanglongbing alters the structure and functional diversity of microbial communities associated with citrus rhizosphere [J]. The ISME Journal, 2012, 6(2): 363.

[4] 程春振，曾继吾，钟云，等. 柑橘黄龙病研究进展 [J]. 园艺学报，2013，40(9)：1656 - 1668.
CHENG Chunzhen, ZENG Jiwu, ZHONG Yun, et al. Research progress on citrus Huanglongbing disease [J]. Acta Horticulturae Sinica, 2013, 40(9): 1656 - 1668. (in Chinese)

[5] 马晓芳. 柑橘木虱转录组分析及与柑橘黄龙病病原菌互作的初步研究 [D]. 杭州：浙江大学，2014.
MA Xiaofang. Transcriptome analysis of citrus psyllid and the study of its interaction with the Huanglongbing pathogen [D]. Hangzhou: Zhejiang University, 2014. (in Chinese)

[6] 贾志成，郑加强，黄雅杰，等. 柑橘黄龙病热处理防治技术研究进展 [J]. 农业工程学报，2015，31(23)：1 - 9.
JIA Zhicheng, ZHENG Jiaqiang, HUANG Yajie, et al. Review and prospect of thermotherapy for citrus Huanglongbing [J]. Transactions of the CSAE, 2015, 31(23): 1 - 9. (in Chinese)

[7] LEE J A, HALBERT S E, DAWSON W O, et al. Asymptomatic spread of Huanglongbing and implications for disease control [J]. Proceedings of the National Academy of Sciences, 2015, 112(24): 7605 - 7610.

[8] 陈凯男，李充璧. 柑橘黄龙病研究概况[J]. 浙江农业科学，2015,56(7):1048－1050,1069.
[9] 梅慧兰，邓小玲，洪添胜，等. 柑橘黄龙病高光谱早期鉴别及病情分级[J]. 农业工程学报，2014,30(9):140－147.
MEI Huilan, DENG Xiaoling, HONG Tiansheng, et al. Early detection and grading of citrus Huanglongbing using hyperspectral imaging technique[J]. Transactions of the CSAE, 2014, 30(9): 140－147. (in Chinese)
[10] 莫元林. 柑橘黄龙病的传播途径及鉴定方法[J]. 现代农业科学，2009(5):64－65.
MO Yuanmei. Citrus Huanglongbing disease transmission and the identification methods[J]. Modern Agricultural Sciences, 2009(5):64－65. (in Chinese)
[11] BOVE J M. Huanglongbing: a destructive, newly-emerging, century-old disease of citrus[J]. Journal of Plant Pathology, 2006,88(1):7－37.
[12] AL-JUMAILI A, EHSANI R. Mobile batch heat treatment system for treating HLB-infected citrus trees[C]// 2015 ASABE Annual International Meeting. American Society of Agricultural and Biological Engineers, 2015.
[13] 林丽萍，陈于陇，朱丽琴，等. 热处理对柑橘霉菌生活力和致病力的影响[J]. 现代食品科技，2015,31(4):222－227.
LIN Liping, CHEN Yulong, ZHU Liqin, et al. The effect of heat treatment on the vitality and pathogenicity of citrus fungi[J]. Modern Food Science and Technology, 2015, 31(4):222－227. (in Chinese)
[14] DESVIGNES J C, BOYER, CORNAGGIA D, et al. Virus diseases of fruit trees[D]. Paris: Centre Technique Interprofessionnel des Fruits et Légumes, 1999.
[15] 林雄杰，范国成，胡高青，等. 湿度对田间自然热处理防治柑橘黄龙病的影响[J]. 福建农业学报，2014,29(5):475－482.
LIN Xiongjie, FAN Guocheng, HU Hanqing, et al. The effect of humidity on citrus Huanglongbing thermotherapy in the field[J]. Fujian Journal of Agricultural Sciences, 2014, 29(5):475－482. (in Chinese)
[16] DOUD M, ZHANG M Q, POWELL C A, et al. Thermotherapy and chemotherapy to control citrus HLB in the field[J/OL]. Journal of Citrus Pathology, 2014,1(1). https://escholarship.org/uc/item/7h95n7j4.
[17] 邓晓玲，许美容，关磊，等. 一种利用热处理防治柑橘黄龙病的方法:103404397 A[P]. 2013-11-27.
[18] DENG X, GUAB L, D I, M, et al. Heat treatment of Huanglongbing-affected citrus trees in field for reduction of "Candidatus Liberibacter Asiaticus"[C]// International Citrus Congress Proceedings, 2012.
[19] 关磊，梁美丹，仇琦琪，等. 利用热处理技术降低柑橘黄龙病菌的浓度[C]// 中国植物病理学会 2012 年学术年会，青岛，2012.
[20] 贾志成，EHSANI Reza，耿加强，等. 柑橘黄龙病蒸汽快速热处理升温特性及田间防治效果[J]. 农业工程学报，2017,33(11):219－225.
JIA Zhicheng, EHSANI Reza, ZHENG Jiaqiang, et al. Heating characteristics and field control effect of rapid citrus Huanglongbing steam heat treatment[J]. Transactions of the CSAE, 2017, 33(11):219－225. (in Chinese)
[21] 姚林建，易龙，李双花，等. 不同温度组合热处理治疗柑橘黄龙病的田间效果分析[J]. 南方农业学报，2018,49(7):1346－1350.
YAO Linjian, YI Long, LI Shuanghua, et al. Efficacy of heat treatment in controlling citrus Huanglongbing by different temperatures combinations in field[J]. Journal of Southern Agriculture, 2018, 49(7):1346－1350. (in Chinese)
[22] GHATREHSAMANI S, ABDULRIDHA J, BALAFOUTIS A, et al. Development and evaluation of a mobile thermotherapy technology for in-field treatment of Huanglongbing (HLB) affected trees[J]. Biosystems Engineering, 2019, 182: 1－15.
[23] ABDULRIDHA J, AMPATZIDIS Y, GHATREHSAMANIS, et al. Mobile thermotherapy system for treating HLB-infected citrus trees utilizing hot water and steam[C]// 2018 ASABE Annual International Meeting. American Society of Agricultural and Biological Engineers, 2018.
[24] KELLEY A J, PELZ K S. Effect of thermotherapy on the acquisition of Candidatus Liberibacter asiaticus by the Asian citrus psyllid (Hemiptera: Liviidae)[J]. Florida Entomologist, 2019, 102(1): 107－112.
[25] 范国成，林雄杰，王贤达，等. 田间自然热罩治疗柑橘黄龙病的效果分析[J]. 果树学报，2016,33(9):1139－1147.
FAN Guocheng, LIN Xiongjie, WANG Xianda, et al. A field study of the efficacy of PVC film cover in controlling Huanglongbing[J]. Journal of Fruit Science, 2016,33(9):1139－1147. (in Chinese)
[26] BRIEN D O, DUAN Y. Prescription for curing citrus greening[J]. Agricultural Research, 2013:4－6.
[27] HOFFMAN M T, DOUD M S, WILLIAMS L, et al. Heat treatment eliminates *'Candidatus* Liberibacter asiaticus' from infected citrus trees under controlled conditions[J]. Phytopathology, 2013, 103(1):15－22.
[28] 张建桃，陈鸿，文晟，等. 柑橘黄龙病热空气快速处理温度场分布特性试验研究[J]. 农业工程学报，2017,33(8):267－277.
ZHANG Jiantao, CHEN Hong, WEN Sheng, et al. Experiment on temperature field distribution characteristics of citrus Huanglongbing hot air rapid treatment[J]. Transactions of the CSAE, 2017, 33(8):267－277. (in Chinese)
[29] 何晶. 远红外加热技术应用的初识[C]// 第十三届全国红外加热暨红外医学发展研讨会论文及论文摘要集，2011.
[30] 符凯，刘智垒，丁珠玉，等. 远红外加热技术在桑葚菌核病防治上的研究[J]. 农机化研究，2012,34(11):83－86.
FU Kai, LIU Zhilei, DING Zhuyu, et al. Study on the prevention of mulberry sclerotinia rot with far-infrared heating technology[J]. Journal of Agricultural Mechanization Research, 2012,34(11):83－86. (in Chinese)
[31] 刘守文，裴一飞，孙来燕. 航天器真空热实验用红外灯光谱分布研究[J]. 宇航学报，2010, 31(1):254－258.
LIU Shouwen, PEI Yifei, SUN Laiyan. Research on spectral pattern of infrared lamp for thermal vacuum test of spacecraft[J]. Journal of Astronautics, 2010, 31(1):254－258. (in Chinese)
[32] 牛成诚. 光刻机双驱动微动台温度场研究[D]. 哈尔滨:哈尔滨工业大学，2013.
NIU Chengcheng. Research on temperature field of lithography dual drive wafer stage[D]. Harbin: Harbin Institute of Technology, 2013. (in Chinese)
[33] 胡长华. 概率与数理统计简明辅导[M]. 南宁:广西科学技术出版社，1989.
[34] 陈旭，齐凤坤，康立功，等. 实时荧光定量 PCR 技术研究进展及其应用[J]. 东北农业大学学报，2010, 41(8):148－155.
CHEN Xu, QI Fengkun, KANG Ligong, et al. Advance and application of real-time fluorescent quantitative PCR[J]. Journal of Northeast Agricultural University, 2010, 41(8):148－155. (in Chinese)

《农业机械学报》第九届编辑委员会(2018～2021)

(按姓氏笔画为序)

荣誉主任委员：汪懋华　蒋亦元　冯炳元　诸慎友

主　任　委　员：罗锡文

常务副主任委员兼主编：任露泉

副主任委员兼执行主编：陈　志

副主任委员：王　博　方宪法　闫楚良　陈学庚　应义斌　赵春江　赵剡水　袁寿其　郭文聚　康绍忠　傅泽田

副主编：于海业　毛罕平　吴普特　张威胜　韩鲁佳　Zhongli Pan

编委：丁为民　马　旭　王　俊　王相友　王春光　王全九　王金武　王景立　王福军　王德成　王绍金　毛恩荣　付　强　冯仲科　权　龙　刘木华　刘荣厚　刘东红　刘成良　刘瑞雯　朱　艳　朱德海　衣淑娟　江连洲　汤方平　何　勇　汪小旵　杨　洲　杨学军　李萍萍　李成华　李建桥　李洪文　李民赞　李道亮　李久生　李耀明　李瑞川　李　红　何东健　邹小波　沈明霞　张本华　张全国　张兆国　张晓辉　陆海燕　陈　龙　陈巧敏　陈海涛　陈　建　陈立平　陈坤杰　坎　杂　尚书旗　尚松浩　易维明　岳德鹏　周志立　屈忠义　苑　进　苑严伟　赵燕东　赵武云　赵凤敏　俞高红　贾洪雷　郭玉明　姬江涛　姬长英　徐惠荣　黄文江　黄冠华　曹成茂　韩志武　韩　英　董红敏　蒋雪松　蒋恩臣　雷廷武　蔡焕杰　廖庆喜　薛新宇　魏新华

外籍编委：Bill Stout　Vilas M Salokhe　Naiqian Zhang　Zhongli Pan　Yubin Lan　Shujun Zhang　Ning Wang　Heping Zhu　Tadeusz Juliszewski　Qin Zhang

农业机械学报

NONGYE JIXIE XUEBAO

2019 年　第 50 卷　第 10 期

(月刊,1957 年创刊)

2019 年 10 月 25 日出版

Transactions of the Chinese Society for Agricultural Machinery

No. 10　Vol. 50　2019

(Monthly, started in 1957)

Published on 25, October 2019

主　管	中国科学技术协会
主　办	中国农业机械学会 中国农业机械化科学研究院
编辑出版	中国农业机械学会 (地址：北京德外北沙滩 1 号 6 信箱) 邮政编码　100083
主　编	任露泉
印　刷	北京富泰印刷有限责任公司
国内发行	中国邮政集团公司北京报刊发行局
订 购 处	全国各地邮局
国外发行	中国国际图书贸易集团有限公司 (北京 399 信箱)

Responsible Department: China Association for Science and Technology

Sponsored by: Chinese Society for Agricultural Machinery; Chinese Academy of Agricultural Mechanization Sciences

Published by: Chinese Society for Agricultural Machinery

Editor in Chief: Ren Luquan

Editorial Office: No. 1 Beishatan, Deshengmen Wai, Beijing 100083, China

Tel: 86-10-64882610/64882231

Fax: 86-10-64867367

http: //www.j-csam.org

E-mail: njxb@caams.org.cn

Overseas Distributor: China International Book Trading Corporation (P. O. Box 399, Beijing, China)

ISSN 1000－1298　CN 11－1964/S　国内邮发代号 2－363　国外邮发代号 M289　国内定价 80.00 元

万方数据

2.6 Application of artificial neural network (ANN) and response surface methodology (RSM) for modeling and optimization of the contact angle of rice leaf surfaces



Acta Physiologiae Plantarum

Publishing model
Hybrid

Submit your manuscript

Editorial board | Aims and scope

Overview

Acta Physiologiae Plantarum is an international journal that publishes peer-reviewed articles on all aspects of plant physiology across all levels of biological organization.

- Coverage ranges from molecular and cell biology to biochemistry.
- Range of topics includes the effects of environmental pollution on crop species, climate conditions on plants, photosynthesis in ornamental plants, genome organization, and more.
- Established in 1978, *Acta Physiologiae Plantarum* is published on behalf of the Franciszek Górski Institute of Plant Physiology, Polish Academy of Sciences, Kraków.

Editor-in-Chief
Przemysław Wojtaszek

Impact factor
2.6 (2022)

5 year impact factor
2.9 (2022)

Submission to first decision (median)
25 days

Downloads
381,956 (2023)

Societies and partnerships

Polish Academy of Sciences

For authors

Submission guidelines

Language editing services

Ethics and disclosures

How to publish with us

Open Access fees and funding

Contact the journal



Language quality checker
Get your manuscript edited for free

Latest articles



Acta Physiologiae Plantarum

Publishing model
Hybrid

Submit your manuscript

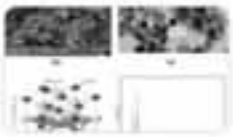


Volume 42, Issue 4

April 2020

25 articles in this issue

Effects of zinc oxide nanoelicitors on yield, secondary metabolites, zinc and iron absorption of Feverfew (*Tanacetum parthenium* (L.) Schultz Bip.)



Reza Shahhoseini, Majid Azizi ... Leila Samiei
Original Article | 30 March 2020 | Article: 52

Application of artificial neural network (ANN) and response surface methodology (RSM) for modeling and optimization of the contact angle of rice leaf surfaces



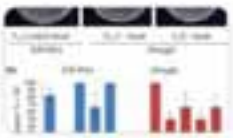
Jiantao Zhang, Gengchun Lin ... Yubin Lan
Original Article | 29 March 2020 | Article: 51

Protective effect of *Pseudomonas* spp. isolates and zinc on seed germination and β-amylase activity in wheat cultivars under cadmium stress



Marzieh Safari, Hossein Kari Dolatabad ... Nelson A. Rivera
Original Article | 28 March 2020 | Article: 50

Transgenerational benefits of endophytes on resilience and antioxidant genes expressions in pea (*Pisum sativum* L.) under osmotic stress



Vipul Kumar | Vladimir Vujanovic

For authors

Submission guidelines
Language editing services
Ethics and disclosures
How to publish with us
Open Access fees and funding

Acta Physiologiae Plantarum (2020) 42:51
https://doi.org/10.1007/s11738-020-03040-0

ORIGINAL ARTICLE

Application of artificial neural network (ANN) and response surface methodology (RSM) for modeling and optimization of the contact angle of rice leaf surfaces

Jiantao Zhang[1,2] · Gengchun Lin[1,2] · Xuanchun Yin[2,3] · Jiajun Zeng[1,2] · Sheng Wen[2,4] · Yubin Lan[2,3]

Received: 20 August 2019 / Revised: 4 March 2020 / Accepted: 17 March 2020 / Published online: 29 March 2020
© Franciszek Górski Institute of Plant Physiology, Polish Academy of Sciences, Kraków 2020

Abstract

In this paper, a novel method for modeling and optimization of the contact angle of rice leaf surfaces by comparing the analytical result of the artificial neural network (ANN) and response surface methodology (RSM), to minimize the contact angle of the rice leaf surfaces. Three factors and three levels Box-Behnken design was used to analyze the external factors influencing the contact angle of the rice leaf surfaces, which consisted of temperature, humidity and the chemical pesticide concentration. By optimizing the designing parameters, the optimum input parameters were obtained. The best input conditions were temperature (25.96 °C), humidity (60.00%), chemical pesticide concentration (131.89 mg/L), and a minimum contact angle of 103.565° was obtained. Moreover, the ANN sensitivity analysis was used to study the weight of three external factors affecting the contact angle. Experiments showed the concentration of chemical pesticides to be the chief factor, as it has a weight is 55.61%, followed by humidity with a weight of 31.15% and temperature with 13.24%. Finally, the reliability of the RSM and ANN methods in modeling and predicting the contact angle was compared by analyzing the value of mean squared error (MSE) and determination coefficient (R^2).The result showed that both models have better performance, and both RSM and ANN have better determination coefficients. The experiments also illustrated that the ANN method get better results than RSM in fitting experimental data, prediction and modeling.

Keywords Rice leaf surfaces · Contact angle · Artificial neural network · Response surface methodology · Optimization

Introduction

Rice is an indispensable crop in the world (Matsumoto et al. 2005). However, pests, diseases and weeds reduce the rice yields and cause serious ecological and economic losses (Nairn and Forster 2017). In modern agriculture, spraying chemical pesticides is still one of the most effective ways to remove pests, diseases and weeds (Cai et al. 2013). However, due to the hydrophobicity of rice leaf surfaces, it is difficult to effectively spray pesticides (Zhu et al. 2018). Only 20 ~ 30% of the pesticides sprayed in China are deposited on the target, with the remaining 70–80% lost to the soil, thus polluting the living environment of animals and humans (Bergeron et al. 2000; Damak et al. 2016). Therefore, improving the wettability of spray pesticide on the leaf surface of rice is an effective technique to reduce the loss of spray pesticide (Yao et al. 2014; Bonn et al. 2009).

When an isotropic substance makes contacts with a liquid substance and forms an interface, the adsorption phenomenon that reduces surface energy occurs, and the liquid substance spreads out on the surface of the isotropic substance (Zhu et al. 2018). The phenomenon of liquid spreading on the isotropic surface is called wetting, and the ability of liquid to spread on the same surface is called the wettability of liquid to solid (Li et al. 2017; Cao et al. 2018). In many

Communicated by H. Peng.

✉ Xuanchun Yin
xc_yin@scau.edu.cn

1 College of Mathematics and Informatics, South China Agricultural University, Guangzhou 510642, China

2 National Center for International Collaboration Research on Precision Agricultural Aviation Pesticide Spraying Technology, Guangzhou 510642, China

3 Engineering College, South China Agricultural University, Guangzhou 510642, China

4 Engineering Foundation Teaching and Training Center, South China Agricultural University, Guangzhou 510642, China

studies, a static value of the contact angle of the characteristic liquid has been used to represent the wettability of the leaf surface, with smaller values indicating better wettability (Zhu et al. 2014). According to relevant research, leaf surface wettability is mainly affected by internal and external factors. The chemical composition and microstructure of the surface of the wax-deposited leaves are the internal factors (Koch et al. 2008). While external factors such as temperature, humidity (Hunsche and Noga 2011) and industrial pollution (Kupcinskiene and Huttunen 2005) have also been reported and gained extensive attention.

Recently, many researchers have studied the effects of atmospheric temperature (Venkatesan et al. 2016) and humidity (Jiang et al. 2018) on the contact angle and found that both have different degrees of influence. Baker studied the effect of environmental conditions on the wettability of cabbage and concluded that a decrease in temperature would enhance the wettability of its surface (Baker 1974). However, these studies did not focus on the contact angle of rice leaf surfaces, nor did they comprehensively consider the influence of external factors on the contact angle of rice leaf surfaces.

One of the most important stages of wetting distribution is modeling and optimization to improve leaf surface wettability (Bas and Boyaci 2007). The complexity of the wettability mechanism is due to the myriad interactions between multiple variables and the nonlinear behavior of these processes (Yadav et al. 2018). Therefore, determining the optimal variable conditions is of great importance to obtain the best wettability. In some classic optimization methods, only one variable is considered at a time, while the others remain unchanged (Chary and Dastidar 2012). These methods are not only complex and long-running, but also fail to account for the full role of each change in the process as they ignore the interaction between multiple variables and cannot obtain true optimal variable conditions (Nair et al. 2014). The researchers adopted the method of multivariate experimental design to solve this problem.

Response surface methodology (RSM), as a method of multivariate nonlinear modeling method, is increasingly gaining researchers' attention (Ayodele and Cheng 2015). RSM can obtain the effect of input variables on the response output and define the role of independent or combined independent variables in the process (Montgomery 2008; Basri et al. 2007). This method has the advantages of short time, few experiments, and response prediction (Shojaeimehr et al. 2014).

Artificial neural network (ANN) modeling has become a hot topic by researchers, because it can obtain the nonlinear relationship between independent variables and solve problems unsolvable by traditional statistical methods (Gadekar and Ahammed 2019; Elfghi 2016; Ehrahimpour et al. 2008). In view of the complexity of predicting the contact angle of the droplet surface, Mehran proposed using ANN. Using this model could produce accurate results well-suited for practical application (Taghipour-Gorjikolaie and Motlagh 2018). However, Mehran studied the influence of factors such as surface tension on the contact angle of the metal surface, and did not involve the contact angle of rice leaf surfaces. Naser proposed a neural network model based on heuristic development methods that can be used to predict the hydrophobic properties of surfaces (Motlagh and Taghipour-Gorjikolaie 2018). The disadvantage of RSM is that it cannot include uncontrollable variables, but any physical or chemical process will not affect the accuracy of neural network modeling, so using ANN can establish a stable nonlinear simulation model (Gadekar and Ahammed et al. 2019). Therefore, using RSM-ANN modeling, the shortcomings of RSM can be resolved and the actual relationship between independent and response parameters can be studied through experimental data (Moghadam et al. 2013).

In this paper, ANN and RSM methods were used to construct the contact angle model of rice leaves, and the effects of temperature, humidity, chemical pesticide concentration on the contact angle were studied. The relationship between the temperature, humidity, chemical pesticide concentration and contact angle and the best conditions for obtaining the optimal contact angle were then obtained. Then determined the weight of the influence of three external factors on the contact angle.Finally, the performance of both models in assessing the contact angle of rice leaf surfaces was compared.

Materials and methods

Samples preparation and basic measurement

The rice leaves used in the experiment were those of the agriculturally dominant variety released by the Guangdong Provincial Department of Agriculture in 2018, Guang 8 You 169, which widely used in Guangdong and South China rice areas. The rice leaves were uniformly selected from the penultimate leaves of rice at the jointing stage. Then rinsed them with clean water to remove the influence of residual pollutants (Cao et al. 2018). The fresh leaves were then cut into rectangular strips having a growth degree of approximately 8 cm and avoiding the middle veins. To prevent the leaf from bending, the leaf was fixed on the glass slide with a special film for experiment (Zhu et al. 2014; Zhao et al. 2018). Finally, put the leaves into the droplet angle tester.

An automatic water drop angle tester (Dong Guan Precise Test Equipment CO., LTD, China) was used to measure the contact angle. The experiment was carried out in a programmable, constant temperature and humidity laboratory (Shang Hai Jiang Kai Machine CO., LTD, China) to control

both factors. The experimental device is shown in Fig. 1. The drop angle tester was equipped with a high-speed camera, which quickly recorded the image of a droplet touching the leave surface and then transmitted it to the computer. Then, the contact angle of the droplet was then obtained by the ellipse fitting method in the Contact Angle Meter (KRUSS DSA25 100 W, Germany).

Box-Behnken design

There are many kinds of experimental designs for response surface methodology, most commonly used of which are Box-Behnken Design (BBD) and Central Composite Design (CCD). In this paper, BBD experimental design was used to analyze the effects of temperature (X_1), humidity (X_2) and chemical pesticide concentration (X_3) on the contact angle of rice leaf. The experiment run times were shown in the following formula (Zhang et al. 2013):

$$N = 2k(k-1) + C_O, \tag{1}$$

where k, C_O are the number of independent variables, center points, respectively. As shown in Table 1, the BBD experiment was designed with three factors and three levels, where the both actual and coded values were given (Yadav et al. 2017; Vijayakumar et al. 2018). Take temperature (X_1), humidity (X_2) and concentration (X_3) as the optimized independent variables. Take three horizontal encoding values for each independent variable, which are $-1, 0, +1$, whereas temperature: 20–30 °C; humidity: 60–80%; chemical pesticide concentration: 0–200 mg/L, respectively (Maran and Sivakumar 2013). In this study, a total of 17 repeated experiments (3 input variables, 5 center points) were carried out and each experiment was repeated three times and the average value was taken. BBD experimental design matrix and prediction results are shown in Table 2. From Table 2, the residual between the predicted value and the real value of the experiment was very small, which indicated that the BBD experiment of RSM model can well fit the experimental data and had a more accurate predictability. The relationship and interaction between the independent variable and the response factor were analyzed by fitting the data which were obtained by the second-order polynomial equation (Bezerra et al. 2008):

Table 1 Independent variables of BBD experiment

Factors	Coded	Levels		
		−1	0	1
Temperature (°C)	X_1	20	25	30
Humidity (%)	X_2	60	80	100
Concentration (mg/L)	X_3	0	100	200

$$y = \beta_0 + \sum_{j=1}^{k} \beta_j X_j + \sum_{j=1}^{k} \beta_{jj} X_j^2 + \sum \sum_{i<j}^{k} \beta_{ij} X_i X_j, \tag{2}$$

where y is the predicted value of response, β_0 is the offset term, β_j, β_{ij} and β_{jj} are the linear coefficients, the quadratic coefficients and the cross-product coefficients, respectively. X_i and X_j are the independent variables. The Design Expert Version 8.0.6 (Stat-Ease, USA) was used to analyze the experimental data and analysis of variance (ANOVA). A significance test to assess the quality of the model's fit.



Fig. 1 Contact angle test equipment **a** measuring computer; **b** automatic water drop angle tester; **c** programmable constant temperature and humidity laboratory

ANN modeling

Artificial neural network

Artificial neural network is a system composed of a large number of processing units interconnected (Esfe et al. 2018). The network consists of a large number of neurons linked to each other, with each node outputting a specific function called the excitation function. The connection between every two nodes is represented by a value, or

Table 2 BBD experiment design and the observed and predicted value of contact angle

Run no	Code values			Real values			Contact angle (°)		
	X_1: Temp	X_2: Humi	X_3: Conc	X_1: Temp	X_2: Humi	X_3: Conc	Experimental	Predicted	Residual
1	1	0	1	30	80	200	112.24	114.08	−1.85
2	1	0	−1	30	80	0	121.70	124.78	−3.08
3	1	1	0	30	100	100	122.41	119.64	2.77
4	1	−1	0	30	60	100	108.66	106.50	2.16
5	−1	−1	0	20	60	100	104.84	107.61	−2.77
6	−1	1	0	20	100	100	112.37	114.53	−2.16
7	−1	0	−1	20	80	0	121.04	119.19	1.85
8	−1	0	1	20	80	200	118.75	115.67	3.08
9	0	1	1	25	100	200	115.03	115.95	−0.92
10	0	1	−1	25	100	0	123.97	123.66	0.31
11	0	−1	1	25	60	200	106.22	106.53	−0.31
12	0	−1	−1	25	60	0	113.95	113.03	0.92
13	0	0	0	25	80	100	109.87	109.87	0.000
14	0	0	0	25	80	100	109.87	109.87	0.000
15	0	0	0	25	80	100	109.87	109.87	0.000
16	0	0	0	25	80	100	109.87	109.87	0.000
17	0	0	0	25	80	100	109.87	109.87	0.000

Table 3 Different neural network model structures

Structure	Transfer (*T* Tan-sig) function (*L* Log-sig) (*P* Linear)	Learning algorithm	*MSE*	R^2
3–10–1	*T-P*	*LM*	0.14940	0.99567
3–20–1	*T-P*	*LM*	0.14601	0.99856
3–30–1	*T-P*	*LM*	0.14897	0.99648
3–30–1	*L-P*	*LM*	0.15064	0.99423
3–10–5–1	*T-T-P*	*LM*	0.13215	0.99924
3–10–10–1	*T-T-P*	*LM*	0.02178	0.99996
3–20–10–1	*T-T-P*	*LM*	0.09577	0.99983
3–20–20–1	*T-T-P*	*LM*	0.02620	0.99993
3–20–20–1	*L-L-P*	*LM*	0.06044	0.99989
3–20–20–1	*T-L-P*	*LM*	0.02710	0.99995
3–10–10–5-1	*T-T-T-P*	*LM*	0.03372	0.99994
3–10–10–10-1	*T-T-T-P*	*LM*	0.01500	0.99997

weight, for assessing the signal strength (Yadav et al. 2018). Due to the uncertainty of the model, the experimental results can be achieved by adjusting the structure of the network, the connection mode of the network, the excitation function and the weight of interconnection among internal nodes (Esfe et al. 2018; Notton et al. 2019; Wen et al. 2019). The accuracy of the neural network is mainly affected by the hidden layers, the number of nodes, the training algorithm, the learning rate, and the transfer function. In this study, through a large number of experiments, the structure of neural network is debugged to find the most appropriate hidden layers, nodes and transfer functions. The results are shown in Table 3. The structure corresponding to the minimum mean squared error (MSE*)* value and the maximum determination coefficient (R^2) value was selected. It can be seen that the optimal structure of the neural network had three hidden layers and each hidden layer had 10 neurons (3–10–10–10–1) and the optimal transfer function was tan-sigmoid and linear. Input variables for the neural network were temperature, humidity, chemical pesticide concentration, while the output was the contact angle. Based on the optimal network structure in Table 3, a diagram of the neural network structure can be drawn. The diagram was shown in Fig. 2.

Data set formation and model evaluation coefficient

To avoid overfitting of the neural network model, the experimental samples were divided into the training set, verification set and test set. They played different roles in the model formation. The function of training set was to determine the parameters of neural network model and training model, the verification set was used to calculate a single evaluation index, and the test set can verify the fitting ability of the neural network model (Maleki et al. 2014). Therefore, 116 groups of experimental data were divided into three subsets which were training set (80 groups), verification set (18 groups) and test set (18 groups). In the artificial neural network, to reduce the effect of input variables due to very large or very small weight, it is necessary to carry out standard

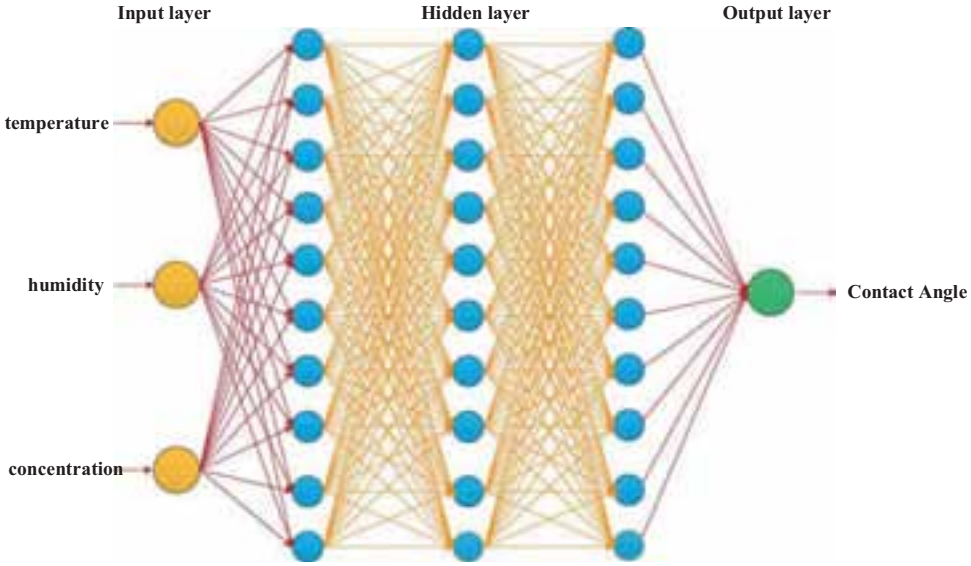


Fig. 2 Architecture of artificial neural network (the ANN has three hidden layers with ten hidden neurons and one output layer with one output, briefly written as 3–10–10–10–1)

normalization of the data set and control the values of output variables within the range of 0.1–0.9. The normalization equation is as follows (Karri et al. 2018):

$$y = 0.1 + 0.8 * \frac{x_{\mathrm{i}} - x_{\min}}{x_{\max} - x_{\min}}, \tag{3}$$

where $x_{\min}, x_{\max}$, x_{i} and y are the minimum value, the maximum value, the original data and the output value, respectively.

The error function is used to evaluate the generalization ability of the neural network model *MSE* and R^2 are the two most commonly used error functions in model evaluation, and their expressions are shown in Eqs. (4) and (5), respectively (Betiku and Taiwo 2015; Shabanzadeh et al. 2015):

$$MSE = \frac{1}{\mathrm{r}} \sum_{i=1}^{r} \left(y_{\mathrm{i}} - y_{\mathrm{di}}\right)^2 \tag{4}$$

$$R^2 = 1 - \frac{\sum_{i=1}^{r} \left(y_{\mathrm{i}} - y_{\mathrm{di}}\right)^2}{\sum_{i=1}^{r} \left(y_{\mathrm{i}} - y_{\mathrm{m}}\right)^2}, \tag{5}$$

where r is the number of points and $y_{\mathrm{di}}, y_{\mathrm{i}}$, y_{m} are the actual value, the predicted value, and the average of the actual values, respectively.

Training algorithm and transfer function

Since the results of the information processing of the neural network are affected by the transfer function (excitation function), selecting the appropriate transfer function is crucial to the neural network model. The three transfer functions commonly used in multilayer neural network are log- sigmoid (*L*), tan-sigmoid (*T*) and linear, as shown in Eqs. (6), (7) and (8), respectively (Rostamizadeh and Rizi 2012):

$$f(x) = \frac{1}{1 + e^{-x}} \tag{6}$$

$$f(x) = \frac{2}{1 + e^{-2x}} \tag{7}$$

$$f(x) = x. \tag{8}$$

There are many training algorithms to train neural network models but no algorithm is suitable for training all of them. Compared with other training algorithms, the Levenberg Marquardt (LM) algorithm has the characteristics of fast convergence and high precision. It is often used to train network structure (Liu and Kim 2008). Since the neural network structure of this study needs to have high precision and fast convergence speed, using LM back propagation learning algorithm as a training algorithm for neural networks, which is consistent with the algorithm selected in (Liu and Kim 2008; Sadrzadeha et al. 2008; Karaci et al. 2016; Chamoli 2015).

Results and discussion

RSM model

Results of the ANOVA, which can be used as a significance test of sample mean difference, the RSM quadratic model

Table 4 Results of variance analysis of BBD experimental design

Source	Sum of squares	Degree of freedom	Mean square	*F*-value	*P*-value	
Model	511.04	9	56.78	7.61	0.0070	Significant
X_1: Temp	8.01	1	8.01	1.07	0.3346	
X_2: Humi	201.16	1	201.16	26.95	0.0045	Significant
X_3: Conc	101.07	1	101.07	13.54	0.0013	Significant
X_1X_2	9.66	1	9.66	1.29	0.2926	
X_1X_3	12.87	1	12.87	1.72	0.2306	
X_2X_3	0.36	1	0.36	0.049	0.8318	
X_1^2	35.84	1	35.84	4.80	0.0646	
X_2^2	2.18	1	2.18	0.29	0.6054	
X_3^2	134.03	1	134.03	17.95	0.0039	Significant
Residual	52.25	7	7.46			
Lack of fit	52.25	3	17.42			
Pure error	0.000	4	0.000			
Cor total	563.29	16				
Std. dev	2.73	R-squared	0.9072			
Mean	113.56	Adj R-squared	0.7880			
C.V. %	2.41	Pred R-squared	0.7658			
PRESS	836.05	Adeq precision	8.723			

are shown in Table 4. When taking the 95% confidence level, the significance level is 0.05. The "*P* value" of the model is 0.0070 and "*F*-value" of the model is 7.61 indicating that the RSM model was significant. The applicability of the model can be judged by the predicted *R*-Squared and adjusted *R*-Squared values. The value of the predicted *R*-Squared was 0.7658 and the adjusted *R*-Squared was 0.7880. Therefore, the model can accurately predict the output parameters within the range of using conditions. The Adep Precision value can be used to describe the signal-to-noise ratio of the model and needs to be greater than 4. Table 4 shows that the value of "Adeq Precision" is 8.723, indicating that the signal generated by this model is enough (Chamoli 2015). The dispersion between the experimental real value and the model predicted value can be expressed by the coefficient of variation (C.V. %) (Maran et al. 2013). In this case, the value of C.V. % was 2.41, indicating that the deviation between the real value and response output value is very small. The significance of the model can be described by the size of the "*p*-value" which should less than 0.05. In this study, X_2, X_3 and X_3^2 were significant model terms. As seen in the case, X_1, X_1X_2, X_1X_3, X_2X_3 and X_2X_3 and X_2^2 were not significant model terms. The reliability of the model can be evaluated by the proximity of the experimental data to the predicted values. According to the data in Table 4, a fitting diagram shown in Fig. 3 was drawn. Known from Fig. 3a that the prediction data fit the test model well and the coefficient "R-Squared" was determined to be 0.9072. Assuming that the experimental data are normally distributed, the residual normal distribution diagram, as shown in Fig. 3b was drawn. As seen from Fig. 3b, the 17 experimental values are very close to the diagonal, indicating that the errors of the model are normally distributed. In Fig. 3c, , the data located within the red region were acceptable and it can be seen that all the data were within the specified region, indicating the reliability of this model to evaluate the size of the contact angle. Through linear, curved surface fitting and equation analysis of the experimental results, a model describing the interaction between variables was obtained according to the coding factor:

$$\begin{aligned} Contactangle\,(^\circ) = {} & +109.87 + 1.00X_1 + 5.01X_2 - 3.55X_3 \\ & + 1.55X_1X_2 - 1.79X_1X_3 - 0.30X_2X_3 \\ & + 2.92X_1^2 - 0.72X_2^2 + 5.64X_3^2, \end{aligned} \tag{9}$$

where X_1 is the temperature, X_2 is the humidity and X_3 is the chemical pesticide concentration.

Three-dimensional response surface and contour plots

The relationship between humidity, temperature, chemical pesticide concentration and the surface contact angle of rice leaves were studied in this paper, the effect of a single factor on contact angle was investigated before discussing the response surface analysis. Figure 4a–c shows the relationship between temperature, humidity, chemical pesticide concentration and the contact angle, respectively. The red dot in Fig. 4 represents the center point with a value

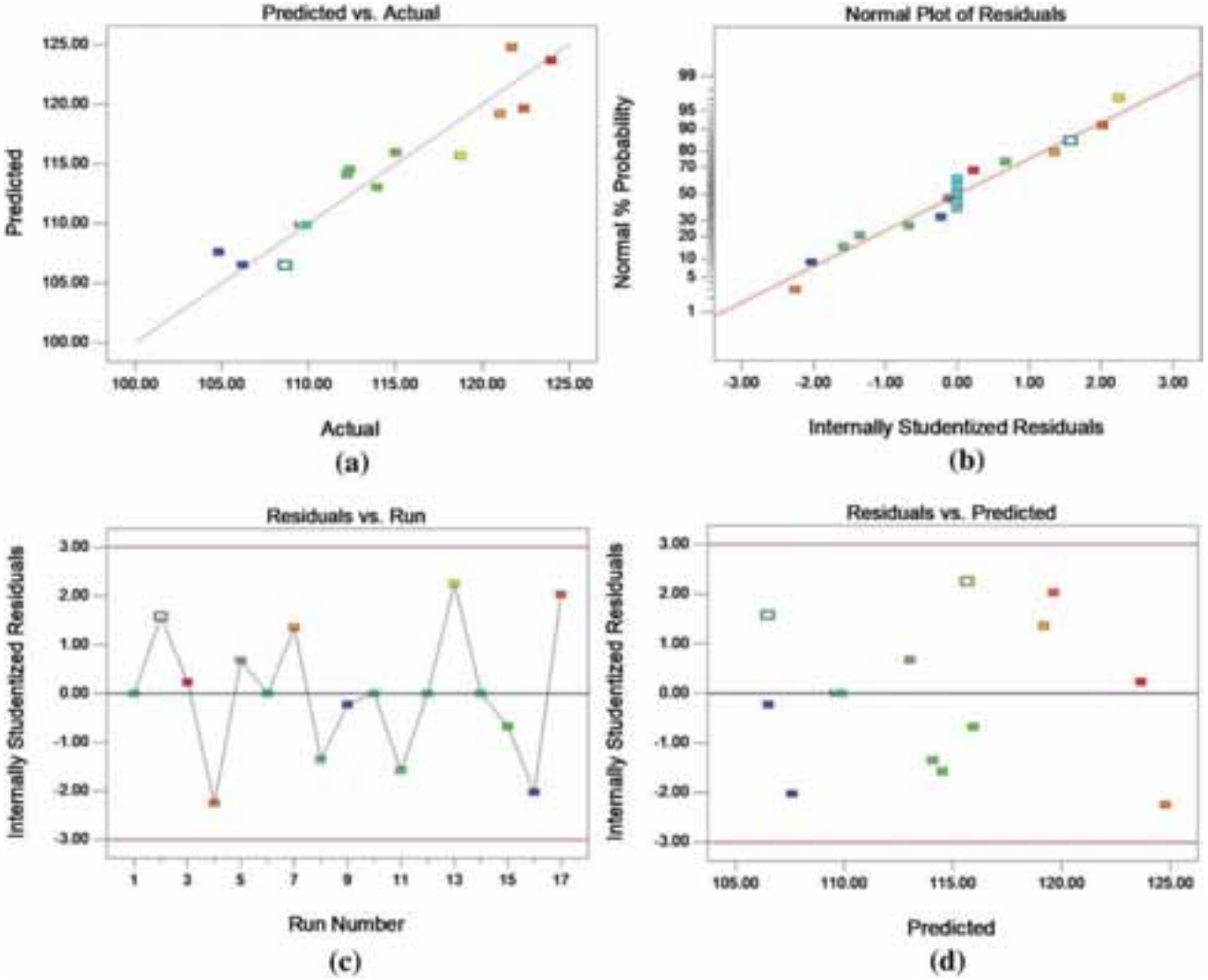


Fig. 3 **a** Plot of RSM predicted value versus experimental real value; **b** plot of the Internally Studentized Residuals, indicating that the error had a normal distribution; **c** plot of experimental run number versus Internally Studentized Residuals; **d** plot of RSM predicted value versus Internally Studentized Residuals (plot **c** and **d** showing the reliability of this model to evaluate the size of the contact angle)

of 5, the middle black line represents the actual change and the upper and lower blue lines are the trend lines. Since the gradient change of contact angle value in Fig. 4a is very small, temperature had little effect on the contact angle. According to Fig. 4b, the contact angle increases with the increase of humidity, and the relationship between the two is approximately proportional. According to Fig. 4c that the contact angle decreases rapidly with the increase of chemical pesticide concentration within the range of 0–100 mg/L, and changes little within the range of 100–200 mg/ L. Indicating a significant influence of humidity and chemical pesticide concentration on the contact angle from Fig. 4b. The conclusions drawn from Fig. 4 were consistent with those drawn from the analysis of variance. The interaction effects of temperature, humidity and chemical pesticide concentration on the contact angle of rice leaf surfaces were studied by three-dimensional response surface diagram and contour diagram, Fig. 5a shows the influence of the interaction between temperature and humidity on contact angle. When the temperature was 25.96 °C and the humidity was 60%, sawing a minimum value of the contact angle at 104.84°. As the humidity decreased, the contact angle decreased gradually, while temperature had minimal effect on the value of the contact angle. The influence of humidity and chemical pesticide concentration on contact angle are shown in Fig. 5b. Chemical pesticide concentration was the significant parameter affecting the contact angle which reached its minimum when the concentration was 131.89 mg/L and the humidity was 60%. At constant humidity, the contact angle remains at a minimum for the concentration of 131.89 mg/L. When the concentration increased or

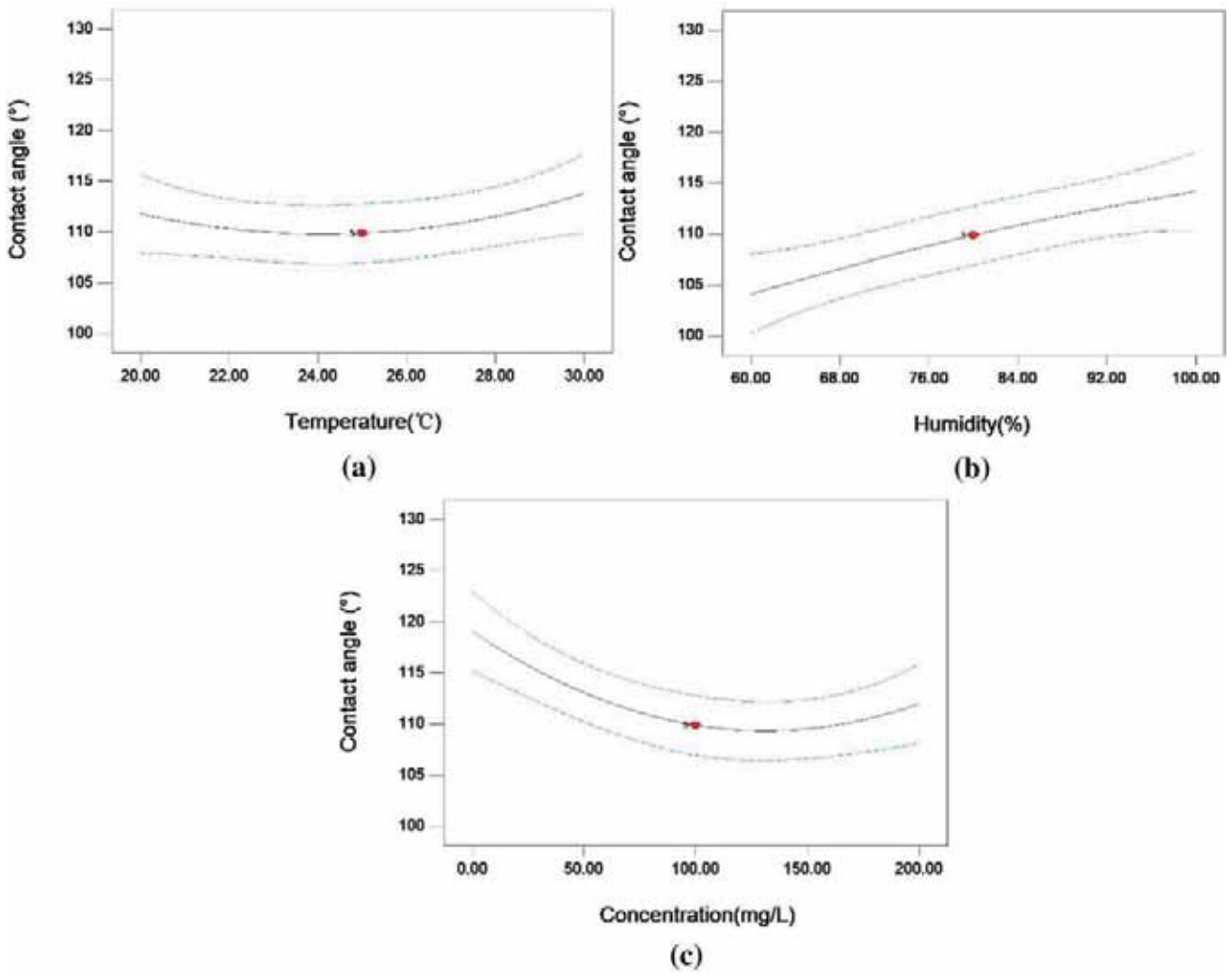


Fig. 4 Single chart showing the effect of a single variable to contact angle. **a** Temperature versus contact angle; **b** humidity versus contact angle; **c** chemical pesticide concentration versus contact angle

decreased, the contact angle gradually increased at constant humidity. Figure 5c shows the influence of the interaction between chemical pesticide concentration and temperature on contact angle. When the temperature is 25 °C and the concentration is 131.89 mg/L, the contact angle is the smallest. When the temperature was kept constant, the contact angle was at a minimum for the concentration of 131.89 mg/L. However, the contact angle gradually increased as the concentration changed.

Optimization of designing parameters

In this study, it is necessary to obtain the experimental conditions of minimum contact angle. To achieve multi-response optimization, the desirability function method which was followed to optimize the operating condition was utilized. The rice studied in this paper is planted in South China. During the rice planting in this area, most of the climate is between 20 and 30 °C and the humidity is between 60 and 100% (Hang et al. 2019). Therefore, the value range of the three independent variables was limited, and the value range and response target were shown in Table 5. Temperature ranged from 20 to 30 °C, humidity ranged from 60 to 100% and chemical pesticide concentration from 0 to 200 mg/L. A combination of parameters of the independent variables was selected according to the desired bar chart value of the combined target. The optimization analysis of the experiment was carried out using Design-Expert 8.0.6. Desirability is used to indicate the effect of optimization, and desirability ranges from 0 to 1, and one is the maximum desirability achieved for multi-response (Singh and Misra 2019; Chamoli 2015). The desirability bar explain the extent to which each variable meets the criteria. As seen from Fig. 6, the overall

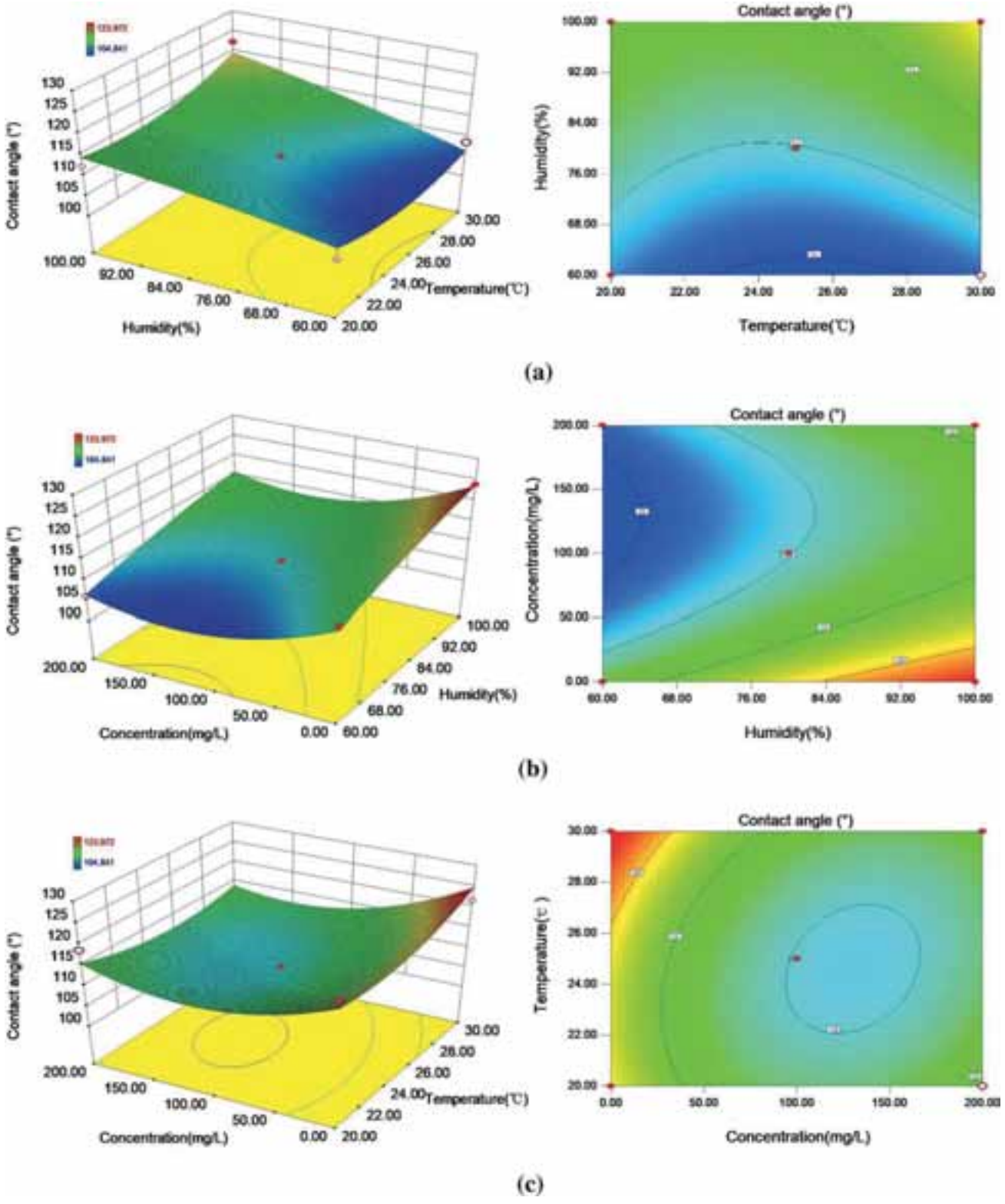


Fig. 5 **a** Temperature and humidity versus contact angle; **b** chemical pesticide concentration and humidity versus contact angle; **c** chemical pesticide concentration and temperature versus contact angle

Table 5 Value range and target of the independent variable

Parameter	Objective	Lower limit	Upper limit
Temperature (°C)	Within range	20	30
Humidity (%)	Within range	60	100
Concentration (mg/L)	Within range	0	200
Contact angle (°)	Minimum	100	124

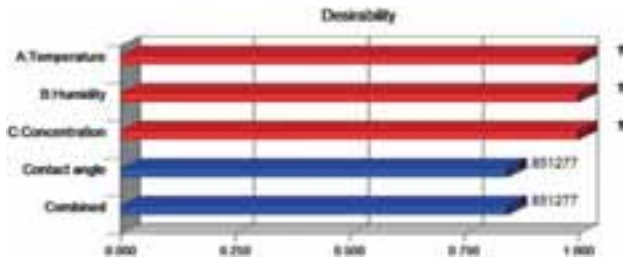


Fig. 6 Desirability bar plot of combined objective (explain the extent to which each variable meets the criteria, one is the maximum desirability achieved for multi-response)

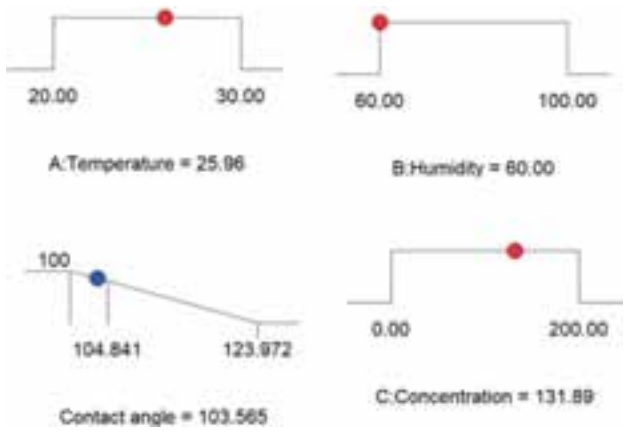


Fig. 7 Ramp function plot of combined objective(showing the optimal input parameter values and predicted output responses, red point represents the optimal input parameter and blue dot represents the optimal output value)

expected response value was 0.851 which is close to the maximum value of 1. From Fig. 7, it can be concluded that the optimal input parameter values and predicted output responses are considered simultaneously in the optimization process. The red dot represents the optimal input parameter value and the blue dot represents the optimal output value. The optimal input parameters were temperature of 25.96 °C, humidity of 60.00% and concentration of 131.89 mg/L, and the optimal output predicted response value was 103.565°.

Artificial neural network results

The ANN model was built in Spyder (Python 3.6) with a Lenovo-PC computer configured with 2.40 GHz and 32.0 GB of RAM. Figure 8a–d shows the regression curves of the training set, verification set, test set and the total experimental set with the LM algorithm, respectively. As seen from Fig. 8, the predicted data were basically near the line of Y = X, which represents the line of best fit between the predicted and the experimental values. The *R* values of the training set, validation set, test set and total set were 0.99752, 0.99563, 0.99012, and 0.9997. The valued of *R* were obtained after rigorous training of the established neural network model. The value of *R* is used to determine the fitting performance of the model. The experimental results show that the predicted values fit the experimental data well. After specifying training data, transfer function, hidden layer number and neuron number, the performance of the network needs to be evaluated (Esfe et al. 2018). Using the LM algorithm for the predicted residual values, Fig. 9a–d shows the residual graphs of the training set, the verification set, the test set, and the total experimental set, respectively. As seen from Fig. 9, the residual values were basically between −2 to 2 with most of the data concentrated near the zero line indicating a small range of experimental error. Thus, the model trained with neural network is seen to be reliable (Gherman et al. 2018).

Sensitivity analysis

Sensitivity analysis is a very important topic in the field of neural network research. It is defined by assuming that there are multiple parameters of independent variables in the model which take on different values within a specified range (Gevrey et al. 2003). Then through studying and predicting the influence of changes in these variables on the output value of the model. This degree of influence, which can be referred to as the sensitivity coefficient, can quantitatively study the influence of the independent variable X_i on the output value Y, and can also be described as weight. The closer the weight is to 1, the greater the impact of input independent variables on the output results. The neural network can be trained to obtain the connection weight of the interlayer neurons, and the sensitivity analysis can use it to get the weight of the independent variable affecting the output variable. The input variables with larger weight values were retained and those with less influence were removed to reduce the complexity of model calculation. According to different implementation methods, the sensitivity analysis can be divided into the following categories: (1) based on connection weight; (2) based on partial derivatives of output variables with input variables;

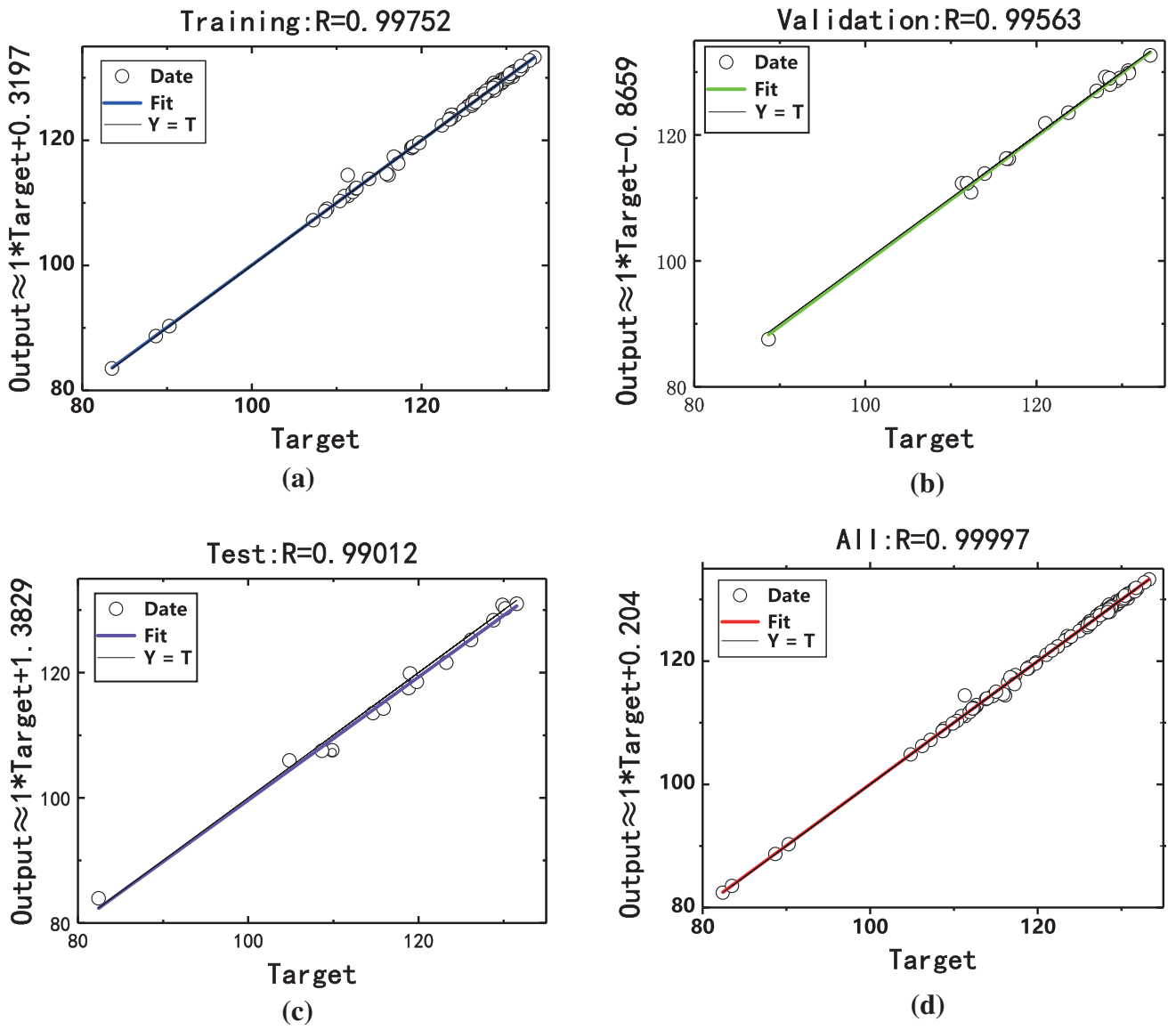


Fig. 8 **a** Plot of predicted of validation set versus actual value; **b** plot of predicted of test set versus actual value; **c** plot of predicted of training set versus actual value; **d** plot of predicted of all set versus actual value

(3) sensitivity analysis method combined with statistical methods; and (4) based on input variable disturbance. The sensitivity analysis method based on connection weight is adopted in this paper, which is a quantization method based on the connection weight of each neural network layer (Podstawczyk et al. 2015; Olden et al. 2004). Using the connection weight method by Spyder software (Python 3.6), the weight of the contact angle output of the three variables of temperature, humidity and chemical pesticide concentration were obtained. The connection weight method is calculated as follows (Olden et al. 2004):

$$W = \frac{\sum_{j=1}^{N} \left(\text{Input}_j + \text{Output}_j\right)}{\sum_{I=1}^{X} (\sum_{j=1}^{N} \left(\text{Input}_j + \text{Output}_j\right))} \times 100\%, \tag{10}$$

where X and N are the number of nodes in the input layer and the hidden layer, respectively, $Input_j$ is the weight of the connection between the input layer and the hidden layer. $Output_j$ is the connection weight between the hidden layer and the output layer. Table 6 shows the connection weights of the neural network model. Figure 10 shows that the chemical pesticide concentration had the greatest influence on the contact angle, with a weight of 55.61%, followed by

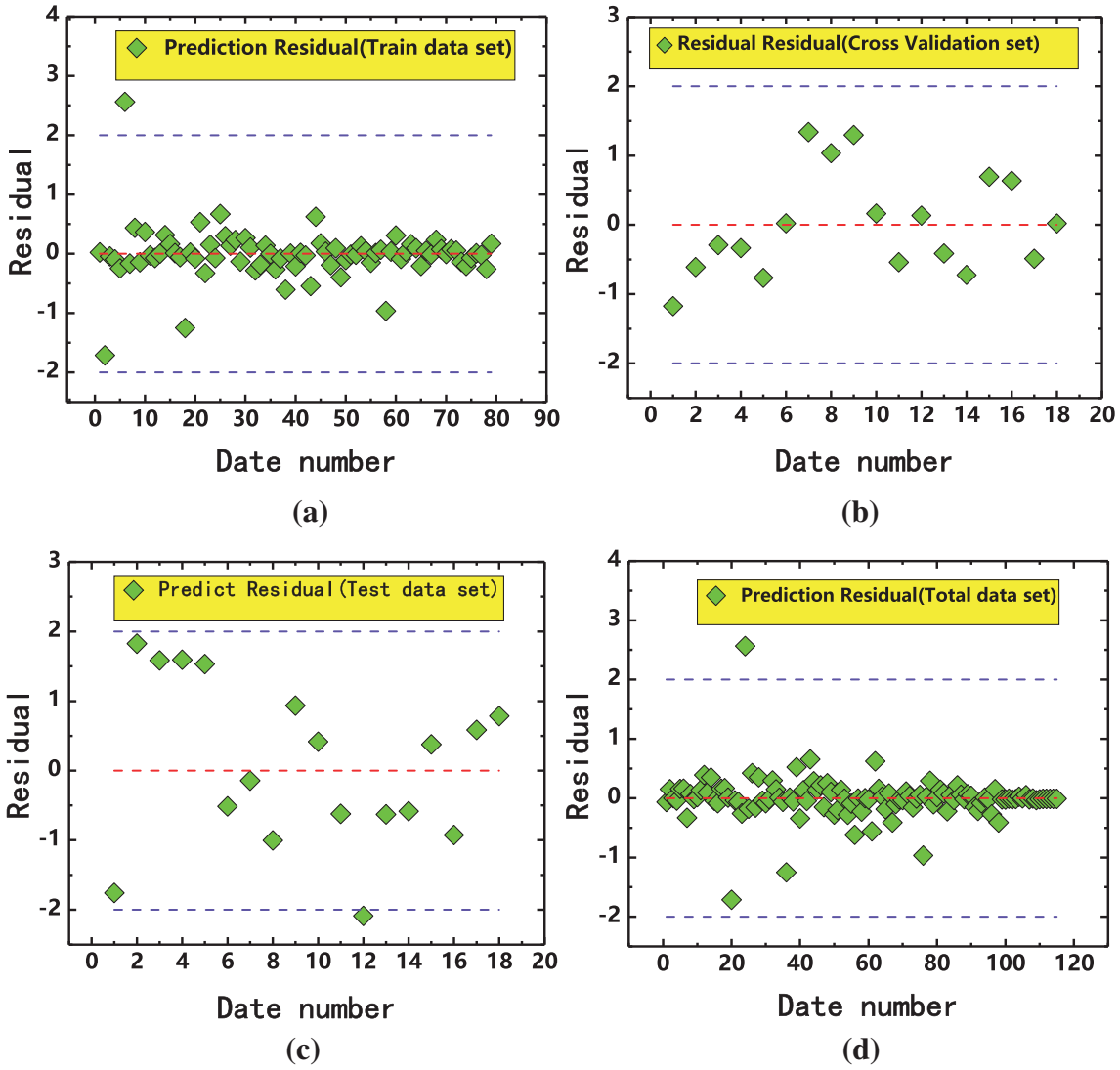


Fig. 9 **a** Plot of train data set residual versus data number; **b** plot of cross validation set residual versus data number; **c** plot of test data set residual versus data number; **d** plot of total data set residual versus data number

humidity with a weight of 31.15%. The least effect on the contact angle was temperature, with a weight of 13.24%.

RSM is a common nonlinear modeling method, which is often used to study the relationship between independent variables and output variables The Artificial neural network method (ANN) can build a multiorder nonlinear model to fit any data; therefore, it is also widely used in data analysis. In this paper, the experimental real value was compared with the prediction results of ANN and RSM. In this study, the evaluation parameters of the two models were analyzed, and the mean square error (MSE) and the determination coefficient (R^2) values of the two models are compared in Table 7. The R^2 and MSE of the artificial neural network model were 0.99997 and 0.169, respectively, and 0.9027 and 3.079, respectively, for the response surface methodology. The closer *MSE* get to 0, the more accurate the model is. The closer R^2 gets to 1, the more accurate the model is. Thus indicating both models have strong ability to predict experimental data. The comparison between R^2 and *MSE* of the two models showed that the ANN was superior to the RSM in predicting contact angle response output. To better visually compare the prediction ability and reliability of the two models, a comparison diagram is drawn in Fig. 11. Figure 11 shows the predicted values for experiments using ANN and RSM and the predicted values of the ANN model basically lie on the Y = X line, the line of best fit between the predicted and experiment value. On the other hand, the predicted values of RSM model were scattered on both sides of and with a large deviation from the Y = X line. It was also concluded that the ANN was superior to the RSM due to the distribution of the predicted values. Although both methods were suitable for modeling and predicting, they did have some limitations. The response surface methodology can

Table 6 Neural network connection weight

Neuron number	Connection weight			
	Input1(X_1)	Input2(X_2)	Input3(X_3)	Output
1	−1.96331	4.70163	2.183706	1.705278
2	6.298675	−6.77046	0.503807	0.045149
3	−6.30913	−1.39579	3.598383	0.198365
4	0.565787	−1.8566	4.648746	1.611957
5	3.619049	−1.43521	5.427927	1.619282
6	0.152521	−13.2501	2.820596	−0.32667
7	−0.06099	−1.26554	8.223463	−2.02041
8	−1.18414	0.484645	12.39567	0.367824
9	0.267144	0.86103	1.075431	1.081194
10	1.034847	−0.96971	5.168459	1.322968
Sum of product ∑(input × output)	3.752919	8.829941	15.766977	–
Percent importance (%)	13.24	31.15	55.61	
Importance	3	2	1	–

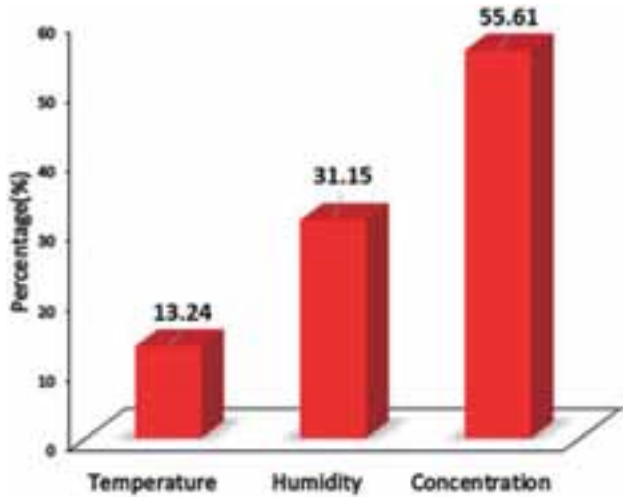


Fig. 10 Plot showing the independent variable parameter weight percentage of contact angle

Table 7 Evaluation coefficients of the two models

Parameter	RSM	ANN
MSE	3.079	0.169
R^2	0.9072	0.99997

only solve second-order nonlinear regression analysis, rather than a multiorder nonlinear regression analysis. The artificial neural network requires a large amount of experimental data to produce reliable models, uses long training times and is unable to analyze interactions between variables. Therefore, using both the ANN and RSM modeling methods to predict the contact angle can maximize their respective advantages, and avoiding the limitations of a single analysis method that would fail to produce optimal results.

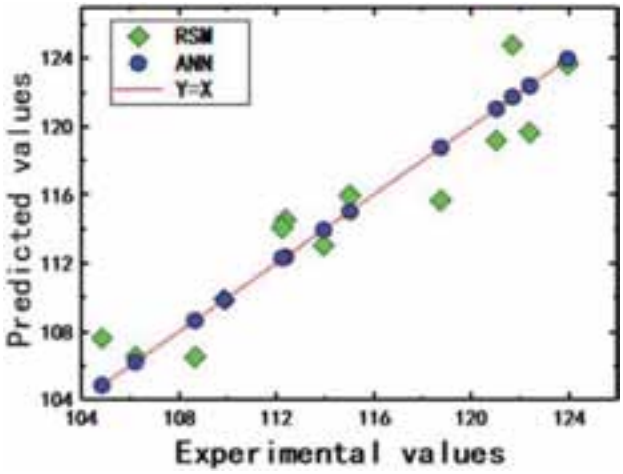


Fig. 11 Plot of experimental value and two model predicted value

Conclusions

In this paper, the application of ANN and RSM in the modeling and optimization of the contact angle of rice leaf surfaces was studied to minimize the contact angle. The following inferences are drawn from the analysis:

The effects of temperature, humidity and chemical pesticide concentration on the contact angle of rice leaf surfaces were studied through the modeling method of RSM. The functional relationship between temperature, humidity, chemical pesticide concentration and the response output (contact angle) was analyzed and built the second-order regression equation. By optimizing the design parameters, the optimal input variables conditions and minimum contact angle values were obtained. The best input conditions were temperature (25.96 °C), humidity (60.00%), and concentration (131.89 mg/L), a minimum contact angle of 103.565° can be obtained.

The degree of influence and relative weight of temperature, humidity and chemical pesticide concentration on contact angle were obtained by RSM analysis of variance and sensitivity analysis of the ANN. The chemical pesticide concentration had the greatest influence on contact angle, with a weight of 55.61%, followed by humidity with a weight of 31.15%. The least effect on contact angle was temperature, with a weight of 13.24%.

Comparing the ANN and RSM modeling methods show that both methods can accurately predict the contact angle, while the accuracy of ANN model is higher than RSM model.

Author contribution statement Conceptualization, J.Z., G.L.; funding acquisition, J.Z., Y.L.; software, J.Z. and X.Y.; writing-original draft preparation, G.L., J.Z., and Y.L.

Funding This research was funded by National Natural Science Foundation (Grant No. 61773171, 61675003), the Characteristic Innovation Projects of Colleges and Universities in Guangdong Province (Grant No. 2018KTSCX019), the leading talents of Guangdong province program (Grant No. 2016LJ06G689), Science and Technology Planning Project of Guangdong Province (Grant No. 2017B010117010) and the 111 Project (Grant No. D18019).

References

Ayodele BV, Cheng CK (2015) Modelling and optimization of syngas production from methane dry reforming over ceria-supported cobalt catalyst using artificial neural networks and Box-Behnken design. J Ind Eng Chem 32:246–258

Baker EA (1974) The influence of environment on leaf wax development in Brassica oleracea var. gemmifera. New Phytologist 73(5):955–966

Baş D, Boyacı IH (2007) Modeling and optimization II: Comparison of estimation capabilities of response surface methodology with artificial neural networks in a biochemical reaction. J Food Eng 78(3):846–854

Basri M, Rahman RNZRA, Ebrahimpour A, Salleh AB, Gunawan ER, Rahman, MBA (2007) Comparison of estimation capabilities of response surface methodology (RSM) with artificial neural network (ANN) in

Chary GHVC, Dastidar MG (2012) Investigation of optimum conditions in coal–oil agglomeration using Taguchi experimental design. Fuel 98:259–264

Chamoli S (2015) ANN and RSM approach for modeling and optimization of designing parameters for a V down perforated baffle roughened rectangular channel. Alex Eng J 54(3):429–446

Damak M, Mahmoudi SR, Hyder MN, Varanasi KK (2016) Enhancing droplet deposition through in-situ precipitation. Nat Commun 7:12560

Ebrahimpour A, Rahman RNZRA, Ch'ng DHE, Basri M, Salleh AB (2008) A modeling study by response surface methodology and artificial neural network on culture parameters optimization for thermostable lipase production from a newly isolated thermophilic Geobacillus sp. strain ARM. BMC Biotechnol 8(1):96

Elfghi FM (2016) A hybrid statistical approach for modeling and optimization of RON: A comparative study and combined application of response surface methodology (RSM) and artificial neural network (ANN) based on design of experiment (DOE). Chem Eng Res Des 113:264–272

Esfe MH, Reiszadeh M, Esfandeh S, Afrand M (2018) Optimization of MWCNTs (10%)–Al2O3 (90%)/5W50 nanofluid viscosity using experimental data and artificial neural network. Phys A 512:731–744

Gadekar MR, Ahammed MM (2019) Modelling dye removal by adsorption onto water treatment residuals using combined response surface methodology-artificial neural network approach. J Environ Manage 231:241–248

Gevrey M, Dimopoulos I, Lek S (2003) Review and comparison of methods to study the contribution of variables in artificial neural network models. Ecol Model 160(3):249–264

Hang FY, Zhang JB, Chen LL, Tong QM, Liu Y (2019) Impact of climate change on rice yield and its regional heterogeneity in China. J Ecol Rural Environ 35(3):283–289

Hunsche M, Noga G (2011) Cuticular wax load and surface wettability of leaves and fruits collected from sweet cherry (Prunus avium) trees grown under field conditions or inside a polytunnel. Acta Physiol Plant 33(5):1785–1792

Jiang X, Wan J, Han H, Wang Y, Li K, Wang Q (2018) Sliding and rolling behavior of water droplets on an ordered nanoball matrix fluorocarbon polymer layer under simulated weather conditions. Surf Sci 675:91–98

Karri R, Tanzifi M, Yaraki MT, Sahu JN (2018) Optimization and modeling of methyl orange adsorption onto polyaniline nano-adsorbent through response surface methodology and differential evolution embedded neural network. J Environ Manage 223:517–529

Karaci A, Caglar A, Aydinli B, Pekol S (2016) The pyrolysis process verification of hydrogen rich gas (H–rG) production by artificial neural network (ANN). Int J Hydrogen Energy 41(8):4570–4578

Koch K, Bhushan B, Barthlott W (2008) Diversity of structure, morphology and wetting of plant surfaces. Soft Matter 4(10):1943–1963

Kupcinskiene E, Huttunen S (2005) Long-term evaluation of the needle surface wax condition of Pinus sylvestris around different industries in Lithuania. Environ Pollut 137(3):610–618

Li S, Huang J, Chen Z, Chen G, Lai Y (2017) A review on special wettability textiles: theoretical models, fabrication technologies and multifunctional applications. J Mater Chem A 5(1):31–55

Liu QF, Kim SH (2008) Evaluation of membrane fouling models based on bench-scale experiments: a comparison between constant flowrate blocking laws and artificial neural network (ANNs) model. J Membr Sci 310(1–2):393–401

Nair AT, Makwana AR, Ahammed MM (2014) The use of response surface methodology for modelling and analysis of water and wastewater treatment processes: a review. Water Sci Technol 69(3):464–478

Nairn JJ, Forster WA (2017) Methods for evaluating leaf surface free energy and polarity having accounted for surface roughness. Pest Manag Sci 73:1854–1865

Maleki A, Daraei H, Shahmoradi B, Razee S, Ghobadi N (2014) Electrocoagulation efficiency and energy consumption probing by artificial intelligent approaches. Desalination Water Treat 52(13–15):2400–2411

Maran JP, Sivakumar V, Thirugnanasambandham K, Sridhar R (2013) Artificial neural network and response surface methodology modeling in mass transfer parameters predictions during osmotic dehydration of Carica papaya L. Alex Eng J 52(3):507–516

Matsumoto T, Wu J, Kanamori H, Katayose Y, Fujisawa M, Namiki N, Sakata K (2005) The map-based sequence of the rice genome. Nature 436:793–800

Moghaddam SS, Moghaddam MA, Arami M (2010) Coagulation/flocculation process for dye removal using sludge from water treatment plant: optimization through response surface methodology. J Hazard Mater 175(1–3):651–657

Notton G, Voyant C, Fouilloy A, Duchaud JL, Nivet ML (2019) Some applications of ANN to solar radiation estimation and forecasting for energy applications. Appl Sci 9(1):209

Moghadam BH, Hasanzadeh M, Haghi AK (2013) On the contact angle of electrospun polyacrylonitrile nanofiber mat. System 22:23

Montgomery DC (2017) Design and analysis of experiments. John wiley sons.

Motlagh NV, Taghipour-Gorjikolaie M (2018) Comparison of heuristic methods for developing optimized neural network based models to predict amphiphobic behavior of fluorosilica coated surfaces. Surf Coat Technol 349:289–295

Olden JD, Joy MK, Death RG (2004) An accurate comparison of methods for quantifying variable importance in artificial neural network using simulated data. Ecol Model 178(3–4):389–397

Podstawczyk D, Witek-Krowiak A, Dawiec A, Bhatnagar A (2015) Biosorption of copper (II) ions by flax meal: empirical modeling

and process optimization by response surface methodology (RSM) and artificial neural network (ANN) simulation. Ecol Eng 83:364–379

Qu D, Cai X, Chang W (2018) Evaluating the effects of steel fibers on mechanical properties of ultra-high performance concrete using artificial neural network. Appl Sci 8(7):1120

Rostamizadeh M, Rizi SMH (2012) Predicting gas flux in silicalite-1 zeolite membrane using artificial neural networks. J Membr Sci 403:146–151

Sadrzadeh M, Mohammadi T, Ivakpour J, Kasiri N (2008) Separation of lead ions from wastewater using electrodialysis: comparing mathematical and neural network modeling. Chem Eng J 144(3):431–441

Shabanzadeh P, Yusof R, Shameli K (2015) Artificial neural network for modeling the size of silver nanoparticles' prepared in montmorillonite/starch bionanocomposites. J Ind Eng Chem 24:42–50

Shojaeimehr T, Rahimpour F, Khadivi MA, Sadeghi M (2014) A modeling study by response surface methodology (RSM) and artificial neural network (ANN) on Cu2+ adsorption optimization using light expended clay aggregate (LECA). J Ind Eng Chem 20(3):870–880

Singh B, Misra JP (2019) Surface finish analysis of wire electric discharge machined specimens by RSM and ANN modeling. Measurement 137:225–237

Taghipour-Gorjikolaie M, Motlagh NV (2018) Predicting wettability behavior of fluorosilica coated metal surface using optimum neural network. Surf Sci 668:47–53

Venkatesan J, Rajasekaran S, Das A, Ganesan S (2016) Effects of temperature-dependent contact angle on the flow dynamics of an impinging droplet on a hot solid substrate. Int J Heat Fluid Flow 62:282–298

Vijayakumar R, Abd Gani S, Zaidan U, Halmi M (2018) Optimization of the antioxidant potentials of red pitaya peels and its in vitro skin whitening properties. Appl Sci 8(9):1516

Wen S, Zhang Q, Yin X, Lan Y, Zhang J, Ge Y (2019) Design of plant protection UAV variable spray system based on neural networks. Sensors 19(5):1112

Yadav AM, Chaurasia RC, Suresh N, Gajbhiye P (2018) Application of artificial neural networks and response surface methodology approaches for the prediction of oil agglomeration process. Fuel 220:826–836

Yadav AM, Nikkam S, Gajbhiye P, Tyeb MH (2017) Modeling and optimization of coal oil agglomeration using response surface methodology and artificial neural network approaches. Int J Miner Process 163:55–63

Yao C, Myung K, Wang N, Johnson A (2014) Spray retention of crop protection agrochemicals on the plant surface retention, uptake, and translocation of agrochemicals in plants. Am Chem Soc 2014:1–22

Zhang W, Lin Y, Zhang Q, Wang X, Wu D, Kong H (2013) Optimisation of simultaneous saccharification and fermentation of wheat straw for ethanol production. Fuel 112:331–337

Zhao X, Gao Y, Zhang C, Zhu Y, Lei J, Ma Y, Du F (2018) Wettability of ionic surfactants SDS and DTAB on wheat (Triticum aestivum) leaf surfaces. J Dispersion Sci Technol 39(12):1820–1828

Zhu Y, Gao Y, Zhang C, Zhao X, Ma Y, Du F (2018) Static and dynamic wetting behavior of TX-100 solution on super-hydrophobic rice (*Oryza sativa*.) leaf surfaces. Colloids Surf A 547:148–156

Zhu YQ, Yu CX, Li Y, Zhu QQ, Zhou L, Cao C, Du FP (2014) Research on the changes in wettability of rice (*Oryza sativa*) leaf surfaces at different development stages using the OWRK method. Pest Manag Sci 70(3):462–469

Publisher's Note Springer Nature remains neutral with regard to jurisdictional claims in published maps and institutional affiliations.

SCAU1820240522

检索证明

根据委托人提供的论文材料，委托人华南农业大学数学与信息学院 张建锋 2篇论文收录情况如下表。

序号	论文名称	发表刊物及发表的年月卷期/页码等	作者排名	论文字数	作者文字单位	收录情况	影响因子	中科院大类分区
1	Effects of temperature and humidity on the contact angle of pesticide droplets on rice leaf surfaces	JOURNAL OF PESTICIDE SCIENCE 出版年：2022 卷期：47 2 页码：59-68 文献号： 文献类型：Article	第一作者	8页	华南农业大学	SCI	IF2-year=2.4 IF5-year=2.8 (2022)	农林科学 4区 Top期刊：否 (2022)
2	Application of artificial neural network (ANN) and response surface methodology (RSM) for modeling and optimization of the contact angle of rice leaf surfaces	ACTA PHYSIOLOGIAE PLANTARUM 出版年：2019 卷期：42 6 页码： 文献号：51 文献类型：Article	第一作者	8页	华南农业大学	SCI	IF2-year=2.304 IF5-year=2.721 (2020)	生物学 4区 Top期刊：否 (2020)

备注：论文检索中如论文发表年月卷期页码等为（）则表示论文尚未正式发表或检索时未找到。

报告免责声明：如未盖章，报告无效

检索员：张进

华南农业大学图书馆

2.7 Effects of temperature and humidity on the contact angle of pesticide droplets on rice leaf surfaces

J-STAGE上の記事を検索

検索条件の詳細設定

5,657,730 記事 (5,430,622 記事)　3,969 資料 (3,471 資料)　25 専門分野

＊2024/03/22 現在

注目トピックス



New 2023年度第1回 J-STAGEセミナーの開催報告書を掲載しました

New 1月30日開催「ジャーナル・インパクトファクター向上をめざすセミナー」関連資料を公開しました

New 2022年度第3回 J-STAGEセミナーの開催報告書を掲載しました。

新着資料

乳幼児教育・保育者養成研究 2024/03/21
日本手外科学会雑誌 2024/03/21
仏教文化 2024/03/21
コギタータ 2024/03/18
Proceedings of the Arthropodan... 2024/03/18
Language in Japan 2024/03/15
ゴルフ教育研究 2024/03/15
Journal of Corpus-based Lexicology... 2024/03/13
日本作物学会関東部会報 2024/03/13
日本臨床スポーツ医学会誌 2024/03/13
三次元画像コンファレンス講演論文集 2024/03/13
日本作物学会四国部会会報 2024/03/12
土木構造・材料論文集 2024/03/07
北方民族文化シンポジウム概報告書 2024/03/06
日本がん・リンパ浮遊療学療法学会誌 2024/03/06

表示数を増やす

バックナンバー

新着号

応用糖質科学：日本応用糖質科学...
エアロゾル研究

My J-STAGEにサインイン

資料を探す：資料タイトルから
資料を探す：分野から
資料を探す：発行機関から
データを探す(J-STAGE Data)

最新情報

- 【発行機関向け】書誌XML作成ツール　サービス提供終了のお知らせ（2025年3月予定）
- 2024年3月14日 2023年度第1回 J-STAGEセミナーの開催報告書を掲載しました。
- 2024年3月12日 【システムメンテナンス】2024年3月27日、メンテナンスのため一部機能が利用できません。
- 2024年3月8日 一部の資料の書誌画面に試行的に表示していたAltmetricsの表示を2024年3月29日をもって終了します。
- 2024年2月27日 1月30日開催「ジャーナル・インパクトファクター向上をめざすセミナー」の関連資料を公開しました。
- 2024年2月9日 2022年度第3回 J-STAGEセミナーの開催報告書を掲載しました。
- 2024年1月25日 「J-STAGE中長期戦略（改定）」

feedback

Journal of Pesticide Science

Online ISSN : 1349-0923
Print ISSN : 1348-589X
ISSN-L : 0385-1559

巻号一覧



49 巻 (2024) +
48 巻 (2023) +
47 巻 (2022) −
4 号 p. 155-
3 号 p. 101-
2 号 p. 47-
1 号 p. 1-
46 巻 (2021) +
45 巻 (2020) +
44 巻 (2019) +
43 巻 (2018) +
42 巻 (2017) +
41 巻 (2016) +
40 巻 (2015) +
39 巻 (2014) +

47 巻, 2 号

選択された号の論文の6件中1～6を表示しています

メタデータをダウンロード すべての抄録を表示する

|< < 1 > >|

Review

Engineering of *Bacillus thuringiensis* insecticidal proteins

Takashi Yamamoto

2022 年 47 巻 2 号 p. 47-58
発行日: 2022/05/20
公開日: 2022/05/28
[早期公開] 公開日: 2022/05/18

DOI https://doi.org/10.1584/jpestics.D22-016

ジャーナル オープンアクセス HTML
電子付録

▸ 抄録を表示する PDF形式でダウンロード (4033K) HTML形式で全画面表示

Regular Articles

Effects of temperature and humidity on the contact angle of pesticide droplets on rice leaf surfaces

Jiantao Zhang, Tengyuan Zhou, Jiajun Zeng, Xuanchun Yin, Yubin Lan, Sh ...

2022 年 47 巻 2 号 p. 59-68
発行日: 2022/05/20
公開日: 2022/05/28
[早期公開] 公開日: 2022/04/23

DOI https://doi.org/10.1584/jpestics.D21-068

ジャーナル オープンアクセス HTML

feedback

J. Pestic. Sci. **47**(2), 59–68 (2022)
DOI: 10.1584/jpestics.D21-068

JOURNAL OF PESTICIDE SCIENCE

Regular Article

Effects of temperature and humidity on the contact angle of pesticide droplets on rice leaf surfaces

Jiantao Zhang,[1,2] Tengyuan Zhou,[1,2] Jiajun Zeng,[1,2] Xuanchun Yin,[2,3] Yubin Lan[2] and Sheng Wen[2,3,*]

[1] *College of Mathematics and Informatics, South China Agricultural University, Guangzhou 510642, China*
[2] *National Center for International Collaboration Research on Precision Agricultural Aviation Pesticide Spraying Technology, Guangzhou 510642, China*
[3] *Engineering College, South China Agricultural University, Guangzhou 510642, China*

(Received November 30, 2021; Accepted February 17, 2022)

The effects of external factors such as temperature, humidity, pesticide formulation, and pesticide concentration on the contact angle of pesticide droplets on rice leaf surfaces were analyzed. The experiments showed that there were significant differences in the contact angles of droplets on the leaf surfaces under different temperatures and humidity. As the ambient temperature increased, the contact angle first decreased and then increased, reaching a minimum value at 25°C. With a gradual increase in humidity, the contact angle significantly increased and reached a maximum at 100% humidity. Finally, it was concluded that both the formulation and concentration of the pesticide had a significant effect on the contact angle of droplets on rice leaf surfaces. The experiments also illustrated that the effects of the pesticide formulation and concentration on the contact angle were more significant than those of temperature and humidity.



Keywords: contact angle, rice leaf surfaces, temperature, humidity, pesticide formulation, pesticide concentration.

Introduction

Rice is an important grain planted in large areas in China.[1)] Recently, rice diseases, insects, and weeds have been increasing annually. Currently, chemical control is the main prevention and control method.[2)] Pesticides play an extremely important role in agricultural production.[3)] Although pesticide use can increase crop yields in the short term, their excessive use leaves many hidden dangers that can be easy to ignore. For example, pesticide droplets can easily roll off the surface of rice leaves,[4,5)] causing only 20–30% of the pesticides to be deposited on the target. The remaining 70–80% is lost to the soil,[6)] which leads to the pesticide having a low degree of wet spreading on the plant foliage[7,8)] and causing ecological pollution.[9–12)] Therefore, one of the key challenges regarding current pesticide application technology is to improve the utilization rate of pesticides, which can be accomplished by studying the wet-distribution effect of liquid pesticides on the surface of rice leaves.[13,14)]

The leaf surface is a barrier that separates plant tissues from the environment.[15)] It plays an important role in protecting the internal structure of the leaf, and it resists the influence of different external environments.[16,17)] Spray droplets can attach to the leaf surface to improve the utilization of pesticides. The contact angle on the surface of the plant leaves is an important indicator that can be used to measure the wetting properties of a liquid.[18–20)]

The phenomenon of liquid diffusion on the surface of isotropic plant leaves is called wetting.[21,22)] The ability of a liquid to diffuse on a solid surface is called the wettability of the liquid to the solid.[23,24)] Wetting spread is a phenomenon in which one fluid replaces another fluid on the interface, usually referring to the process by which a liquid replaces a gas on a solid surface. The wetting and distribution of a liquid on the surface of rice leaves, which is generally represented by the contact angle,[25,26)] reflects the affinity of the rice leaf surface for pesticide droplets. The contact angle of droplets on rice leaves is affected by internal and external factors. Internal factors mainly include the rice variety, the chemical fractionation of wax deposited on the leaf surface,[27)] physical microstructures,[28)] leaf position, and the plant growth

* To whom correspondence should be addressed.
E-mail: vincen@scau.edu.cn
Published online April 23, 2022

BY-NC-ND © Pesticide Science Society of Japan 2022. This is an open access article distributed under the Creative Commons Attribution-NonCommercial-NoDerivatives 4.0 International (CC BY-NC-ND 4.0) License (https://creativecommons.org/licenses/by-nc-nd/4.0/)

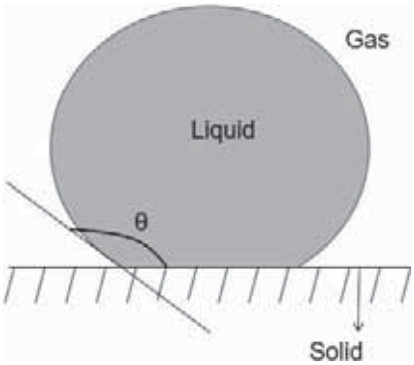


Fig. 1. Contact angle schematic.

cycle. External factors affect the contact angle by changing the environmental conditions around the leaf surface and the properties of the liquid, including the type and concentration of surfactants, the type and concentration of organic solvents, the solution viscosity, droplet volume, temperature, and humidity.

Contact angle is the most direct indicator of wetting and spreading properties. For most plants, the wetting and spreading performance on plant leaves can be analyzed by measuring the contact angle between droplets and the leaf surface. Contact angles less than 90° indicate wetting, and the droplets can adhere to the solid surface or even spread. Contact angles greater than 90° indicate non-wetting. If the contact angle is much larger than 90°, the droplets will aggregate into water droplets and roll off.[29] The contact angle is shown in Fig. 1.

During plant growth, the temperature and relative humidity of the environment are critical external factors.[30,31] These two environmental factors greatly affect the physical and chemical properties of leaf surfaces, thus affecting the contact angle of droplets on the surface of rice leaves. Therefore, many researchers have recently explored the effects of temperature[32] and humidity[33] on the droplet contact angle. Baker[34] explored the effects of temperature and relative humidity on the wettability of cabbage leaf surfaces and concluded that a decrease in temperature or relative humidity would reduce the wettability. In a study on rice and lotus leaves, Sun[35] also mentioned the important influence of temperature on leaf surface wetting diffusion. The results of the study showed that the contact angle of droplets on the surfaces of experimental plant leaves remained constant within a certain temperature range. After reaching a certain temperature, the contact angle began to linearly decline. When the experimental temperature reached 56°C, the contact angle of the droplets on the surface of the lotus and rice leaves was approximately 120°. At this temperature, the rice leaf contact angle decreased at the highest rate. As the ambient temperature continued to rise, the contact angle of the droplets on the surfaces of the lotus and rice leaves decreased, and it was minimized when the ambient temperature reached 69°C. In the ambient temperature range of 56–69°C, the contact angle of the droplets on the surfaces of the lotus and rice leaves changed significantly.

In this study, the effects of four main external factors, namely ambient temperature, relative humidity, pesticide formulation, and pesticide concentration, on the contact angle of droplets on rice leaves during a simulated agricultural aviation rice-field spraying operation were investigated using an automatic contact-angle tester. The impacts of these four factors were then obtained. This study considered the temperature and humidity

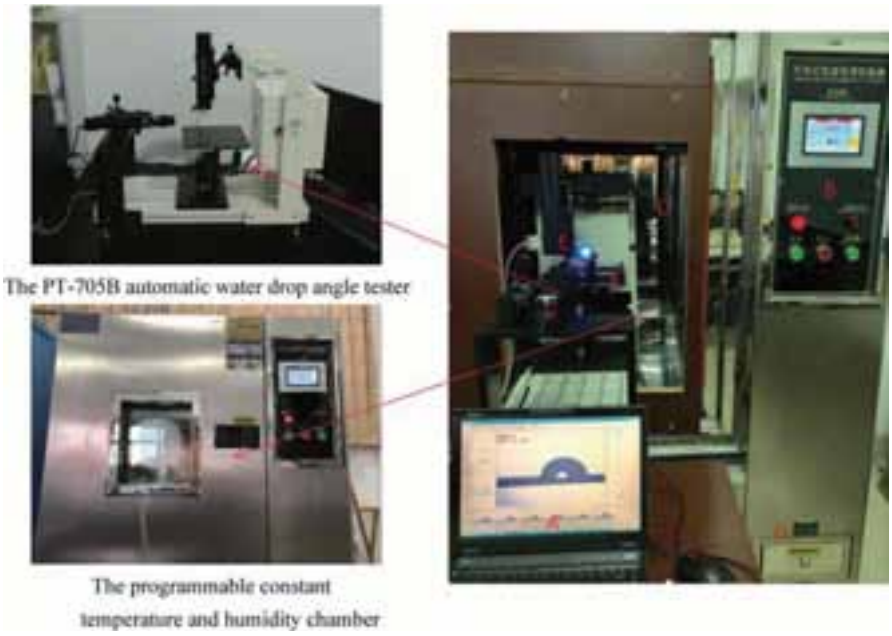


Fig. 2. The experimental environment was designed and constructed to measure the contact angle of droplets on the surface of rice leaves under different temperature and humidity conditions. (A) Measuring computer; (B) numerical control board for the incubator; (C) high-speed camera; (D) internal environment of the test chamber with constant temperature and humidity; (E) drop injector; (F) fixed experimental platform; (G) water tank.

Table 1. Experimental factors and levels

Experimental factors	Levels						
Temperature	15°C	20°C	25°C	30°C	35°C	40°C	45°C
Humidity	40%	50%	60%	70%	80%	90%	100%
Pesticide formulation	EC	SC	WP	WG	SL		
Pesticide concentration	1 : 100	1 : 200	1 : 500	1 : 1000	1 : 2000	1 : 3000	1 : 4000

ranges of rice plants in the general planting environment to be the independent variables and the rice leaf contact angle to be the dependent variable. Finally, this study explored the interaction effect of ambient temperature and relative humidity on the leaf contact angle of rice plants.

Materials and methods

1. Materials

Three rice varieties (Guang 8 You 169, He Mei Zhan, and Mei Xiang Zhan 2) were selected from the agriculturally dominant rice varieties released by the Guangdong Provincial Department of Agriculture. These varieties are widely used in Guangdong and the rice-planting regions of southern China, and they have good prospects for popularization and application.

To avoid any effects of other variables on the experiment, the test rice materials were uniformly planted in a rice test field at the South China Agricultural University. The penultimate leaves in the middle of the rice plants were selected as the experimental samples. In order to keep the rice leaves fresh, they were packed and sealed in polyethylene bags and transported to the laboratory immediately after each field-sampling session. The bottoms of the rice leaves were immediately placed in a container of distilled water to prevent the leaves from curling up, which would have prevented the contact angle of the droplets on the leaf surfaces from being measured. Before the experiment, the rice leaves were cut into 8 cm-long rectangles. The samples were then adhered to glass slides with double-sided tape, and the edges were lightly compacted to prevent curling. Finally, the slides were placed on a platform for measurement. During the measurements, external objects were prevented from contacting the rice leaf surfaces to avoid damaging the leaf surface structures.

2. Experimental instruments and tools

A PT-705B automatic water-drop angle tester (Dong Guan Precise Test Equipment Co., Ltd., China) and a programmable constant temperature and humidity tester (Shang Hai Jiang Kai Machine Co., Ltd., China) were used in the experiment, as shown in Fig. 2. The automatic water-drop angle tester was equipped with a precise automatic liquid-distribution system. The programmable constant temperature and humidity tester had a temperature accuracy of 0.1°C and a humidity accuracy of 0.1%.

3. Methods

The external factors considered in this study were categorized as environmental or chemical factors. The environmental factors were temperature and relative humidity. The chemical factors were pesticide formulation and pesticide concentration.

The experimental platform that was built for this study is shown in Fig. 2. The contact angle was measured using an automatic water-drop angle tester. The experiment was carried out in a chamber with programmable constant temperature and humidity, and the temperature and humidity were adjusted according to the experimental requirements. A high-speed camera equipped with the drop angle tester was used to capture the droplet, and the shape of the droplet was collected using an optical amplification system and an image acquisition system. Finally, the contact angles of droplets on the rice leaf surfaces were measured using the ellipse fitting method[36] with the automatic water-drop angle tester.

3.1. Experiment on the influence of single factors on the contact angle of rice leaves

First, the effects of temperature and humidity on the surface contact angle of rice leaves were explored. The three rice varieties (Guang 8 You 169, He Mei Zhan, and Mei Xiang Zhan 2) were arranged for measurement of the contact angle at different temperatures and humidity levels using a uniform pesticide formulation with a dilution ratio of 1 : 200 as the suspension agent. The experimental factors and levels are shown in Table 1. The temperature levels were 15°C, 20°C, 25°C, 30°C, 35°C, 40°C, and 45°C, and the humidity levels were 40%, 50%, 60%, 70%, 80%, 90%, and 100%. Then the effects of the pesticide formulation and concentration on the rice leaf surface contact angle were studied. The experiment to measure the contact angle on rice variety Guang 8 You 169 was designed under unified conditions of 30°C, 70% humidity, and different pesticide formulations and concentrations. Five widely used pesticide formulations were

Table 2. Experimental factors and levels

Experimental factors	Levels				
Temperature	20°C	25°C	30°C	35°C	40°C
Relative humidity	40%	60%	80%	100%	
Pesticide formulation	EC	SC	WP	WG	SL
Pesticide concentration	1 : 100	1 : 200	1 : 500	1 : 1000	

utilized in this experiment: a 5% imidacloprid emulsion (5% imidacloprid EC), a 35% imidacloprid suspension (35% imidacloprid SC), a 10% imidacloprid wettable powder (10% imidacloprid WP), a 70% imidacloprid water dispersible granule (70% imidacloprid WG), and a 10% imidacloprid soluble concentrate (10% imidacloprid SL). They were produced by Xinyi Nong Plant Protection, Jiaduo Collects Genuine Agricultural Materials, Fengge China Agricultural Materials, MinYuan Agricultural Materials, and Green Field Plant Protection, respectively. Different concentrations of pesticides were distinguished by the dilution ratio of the pesticide stock solution, which was obtained by adding deionized water to an imidacloprid pesticide stock solution. The specific dilution ratios were 1 : 100, 1 : 200, 1 : 500, 1 : 1000, 1 : 2000, 1 : 3000, and 1 : 4000.

3.2. Effect of temperature and humidity interaction on rice leaf contact angle

The leaf contact angles of the three rice varieties under different combinations of temperature and humidity were determined under the condition that the pesticide formulation was a suspension agent and the pesticide concentration was 1 : 200. The ambient temperature levels were 20°C, 25°C, 30°C, and 35°C, and the ambient relative humidity levels were 40%, 50%, 60%, 70%, 80%, 90%, and 100%. Contact angle measurement experiments with different combinations of temperature and humidity were conducted, and each experiment was repeated 12 times. The maximum and minimum values were removed, and the average value of the remaining 10 contact angles was taken as the final experimental result. Finally, IBM SPSS Statistics Software (SPSS Inc., USA) and Design-Expert software (Stat-Ease, USA) were used to analyze the influence of temperature and humidity on the contact angle of droplets on the rice leaf surface.

3.3. Multilevel mixed orthogonal experiment

To explore the influence of the four external factors (temperature, relative humidity, pesticide formulation, and pesticide concentration) on the contact angle of the rice leaf surfaces, 25 groups of mixed orthogonal experiments were designed according to the experimental factors and levels in Table 2. The measurements were repeated 12 times for each group, and the maximum and minimum values were removed. The average value of the remaining 10 contact angles was taken as the final experimental result. SPSS software was used to analyze the experimental data using a multifactor analysis of the general linear model. Finally, the degree of influence of each factor was recorded, and the degree of influence of each external factor was obtained through analysis with Design-Expert software.

Results

1. Univariate analysis

1.1. Effect of temperature on the contact angle of droplets on rice leaf surfaces

The experimental results showed that the measured contact angles on the leaf surfaces of the three rice varieties varied with the ambient temperature, as shown in Fig. 3. At different ambient temperatures, the contact angles of the droplets on the surfaces of the rice leaves were significantly different. With an increase in ambient temperature from 15 to 45°C, the leaf contact angles of the three rice varieties changed significantly. The leaf contact angles of the three tested varieties ranged from 120 to 135°. The contact angle of Guang 8 You 169 increased from 127.331 to 136.384°, which was an increase of 7.1%; that of He Mei Zhan increased from 127.279 to 134.327°, an increase of 5.6%; and that of Mei Xiang Zhan 2 rose from 125.503 to 134.676°, an increase of 7.3%. In the ambient temperature range of 15–25°C, the rice leaf contact angle decreased significantly and reached its minimum at approximately 25°C. When the ambient temperature continued to rise from 25 to 45°C, the contact angle tended to increase, and the wetting and spreading effects became weaker. Therefore, in the rice-planting environment, when the external temperature was approximately 25°C, the contact angle was the smallest, and the droplets had the best wettable spreading effects on the surface of rice leaves.

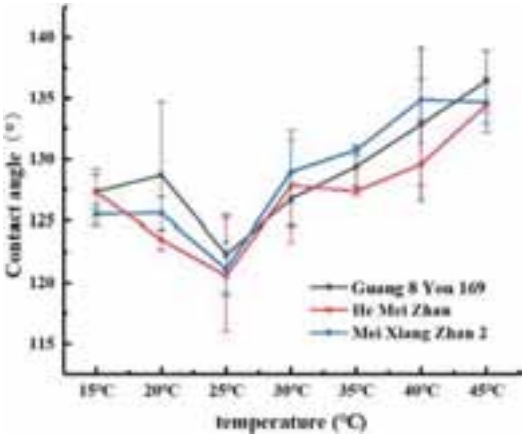


Fig. 3. Relationships between the leaf contact angles of three rice cultivars and temperature.

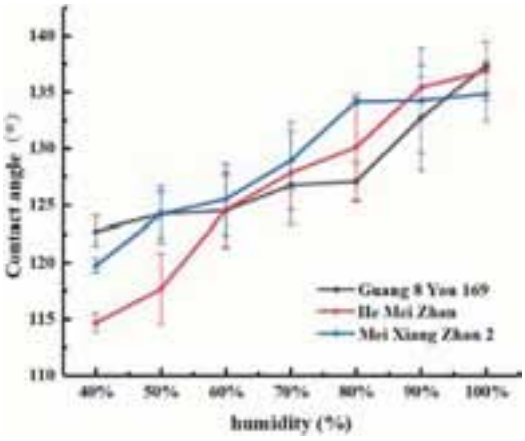


Fig. 4. Relationships between the leaf contact angles of three rice cultivars and relative humidity.

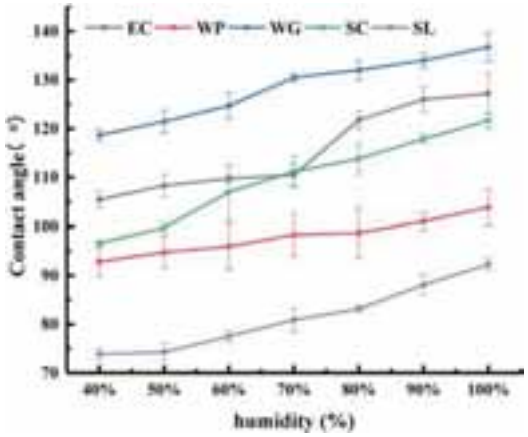


Fig. 5. Relationships between the leaf contact angle of rice and relative humidity under different formulations of imidacloprid.

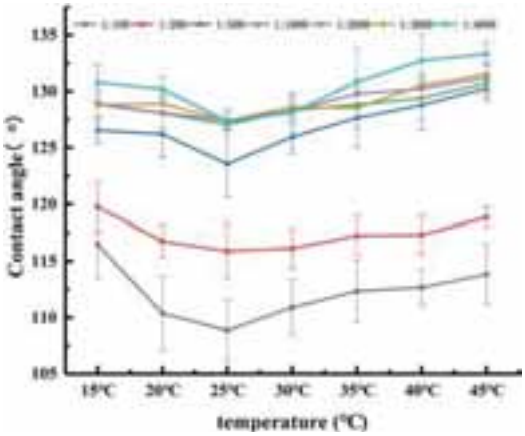


Fig. 7. Relationships between the leaf contact angle and temperature under different concentrations of imidacloprid.

1.2. Effect of humidity on the contact angle of droplets on rice leaf surfaces

The change in the leaf contact angle of the three rice varieties with humidity was measured experimentally. As shown in Fig. 4, the leaf contact angles of the three rice varieties exhibited obvious changes with an increase in environmental humidity from 40 to 100%. The leaf contact angles of the three rice varieties were all in the range of 115.0–137.5°. The contact angle of Guang 8 You 169 increased from 122.766 to 137.361°, which was an increase of 11.9%. The contact angle of He Mei Zhan increased from 114.67 to 136.901°, an increase of 19.4%. The contact angle of Mei Xiang Zhan 2 increased from 119.758 to 134.867°, an increase of 12.6%. In the range of 40–100% relative humidity, the rice leaf contact angle increased with the gradual increase in environmental relative humidity. The contact angle reached its maximum when the relative humidity was 100%, when the wetting and spreading effects of the liquid on the rice leaf surface were the worst. The contact angle reached its minimum when the relative humidity was 40%, when the wetting and spreading effects of the liquid on the rice leaf surface were the best.

1.3. Effect of pesticide formulation on the contact angle of rice leaf surfaces

For five different formulations of the pesticide imidacloprid, the droplet contact angle on the rice leaf surface varied with ambient temperature and relative humidity, as shown in Fig. 5 and Fig. 6. It can be concluded from the figures that the variable trends in the contact angles with the five pesticide formulations on the rice leaf surface under different temperatures and humidity are consistent with the results presented in Sections 3.1.1 and 3.1.2. Finally, the values of the contact angles for the five pesticide formulations were ranked as follows: WG>EC>SC>WP>SL. Therefore, the differences in the numerical values of the droplet contact angles for the five pesticide formulations suggest that the effects of different formulations of the same pesticide on the rice leaf contact angle are significantly different.

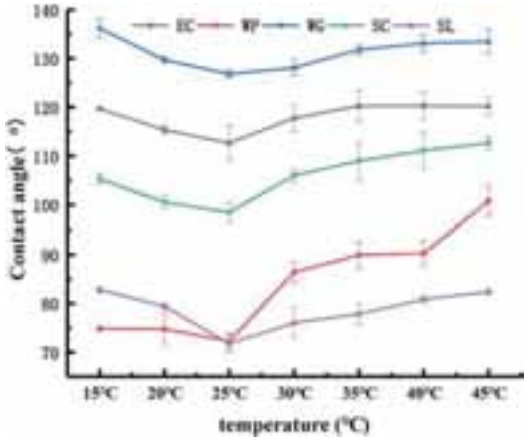


Fig. 6. Relationships between the leaf contact angle of rice and temperature under different formulations of imidacloprid.

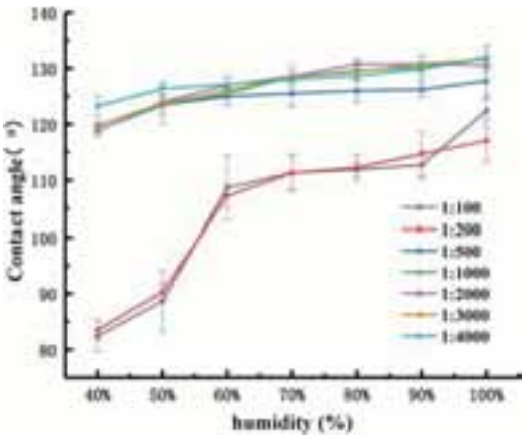


Fig. 8. Relationships between the leaf contact angle and humidity under different concentrations of imidacloprid.

Table 3. Tests of Between-Subject Effects

Source	Type III Sum of Squares	df	Mean Square	F	*p*-value
Corrected Model	674.236[a)]	26	25.932	7.643	0.280
Intercept	381792.777	1	381792.777	112523.245	0.002
Temperature*humidity	15.954	17	0.938	0.277	0.926
Temperature	98.100	3	32.700	9.637	0.231
Humidity	551.179	6	91.863	27.074	0.146
Error	3.393	1	3.393		
Total	390200.428	28			
Corrected Total	677.629	27			

[a)] R-Squared=0.995 (Adjusted R-Squared=0.865)

1.4. Effect of pesticide concentration on the droplet contact angle on rice leaf surfaces

Figure 7 shows the change in the contact angle of seven different concentrations of imidacloprid on the surface of rice leaves at different environmental temperatures. As shown in the figure, the trends of the contact angles of the seven pesticide concentrations on rice leaf surfaces with changing temperature were consistent with the results presented in Section 3.1.1. Overall, the contact angles of the droplets on the rice leaf surfaces were significantly different for different pesticide concentrations, and they were roughly divided into three categories. In the first category, the contact angles of pesticides with the highest dilutions (1:1000, 1:2000, 1:3000, and 1:4000) were the largest, similar to the contact angle of water on the rice leaf surface. In the second category, the contact angle of the moderately diluted solution (1:500) decreased by approximately 2.5–3° compared with those in the first category. In the third category, the contact angles of the pesticides with the lowest dilutions (1:100 and 1:200) were significantly lower, with the lowest contact angle being approximately 107° at 25°C.

Figure 8 shows the curves of the contact angles of seven concentrations of imidacloprid on the surface of rice leaves in relation to the environmental relative humidity. As can be seen from the figure, the trends of the contact angles of the seven pesticide concentration solutions with increasing relative humidity were consistent with the results presented in Section 3.1.2. Overall, the contact angle was significantly different for different pesticide concentrations. The contact angles were divided into three categories. In the first category, the contact angles of the liquids with a high degree of dilution (1:500, 1:1000, 1:2000, 1:3000, and 1:4000) were large, similar to the contact angle of water on the surface of rice leaves. In the second category, the contact angle of the moderately diluted solution (1:500) was slightly decreased compared to those in the first category, but the reduction degree was not as significant as that presented in Fig. 8. In the third category, the contact angles of the liquid with the lowest dilution levels (1:100 and 1:200) decreased significantly compared to the other categories, and the contact angle reached a minimum of approximately 85° under the condition of 40% relative humidity.

2. Two-factor interaction analysis of temperature and humidity

The two-factor univariate analysis of the leaf contact angle of rice plants with different combinations of ambient temperature and relative humidity was performed using SPSS. Finally, the influence of the two main factors, temperature and relative humidity, on the contact angle was determined. The results of the specific analysis are presented in Table 3. The results show that the effects of temperature (p=0.231) and relative humidity (p=0.146) on the contact angle of droplets on the surface of rice leaves were not significant (at a level of p=0.05). Under the interaction of temperature and relative humidity, the influence of the contact angle was not significant (p=0.926).

In addition, a response surface analysis of rice leaf contact angles under different temperature and relative humidity combinations was performed using Design-Expert software. Surface response maps and contour maps of the temperature and relative humidity are shown in Fig. 9.

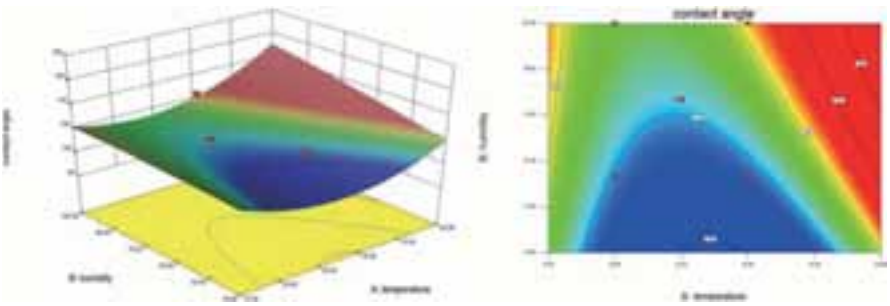


Fig. 9. Temperature and humidity *versus* contact angle.

Table 4. Orthogonal experimental results

Number	Temperature	Relative humidity	Pesticide formulation	Pesticide concentration	Contact angle
1	25°C	60%	WP	1:200	92.850±1.941
2	40°C	40%	SL	1:200	85.526±1.004
3	35°C	40%	WG	1:500	122.830±1.894
4	20°C	60%	SC	1:500	114.090±1.222
5	30°C	40%	WP	1:1000	118.339±1.073
6	25°C	80%	WG	1:1000	128.799±1.458
7	35°C	60%	SL	1:100	77.373±0.968
8	40°C	60%	EC	1:1000	127.889±1.129
9	40°C	100%	WP	1:500	115.055±0.731
10	35°C	100%	SC	1:1000	121.440±2.743
11	30°C	100%	EC	1:100	109.986±1.352
12	25°C	100%	SL	1:100	79.625±0.730
13	25°C	40%	SC	1:100	106.339±1.055
14	35°C	80%	EC	1:200	118.220±0.664
15	20°C	80%	WP	1:100	86.968±2.049
16	20°C	40%	EC	1:100	112.953±1.582
17	30°C	60%	WG	1:100	107.017±1.328
18	40°C	40%	WG	1:100	104.194±1.240
19	20°C	100%	WG	1:200	113.047±2.575
20	30°C	40%	SC	1:200	109.760±1.314
21	25°C	40%	EC	1:500	123.379±1.261
22	35°C	40%	WP	1:100	82.381±0.610
23	40°C	80%	SC	1:100	104.089±1.495
24	20°C	40%	SL	1:1000	119.042±1.952
25	30°C	80%	SL	1:500	108.678±1.316

As shown in Fig. 9, as the relative humidity gradually decreased from 100%, the contact angle tended to gradually decrease. As the temperature changed from 15 to 40°C, the contact angle decreased. At 25°C and 40% relative humidity, the minimum contact angle was reached (approximately 113.5°). The trend of the contact angle increased after reaching this minimum value. In addition, as the surface steadily changed, the values of the contour line and the color changed smoothly and gradually. The temperature and relative humidity had little effect on the contact angle. However, compared to temperature, humidity had a greater impact on the contact angle of droplets on the rice leaf surface.

Under the interaction of temperature and relative humidity, the change in the leaf contact angle of rice plants was also relatively stable. Therefore, it can be concluded that environmental temperature and relative humidity have no significant interactive effect on the contact angle of droplets on the surface of rice leaves.

3. Orthogonal experimental analysis

The experimental results of the 25 sets of the contact angle mixed orthogonal experimental data are presented in Table 4. The multifactor univariate analysis of the general linear model was carried out using SPSS, and the inter-subject effect test results are shown in Table 5. It can be seen from Table 5 that the effects of pesticide formulation and pesticide concentration were both significant ($p<0.05$), indicating that they each had a significant influence on the contact angle of droplets on the surface of rice leaves. However, the F-value of the pesticide concentration factor was 29.756, and that of the pesticide formulation factor was 17.705. Therefore, the pesticide concentration had a greater influence on the contact angle than did the pesticide formulation. In contrast, the effects of ambient temperature and relative humidity were insignificant ($p>0.05$). As discussed in Sections 3.1.1 and 3.1.2, temperature and humidity had an insignificant influence on the contact angle of droplets on the surface of rice leaves. However, humidity ($p=0.433$) had a greater influence on the contact angle than did ambient temperature ($p=0.461$).

The above four factors had a descending order of influence on the contact angle of droplets on the surface of rice leaves: pesticide concentration>pesticide formulation>relative humidity>temperature. When the other parameters were consistent and the dilution ratio of the pesticide concentration was 1,000 times or higher, the contact angle of droplets on the surface of rice leaves was more than 120°, and the rice leaves were hydrophobic. When the dilution ratio of the pesticide concentration was 100 times, the contact angle was approximately 85°, and the reduction rate was 29.2%.

Table 5. Tests of Between-Subjects Effects

Source	Type III Sum of Squares	df	Mean Square	F	*p*-value
Corrected Model	5235.184[a)]	14	373.942	11.928	0.000
Intercept	254739.223	1	254739.223	8125.685	0.000
Temperature	122.702	4	30.676	0.978	0.461
Humidity	93.784	3	31.261	0.997	0.433
Pesticide formulation	2220.157	4	555.039	17.705	0.000
Pesticide concentration	2798.541	3	932.847	29.756	0.000
Error	313.499	10	31.350		
Total	294965.009	25			
Corrected Total	5548.683	24			

[a)] R-Squared=0.944 (Adjusted R-Squared=0.864)

In addition, 29 experimental groups were designed using Design-Expert software. The interference effects of the four external factors (ambient temperature, relative humidity, pesticide formulation, and pesticide concentration) on the contact angle of droplets on the rice leaf surface were analyzed. In Fig. 10, as the design factor increased from −1 to 1, there was a larger variation in the curve and a greater influence of the influencing factor on the contact angle of the droplet on the rice leaf surface.

The overall change in the amplitude of ambient temperature (impact factor A) was the smallest, while that of pesticide concentration (impact factor C) was the largest, and the relative humidity and pesticide formulation were in the middle (Fig. 10). Therefore, ambient temperature had the least influence on the contact angle of droplets on the rice leaf surface, while pesticide concentration had the largest influence. The degree of influence on the contact angle was pesticide concentration>pesticide formulation>relative humidity>temperature, which was consistent with the orthogonal experimental results obtained through SPSS.

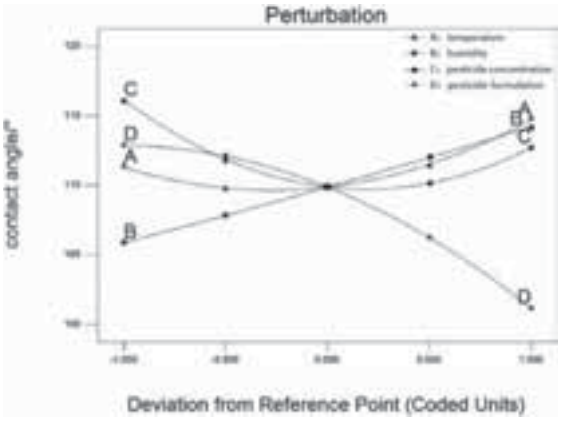


Fig. 10. Interference diagram of (A) temperature, (B) humidity, (C) pesticide concentration, and (D) pesticide formulation. NOTE: The horizontal axis of the interference graph represents the design factor of the experimental group, and the level ranges from the minimum (−1) on the left to the maximum (1) on the right, indicating that the impacts of the four external influence factors increased from small to large.

Discussion

The above experimental results show that the temperature and relative humidity of the ambient air have an effect on the contact angle of the droplets on the surface of rice leaves during plant growth. Koch *et al.*[29)] investigated the effects of relative humidity on the physical and chemical composition of leaf surface wax, morphology, and wettability of cabbage, eucalyptus, and nasturtium. The contact angles of droplets on the leaf surfaces of these three species of hydrophobic plants were measured, and gas chromatography was used to estimate the amount of wax on the leaf surfaces. The experimental results showed that high relative humidity (98%) resulted in a significantly higher amount of water contained in the leaves of cabbage, eucalyptus, and nasturtium compared to that under lower relative humidity (20–30%). The contact angle of the corresponding droplets on the blade surface was also small. In addition, the decrease in relative humidity in the air caused an increase in the amount of wax deposited on the leaf surfaces of the three plants. Therefore, the relative humidity of the air is positively correlated with the increase in wax crystal density on the surface of plant leaves and a decrease in leaf surface wettability. This is inconsistent with the change in the contact angle of droplets on the surface of rice leaves with increasing relative humidity in the air. This may be due to the uneven microstructure of the surface of the rice leaf, as it has striped grooves, stomata, many fine hairs, and a high degree of roughness.[37)]

Chhasatia *et al.*[38)] studied the influence of relative humidity on the contact angle and particle deposition morphology of evaporating colloidal droplets. A high-resolution goniometer was used to measure the contact angle of droplets on a glass substrate by changing the relative humidity in the air while controlling the relevant variables. The results showed that with the increase in relative humidity, the contact angle of the droplets on the glass substrate gradually increased, which was consistent with the contact angle rule obtained by Koch *et al.*[30)] In addition, Chhasatia *et al.*[38)] used fluorescence microscopy to study the deposition behavior of inkjet-printed aqueous colloidal droplets on a glass substrate. The relative humidity in the air also affected the extent to which the droplets spread after hitting the

glass substrate. The evaporation rate at the surface of the falling glass substrate and the evaporation-driven flow conditions inside the droplets drove the suspended particles toward the contact line between the droplets and the solid surface. Chhasatia *et al.*[38] concluded that the droplet particle deposition area and the droplet contact angle changed significantly with the relative humidity of the air. Higher deposition diameters can be observed at higher relative humidity and lower evaporation rates. This can be attributed to the lower contact angle during diffusion.

Leelamanie *et al.*[39] found that with a decreasing relative humidity (94 to 33%) and an equivalent stearic acid content, the surface free energy of sand sample surfaces gradually increased, while the contact angle of the water droplet on the sand sample surface gradually decreased. Thus, these results on the influence of relative humidity on the contact angle of droplets on a hydrophobic fine sand surface are consistent with the results of the present study on the relationship between environmental relative humidity and the wettability of the rice leaf surface (as discussed in Section 3.1.2).

Based on the results of the above three studies, it can be concluded that the contact angle of droplets on the surfaces of materials that are hydrophobic varies with the relative humidity of the ambient air, but there is a considerable difference depending on the type of material. The reasons for this large contrast may be the result of differences in the structure of the composite materials and the surface of plant leaves. Therefore, this study has determined that the contact angle of droplets on the surface of rice leaves changes with the relative humidity of the air.

Conclusions

To improve the effect of pesticide spraying in agricultural rice fields and to reduce the necessary amount of pesticide, four external environmental factors that affect the wettability of liquid droplets in contact with the surface of rice leaves were studied. The following conclusions were drawn:

(1) The ambient temperature and relative humidity influence the contact angle of droplets on the surface of rice leaves. In the natural environment of rice growth in southern China, the contact angle did not change with a single trend of a rise in ambient temperature. With an increase in ambient temperature from 15 to 25°C, the contact angle decreased, and the effect of the droplets was gradually enhanced. With an increase from 25 to 45°C, the contact angle of the droplets on the surface of the rice leaves increased. Therefore, at an ambient temperature of approximately 25°C, the contact angle was minimized, and the wet spreading effect was optimal. In contrast, the contact angle of droplets on the surface of rice leaves changed with a single trend of an increase in environmental relative humidity. With an increase in relative humidity from 40 to 100%, the contact angle increased. Therefore, when the relative humidity of the environment was 40%, the contact angle was the smallest, and the wet spreading effect was optimal.

(2) The formulation and concentration of the pesticide solution had a significant influence on the contact angle of droplets on the surface of rice leaves. Different formulations of the same pesticide had a significant influence on the contact angle. The five widely used pesticide formulations that were used in this study resulted in the following ranking of contact angles: WG>EC>SC>WP>SL. WP and SL had smaller contact angles than did the other pesticide formulations, and they therefore exhibited the best wet spreading effects. In addition, when using the same pesticide suspension formulation, the contact angles of different concentrations of the pesticide solution also exhibited significant differences. With increasing pesticide concentration, the contact angle gradually increased, and the wetting and spreading effects gradually decreased. Therefore, the use of high-concentration (1:100 or 1:200) WP or SL formulations during spraying operations can improve the spreading effect of the liquid on the surface of rice leaves.

(3) By designing 25 sets of contact angle orthogonal experiments, the degrees of influence of the four external factors were ranked from large to small as pesticide concentration, pesticide formulation, relative humidity, and temperature. The most important external environmental factors affecting the wetting properties of droplets on rice leaves were pesticide formulation and pesticide concentration. According to the results of the hybrid orthogonal test and the single factor test, when the concentration of sprayed pesticide was increased and the pesticide formulation was WP or SL, the contact angle was greatly reduced. When the droplets are in contact with the surface of rice leaves, the wetting and spreading effects are greatly enhanced, and the rice leaves can be converted from hydrophobic to hydrophilic.

Acknowledgements

This work was financially supported by the National Natural Science Foundation of China (No. 61773171).

Funding

This research was funded by the key areas special project "Artificial Intelligence" of the ordinary universities in Guangdong Province (2019KZDZX1002), the National Natural Science Foundation (Grant No. 61773171), and the Characteristic Innovation Projects of Colleges and Universities in Guangdong Province (2019KTSCX016).

Conflicts of interest

The authors declare no conflicts of interest.

Author contribution statement

Conceptualization, J.Z. and T.Z.; funding acquisition, J.Z. and S.W.; software, J.Z. and S.W.; writing—original draft preparation, T.Z., J.Z., and S.W.

References

1) T. Sasaki; International Rice Genome Sequencing Project: The map-based sequence of the rice genome. *Nature* **436**, 793–800 (2005).
2) V. T. Xuan: Rice production, agricultural research, and the environment. In "Vietnam's rural transformation" pp. 185–200, 2018.
3) D. Cai, L. Wang, G. Zhang, X. Zhang and Z. Wu: Controlling pesticide loss by natural porous micro/Nano composites: Straw ash-based biochar and biosilica. *ACS Appl. Mater. Interfaces* **5**, 9212–9216

(2013).
4) C. A. Brewer, W. K. Smith and T. C. Vogelmann: Functional interaction between leaf trichomes, leaf wettability and the optical properties of water droplets. *Plant Cell Environ.* **14**, 955–962 (1991).
5) J. Venkatesan, S. Rajasekaran, A. Das and S. Ganesan: Effects of temperature-dependent contact angle on the flow dynamics of an impinging droplet on a hot solid substrate. *Int. J. Heat Fluid Flow* **62**, 282–298 (2016).
6) X. You, M. He, W. Zhang, H. Wei, Q. He, X. Lyu and L. Li: Molecular dynamics simulations and contact angle of surfactant at the coal–water interface. *Mol. Simul.* **44**, 722–727 (2018).
7) C. Zhang, X. Zhao, J. Lei, Y. Ma and F. Du: The wetting behavior of aqueous surfactant solutions on wheat (Triticum aestivum) leaf surfaces. *Soft Matter* **13**, 503–513 (2017).
8) S. Wang, H. Wang, T. Li, C. Li, X. Zhong and Y. Zhou: Wetting property representation of pesticides on the crop leaf surfaces. *Bangladesh J. Bot.* **45**, 1027–1033 (2016).
9) V. Bergeron, D. Bonn, J. Y. Martin and L. Vovelle: Controlling droplet deposition with polymer additives. *Nature* **405**, 772–775 (2000).
10) M. Damak, M. N. Hyder and K. K. Varanasi: Enhancing droplet deposition through *in-situ* precipitation. *Nat. Commun.* **7**, 12560 (2016).
11) D. Pimentel, L. McLaughlin, A. Zepp, B. Lakitan, T. Kraus, P. Kleinman and G. Selig: Environmental and economic effects of reducing pesticide use in agriculture. *Agric. Ecosyst. Environ.* **46**, 273–288 (1993).
12) M. Lechenet, F. Dessaint, G. Py, D. Makowski and N. Munier-Jolain: Reducing pesticide use while preserving crop productivity and profitability on arable farms. *Nat. Plants* **3**, 17008 (2017).
13) C. Yao, K. Myung, N. Wang and A. Johnson: Spray retention of crop protection agrochemicals on the plant surface. In "Retention, Uptake, and Translocation of Agrochemicals in Plants," American Chemical Society, pp. 1–22, 2014.
14) D. Bonn, J. Eggers, J. Indekeu, J. Meunier and E. Rolley: Wetting and spreading. *Rev. Mod. Phys.* **81**, 739–805 (2009).
15) K. Koch, B. Bhushan and W. Barthlott: Diversity of structure, morphology and wetting of plant surfaces. *Soft Matter* **4**, 1943–1963 (2008).
16) X. Zhao, Y. Gao, C. Zhang, Y. Zhu, J. Lei, Y. Ma and F. Du: Wettability of ionic surfactants SDS and DTAB on wheat (Triticum aestivum) leaf surfaces. *J. Dispers. Sci. Technol.* **39**, 1820–1828 (2018).
17) Y. Q. Zhu, C. X. Yu, Y. Li, Q. Q. Zhu, L. Zhou, C. Cao and F. P. Du: Research on the changes in wettability of rice (*Oryza sativa*.) leaf surfaces at different development stages using the OWRK method. *Pest Manag. Sci.* **70**, 462–469 (2014).
18) K. L. Mittal (Ed.): Advances in contact angle, wettability and adhesion. John Wiley & Sons. (2015).
19) J. H. Troughton and D. M. Hall: Extracuticular wax and contact angle measurements on wheat (Triticum vulgare L.). *Aust. J. Biol. Sci.* **20**, 509–526 (1967).
20) N. J. Shirtcliffe, G. McHale, S. Atherton and M. I. Newton: An introduction to superhydrophobicity. *Adv. Colloid Interface Sci.* **161**, 124–138 (2010).
21) E. Bormashenko: Progress in understanding wetting transitions on rough surfaces. *Adv. Colloid Interface Sci.* **222**, 92–103 (2015).
22) M. Hunsche and G. Noga: Cuticular wax load and surface wettability of leaves and fruits collected from sweet cherry (Prunus avium) trees grown under field conditions or inside a polytunnel. *Acta Physiol. Plant.* **33**, 1785–1792 (2011).
23) Y. Zhu, Y. Gao, C. Zhang, X. Zhao, Y. Ma and F. Du: Static and dynamic wetting behavior of TX-100 solution on super-hydrophobic rice (*Oryza sativa*.) leaf surfaces. *Colloids Surf. A Physicochem. Eng. Asp.* **547**, 148–156 (2018).
24) C. Cao, Y. Y. Song, Z. L. Zhou, L. D. Cao, F. M. Li and Q. L. Huang: The role of adhesion force in the bouncing height of pesticide nanoparticles on the rice (*Oryza sativa*) leaf surface. *J. Mol. Liq.* **272**, 92–96 (2018).
25) R. J. Good: A thermodynamic derivation of Wenzel's modification of Young's equation for contact angles; together with a theory of Hysteresis1. *J. Am. Chem. Soc.* **74**, 5041–5042 (1952).
26) A. M. Karim, J. P. Rothstein and H. P. Kavehpour: Experimental study of dynamic contact angles on rough hydrophobic surfaces. *J. Colloid Interface Sci.* **513**, 658–665 (2018).
27) G. A. Beattie and L. M. Marcell: Effect of alterations in cuticular wax biosynthesis on the physicochemical properties and topography of maize leaf surfaces. *Plant Cell Environ.* **25**, 1–16 (2002).
28) Y. Chen, W. Xia and G. Xie: Contact angle and induction time of air bubble on flat coal surface of different roughness. *Fuel* **222**, 35–41 (2018).
29) Y. Yuehua and T. R. Lee: Contact angle and wetting properties. In "Surface Science Techniques," pp. 3–34, 2013.
30) K. Koch, K. D. Hartmann, L. Schreiber, W. Barthlott and C. Neinhuis: Influences of air humidity during the cultivation of plants on wax chemical composition, morphology and leaf surface wettability. *Environ. Exp. Bot.* **56**, 1–9 (2006).
31) S. H. Doerr, L. W. Dekker, C. J. Ritsema, R. A. Shakesby and R. Bryant: Water repellency of soils. *Soil Sci. Soc. Am. J.* **66**, 401–405 (2002).
32) M. E. Diaz, M. D. Savage and R. L. Cerro: The effect of temperature on contact angles and wetting transitions for *n*-alkanes on PTFE. *J. Colloid Interface Sci.* **503**, 159–167 (2017).
33) X. Jiang, J. Wan, H. Han, Y. Wang, K. Li and Q. Wang: Sliding and rolling behavior of water droplets on an ordered nanoball matrix fluorocarbon polymer layer under simulated weather conditions. *Surf. Sci.* **675**, 91–98 (2018).
34) E. A. Baker: The influence of environment on leaf wax development in *Brassica oleracea* var. gemmifera. *New Phytol.* **73**, 955–966 (1974).
35) Y. Sun, Y. Zhang and Z. Yang: Experimental research on the change of contact angle of lotus leaf and rice leaf with temperature. *J. Jilin Teach. College Eng. Technol.* **33**, 102–104 (2017).
36) D. K. Prasad, M. K. Leung and C. Quek: ElliFit: An unconstrained, non-iterative, least squares based geometric Ellipse Fitting method. *Pattern Recognit.* **46**, 1449–1465 (2013).
37) X. Tang, J. Dong and X. Li: A comparison of spreading behaviors of Silwet L-77 on dry and wet lotus leaves. *J. Colloid Interface Sci.* **325**, 223–227 (2008).
38) V. H. Chhasatia, A. S. Joshi and Y. Sun: Effect of relative humidity on contact angle and particle deposition morphology of an evaporating colloidal drop. *Appl. Phys. Lett.* **97**, 827 (2010).
39) D. A. L. Leelamanie, J. Karube and A. Yoshida: Relative humidity effects on contact angle and water drop penetration time of hydrophobized fine sand. *Soil Sci. Plant Nutr.* **54**, 695–700 (2008).

SCAULIB202405422

检索证明

根据委托人提供的论文材料，委托人华南农业大学数学与信息学院 张建桃 2 篇论文收录情况如下表。

序号	论文名称	发表刊物及发表的年月卷期/页码等	作者排名	论文等级	作者文中单位	收录情况	影响因子	中科院大类分区
1	Effects of temperature and humidity on the contact angle of pesticide droplets on rice leaf surfaces	JOURNAL OF PESTICIDE SCIENCE 出版年：2022 卷期：47 2 页码：59-68 文献号： 文献类型：Article	第一作者	B 类	华南农业大学	SCI	IF2-year=2.4 IF5-year=2.3 （2022）	农林科学 4 区 Top 期刊：否 （2022）
2	Application of artificial neural network (ANN) and response surface methodology (RSM) for modeling and optimization of the contact angle of rice leaf surfaces	ACTA PHYSIOLOGIAE PLANTARUM 出版年：2020 卷期：42 4 页码：- 文献号：51 文献类型：Article	第一作者	B 类	华南农业大学	SCI	IF2-year=2.354 IF5-year=2.711 （2020）	生物学 4 区 Top 期刊：否 （2020）

说明：论文等级和中科院大类分区按《华南农业大学学术论文评价方案（试行）》划分。

华南农业大学图书馆SCAULIB202405422

华南农业大学图书馆 信息检索专用章

报告免责声明:如未盖章,报告无效

检索员：张进

华南农业大学图书馆

3. **以通讯作者发表本专业论文情况**

3.1 A Human Finger-Inspired Shape-Locking Pneumatic Gripper Enabled by Folding Laminar Jamming Structure

IEEE/ASME TRANSACTIONS ON MECHATRONICS

This TRANSACTIONS is a joint publication of the IEEE and ASME. For membership and subscription information and pricing, please visit www.ieee.org/membership-catalog.

IEEE/ASME TRANSACTIONS ON MECHATRONICS MANAGEMENT COMMITTEE

Chairman: TOMOYUKI SHIMONO (IES), *Treasurer:* I-MING CHEN (RAS), *Secretary:* XIANG CHEN (DSCD), JINGANG YI (DSCD), HEIKI VALLERY (RAS), and SEHOON OH (IES)

EDITOR-IN-CHIEF

HUIJUN GAO
Harbin Institute of Technology, China

PAST EDITOR-IN-CHIEF

I-MING CHEN
Nanyang Technological University, Singapore

SENIOR EDITORS

CHIEN CHEAH
Nanyang Technological University, Singapore

DONGMEI CHEN
The University of Texas at Austin, USA

XINKAI CHEN
Shibaura Institute of Technology, Japan

CÉDRIC CLEVY
Femto-St, France

HIROSHI FUJIMOTO
University of Tokyo, Japan

MARINA INDRI
Politecnico di Torino, Italy

SEIICHIRO KATSURA
Keio University, Japan

KENN OLDHAM
University of Michigan, USA

YA-JUN PAN
Dalhousie University, Canada

ZONGXUAN SUN
University of Minnesota, USA

JUN UEDA
Georgia Institute of Technology, USA

HESHENG WANG
Shangai Jiao Tong University, China

TECHNICAL EDITORS

AHMAD AL-DABBAGH
The University of British Columbia, Canada

KUN BAI
Huazhong University of Science and Technology, China

SIMONE BALDI
Southeast University, China

LUCA BASCETTA
Politecnico di Milano, Italy

MOKRANE BOUDAOUD
Sorbonne University, France

RAFFAELLA CARLONI
University of Groningen, The Netherlands

YOUNGSU CHA
Korea University, South Korea

AHMED CHEMORI
LIRMM, France

CHAO CHEN
Monash University, Australia

JIAN CHEN
Southern University of Science and Technology, China

SILU CHEN
Ningbo Inst of Material Tech, Chinese Acad of Sciences, China

XU CHEN
University of Washington, USA

ZHENG CHEN
Zhejiang University, China

LONG CHENG
Institute of Automation, Chinese Academy of Sciences, China

TUHIN DAS
Central Florida University, USA

MICHAEL DEFOORT
University Polytechnic Hauts-de-France (UPHF), France

STEFANO DI GENNARO
University of L'Aquila, Italy

BARIS FIDAN
University of Waterloo, Canada

YAN GU
Purdue University, USA

SOOHEE HAN
Pohang University of Science and Technology, Korea

JONATHAN HEY
Singapore Inst. Manufacturing Technology, Singapore

SOO JEON
University of Waterloo, Canada

HOSHIAR ALI KAFASH
University of Essex, UK

YIANNIS KARAYIANNIDIS
Lund University, Sweden

ERKAN KAYACAN
The University of Oklahoma, USA

SEKI KENTA
Nagoya Institute of Technology, Japan

WONHEE KIM
Chung-Ang University, Korea

YAGUO LEI
Xi'an Jiaotong University, China

BIN LIANG
Tsinghua University, China

MINAS LIAROKAPIS
University of Auckland, New Zealand

PEI-CHUN LIN
National Taiwan University, Taiwan

XINGJIAN LIU
Dalian University of Technology, China

YU LIU
South China University of Technology, China

SANTHAKUMAR MOHAN
Indian Institute of Technology Palakkad, India

NAOKI MOTOI
Kobe University, Japan

ANH-TU NGUYEN
LAMIH-CNRS laboratory, INSA Hauts-de-France, Université Polytechnique Hauts-de-France, France

SUKHO PARK
DGIST, Republic of Korea

SALVATORE PIROZZI
Università degli Studi della Campania "L. Vanvitelli", Italy

MICKY RAKOTONDRABE
ENIT, University of Toulouse, France

JUAN REN
Iowa State University, USA

LEI REN
Beihang University, China

GIANLUCA RIZZELLO
Saarland University, Germany

SPANDAN ROY
IIIT Hyderabad, India

JEONG SEOKHWAN
Sogang University, South Korea

CHAO SHEN
Carleton University, Canada

BARYS SHYROKAU
Delft University of Technology, Netherlands

XIAOSHENG SI
Rocket Force University of Engineering, China

HAO SU
North Carolina State University, USA

WEICHAO SUN
Harbin Institute of Technology, China

YANG TANG
East China University of Science and Technology, China

ANA LUISA TREJOS
Western University, Canada

ANTONIO VISIOLI
University of Brescia, Italy

ARNE WAHRBURG
ABB AG Corporate Research, Germany

CHARLIE C.L. WANG
University of Manchester, UK

WILSON WANG
Lakehead University, Canada

GUANGHUI WEN
Southeast University, China

ZEYANG XIA
Shenzhen Institutes of Advanced Technology, Chinese Academy of Sciences, China

TIANTIAN XU
Shenzhen Institute of Advanced Technology, Chinese Academy of Sciences, China

WEI XU
Chinese Academy of Sciences, China

CHENGUANG YANG
University of the West of England, Bristol, UK

CHUNHUA YANG
Central South University, China

JUN YANG
Loughborough University, UK

JIANYONG YAO
Nanjing University of Science and Technology, China

SE YOUNG (PABLO) YOON
University of New Hampshire, USA

HAOYONG YU
National University of Singapore, Singapore

WENLONG ZHANG
Arizona State University, USA

YONG ZHAO
Northeastern University, China

YE ZHAO
Georgia Institute of Technology, USA

SONGLIN ZHUANG
Yongjiang Laboratory, China

PARTICIPATING ORGANIZATIONS: IEEE
THE AMERICAN SOCIETY OF MECHANICAL ENGINEERS

IEEE OFFICERS

THOMAS M. COUGHLIN, *IEEE President and CEO*
KATHLEEN A. KRAMER, *IEEE President-Elect*
SAIFUR RAHMAN, *IEEE Past President*
FORREST D. WRIGHT, *Director & Secretary*
GERARDO BARBOSA, *Director & Treasurer*
RABAB KREIDIEH WARD, *Director & Vice President, Educational Activities*
DEEPAK MATHUR, *Director & Vice President, Member & Geographic Activities*
SERGIO BENEDETTO, *Director & Vice President, Publication Services and Products*
JAMES E. MATTHEWS III, *Director & President, Standards Association*
MANFRED J. SCHINDLER, *Director & Vice President, Technical Activities*
KEITH A. MOORE, *Director & President IEEE-USA*

ASME 2024 BOARD OF GOVERNORS

TOM KURFESS, *President*
KAREN OHLAND, *Immediate Past President*
THOMAS COSTABILE, *Executive Director/CEO*
ANDREW BICOS, ALMA FALLON, TOMMY GARDNER, SUSAN IPRI BROWN, KATHRYN JABLOKOW, SAM KORELLIS, MONICA MOMAN-SAUNDERS, JARED OEHRING, DAVE SCHLESINGER, PATRICK VIETH, WOLF YEIGH, *Members*

IEEE Periodicals
Transactions/Journals Department

Senior Director, Publishing Operations: DAWN MELLEY
Director, Editorial Services: KEVIN LISANKIE *Director, Production Services:* PETER M. TUOHY
Associate Director, Information Conversion and Editorial Support: NEELAM KHINVASARA
Manager, Journals Production: PATRICK KEMPF *Journals Production Manager:* CHRISTIE INMAN

IEEE/ASME TRANSACTIONS ON MECHATRONICS (ISSN 1083-4435) is published bimonthly by The Institute of Electrical and Electronics Engineers, Inc. Responsibility for the contents rests upon the authors and not the IEEE, the Society/Council, or its members. **IEEE Corporate Office:** 3 Park Avenue, 17th Floor, New York, NY 10016. **IEEE Operations Center:** 445 Hoes Lane, Piscataway, NJ 08854. **NJ Telephone:** +1 732 981 0060. **Price/Publication Information:** To order individual copies for members and nonmembers, please email the IEEE Contact Center at contactcenter@ieee.org. **Copyright and Reprint Permissions:** Abstracting is permitted with credit to the source. Libraries are permitted to photocopy for private use of patrons, provided the per-copy fee of $31.00 is paid through the Copyright Clearance Center, 222 Rosewood Drive, Danvers, MA 01923. For all other copying, reprint, or republication permission, write to Copyrights and Permissions Department, IEEE Publications Administration, 445 Hoes Lane, Piscataway, NJ 08854. Copyright © 2024 by The Institute of Electrical and Electronics Engineers, Inc. All rights reserved. Periodicals Postage Paid at New York, NY and at additional mailing offices. **Postmaster:** Send address changes to IEEE/ASME TRANSACTIONS ON MECHATRONICS, IEEE, 445 Hoes Lane, Piscataway, NJ 08854. GST Registration No. 125634188. CPC Sales Agreement #40013087. Return undeliverable Canada addresses to: Pitney Bowes IMEX, P.O. Box 4332, Stanton Rd., Toronto, ON M5W 3J4, Canada. IEEE prohibits discrimination, harassment and bullying. For more information, visit http://www.ieee.org/nondiscrimination. Printed in U.S.A.

Digital Object Identifier 10.1109/TMECH.2024.3470411

IEEE/ASME TRANSACTIONS ON
MECHATRONICS

OCTOBER 2024 VOLUME 29 NUMBER 5 IATEFW (ISSN 1083-4435)

REGULAR PAPERS

Tight-Space Maneuvering of a Hybrid-Driven Robotic Fish Using Backstepping-Based Adaptive Control ..... *S. Li, Z. Wu, S. Dai, J. Wang, M. Tan, and J. Yu* 3219
An Autonomous Aerial Refueling Controllable Drogue With Adjustable Strut Angle: Control and Test ..... *Z. Meng, J. Bai, B. Yan, and S. Li* 3232
Electromagnetic-Actuated High-Resolution Tactile Device With Actuating and Sensing Capabilities ..... *Y. Guo, C. Shang, Q. Tong, Y. Zhang, Z. Peng, and D. Wang* 3243
Antagonistic Pump With Multiple Pumping Modes for On-Demand Soft Robot Actuation and Control ..... *J. Zhou, W. Chen, H. Cao, Q. He, and Y. Liu* 3252
Design of Axial Flux Permanent Magnet Machine for Miniaturized Integrated Starter–Generator System Applications ..... *G. Li, Y. Xu, Y. Zhang, and F. Xu* 3265
A 7 cm-Scale Spherical Underwater Robot Using Piezoelectric Double-Jet Actuator for Deep-Sea Environment ..... *X. Zhou, W. Chen, K. Li, H. Zheng, B. Liu, S. Chen, L. Zhang, and N. Qi* 3277
Hierarchical Viewpoint Planning for Complex Surfaces in Industrial Product Inspection ..... *S. Wang, Y. Tong, X. Shang, and Z. Zhang* 3289
Hierarchical Cloud-Supported Control Framework for Space Teleoperation With Networked-Follower Robots ..... *J.-Z. Xu, M.-F. Ge, Z.-W. Liu, H. Yan, C.-D. Liang, and Y.-D. Wu* 3300
Cavity-Membrane-Based Water-Jet Bio-Inspired Thruster With Multidirectional Accelerating Capability ..... *X. Wang, X. Pei, R. Zhu, T. Hou, and X. Yang* 3312
Force-Closure Analysis of Multilink Cable-Driven Redundant Manipulators Considering Cable Coupling and Friction Effects ..... *Z. Liang, B. Jiang, P. Quan, H. Lin, Y. Lou, and S. Di* 3324
Safety Assessment Approach to UAVs Based on Profust Safety Index and HIL Simulation ..... *X. Dai, J. Tu, and Q. Quan* 3336
Fixed-Time Safe-by-Design Control for Uncertain Active Vehicle Suspension Systems With Nonlinear Reference Dynamics ..... *Z. Zhou, M. Zhang, H. Liu, and X. Jing* 3348
Torque-Bounded Admittance Control With Implicit Euler Realization of Set-Valued Operators ..... *X. Yuan, Y. Ding, X. Xiong, and Y. Lou* 3360
Vacuum-Driven Parallel Continuum Robots With Self-Sensing Origami Linkages ..... *W. Fan, J. Wang, Z. Zhang, G. Chen, and H. Wang* 3370
A Nonresonant and Frequency Up-Conversion Motion Converter for Footstep Energy Harvesting ..... *Q. Pan, S. Bai, Z. Long, Y. Zheng, Y. Wang, P. Chirarattananon, and Z. Yang* 3381
Optimization of the Control Performance of a Novel 3/2 Water Proportional Directional Valve With a Special Position Following Servo Mechanism ..... *Y. Liao, W. Zhao, J. Feng, and Z. Lian* 3391
Design of a Parallel Wrist Rehabilitation Robot and Analysis of Physiological Effect on Training ..... *L. Zhang, Z. Yu, P. Su, J. Li, and R. Ge* 3401
Pneumatic Exoskeleton Joint With a Self-Supporting Air Tank and Stiffness Modulation: Design, Modeling, and Experimental Evaluation ..... *L. Mišković, M. Dežman, and T. Petrič* 3415
Design Optimization of Pyramid-Shaped Transmission System for Multiarm Concentric-Tube Robots ..... *C. Zhang, G. Cen, X. Yang, X. Xu, M. Q.-H. Meng, S. Song, and J. Wang* 3427

(Contents Continued on Page 3217)

A JOINT PUBLICATION OF THE IEEE INDUSTRIAL ELECTRONICS SOCIETY,
THE IEEE ROBOTICS AND AUTOMATION SOCIETY,
AND THE ASME DYNAMIC SYSTEMS AND CONTROL DIVISION

(Contents Continued from Front Cover)

Design of Novel Double-Stator Switched Reluctance Motor Drive System for Electric Vehicles ..... *W. Yan, D. Zhang, K. Zhang, H. Chen, H. Li, W. Wang, and Q. Wang* 3439
Design and Control of a Collision-Resilient Aerial Vehicle With an Icosahedron Tensegrity Structure ..... *J. Zha, X. Wu, R. Dimick, and M. W. Mueller* 3449
Motion State Estimation of Preceding Vehicles With Packet Loss and Unknown Model Parameters ..... *Y. Wang, H. Chen, G. Yin, Y. Mo, N. de Boer, and C. Lv* 3461
Dual Weighted-Class Adversarial Network for Rotary Machine Fault Diagnosis Using Multisource Domain with Class-Inconsistent Data ..... *S. Yang, B. Lei, Q. Wang, J. Chang, X. Kong, and H. Cheng* 3473
Taylor Neural Network for Unseen Object Instance Segmentation in Hierarchical Grasping ..... *K. Fu, X. Dang, and Y. Zhang* 3485
Fault Diagnosis of Multichannel Bearing-Rotor System via Multistructure Collaborative Discriminative Embedding ..... *J. Yuan, R. Zhao, K. Wei, P. Chen, and T. He* 3497
Robust Photogrammetry Sensor-Based Real-Time Pose Control of Industrial Robots ..... *E. Zakeri and W.-F. Xie* 3509
Multifingered Grasp Planning Based on Gaussian Process Implicit Surface and its Partial Differentials ..... *H. Liu, S. K. Sampath, N. Wang, and C. Yang* 3522
Chained Spatial Beam Constraint Model: A General Kinetostatic Model for Tendon-Driven Continuum Robots ..... *Y. Chen, S. Yao, M. Q.-H. Meng, and L. Liu* 3534
Physics-Informed Neural Network for Spacecraft Lithium-Ion Battery Modeling and Health Diagnosis ..... *H. Fu, Z. Liu, K. Cui, Q. Du, J. Wang, and D. Shi* 3546
MCOV-SLAM: A Multicamera Omnidirectional Visual SLAM System ..... *Y. Yang, M. Pan, D. Tang, T. Wang, Y. Yue, T. Liu, and M. Fu* 3556
Deep Koopman Operator-Informed Safety Command Governor for Autonomous Vehicles ..... *H. Chen, X. He, S. Cheng, and C. Lv* 3568
A 6-DOF Extended Unified Wrench Model for Maglev Planar Motor ..... *C. Hu, H. Fu, Y. Zhu, and M. Zhang* 3579
Spatial Position–Force Perception for a Soft Parallel Joint via Pressure-Deformation Self-Sensing ..... *Y. Su, X. Chen, Z. Fang, D. Liu, J. Lam, and Z. Wang* 3590
Adaptive Conditional Disturbance Negation-Based Nonsmooth-Integral Control for PMSM Drive System ..... *J. Sun, S. Xu, S. Ding, Z. Pu, and J. Yi* 3602
Fault Detection and Diagnosis Based on Interactive Multi-Model Moving Horizon Estimation and Neuro-Tire Model ..... *B. Zhang, S. Lu, W. Xie, and F. Xie* 3614
A Human Finger-Inspired Shape-Locking Pneumatic Gripper Enabled by Folding Laminar Jamming Structure ..... *X. Yin, P. Zhou, J. Xie, S. Tang, S. Wen, J. Zhang, and J. Li* 3626
Analysis of Hybrid Rotor PM Motor Caused by Atypical Vibration Sources ..... *G. Xu, Y. Cai, Q. Chen, Z. Jia, Z. Liu, and H. Shi* 3638
A Real-Time Maximum Tire-Road Friction Tracking Control Method for Aircraft Braking System With Disturbance Compensation ..... *Z. Wang, X. Liu, D. Sun, N. Bai, P. Qi, and Z. Jiao* 3649
Grasping Control for Kinematically Redundant Parallel Robots With a Remotely Operated Gripper ..... *Z. Zhou, T. S. Nguyen, and C. Gosselin* 3661
Sensorless Ground Reaction Force Observation With Disturbance Compensation in Heavy-Legged Robots ..... *S. Liu, Z. Pan, S. Zhou, Z. Niu, and R. Wang* 3672
Mathematical Modeling of an Armature Assembly in a Flapper–Nozzle Servo Valve Based on the Finite Element Method ..... *X. Lv, J. Yang, Q. Qi, J. Peng, and C. Wang* 3684
Design of a Square Rotor Driven Pneumatic Stepper Actuator for MR-Guided Therapy ..... *H. Liang, W. Zuo, and Z. T. H. Tse* 3696
Design and Evaluation of an Integrated Active and Passive Body Weight Support System for Variable Gravity and Inertia Compensation ..... *J. Zhang, A. Zhu, P. Ma, C. Zheng, X. Zhang, and G. Cao* 3706
High-Order Fully Actuated Control Approach for Servo Systems Based on Dynamical Compensator and Extended State Observer ..... *P. Li and G.-R. Duan* 3717
A MOEMS Safety and Arming Device Based on Coupled Electrothermal and Centrifugal Actuators ..... *X. Kong, Y. Cao, W. Ma, H. Zhu, F. Xiu, L. Liu, W. Nie, and Z. Xi* 3727
Analysis of No-Load Operation of Cup Winding Permanent Magnet Synchronous Machine in Flywheel Energy Storage Application ..... *M. Sun, Y. Xu, and G. Li* 3739
Mechanism and Validation of a Long-Stroke Ultraprecision Atmospheric Pressure Driven Actuator ..... *Y. Zhang, X. Zhang, D. Xie, S. Cao, and B. Yang* 3750

(Contents Continued on Page 3218)

A Human Finger-Inspired Shape-Locking Pneumatic Gripper Enabled by Folding Laminar Jamming Structure

Xuanchun Yin, *Member, IEEE*, Pengyu Zhou, Junliang Xie, Shijie Tang, Sheng Wen, Jiantao Zhang, and Jiehao Li, *Member, IEEE*

***Abstract*—Bio-inspired soft grippers based on impactive gripping with the advantages of flexibility and universality have been widely used in take-and-place tasks. However, this type of gripper has the risk of breaking fragile objects with deformable surfaces due to the inevitable impactive force applied to the objects. Inspired by the grasping method of human fingers, this article presents a gripper containing two shape-locking fingers that can simultaneously control the span and grasping force to reduce the impact and grasp fragile objects safely. The shape-locking finger composes of three parts, including a soft pneumatic actuator, a folding laminar jamming structure, and a typical laminar jamming structure and the function of the three parts are driving, locking the shape, and improving the stiffness of the finger, respectively. In addition, combined with finite element analysis, we establish a theoretical model to predict the finger's bending angle and tip force, and the experimental results demonstrate the reliability of the model. Through a specific grasping process: pregrasp, shape-locking, and improving the grasping force, the controllable span and force (CSF) gripper can safely grasp deformable objects, such as a plastic cup with a 100-g weight, tofu, cake, mochi, and jelly, which shows that the CSF gripper has the potential for fragile foods tasks.**

***Index Terms*—Controllable span and force (CSF), fragile foods, modeling of soft pneumatic gripper (SPG), shape-locking.**

Manuscript received 2 October 2023; revised 12 December 2023; accepted 2 January 2024. Date of publication 31 January 2024; date of current version 17 October 2024. Recommended by Technical Editor G. Carbone and Senior Editor J. Ueda. This work was supported in part by the National Natural Science Foundation of China under Grant 61773171 and Grant 32271985, in part by the Characteristic innovation projects of universities in Guangdong province under Grant 2019KTSCX016 and Grant 2019KZDZX1002, and in part by Guangdong province education project, under Grant 2018KTSCX019. *(Corresponding authors: Xuanchun Yin; Jiantao Zhang.)*

Xuanchun Yin, Pengyu Zhou, Junliang Xie, Sheng Wen, and Jiehao Li are with the College of Engineering, South China Agricultural University, Guangzhou 510642, China (e-mail: xc_yin@scau.edu.cn; pengyu@stu.scau.edu.cn; 20212156009@stu.scau.edu.cn; vincen@scau.edu.cn; jiehao.li@ieee.org).

Shijie Tang is with the School of Mechatronic Engineering and Automation, Foshan University, Foshan 528011, China (e-mail: 2112051018@stu.fosu.edu.cn).

Jiantao Zhang is with the College of Mathematics and Informatics, South China Agricultural University, Guangzhou 510642, China (e-mail: zhangjiantao@yeah.net).

This article has supplementary material provided by the authors and color versions of one or more figures available at https://doi.org/10.1109/TMECH.2024.3352643.

Digital Object Identifier 10.1109/TMECH.2024.3352643

I. Introduction

ROBOTIC grippers have been applied in various fields, such as take-and-place tasks [1], medical devices [2], and human–machine interaction [3]. Rigid grippers are characterized by high load and precise repetitive motion in take-and-place tasks. However, due to the low safety performance, the rigid grippers require extra sensors and sophisticated control when grasping fragile objects. Compared to rigid grippers, grippers made of soft materials have better protection for fragile objects by different grasping methods [4].

Soft robotic grippers based on impactive gripping have attracted considerable attention, and most of them are designed in bionic forms [5], [6]. Inspired by an octopus arm, a tapered gripper with suction cups is developed to grip, move, and place different types of objects, including a fragile object: an egg [7]. Equipping with suction cups for a soft gripper is an effective method to grasp fragile objects, and it helps to hold diverse shapes, sizes, and poses objects [8]. However, applying the suction cup is limited to objects with rigid surfaces because suction may damage objects with deformable surfaces. A gecko-inspired adhesion [9], [10] and electroadhesion [11] can provide enough shear or normal adhesion to grip these objects without a normal squeezing force. Whereas, the gecko-inspired adhesion gripper depends on an additional preloading mechanism to assist in adhering, which may lead to unpredictable deformation or damage to the object. Moreover, the force generated by electroadhesion needs high voltage, which is challenging to the stability of materials. Therefore, to ensure the versatility of the gripper and extraordinary protection for deformable fragile objects, such as tofu, cake, and jelly, impactive gripping is a suitable approach through reducing the impactive force and pinching carefully.

For example, to solve the limitation of handling fragile objects, including tofu, a shape-adaptive parallel gripper first matches the target object with an extremely low stiffness skin and then transits the stiffness of the skin from a soft to a rigid state to hold [12]. It is an efficient method to apply an extremely low stiffness gripper surface to reduce the impactive force. Impactive

1083-4435 © 2024 IEEE. Personal use is permitted, but republication/redistribution requires IEEE permission.
See https://www.ieee.org/publications/rights/index.html for more information.

Authorized licensed use limited to: XIDIAN UNIVERSITY. Downloaded on October 18,2024 at 07:13:14 UTC from IEEE Xplore. Restrictions apply.

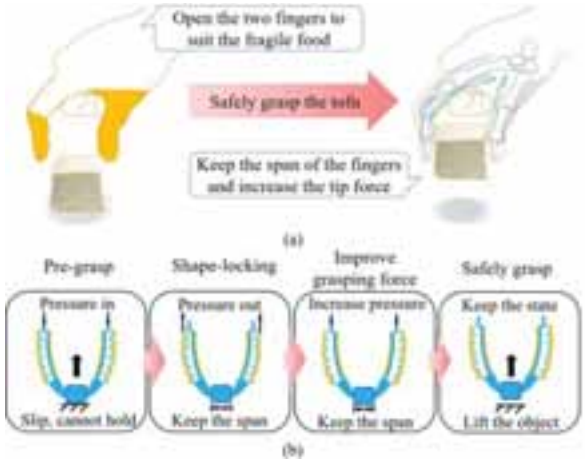


Fig. 1. (a) Strategy of humans' grasping tofu. (b) Grasping process of the CSF gripper inspired by humans.

gripping soft pneumatic grippers (SPGs), with the advantages of versatility, high forces, robustness, safety, and a relatively simple structure, have been widely used in different fields [5]. Although soft pneumatic actuators (SPAs) are generally made of soft silicone rubber, an extremely low modulus elastomer makes it hard to sustain high input pressure to output enough force. Li et al. [13] developed a precharged pneumatic gripper combined with tendon actuation that can bend slowly to grasp delicate objects, such as tofu, by controlling the tendon's releasing speed and displacement. It shows excellent cooperation between fluid and tendon actuation, realizing a controllable bending speed and displacement of the soft finger, but the volume of the gripper becomes bulky. Therefore, it is an effective way to reduce the impact on fragile objects by controlling the finger's bending speed or displacement (bending angle) for two-finger SPGs.

The human finger provides abundant inspiration for robotic gripper design, such as tendon actuation [14], joints [15], and grasping strategies [16]. A robotic gripper even can be designed as an anthropomorphic hand [17]. Inspired by the hybrid design of human fingers, Zhu et al. [18] developed a rigid–soft coupled finger that can grasp tofu by activating the soft actuator (to touch the object gently) and the rigid actuator (to provide sufficient grasping force) in sequence. The human hand consists of bones, joints, ligaments, tendons, muscles, nerves, and blood vessels [19], [20]. The tendons can be divided into two categories: 1) extensor tendons on top of the hand and 2) flexor tendons on the palm side. The extensor tendons allow each finger to straighten, and the flexor tendons allow the finger and thumb to flex or bend to grip objects in the palm. The two types of tendons enable human hands to exhibit excellent ability to grasp fragile foods. To safely grasp tofu, humans will first open the fingers to suit the size of the object and then improve the grasping force with the span unchanged through the antagonism between the extensor tendons and flexor tendons [Fig. 1(a)]. In the grasping process, the flexor tendons provide enough grasping force to hold the object, while the extensor tendons keep the bending state of the fingers. Inspired by the grasping process of humans, we developed a method for a SPG to grasp a fragile object with deformable surfaces, as shown in Fig. 1(b). First, the gripper gently touches and suits the size of the object at a relatively low input pressure, which causes the object to be hardly held. Second, the gripper keeps the span constant by locking the shape of the finger. Finally, the gripper improves the grasping force by increasing the input pressure. Eventually, it lifts the object safely and stably.

The function of shape locking is to enhance the stiffness of the soft finger essentially. Variable stiffness of soft robots can effectively improve the capacity to interact with the environment, and it can be achieved by different technologies, including shape memory materials, electroactive polymers, material jamming, and so on [21]. Jamming structures are typically composed of grains, fibers, or layers. Layer jamming structures (i.e., laminar jamming structures) are widely used to enhance the stiffness to lock the finger's bending state and improve the grippers' load performance because of their unique features of low-cost, lightweight, easy-to-fabricate, and fast response time [22], [23], [24]. With negative pressure applied, the increased frictional interactions of laminates will dramatically enhance the bending stiffness of laminar jamming structures. Therefore, employing a laminar jamming structure is promising to lock the bending curvature of a soft pneumatic finger.

In this article, we presented a simultaneously controllable span and force (CSF) gripper to grasp fragile foods inspired by the pinching process of human fingers for those objects with deformable surfaces. Different from using an extremely soft material and rigid actuators, this method reduces the impactive force of the SPG by mimicking the grasping strategy of human fingers. The shape-locking finger controls both the bending curvature and the tip force simultaneously with the help of the rigid–soft transformation ability of the laminar jamming structure. The laminar jamming structure is improved and folded to adapt to the SPA, utilizing the deployable ability of origami. Moreover, the folding laminar jamming structure (FLJS) is activated to maintain the shape of the finger, different from its typical application of improving load performance. In addition, an analytical model combined with finite element analysis (FEA) is established to predict the soft finger's bending angle and output force in different pressure conditions. In addition, experiments have demonstrated the model's reliability, the function of the CSF gripper, and the ability to safely grasp fragile foods, such as tofu, jelly, cake, and mochi. The main contributions of this article are summarized as follows.

1) Taking inspiration from the grasping process of humans, we present a shape-locking pneumatic gripper that can simultaneously control the span and force to reduce the impactive force when grasping fragile foods.
2) We established an FEA-based theoretical model to predict the finger's bending angle and output force in different pressure conditions, showing a modeling method for large chamber gap SPAs with laminar jamming structures.

The rest of this article is organized as follows. Section II describes the design of the CSF gripper and shape-locking finger. Section III establishes a theoretical model to characterize the relation of the finger's bending angle and input pressure and derive the moment of inertia of the FLJS, followed by the tip

Authorized licensed use limited to: XIDIAN UNIVERSITY. Downloaded on October 18,2024 at 07:13:14 UTC from IEEE Xplore. Restrictions apply.

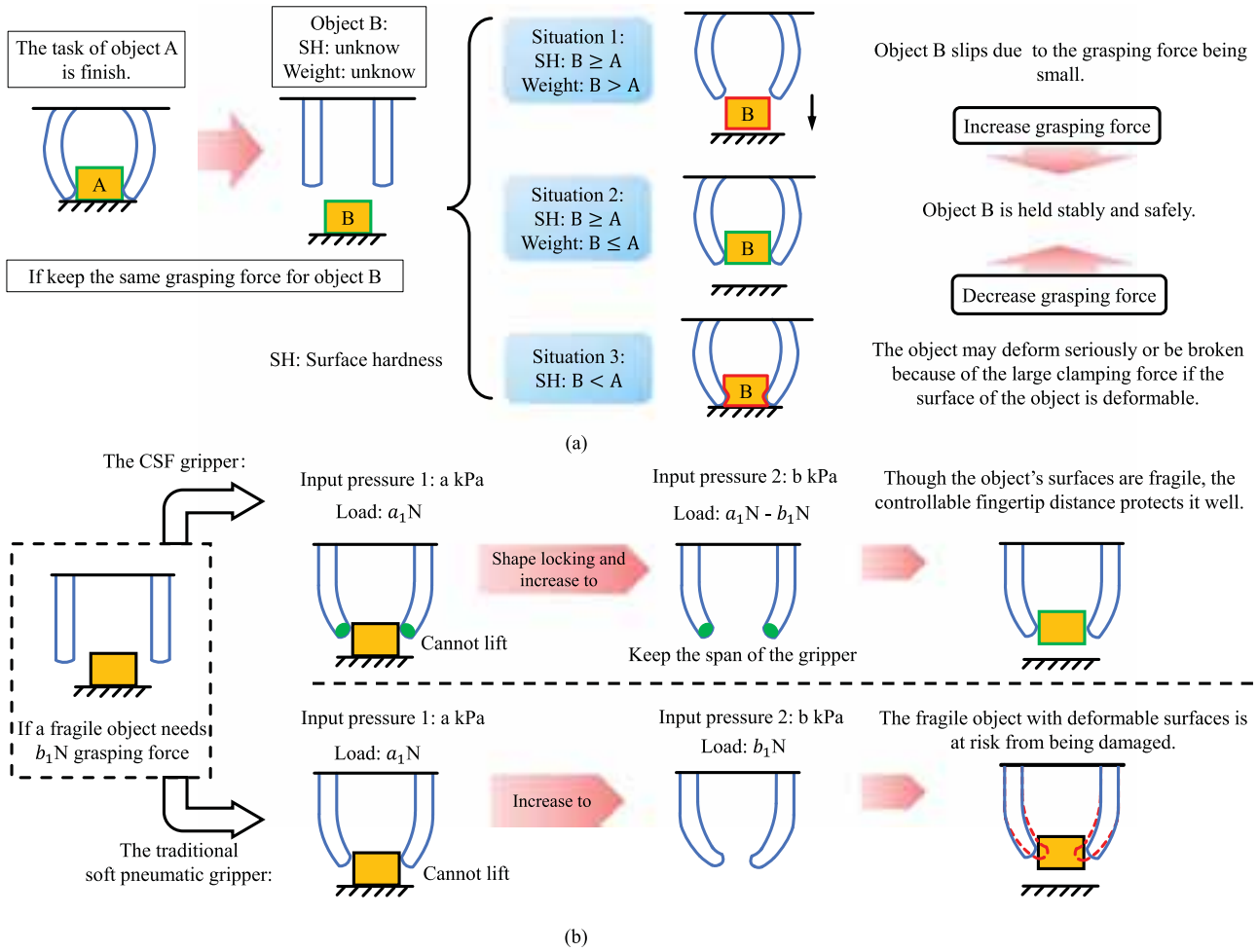


Fig. 2. Design of the CSF gripper. (a) Traditional soft pneumatic gripper will face three situations when beginning to grip the next object whose information is unknown. (b) Comparison of the CSF gripper and the traditional soft pneumatic gripper when they grasp a fragile object.

force model. In Section IV, experiments and discussions are conducted to demonstrate the model's reliability and the capacities of the gripper. Finally, Section V concludes this article.

II. Design

A. Design of the CSF Gripper

SPGs are widely used in take-and-place tasks, especially to take fragile objects. As shown in Fig. 2(a), the gripper faces the problem of how much force should be used to grip object B after finishing the task of object A. We assume that the surface hardness (SH) and the weight information of object B are unknown, and its size is the same as object A. Three situations will happen if a traditional SPG begins gripping object B with the grasping force unchanged.

1) *Situation 1:* SH: B $\geq$ A, weight: B $>$ A. The object may slip during holding due to the grasping force not being enough to lift the object.
2) *Situation 2:* SH: B $\geq$ A, weight: B $\leq$ A. The object can be held stably and safely.
3) *Situation 3:* SH: B $<$ A. The object may deform seriously or be broken because of the large clamping force if the surface of the object is deformable.

A traditional SPG can increase the force in situation 1 or decrease the force in situation 3 to safely hold the object. In general, the gripper with a soft body has good protection for target objects, making soft grippers can ignore the applied force on the objects when contacting objects. However, if a fragile object with highly deformable surfaces whose stiffness is smaller than the common soft materials, most traditional SPGs face the problem of large impactive force on the object. Therefore, it is essential to reduce the impact on objects for an impactive gripping griper. To decrease the impactive force and hold the fragile food stably, we developed a CSF gripper that can improve the grasping force with the span of two fingers constant, inspired by the pinching process of human fingers for those objects with deformable surfaces. As shown in Fig. 2(b), we assume that a traditional SPG and the CSF gripper have the same coefficient of friction, and the fragile object needs b_1 N grasping force to be held. A relatively low input pressure can gently touch and suit the size of the object, but the generated load a_1 N (is smaller than b_1 N) cannot lift the object. Before increasing the input pressure, the shape of the fingers is locked to keep the span of the CSF gripper constant. Eventually, with a suitable span, the CSF gripper enhances the force to b_1 N to hold the object, similar to the grasping method of humans. In contrast, the span of

Authorized licensed use limited to: XIDIAN UNIVERSITY. Downloaded on October 18,2024 at 07:13:14 UTC from IEEE Xplore. Restrictions apply.

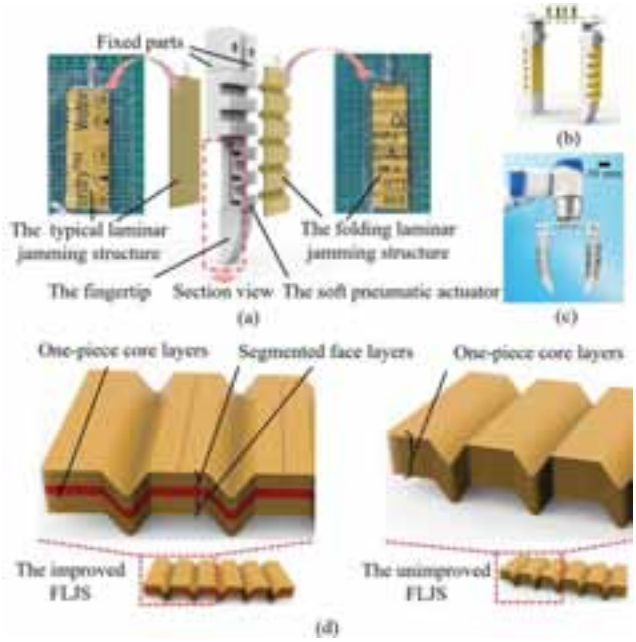


Fig. 3. Design of the shape-locking finger. (a) Explosive view of the shape-locking finger. (b) CAD model of the CSF gripper. (c) Prototype of the CSF gripper. (d) Improved and unimproved FLJS.

traditional SPGs decreases with the tip force increasing, which has a risk of damaging the object with deformable surfaces. In short, compared to the one span corresponding to one grasping force, the CSF gripper can output a range of forces with a constant span, providing enough load and protectiveness for objects.

B. Design of the Shape-Locking Finger

The CSF gripper consists of two shape-locking fingers and an assembled board [see Fig. 3(a)], and the computer-aided design (CAD) model and photographs of the gripper are shown in Fig. 3(b) and (c). The shape-locking finger is composed of an SPA, an FLJS, a typical LJS (TLJS), and a fingertip. Due to the rigid–soft transformation capacity of laminar jamming structures, they are popularly applied in the soft gripper and activated to improve the stiffness and load performance. Different from the variable stiffness role, we design an order of use: inputting pressure, activating the FLJS, and increasing the pressure, achieving the shape-locking function of the soft finger. Therefore, the target object can be held safely and steadily through the specific grasping process [shown in Fig. 1(b)]: pregrasp (with relatively low pressure), shape-locking (by activating the FLJS), and improving the grasping force (by increasing the input pressure). In addition, the CSF gripper can be used as a typical soft gripper by deactivating the FLJS when grasping objects that are not easily deformed. A laminar jamming structure is folded and then installed on the top surface of the SPA's chamber, which achieves a compact structure and an ideal locking result of the finger without affecting the bending motion of the SPA. However, the FLJS will generate a restoring torque in the folded state, resisting the SPA from the bending state to the ideal initial state: 0°. To reduce the influence of this recovery moment, the FLJS is improved by employing a sandwich structure, including one-piece core layers and segmented face layers [see Fig. 3(d)]. Due to the maximum bending angle of the SPA limited by the FLJS, the total length of the FLJS and the length of the chamber gap can be changed to adjust the bending range of the finger. Moreover, to enhance the load performance of the finger, a TLJS is used as a variable stiffness mechanism, which is assembled on the bottom of the SPA.

III. Theoretical Model

Different solutions have been developed to solve the modeling issue of soft robots [25], [26]. As typical actuators used in soft grippers, SPAs have been studied and established the theoretical model of bending angle and output force, such as single chamber actuators [27], [28], multichambers [29], [30], [31], and symmetrically distributed chambers [32]. However, the multichambers researches mainly focus on small chamber gap and pure SPA grippers. Thus, this part introduces a theoretical model for multichamber SPA with a large chamber gap (the wall of chambers cannot contact each other when inflated) and equipping with laminar jamming structures. Section A presents the model of the finger's bending angle when the variable stiffness mechanism works and not works. Section B deduces the moment of inertia of the FLJS. Section C calculates the tip force of the finger applied to the object.

A. Modeling the Bending Angle of the Finger

With the TLJS in a deactivated state or an activated state, the movement of the finger shows different characteristics. Because the SPA dominates the finger's motion when the variable stiffness mechanism not working, and the motion of the SPA is affected by the TLJS when the TLJS (variable stiffness mechanism) is activated. Therefore, the model of the bending angle is established into two parts as follows.

1) Variable Stiffness Mechanism Off: The FLJS and the TLJS are considered inextensible and compliant materials when deactivated. The expansion of the SPA's chambers dominates the bending motion of the finger when the variable stiffness mechanism is off. To constrain the radial expansion of SPAs, measures can be adopted, such as adding fiber windings and separating chambers by rigid ribs [27], [28], [29]. In this article, the radial expansion of the actuator is restricted by the FLJS and TLJS. Therefore, the radial expansion of the SPA is considered negligible, and the axial expansion is analyzed to derive the relationship between the input pressure and the bending angle. Fig. 4(a) and Table I show the parameters of the fingers. The plane relation can be written as [33]

$$P = \frac{T}{\rho} \tag{1}$$

where P is the input pressure of the finger. ρ is the radius of the deformed chamber wall. T is the line tension.

The chamber's lateral wall is regarded as a plane strain membrane, and its line tension T is related to the strain energy function W. Due to the material being considered incompressible, the extension ratio in the thickness direction is equal to $1/(\lambda_\xi \lambda_\phi)$.

Authorized licensed use limited to: XIDIAN UNIVERSITY. Downloaded on October 18,2024 at 07:13:14 UTC from IEEE Xplore. Restrictions apply.

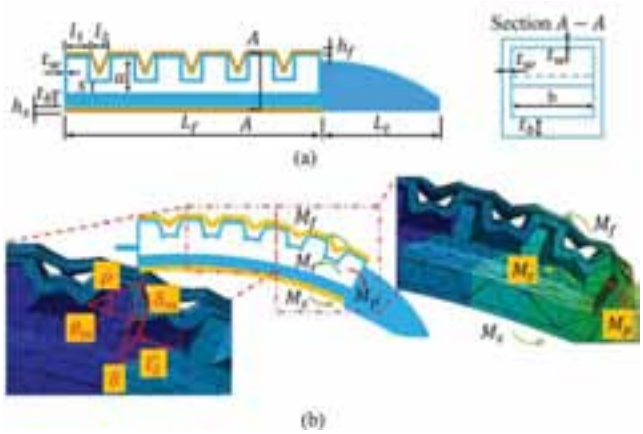


Fig. 4. Schematic for modeling the bending angle of the shape-locking finger. (a) Geometric parameters of the finger in the undeformed state. (b) Moments of the finger in a bending state.

TABLE I
PARAMENTERS OF THE SHAPE-LOCKING FINGER

Parameters	Symbol	Value	Unit
The number of the chamber	N	6	
The thickness of the chamber	t_w	2	mm
The inside height of the chamber	a	10	mm
The inside width of the chamber	b	34	mm
The gap height of the SPA	s	2	mm
The thickness of the SPA's bottom	t_b	7	mm
The number of the TLJS layers	n_2	12	mm
The length of the chamber gap	l_2	8	mm
The length of the finger tip	L_t	42	mm

The lateral chamber wall is regarded as an equi-biaxial stretch, meaning that $\lambda_\xi = \lambda_\phi = \lambda$ and $T_\xi = T_\phi = T$ at the pole are always right [34], [35]. Therefore, the tension of a chamber lateral wall is expresses as follows:

$$\begin{cases} T = \frac{2t_w}{\lambda}\left(\lambda^2 - \frac{1}{\lambda^2}\right)\left(\frac{\partial W}{\partial I_1} + \frac{\partial W}{\partial I_2}\right) \\ I_1 = \lambda_\xi^2 + \lambda_\phi^2 + 1/(\lambda_\xi\lambda_\phi)^2 \\ I_2 = (\lambda_\xi\lambda_\phi)^2 + 1/\lambda_\xi^2 + 1/\lambda_\phi^2 \end{cases} \tag{2}$$

where I_1 and I_2 are the first and second invariants of the left Cauchy–Green tensor, respectively. t_w, λ_ϕ, and λ_ξ are the thickness of the chamber wall, the longitudinal stretch, and the latitudinal stretch, respectively. The strain energy density of the Neo-Hookean (NH) model is given as

$$W = \frac{\mu}{2}(I_1 - 3) \tag{3}$$

where μ is the shear modulus of the material. Therefore, we get the following formulas:

$$\begin{cases} T = \mu t_w\left(\lambda - \frac{1}{\lambda^3}\right) \\ \lambda = \frac{\theta_m}{\sin\theta_m} \end{cases} \tag{4}$$

where θ_m is the maximum angle of the chamber wall at the clamped edge.

As shown in Fig. 4(b), the radius of the deformed chamber wall ρ is expressed as follows:

$$\rho = \frac{R_e^2 + \delta_m^2}{2\delta_m} \tag{5}$$

where R_e is the equivalent radius of the chamber's lateral wall, and $R_e = \sqrt{\frac{ab}{\pi}}$. δ_m is the max deflection of the chamber wall, and $\delta_m = a \cdot \tan(\frac{\theta_m}{2})$. a and b are inside height of the chamber and the inside width of the chamber, respectively. θ_m is the maximum angle of the chamber wall at the clamped edge. The deflection of the chamber wall δ can be calculated by the geometric relation

$$\delta = \frac{2s}{a}\delta_m. \tag{6}$$

The bending curvature of the SPA can be considered uniform [27], [29], [32]. Therefore, the relation of the bending angle θ and δ in deformed state can be written as follows:

$$\theta\ (R + h_s + t_b + s) = Nl_1 + (N-1)\,l_2' + 2\,(N-1)\,\delta \tag{7}$$

where R, h_s, t_b, and s are the parameters of the finger shown in the Fig. 4. Furthermore, N, l_1, and l_2' are the number of the chamber, the length of single chamber, and the length of chamber's gap when the finger is working, respectively. θ_m and l_2' can be obtained by the FEA results. Eventually, the bending angle θ of the finger can be written as follows:

$$\theta = \frac{Nl_1 + (N-1)\,l_2' + 2\,(N-1)\,\delta - L_f}{h_s + t_b + s}. \tag{8}$$

2) Variable Stiffness Mechanism On: The TLJS will generate a resistive moment to the SPA when activated, which improves the stiffness of the finger, allowing the finger to withstand a larger input pressure. Thus, the model of the bending angle is established based on the equilibrium moment [see Fig. 4(b)]

$$M_p - (N-1)\,M_r - M_s - M_f = 0 \tag{9}$$

where M_p is the moment generated by the internal air pressure that works on the SPA, M_r is the restoring moment of each gap layer of the SPA, M_f is the resistive moment of the FLJS, and M_s is the resistive moment of the TLJS.

The moment M_p generated by the internal air pressure can be expressed as follows [27]:

$$M_p = P\,(a-s)\,b\left(\frac{1}{2}a + \frac{1}{2}s + t_b\right). \tag{10}$$

The restoring moment M_r of each gap layer of the SPA can be written as follows:

$$M_r = \frac{E_r I_r}{R_r} \tag{11}$$

where E_r is the Young's modulus of the rubber elastomer. I_r is the moment of inertia of the gap layer, and $I_r = \frac{bt_w^3}{12}$. R_r is the radius of the deformed gap layer

$$\begin{cases} R_r = \frac{T}{P} \\ T = \mu t_w\left(\lambda - \frac{1}{\lambda^3}\right) \\ \lambda = \frac{\theta_r}{\sin\theta_r} \end{cases} \tag{12}$$

Authorized licensed use limited to: XIDIAN UNIVERSITY. Downloaded on October 18,2024 at 07:13:14 UTC from IEEE Xplore. Restrictions apply.

TABLE II
PARAMENTERS OF THE FLJS

Parameters	Symbol	Value	Unit
The number of the FLJS layers	n_1	10	
The thickness of one sandpaper	h_0	0.167	mm
The length of the SPA	L_f	100	mm
The length of one chamber	l_1	10	mm
The length of one part of the FLJS	l_b	8	mm

where θ_r is the bending angle of the gap layer.

The resistive moment M_s of the variable stiffness mechanism can be expressed as follows:

$$\begin{cases} M_s = \kappa E_s I_{s,on} \\ I_{s,on} = \frac{b(n_2 h_0)^3}{12} \end{cases} \tag{13}$$

where E_s is the Young's modulus of the sandpaper. κ is the bending curvature of the laminar jamming structure. $I_{s,on}$ is the moment of inertia of the TLJS when it is working. n_2 is the TLJS's number of layers.

Different to the function of the TLJS, the FLJS is in inactive state when the finger bends. Therefore, the resistive moment of the FLJS can be calculated as follows:

$$M_f = \kappa_f \, E_s I_{\text{off}} \tag{14}$$

where κ_f is the bending curvature of the FLJS, and $\kappa_f = \frac{1}{R+h_s+t_b+a+t_w}$. I_{off} is the moment of inertia of the FLJS.

B. Modeling the FLJS

The FLJS consists of a thermoplastic polyurethane (TPU) enveloper, sandpapers (P15000, 3M), and a 4-mm outer diameter PU tube, and these components are heat-sealed by a heat press machine. To obtain the moment of inertia of the FLJS, this part presents the modeling of the FLJS.

1) FLJS in Activated State: To maximize the performance of the FLJS, the FLJS is designed to be used in preslip regime, meaning that all sections are cohesive [36]. Fig. 5 shows the schematic diagrams used for analyzing the FLJS, and the FLJS can be regarded as a simply supported beam with a variable moment of inertia. A part of the FLJS is utilized to calculate the variable moment of inertia [Fig. 5(a)]. To simplify the analytical model, an equivalent simply supported beam with a constant moment of inertia is presented [see Fig. 5(b)] [37]. Table II lists the parameters of the FLJS.

A piecewise function $I_{on}(x)$ can denote the moment of inertia of the FLJS from the cross-section to the clamped end, and it can be expressed as follows:

$$I_{on}(x) = \begin{cases} I_{on1}(x) & (0, l_1) \\ I_{on2}(x) & \left(l_1,\ l_1 + l_b \sin\frac{\alpha}{2}\right) \\ I_{on3}(x) & \left(l_1 + l_b \sin\frac{\alpha}{2},\ l\right) \end{cases} \tag{15}$$

where $I_{on1}(x)$, $I_{on2}(x)$, and $I_{on3}(x)$ are the moment of inertia in segment I, segment II, and segment III, respectively.

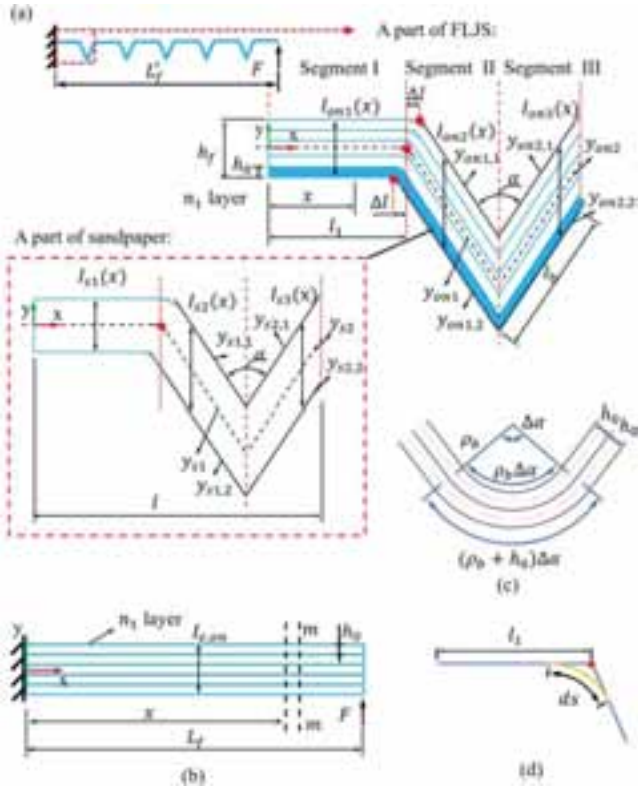


Fig. 5. Schematic diagrams used for analyzing the FLJS. (a) Analytical model of the FLJS used for calculating the moment of inertia. (b) Equivalent laminar jamming structure with constant moment of inertia. (c) Analytical model of a two-layers article in bending state. (d) Simplified model of the FLJS in one crease.

$I_{on1}(x)$ can be written as follows:

$$I_{on1}(x) = \frac{b h_f^3}{12} \tag{16}$$

where b is the width of the FLJS, which is same to the inside width of the chamber. h_f is the thickness of the FLJS.

In general, the bending area of a thick-sheet origami can be considered a joint area [38], as shown in Fig. 5(c). However, it is a is noncurvature bending crease in this article, as shown in Fig. 5(d), because the bending arc length ds in each bending area is small. Different from the unimproved laminar jamming structure, each sandpaper of the segmented face layers only has three creases, in which the loss of the folding area of each sandpaper can be ignored. Owing to the thickness of each layer h_0 being minimal in this article, it is assumed that the crease of the sandpapers is in the same vertical line, which means that the distance Δl between outer creases and middle crease in the x-axis is equal to 0. Therefore, the moment of inertia in segment II $I_{on2}(x)$ can be written as follows:

$$I_{on2}(x) = \int_{y_{on1,2}}^{y_{on1,1}} (y - y_{on1})^2 \text{bdy} \tag{17}$$

where $y_{on1,1}$, $y_{on1,2}$, and y_{on1} are the top line, bottom line, and neutral axis of the FLJS, respectively. They can be expressed as

Authorized licensed use limited to: XIDIAN UNIVERSITY. Downloaded on October 18,2024 at 07:13:14 UTC from IEEE Xplore. Restrictions apply.

follows:

$$\begin{cases} y_{on1,1} = -\cot\left(\frac{\alpha}{2}\right)x + l_1\cot\left(\frac{\alpha}{2}\right) + \frac{h_f}{2} \\ y_{on1,2} = -\cot\left(\frac{\alpha}{2}\right)x + l_1\cot\left(\frac{\alpha}{2}\right) - \frac{h_f}{2} \\ y_{on1} = -\cot\left(\frac{\alpha}{2}\right)x + l_1\cot\left(\frac{\alpha}{2}\right) \end{cases} \tag{18}$$

where α and l_1 are the folding angle of the FLJS and the length of one chamber, respectively.

The moment of inertia in segment III $I_{on3}(x)$ can be written as follows:

$$I_{on3}\ (x) = \int_{y_{on2,2}}^{y_{on2,1}} (y - y_{on2})^2 \mathrm{bdy} \tag{19}$$

where $y_{on2,1}$, $y_{on2,2}$, and y_{on2} can be expressed as follows:

$$\begin{cases} y_{on2,1} = \cot\left(\frac{\alpha}{2}\right)\ x - l\cot\left(\frac{\alpha}{2}\right) + \frac{h_f}{2} \\ y_{on2,2} = \cot\left(\frac{\alpha}{2}\right)\ x - l\cot\left(\frac{\alpha}{2}\right) - \frac{h_f}{2} \\ y_{on2} = \cot\left(\frac{\alpha}{2}\right)\ x - l\cot\left(\frac{\alpha}{2}\right). \end{cases} \tag{20}$$

Hence, $I_{on}(x)$ can be represented by the following Fourier series:

$$I_{on}\ (x) = \sum_{n_f=1}^{\infty} b_{on,n_f}\ \sin\left(\frac{n_f\pi x}{l}\right)\ (\ n_f = \ 1,\ 2,\ 3\ldots) \tag{21}$$

where b_{on,n_f} is coefficient of the Fourier series, and it can be expressed as follows:

$$\begin{aligned} b_{on,n_f} = \frac{2}{l}\ \Bigg[& \int_0^{l_1} I_{on1}\,(x)\sin\left(\frac{n_f\pi x}{l}\right)dx \\ & + \int_{l_1}^{l_1+l_b\sin\left(\frac{\alpha}{2}\right)} I_{on2}\,(x)\sin\left(\frac{n_f\pi x}{l}\right)dx \\ & + \int_{l_1+l_b\sin\left(\frac{\alpha}{2}\right)}^{l} I_{on3}\,(x)\sin\left(\frac{n_f\pi x}{l}\right)dx\Bigg]. \end{aligned} \tag{22}$$

Therefore, the first term of b_{on,n_f} is described as follows:

$$\begin{aligned} b_{on,1} = \frac{2}{l}\ \Bigg[& \int_0^{l_1} I_{on1}\,(x)\sin\left(\frac{\pi x}{l}\right)dx \\ & + \int_{l_1}^{l_1+l_b\sin\left(\frac{\alpha}{2}\right)} I_{on2}\,(x)\sin\left(\frac{\pi x}{l}\right)dx \\ & + \int_{l_1+l_b\sin\left(\frac{\alpha}{2}\right)}^{l} I_{on3}\,(x)\sin\left(\frac{\pi x}{l}\right)dx\Bigg]. \end{aligned} \tag{23}$$

It is postulated that the behavior of the FLJS with variable moment of inertia can be closely represented by an equivalent simply supported beam with constant moment of inertia $I_{e,on}$. The moment of inertia $I_{e,on}(x)$ in the equivalent beam is expressed as follows:

$$I_{e,on}\ (x) = I_{on}\ (x) = I_{e,on}. \tag{24}$$

To calculate $I_{e,on}$, the moment of inertia $I_{e,on}(x)$ can be expanded into the following Fourier series:

$$I_{e,on}\,(x)\ = \sum_{n_e=1}^{\infty} b_{e,n_e}\ \sin\left(\frac{n_e\pi x}{l}\right)\ (\ n_e = \ 1,\ 2,\ 3\ldots) \tag{25}$$

where b_{on,n_e} is coefficient of the Fourier series

$$b_{e,n_e} = \frac{2I_{e,on}}{n_e\pi}\ [1 - \cos(n_e\pi)]. \tag{26}$$

The first term of the Fourier series of $I_{on}(x)$ and $I_{e,on}(x)$ are equal. Therefore, we get the following formula:

$$I_{e,on} = \frac{\pi}{4}\ b_{on,1}. \tag{27}$$

2) FLJS in Free State: Each of the sandpapers is in a free state when the FLJS does not work. Thus, the moment of inertia of the FLJS in free state I_{off} can be written [39] as

$$I_{\text{off}} = n_1 I_s \tag{28}$$

where n_1 and I_s are the number of the FLJS's layer and one layer sandpaper's equivalent moment of inertia in the free state, respectively. And, I_s can be calculated as follows:

$$I_s(x) = \begin{cases} I_{s1}\ (x) = \frac{bh_0^3}{12} & (0,\ l_1) \\ I_{s2}\ (x) = \int_{y_{s1,2}}^{y_{s1,1}} (y - y_{s1})^2 \mathrm{bdy} & \left(l_1,\ l_1 + l_b\sin\frac{\alpha}{2}\right) \\ I_{s3}\ (x) = \int_{y_{s2,2}}^{y_{s2,1}} (y - y_{s2})^2 \mathrm{bdy} & \left(l_1 + l_b\sin\frac{\alpha}{2},\ l\right) \end{cases} \tag{29}$$

where $I_{s1}(x)$, $I_{s2}(x)$, and $I_{s3}(x)$ are the moment of inertia in segment I, segment II, and segment III, respectively [Fig. 5(a)]. And, they can be calculated using the aforementioned method.

Hence, $I_s(x)$ can be represented by the following Fourier series:

$$I_s\,(x) = \sum_{n_f=1}^{\infty} b_{s,n_f}\ \sin\left(\frac{n_f\pi x}{l}\right)\ (\ n_f = \ 1,\ 2,\ 3\ldots) \tag{30}$$

where b_{s,n_f} is coefficient of the Fourier series, and the first term of the coefficient $b_{s,1}$ is described as follows:

$$\begin{aligned} b_{s,1} = \ \Bigg[& \int_0^{l_1} I_{s1}\,(x)\sin\left(\frac{\pi x}{l}\right)dx \\ & + \int_{l_1}^{l_1+l_b\sin\left(\frac{\alpha}{2}\right)} I_{s2}\,(x)\sin\left(\frac{\pi x}{l}\right)dx \\ & + \int_{l_1+l_b\sin\left(\frac{\alpha}{2}\right)}^{l} I_{s3}\,(x)\sin\left(\frac{\pi x}{l}\right)dx\Bigg]\frac{2}{l}. \end{aligned} \tag{31}$$

The one-layer FLJS's moment of inertia I_s is simplified to a constant moment of inertia $I_{s,e}$. Moreover, the moment of inertia $I_{s,e}(x)$ in the equivalent beam is expressed as follows:

$$I_{s,e}\,(x) = I_s\,(x) = I_{s,e}. \tag{32}$$

Authorized licensed use limited to: XIDIAN UNIVERSITY. Downloaded on October 18,2024 at 07:13:14 UTC from IEEE Xplore. Restrictions apply.

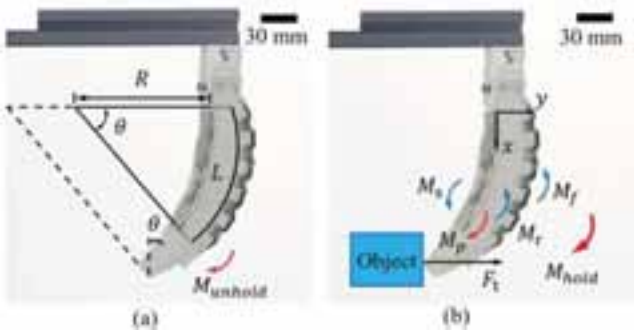


Fig. 6. Schematic for modeling the tip force of the shape-locking finger. (a) Bending finger in no-load state. (b) Bending finger in load state.

To calculate $I_{s,e}$, the moment of inertia $I_{s,e}(x)$ can be expanded into the following Fourier series:

$$\begin{cases} I_{s,e}(x) = \sum_{n_e=1}^{\infty} b_{se,n_e} \sin\left(\frac{n_e \pi x}{l}\right) \ (n_e = 1, 2, 3 \ldots) \\ b_{se,n_e} = \frac{2I_{s,e}}{n_e \pi} \left[1 - \cos(n_e \pi)\right] \end{cases} \tag{33}$$

where b_{se,n_e} is the coefficient of the Fourier series. The first term of the Fourier series of $I_s(x)$ and $I_{s,e}(x)$ are equal. Therefore, we obtain the following formula:

$$I_{s,e} = \frac{\pi}{4} b_{s,1}. \tag{34}$$

C. Modeling the Tip Force of the Finger

The tip force generated by the finger is calculated when the gripper contacts an object. It is assumed that the moments of the four parts mentioned above can be considered as a resultant moment M_{gripper} generated by the finger (see Fig. 6)

$$M_{\text{gripper}} = M_p - (N-1) M_r - M_f - M_s \tag{35}$$

when the gripper bends in no-load state, the resultant moment M_{gripper} names M_{unhold}, and $M_{\text{unhold}} = 0$. When the gripper holds an object, the resultant moment M_{gripper} names M_{hold}. $M_{\text{hold}} \neq 0$ and it can be expressed as follows:

$$M_{\text{hold}} = M_t = \frac{E_{\text{gripper}} I_{\text{gripper}}}{R} \tag{36}$$

where $E_{\text{gripper}} I_{\text{gripper}}$ is the bending stiffness of the shape-locking finger, and it can be measured by the experiments [29]. M_t is the moment generated by the tip force F_t and it can be expressed on the basis of equilibrium moment

$$M_t = (R \sin\theta + L_t \cos\theta) F_t \tag{37}$$

where θ and L_t are the bending angle of the finger and the length of the fingertip, respectively.

An additional deflection will be generated when the actuator contacts the target object, causing the bending shape of the finger to deform slightly. However, this effect will decrease when the bending angle increases and the input pressure decreases [31]. In addition, it is not easy to obtain the deflection shape of the actuator in real time. Therefore, to simplify the model, we neglect the slight displacement of the actuator, meaning that $\theta_{\text{unhold}} = \theta_{\text{hold}} = \theta$. Eventually, the tip force F_t can be written as

$$F_t = \frac{E_{\text{gripper}} I_{\text{gripper}}}{R(R \sin\theta + L_t \cos\theta)}. \tag{38}$$

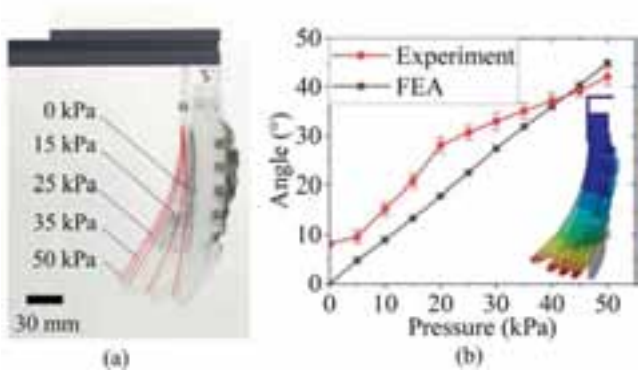


Fig. 7. Bending angle of the shape-locking finger. (a) Bending states of the finger in 0 kPa, 15 kPa, 25 kPa, 35 kPa, and 50 kPa. (b) Relationship between the input pressure and the bending angle obtained from experimental data and FEA.

IV. Verification and Discussion

In this section, the shape-locking finger's bending angle and tip forces are measured to prove the reliability of the theoretical model. In addition, we demonstrate that the CSF gripper can improve the grasping force with the span constant and can safely hold fragile foods with deformable surfaces.

A. Bending Angle of the Finger

A shape-locking finger is composed of an SPA, a TLJS, an FLJS, and a fingertip. The SPA and fingertip are cast in commercial soft and stretchable rubber (Dragon skin 30, Smooth-on Inc., USA). The TLJS is fabricated by the same method of the FLJS. Eventually, the FLJS and the TLJS are bonded to the SPA using silicone glue. The shape-locking finger is mounted on the aluminous support by a 3-D printing connecting component, and a camera captures the movement to measure the bending angle. Fig. 7(a) and (b) show the comparison of the finger's bending angles in different input pressure. The bending angle of the finger exhibits a linear increasing relationship with the input pressure, and the FEA results can roughly describe the bending trajectory of the shape-locking finger. The SPA's density is set to 1917.4 kg·m^3 in FEA. Moreover, the data collected from the uniaxial tensile test [ISO 37:2017(E)] are fitted based on the Yeoh model, and the material constants are C10 = 0.14 MPa and C20 = 0.001 MPa, respectively. It can be observed that the bending angle of the prototype is 8.2° when the input pressure is 0 kPa. The case is because the FLJS will generate a restoring torque in the folded state, resisting the SPA from the bending state to the ideal initial state: 0°, but it does not affect the performance of the finger.

As shown in Fig. 8(a) and (b), the curves of the theoretical model and experimental data have a satisfactory degree of fitting whether the variable stiffness mechanism work or not. With the

Authorized licensed use limited to: XIDIAN UNIVERSITY. Downloaded on October 18,2024 at 07:13:14 UTC from IEEE Xplore. Restrictions apply.

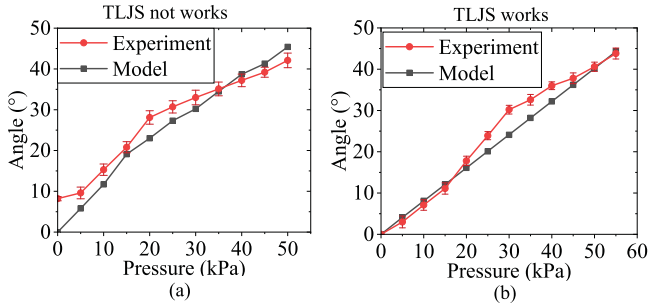


Fig. 8. Relationship between the input pressure and the bending angle obtained from experimental data and the theoretical model when the TLJS (a) not works and (b) works.

TLJS deactivated, the curves increase sharply at less than 20 kPa and then slow down. However, the growth rate becomes gentle after the TLJS works. This is because the motion of SPA is the leading role when the TLJS not works, while the activated TLJS can be regarded as a uniform curved beam, weakening the rapid deformation of the SPA. With the TLJS not working, the maximum bending angles of the experiment and model are 42.1° and 45.4° at 50 kPa, respectively, showing a 7.8% error. With the TLJS working, the maximum bending angles of the experiment and model are 43.8° and 44.3° at 55 kPa, respectively, showing a 1.2% error. Due to the stiffness enhanced by the activated TLJS, the shape-locking finger can sustain a larger maximum input pressure. However, the maximum bending angle is limited by the FLJS, resulting in similar maximum bending angles in the two cases. Thus, the shape-locking finger can adjust the length of the chamber gap and the length of the FLJS to increase the bending range of the finger for different application scenarios. In summary, the theoretical model can predict the movement of the shape-locking finger.

B. Tip Force of the Finger

Fig. 9(a) exbibits the experiment platform to measure the tip force of the shape-locking finger, mainly including a load cell, a proportional valve (ITV2031-212L, SMC), a solenoid valve, a vacuum meter, the STM 32, a relay and a power supply, and so on. To measure the tip force, the shape-locking finger, and the load cell are fixed on the table, with the fingertip contacting the surface of the load cell. High-pressure gas is generated by a compressor and regulated by the proportional valve before entering into the SPA. The solenoid valve switches the bending states of the finger, and valves are controlled by the STM 32. Two ball valves and a vacuum meter are applied to realize the seal, decompression, and vacuum degree monitor of the FLJS and TLJS.

The load cell directly measures and records the tip force when the finger bends, and the experimental and model results are shown in Fig. 9(b) and (c). With the TLJS not working, the maximum tip forces of the experiment and model are 1.14 and 0.72 N at 50 kPa, respectively, showing a 36.8% error. With the TLJS working, the maximum tip forces of the experiment and model are 1.44 and 1.75 N at 55 kPa, respectively, showing a 21.5% error. However, when the TLJS is deactivated, the model

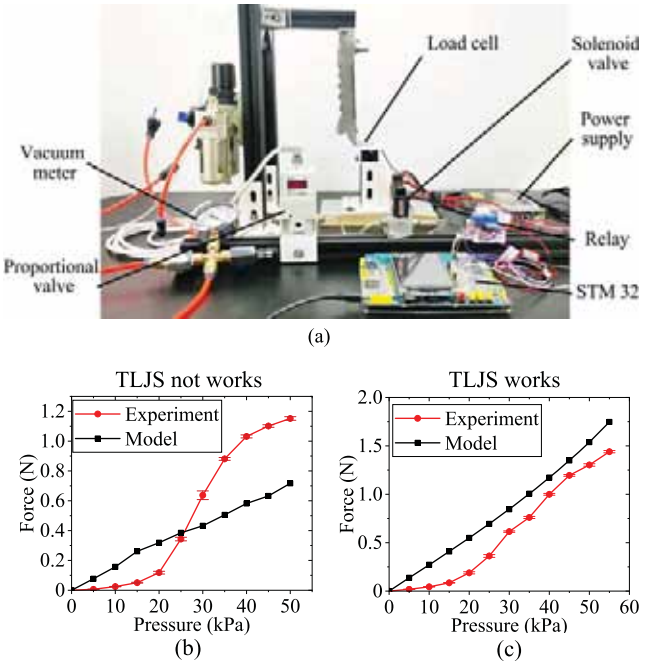


Fig. 9. Tip force of the shape-locking finger. (a) Experimental platform for measuring the tip force of the finger. The relationship between the input pressure and the tip force obtained from experimental data and theoretical model when the variable stiffness mechanism (b) not works and (c) works.

fails to catch the trend accurately and has a large deviation. This is because the SPA dominates the finger's motion when the TLJS does not work. The model tries to conclude the two situations of the TLJS when it turns ON and OFF, missing the large and rapid deformation of the soft material. In contrast, the model shows good predictability when the TLJS works because the TLJS dominates the finger's motion when it is activated. In addition, the TLJS can improve the load performance of the finger, even though the FLJS limits the maximum bending angle. The theoretical model will be improved to solve this problem caused by the SPA in the future.

C. Verification of the CSF Gripper

The CSF gripper assembled by two shape-locking fingers holds a deformable plastic cup and a 100-g weight when the FLJS is activated or not to verify the function of the gripper (Supplementary Video). Without activating the shape-locking, the gripper can be regarded as a typical impactive gripping gripper. As shown in Fig. 10(a), the gripper can readily grip a plastic cup at 16 kPa. However, if a 100-g weight is put into the cup, the gripper cannot hold it. To grasp a plastic cup with the 100-g weight inside it, the gripper increases the input pressure to 49 kPa. However, the span of the gripper decreases when the grasping force increases, which makes the cup deform seriously. Fig. 10(b) shows the grasping process of the finger with activating the FLJS. Before increasing the input pressure, the finger is locked by vacuumizing the bladder of the FLJS. Contrary to typical gripping, the cup hardly deforms when the gripper improves the grasping force with the span unchanged.

Authorized licensed use limited to: XIDIAN UNIVERSITY. Downloaded on October 18,2024 at 07:13:14 UTC from IEEE Xplore. Restrictions apply.

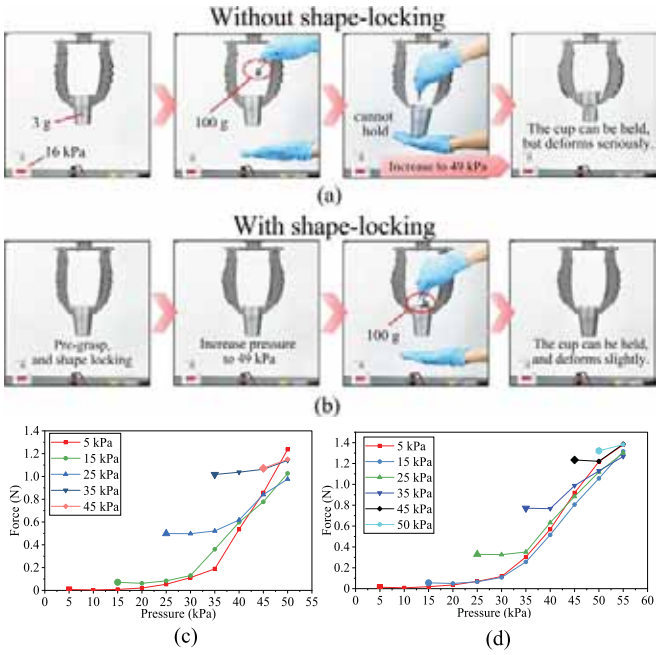


Fig. 10. Validation of the CSF gripper. The process of grasping a plastic cup and a 100g weight when the CSF gripper (a) not employs the shape-locking and (b) employs the shape-locking. (c) Finger's tip force versus input pressure with the finger locked at 5, 15, 25, 35, and 45 kPa when the TLJS not works. (d) Finger's tip force vs. input pressure with the finger locked at 5, 15, 25, 35, 45, and 50 kPa when the TLJS works.

Therefore, the experiments demonstrate that the design of the CSF gripper achieves the control of the span and grasping force simultaneously.

In addition, we measured the tip force after shape-locking to understand the output characteristic of the finger. First, the finger bends with a small input pressure to simulate the pregrasp. Then, we increased the input pressure and recorded the tip force, after the FLJS locked the finger. As shown in Fig. 10(c), when the finger is locked at 5, 15, 25, 35, and 45 kPa (the large solid dots in the figure), the ranges of the output force are 0.007–1.237 N, 0.071–1.026 N, 0.499–0.977 N, 1.040–1.140 N, and 1.071–1.150 N, respectively. Fig. 10(d) shows the output force of the fingertip when the finger is locked at 5, 15, 25, 35, 45, and 50 kPa, with activating the TLJS. The ranges of the output force are 0.014–1.380 N, 0.056–1.267 N, 0.330–1.300 N, 0.771–1.317 N, 1.234–1.386 N, and 1.321–1.382 N, respectively. The results show that the finger can output a range of the forces with a constant span, and has a larger adjustment range when the finger is locked at a smaller pressure.

To further verify the protective capacity of the CSF gripper, the gripper is used to grasp fragile foods with deformable surfaces, such as tofu, cake, mochi, and jelly, with the shape-locking mechanism activated and not activated. The grasping processes are included in the supplementary video. As shown in Fig. 11, the 49.5-g tofu, the 13.4-g cake, the 38.7-g mochi, and the 80-g jelly are safely held through the designed grasping strategy. However, without the shape-locking, the tofu and the jelly are destroyed, and the cake and mochi deform seriously. Though the activated FLJS generates a little reverse displacement of the fingertip,



Fig. 11. Exhibition of grasping fragile foods, such as (a) tofu, (b) cake, (c) mochi, and (d) jelly, with shape-locking and without shape-locking.

it will be compensated by the following step of increasing input pressure. Therefore, the experiments demonstrate that the proposed grasping strategy can effectively reduce the impact of the impactive gripping gripper. There are many similar designs combining jamming technology and SPAs to improve the load performance of soft grippers [22], [24], and [40], [41], [42], [43]. Different from their application scenarios, layer jamming technology is applied for safely grasping fragile foods in this article. Without employing extremely soft materials, the CSF gripper shows a promising method for grasping fragile foods.

V. Conclusion

In this article, we develop a CSF gripper that can improve the grasping force with the span constant to grip fragile foods with deformable surfaces inspired by the grasping method of humans. The CSF gripper is achieved by two shape-locking fingers, and a finger mainly consists of an SPA, an FLJS, and a TLJS. The roles of the three components are driving, locking the shape, and improving the load performance of the finger. In addition, an analytical model combined with FEA and experiments is established to predict the finger's bending angle and the finger's tip force, and experiment results validate the model's reliability. Through the specific grasping process, the CSF gripper safely and stably holds a plastic cup with a 100-g weight inside it, 49.5-g tofu, 13.4-g cake, 38.7-g mochi, and 80-g jelly. Experiments demonstrate that the FLJS can lock the shape of the SPA, and the CSF gripper can effectively decrease the impactive force applied on the objects, showing good protection for fragile foods with deformable surfaces.

Future work will focus on the proprioceptive ability of the finger to sense the target object's shape and size and realize automatic grasping. Besides, we will improve the theoretical model to describe the shape-locking finger's bending motion and tip forces more precisely.

References

[1] W. Xu, H. Zhang, H. Yuan, and B. Liang, "A compliant adaptive gripper and its intrinsic force sensing method," *IEEE Trans. Robot.*, vol. 37, no. 5, pp. 1584–1603, Oct. 2021.

[2] S. Park et al., "A tele-operated microsurgical forceps-driver with a variable stiff-ness haptic feedback master device," *IEEE Robot. Automat. Lett.*, vol. 5, no. 2, pp. 1946–1953, Apr. 2020.

Authorized licensed use limited to: XIDIAN UNIVERSITY. Downloaded on October 18,2024 at 07:13:14 UTC from IEEE Xplore. Restrictions apply.

[3] F. J. Ruiz-Ruiz, J. Ventura, C. Urdiales, and J. M. Gómez-de-Gabriel, "Compliant gripper with force estimation for physical human-robot interaction," *Mechanism Mach. Theory*, vol. 178, 2022, Art. no. 105062.
[4] J. Shintake, V. Cacucciolo, D. Floreano, and H. Shea, "Soft robotic grippers," *Adv. Materials*, vol. 30, no. 29, 2018, Art. no. 1707035.
[5] L. Zhou, L. Ren, Y. Chen, S. Niu, Z. Han, and L. Ren, "Bio-inspired soft grippers based on impactive gripping," *Adv. Sci.*, vol. 8, no. 9, 2021, Art. no. 2002017.
[6] J. K. A. Langowski, P. Sharma, and A. L. Shoushtari, "In the soft grip of nature," *Sci. Robot.*, vol. 5, no. 49, 2020, Art. no. eabd9120.
[7] Z. Xie et al., "Octopus arm-inspired tapered soft actuators with suckers for improved grasping," *Soft Robot.*, vol. 7, no. 5, pp. 639–648, 2020.
[8] Y. Hao et al., "A multimodal, enveloping soft gripper: Shape conformation, bioinspired adhesion, and expansion-driven suction," *IEEE Trans. Robot.*, vol. 37, no. 2, pp. 350–362, Apr. 2021.
[9] E. W. Hawkes, D. L. Christensen, A. K. Han, H. Jiang, and M. R. Cutkosky, "Grasping without squeezing: Shear adhesion gripper with fibrillar thin film," in *Proc. IEEE Int. Conf. Robot. Automat.*, May 2015, pp. 2305–2312.
[10] S. Kim, M. Spenko, S. Trujillo, B. Heyneman, D. Santos, and M. R. Cutkosky, "Smooth vertical surface climbing with directional adhesion," *IEEE Trans. Robot.*, vol. 24, no. 1, pp. 65–74, Feb. 2008.
[11] J. Shintake, S. Rosset, B. Schubert, D. Floreano, and H. Shea, "Versatile soft grippers with intrinsic electroadhesion based on multifunctional polymer actuators," *Adv. Materials*, vol. 28, no. 2, pp. 231–238, 2016.
[12] J. Y. Lee et al., "Shape-adaptive universal soft parallel gripper for delicate grasping using a stiffness-variable composite structure," *IEEE Trans. Ind. Electron.*, vol. 68, no. 12, pp. 12441–12451, Dec. 2021.
[13] Y. Li, Y. Chen, T. Ren, Y. Li, and S. H. Choi, "Precharged pneumatic soft actuators and their applications to untethered soft robots," *Soft Robot.*, vol. 5, no. 5, pp. 567–575, 2018.
[14] R. Konda, D. Bombara, S. Swanbeck, and J. Zhang, "Anthropomorphic twisted string-actuated soft robotic gripper with tendon-based stiffening," *IEEE Trans Robot.*, vol. 39, no. 2, pp. 1178–1195, Apr. 2023.
[15] W. Zhu et al., "A soft-rigid hybrid gripper with lateral compliance and dexterous in-hand manipulation," *IEEE/ASME Trans. Mechatron.*, vol. 28, no. 1, pp. 104–115, Feb. 2023.
[16] D. Yoon and K. Kim, "Fully passive robotic finger for Human-inspired adaptive grasping in environmental constraints," *IEEE/ASME Trans. Mechatron.*, vol. 27, no. 5, pp. 3841–3852, Oct. 2022.
[17] Y. Zhu, G. Wei, L. Ren, Z. Luo, and J. Shang, "An anthropomorphic robotic finger with innate human-finger-like biomechanical advantages Part I: Design, ligamentous joint, and extensor mechanism," *IEEE Trans Robot.*, vol. 39, no. 1, pp. 485–504, Feb. 2023.
[18] J. Zhu et al., "Bioinspired multimodal multipose hybrid fingers for wide-range force, compliant, and stable grasping," *Soft Robot.*, vol. 10, no. 1, pp. 30–39, 2023.
[19] C. L. Taylor and R. J. Schwarz, "The anatomy and mechanics of the human hand," *Artif. Limbs*, vol. 2, no. 2, pp. 22–35, May 1955.
[20] Z. Xu and E. Todorov, "Design of a highly biomimetic anthropomorphic robotic hand towards artificial limb regeneration," in *Proc. IEEE Int. Conf. Robot. Automat.*, May 2016, pp. 3485–3492.
[21] M. Manti, V. Cacucciolo, and M. Cianchetti, "Stiffening in soft robotics: A review of the state of the art," *IEEE Robot. Automat. Mag.*, vol. 23, no. 3, pp. 93–106, Sep. 2016.
[22] X. Zeng and H. J. Su, "A high performance pneumatically actuated soft gripper based on layer jamming," *J. Mechanisms Robot.*, vol. 15, no. 1, 2023, Art. no. 014501.
[23] R. Chen, L. Wu, Y. Sun, J. Q. Chen, and J. L. Guo, "Variable stiffness soft pneumatic grippers augmented with active vacuum adhesion," *Smart Materials Structures*, vol. 29, no. 10, 2020, Art. no. 105028.
[24] Y. Yang, Y. Zhang, Z. Kan, J. Zeng, and M. Y. Wang, "Hybrid jamming for bioinspired soft robotic fingers," *Soft Robot.*, vol. 7, no. 3, pp. 292–308, 2020.
[25] C. Armanini, F. Boyer, A. T. Mathew, C. Duriez, and F. Renda, "Soft robots modeling: A structured overview," *IEEE Trans. Robot.*, vol. 39, no. 3, pp. 1728–1748, Jun. 2023.
[26] M. Russo et al., "Continuum robots: An overview," *Adv. Intell. Syst.*, vol. 5, no. 5, 2023, Art. no. 2200367.
[27] P. Polygerinos et al., "Modeling of soft fiber-reinforced bending actuators," *IEEE Trans Robot.*, vol. 31, no. 3, pp. 778–789, Jun. 2015.
[28] Z. Wang, P. Polygerinos, J. T. Overvelde, K. C. Galloway, K. Bertoldi, and C. J. Walsh, "Interaction forces of soft fiber reinforced bending actuators," *IEEE/ASME Trans. Mechatron.*, vol. 22, no. 2, pp. 717–727, Apr. 2017.
[29] G. Alici, T. Canty, R. Mutlu, W. Hu, and V. Sencadas, "Modeling and experimental evaluation of bending behavior of soft pneumatic actuators made of discrete actuation chambers," *Soft Robot.*, vol. 5, no. 1, pp. 24–35, 2018.
[30] J. Wang, Y. Fei, and W. Pang, "Design, modeling, and testing of a soft pneumatic glove with segmented PneuNets bending actuators," *IEEE/ASME Trans. Mechatron.*, vol. 24, no. 3, pp. 990–1001, Jun. 2019.
[31] G. Zhong, W. Dou, X. Zhang, and H. Yi, "Bending analysis and contact force modeling of soft pneumatic actuators with pleated structures," *Int. J. Mech. Sci.*, vol. 193, 2021, Art. no. 106150.
[32] W. Zhou and Y. Li, "Modeling and analysis of soft pneumatic actuator with symmetrical chambers used for bionic robotic fish," *Soft Robot.*, vol. 7, no. 2, pp. 168–178, 2020.
[33] A. Srivastava and C. Y. Hui, "Large deformation contact mechanics of long rectangular membranes. I. Adhesionless contact," *Proc. Math. Phys. Eng. Sci.*, vol. 469, no. 2160, 2013, Art. no. 20130424.
[34] Z. Liu, F. Wang, S. Liu, Y. Tian, and D. Zhang, "Modeling and analysis of soft pneumatic network bending actuators," *IEEE/ASME Trans. Mechatron.*, vol. 26, no. 4, pp. 2195–2203, Aug. 2021.
[35] Z. Zhang, J. Sang, and Y. Zhang, "Inflation analyses of a circular elastomeric membrane with hydrostatic pressure," *Theor. Appl. Mechanics Lett.*, vol. 2, no. 6, 2012, Art. no. 061002.
[36] Y. S. Narang, J. J. Vlassak, and R. D. Howe, "Mechanically versatile soft machines through laminar jamming," *Adv. Funct. Materials*, vol. 28, no. 17, 2018, Art. no. 1707136.
[37] B. Bakht and L. G. Jaeger, "Dealing with varying moments of inertia of girders in bridge analysis," *Can. J. Civil Eng.*, vol. 15, no. 2, pp. 232–239, 1988.
[38] N. A. Pehrson, S. P. Magleby, R. J. Lang, and L. L. Howell, "Introduction of monolithic origami with thick-sheet materials," in *Proc. IASS Annu. Symposia*, 2016, pp. 1–10.
[39] Y. S. Narang, B. Aktaş, S. Ornellas, J. J. Vlassak, and R. D. Howe, "Lightweight highly tunable jamming-based composites," *Soft. Robot.*, vol. 7, no. 6, pp. 724–735, 2020.
[40] M. Zhu, Y. Mori, T. Wakayama, A. Wada, and S. Kawamura, "A fully multi-material three-dimensional printed soft gripper with variable stiffness for robust grasping," *Soft Robot.*, vol. 6, no. 4, pp. 507–519, 2019.
[41] M. Zhu, M. Xie, Y. Mori, J. Dai, S. Kawamura, and X. Yue, "A variable stiffness soft gripper based on rotational layer jamming," *Soft Robot.*, 2023, doi: 10.1089/soro.2022.0232.
[42] H. Wei, Y. Shan, Y. Zhao, L. Qi, and X. Zhao, "A soft robot with variable stiffness multidirectional grasping based on a folded plate mechanism and particle jamming," *IEEE Trans. Robot.*, vol. 38, no. 6, pp. 3821–3831, Dec. 2022.
[43] L. Liu, J. Zhang, G. Liu, Z. Zhu, Q. Hu, and P. Li, "Three-fingered soft pneumatic gripper integrating joint-tuning capability," *Soft Robot.*, vol. 9, no. 5, pp. 948–959, 2022.



Xuanchun Yin (Member, IEEE) received the B.S. degree in mechanical engineering from the Changchun University of Science and Technology, Changchun, China, in 2005, the M.S. degree in mechatronic engineering from South China Agricultural University, Beijing, China, in 2012, and the Ph.D. degree in intelligent mechanical systems engineering from Kagawa University, Takamatsu, Japan, in 2016.

He was a Visiting Scholar with the Department of Mechanical and Aerospace Engineering, Case Western Reserve University, Cleveland, OH, USA, from 2019 to 2020. He is currently an Associate Professor with the School of Engineering, South China Agricultural University. His research interests include haptics, human-robot interaction, teleoperation system, artificial intelligence, bio-inspired robotics, medical robotics, and agricultural robotics.

Authorized licensed use limited to: XIDIAN UNIVERSITY. Downloaded on October 18,2024 at 07:13:14 UTC from IEEE Xplore. Restrictions apply.



Pengyu Zhou received the M.S. degree in mechanical engineering from the College of Engineering, South China Agricultural University, Guangzhou, China, in 2023. He is currently working toward the Ph.D. degree in computer science and technology with the Academy for Engineering and Technology, Fudan University, Shanghai, China.

His research interests include the design and control of bio-inspired and soft robots, origami robots, and dielectric elastomer actuation.



Junliang Xie received the B.S. degree in mechanical and electrical engineering from the Guangdong University of Technology, Guangdong, China, in 2021. He is currently working toward the M.S. degree with the College of Engineering, South China Agricultural University, Guangzhou, China.

His research interests include the design and control of the bionic robot, soft gripper.



Shijie Tang received the master's degree in mechanical engineering with Foshan University, Foshan, China, 2023. He is currently working toward the Ph.D. degree in mechanical engineering from the Changchun University of Science and Technology, Changchun, China.

His research interests on soft robotics.



Sheng Wen received the Ph.D. degree in agricultural electrification and automation from South China Agricultural University, Guangzhou, China, in 2011.

He is currently an Associate Professor with the School of Engineering, South China Agricultural University. His research interests include agricultural artificial intelligence, haptics, human-robot interaction, and teleoperation.



Jiantao Zhang received the B.S., M.S., and Ph.D. degrees in agricultural electrification and automation from South China Agricultural University, Guangzhou, China, in 2004, 2006, and 2011, respectively.

He is currently an Associate Professor with the School of Mathematics and Informatics, South China Agricultural University. His research interests include agricultural artificial intelligence, haptics, teleoperated robotics system, unmanned aerial vehicle, and precision agriculture.



Jiehao Li (Member, IEEE) received the M.Sc. degree in control engineering from the South China University of Technology, Guangzhou, China, in 2017, and the Ph.D. degree in control science and engineering from the State Key Laboratory of Intelligent Control and Decision of Complex Systems, School of Automation, Beijing Institute of Technology, Beijing, China, in 2022.

He is currently an Associate Professor with the College of Engineering, South China Agricultural University, Guangzhou. He is also a Research Fellow with the School of Computer Science and Engineering, South China University of Technology, supervised by C. L. Philip Chen. His research interests include agricultural robotics, robot control, and image processing.

Authorized licensed use limited to: XIDIAN UNIVERSITY. Downloaded on October 18,2024 at 07:13:14 UTC from IEEE Xplore. Restrictions apply.

3.2 Single-rotor UAV flow field simulation using generative adversarial networks

Volume 217, February 2024

ISSN 0168-1699

Computers and electronics in agriculture





ScienceDirect

Computers and Electronics in Agriculture

Supports *open access*

13.6	8.3
CiteScore	Impact Factor

Submit your article | Guide for authors

Menu | Search in this journal

Volume 167

December 2019

Download full issue

< Previous vol/issue | Next vol/issue >

Receive an update when the latest issues in this journal are published

Sign in to set up alerts

Full text access

Editorial Board

Article 105131

View PDF

Full Length Articles

FEEDBACK

Research article ○ Abstract only

Spatio-temporal monitoring of wheat yellow rust using UAV multispectral imagery

Jinya Su, Cunjia Liu, Xiaoping Hu, Xiangming Xu, ... Wen-Hua Chen
Article 105035

Article preview

Research article ○ Abstract only

Effects of application costs on fertilizer application strategy

Michael Friedrich Tröster, Hubert Pahl, Johannes Sauer
Article 105033

Article preview

Research article ○ Abstract only

Field detection and classification of citrus Huanglongbing based on hyperspectral reflectance

Xiaoling Deng, Zixiao Huang, Zheng Zheng, Yubin Lan, Fen Dai
Article 105006

Article preview

Research article ○ Abstract only

Real-time forest smoke detection using hand-designed features and deep learning

Yingshu Peng, Yi Wang
Article 105029

Article preview

Research article ○ Abstract only

Automated system for characterizing short-term feeding behavior and real-time forestomach motility in cattle

Amanda M. Egert-McLean, Michael P. Sama, James L. Klotz, Kyle R. McLeod, ... David L. Harmon
Article 105037

Article preview

FEEDBACK

Barry Watkins, Adriaan Van Niekerk
Article 105078

Article preview

Research article ○ Abstract only

Miniaturized wireless water content and conductivity soil sensor system

Cristina Rusu, Anatol Krozer, Christer Johansson, Fredrik Ahrentorp, ... Antonio Montagnoli
Article 105076

Article preview

Research article ○ Abstract only

Visual features based automated identification of fish species using deep convolutional neural networks

Hafiz Tayyab Rauf, M. Ikram Ullah Lali, Saliha Zahoor, Syed Zakir Hussain Shah, ... Syed Ahmad Chan Bukhari
Article 105075

Article preview

Research article ○ Abstract only

Single-rotor UAV flow field simulation using generative adversarial networks

Sheng Wen, Ningwen Shen, Jiantao Zhang, Yubin Lan, ... Yufeng Ge
Article 105004

Article preview

Research article ○ Abstract only

Three dimensional radio-frequency electromagnetic imaging of an in-bin grain conditioning process

Colin Gilmore, Mohammad Asefi, Kyle Nemez, Jitendra Paliwal, Joe LoVetri
Article 105059

Article preview

Research article ○ Abstract only

FEEDBACK

A new proposal for automatic identification of multiple soybean diseases

Juliana Mariana Macedo Araujo, Zelia Myriam Assis Peixoto
Article 105060

Article preview

Research article ○ Abstract only

MOEA/D-DE based bivariate control sequence optimization of a variable-rate fertilizer applicator

Jiqin Zhang, Gang Liu, Chengming Luo, Hao Hu, Jiayun Huang
Article 105063

Article preview

Research article ○ Abstract only

Using hybrid algorithm to reduce non-working distance in intra- and inter-field logistics simultaneously for heterogeneous harvesters

Pengfei He, Jing Li, Hailong Qin, Yanping He, Guangqiao Cao
Article 105065

Article preview

Research article ○ Abstract only

An Analytical Hierarchy Process to manage water quality in white fish (Chirostoma estor estor) intensive culture

José Luis Vázquez-Burgos, José J. Carbajal-Hernández, Luis P. Sánchez-Fernández, Marco A. Moreno-Armendáriz, ... Ignacio Hernández-Bautista
Article 105071

Article preview

Research article *Open access*

A spatio-temporal recurrent network for salmon feeding action recognition from underwater videos in aquaculture

Håkon Måløy, Agnar Aamodt, Ekrem Misimi
Article 105087

FEEDBACK



Copyright © 2023 Elsevier B.V. or its licensors or contributors.
ScienceDirect® is a registered trademark of Elsevier B.V.



FEEDBACK

Computers and Electronics in Agriculture 167 (2019) 105004

Contents lists available at ScienceDirect

Computers and Electronics in Agriculture

journal homepage: www.elsevier.com/locate/compag

Single-rotor UAV flow field simulation using generative adversarial networks

Sheng Wen[a,b], Ningwen Shen[b,c], Jiantao Zhang[b,d,*], Yubin Lan[b,c], Jie Han[b,c], Xuanchun Yin[b,c], Quanyong Zhang[b,c], Yufeng Ge[e]

[a] Engineering Foundation Teaching and Training Center, South China Agricultural University, Guangzhou 510642, China
[b] National Center for International Collaboration Research on Precision Agriculture Aviation Pesticides Spraying Technology, Guangzhou 510642, China
[c] Engineering College, South China Agricultural University, Guangzhou 510642, China
[d] Mathematics and Informatics College of South China Agricultural University, Guangzhou 510642, China
[e] Biological Systems Engineering Department, University of Nebraska-Lincoln, Lincoln 68505, USA

ARTICLE INFO

Keywords:
Flow-field
CFD
GAN
Flow field prediction
Feature extraction

ABSTRACT

In recent years, with the large-scale application of unmanned aerial vehicles (UAV) in agricultural plant protection, various shortcomings of have been identified; for example, the rotor flow field of the UAV will cause drift of the droplets, resulting in waste and secondary disaster. Therefore, digital simulation has become a necessity. However, due to the complexity of the rotor flow field of the rotor UAV and the operating environment of the UAV, digital simulation is associated with a large workload and great computational costs. It is urgent to explore new models using deep learning to identify the law of the rotor flow field. To address this problem, deep learning, in combination with flow field methods, is used to explore new models in this paper. A generative adversarial network (GAN) prediction model is proposed in this paper. The GAN includes a generation network and a discrimination network. In this paper, the features of the flow field are learned by the generative network to identify deep features of the flow field. The discrimination network distinguishes between true and false pictures by extracting features during training to realize adversarial training. This model can predict the flow field by identifying features of the flow-field distribution in training samples to build a predictive model. The compression effects of the computational fluid dynamics (CFD) model and the GAN model are compared in this paper. The GAN model outperforms the CFD model in predicting the flow field and compressing the data.

1. Introduction

With the continuous development of UAV technology, agricultural UAVs have been widely used around the world, especially in East Asian countries such as Japan, China and South Korea. In the past ten years, China's agricultural UAVs have been rapidly developed for low-altitude and small-volume applications. Up to 2017, 95% of Chinese agricultural aviation technology was applied in aerial plant protection operations, and the remaining 5% was applied in agricultural information acquisition, aerial photography, and assisted breeding, among other areas (Xiongkui et al., 2017). Japan is the first country in the world to use unmanned helicopters for agricultural pesticide applications and is one of the leading countries in the commercialization of this technology. As of the end of October 2005, the number of registered agricultural UAVs in Japan had increased to 2002 from 307 in 1995, with an average annual growth rate of 13.80%. The Yamaha RMAX series already has 2400 UAVs in 2017 (Xiongkui et al., 2017).

With the continuous and widespread application of agricultural UAV plant protection technology, various risks have been identified. The drift of spray droplets that is caused by the rotor flow field of the UAV is one of the major technical risks (Preftakes, 2017). Because the concentration of the liquid that is sprayed by the UAV is much higher than the concentration of the liquid that is used by the ground plant protection machine, it is easy to cause secondary disasters.

Existing spray drift models, such as a model for estimating the near-field spray drift from aerial applications (AGDRIFT) and a spray behavior simulation program (AGDISP), are aimed at manned fixed-wing aircraft and helicopters (Reeg et al., 2017). Because the flying height

* Corresponding author at: National Center for International Collaboration Research on Precision Agriculture Aviation Pesticides Spraying Technology, Guangzhou 510642, China.
E-mail addresses: vincen@scau.edu.cn (S. Wen), 2846833826@qq.com (N. Shen), zhangjiantao@yeah.net (J. Zhang), ylan@scau.edu.cn (Y. Lan), 2048570351@qq.com (J. Han), xc_yin@scau.edu.cn (X. Yin), qy_zhang@stu.scau.edu.cn (Q. Zhang), yge2@unl.edu (Y. Ge).

https://doi.org/10.1016/j.compag.2019.105004
Received 18 April 2019; Received in revised form 9 September 2019; Accepted 11 September 2019
Available online 18 November 2019
0168-1699/ © 2019 Elsevier B.V. All rights reserved.

and speed of manned machines are much larger than those of agricultural UAVs, these models are not suitable for research on UAVs (Teske et al., 2018). Many researchers have studied the problem of droplet drift that is caused by the rotor flow field of the UAV. The droplet drift distribution characteristics of the oil-operated single-rotor plant protection UAV have been investigated by Xiaonan et al. (2017) under precise operating parameters, such as speed and height, by establishing a droplet drift collection test platform. CFD simulation of single-rotor UAV wing tip vortex (Sheng et al., 2018) is used to analyze the effect of an eddy current on the spray. The Porous model (Hao et al., 2019) was adopted to study the space-time distribution of the multi-rotor UAV's underwashing flow. A simulation method that is based on the compressible Reynolds-averaged Navier-Stokes (RANS) equations with an RNG k-ε turbulence model and dynamic mesh technology (Fengbo et al., 2017) was used to analyze the discipline of the six-rotor agricultural UAV hovering airflow. However, these studies mainly analyze the flow field of the rotor of the UAV from the perspective of experimental and numerical simulation. These methods have various shortcomings, e.g., experiments on a large farm are difficult to repeat, the simulation time under a preset condition takes more than a week and the results of numerical simulations are difficult to further investigate. With the continuous development of deep learning and neural network technologies, these technologies are being applied in the field of agricultural engineering. Neural network technology has been applied to remote sensing for land cover and crop classification, yield estimation, and weed detection (Kamilaris and Prenafeta-Boldú, 2018) in the field of agriculture. Deep learning techniques (Kussul et al., 2017) are used to identify land cover and crops based on remote sensing data. A fully convolutional network was applied to weed mapping of unmanned aerial vehicle (UAV) imagery. Convolutional neural networks (dos Santos Ferreira et al., 2017) were employed for weed detection in soybean crop images and classification of these weeds among grass and broadleaf. Convolutional neural network models (Ferentinos, 2018) are used to detect and diagnose plant diseases. The results of these studies have demonstrated the advantages of deep learning in the field of agriculture. Therefore, the use of deep learning and neural network methods to solve the problems regarding the UAV rotor flow that are described above has become our focus.

In the last few years, preliminary progress has been made in using machine learning to process the flow field. For example, deep learning was applied on a fluid flow by Lee and You (2017), who used a generative adversarial network (GAN) to predict laminar vortex shedding over a cylinder in a cylinder. Jin et al. (2018) employed a fusion convolutional neural network to predict the velocity field around a circular cylinder for various Reynolds numbers by utilizing the pressure field on the cylinder. Pandya et al. (2017) developed an artificial network model that was based on computational fluid dynamics for predicting solid particle erosion. Zhang et al. (2018) applied a convolutional neural network to predict the airfoil lift coefficient. However, the flow fields that have been handled by deep learning are not highly complicated; hence, the study of the combination of a flow field and a neural network has only just begun. Therefore, further research on the combination of deep learning and flow fields has become a substantial problem we need to solve.

In this paper, a generative adversarial network is used to predict the vorticity and fluid-velocity distribution of the rotor flow field in a single-rotor plant-protection UAV. In this process, the relationship between the input flow field and the output flow field is learned using the network by exploring the characteristics and laws of the drift field distribution of the UAV. After learning, the network can use these features to establish a connection between the front and back flow fields in chronological order. This approach can also replace the CFD model that uses physical formulas to realize fluid motion simulation through this network model.

The remainder of this paper is organized as follows. The utilized datasets are described in Section 2. The model of deep learning for the generation of the training data, the architecture of the GAN and the loss function are explained in Section 3. The training progress and training result are presented and discussed in Section 3, and the conclusions of this work are discussed in Section 4.

2. Deep learning model structure

With the development of artificial intelligence, the GAN has emerged and been well developed (Creswell et al., 2018). The network structure is also constantly improving. In the process, advantages of the GAN are demonstrated; e.g., according to the actual results, the results that are generated by the network produce better samples than other network models, and a confrontational network framework is provided for training any type of generation network. Therefore, the generative adversarial network was used for deep learning of the prediction model of the flow field.

2.1. Framework of the GAN

In this section, the overall framework and operating principle of the GAN are introduced. In the study, generative adversarial networks were adopted to predict the flow field. The GAN is composed of a generative network and a discriminative network, and the two networks are confrontational in the training process to yield more accurate predictions (Durugkar et al., 2016). In Fig. 1, the generated network is composed of a convolutional layer, which is used to read the input image feature, and a deconvolutional layer, which generates the picture.

Six types of flow fields were predicted by deep neural networks in our work. Therefore, six generators $\{ G_f^V, G_s^V, G_t^V, G_f^U, G_s^U, G_t^U \}$ are used for prediction in Fig. 1, where V and U denote the vorticity and velocity distributions, respectively. Subscripts f, s and t denote the front view, side view and top view, respectively. The structures of the six generation networks are the same as in Fig. 1; however, some of the parameters of the neural network differ. In our neural network training, the weights and bias values in the network are randomly selected and the random acquisition values follow the random distribution law. Therefore, in training on pictures, it is necessary to adjust the mean and standard deviation in the random number function. A set of four consecutive flow-field images, namely, $A_{ij} = \{T_{ij}^n, T_{ij}^{n+1}, T_{ij}^{n+2}, T_{ij}^{n+3}\}$, are used as input for the generator network G, where T denotes the input image. Subscript i denotes the flow-field vorticity image (the fluid velocity distribution plot) and subscript j denotes the visual angle of the UAV's rotor flow-field distribution, which includes a side view, top view and face view. When the image data A_{ij} are input into the generation network, the first step is to pass through a series of convolutional layers, namely, C_g, which are used to read the characteristics of the image. After this process, each of the four flow-field images is compressed to 1/8 its original pixel size, and the number of channels of the image is expanded from 3 to 256. Then, the four images are convolved into an image feature map and concatenated to a cube F_K^L of size 16 × 16 with 1024 channels, as illustrated in Fig. 2, where k is the index of the flow field that is processed by the neural network and $k \in \{1, 2, 3, 4, 5, 6\}$:

$$F_k^L = C_g(T_{ij}^n) + C_g(T_{ij}^{n+1}) + C_g(T_{ij}^{n+2}) + C_g(T_{ij}^{n+3})$$

$$k \in \{1, 2, 3, 4, 5, 6\},\ i \in \{1, 2, 3\} \quad (1)$$

Then, the feature that is obtained after convolution is input into a series of deconvolutional layers. Finally, the deconvolution of the deconvolutional layer generates a fake image, which is denoted as B_{ij}^F and expressed as follows:

$$B_{ij}^F = \begin{cases} G_f^V(F_k^L), & k = 1; \\ G_s^V(F_k^L), & k = 2; (i = 1, j = \{1, 2, 3\}) \\ G_s^V(F_k^L), & k = 3; \end{cases} \quad (2)$$

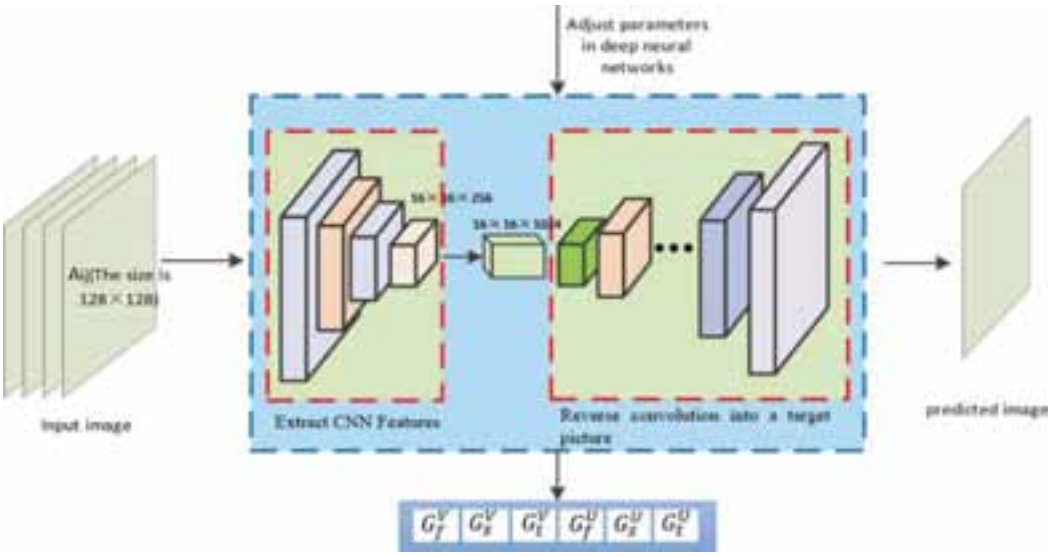


Fig. 1. Six generation networks.

$$B_{ij}^{F} = \begin{cases} G_f^S(F_k^L),\ k = 3; \\ G_s^S(F_k^L),\ k = 5; (i = 2, j = \{1, 2, 3\}) \\ G_t^S(F_k^L),\ k = 6; \end{cases} \tag{3}$$

where 1 and 2 are the low-field vorticity image and the fluid-velocity-distribution image, respectively, for i, with i = 1, 2, and 3 representing the side view, top view and face view, respectively, for j; and B_{ij}^{F} is is the result of generator network generation. The result B_{ij}^{F} that is generated by the generator is input into the discriminator network, which is denoted as D_m, to discriminate between true and false; similarly, the real picture, namely, B_{ij}^{F}, is also input into the discriminator D_m to improve its discriminating ability:

$$(0|1) = \begin{cases} D_m(B_{ij}^{F}); \\ D_m(B_{ij}^{R}); \end{cases}$$

$$i \in \{1, 2\}, j \in \{1, 2, 3\}, m \in \{1, 2, 3, 4, 5, 6\} \tag{4}$$

where m denotes the discriminator for handling flow fields.

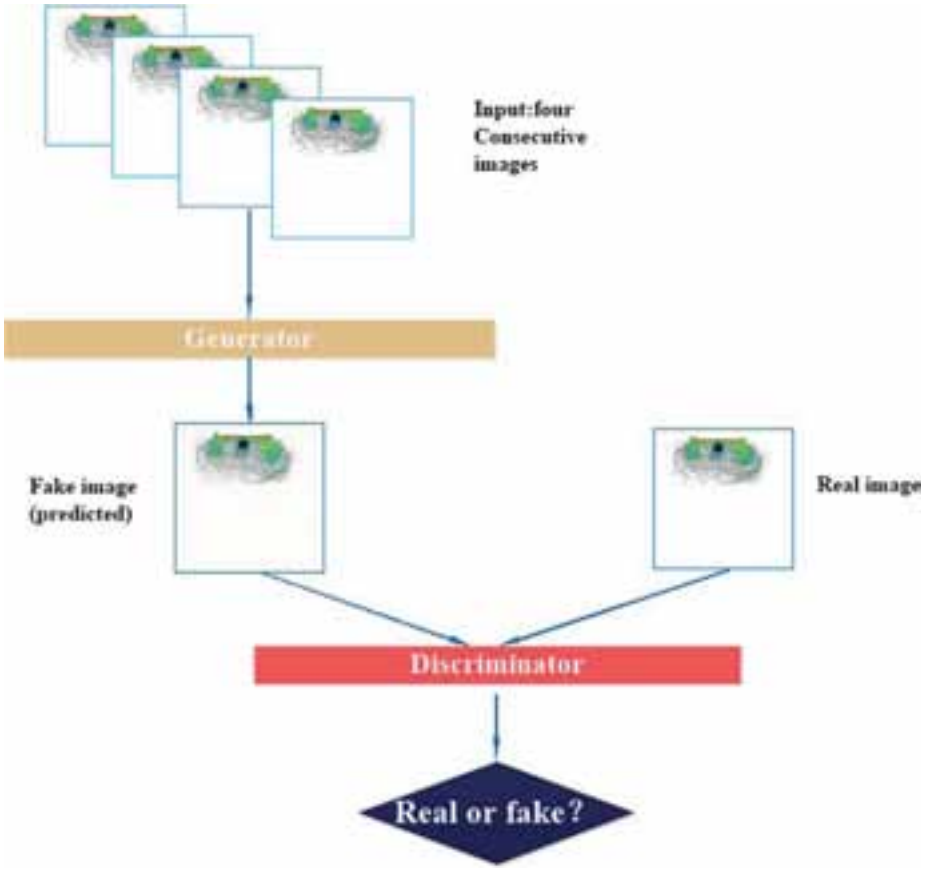


Fig. 2. Overall framework of the generation adversarial network. The flow-field vorticity distribution map is applied to the neural network structure.

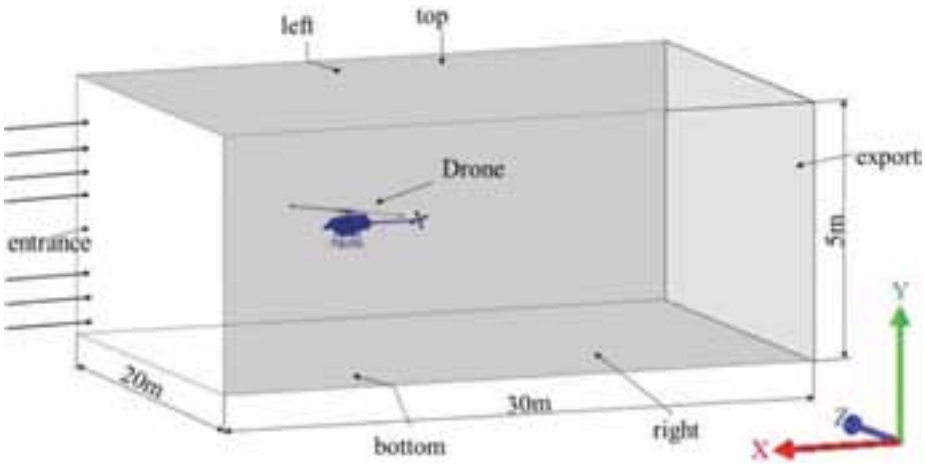


Fig. 3. Schematic diagram of the computational domain.

In summary, based on these architectures of generative adversarial networks, the generator network tries to generate a flow field that satisfies $B^F = B^R$. The architecture of the entire GAN is illustrated in Fig. 2.

2.2. Datasets

2.2.1. Model description

To obtain a higher quality single-rotor UAV rotor flow field data set, the XFlow software (Dassault Systèmes) is utilized for rotor flow field simulation of a single-rotor UAV in this work. The versions of the simulation tool are designed by Next, Limit Technology for solving problems in computational fluid dynamics (CFD). XFlow uses the lattice Boltzmann method (LBM) to solve complex problems in CFD (Santana et al., 2011). Previous studies have demonstrated that XFlow can be used to simulate the flow fields of four-rotor and single-rotor UAVs and yields accurate results (Thibault et al., 2017; Sheng et al., 2018).

According to Fig. 3, the size of the computational domain was 30 m × 5 m × 20 m in the X-, Y-, and Z-directions, respectively. The four colored boundaries are fixed-wall boundaries. The velocity inlet is the air inlet and the direction of the velocity is the negative direction along the X-axis. The velocity at the inlet is set to 0–7 m/s to simulate the flight speeds of the single-rotor UAV. In the computational domain, the height of the main rotor of the UAV is 3 m from the bottom. The objective of the simulation is to build deep-learning model data sets.

To better represent the flow-field distribution, the three directions of the calculation domain are adopted. Three views, namely, a front view, side view and top view, are shown in Fig. 4. The three perspectives of the computational domain can better lay the foundation for constructing the neural network model.

2.2.2. Mathematical description

For UAV simulation of the UAV rotor flow field, the lattice of the D3Q27 model (Sheng et al., 2018) in Fig. 5 was adopted as the characteristic lattice structure of the uniform cubic unit of LBM. The simulation of the fluid is controlled by several governing equations. In our work, the lattice Boltzmann equation was selected for solving the

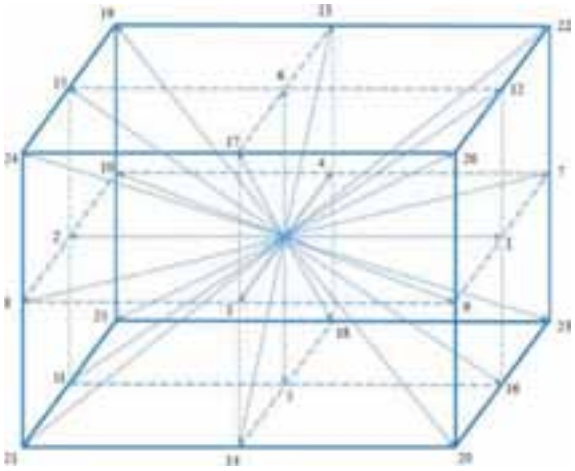


Fig. 5. Lattice of the D3Q27 model.

equation of the flow field simulation. The lattice Boltzmann equation can be expressed as (Brionnaud et al., 2016)

$$u_i(y + \theta_i, \alpha + d\alpha) = u_i(y, \alpha) + M_i(y, \alpha) \tag{5}$$

and

$$M_i = \frac{1}{\mu}(u_i - u_i^{\theta}) \tag{6}$$

where u_i, θ_i, $d\alpha$, $u_i(y,\alpha)$, M_i, u_i^{θ} and μ are the particle velocity distribution function, the speed along the i-th direction, the time step, the particle velocity distribution function in the i-th direction at point y at time $\alpha\alpha$, the collision operator, the single-particle equilibrium distribution function and the dimensionless relaxation parameter, respectively.

The wall-adapting local-eddy LES turbulence model was employed by XFlow, which maintains a consistent local eddy viscosity and near-wall behavior (Ducros et al., 1998). In practice, large eddy simulation



Fig. 4. Three views of the computing domain.

(LES) is used as a wall-adaptive local eddy viscosity model to accurately simulate the flow field characteristics of the rotor. The execution formula can be expressed as (Men et al., 2017)

$$r_t = \Delta_u^2 \frac{(C_{\alpha\beta}^d C_{\alpha\beta}^d)^{\frac{3}{2}}}{(H_{\alpha\beta}H_{\beta\alpha})^{\frac{5}{2}} + (C_{\alpha\beta}C_{\beta\alpha})^{\frac{5}{4}}} \tag{7}$$

and

$$\Delta_u = s_w \Delta \tag{8}$$

$$H_{\alpha\beta} = \frac{c_{\alpha\beta} + c_{\beta\alpha}}{2} \tag{9}$$

$$C_{\alpha\beta}^d = \frac{1}{2}(c_{\alpha\beta}^2 + c_{\beta\alpha}^2) - \frac{1}{3}\varphi_{\alpha\beta}c_{\gamma\gamma}^2 \tag{10}$$

where r_t is the simulated turbulent eddy viscosity; Δ_u is the filter scale; s_w is a constant, which is equal to 0.325; Δ is the unit grid scale; $H_{\alpha\beta}$ and $C_{\alpha\beta}^d$ are the resolving scale strain rate tensors; $\varphi_{\alpha\beta}$ is the Kronecker symbol; and $c_{\alpha\beta}$, $c_{\beta\alpha}$ and $c_{\gamma\gamma}$ are the components of the strain rate tensor, which were obtained from the second-order moment via the LBM method. In the above equations, the subscripts α, β and γ denote directions in space.

2.2.3. Boundary conditions

Using XFlow based on LEM for flow field simulation, the setting of parameters determines the quality of the simulation. The global space refinement resolution size of the calculation domain is set to 0.2 m. The fuselage, main rotor, and tail surface refinement algorithms are set to adaptive methods. The body resolution is set to 0.05 m. The fine resolution of the main rotor and tail is set to 0.025 m. To capture the characteristics of the wake of the lower wash field, the fine resolution size of the wake of the lower wash field is set to 0.0125 m and the threshold of the wake refinement is set to 5×10^{-5} m. The effect of automatic discretization after parameter setting is illustrated in Fig. 6.

2.2.4. Data sampling and preprocessing

To more effectively construct the data sets of the deep learning model, after the simulation has been completed, the two-dimensional map that is derived from simulation software is used as the raw data to train the neural network model. The two-dimensional image is divided into a top view, side view and front view, as shown in Fig. 7. In Fig. 7, (a) and (b) are the vortex and velocity maps from a top view. (c) and (d) are the vortex and velocity maps from a front view. (e) and (f) are the vortex and velocity maps from a side view.

In our work, the pixels and size of the UAV rotor flow-field image that is generated by the flow field analysis software cannot be input into the deep learning model for training due to computer configuration restrictions. These software-generated flow-field images must be compressed prior to being input into the deep neural network. Each image is preprocessed with Python code, and the processed image can be used as input data for the deep learning model. A flow diagram of the preprocessing steps is presented in Fig. 8. The resulting flow-field image has a pixel size of 128 by 128. The data are highly compressed during this process.

The six data sets that are used for deep learning training are flow-field vorticity and fluid velocity distribution images that are generated by data simulation. In each data set, every five consecutive pictures compose a slice, that the time interval between pictures is 0.01 s. In a slice, the first four consecutive pictures are used as input, and the last image is used as the picture to predict. In Fig. 9, two types of data sets are shown: the top view of the rotor vorticity of the UAV operation and the side view of the rotor vorticity of the UAV operation. These images are in jpg format with three feature figures (R(red)G(green)B(blue)). In the next section, these data sets are used for training in generating network extraction flow-field features.

2.3. Generator network

The generator is a core component of the GAN and a key factor in generating the flow-field map. To generate a good flow-field image, the generation network must have an appropriate neural network structure. The architecture of the generation network is illustrated in Fig. 10. The structure of this generation network consists of two parts: a convolutional layer for reading the flow-field features as input data and a deconvolutional layer for generating the flow-field image. As illustrated in the upper part of Fig. 10, the convolutional layer for reading the features of the image is composed of four convolutional layers. Each convolutional layer is composed of a convolution function, a pooling function and an activation function. In our work, to read the image features accurately, the average pooling function is used in the convolutional layer. The LRelu activation function was adopted to reduce overfitting while improving the fault tolerance

of the model. The LRelu function is as follows:

$$I_{output} = \max\{0.2 \times I_{intput}, I_{intput}\} \tag{11}$$

where I_{input} is output result of each layer of the convolutional layer and I_{output} is the maximum between $0.2 \times I_{input}$ and I_{input}. In these convolutional layers, the convolution kernel is 9×9 in size with a stride of 1, and the pooling window is 7×7 in size. The detailed parameters of the convolutional layer are listed in Table 1.

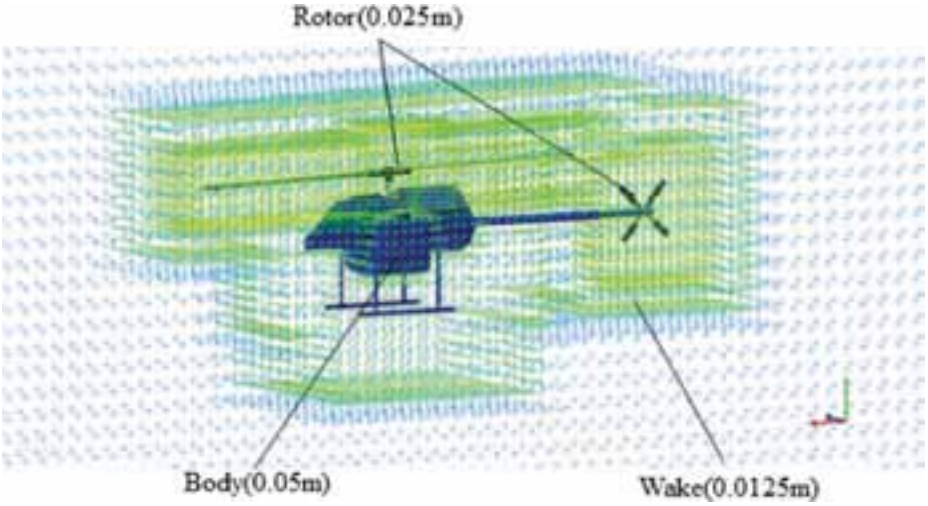


Fig. 6. Discrete division of computing regions.

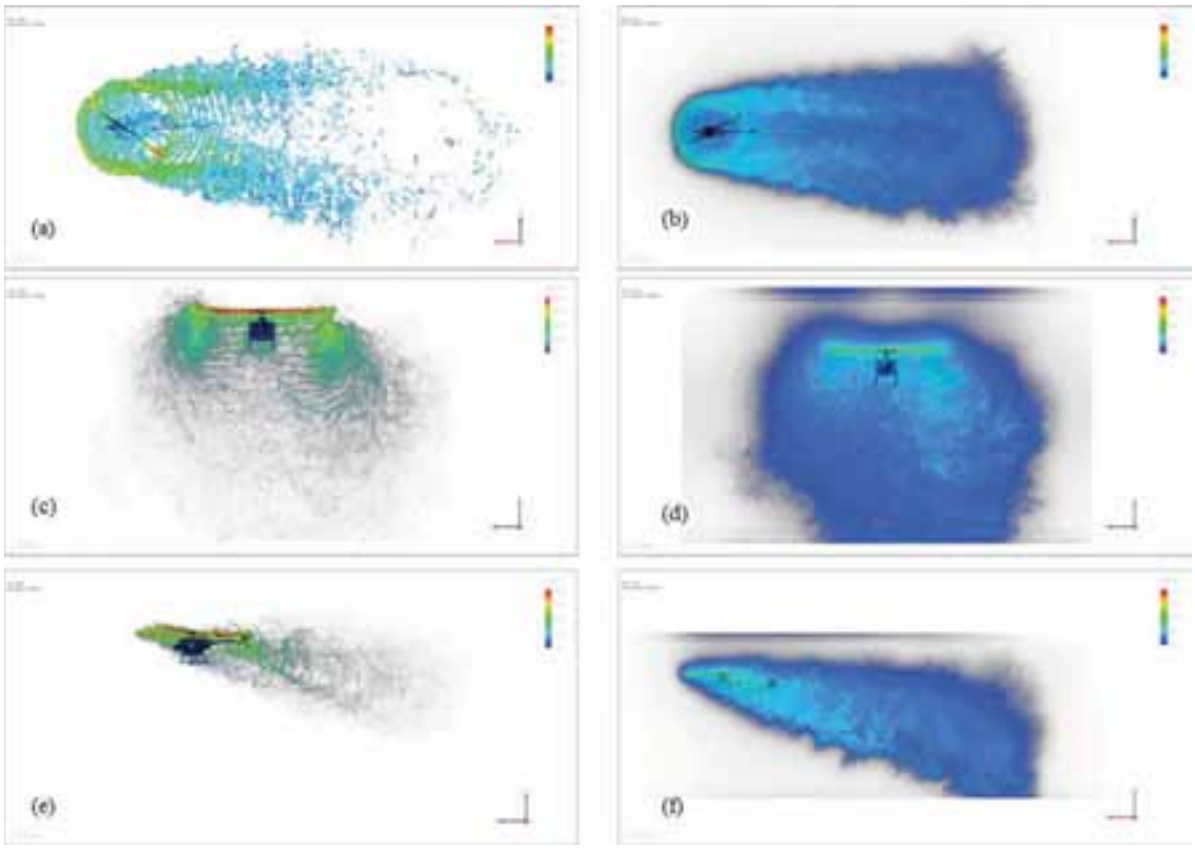


Fig. 7. UAV rotor flow field original maps. (a) is the side view of fluid-vorticity-distribution image; (b) is the top view of fluid-velocity-distribution image; (c) is face view of fluid-vorticity-distribution image; (d) is face view of fluid-velocity-distribution image; (e) is the side view of fluid-vorticity-distribution image; (f) is is the side view of fluid-velocity-distribution image.

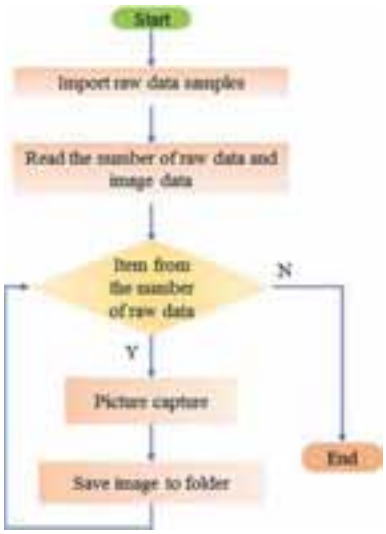


Fig. 8. Flow-field image preprocessing flowchart. The original image is flow field image from result of the data simulation. Number of raw data is amount of raw data samples. Image data is flow field image in raw data samples.

To generate an improved flow-field image based on the feature map that was extracted by the convolutional layer prior to the deconvolution, a 10-layer deconvolutional structure is employed by this paper, as illustrated in the lower half of Fig. 10. In these deconvolutional layers, a deconvolutional function, batch-normalization (BN) function and LRelu activation function are employed in each of the first nine layers, where the batch-normalization function was selected because it accelerates the deep network training by reducing the internal covariate shift (Ioffe and Szegedy, 2015). In the 10th deconvolutional layer, a deconvolutional function and the tanh function are used to generate the picture, where the tanh function is the activation function.

In these deconvolutional layers, the deconvolution kernel is 9×9 in size. The parameters of the deconvolutional structure are listed in Table 2. By the construction of these structures in the subsequent training, the generation network can learn the distribution law of the flow field in the sample data set and use it for prediction. In Fig. 10, when image data A_{ij} are entered into the convolutional layer and considering the convolution of the convolutional layer, four chronological flow-field images are read in parallel by four convolutional layers; then, the features that have been read by the convolutional layers are input into a 10-layer deconvolutional structure to generate a predicted flow-field image. In the process of generating this flow-field image, the flow-field image is under the action of the first convolutional layer; the size of the feature image that is obtained by the first convolutional layer is 128×128, and the number of feature maps is 128, as illustrated in the upper part of Fig. 10. Similarly, the sizes of the feature pictures that were obtained by the second convolutional layer, the third convolutional layer and the fourth convolutional layer are 64×64, 32×32 and 16×16, respectively, and the numbers of feature maps are 256, 256 and 512, respectively. Subsequently, the final feature map of the four input flow-field images is represented as a matrix of size $16 \times 16 \times 1024$ by the CANCAT function as input of the generator, as illustrated in Fig. 10.

To study the law of the variation of the characteristics of the flow-field distribution map during the convolution process (Kutz, 2017; Zeiler and Fergus, 2014; Chen et al., 2016), the feature extraction process for the first frame of the input picture of four consecutive frames is shown in Fig. 11. First, the features that are extracted by the

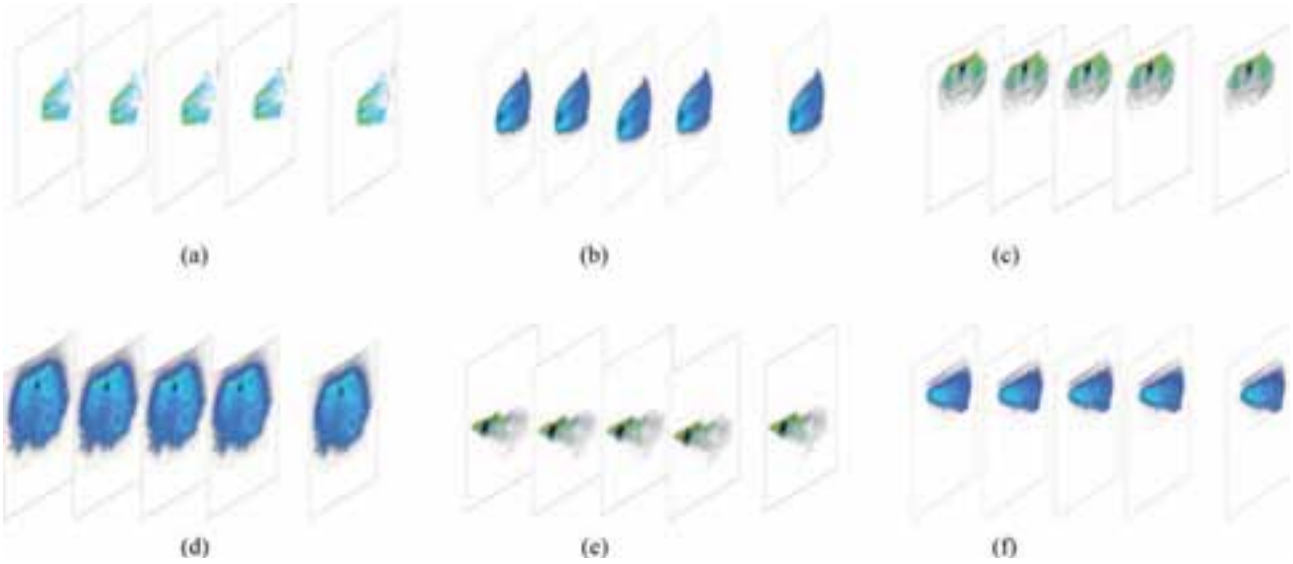


Fig. 9. (a) These five pictures are top views of the single-rotor UAV rotor vorticity map, of which the first four pictures are the input data for the neural network, and the last image is the ground-truth picture. (b) These five pictures are side views of the single-rotor UAV rotor vorticity map and are the input data for deep learning, of which first four pictures are the input data for the neural network, and the last image is the ground-truth picture. (c) These five pictures are front views of the single-rotor UAV rotor vorticity map and are input data for deep learning, of which the first four pictures are the input data for the neural network, and the last image is the ground-truth pictures. (d) These five images compose a data set for the prediction of a smooth velocity distribution. (e) These five picture are top views of the single-rotor UAV rotor flow field velocity distribution. As in the previous midstream dataset, the first four images are input data, and the last image is the ground-truth image for neural network training. (f) These five images are side views of the velocity distribution of the flow field that is distributed by the rotor flow.

first layer of the convolutional layer are mainly texture features, followed by color features. In Fig. 11, (4) corresponds to the color feature of the flow-field distribution map that was extracted by the convolutional layer; the remaining images correspond to the texture feature in convolutional layer 1. In convolutional layer 2, color features (1), (2), (6), and (7) and texture features (3), (4), (5), (8), and (9) are primarily extracted based on the feature map of the first layer. The texture is a type of visual feature that reflects the homogeneity of an image. The edge features, which include the horizontal edge features and the vertical edge features, reflect the overall contour and frame of the image.

The color characteristics reflect the depth of the colors in areas of the image. In the third layer and the fourth layer of the convolutional layer, the extracted feature map mainly includes color features in Fig. 11(d) and (e). After the feature extraction of the flow-field image by the convolutional layer, the convolutional layer abstracts the

Table 1
Parameters of the architecture of the convolutional network.

Layer	Depth	Kernel	Stride	Activation
conv1	64	9 × 9	1 × 1	LRelu
avg_pool1	—	7 × 7	1 × 1	—
conv2	128	9 × 9	1 × 1	LRelu
avg_pool2	—	7 × 7	2 × 2	—
conv3	256	9 × 9	1 × 1	LRelu
avg_pool3	—	7 × 7	2 × 2	—
conv4	256	9 × 9	1 × 1	LRelu
avg_pool4	—	7 × 7	2 × 2	—

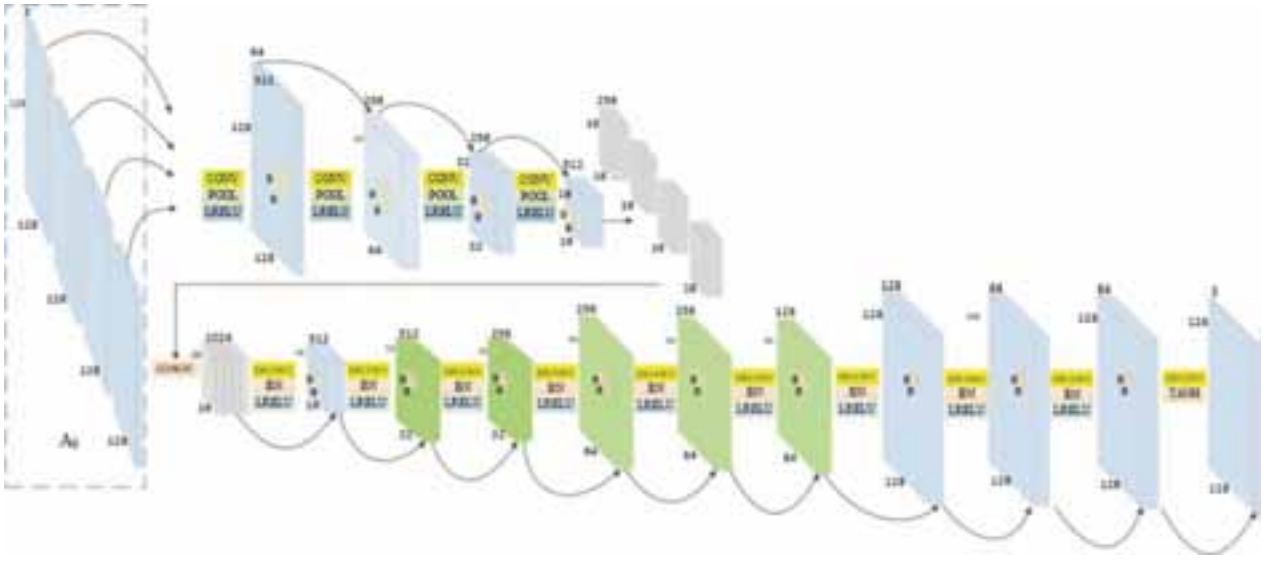


Fig. 10. Generator network structure.

Table 2
The parameter of architecture of deconvolution network.

Layer	Depth	Kernel	Stride	Activation
deconv1	512	9 × 9	1 × 1	LRelu
deconv2	512	9 × 9	2 × 2	LRelu
deconv3	256	9 × 9	1 × 1	LRelu
deconv4	256	9 × 9	2 × 2	LRelu
deconv5	256	9 × 9	1 × 1	LRelu
deconv6	128	9 × 9	1 × 1	LRelu
deconv7	128	9 × 9	2 × 2	LRelu
deconv8	64	9 × 9	1 × 1	LRelu
deconv9	64	9 × 9	1 × 1	LRelu
deconv10	3	9 × 9	1 × 1	Tanh

features step by step to abstractly represent the image so that the neural network can well understand and distinguish the image.

For the flow field prediction, the data sets that are composed of the flow-field images are utilized. In this process, by using these data sets to train the generation network, the generation network can learn implicit laws continuously from the entire flow field data set. The well-trained generation network can reconstruct the flow field for prediction. The reconstruction process of generating the network model for flow field after training is illustrated in Fig. 12. In these figures, after the flow-field feature data with data type 16 × 16 × 1024 have been input into the deconvolutional layer, the input data are reverse-convolved by the deconvolutional layer and, finally, the prediction of the flow-field image is realized. As shown in Fig. 12(a), the feature map of the first layer of the deconvolutional layer is extracted. The deconvolutional layer of the first layer in the feature does not learn the potential features of the flow-field distribution. Then, these features are used as input to the second layer. After the second layer of deconvolution, the extracted feature map is as shown in Fig. 12(b). The feature maps begin to change as the weights and bias values are adjusted in the generator. In Fig. 12(c), the characteristics of the flow field begin to appear in these feature maps. In Fig. 12(d), the contour of the flow field begins to appear. In the 4th-to-10th-layer deconvolution process, the generator continuously adjusts the biases and weights so that the characteristics of the learned flow field become clearer. Finally, via the above learning process, the generator learns the texture features of the flow field to reconstruct the flow field as the prediction.

During the reconstruction of this flow field, after the network has been sufficiently well trained, it extracts the feature maps that were processed by the convolutional layer before the deconvolutional layer and interprets them via a unique approach. Then, according to these feature maps, it reconstructs the features of the flow-field distribution picture that we want to predict layer by layer via our unique approach. That is to say, after the training network has completed its training, it can learn common features and predict the flow field.

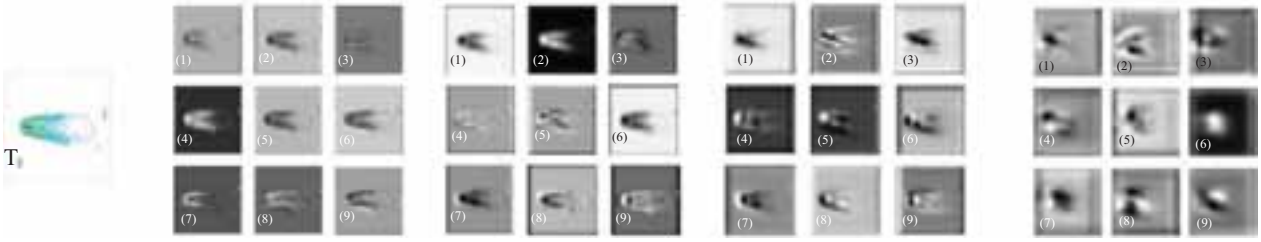
2.4. Discriminator network

The discriminator network is an important element that constitutes GAN and an integral part of the adversarial structure in GAN. The discriminator network is mainly used to judge the authenticity of the generated picture of the network in order to optimize the generated network so that it can generate high quality flow field map. The detailed structure of the discriminator, some parameters in the structure and discriminating process of true and false pictures is introduced in this section. The structure of this discriminator network consists of 6 convolutional layer structures and 2 fully connected layers as shown in Fig. 13. Each layer of convolution is made up of a convolutional function, batch-normalization functions are associated with an average pooling function. In the discriminator, which consists of these components, to more accurately judge the authenticity of the input picture, a convolution kernel of size 5 × 5 and a pooling window of size 7 × 7 are utilized. The parameters of the discrimination network are listed in Table 3.

In Fig. 13, the predicted image is a generated graph demonstrating that the generative model does not fully capture the features of the training data, and the real image is the picture in the dataset. When a real picture is input, the data are subjected to feature extraction by the convolutional layer and conversion by the fully connected layer to finally output a high probability value, which we expect to be close to 1. Sometimes, through the continuous input of real pictures, the discriminator is also trained, which constantly improves the discriminator's ability to judge true and false pictures. When a fake picture is input into the discrimination network, the picture is also subjected feature extraction by the convolutional layer and conversion by the fully connected layer to finally output a low probability value that is close to 0. In the training process, the flow-field image that is generated by the generated model must deceive the discriminator as much as possible so that its output probability is close to 1, thus achieving the role of the fraud deception the discriminator model.

After the final training, the predicted image that is generated by the generator is realistic and, thus, successfully realizes deception. In this process, the discriminant model extracts the features of the input data, including the real picture and the predicted picture, inputs them into the fully connected layer, and obtains the expected value. In the later stages of training, when predicting pictures and real picture input, the expected value of the discriminator input will be close to 1 because the predicted picture that is generated by the generated network is sufficiently realistic, and the discriminator cannot distinguish it from the real image. The feature extraction process for true and false pictures is illustrated in Fig. 14. This figure shows that the discriminator network identifies the law of the flow-field distribution characteristics of the true and false pictures.

In Fig. 15, when the true and false pictures pass through the first layer of the convolutional layer, the convolutional layer extracts 64 feature maps of size 128 × 128. The feature of the first layer is input as the second layer, and the second layer extracts 128 feature maps of size 128 × 128. The feature that is extracted by the third layer consists of 128 feature maps of size 64 × 64. The feature that is extracted by the fourth layer consists of 128 feature maps of size 64 × 64. The feature that is extracted by the fifth layer consists of 128 feature maps of size 32 × 32. The feature that is extracted by the sixth layer consists of 128 feature maps of size 32 × 32. Finally, the discriminator can distinguish



(a) Original Image (b) Convolutional layer 1 (c) Convolutional layer 2 (d) Convolutional layer 3 (e) Convolutional layer 4

Fig. 11. Evolution of a randomly selected subset of learned features during the training process. Nine maps are shown for each layer.

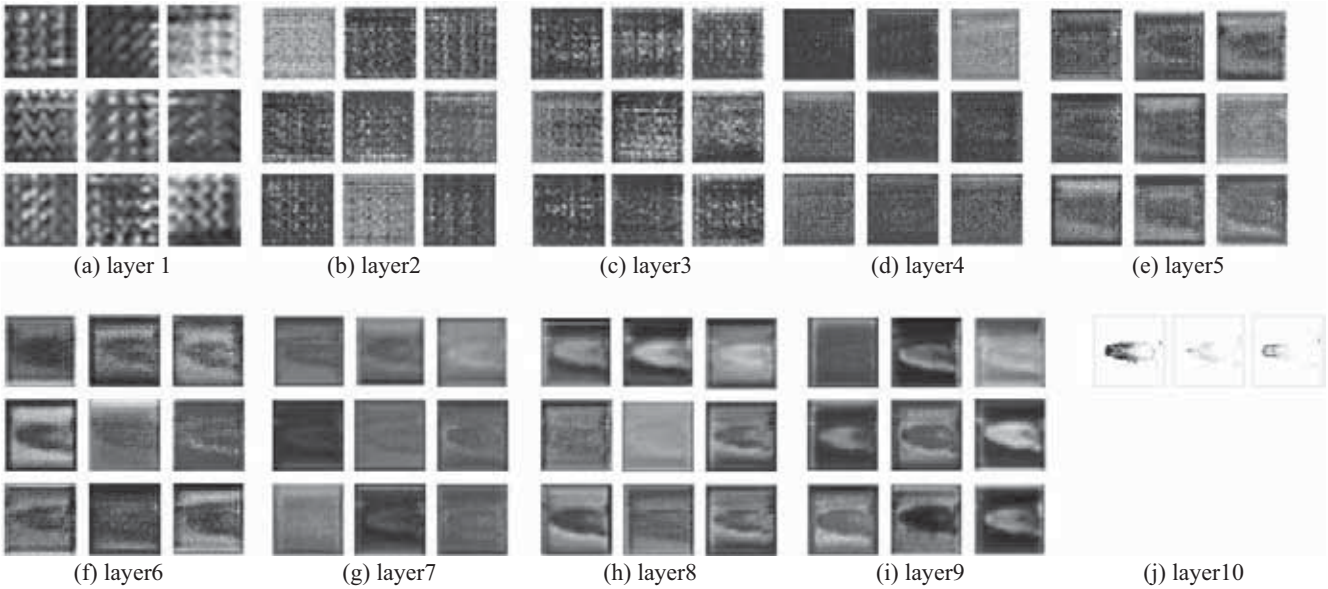


Fig. 12. Evolution of a randomly chosen subset of features map through the refactoring process in the vortex top view prediction process. Nine maps are listed for the first to the ninth layer. The tenth layer lists three maps because there are three feature maps in total.

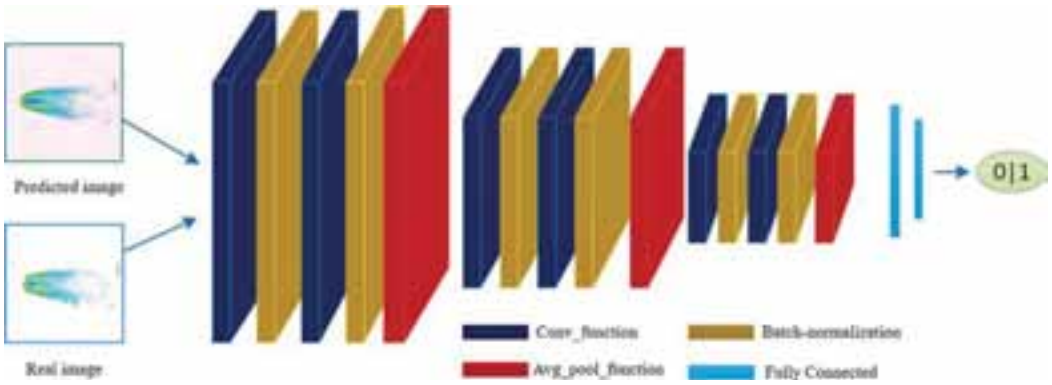


Fig. 13. Discriminator architecture for judging true and false pictures.

Table 3
The parameter of architecture of discriminator network.

Layer	Depth	Kernel	Stride	Activation function
conv1	64	5 × 5	1 × 1	LRelu
conv2	128	5 × 5	2 × 2	LRelu
avg_pool1	—	7 × 7	1 × 1	—
conv3	128	5 × 5	1 × 1	LRelu
conv4	128	5 × 5	1 × 1	LRelu
avg_pool2	—	7 × 7	2 × 2	—
conv5	128	5 × 5	1 × 1	LRelu
conv6	128	5 × 5	1 × 1	LRelu
avg_pool3	—	7 × 7	2 × 2	—

between true and false pictures by using the extracted feature of the last layer and the final obtained features, in combination with the fully connected layer.

The discriminator distinguishes between true and false pictures by autonomously extracting the feature distribution law of the true and false flow-field maps. In the real map convolution process, the feature map that is obtained via convolution gradually changes from concrete to abstract. In the real picture convolution process in Fig. 14, the attributes of the features that are extracted by convolutional layer 1 include texture, color, and edge features. In convolutional layer 1, texture features are displayed in (c) and (f), color features in (b) and (i), and edge features in (a), (d), (g) and (h). In convolutional layer 2, the color feature (e) and texture features (a), (b), (c), (d), (f), (g), (h) and (i) are extracted based on the first convolutional layer. Starting with the third convolutional layer, the extracted features become increasingly abstract. In the third and fourth convolutional layers, the features are slightly abstract. The feature map of the flow-field map that is extracted by this layer still includes texture features and color features in the third and fourth layers. In Fig. 14(Ad), pictures (a), (b), (c), (e), (g) and (h) correspond to texture features, and picture (d), (f) and (i) correspond to color features. In Fig. 14(Ae), pictures (a), (c), (e), (h) and (i) correspond to color features, and pictures (b), (d), (f) and (g) correspond to texture features. In the fifth and sixth convolutional layers, the extracted feature map becomes more abstract and the extracted feature types only include color features in Fig. 14(Af) and Fig. 14(Ag). In the predicted picture convolution process, as in the feature extraction process of a real image, the features that are extracted by the first and second convolutional layers include texture, color, and edge features. The features that are extracted by the third and fourth convolutional layers include textures and color features. The features that are extracted by the fifth and sixth convolutional layers include color features. In the prediction map feature extraction picture in Fig. 14, pictures (e), (f) and (h) are color features, pictures (c), (d) and (i) are texture features and pictures (a), and (b) and (g) are edge features in Fig. 14(Bb). In Fig. 14(Bc), pictures (a), (e), (g) and (i) are color

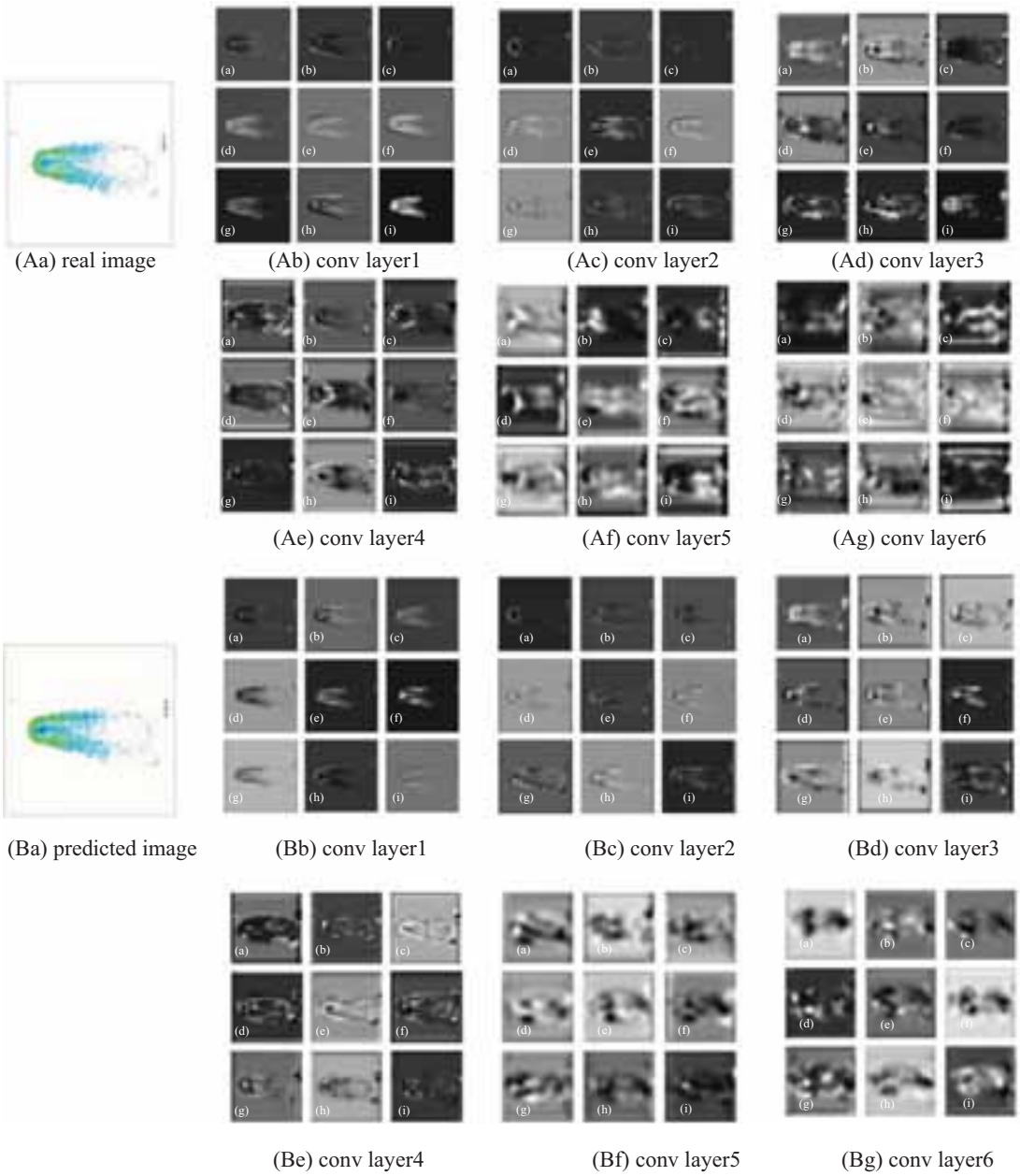


Fig. 14. The presentation of each layer of the convolutional layer feature map of the feature extraction process of the true and false flow field distribution map, each layer randomly extracts nine pictures to represent.

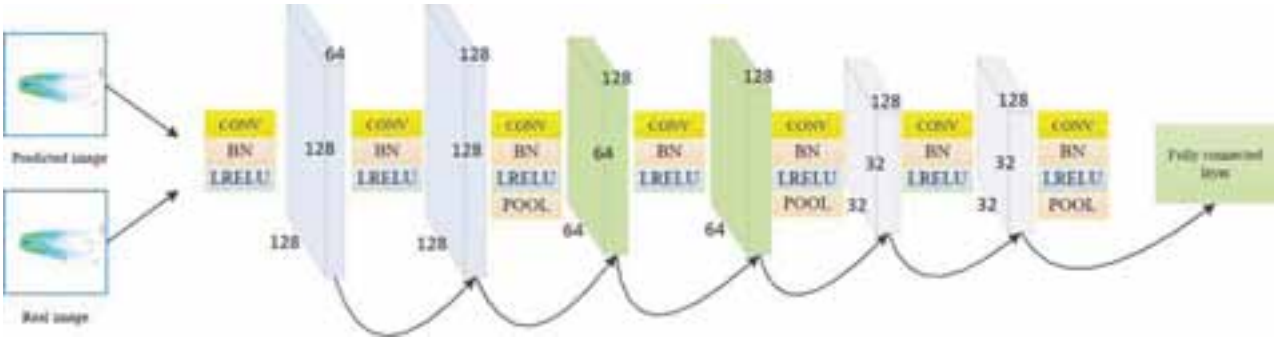
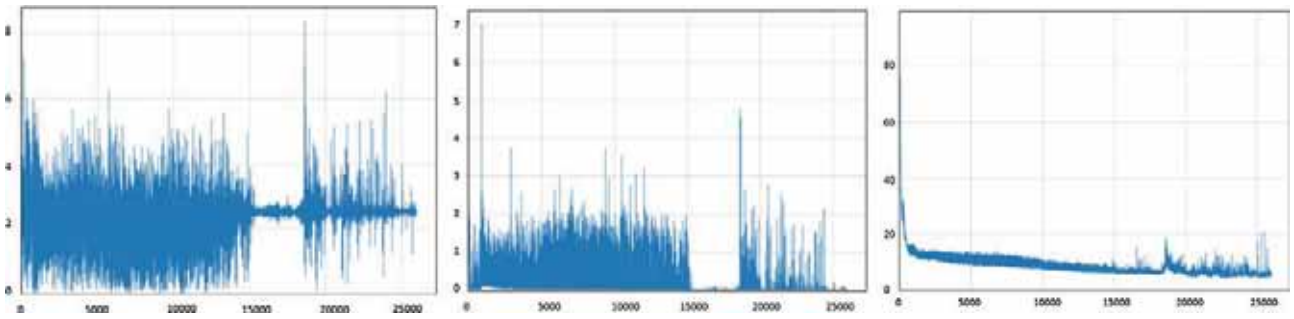


Fig. 15. Process of changing the feature map in the discriminator.



(a) Generative model loss function (b) Discriminative model loss function (c) Content loss function

Fig. 16. Loss function graphs for model iteration when predicting the vortex flow-field top view.

features, pictures (b), (d), (f) and (h) are texture features and picture (c) is an edge feature. In Fig. 14(Bd), pictures (d), (f) and (i) are color features, and pictures (a), (b), (c), (e), (g) and (h) are texture features. In Fig. 14(Be), pictures (b), (d), (h) and (i) are color features, and pictures (a), (c), (e), (f), (g) are texture features. In Fig. 14(Bf) and Fig. 14(Bg), the feature maps are all color features. The entire discriminator finally distinguishes between true and false pictures by using the above extracted features.

In summary, in the training process, the discrimination network employs the convolutional neural network to extract the features of the real picture and the predicted picture to continuously improve the judgment performance and, finally, realize satisfactory discrimination performance between true and false images. At the same time, the discriminating network ultimately realizes the objective of training the generated network via a confrontational approach.

2.5. Loss function

The loss function of a deep neural network is important for the successful prediction by the deep learning model of the flow field of a single-rotor UAV. In terms of the loss function, reducing the gap between the real flow-field image and the model prediction result is of great significance. At the same time, the results of the neural network model that are used to predict images must also be associated with a suitable loss function. In addition, the antagonistic loss function is indispensable for GAN because it is a key factor in the formation of resistance to GAN. In this study, using a classic approach, the predicted flow-field distribution image is compared pixel-wise with the corresponding distribution from the real image using a content loss function. The adversarial loss function is the decisive factor in the network confrontation for the real/synthetic prediction of the discriminator from the generated flow-field map.

To make the flow-field image that is predicted by the generator realistic, the gap between the predicted picture of the flow field and the real flow-field image must be expressed as a content loss function. Given a set of input flow-field images and a real flow field R_i of dimensions $M = W \times H$, the generation network G generates a flow field F_i as a vector of probabilities, where W and H describe the dimensions of the corresponding flow-field map within the GAN. The GAN-based content loss, which is denoted as $L(R_iF_i)$, is the Euclidean loss (Shi et al., 2016; Pan et al., 2017), which is defined as

$$L_{EL} = \frac{1}{M}\sum_{i=1}^{M}((R_i - F_i))^2 \tag{12}$$

In our work, the content loss is important for the smooth prediction of the flow field results by the GAN. In the training of the neural network, the flow-field image F_i that is generated by the generation network approaches the ideal result and is almost able to deceive the discriminator.

The adversarial loss function is also highly important for the generative adversarial network. The loss function mainly depends on the performance and results of the discriminator network. In our work, the real flow-field image and the flow field that is generated by generation network must be distinguished by discriminator network and assigned values of 0 and 1, where 0 corresponds to the real image and 1 to the false image. Both outcomes of the discriminator network are eventually used as input data and input into the adversarial loss function for true/false judgements. The adversarial loss function is divided into a generative loss function and a discriminative loss function. The generative loss is based on the probabilities of the discriminator $D(G(X^i))$ over all training images and encourages the network to favor solutions that reside on the manifold of natural images to fool the discriminator network. The generative loss function (Xie et al., 2018; Isola et al., 2017) is defined as follows:

$$L_G = \sum_{i=1}^{N} -\log(G(X^i)) \tag{13}$$

where $G(X^i)$ is the generative network, which generates the distribution of the flow field for the four consecutive flow-field images for input data X^i.

The discriminator loss is trained to distinguish between specimens from the real distribution of the flow field and the specimens that are generated by the generative network. During training, generated and real samples are used to train the discriminator to promote its discrimination performance. Meanwhile, the sample also trains the generative network to promote its performance in deceiving the discriminator. The discriminative loss function (Isola et al., 2017; Zhang et al., 2017) is defined as follows:

$$L_G = \sum_{i=1}^{N} [\log D(y^i) + \log(1 - D(G(X^i)))] \tag{14}$$

where $D(y^i)$ is the value of the discrimination network after y^i, y^i is a real picture in the training sample, $D(G(X^i))$ is the value after the predicted image has been generated by the generation network, $G(X^i)$ is a series of consecutive frames of images that are obtained after generating the network, and X^i is the flow-field image input to a series of consecutive frames in the generated network.

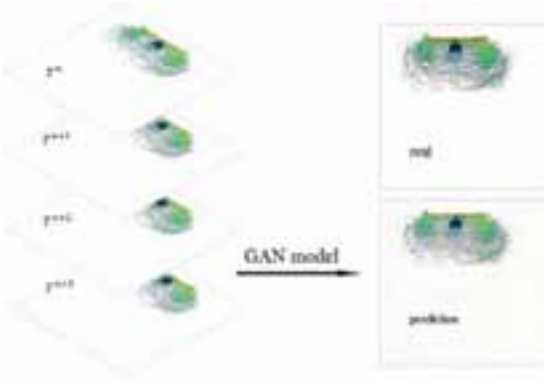
In Fig. 16, three loss function maps for predicting the vortex flow-field top view are presented. This figure demonstrates the variations of the generated model loss function, the discriminant model loss function, and the content loss function during the training process. During the training process, a joint loss that consists of the generative model loss, the discriminative model loss, and the content loss is minimized.

In our study, the flow field is predicted by constructing a neural network model. The neural network model must be trained on the flow-field image distribution data set. In neural network training, the loss function is the core component of the neural network model. In our work, neural network training is performed on the TensorFlow platform using the Python programming language. The training algorithm of the model is presented in Table 4.

Table 4
GAN training algorithm.

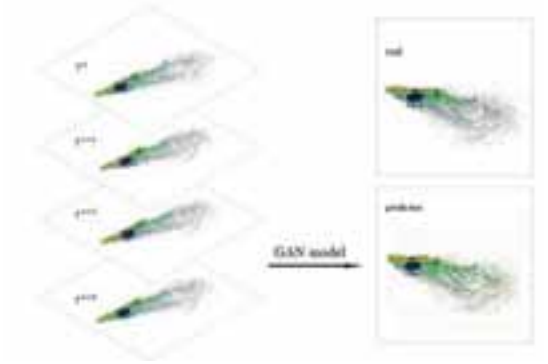
Algorithm: GAN training

```
# d denotes the training data sets.
# x1, x2, x3, x4 and y denote data patches.
# φ is the output of generation network G-Net.
# f and r are the outputs of D-Net with the fully connected layer.
# num_batch is the total data volume.
# E is the step size for training the network.
for each i ∈ E do
    for each j ∈ num_batch do
        x1, x2, x3, x4, y ← Randomsample(d)
        φ ← G(x1, x2, x3, x4)
        f ← D(y)
        rr ← D(φ)
        update G-Net by minimizing LEL loss with Eq. (12)
        update D-Net by minimizing LD loss with Eq. (14)
        update G-Net and D-Net by minimizing LG loss with Eq. (13)
end for
```



(a)Input images (b) Predicted image and real image

(I)



(c) Input images (d) Predicted image and real image

(II)

Fig. 17. (a) and (b) Prediction of the front view of the flow-field vorticity image. (c) and (d) Prediction of the side view of the flow-field vorticity. (a) and (c) Input data of the neural network model. (b) and (d) Comparison between the predicted image and the real image. Neural network prediction model: (I) and (II) show the GAN model that was trained using the top view of the rotor vortex flow field. The four flow-field images, which are arranged in chronological order, are input into the GAN model to generate a fifth frame model.

3. Results and discussion

In our study, the two types of flow fields are divided into six types of prediction studies, which are used for deep learning. The six flow fields are the side view, the front view and the top view of the vorticity flow field of the single-rotor UAV rotor flow field and the side view, front view and top view of the velocity flow field of the flow field. Using these flow field data, every five chronological flow field data constitute a single data item, wherein the first four data $\{T^n, T^{n+1}, T^{n+2}, T^{n+3}\}$ of each such data item are input data and the last is output data. Then, the collection of these data constitute a data set. In model prediction, the first four flow-field maps are used to predict the last stream field image, which will be used to construct the model's input and output. After our experiments, the trained deep neural network model can predict the flow field and the predicted result is used in practical applications. A set of input pictures, the corresponding predicted picture, and the real picture are shown in Fig. 17. The figure shows the prediction results for the front and side views of the vorticity flow field. In this figure, when flow-field image (a) or (c) is input, the difference between the predicted picture and the real picture is extremely small.

To further demonstrate the predictive power of the deep neural network model, this study used a variety of flow-field images for prediction experiments. In Fig. 18, six flow fields map are used for the training and prediction of neural network models: (a) the vorticity flow field top view, (b) the vorticity flow field front view, (c) the vorticity flow field side view, (d) the velocity flow field front view, (e) the velocity flow field side view, (f) the velocity flow field top view. In this picture, the first row presents a top view of the velocity field that was obtained via the CFD approach for 10 flow fields. The second row presents the resulting flow-field top maps that were predicted by the GAN. The third row presents a front view of the velocity field that was obtained via the CFD approach for 10 flow fields. The fourth row presents the resulting flow-field maps that were predicted by the GAN. The fifth row presents side views of 10 vorticity flow fields. The sixth row contains vortex flow field side views that were predicted by the GAN model. The seventh row contains 10 velocity flow field front views that were generated by the CFD model. The eighth row presents the velocity flow field front views that were predicted by the GAN model. The ninth row contains 10 velocity flow field side views that were generated by the CFD model. The tenth row presents the velocity flow field side views that were predicted by the GAN model. The eleventh row contains 10 velocity flow field top views that were generated by the CFD model. The twelfth row presents the velocity flow field top views that were predicted by the GAN model. According to the figure, comparing the flow-field maps in the first and second rows, the third and fourth rows, the fifth and sixth rows, the seventh and eighth rows, the ninth and tenth rows, and the eleventh and twelfth row, the results of the data simulation are consistent with the results that were predicted by the GAN model. Thus, in our research, the GAN prediction model can predict the flow field.

To better represent the predicted performance of GAN, this part is combined with the real and predicted images shown in Fig. 18 for quantitative analysis. The structural similarity index method (SSIM) is applied to evaluate the similarity between the real graph and the predicted result. There is a strong correlation between the pixels of a natural image. Using this relationship, the SSIM index obtains the similarity of the picture by measuring the values of the three modules of brightness, contrast and structure (Wang et al., 2004). In this method, the average pixel value of the pixels of the picture is taken as an estimate of the brightness (Zhu et al., 2018):

$$\mu_x = \frac{1}{N}\sum_{1}^{N} x_i \tag{15}$$

where N is the number of all pixels in the image, x is the pixel value of the image and x includes r or p. The average standard deviation of the pixels of the picture is used as an estimate of the contrast value of the picture, the measured value of contrast is (Zhu et al., 2018):

$$\sigma_x = \left(\frac{1}{N-1}\sum_{i=1}^{N}(x_i - \mu_x)^2\right)^{\frac{1}{2}} \tag{16}$$

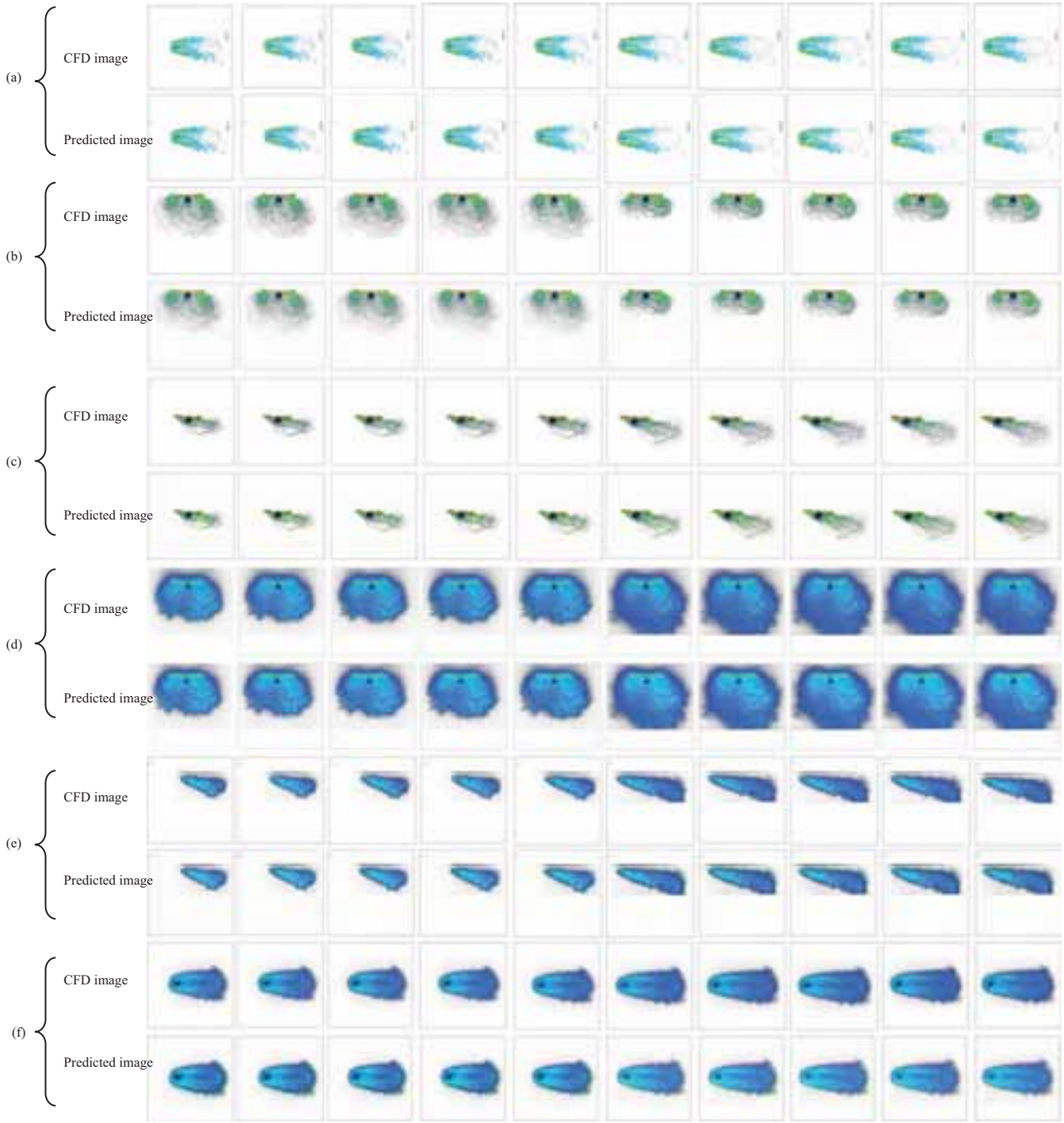


Fig. 18. Comparison of predicted images with real images.

where N is the number of all pixels in the image, x is the pixel value of the image and x includes r or p. The value of SSIM needs to compare the brightness, contrast and structure of the two pictures. The brightness contrast function, contrast function and structure contrast function were given as follows (Zhu et al., 2018):

$$l(r, p) = \frac{2\mu_r\mu_p + C_1}{\mu_r^2\mu_p^2 + C_1}, \tag{17}$$

$$c(r, p) = \frac{2\sigma_r\sigma_p + C_2}{\sigma_r^2\sigma_p^2 + C_2}, \tag{18}$$

$$s(r, p) = \frac{2\sigma_{rp} + C_3}{\sigma_r\sigma_p + C_3}, \tag{19}$$

and

$$\sigma_{rp} = \frac{1}{N-1}\sum_{1}^{N}(r_i - \mu_r)(p_i - \sigma_p) \tag{20}$$

where r is discrete signals of real image, p is discrete signals of predicted image, C_1, C_2 and C_3 is three constants to avoid the case where the denominator is 0. The form of SSIM between signal r and p is defined as (Hasan et al., 2018):

Table 5
The result SIMM for real images and predicted images.

Row number	Column number									
	1	2	3	4	5	6	7	8	9	10
	Value of SSIM									
1	0.979	0.972	0.973	0.950	0.986	0.956	0.983	0.982	0.967	0.985
2	0.971	0.973	0.967	0.975	0.971	0.960	0.966	0.959	0.955	0.961
3	0.986	0.983	0.982	0.981	0.982	0.979	0.985	0.983	0.978	0.980
4	0.969	0.966	0.980	0.966	0.967	0.966	0.968	0.981	0.981	0.980
5	0.973	0.973	0.972	0.972	0.971	0.961	0.970	0.977	0.961	0.972
6	0.965	0.964	0.969	0.969	0.968	0.970	0.961	0.970	0.966	0.959

$$SSIM(r, p) = l(r, p)\cdot c(r, p)\cdot s(r, p) = \frac{(2\mu_r\mu_p + C_1)(2\sigma_r\sigma_p + C_2)}{(\mu_r^2 + \mu_p^2 + C_1)(\sigma_r^2 + \sigma_p^2 + C2)} \quad (21)$$

In fact operation, C_1 is generally 1.275, C_2 is 3.825, C_3 is 1.9125, and the value of SSIM belongs to between 0 and 1; when the value is larger, the two pictures are more similar (Wang et al., 2004). By the SSIM method given above, the similarity comparison between the real map and the predicted graph in Fig. 18 is performed. The results of the similarity are shown in Table 5. In this table, the data in the first line is the result of the comparison of the similarity between the true and the false pictures of the first line and the second line in Fig. 18; by analogy, the SSIM indices of the 11-line and 12-line pictures in Fig. 18 correspond to the last line in Table 5. According to the results of the SSIM value data in Table 5, The SSIM value of the prediction result of each picture is basically greater than 0.960. According to the paper by Reisenhofer et al. (2018), for the graph in Fig. 18, the result of SSIM indicate that our predicted results performs favorably in terms of visual quality.

In our research, the GAN model is used to predict the flow field as it yields realistic results, which is because after training, the deep learning model can identify and utilize the hidden features of the flow-field image. By utilizing these trained and learned flow-field features, the GAN model can establish a connection between the input data, namely, four chronological maps, and the output data, namely, a flow-field image, to realize the desired predictive performance. This connection is equivalent to the physical formula in the CFD model, in which the physical model is determined via the physical equation control method to obtain the flow-field simulation map. Similarly, the deep neural network model can use its connection to the physical model to generate a flow-field image. In Fig. 17, (I) is a front-view model of the vorticity flow field and (II) is a side-view model of the vorticity flow field. These models demonstrate that the GAN prediction model can generate subsequent flow fields by utilizing the previously generated flow field, which is similar to the physical-model-controlled CFD model. The deep learning model and the CFD model can realize the same flow field generation performance and have similar advantages. In practice, when the neural network model that is obtained by training the GAN on the appropriate data set predicts the flow field, the operation speed of the model is much faster compared to the CFD model. In the experiment, the CFD model consumes more than 24 h in the process of generating 400 flow-field images. The average time that is required to generate a flow-field image is at least 216 s. The GAN model only takes less than a second to generate a flow-field image. This difference substantially reduces the computation time and computational cost.

In our study, the GAN model also yielded satisfactory results in compressing data in terms of the compression calculation time. In Fig. 19, top views of the rotor flow fields of five groups of UAVs that were predicted by the model are shown. The first column in Fig. 19 presents the raw data, which have not been processed; the second column presents the images that can be used as the predictions in the data set after processing, and the third column presents the predicted flow-field maps of the GAN model. In Fig. 19, each row of pictures is considered a set of data. The memory sizes of the original picture, the processed picture, and the predicted picture are listed in Table 6. In the table, the compression ratio is the result of comparing the storage sizes of the original picture, the preprocessed picture, and the predicted picture. According to the compression ratio values in the table, the GAN model occupies the smallest storage space. Therefore, the GAN model has satisfactory data compression performance, which reduces the computer storage costs.

4. Conclusions

In this paper, a prediction model that is based on a GAN was proposed for predicting flow fields. By constructing a GAN that consists of multiple convolutional layers and training the GAN using six flow field data sets applied in combination with loss functions, the GAN can extract and learn the characteristics of the flow field. Comparing the flow-field map that was predicted by the GAN with the flow-field map that was generated by CFD, the GAN can predict the flow-field distribution of the next frame based on the flow-field distributions of the previous four frames.

In our study, the GAN successfully constructs a network model that can predict the flow field by learning the flow-field features in the original data to successfully establish the relationship between the input flow field data and the output flow field. In this process, the model does not depend on physical equations; hence, the model can provide an alternative data simulation method.

It takes much less time for the GAN model to generate a flow field image than the CFD model. The storage space that is occupied by the generated flow-field image that is generated by the network model is smaller than that of the CFD model. Therefore, compared to the CFD model, the GAN model can compress data faster and with a higher compression ratio, which can reduce the computing cost.

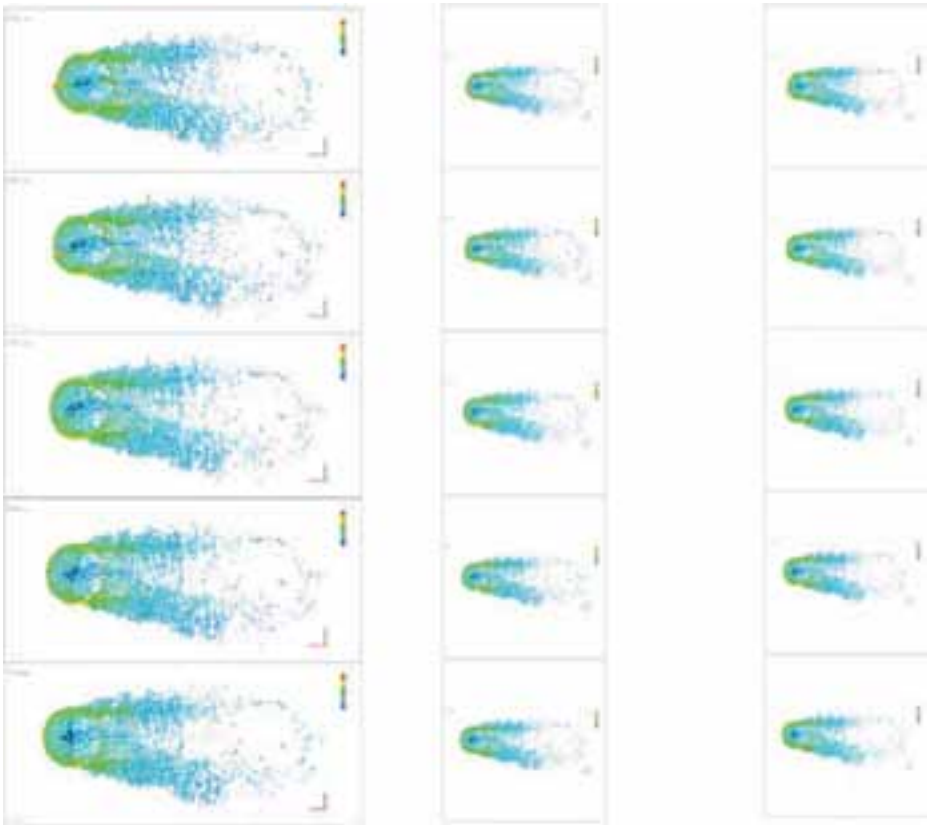
More integrated thinking and more purposeful research will continue to be necessary for tackling all the challenges that different time intervals may have an impact on the prediction of GAN.

Declaration of Competing Interest

The authors declared that they have no conflicts of interest to this work. We declare that we do not have any commercial or associative interest that represents a conflict of interest in connection with the work submitted.

Acknowledgement

The authors gratefully acknowledge the support of Characteristic Innovation Projects of Colleges and Universities in Guangdong Province (2018KTSCX019), Guangzhou Science and Technology Project (201707010047), Guangdong Leading Talent Project (2016LJ06G689) and National Natural Science Foundation of China (Grant No. 61773171).



(a) The original image (b) The program processing result (c) The predicted result

Fig. 19. Comparison between the CFD model and the predictive model.

Table 6
Compression ratios.

Case	Original image	Processed image	Predicted image	Compression ratio
1	739 KB	65 KB	12.5 KB	59.12:5.20:1
2	740 KB	65 KB	12.8 KB	57.81:5.07:1
3	736 KB	65 KB	12.7 KB	57.95:5.12:1
4	729 KB	65 KB	12.5 KB	58.32:5.20:1
5	731 KB	65 KB	12.7 KB	57.56:5.12:1
Method	CFD model	—	GAN model	—

Appendix A. Supplementary material

Supplementary data to this article can be found online at https://doi.org/10.1016/j.compag.2019.105004.

References

Brionnaud, R., Chávez Modena, M., Trapani, G., M. Holman, D., 2016. Direct noise computation with a lattice-Boltzmann method and application to industrial test cases. In: 22nd AIAA/CEAS Aeroacoustics Conference, pp. 2969.

Creswell, A., White, T., Dumoulin, V., Arulkumaran, K., Sengupta, B., Bharath, A.A., 2018. Generative adversarial networks: an overview. IEEE Signal Process Mag. 35 (1), 53–65.

Chen, Y., Jiang, H., Li, C., Jia, X., Ghamisi, P., 2016. Deep feature extraction and classification of hyperspectral images based on convolutional neural networks. IEEE Trans. Geosci. Remote Sens. 54 (10), 6232–6251.

dos Santos Ferreira, A., Freitas, D.M., da Silva, G.G., Pistori, H., Folhes, M.T., 2017. Weed detection in soybean crops using ConvNets. Comput. Electron. Agric. 143, 314–324.

Durugkar, I., Gemp, I., Mahadevan, S. (2016). Generative multi-adversarial networks. arXiv preprint arXiv:1611.01673.

Ducros, F., Nicoud, F., Poinsot, T., 1998. Wall-adapting local eddy-viscosity models for simulations in complex geometries. Numer. Methods Fluid Dynamics VI 293–299.

Fengbo, Y., Xinyu, X., Ling, Z., Zhu, S., 2017. Numerical simulation and experimental verification on downwash air flow of six-rotor agricultural unmanned aerial vehicle in hover. Int. J. Agric. Biol. Eng. 10 (4), 41–53.

Ferentinos, K.P., 2018. Deep learning models for plant disease detection and diagnosis. Comput. Electron. Agric. 145, 311–318.

Hao, Z., Lijun, Q., Yallei, W., et al., 2019. Research on spatio-temporal distribution of down-wash airflow for multi-rotor plant protection UAV based on porous model. Trans. Chin. Soc. Agric. Mach. 50 (1000–1298), 112–122.

Hasan, M., El-Sakka, M.R., 2018. Improved BM3D image denoising using SSIM-optimized Wiener filter. EURASIP J. Image Video Process. 2018 (1), 25.

Ioffe, S., Szegedy, C. (2015). Batch normalization: Accelerating deep network training by reducing internal covariate shift. arXiv preprint arXiv:1502.03167.

Isola, P., Zhu, J.Y., Zhou, T., Efros, A.A., 2017. Image-to-image translation with conditional adversarial networks. In: Proceedings of the IEEE Conference on Computer Vision and Pattern Recognition, pp. 1125–1134.

Jin, X., Cheng, P., Chen, W.L., Li, H., 2018. Prediction model of velocity field around circular cylinder over various Reynolds numbers by fusion convolutional neural networks based on pressure on the cylinder. Phys. Fluids 30 (4), 047105.

Kamilaris, A., Prenafeta-Boldú, F.X., 2018. Deep learning in agriculture: A survey. Comput. Electron. Agric. 147, 70–90.

Kussul, N., Lavreniuk, M., Skakun, S., Shelestov, A., 2017. Deep learning classification of land cover and crop types using remote sensing data. IEEE Geosci. Remote Sens. Lett. 14 (5), 778–782.

Kutz, J.N., 2017. Deep learning in fluid dynamics. J. Fluid Mech. 814, 1–4.

Lee, S., You, D. (2017). Prediction of laminar vortex shedding over a cylinder using deep learning. arXiv preprint arXiv:1712.07854.

Men, Y., Lai, Y., Dong, S., Du, X., Liu, Y., 2017. Research on CO dispersion of a vehicular exhaust plume using Lattice Boltzmann Method and Large Eddy Simulation. Transport. Res. Part D: Transport Environ. 52, 202–214.

Preftakes, C.J., 2017. Exposure and Risk to Non-Target Receptors for Agricultural Spray Drift of Formulation Types and Adjuvants. Doctoral dissertation. State University-Bozeman, College of Agriculture, Montana.

Pandya, D.A., Dennis, B.H., Russell, R.D., 2017. A computational fluid dynamics based artificial neural network model to predict solid particle erosion. Wear 378, 198–210.

Pan, J., Ferrer, C., Mcguinness, K., et al. (2017), SalGAN: Visual Saliency Prediction with Generative Adversarial Networks.

Reeg, J., Schad, T., Preuss, T.G., Solga, A., Körner, K., Mihan, C., Jeltsch, F., 2017. Modelling direct and indirect effects of herbicides on non-target grassland communities. Ecol. Model. 348, 44–55.

Reisenhofer, R., Bosse, S., Kutyniok, G., Wiegand, T., 2018. A Haar wavelet-based perceptual similarity index for image quality assessment. Signal Process. Image Commun. 61, 33–43.

Santana, F., Oliva, G., de Souza, C.R., Gerosa, M.A., 2011. Xflow: An extensible tool for empirical analysis of software systems evolution. Proceedings of the VIII Experimental Software Engineering Latin American Workshop, ESELAW, vol. 11.

Sheng, W., Jie, H., Yubin, L., Xuanchun, Y., Yuhua, L., et al., 2018. Influence of wing tip vortex on drift of singe rotor plant protection unmanned aerial vehicle. Trans. Chin. Soc. Agric. Mach. 49 (1000–1298), 127–137 + 160.

Shi, W., Caballero, J., Huszár, F., Totz, J., Aitken, A.P., Bishop, R., et al., 2016. Real-time single image and video super-resolution using an efficient sub-pixel convolutional neural network. In: Proceedings of the IEEE Conference on Computer Vision and Pattern Recognition, pp. 1874–1883.

Teske, M.E., Wachspress, D.A., Thistle, H.W. (2018). Prediction of Aerial Spray Release from UAVs.

Thibault, S., Holman, D., Garcia, S., Trapani, G., 2017. CFD simulation of a quad-rotor UAV with rotors in motion explicitly modeled using an LBM approach with adaptive refinement. In: 55th AIAA Aerospace Sciences Meeting, pp. 0583.

Wang, Z., Bovik, A.C., Sheikh, H.R., Simoncelli, E.P., 2004. Image quality assessment: from error visibility to structural similarity. IEEE Trans. Image Process. 13 (4), 600–612.

Xiongkui, H., Bonds, J., Herbst, A., Langenakens, J., 2017. Recent development of unmanned aerial vehicle for plant protection in East Asia. Int. J. Agric. Biol. Eng. 10 (3), 18–30.

Xiaonan, W., Xiongkui, H., Changling, W., Zhichong, W., et al., 2017. Spray drift characteristics of fuel powered single-rotor UAV for plant protection. Trans. Chin. Soc. Agric. Eng. (Transactions of the CSAE) 33 (1), 117–123.

Xie, Y., Franz, E., Chu, M., Thuerey, N., 2018. Tempogan: a temporally coherent, volumetric gan for super-resolution fluid flow. ACM Trans. Graphics (TOG) 37 (4), 95.

Zhang, Y., Sung, W.J., Mavris, D.N., 2018. Application of Convolutional Neural Network to Predict Airfoil Lift Coefficient. In: 2018 AIAA/ASCE/AHS/ASC Structures, Structural Dynamics, and Materials Conference, pp. 1903.

Zeiler, M.D., Fergus, R., 2014. Visualizing and understanding convolutional networks. In: European Conference on Computer Vision. Springer, Cham, pp. 818–833.

Zhang, H., Sindagi, V., Patel, V. M. (2017). Image de-raining using a conditional generative adversarial network. arXiv preprint arXiv:1701.05957.

Zhu, R., Zhou, F., Xue, J.H., 2018. MvSSIM: A quality assessment index for hyperspectral images. Neurocomputing 272, 250–257.

SCAULIB202405438

检索证明

根据委托人提供的论文材料，委托人华南农业大学数学与信息学院 张建桃 3 篇论文收录情况如下表。

序号	论文名称	发表刊物及发表的年月卷期/页码等	作者排名	论文等级	作者文中单位	收录情况	影响因子	中科院大类分区
1	Origami Improved Dielectric Elastomer Actuation for Tunable Lens	IEEE TRANSACTIONS ON INSTRUMENTATION AND MEASUREMENT 出版年：2022 卷期：71 页码：- 文献号：7502709 文献类型：Article	共同通讯作者（倒数第一）	A 类	华南农业大学	SCI	IF2-year=5.6 IF5-year=5.4 （2022）	工程技术 2 区 Top 期刊：否 （2022）
2	Single-rotor UAV flow field simulation using generative adversarial networks	COMPUTERS AND ELECTRONICS IN AGRICULTURE 出版年：2019 卷期：167 页码：- 文献号：105004 文献类型：Article	通讯作者	A 类	华南农业大学	SCI	IF2-year=3.858 IF5-year=4.008 （2019）	农林科学 2 区 Top 期刊：是 （2019）
3	FLUID-SOLID COUPLING AND EXPERIMENTAL REALIZATION OF A PIEZOELECTRIC ATOMIZER UNDER STANDING-WAVE RESONANCE	APPLIED ENGINEERING IN AGRICULTURE 出版年：2016 卷期：32 3 页码：327-340 文献号： 文献类型：Article	通讯作者	B 类	华南农业大学	SCI	IF2-year=0.505 IF5-year=0.667 （2016）	农林科学 4 区 Top 期刊：否 （2016）

华南农业大学图书馆SCAULIB202405438

3.3 农用无人机超低容量旋流喷嘴的雾化特性分析与试验

《中文核心期刊要目总览》收录
Ei Compendex(核心版)收录
百种中国杰出学术期刊
RCCSE中国权威学术期刊

2016.20
第32卷 VOL. 32

ISSN 1002-6819
CN 11-2047/S
CODEN NGOXEO

农业工程学报

TRANSACTIONS OF THE CHINESE SOCIETY OF AGRICULTURAL ENGINEERING

NONGYE GONGCHENG XUEBAO



ISSN 1002-6819
9 771002 681160 20

中国农业工程学会 主办

万方数据

农业工程学报
二〇一六年十月
第三十二卷
第二十期
中国农业工程学会

农 业 工 程 学 报

2016 年 10 月第 20 期　总第 297 期（第 32 卷）

目　次

·综合研究·

信息技术提升农业机械化水平 …… 罗锡文，廖　娟，邹湘军，张智刚，周志艳，臧　英，胡　炼（1）

·农业装备工程与机械化·

“洁区播种”思路下麦茬全秸秆覆盖地花生免耕播种机研制 …… 顾峰玮，胡志超，陈有庆，吴　峰（15）
对置斜盘高速精密大豆排种器设计与充种机理分析 …… 刘宏新，刘俊孝，唐师法，徐晓萌（24）
双层种箱式马铃薯排种装置设计与试验 …… 牛　康，苑严伟，罗　敏，刘阳春，吕程序，方宪法（32）
气吸式马铃薯排种器正压吹种零速投种性能优化试验
…… 吕金庆，杨　颖，尚琴琴，李紫辉，李季成，刘中原，王英博（40）
马铃薯专用中耕培土犁的应用及增产效果 …… 高中超，刘　峰，王秋菊，姜　辉，张劲松，姚春雨，高　盼（49）
滚筒刮拉式香蕉茎秆纤维刮取装置参数优化与试验 …… 张喜瑞，王　超，梁　栋，李　粤（55）
车削刀具磨损声发射信号的云特征分析 …… 关　山，康振兴，彭　昶（63）
柴油机双卷流燃烧室内外室燃油匹配分析 …… 李向荣，周海琴，万远亮，苏立旺，刘福水（70）
输送多组分介质的离心泵内部固液两相流特性 …… 黄思杰，邵春雷（77）

·农业航空工程·

农用无人机超低容量旋流喷嘴的雾化特性分析与试验
…… 文　晟，兰玉彬，张建桃，李晟华，张海艳，邢　航（85）
航空植保作业用喷头在风洞和飞行条件下的雾滴粒径分布 …… 茹　煜，朱传银，包　瑞，李宗飞，丁　涛（94）

·农业水土工程·

考虑工作压力的垂直摇臂式喷头可调结构参数优化与试验 …… 汤　攀，李　红，陈　超，孙彩珍（99）
覆膜耕作方式对河套灌区土壤水热效应及玉米产量的影响 …… 齐智娟，冯　浩，张体彬，周立峰（108）
灌水频率对辣椒各生育期设施土壤盐分迁移规律的影响 …… 杜　磊，郑子成，李廷轩（114）
基于生理发育时间的压砂地西瓜发育动态模型及验证 …… 马　波，田军仓（122）
压砂地西瓜光合作用干物质及产量水氮耦合模型及验证 …… 马　波，田军仓，沈　晖，李王成（129）
AMSR2 缺失数据重建及其土壤湿度反演精度评价 …… 张桂欣，郝振纯，祝善友，周楚炫，华俊玮（137）
基于物联网的荔枝园信息获取与智能灌溉专家决策系统
…… 余国雄，王卫星，谢家兴，陆华忠，林进彬，莫昊凡（144）
紫色土坡耕地埂坎土壤抗剪性能对含水率的响应 …… 韦　杰，史炳林，李进林（153）
冲刷条件下黄土丘陵区浅沟侵蚀形态及产流产沙特征
…… 康宏亮，王文龙，薛智德，郭明明，史倩华，李建明，郭军权（161）
中国农村水利现代化指标体系构建 …… 邱元锋，孟　戈，雷声隆（171）

万方数据

·农业航空工程·

农用无人机超低容量旋流喷嘴的雾化特性分析与试验

文　晟[1,2]，兰玉彬[1,2]，张建桃[2,3※]，李晟华[1]，张海艳[1]，邢　航[1,2]

（1. 华南农业大学工程学院，广州 510642；2. 国际农业航空施药技术联合实验室，广州 510642；
3. 华南农业大学数学与信息学院，广州 510642）

摘　要：针对农用植保无人机超低容量喷施作业时，使用液力喷嘴产生的雾滴粒径较大，离心喷嘴结构复杂、价格较高等不足，基于旋流雾化的原理并采用模块化方法，提出了一种超低容量旋流喷嘴结构。通过对旋流喷嘴内流场的流体动力学行为和雾化特性进行数值分析与试验，明确了流体的物理特性和旋流喷嘴的结构参数等对雾化性能的影响规律。研究结果表明，液膜表面的正弦波失稳是导致锥形液膜碎化为雾滴的主要原因，在旋流喷嘴的结构参数中，喷嘴出口直径是喷嘴雾化性能的主要影响因素。当喷嘴出口直径从 1 增大至 1.5 mm，喷雾流量平均增大了 46.23%，喷雾角平均增大了 29.77%，产生雾滴的索特平均直径平均增大了 15%。此外，喷雾流量还与旋流槽数量成比例，旋流槽的螺旋角主要影响喷雾角。喷嘴入口处的流体相对压强则对喷雾角及雾滴粒径有较大的影响，其中喷雾角随着相对压强的增大而增大，而雾滴的索特平均直径随压强的增大呈非线性递减，当流体的相对压强从 70 增大至 160 kPa 时，系列化旋流喷嘴的索特平均直径降低了约 25%～35%。此外对于旋流喷嘴而言，流体黏度的增大会导致喷雾角的减小，但适当增加流体的黏度（不超过纯水黏度的 200%）可显著降低雾滴的平均粒径，提高喷嘴的雾化质量。该研究可为农用无人机超低容量变量喷洒系统的研发提供参考。

关键词：机械化；喷雾；计算机仿真；超低容量；旋流喷嘴；农用无人机；雾化特性

doi：10.11975/j.issn.1002-6819.2016.20.011

中图分类号：S49　　**文献标志码：**A　　**文章编号：**1002-6819(2016)-20-0085-09

文　晟，兰玉彬，张建桃，李晟华，张海艳，邢　航. 农用无人机超低容量旋流喷嘴的雾化特性分析与试验[J]. 农业工程学报，2016，32(20)：85－93.　doi：10.11975/j.issn.1002-6819.2016.20.011　http://www.tcsae.org

Wen Sheng, Lan Yubin, Zhang Jiantao, Li Shenghua, Zhang Haiyan, Xing Hang. Analysis and experiment on atomization characteristics of ultra-low-volume swirl nozzle for agricultural unmanned aviation vehicle[J]. Transactions of the Chinese Society of Agricultural Engineering (Transactions of the CSAE), 2016, 32(20): 85－93. (in Chinese with English abstract) doi：10.11975/j.issn.1002-6819.2016.20.011　http://www.tcsae.org

0　引　言

农业是中国国民经济持续发展的基础产业，保障粮食安全是中国的基本国策，目前病虫草害已成为中国农业减产和农产品质量受损的重要原因。据统计，中国每年因防治不及时，病虫草害造成的粮食作物产量损失高达 10%以上[1]。农用药剂防治因具有功效高、防治及时等特点，是现阶段中国防治农业有害生物的主要方法[2]。无人机因其体积小、无需跑道及操控灵活等特点，适用于在丘陵地区中、小田块的病虫草害防治工作，故基于无人机的农业植保技术在国外得到了较好发展[3-5]。近年来，利用无人机进行植保工作的研究在中国也受到了重视[6]。茹煜等[7]基于德国 VARIO 公司多用途无人机，设计了一种远程控制低量喷雾系统，并对影响离心喷雾效果的主要因素进行了理论研究和性能试验。秦维彩等[8]基于 N-3 型农用无人机，对玉米生长后期雾滴的沉积效果进行了试验分析，并就喷洒参数对玉米冠层雾滴沉积分布的影响规律进行了研究。张宋超等[9]基于计算流体力学方法，对 N-3 型农用无人机作业过程中旋翼风场和农药喷洒漂移特性进行了数值模拟和户外试验，重点研究了雾滴的沉积规律。张京等[10]基于红外热像仪，对 WPH642 型无人驾驶直升机航空喷施时药液雾滴的沉积效果进行了大田试验与分析。

超低容量精确喷雾技术可提高农药利用率，减少农药使用量。根据民用航空行业标准 MH/T1002.1[11]，超低容量喷洒的雾滴平均粒径应不超过 120 μm。但较小的雾滴粒径容易造成飘失，而农用无人机是超低容量喷雾技术实施较为理想的航空植保器械。首先，农用无人机的作业高度较低，一般位于作物冠层上方的 0.5～1.5 m，喷施效果较好；其次，农用无人机旋翼产生的下洗气流可起到较好的雾滴输送作用。超低容量喷洒系统的关键技术之一是雾化喷嘴的设计，其中超低容量雾化喷嘴应具有可持续产生雾滴平均粒径小于 120 μm 的雾化能力。现阶段中国农用无人机喷洒系统使用的喷嘴主要有液力喷嘴和离心喷嘴。这 2 种喷嘴技术源于地面植保机械，虽具有技术成熟可靠等优点，但对于植保无人机的超低容量喷施作业还存在着不足[12-13]。以中国农用无人机目前普遍采用的狭缝式液力喷嘴为例，其工作压力通常为

收稿日期：2016-01-17　　修订日期：2016-08-15
基金项目：国家重点研发计划资助项目（2016YFD0200700）；广东省自然科学基金资助项目（2015A030310182）；广东省科技计划资助项目（2016A020210100，2016A020210092）。
作者简介：文　晟，男，湖南长沙人，博士，副教授，硕士生导师，主要从事植保机械和精准喷雾技术的研究。广州　华南农业大学工程学院，510642。Email：vincen@scau.edu.cn
※通信作者：张建桃，男，湖南双峰人，博士，副教授，硕士生导师，主要从事精细农业方面的研究。广州　国际农业航空施药技术联合实验室，510642。Email：zhangjiantao@yeah.net

300～500 kPa，产生雾滴的平均粒径通常为200～500 μm，喷施的药剂用量较多（约 1～2 L/min），属于常量喷雾范围，难以实现超低容量喷施。

王玲等[14]构建了一个适用于农用无人机的变量喷雾系统，其喷嘴部分采用了英国 Micro 公司的 Ulva+型低量离心喷嘴，试验结果表明，该型离心喷嘴产生的雾滴粒径范围为 101.74～228.16 μm。茹煜等[15]设计了用于无人机航空喷雾的低量离心式雾化喷嘴，并进行了喷雾试验研究。结果表明，该离心喷嘴工作时产生的雾滴粒径范围为 78.24～200.45 μm。离心喷嘴产生的雾滴粒径比液力雾化喷嘴的小，且雾滴谱较窄，但其结构较复杂、价格高，且高速旋转的部件易磨损并引起无人机振动，此外在喷施作业时也易发生触碰而损坏。

旋流喷嘴因具有较好的雾化能力，已被应用于燃气涡轮发动机的燃油喷射[16]、喷雾干燥及烟气脱硫[17]等工业领域。其工作原理是使流体进入旋流腔并产生螺旋运动，当流体从喷嘴出口处喷出后，因具有较大的旋转速度而形成一个中空的液膜锥，并最终碎化为较为均匀的雾滴。课题组利用旋流雾化的原理，研发了一种用于农用无人机的低压超低容量旋流喷嘴，通过对旋流喷嘴进行流场分析及喷雾试验，明确流体的物理性质和旋流喷嘴的结构参数等对喷雾角、流量、雾滴的平均粒径及雾滴谱分布等雾化特性的影响规律。此外针对旋流喷嘴采用的模块化方法，可实现仅通过更换内部少量零部件即能改变喷嘴的雾化性能，从而满足为防治不同病虫草害而提出的生物最佳粒径要求。

1 超低容量旋流喷嘴的结构

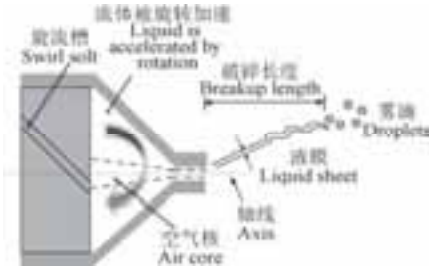
课题组研究的农用无人机超低容量旋流喷嘴如图 1a 所示，主要由基座 1、旋流腔 2、旋流线轴 3、旋流塞 4、橡胶密封圈 5 及端盖 6 等部分组成。外部流体从端盖 6 的进水口流入，并通过旋流塞 4 的内流道进入旋流喷嘴的内部。当流体在外部压力作用下经过旋流线轴 3 上的旋流槽后，将产生角动量并形成螺旋运动，且在旋流腔 2 中被旋转加速。当流体离开喷嘴出口后，在离心力的作用下展开并形成一个中空的锥形液膜。随着锥形液膜的持续发展，在液体表面张力和离心力的共同作用下，液膜迅速发展为丝带状，并最终破碎成较为均匀的雾滴，旋流喷嘴的雾化机理如图 1b 所示。

2 雾化性能的流场数值分析

由于旋流喷嘴的内部流场是湍流，因此流体在旋流腔内的运动形态复杂且不稳定。此外，旋流喷嘴内流场的流体动力学行为既难以直接观察，也难以通过试验进行测量，因此基于计算流体力学的数值分析技术是对旋流喷嘴内流场特性进行分析的一种重要方法[18-19]。本文采用计算流体力学的流体体积函数法（volume of fluid，VOF）对图 1 所示超低容量旋流喷嘴的内流场进行数值模拟，并对喷嘴内部流体的运动形态、流量及喷雾角等参数进行分析，以明确旋流喷嘴内流场的流体动力学特性。



a. 超低量旋流喷嘴的结构示意图
a. Schematic of ultra-low-volume swirl nozzle



b. 旋流喷嘴的雾化机理
b. Atomization mechanism of swirl nozzle

图 1 超低容量旋流喷嘴的结构及雾化机理

Fig.1 Schematic and atomization mechanism of ultra-low-volume swirl nozzle

2.1 控制方程

VOF 数值分析方法通过对流体运动界面的追踪，可有效模拟有多个自由表面流体的动力学特性，尤其适用于对流体喷射等问题的分析。本文采用 RANS（Reynolds-Averaged Navier-Stokes）技术模拟多相流问题，气液两相流的控制方程如下所示[20]

$$\frac{\partial \overline{\rho}}{\partial t}+\frac{\partial \overline{\rho_i}\overline{u}_i}{\partial x_i}=0 \tag{1}$$

$$\frac{\partial \overline{\gamma}}{\partial t}+\frac{\partial}{\partial x_i}(\overline{\gamma}\overline{u}_i+\overline{\gamma' u_i'})=0 \tag{2}$$

$$\frac{\partial \overline{\rho u}_i}{\partial t}+\frac{\partial}{\partial x_i}(\overline{\rho}\overline{u}_i\overline{u}_j+\overline{\rho}\overline{u_i'u_j'})= -\frac{\partial \overline{p}}{\partial x_j}+\frac{\partial}{\partial x_j}\left[\overline{\mu}\cdot(\frac{\partial u_i}{\partial x_j})\right]+(\overline{F}_V)_i \tag{3}$$

$$(F_V)_i=\sigma\cdot\kappa\cdot\delta\cdot\boldsymbol{n} \tag{4}$$

式中 ρ 表示密度，kg/m^3；u_i 表示速度分量，m/s；t 表示时间，s；x_i 和 x_j 分别表示空间坐标，m；p 表示压强，Pa；γ 为体积分数；μ 表示黏度，Pa·s；F_V 为施加到体单元上的力，N；σ 表示表面张力系数，N/m；κ 表示界面曲率，m^{-1}；δ 表示狄拉克函数；$\boldsymbol{n}$ 表示交界面上的法线向量；上划线表示时间平均值，撇号表示波动量。式（1）－式（4）中密度与黏度的平均值可表示为[21]

$$\begin{aligned}\overline{\rho}&=\overline{\gamma}\cdot\rho_1+(1-\overline{\gamma})\rho_2\\ \overline{\mu}&=\overline{\gamma}\cdot\mu_1+(1-\overline{\gamma})\mu_2\end{aligned} \tag{5}$$

式中下标 1 和 2 分别表示液相和气相。

2.2 数值模型与边界条件

由于流体进入旋流腔后不仅有轴向运动，还有周向旋转运动，难以用二维模型较为准确地模拟流体的运动

特性，因此建立旋流喷嘴流场的三维有限元模型如图 2 所示。整个三维模型由两部分组成，其中：上半部分为旋流喷嘴的内流场，用于模拟流体通过旋流线轴的旋流槽进入旋流腔后的流体动力学行为；下半部分为外流场，用于模拟流体从旋流喷嘴的出口流出后，在外部大气环境中的流体动力学特征。数值计算时，旋流槽的顶面设为入口边界，旋流腔的外表面及外部流场的顶面设为固壁边界，外部流场的侧面与底面设为出口边界。

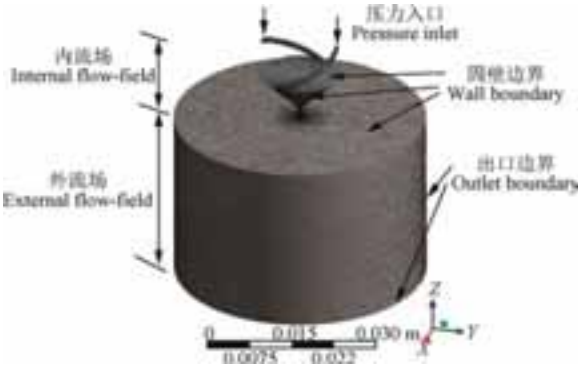


图 2　旋流喷嘴流场的三维有限元模型

Fig.2　3-D finite element model for flow-field of swirl nozzle

气液两相流的控制方程利用计算流体力学数值软件 Fluent®（ANSYS 公司，美国）求解，数值计算时设置的边界条件和假设如下所示：

1）模型的出入口设置为压力入口（pressure inlet）和压力出口（pressure outlet）边界条件，其中入口处的相对压强 p_{in}=160 kPa，出口处的相对压强 p_{out}=0，即为标准大气压，并且不考虑液相与气相之间的热交换。

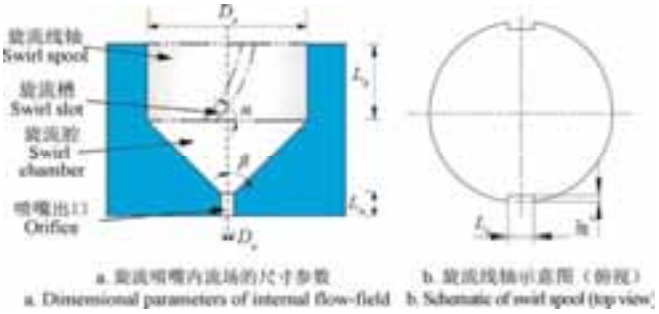
2）在流场计算的初始时刻，各节点的速度及相对压强为 0，即 u_i=0 且 p_i=0。数值计算时的工作流体为水，其物理特性为：密度 ρ_1=998.2 kg/m^3，黏度 μ_1=8.5×10^{-4} Pa·s，表面张力系数 σ=7.15×10^{-2} N/m；空气的物理特性为密度 ρ_2=1.225 kg/m，黏度 μ_2=1.7894×10^{-5} Pa·s。

3）整个流场计算域基于 VOF 多相流模型，并使用 k-ε 湍流模型求解。压力-速度耦合项采用 PISO 算法求解，动量方程使用二阶迎风格式，压力方程用二阶精度离散。为准确捕获流场的瞬态动力学行为，时间步长Δt 设为2×10^{-6} s。

2.3　喷嘴内流场几何参数与流场的速度云图

旋流喷嘴内流场各部分的尺寸参数如图 3 所示，初始计算时旋流线轴的直径 D_s=14 mm，高度 L_s=6 mm；旋流线轴上开有 2 条旋流槽，旋流槽宽度 L_c=2 mm，深度 W_c=0.5 mm，旋流槽螺旋线的螺旋角 α=30°，旋流腔的收敛角 β=45°；喷嘴出口处的直径 D_o=1 mm，长度 L_o=2 mm。用于模拟外流域流场特性的圆柱直径 D_f=45 mm，长度 L_f=30 mm，整个三维流场计算域的单元与节点数分别为 549 631 和 101 179。

图 4 为入口处相对压强为Δp=160 kPa 时旋流喷嘴流场的速度云图。由图 4 可知，液体在外部压强作用下经旋流槽进入旋流腔后，在旋流腔内部被旋转加速，并在腔体内部形成一个低压区。由于具有轴向和周向速度，当流体从喷嘴出口处流出后形成了锥形液膜，并在液体的表面张力和离心力共同作用下碎化为雾滴。



注：D_s为旋流线轴的直径，mm；L_s为旋流线轴的高度，mm；α为旋流槽螺旋线的螺旋角，(°)；β为旋流腔的收敛角，(°)；D_o为喷嘴出口的直径，mm；L_o为喷嘴出口的长度，mm；L_c为旋流槽的宽度，mm；W_c为旋流槽的深度，mm。

Note: D_s is swirl spool diameter, mm; L_s is swirl spool length, mm; α is helical angle of spiral line, (°); β is cone angle of swirl chamber, (°); D_o is orifice diameter, mm; L_o is orifice length, mm; L_c is width of swirl slots, mm; W_c is depth of swirl slots, mm.

图 3　旋流喷嘴内流场的结构示意图

Fig.3　Schematic of internal flow-field in swirl nozzle

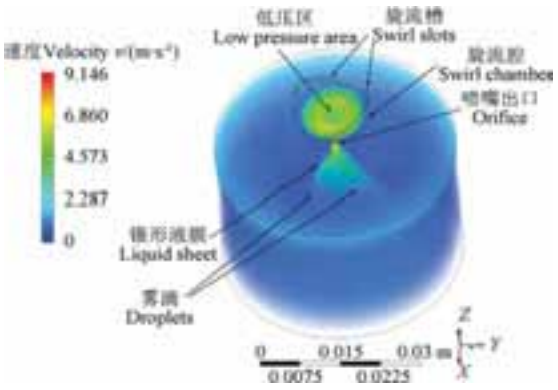


图 4　入口压强为 160 kPa 时旋流喷嘴流场的速度云图

Fig.4　Velocity contour of swirl nozzle flow-field at inlet pressure of 160 kPa

2.4　喷雾角和流量

喷雾角θ直接影响雾滴的沉积分布特性，是一个描述旋流喷嘴雾化性能的特征参数。Rizk 等[22]的研究表明喷雾角θ与喷嘴常数成反比，其在大量试验的基础上，推导出喷雾角与旋流喷嘴结构参数等的经验公式为

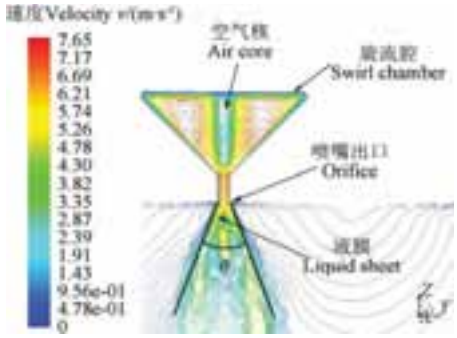
$$\theta=6K^{-0.15}\left[\frac{\Delta p\cdot D_o^2\cdot\rho_1}{\mu_1}\right]^{0.11} \quad (6)$$

式中 K 为喷嘴常数，表达式为

$$K=\frac{A_p}{D_s\cdot D_o} \quad (7)$$

式中 D_s为旋流线轴的直径，mm；D_o为喷嘴出口的直径，mm；Δp=p_{in}-p_{out}为旋流喷嘴入口与出口的压强差，Pa；θ为喷雾角，(°)；A_p为旋流槽入口端的总面积，m^2。由式（6）和式（7）可知，当入口处相对压强Δp=160 kPa 时，旋流喷嘴的喷雾角 θ=42.5°。图 5 为在相同条件下，利用 Fluent 求得的流场数值解，此时喷雾角 θ=46.2°，数值结果与经验公式的相对误差为 8.0%。产生误差的主要原因是：为满足不同类型植保作业对喷雾角和雾滴粒径等的

变化需求，课题组研究的旋流喷嘴采用了旋流线轴这一结构（图 1a），其中的旋流槽对液体起到了导流作用。Rizk 等[22]设计的旋流喷嘴没有旋流线轴，因此其经验式（6）和式（7）没有考虑旋流槽对喷雾角的影响。



注：θ 为喷雾角，(°)，且 θ=46.2°。
Note: θ is spray angle, (°), and θ=46.2°.

图 5 内流场的速度云图及喷雾角
Fig.5 Velocity contour of internal flow-field and spray angle

喷嘴流量与流体的物理性质、喷嘴的结构参数和相对压强等有关，是一个需试验测量的参数。图 6 为喷嘴出口处流量曲线的数值分析结果，从图 6 可知，当相对压强Δp =160 kPa 的流体从旋流槽顶端入口处进入喷嘴内部后，在 0.016 s 开始从喷嘴流出，且在约 0.024 s 后达到较稳定状态，此时其质量流量为 0.0114 kg/s，对于水而言，相应的体积流量 Q 为 0.684 L/min。

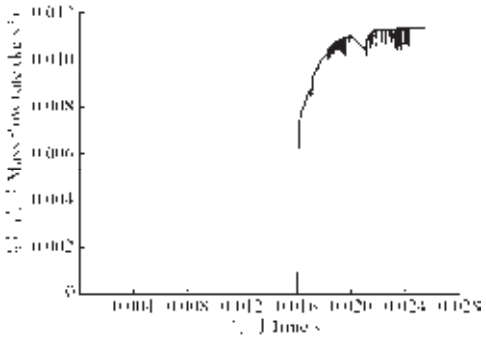


图 6 旋流喷嘴出口的质量流量
Fig.6 Mass flow rate of swirl nozzle outlet

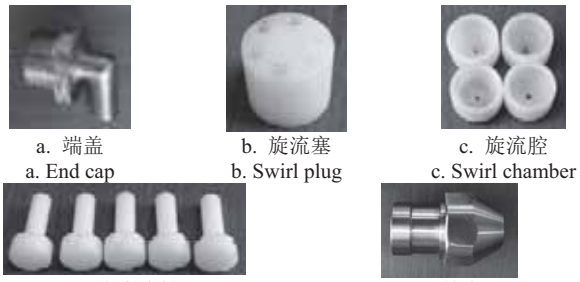
3 试验与分析

超低容量旋流喷嘴雾化特性的试验台架如图 7 所示，主要由水泵 2 （WZBHR-128A，浙江韩羽公司）、调压阀 4、数显流量计 5（K24，温州永嘉机械公司）和数字压力表 6 （MD-S260，杭州雪辰仪表公司）等组成。水箱 1 中的液体由水泵加压后，经管道送至旋流喷嘴 7 的入口处。管道中流体的压强可通过调压阀进行调节，旋流喷雾的流量以及喷嘴入口处的流体压强，可分别从流量计和压力表获得。旋流喷嘴出口处的流体特性拟基于图象法进行研究，喷嘴的喷雾角、液膜失稳后形成的表面波等特征利用单反相机（ILCE-5100，日本索尼公司）进行捕捉，其生成图像的最高分辨率可达 6 000×4 000 像素。旋流喷嘴产生的雾滴平均粒径及雾滴谱利用激光粒度仪（Winner318B，济南微纳公司）进行测试，每组试验均重复 3 次。



图 7 喷雾试验台架
Fig.7 Experiment platform of spraying

为研究不同结构参数对旋流喷嘴雾化特性的影响规律，课题组加工了多种不同形状尺寸的旋流腔和旋流线轴，如图 8 所示。通过采用模块化方法，超低容量旋流喷嘴可方便地更换零部件形成不同尺寸的旋流喷嘴，以满足生物最佳粒径对不同雾滴尺寸的要求，喷嘴的结构参数如表 1 所示。



a. 端盖 a. End cap
b. 旋流塞 b. Swirl plug
c. 旋流腔 c. Swirl chamber
d. 旋流线轴 d. Swirl spool
e. 基座 e. Base

图 8 试验用的超低量旋流喷嘴
Fig.8 Ultra-low-volume swirl nozzle for testing

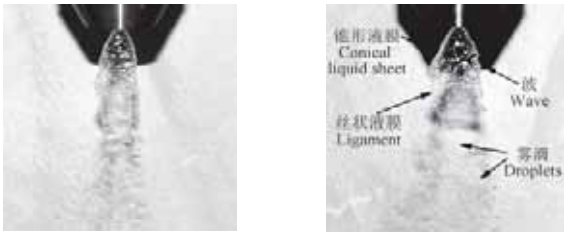
表 1 喷嘴的结构参数
Table 1 Structural parameters of nozzles

喷嘴编号 Nozzle number	喷嘴出口直径 Diameter of orifice D_o /mm	喷嘴出口长度 Length of orifice L_o /mm	旋流槽条数 Number of swirl slot n	旋流槽螺旋角 Helical angle of swirl slot α/(°)	旋流腔直径 Diameter of swirl chamber D_s /mm	喷嘴常数 Nozzle constant K
A_1	1	2	2	30	14	0.14
A_2	1.25	2	2	30	14	0.11
A_3	1.5	2	2	30	14	0.095
A_4	2	2	2	30	14	0.07
A_5	1	2	3	45	14	0.21
A_6	1.25	2	3	45	14	0.17
A_7	1.5	2	3	45	14	0.14
A_8	2	2	3	45	14	0.1

3.1 水的雾化特性

课题组对超低量旋流喷嘴 A_1 至 A_8 在不同流体压强下的雾化特性进行了试验测试。其中，以喷嘴 A_2 为例，用水作为工作流体时的雾化过程如图 9 所示。从图 9 可知，流体从喷嘴出口喷出后形成的锥形液膜、液膜表面的波、丝状液膜以及液膜破碎后形成的雾滴形态均有比较清晰地显示。图 9 表明，对于旋流喷嘴而言，液膜表面的正弦波失稳是锥形液膜破裂的主要原因。当流体从

喷嘴出口流出形成中空的锥形液膜后，具有周向和轴向速度的液膜在持续发展过程中，因受外界气体的扰动作用而在其表面形成正弦波。随着波幅的增大，在液膜的顶端破裂成丝状液膜，并最终碎化为大量细小均匀的雾滴。由图 9a 所示，当喷嘴入口处相对压强Δp=70 kPa 时，喷嘴出口处已形成了中空的锥形液膜并最终碎化为雾滴。但较低的液体压强使得液膜的周向旋转速度不够且离心力较小，整个液膜在重力作用下收缩成条形鹅卵石的形状。如图 9b 所示，当Δp 增大至 95 kPa 后，由于周向和轴向速度的增大，锥形液膜得到了较好的发展，形成了类似于郁金香的形状，且液膜碎化为较为均匀的雾滴。如图 9c 与 9d 所示，当相对压强Δp 超过 125 kPa 后，液体从喷嘴出口处流出后形成了展开的锥形液膜，且最终碎化形成的雾滴更为细小和均匀（如图 9c 与图 9d 所示）。



a. Δp=70 kPa　　b. Δp=95 kPa
Q=0.640 L·min^{-1}　　Q=0.748 L·min^{-1}

c. Δp=125 kPa　　d. Δp=160 kPa
Q=0.876 L·min^{-1}　　Q=1.011 L·min^{-1}

注：Q 为旋流喷嘴的体积流量，L·min^{-1}。
Note: Q is volume flow rate of swirl nozzle, L·min^{-1}.

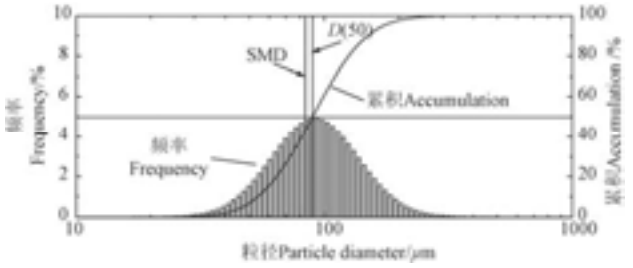
图 9　喷嘴 A_2 在不同压强及体积流量下的雾化特征
Fig.9　Atomization characteristics of nozzle A_2 under different pressures and volume flow rates

雾滴平均粒径和雾滴谱分布是评价喷嘴效能及雾化质量的重要参数之一。美国农业生物工程师学会（american society of agricultural and biological engineers, ASABE）制定了喷嘴的分类标准 S-572.1[23]，该标准根据雾滴的尺寸将喷嘴分为极好（<60 μm）、非常好（61～105 μm）、好（106～235 μm）、中等（236～340 μm）、粗糙（341～403 μm）、非常粗糙（404～502 μm）和极粗糙（>503 μm）等多种类型。由于喷嘴产生的雾滴尺寸并非完全一致，因此关于喷雾的研究通常采用雾滴平均尺寸对雾化质量进行评价。喷雾液滴平均直径的表示方法较多，其中索特平均直径（sauter mean diameter，SMD）是目前评价液体雾化平均直径的一个主要参数[24-25]，其表达式为[26]

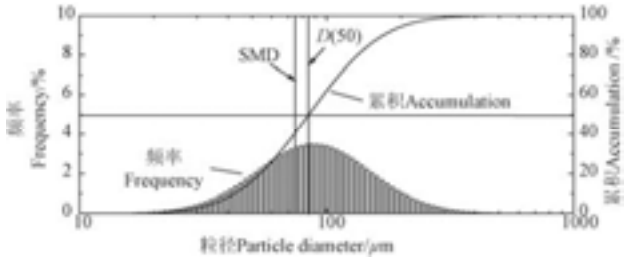
$$D_{pq}=\left[\frac{\sum_{i=1}^{\infty}n_iD_i^3}{\sum_{i=1}^{\infty}n_iD_i^2}\right]^{1/(p-q)} \quad (8)$$

式中 D_{pq} 为索特平均直径，μm；n_i 表示第 i 级尺寸的雾滴数目，p=3，q=2；D_i 为第 i 级尺寸的雾滴直径，μm。

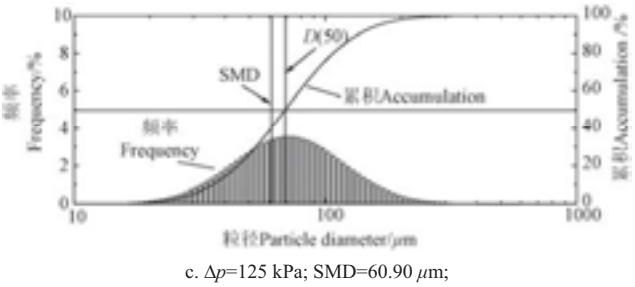
超低量旋流喷嘴 A_2 在不同流体压强下的索特平均直径和雾滴谱分布如图 10 所示。



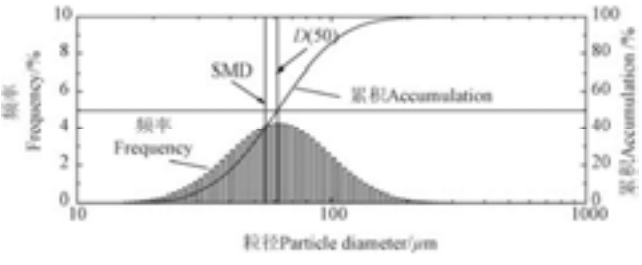
a. Δp=70 kPa; SMD=82.97 μm;
D(10)=54.02 μm; D(50)=89.75 μm; D(90)=149.11 μm



b. Δp=95 kPa; SMD=73.53 μm;
D(10)=42.55 μm; D(50)=84.83 μm; D(90)=169.89 μm



c. Δp=125 kPa; SMD=60.90 μm;
D(10)=35.79 μm; D(50)=69.33 μm; D(90)=134.68 μm



d. Δp=160 kPa; SMD=55.55 μm;
D(10)=34.39 μm; D(50)=61.44 μm; D(90)=109.93 μm

注：SMD 为索特平均直径，μm；D(10)为累积到全部雾滴总体积 10%时的雾滴直径，μm；D(50)为累积到全部雾滴总体积 50%时的雾滴直径，μm；D(90)为累积到全部雾滴总体积 90%时的雾滴直径，μm。
Note: SMD is Sauter mean diameter, μm; D(10) is droplet diameter when accumulated volume reaches 10% of total volume of all droplets, μm; D(50) is droplet diameter when accumulated volume reaches 50% of total volume of all droplets, μm; D(90) is droplet diameter when accumulated volume reaches 90% of total volume of all droplets, μm.

图 10　喷嘴 A_2 在不同流体压强下的索特平均直径和雾滴谱
Fig.10　SMD and droplet spectrums of nozzle A_2 with different pressures

从图 10 中可知，喷嘴产生的雾滴较均匀且雾滴谱呈正态分布，当Δp=70 kPa 时，喷嘴产生的雾滴 SMD 值为 82.97 μm。图 10 也表明，雾滴的 SMD 值随着喷嘴入口处流体相对压强的增大而减小，当相对压强增大至

Δp=160 kPa 时，喷嘴产生雾滴的 SMD 值为 55.55 μm。这是因为随着流体压强的增大，旋流腔内流体的动能增加，这使得流体离开喷嘴后具有更高的周向和轴向速度，因此锥形液膜产生了更大的离心力，且增大了液膜与外界空气间的扰动，并最终导致液膜碎化成更为细小、均匀的雾滴。

旋流喷嘴 A_1～A_8 在不同压强条件下（Δp=70、95、125 及 160 kPa），喷雾参数试验数据如表 2 所示。从表 1 喷嘴的结构参数和表 2 的试验结果可知：

1）在旋流喷嘴的结构参数中，喷嘴出口直径 D_o 对喷嘴的雾化性能影响较大。当喷嘴出口长度 L_o 不变时，旋流喷嘴的体积流量 Q 与 SMD 值随着 D_o 的增大而显著增加。其中，流量的增加比例与 D_o 的增大比例一致；而 SMD 的增大比例与 D_o 的增大比例不完全一致，当 D_o 直径从 1 分别增大至 1.25、1.5 和 2 mm 时，SMD 值分别增大了约 9%、15%及 30%。

2）旋流槽的条数 n 直接影响喷嘴的体积流量 Q，而旋流槽的螺旋角 α（图 3a 所示）则对雾滴的索特平均粒径有较明显影响。试验结果表明，当 α 的角度从 30°增大到 45°时，SMD 的平均值增大了约 9%。显然，在相同流体压强下，随着旋流槽倾角 α 的增大，流体的周向速度减小且轴向速度增大，这使得液膜旋转产生的离心力变小，减小的离心力使得锥形液膜与空气的扰动减弱，这使得液膜碎化产生的雾滴平均粒径增大。

3）对于旋流喷嘴而言，流体的相对压强Δp 对雾滴粒径有较大的影响，SMD 值随Δp 的增大呈非线性递减，当 Δp 从 70 增大至 160 kPa 时，喷嘴 A_1～A_8 的 SMD 值降低了约 25%~35%。这是因为根据旋流喷嘴的工作原理，随着流体压强的增大，锥型液膜的发展更加充分且锥形液膜与空气的扰动增强，从而导致产生的雾滴更为细小和均匀，这个规律与图 9 的表现完全一致。

表 2 旋流喷嘴 A_1～A_8 在不同压强下的雾化试验

Table 2 Spraying test of swirl nozzles A_1~A_8 with different pressures

编号 No.	相对压强 Relative pressure Δp/kPa	喷雾角 Spray angle θ/(°)	体积流量 Volume flow rate Q/(L·min^{-1})	索特平均直径 Sauter mean diameter/μm	编号 No.	相对压强 Relative pressure Δp/kPa	喷雾角 Spray angle θ/(°)	体积流量 Volume flow rate Q/(L·min^{-1})	索特平均直径 Sauter mean diameter/μm
A_1	70	37.9	0.460	75.96	A_5	70	33.2	0.682	79.76
	95	42.4	0.515	66.60		95	36.3	0.768	72.79
	125	44.3	0.667	59.76		125	40.5	1.001	61.01
	160	45.1	0.725	54.29		160	41.2	1.127	59.72
A_2	70	50.3	0.640	82.97	A_6	70	43.5	0.958	91.37
	95	52.8	0.748	73.53		95	45.9	1.122	81.23
	125	58.5	0.876	60.90		125	51.3	1.312	66.78
	160	60.8	1.011	55.55		160	52.8	1.476	61.35
A_3	70	58.9	0.843	86.28	A_7	70	50.7	1.251	93.76
	95	60.9	0.983	78.99		95	52.5	1.374	88.34
	125	66.8	1.151	72.91		125	56.1	1.735	82.57
	160	67.5	1.328	63.38		160	56.6	1.992	76.82
A_4	70	68.6	1.128	102.64	A_8	70	60.6	1.591	116.57
	95	74.1	1.320	84.73		95	64.1	1.879	93.62
	125	78.4	1.547	81.12		125	66.9	2.163	86.31
	160	79.6	1.784	77.19		160	68.7	2.535	82.77

3.2 甘油溶液的雾化特性

农用无人机采用人工遥控及自动导航技术进行喷施作业，保证了工作人员的安全；同时由于农用无人机的续航和负载量有限，因此使用高浓度药液进行超低容量精确喷施是农用无人机植保的一个重要发展方向。为提高药效、减少蒸发和降低雾滴漂移而添加的各种航空喷洒助剂也会极大地改变喷施药液的物理特性，显然仅根据已有的经验公式难以对不同浓度、黏度流体的雾化特性进行较为准确的预测。课题组以不同浓度的甘油溶液作为工作流体，对超低量旋流喷嘴在不同黏度条件下的雾化特性进行研究。其中，甘油溶液的主要物理特性（密度、黏度及表面张力等）是在室温条件下（28℃）利用密度计（M329517，北京远大科技公司）、黏度计（NDJ-5S/8S, 上海越平科学仪器公司）及表面张力仪（BYZ-101, 上海方瑞仪器公司）等进行测量获得，试验测得的详细参数如表 3 所示。

表 3 甘油溶液的物理特性(28℃)

Table 3 Physical properties of water-glycerol mixtures (at 28℃)

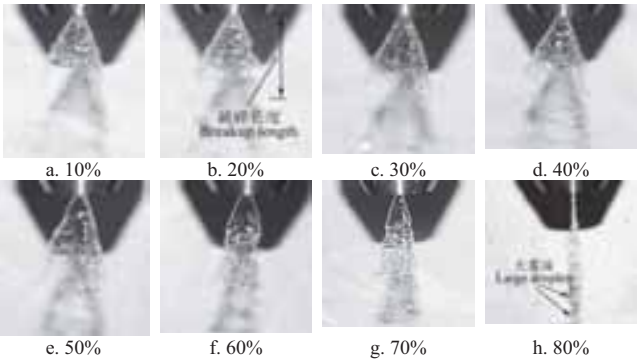
甘油比例 Proportion of glycerol /%	密度 Density ρ/(kg·m^{-3})	黏度 Viscosity μ/(10^{-3} Pa·s)	表面张力 Surface tension/(N·m^{-1})
0	996	0.85	0.0715
10	1 017	1	0.07
20	1 039	1.4	0.0693
30	1 062	1.9	0.069
40	1 086	2.8	0.0684
50	1 138	4.4	0.068
60	1 144	7.5	0.0675
70	1 166	14	0.067
80	1 195	35	0.066

超低量旋流喷嘴 A_2 在相同压强Δp=160 kPa 条件下，针对不同浓度甘油溶液的喷雾特性如图 11 所示。从图 11 可知，当甘油浓度为 10%～40%时，其雾化特性与水相比

（图 9d）差别较小。但随着甘油浓度的进一步增大，喷嘴的雾化特性出现了较为明显的变化：

1）喷雾角 θ 随着甘油浓度的增大而急剧减小。显然随着液体黏度的增加，流体在旋流腔中产生的周向旋转速度变小，这使得流体从喷嘴出口喷出后因动量不足，难以展开并充分发展为中空的锥形液膜。

2）液膜的破碎长度随甘油浓度的增大而逐渐变长，这表明随着流体黏度的增加，液膜越来越难以碎化成较为均匀的雾滴。这是因为流体黏度的增加将使得雷诺数 *Re* 减小，这将减缓湍流的发展且阻碍液膜的碎裂，使得雾滴的尺寸增大。试验结果显示，当甘油浓度达到 80%以后，喷嘴 A_2 只能形成旋转的射流而并未展开成锥形液膜，且随着射流的发展出现了黏连且不均匀的大雾滴（如图 11h 所示）。



a. 10%　b. 20%　c. 30%　d. 40%

e. 50%　f. 60%　g. 70%　h. 80%

图 11 超低量旋流喷嘴 A_2 在不同浓度甘油溶液下的雾化特性(相对压强为 160 kPa)

Fig.11 Atomization characteristics of ultra-low-volume swirl nozzle A_2 under different concentrations of glycerol solution(relative pressure is 160 kPa)

不同浓度甘油溶液经喷嘴 A_2 形成的喷雾角 θ 及索特平均直径的试验结果如表 4 所示。

表 4　喷嘴 A_2 在不同浓度甘油溶液下的雾化试验(相对压强为 160 kPa)

Table 4　Spraying test values of nozzle A_2 under different concentrations of glycerol solution (the relative pressure is 160 kPa)

甘油比例 Proportion of glycerol/%	喷雾角 Spray angle θ/(°)	索特平均直径 Sauter mean diameter/μm	体积流量 Volume flow rate Q/(L·min^{-1})
0	60.8	55.55	1.011
10	60.1	45.38	1.097
20	57.6	47.67	1.135
30	54.9	51.72	1.154
40	53.1	54.93	1.190
50	47.6	58.21	1.205
60	41.5	60.82	1.212
70	33.7	93.61	1.302
80	0	292.26	1.348

由表 4 可知：

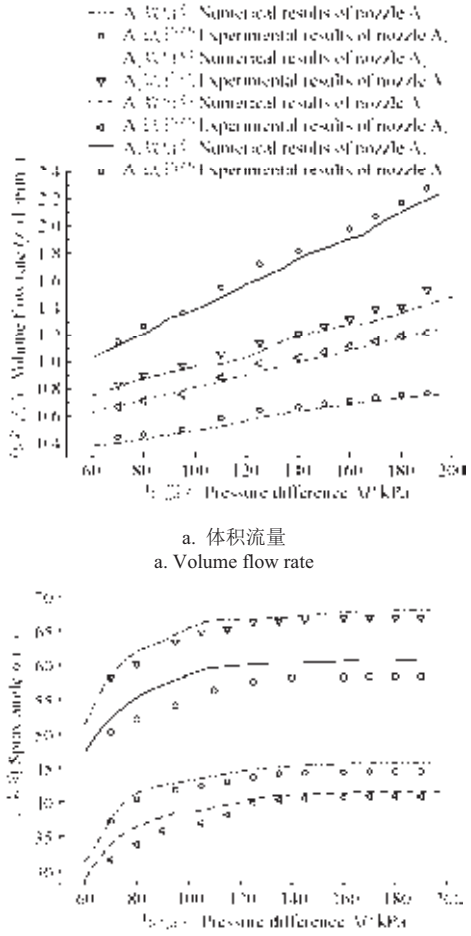
1）当甘油浓度从 10%增大到 40%时，喷雾角 θ 随流体黏度的增大而减小，但减小的幅度不大，与表 2 中黏度增加的幅度相当。

2）随着甘油浓度的继续增大，喷雾角 θ 随着流体黏度的增大而快速减小，且当甘油浓度达到 70%时，喷雾角 θ 约为在相同条件下使用水作为喷施流体的一半。

3）表 4 表明，适当增加流体的黏度（不超过纯水黏度的 200%）可显著降低雾滴平均粒径，提高喷嘴的雾化质量。以 10%浓度的甘油溶液为例，其黏度比水的黏度增加了约 17.6%，当Δp=160 kPa 时，SMD 值为 45.38 μm，比水的降低了约 18.3%，此时喷嘴 A_2 已完全达到 ASABE S-572.1 标准定义的极好类型。

4）表 4 结果还表明，对于旋流喷嘴而言，过高的液体黏度需要较高的流体压强才能获得比较好的雾化性能，这意味着需要农用无人机携带更大功率的液泵设备，将加剧农用无人机的能量消耗。

图 12 为使用 10%的甘油溶液，旋流喷嘴 A_1、A_3、A_5、A_7 在不同流体压强下，流量及喷雾角的数值解和试验曲线。其中，体积流量的数值解与试验结果的平均误差为 4.83%，喷雾角的数值解与试验结果的平均误差为 3.45%。



a. 体积流量
a. Volume flow rate

b. 喷雾角
b. Spray angle

图 12　体积流量和喷雾角的变化曲线（10%甘油溶液）

Fig.12　Curves of volume flow rate and spray angle (10% glycerol solution)

由图 12 可见，流体相对压强Δp 对喷嘴流量的影响较

大，喷嘴流量随Δp的增大成线性递增，但喷雾角θ与Δp并不是简单的线性关系，当Δp小于 80 kPa 时，喷雾角θ随压强的增大而迅速增大；当Δp大于 80 kPa 后，喷雾角θ随压强的增大而增大，但增大的幅度减缓；当Δp大于 180 kPa 后，随着压强的进一步增大，喷嘴喷雾角θ趋于平缓且不再增大。在旋流喷嘴的结构参数中，喷嘴出口直径D_o对喷雾流量和喷雾角均有较大影响，试验结果表明，当D_o从 1 增大至 1.5 mm，喷雾流量平均增大了 46.23%，喷雾角平均增大了 29.77%。旋流槽条数n主要影响喷雾体积流量，当旋流槽条数n从 2 条增大至 3 条，液体平均体积流量增大了 31.96%。此外，旋流槽的螺旋角α主要影响喷雾角θ，试验显示当螺旋角α从 30°增大至 45°时，喷雾角θ平均降低了 11.6%。

4 结论与讨论

1）基于图像法的研究表明，超低容量旋流喷嘴的雾化过程分为：中空的锥形液膜、液膜的表面波、形成丝带状液膜及碎化成较均匀雾滴 4 个阶段。其中，液膜表面的正弦波失稳是锥形液膜破裂的主要原因。

2）在旋流喷嘴的结构参数中，喷嘴出口直径是喷嘴雾化性能的主要影响因素，当喷嘴出口直径从 1 增大至 1.5 mm，喷雾流量平均增大了 46.23%，喷雾角平均增大了 29.77%，产生雾滴的索特平均直径平均增大了 15%。此外，喷雾流量还与旋流槽条数成比例，旋流槽的螺旋角主要影响喷雾角，当螺旋角从 30°增大至 45°后，喷雾角平均降低了 11.6%。

3）流体的相对压强对喷嘴流量和雾滴粒径有较大的影响，喷嘴流量随相对压强的增大成线性递增，而雾滴的索特平均直径随相对压强的增大呈非线性递减，试验表明，当流体的相对压强从 70 增大至 160 kPa 时，旋流喷嘴 A_1～A_8 的索特平均直径降低了约 25%～35%。

在后续研究中，可利用喷洒控制器对液泵进行脉宽调制控制，通过调节液泵产生的流体压强，改变农药药液喷施的流量、雾滴粒径等参数，从而实现变量喷洒。

[参 考 文 献]

[1] 周志艳，臧英，罗锡文，等. 中国农业航空植保产业技术创新发展战略[J]. 农业工程学报，2013，29(24)：1－10.
Zhou Zhiyan, Zang Ying, Luo Xiwen, et al. Technology innovation development strategy on agricultural aviation industry for plant protection in China[J]. Transactions of the Chinese Society of Agricultural Engineering (Transactions of the CSAE), 2013, 29(24): 1－10. (in Chinese with English abstract)

[2] 薛新宇，梁建，傅锡敏. 我国航空植保技术的发展前景[J]. 农机化研究，2008(5)：72－74.
Xue Xinyu, Liang Jian, Fu Ximin. Prospect of aviation plant protection in China[J]. Chinese Agricultural Mechanization. 2008(5): 72－74. (in Chinese with English abstract)

[3] 薛新宇，兰玉彬. 美国农业航空技术现状和发展趋势分析[J]. 农业机械学报，2013，44(5)：194－201.
Xue Xinyu, Lan Yubin. Agricultural aviation applications in USA[J]. Transactions of the Chinese Society of Agricultural Machinery, 2013, 44(5): 194－201. (in Chinese with English abstract)

[4] Huang Y, Hoffmann W C, Lan Y, et al. Development of a spray system for an unmanned aerial vehicle platform[J]. Applied Engineering in Agriculture, 2009, 25(6): 803－809.

[5] Faiçal B S, Costa F G, Pessin G, et al. The use of unmanned aerial vehicles and wireless sensor networks for spraying pesticides[J]. Journal of Systems Architecture, 2014, 60(4): 393－404.

[6] 张东彦，兰玉彬，陈立平，等. 中国农业航空施药技术研究进展与展望[J]. 农业机械学报，2014，45(10)：53－59.
Zhang Dongyan, Lan Yubin, Chen Liping, et al. Current status and future trends of agricultural aerial spraying technology in China[J]. Transactions of the Chinese Society of Agricultural Machinery, 2014, 45(10): 53 － 59. (in Chinese with English abstract)

[7] 茹煜，贾志成，范庆妮. 无人直升机远程控制喷雾系统[J]. 农业机械学报，2012，43(6)：47－52.
Ru Yu, Jia Zhicheng, Fan Qingni, et al. Remote control spraying system based on unmanned helicopter[J]. Transactions of the Chinese Society of Agricultural Machinery, 2012, 43(6): 47－52. (in Chinese with English abstract)

[8] 秦维彩，薛新宇，周立新，等. 无人直升机喷雾参数对玉米冠层雾滴沉积分布的影响[J]. 农业工程学报，2014，30(5)：50－56.
Qin Weicai, Xue Xinyu, Zhou Lixin, et al. Effects of spraying parameters of unmanned aerial vehicle on droplets deposition distribution of maize canopies[J]. Transactions of the Chinese Society of Agricultural Engineering (Transactions of the CSAE), 2014, 30(5): 50－56. (in Chinese with English abstract)

[9] 张宋超，薛新宇，秦维彩，等. N-3 型农用无人直升机航空施药飘移模拟与试验[J]. 农业工程学报，2015，31(3)：87－93.
Zhang Songchao, Xue Xinyu, Qin Weicai, et al. Simulation and experimental verification of aerial spraying drift on N-3unmanned spraying helicopter[J]. Transactions of the Chinese Society of Agricultural Engineering (Transactions of the CSAE), 2015, 31(3): 87－93. (in Chinese with English abstract)

[10] 张京，何雄奎，宋坚利，等. 无人驾驶直升机航空喷雾参数对雾滴沉积的影响[J]. 农业机械学报，2012，43(12)：94－96.
Zhang Jing, He Xiongkui, Song Jianli, et al. Influence of spraying parameters of unmanned aircraft on droplets deposition[J]. Transactions of the Chinese Society for Agricultural Machinery, 2012, 43(12): 94－96. (in Chinese with English abstrct)

[11] MH/T 1002.1-1995，农业航空作业质量技术指标[S]. 北京：中国民用航空总局，1995.

[12] 张建桃，文晟，江定心，等. 超声雾化在超低量喷雾中的应用前景[J]. 中国植保导刊，2014，34(10)：67－70.
Zhang Jiantao, Wen Sheng, Jiang Dingxin, et al. Application of ultrasonic atomization to plant protection machinery[J]. China Plant Protection, 2014, 34(10): 67－70. (in Chinese with English abstrct)

[13] 王潇楠，何雄奎，宋坚利. 助剂类型及浓度对不同喷头雾滴飘移的影响[J]. 农业工程学报，2015，31(22)：49－55.
Wang Xiaonan, He Xiongkui, Song Jianli. Effect of adjuvant types and concentration on spray drift potential of different nozzles[J]. Transactions of the Chinese Society of Agricultural Engineering (Transactions of the CSAE), 2015, 31(22): 49－55. (in Chinese with English abstract)

[14] 王玲，兰玉彬，Hoffmann W C，等. 微型无人机低空变量喷药系统设计与雾滴沉积规律研究[J]. 农业机械学报，2016，47(1)：15－22.
Wang Ling, Lan Yubin, Hoffmann W C, et al. Design of

variable spraying system and influencing factors on droplets deposition of small UAV[J]. Transactions of the Chinese Society for Agricultural Machinery, 2016, 47(1): 15－22. (in Chinese with English abstract)

[15] 茹煜，金兰，周宏平，等. 航空施药旋转液力雾化喷头性能试验[J]. 农业工程学报，2014，30(3)：50－55.
Ru Yu, Jin Lan, Zhou Hongping, et al. Performance experiment of rotary hydraulic atomizing nozzle for aerial spraying application[J]. Transactions of the Chinese Society of Agricultural Engineering (Transactions of the CSAE), 2014, 30(3): 50－55. (in Chinese with English abstract)

[16] Nouri-Borujerdi A, Kebriaee A. Numerical simulation of laminar and turbulent two-phase flow in pressure-swirl atomizers[J]. Journal of American Institute of Aeronautics and Astronautics, 2012, 50(10): 2091－2101.

[17] 闫云飞，张力，高振宇，等. 低压旋流雾化喷嘴的雾化性能[J]. 化工学报，2009，60(5)：1141－1147.
Yan Yunfei, Zhang Li, Gao Zhenyu, et al. Atomization performance of low pressure swirl atomizing nozzle[J]. Journal of Chemical Industry and Engineering, 2009, 60(5): 1141－1147. (in Chinese with English abstrct)

[18] Shirani E, Jafari A, Ashgriz N. Turbulence models for flows with free surfaces and interfaces[J]. Journal of American Institute of Aeronautics and Astronautics, 2006, 44(7): 1454－1462.

[19] Altimira M, Rivas A, Larraona G S, et al. Characterization of fan spray atomizers through numerical simulation[J]. International Journal of Heat and Fluid Flow, 2009, 30(2): 339－355.

[20] Belhadef A, Vallet A, Amielh M, et al. Pressure-swirl atomization: Modeling and experimental approaches[J]. International Journal of Multiphase Flow, 2012, 39: 13－20.

[21] Datta A, Som S K. Numerical prediction of air core diameter, coefficient of discharge and spray cone angle of a swirl spray pressure nozzle[J]. International Journal of Heat and Fluid Flow, 2000, 21(4): 412－419.

[22] Rizk N K, Lefebvre A H. Internal flow characteristics ofsimplex swirl atomizers[J]. Journal of Propulsion and Power, 1985, 1(3): 193－199.

[23] American society of agricultural and biological engineers. S-572.1 spray nozzle classification by droplet spectra[S]. USA: St. Joseph, MI, 2009.

[24] Datta A, Som S K. Numerical prediction of air core diameter, coefficient of discharge and spray cone angle of a swirl spray pressure nozzle[J]. International Journal of Heat and Fluid Flow, 2000, 21(4): 412－419.

[25] Wen X, Yong H. Improved semiempirical correlation to predict sauter mean diameter for pressure-swirl atomizers[J]. Journal of Propulsion and Power, 2014, 30(6): 1628－1635.

[26] Levy M, Levy Y, Sher E. Spray structure as generated under homogeneous flash boiling nucleation regime[J]. Applied Thermal Engineering, 2014, 73(1): 416－423.

Analysis and experiment on atomization characteristics of ultra-low-volume swirl nozzle for agricultural unmanned aviation vehicle

Wen Sheng[1,2], Lan Yubin[1,2], Zhang Jiantao[2,3※], Li Shenghua[1], Zhang Haiyan[1], Xing Hang[1,2]

(1. *Engineering College of South China Agricultural University*, *Guangzhou* 510642, *China*;
2. *International Lab of Agricultural Aviation Pesticide Spraying Technology*, *Guangzhou* 510642, *China*;
3. *College of Mathematics and Informatics of South China Agricultural University*, *Guangzhou* 510642, *China*)

Abstract: The ultra-low-volume precision spraying of agricultural UAV (unmanned aviation vehicle) is a key technology in the field of plant protection. There are still some problems in the application of the ultra-low-volume spraying of agricultural UAV in China, such as relatively large droplet diameter of hydraulic nozzle, complex centrifugal nozzle structure and high price. Based on the mechanism of swirl atomization and the modular approach, a new swirl nozzle is developed in this paper. The hydrodynamics and the atomization characteristics of the flow field in the nozzle are studied numerically and experimentally. The physical properties of the fluid and the effect of the atomizer geometry on the atomization characteristics are obtained. The results show that the breakup of conical liquid sheet occurs via unstable growth of sinuous waves on the surface of the liquid sheet. In the structural parameters of the swirl nozzle, the diameter of the nozzle orifice has a great effect on the atomizer performance. As the diameter of the nozzle orifice increases from 1 to 1.5 mm, the average flow rate of the spraying is increased by 46.23%. At the same time, the average of spray angle is increased by 29.77% and the SMD (Sauter mean diameter) is increased by 15%. In addition, the flow rate of the spraying is linearly proportional to the number of the swirl slots. The spray angle is also impacted by the inclination angle of the swirl slot. When the inclination angle is increased from 30° to 45°, the spray angle is reduced by 11.6%. The relative flow pressure on the nozzle inlet has a significant impact on the flow rate of the spraying and the diameter of the droplet. The flow rate of the spraying linearly increases with the relative flow pressure, while the Sauter mean diameter decreases nonlinearly with the relative flow pressure. The experiments indicate that the Sauter mean diameters of serial swirl nozzles decrease by 25%-35% with an increment in the relative flow pressure from 70 to 160 kPa. In order to achieve the variable spraying, the flow rate and the diameter of the droplet can be changed by using the PWM (pulse width modulation) controller to control the fluid pressure of the pump. The increment in flow viscosity will decrease the spray angle for the swirl nozzle. The Sauter mean diameter decreases monotonously with a proper increment of flow viscosity (less than 200% of the viscosity of pure water), which can produce higher atomization quality. The experiment shows that when the flow viscosity is 17.6% greater than the pure water and the pressure is 160 kPa, the swirl nozzle can produce the droplets with the Sauter mean diameter of 45.38 μm, which is 18.3% less than the case of pure water. The results from the present study have significant implications for the optimal design of ultra-low-volume atomizer in agricultural UAV. The present method and results on the spraying mechanism of swirl nozzle provide the important reference for researching and developing the ultra-low-volume variable spraying system.

Keywords: mechanization; spraying; computer simulation; ultra-low-volume; swirl nozzle; agricultural unmanned aviation vehicle; atomization characteristics

中国农业工程学会第二届特别优秀论文获奖名单

序号	作者	论文题目	年卷期
1	申双和，张方敏，盛 琼	1975－2004 年中国湿润指数时空变化特征	2009, 25(1): 11－15
2	孟力力，杨其长，Gerard.P.A.Bot，王 楠	日光温室热环境模拟模型的构建	2009, 25(1): 164－170
3	邓 辉，李 春，李 飞，陈计亮	棉花秸秆糖化碱预处理条件优化	2009, 25(1): 208－212
4	亮 峰，俞 立，张文安，徐青香，于莉洁	基于无线传感器网络的作物水分状况监测系统研究与设计	2009, 25(2): 107－112
5	李大婧，宋江峰，刘春泉，于 淼	超声波辅助提取黑豆皮色素工艺优化	2009, 25(2): 273－279
6	张宽地，吕宏兴，赵延凤	明流条件下圆形隧洞正常水深与临界水深的直接计算	2009, 25(3): 1－5
7	佟国红，David M. Christopher	墙体材料对日光温室温度环境影响的 CFD 模拟	2009, 25(3): 153－157
8	霍霄妮，李 红，张微微，孙丹峰，周连第，李保国	北京耕作土壤重金属多尺度空间结构	2009, 25(3): 223－229
9	蔡义华，刘 刚，李 莉，刘 卉	基于无线传感器网络的农田信息采集节点设计与试验	2009, 25(4): 176－178
10	刘战广，朱洪光，王 彪，张亚雷	粪草比对干式厌氧发酵产沼气效果的影响	2009, 25(4): 196－200
11	陈荣清，张凤荣，孟 媛，郭力娜	农村居民点整理的现实潜力估算	2009, 25(4): 216－221
12	倪九派，李 萍，魏朝富，谢德体	基于 AHP 和熵权法赋权的区域土地开发整理潜力评价	2009, 25(5): 202－209
13	李 卓，吴普特，冯 浩，赵西宁，黄 俊，庄文化	容重对土壤水分入渗能力影响模拟试验	2009, 25(6): 40－45
14	佟 懿，谢 晶	鲜带鱼不同贮藏温度的货架期预测模型	2009, 25(6): 301－305
15	韩华峰，杜克明，孙忠富，赵 伟，陈 冉，梁聚宝	基于 ZigBee 网络的温室环境远程监控系统设计与应用	2009, 25(7): 158－163
16	高利伟，马 林，张卫峰，王方浩，马文奇，张福锁	中国作物秸秆养分资源数量估算及其利用状况	2009, 25(7): 173－179
17	何英彬，陈佑启，杨 鹏，许新国，佘强毅	农村居民点土地整理及其对耕地的影响	2009, 25(7): 312－316
18	吴大千，刘 建，贺同利，王淑军，三仁卿	基于土地利用变化的黄河三角洲生态服务价值损益分析	2009, 25(8): 256－261
19	李 广，黄高宝	雨强和土地利用方式对黄土丘陵区水土流失的影响	2009, 25(11): 85－90
20	张瑞瑞，赵春江，陈立平，徐 刚	农田信息采集无线传感器网络节点设计	2009, 25(11): 213－218
21	曹秀玲，张清军，尚国琲，安石鑫	河北省农村居民点整理潜力评价分级	2009, 25(11): 318－323
22	姜 莎，陈芹芹，胡雪芳，杨 阳，倪元颖	电子舌在红茶饮料区分辨识中的应用	2009, 25(11): 345－349
23	毕于运，高春雨，王亚静，李宝玉	中国秸秆资源数量估算	2009, 25(12): 211－217
24	朱 明，郭红宇，周新群	现代农业产业工程体系建设方案研究	2010, 26(1): 1－5
25	李 亮，史海滨，贾锦凤，王长生，刘宏云	内蒙古河套灌区荒地水盐运移规律模拟	2010, 26(1): 31－35
26	吕美蓉，李增嘉，张 涛，宁堂原，赵建波，李洪杰	少免耕与秸秆还田对极端土壤水分及冬小麦产量的影响	2010, 26(1): 41－46
27	强小嫚，周新国，李彩霞，郭冬冬，刘祖贵，张俊鹏	不同水分处理下液膜覆盖对夏玉米生长及产量的影响	2010, 26(1): 54－60
28	马文军，程琴娟，李良涛，宇振荣，牛灵安	微咸水灌溉下土壤水盐动态及对作物产量的影响	2010, 26(1): 73－80
29	李汴生，张 微，梅灿辉	超高压和热灭菌对鲜榨菠萝汁品质影响的比较	2010, 26(1): 359－364
30	吴普特，赵西宁	气候变化对中国农业用水和粮食生产的影响	2010, 26(2): 1－6
31	李 震，Wang Ning，洪添胜，文 韬，刘志壮	农田土壤含水率监测的无线传感器网络系统设计	2010, 26(2): 212－217
32	刘 洁，李小昱，李培武，王 为，屠 炜，张 军	基于近红外光谱的板栗水分检测方法	2010, 26(2): 338－341
33	佟 懿，谢 晶，肖 红，杨胜平	基于电子鼻的带鱼货架期预测模型	2010, 26(2): 356－360
34	杨 玮，吕 科，张 栋，吴 松，龙智强，商守海	基于 ZigBee 技术的温室无线智能控制终端开发	2010, 26(3): 198－202
35	尹 令，刘财兴，洪添胜，周皓恩，Kae Hsiang Kwong	基于无线传感器网络的奶牛行为特征监测系统设计	2010, 26(3): 203－208
36	黄辉玲，罗文斌，吴次芳，李冬梅	基于物元分析的土地生态安全评价	2010, 26(3): 316－322
37	陈 博，欧阳竹	基于 BP 神经网络的冬小麦耗水预测	2010, 26(4): 81－86
38	李 楠，刘成良，李彦明，张佳宝，朱安宁	基于 3S 技术联合的农田墒情远程监测系统开发	2010, 26(4): 169－174
39	曹银贵，周 伟，王 静，袁 春，赵 丽	基于主成分分析与层次分析的三峡库区耕地集约利用对比	2010, 26(4): 291－296
40	刘 明，潘磊庆，屠 康，刘 鹏	电子鼻检测鸡蛋货架期新鲜度变化	2010, 26(4): 317－321
41	展 慧，李小昱，王 为，汪成龙，周 竹，黄 懿	基于机器视觉的板栗分级检测方法	2010, 26(4): 327－331
42	黄 艳，黄建立，郑宝东	银耳微波真空干燥特性及动力学模型	2010, 26(4): 362－367
43	张素梅，王宗明，张 柏，宋开山，刘殿伟，李 方，任春颖，黄 健，张惠琳	利用地形和遥感数据预测土壤养分空间分布	2010, 26(5): 188－194
44	罗 娟，侯书林，赵立欣，孟海波，田宜水	典型生物质颗粒燃料燃烧特性试验	2010, 26(5): 220－226
45	张 杰，任小龙，罗诗峰，海江波，贾志宽	环保地膜覆盖对土壤水分及玉米产量的影响	2010, 26(6): 14－19
46	文 韬，洪添胜，李 震，黄 森，李加念，叶智杰	橘园无线传感器网络不同节点部署方式下的射频信号传播试验	2010, 26(6): 211－215
47	戴志刚，鲁剑巍，李小坤，鲁明星，杨文兵，高祥照	不同作物还田秸秆的养分释放特征试验	2010, 26(6): 272－276
48	朱雪欣，王红梅，袁秀杰，侯欣欣	基于 GIS 的农村居民点区位评价与空间格局优化	2010, 26(6): 326－333
49	黄晚华，杨晓光，李茂松，张晓煜，王明田，代姝玮，马洁华	基于标准化降水指数的中国南方季节性干旱近 58 a 演变特征	2010, 26(7): 50－59
50	李江波，饶秀勤，应义斌，王东亭	基于高光谱成像技术检测脐橙溃疡	2010, 26(8): 222－228
51	孔雪松，刘艳芳，邹亚锋，陈奕云	基于农户意愿的农村居民点整理潜力测算与优化	2010, 26(8): 296－301
52	郭力娜，张凤荣，曲衍波，关小克，朱泰峰	基于分等因素组合的农用地整理类型分区	2010, 26(9): 308－314
53	任守纲，徐焕良，黎 安，周光宏	基于 RFID/GIS 物联网的肉品跟踪及追溯系统设计与实现	2010, 26(10): 229－235
54	曲衍波，张凤荣，姜广辉，关小克，郭力娜	基于生态位的农村居民点用地适宜性评价与分区调控	2010, 26(11): 290－296
55	李耀明，秦同娣，陈 进，赵 湛	玉米茎秆往复切割力学特性试验与分析	2011, 27(1): 160－164
56	靳红梅，常志州，叶小梅，马 艳，朱 瑾	江苏省大型沼气工程沼液理化特性分析	2011, 27(1): 291－296

续表见封三

中国标准连续出版物号：ISSN 1002-6819 / CN11-2047/S　　国内邮发代号：18-57　　国内定价：50元

《中文核心期刊要目总览》收录
Ei Compendex(核心版)收录
百种中国杰出学术期刊
RCCSE中国权威学术期刊

ISSN 1002-6819
CN 11-2047/S
CODEN NGOXEO
www.tcsae.org

农业工程学报

NONGYE GONGCHENG XUEBAO | TRANSACTIONS OF THE CHINESE SOCIETY OF AGRICULTURAL ENGINEERING

2022年 第38卷 VOL. 38 20



农 业 工 程 学 报

2022 年 10 月第 20 期 （总第 444 期） 第 38 卷

目 次

·农业装备工程与机械化·

机采棉种植模式对植保机械化学脱叶作业效果的影响
…… 丁宸旸，吕 新，韩小强，郝婷丽，麻向阳，刘世豪，田程程，刘尚昌，侯彤瑜（1）

夹持式鲜菱角脱壳机设计与试验 …… 万志华，张国忠，徐红梅，周 勇，唐楠锐，张 晗（9）

柱塞式能量回收马达配流副锥度角的分析与试验
…… 李少年，梁 涛，包尚令，王 煜，周致元，李 曦（20）

智能施药机器人关键技术研究现状及发展趋势
…… 兰玉彬，闫 瑜，王宝聚，宋灿灿，王国宾（30）

农药液滴在玉米叶片表面铺展面积的影响因素
…… 高 荣，黄路生，文 晟，尹选春，张建桃（41）

用于池塘养殖尾水处理的串联式旋流器水动力特性及分离效率
…… 张 俊，刘奥胜，李 乐，曹守启（49）

泄流激励下水工闸门运行模态参数自动识别 …… 张钰奇，赵华东，付春健，铁 瑛，李何林（59）

·农业航空工程·

低空无人机高光谱影像失真评价指标构建 …… 赵庆展，刘汉青，田文忠，王学文（67）

·农业水土工程·

环境因子与玉米生长对地表温度监测土壤水分的影响
……李志军，于广多，刘 奇，张智韬，黄嘉亮，刘 畅，张秋雨，陈俊英（77）

钠吸附比和盐分浓度对新疆典型砂壤土物理性质的影响
……许尊秋，陈 阳，毛晓敏（86）

植被和梯田措施对坡沟系统细沟侵蚀调控作用
……董敬兵，时 鹏，李占斌，李 鹏，白璐璐，赵 准，宋致华，赵倩卓，慕全鹏（96）

基于电导率和结构稳定性阳离子比的微咸水灌溉水质评估方法
……张体彬，闫思慧，罗 敏，王 春，张通港，程 煜，冯 浩（105）

基于能坡划分原理的大比降山区河流阻力特性 …… 杨奉广，彭清娥（113）

·农业信息与电气技术·

柑橘黄龙病光谱特征波段选择及光谱检测仪研制
…… 兰玉彬，王天伟，郭雅琦，杨冬子，林韶明，胡宇琦，林晓晴，邓小玲（119）

融合多尺度特征和多重注意力的水下目标检测
…… 李 辉，王晓宇，刘 云，陶 冶，付诗佳，吴依凡（129）

基于 RGBD 相机的黑皮鸡枞菌子实体形态视觉测量
…… 王映龙，肖 欢，殷 华，罗 珊，勒 宇，万家兴（140）

非接触式测温鉴定母猪典型生理状态
…… 王晨阳，胡冰艳，李雨晴，寇忠云，李爱赟，李 倩，庞卫军（149）

农药液滴在玉米叶片表面铺展面积的影响因素

高　荣[1,2]，黄路生[1,2]，文　晟[2]，尹选春[2]，张建桃[1,2,3※]

（1. 华南农业大学数学与信息学院，广州 510642；2. 国家精准农业航空施药技术国际联合研究中心，广州 510642；
3. 农业农村部华南热带智慧农业技术重点实验室，广州 510642）

摘　要：农药液滴在植物叶面上最大铺展面积，决定了农药有效成分作用范围、蒸发时间和叶面吸收效果。为了探究液滴粒径、农药润湿性能和叶面倾角对液滴在玉米叶面上铺展面积的影响机理，通过试验方式产生 548、675、756、877、973 μm 粒径的液滴，利用质量分数为 0、0.005%、0.01%、0.1%的 OP-10 表面活性剂代表润湿性能不同的农药，设定叶面倾角为 0°、15°、30°、45°、60°、75°，进行全因子试验。结果表明：液滴粒径、表面活性剂浓度、叶面倾角均对铺展面积影响显著（P<0.001），三者增大均能提高液滴在玉米叶面上的最大铺展面积。在不同角度下，增大液滴粒径和溶液的润湿性能都能增加液滴在玉米叶面上的铺展面积。药液润湿性能差时，铺展面积随叶面倾角的变化不够明显，润湿性能较好时，铺展面积呈现出随叶面倾角先上升后下降的趋势，粒径为 548 μm 液滴铺展面积的最大值出现在叶面倾角 45° 左右。通过表面活性剂的单位浓度铺展面积评估了不同浓度的 OP-10 液滴的铺展能力，发现 0.005%铺展能力大于其他浓度，说明在溶液中加入少量 OP-10 就可以显著改变溶液润湿性能。研究结果有助于理解叶面铺展润湿机理，并为通过调控农药润湿性能和药液粒径来实现农药减量增效提供了理论支撑。

关键词：农药液滴；润湿性能；铺展面积；表面活性剂；液滴粒径；黏附功

doi：10.11975/j.issn.1002-6819.2022.20.005

中图分类号：S48　　**文献标志码：**A　　**文章编号：**1002-6819(2022)-20-0041-08

高荣，黄路生，文晟，等．农药液滴在玉米叶片表面铺展面积的影响因素[J]．农业工程学报，2022，38(20)：41-48.
doi：10.11975/j.issn.1002-6819.2022.20.005　http://www.tcsae.org

Gao Rong, Huang Lusheng, Wen Sheng, et al. Factors influencing the spreading areas of pesticide droplets on the surface of maize leaves[J]. Transactions of the Chinese Society of Agricultural Engineering (Transactions of the CSAE), 2022, 38(20): 41-48. (in Chinese with English abstract)　doi：10.11975/j.issn.1002-6819.2022.20.005　http://www.tcsae.org

0　引　言

农药的低效利用导致大量化学成分进入生态环境，对空气、水体和土壤造成严重的污染，同时造成了许多资源浪费。农药施用主要通过喷雾方式[1-2]，然而大部分农药液滴极其容易在靶标叶片表面蒸发、反弹、滚落，大约只有 0.1%的农药有效成分达到了施用目标[3]。农药液滴在植物叶片上的铺展面积影响农药有效成分的作用范围[4]、蒸发时间[5-6]和叶面吸收效果[7]。调控农药液滴在植物叶片上的铺展面积是提高农药利用率的有效途径，对实现农药减量增效和降低环境污染有重要作用。

农药雾滴在植物叶片表面的润湿性能是决定铺展面积的关键因素。植物叶片表面主要为外蜡质层，其化学成分[8-9]、表面拓扑形貌[10]及表面自由能等[2,11-12]，共同决定了植物叶面的被润湿能力。植物叶面特性是固有属性，在实际农业生产中很难通过改变叶面特性来提高农药雾滴的铺展面积，一般只能通过提高对不同叶面特性的认知水平来开发或选择适合的农药[12]。前人研究表明，在农药制剂中添加适宜的表面活性剂是提高药液对靶润湿的有效方法[11]。Xu 等[13]研究了 4 种不同浓度的助剂在蜡质和多毛植物叶面上铺展、蒸发的过程，发现液滴的铺展面积随助剂浓度的增加而增加，并在一定浓度下达到峰值；不同种类的助剂在两种植物叶面上的最大铺展面积不同，通过调控助剂浓度和种类可以增加不同作物表面上的农药雾滴的覆盖面积，从而实现农药减量增效的目的。Kraemer 等[14]将 0.5 和 1 μL 草甘膦溶液滴加到难润湿和易润湿的两种植物叶片表面上，液滴蒸发后观察液滴扩散面积和草甘膦残留痕迹，发现在难润湿叶片上，液滴体积从 0.5 增加至 1 μL，其铺展面积仅略微增加；在易润湿叶片上，铺展面积显著增大；当在草甘膦溶液中加入表面活性剂时，两种叶片上的铺展面积都有所增大，但难润湿叶片上铺展面积增加更为明显。Oliveira 等[15]研究了 4 种粒径的 2,4-D 除草剂液滴在杂草叶面的铺展。结果表明，800 和 950 μm 的液滴显著增加了除草剂在了两种杂草叶表面的滞留量，且液滴滞留量与叶片表面特性和溶液的物理和化学性质高度相关。上述研究充分说明了液滴在植物叶面上的铺展面积与液滴粒径、溶液性质有关，且两者存在一定交互作用。在实际生产过程中农药液滴需要在不同角度的植物叶面上附着、铺展，目前有关液滴在植物叶面上铺展行为的研究大多集中于平

收稿日期：2022-06-15　修订日期：2022-08-15
基金项目：广东省普通高校特色创新类项目（2019KZDZX1002）；广东省自然科学基金项目（2022A1515011008）；国家自然科学基金面上项目（61773171）；高等学校学科创新引智计划项目（D18019）
作者简介：高荣，研究方向为农业精准喷雾技术。
Email：gaorong17694804202@163.com
※通信作者：张建桃，博士，副教授，研究方向为农用无人机和人工智能。
Email：zhangjiantao@yeah.net

面研究上，而对斜面上的液滴行为研究较少[16]。文献[17-20]研究发现，叶片倾角对液滴在植物叶面上的覆盖面积、覆盖率有显著影响，但试验均采用大规模喷雾方式，药液呈雾滴群形态撞击到植物叶面，液滴的粒径、飞行速度无法保持在同一水平，由粒径、速度造成的铺展面积增加无法评估，所以本文设计单液滴试验来保证液滴粒径和速度相对固定。

综上所述，研究倾斜叶片上的雾滴润湿展布现象对提高农药有效利用率和降低农药面源污染有重要的实际意义，但目前相关研究还不够充足。本文通过试验测定了不同浓度的非离子表面活性剂 OP-10 溶液在玉米叶面上的润湿性能，筛选出润湿性有明显差异的 4 种浓度，利用液滴发生器产生 5 种粒径的单个液滴，对其在不同倾角的玉米叶片上的铺展面积开展研究。分析液滴粒径、溶液润湿性能和叶面倾角对铺展面积的影响及其交互影响，以期为提高农药有效利用率提供理论依据。

1 材料与方法

1.1 试验材料

试验采用非离子表面活性剂 OP-10（烷基酚聚氧乙烯醚，天津市科密欧化学试剂有限公司）配置成不同浓度的水溶液，用于改变液滴在玉米叶面上的润湿性能。OP-10 是农药制剂中常用的润湿剂、展着剂，调控其浓度可以实现不同的润湿效果；染色剂诱惑红（纯度 99%，河南祥意商贸有限公司）；去离子水；新鲜玉米叶片（品种为金香糯），取拔节期玉米叶片进行试验。

1.2 仪器与设备

全自动水滴角测试仪（型号 CAPST-2000At，东莞市普赛特检测设备有限公司）；自动表面张力仪（型号 EZ-Pi Plus，芬兰 Kibron 公司）；体式显微镜（型号 SZX16，日本 Olympus 公司）；液滴发生器（Ultimus I-II 型高精度点胶机，美国 EFD 公司，OLF750AF 型气体压缩机，上海捷豹压缩机制造有限公司）；自制可调整角度的斜板。

1.3 研究方法

1.3.1 溶液表面张力及在玉米叶片上润湿性能测定

试验采用去离子水与 OP-10 试剂配制 5 种浓度的 OP-10 水溶液，质量分数分别为 0.001%、0.005%、0.01%、0.05%、0.1%（溶液配置后 2 h 内完成试验）。然后，通过自动表面张力仪，使用 Wilhelmy 平板法，测量不同浓度溶液的表面张力，每种浓度重复测量 10 次，取平均值，试验温度为（25±1）℃，相对湿度（67±5）%。

接触角测定：取拔节期新鲜玉米叶片，沿玉米主叶脉对称剪下 3×3 cm 部分作为试验样本，保持自然状态平整地固定在全自动水滴角测试仪的载物台上，用微量注射器将 2 μL 液滴点滴在玉米叶面上，用全自动水滴角测试仪上的 CCD 摄像头每 10 s 摄下叶面上的液滴，输入电脑，用测试仪内置的拟合分析法计算出各浓度 OP-10 液滴在玉米叶面上 90 s 时的稳定接触角，测定时的温度为（25±1）℃，相对湿度（67±5）%。

根据热力学定义，在恒温恒压条件下，液滴在接触固体表面时会自动铺展，液–气界面取代固–气界面，黏附功 W_a 是指液体润湿固体界面的过程需要做的功，它是液体能否润湿固体的一种度量[21]。

$$W_a = \gamma_{sg} + \gamma_{lg} - \gamma_{sl} \quad (1)$$

式（1）为热力学表达式，其中 W_a 为黏附功，J/m^2；γ_{sg}、γ_{lg}、γ_{sl} 分别为固-气、液-气、固-液界面张力，mN/m。

当液滴的三相接触线处达到应力平衡状态时，根据 Young 氏方程可得[22]

$$\gamma_{sg} - \gamma_{sl} = \gamma_{lg}\cos\theta \quad (2)$$

式（1）、式（2）联立得到黏附功

$$W_a = \gamma_{lg}(1+\cos\theta) \quad (3)$$

式中 θ 为接触角，（°）。

1.3.2 液滴发生器粒径校准方法

液滴发生器[15,23]由高精度点胶机和空气压缩机构成，液滴发生器能够产生 200～2 000 μm 的单个液滴，可以通过设置触发时间、气压和真空等参数来控制液滴粒径的大小，不受液体性质影响。在试验前，采用 Lin 等[24]的方法，对液滴发生器产生液滴粒径进行校准。液滴发生器产生的液滴直径由水敏纸上的斑点图像面积获得，通过下式计算[25]

$$d = 1.06A^{0.445} \quad (4)$$

式中 A 为液滴在水敏纸上的斑点面积。扫描水敏纸获得液滴在水敏纸上的斑点图像像素，然后除以扫描分辨率得到 A 值，扫描分辨率为 2400 dpi，10.58 μm/pixel。通过改变触发时间、气压和真空参数并在水敏纸上多次测试得到粒径为 548、675、756、877、973 μm 的 5 个液滴。

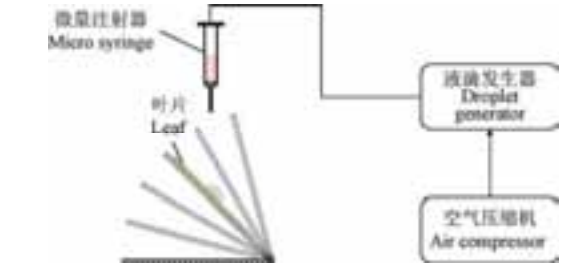
1.3.3 液滴在玉米叶片上的铺展面积

选择新鲜健康的玉米叶片进行液滴铺展试验，将玉米叶片裁剪为 3 cm×5 cm 的长条，用双面胶固定在自制可调角度的斜板上，设置斜板与水平面的角度分别为 0°、15°、30°、45°、60°、75°，斜板角度可以覆盖大部分自然生长的植物叶面倾角。以粒径为 548、675、756、877、973 μm 的液滴为试验对象，研究不同粒径大小的液滴在玉米叶面上的铺展面积。液滴产生后会悬挂在微量注射器的针头处，垂直移动微量注射器，让液滴以零速度接触到植物叶面，液滴与植物叶面接触后，移动微量注射器，针头与液滴脱离，操作过程中避免针头接触到植物叶面，防止破坏叶面结构。试验溶液由表面活性剂 OP-10 和诱惑红复配，根据溶液在玉米叶片上润湿性能的差异，选择 4 种接触角有显著差别的溶液进行试验，OP-10 浓度分别为 0、0.005%、0.01%、0.1%，诱惑红浓度为 0.5%。Gao 等[26]验证了在农药制剂中加入诱惑红，不会对溶液性质产生影响。试验设计为 3 因素多水平的全因子试验，共 120 种不同处理，每种处理重复 10 次。待液滴完全蒸发后，将试验叶片放置在体式显微镜下，用高清数码相机拍摄液滴铺展痕迹。液滴铺展图片用 image J 图像处理软件进行处理，得到实际铺展面积。试验装置如图 1 所示。

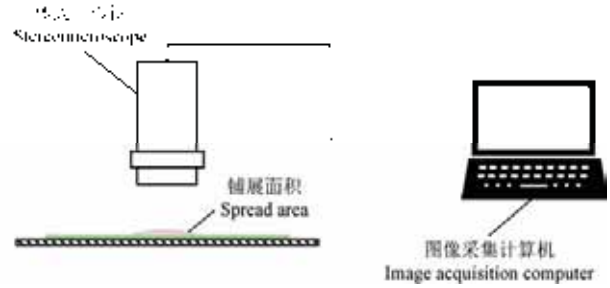
1.3.4 表面活性剂浓度对液滴铺展能力的影响

在溶液中加入表面活性剂会对液滴的铺展产生显著影响。然而，这并不能体现不同 OP-10 浓度对液滴铺展能力的作用。因此，利用液滴的铺展面积与表面活性剂浓度的比值来评估铺展效率[24]。该比值的实际含义为每

百分比表面活性剂浓度的铺展面积，下文中称为单位浓度铺展面积，$mm^2/\%$。



a. 液滴发生装置
a. Droplet generator



b. 图像采集装置
b. Image acquisition device

图 1　试验装置示意图

Fig.1　Schematic diagram of the experimental configurations

1.4　数据处理

在 IBM SPSS Statistics 28（美国 IBM 公司）上进行方差分析（ANOVA）和相关性（Pearson）分析，置信区间设为 95%。采用箱形图剔除极端异常值，并用均值替代。使用 Duncan 新复极差法进行事后比较，分析每种因素不同水平的差异。通过 MATLAB 软件对液滴铺展面积数据进行插值，绘制不同因素交互的曲面响应图，分析各因素之间的交互作用。

2　结果与分析

2.1　不同浓度 OP-10 溶液的表面张力及在玉米叶片上的润湿性能

喷雾药液的表面张力是决定液滴能否在作物叶面上润湿铺展的关键因素，液体表面张力过高会导致液滴撞击植物叶片时发生弹跳、滚落现象，导致药液无法沉积在植物叶面。溶液的表面张力随 OP-10 表面活性剂浓度上升而降低，在到达浓度 0.005%后表面张力保持稳定，其表面张力为 35.9 mN/m，表面活性剂 OP-10 在溶液浓度为 0.005%左右达到临界胶束浓度。溶液在玉米叶片上的稳定接触角，随溶液浓度升高而降低，在到达临界胶束浓度前，接触角迅速下降；当溶液浓度到达临界胶束浓度后，接触角下降趋势减缓，最后达到稳定。黏附功随 OP-10 浓度增加而增加，在溶液浓度为 0.1%时达到最大值 58.82 J/m^2，试验结果如表 1 所示。为模拟不同润湿性能的农药在不同角度玉米叶面上的铺展面积，根据接触角大小选择可代表不同润湿能力的浓度水平，选择浓度为 0、0.1%、0.01%、0.005%OP-10 溶液进行下一步试验。徐广春等[27]研究了常用农药在推荐浓度下的表面张力，大部分农药在推荐浓度下表面张力均在 30～72 mN/m 之间。本文选取的试验溶液可以代表大部分农药在玉米叶面上的润湿性能。

表 1　不同浓度 OP-10 水溶液的表面张力、在玉米叶片上的稳定接触角及黏附功

Table1　Surface tension of different concentrations OP-10 aqueous solutions, stable contact angle and adhesion work of on maize leaves

浓度 Concentration/%	表面张力 Surface tension/($mN\cdot m^{-1}$)	接触角 Contact angle/(°)	黏附功 Adhesion work/($J\cdot m^{-2}$)
0	72.0±0.10	129.2±2.1	26.5
0.001	45.6±0.57	120.1±0.8	22.7
0.005	35.9±0.47	79.6±2.2	42.4
0.01	35.1±0.12	65.8±6.0	49.4
0.05	35.4±0.22	54.8±2.3	55.8
0.1	35.1±0.04	47.4±3.2	58.8

2.2　最大铺展面积的三因素方差分析（ANOVA）

方差分析（ANOVA）结果如表 2 所示。OP-10 浓度、叶面倾角、液滴粒径三种试验因素均对液滴的铺展面积产生了显著影响，且三因素之间存在显著的交互作用（$P<0.001$）。方差整体模型对试验结果有较好的解释性，可解释试验 87.5%（调整后 $R^2=0.875$）的变异来源。其中溶液的偏 Eta 平方值为 0.857，为试验因素及交互作用中的最大值，可认为溶液类型对总体变异的贡献大于其他因素及交互作用。叶面倾角对总体变异的贡献最小，偏 Eta 平方值为 0.073。在交互作用的效应量比较中，液滴粒径×叶面倾角×溶液的偏 Eta 平方（0.257）>叶面倾角×溶液（0.24）>液滴粒径×溶液（0.108）>液滴粒径×叶面倾角（0.1），效应量的比较说明了三因素之间的交互作用对总体变异的贡献大小。

表 2　溶液、叶面倾角、液滴粒径及相互作用对铺展面积影响的方差分析

Table 2　ANOVA on the effects of solution, leaf angle, droplet particle size and interaction on spread area

变异来源 Sources of variability	平方和 Sums of squares	自由度 Degree of freedom	均方 Mean square	*F*	*P*	偏 Eta 平方 Partial Eta square
修正模型 Correction model	719.869	119	6.049	71.410	<0.001	0.887
液滴粒径 Droplet size *A*	82.148	4	20.537	242.429	<0.001	0.473
叶面倾角 Leaf angle *B*	7.229	5	1.446	17.067	<0.001	0.073
OP-10 浓度 OP-10 concentration *C*	548.759	3	182.920	2 159.287	<0.001	0.857
液滴粒径 *A*×叶面倾角 *B*	10.218	20	0.511	6.031	<0.001	0.100
液滴粒径 *A*×OP-10 浓度 *C*	11.036	12	0.920	10.857	<0.001	0.108
叶面倾角 *B*×OP-10 浓度 *C*	28.822	15	1.921	22.682	<0.001	0.240
A×*B*×*C*	32.860	60	0.528	6.228	<0.001	0.257

注：$R^2=0.887$（调整后 $R^2=0.875$）。
Note: $R^2=0.887$ (Adjusted $R^2=0.875$).

为了解各因素不同水平之间的差异，采用 Duncan 新复极差法对不同水平的均数进行事后检验，对液滴粒径、叶面倾角、OP-10 浓度 3 个因素分别进行讨论。在对单一

因素进行事后检验时，铺展面积为另外两种因素所有水平的平均值。由表 3 可知，叶面倾角对铺展面积影响的整体趋势为随叶面倾角增大，铺展面积增加，但 15°、30°、45°、60°倾角的铺展面积较为接近，叶面倾角为 75°时为 1.51 mm^2，相比于 0°、45°角，铺展面积平均增大了 18.0%、11.9%；铺展面积随液滴粒径增加而增加，其中 675、756 μm 的两种液滴的铺展面积没有显著性差异（P>0.05），分析原因可能是两种液滴粒径的初始差值不够大，导致其铺展面积接近。如图 2 所示，液滴粒径和铺展面积之间呈现线性关系，液滴粒径从 548 μm 增加到 973 μm，铺展面积增加了 71.2%。对液滴粒径和铺展面积进行拟合，拟合方程为 y=0.0017x+0.0223，拟合系数 0.969，表明液滴粒径每增加 100 μm，液滴的最大铺展面积平均增加 0.17 mm^2；不同浓度的 OP-10 溶液的铺展面积均有显著差别。液滴的最大铺展面积随溶液表面活性剂浓度增加而增加，在 0.1%的浓度下铺展面积达到最大值 2.22 mm^2，去离子水的平均铺展面积为最小值 0.33 mm^2。与去离子水相比，0.1%浓度下的 OP-10 在玉米叶面上的铺展面积平均增加了 572.7%。

表 3 液滴粒径、叶面倾角、OP-10 浓度的事后检验

Table 3 Post hoc tests of droplet size, leaf angle, and OP-10 concentration

项目 Item		样本数 Samples number	铺展面积 Spread area/mm^2
叶面倾角 Leaf angle/(°)	0	200	1.28a
	15	200	1.30ab
	30	200	1.31ab
	45	200	1.35b
	60	200	1.32ab
	75	200	1.51c
液滴粒径 Droplet size/μm	548	240	1.01a
	675	240	1.20b
	756	240	1.24b
	877	240	1.56c
	973	240	1.73d
OP-10 浓度 OP-10 concentration/%	0	300	0.33a
	0.005	300	1.30b
	0.01	300	1.53c
	0.1	300	2.22d

注：小写字母代表在 0.05 水平下差异显著。

Note: Lowercase letters represent significant differences at the 0.05 level.

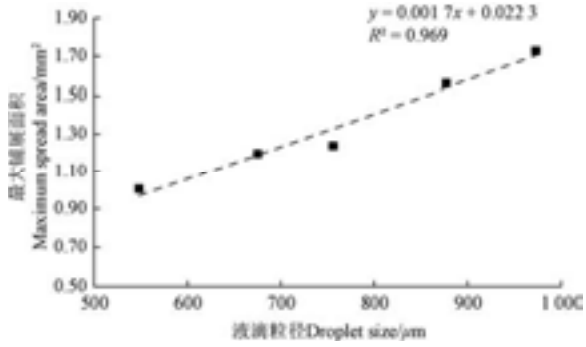


图 2 最大铺展面积和液滴粒径关系

Fig.2 Relationship between maximum spread area and droplet size

综上所述，叶面倾角、液滴粒径、OP-10 浓度都对液滴的铺展有明显影响。在本文设置的试验参数中，OP-10 浓度对液滴的铺展面积影响最大，液滴粒径次之，叶面倾角最小，且三者存在一定交互作用。

2.3 叶面倾角、液滴粒径、溶液润湿性的交互作用分析

对溶液的表面张力、接触角，黏附功和铺展面积之间进行相关性分析，结果如表 4 所示。溶液表面张力和铺展面积之间呈现不显著负相关（r=−0.871，P=0.129），铺展面积增大趋势和液滴在玉米叶片上接触角减小的趋势呈现出一致性（r=−0.986，P=0.014），黏附功 W_a 和铺展面积之间呈现出显著正相关（r=0.995，P=0.009）。接触角和黏附功均是衡量液滴在玉米叶面上润湿性能的指标，但通过相关性分析发现，黏附功的大小可以更好地反应液滴在玉米叶片上的铺展面积趋势。下面将用黏附功代替对应的 OP-10 溶液浓度，分析溶液的润湿性能和叶面倾角、液滴粒径对铺展面积造成的交互影响。

表 4 各变量间相关系数

Table 4 Correlation coefficients between variables

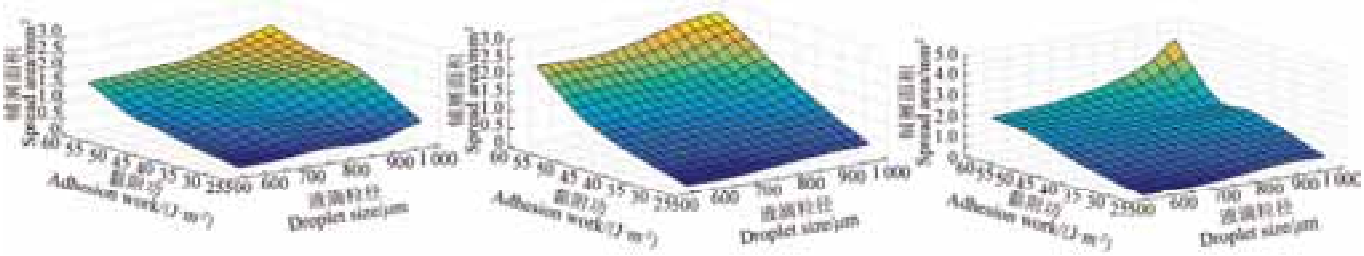
变量 Variable	铺展面积 Spread area	表面张力 Surface tension	接触角 Contact angle
表面张力 Surface tension	-0.871	1	
接触角 Contact angle	-0.986*	0.933	1
黏附功 Adhesion work	0.995**	-0.878	-0.991**

注：*P<0.05 级别（双尾），**P<0.01 级别（双尾），相关性显著。

Note: *P<0.05 level (two-tailed), **P<0.01 level (two-tailed), significant correlation.

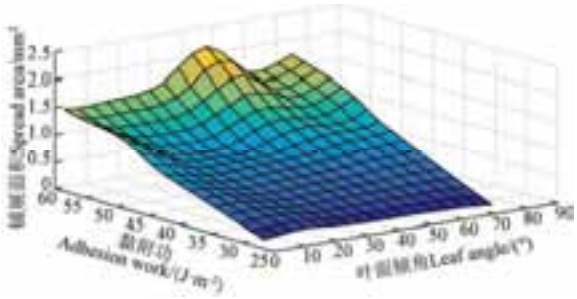
为分析溶液润湿性能和液滴粒径对铺展面积的交互影响，绘制交互效应曲面图，如图 3 所示。在所有角度下，都呈现出随黏附功和液滴粒径的增大，铺展面积也随之增大的趋势，且在黏附功和液滴粒径交叉方向上曲面上升最为陡峭。在叶面倾角为 15°时，曲面整体上升比较平缓，铺展面积最大值为 2.42 mm^2，最小值为 0.24 mm^2，最大值约为最小值的 10 倍。在叶面倾角为 45°时，曲面较 15°时更加陡峭，在黏附功为 58.82 J/m^2，液滴粒径为 973 μm 时铺展面积达到最大值 2.83 mm^2；黏附功为 26.49 J/m^2，液滴粒径 548 μm 时，铺展面积有最小值 0.77 mm^2，最大值约为最小值的 3.7 倍。在叶面倾角为 75°时，在黏附功和液滴粒径增大的方向上，曲面呈现出先平缓上升后陡峭上升的趋势，且在黏附功为 58.82 J/m^2，液滴粒径为 973 μm 时，铺展面积达到最大值 4.31 mm^2 远大于其他条件下的铺展面积。在不同角度下，增大液滴粒径和溶液的润湿性能均能增加液滴在玉米叶面上的铺展面积，但在不同角度下提高铺展面积的能力有所区别，在农药施用过程中可根据靶标叶面的倾角来选择适宜的喷施粒径和溶液润湿性。

在方差分析中发现溶液的润湿性能对液滴铺展面积影响最大，为探究溶液润湿性能和叶面倾角交互作用对液滴铺展面积的影响，固定液滴粒径为 548 μm，绘制铺展面积交互效应曲面图，如图 4 所示。在溶液的黏附功较低时，铺展面积随叶面倾角的变化不够明显；在溶液黏附功较高时，润湿性能较好，铺展面积呈现出随叶面倾角先上升后下降的趋势。铺展面积最大值在叶面倾角为 45°时，黏附功为 58.4 J/m^2 时取得，最大值为 2.24 mm^2。



a. 15° 叶面倾角　　b. 45° 叶面倾角　　c. 75° 叶面倾角
a. 15° leaf angle　　b. 45° leaf angle　　c. 75° leaf angle

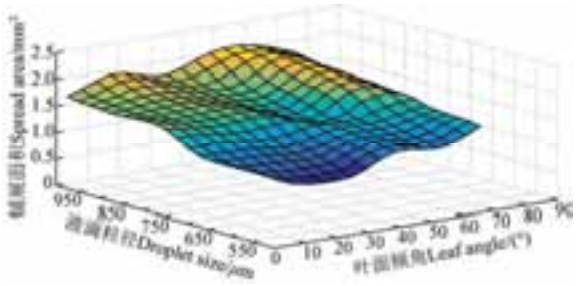
图 3　液滴粒径和润湿性能的交互影响
Fig.3　Interaction between droplet size and wettability



注：固定液滴粒径为 548 μm。
Note: The fixed droplet size is 548 μm.

图 4　润湿性能和叶面倾角的交互影响
Fig.4　Interaction between wettability and leaf angle

图 5 为 0.01%OP-10 溶液的液滴粒径和叶面倾角的交互效应图。液滴粒径和叶面倾角交互作用的整体趋势为铺展面积随液滴粒径和叶面倾角的增大而增大，但叶面倾角对铺展面积的影响不够明显且小于液滴粒径对铺展面积的影响。曲面的整体趋势较为平缓，当液滴粒径和叶面倾角较小时，铺展面积处于曲面上的低点，液滴粒径和叶面倾角较大时，铺展面积为曲面上的高点，最大值和最小值分别为 2.11、0.88 mm^2。

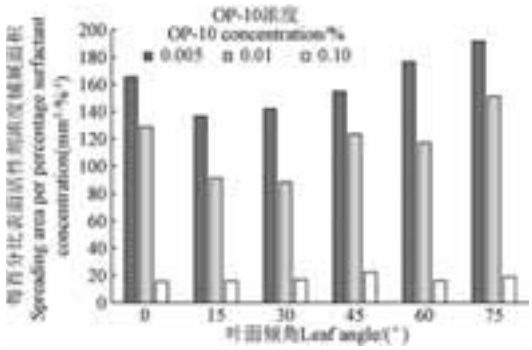


注：固定黏附功为 22.7 J·m^{-2}。
Note: The fixed adhesion work is 22.7 J·m^{-2}.

图 5　液滴粒径和叶面倾角的交互影响
Fig.5　Interaction between droplet size and leaf angle

2.4　表面活性剂浓度对液滴铺展能力的影响

为探究不同浓度 OP-10 对液滴铺展能力的影响，根据 1.3.4 节的研究方法，固定液滴粒径为 548 μm，计算不同叶面倾角下的单位浓度铺展面积，结果如图 6 所示。OP-10 浓度和单位浓度铺展面积之间呈现出明显趋势，6 种叶面倾角的单位浓度铺展面积均为 0.005%浓度>0.01%浓度>0.1%浓度，这表明在 0.005%浓度下的溶液对铺展面积增加的效率最高。OP-10 溶液在浓度 0.005%时达到临界胶束浓度，浓度从 0.005%增加到 0.01%、0.1%的过程中，溶液的表面张力保持稳定不再变化，但继续增加表面活性剂浓度还会增加铺展面积，但铺展面积增加效率显著降低，OP-10 浓度达到 0.1%时，降到最低。根据单位浓度铺展面积随溶液浓度降低的趋势，推断继续增大表面活性剂的浓度，液滴的铺展面积达到最大值后也将维持稳定。叶面倾角对单位浓度铺展面积的影响没有明显规律，但从图 6 可以看出，在叶面倾角为 75° 时，0.005%浓度下液滴的铺展能力最高，191.5 mm^2/%，叶面倾角为 0° 时，0.1%浓度下液滴的铺展能力最低，15.4 mm^2/%。



注：固定液滴粒径为 548 μm。
Note: The fixed droplet size is 548 μm.

图 6　不同角度下的单位浓度铺展面积
Fig.6　Unit concentration spread area at different angles

去离子水在玉米叶面上的接触角约为 129.2°，难以铺展。在去离子水中加入 OP-10 表面活性剂后溶液表面张力显著降低，同时接触角快速下降，当 OP-10 浓度达到 0.005%后表面张力不再降低，但 0.01%、0.1%OP-10 溶液在玉米叶面上的最大铺展面积仍然增大。表面活性剂分子结构具有双向性，一端为亲水基团，另一端为疏水基团，当溶液中的表面活性剂含量较少时，表面活性剂分子的亲水基向水，疏水基向空气，被吸附在水的表面上，形成定向的单分子层，使得水−空气界面被表面活性剂的亲油基−空气界面所取代，水表面的亲水性变成了亲油性，从而降低了水的表面张力[27]。当表面活性剂分子达到饱和状态时，溶液内部的表面活性剂分子形成亲油基向内、亲水基向外的胶束，即达到了临界胶束浓度，此时继续增大表面活性剂浓度，溶液的表面张力将不再降低。表面活性剂 OP-10 溶液形成液滴后，在玉米叶面

上进行铺展，此时液滴表面积扩大，产生了新的气-液界面，溶液内部的胶束便向新生成界面转移，继续在气-液界面处形成定向的单分子层。在试验中，0.005%OP-10溶液的表面活性剂分子刚达到饱和的临界值，变成液滴后溶液内部的表面活性剂分子向新形成的气-液界面转移上，此时由于溶液内部的表面活性剂分子数量较少，导致气-液界面的表面活性剂分子密度降低[28]，所以润湿性有限。在 0.01%、0.1%浓度下的 OP-10 溶液内部含有的表面活性剂分子更多，变成液滴扩大气-液界面后，界面处的表面活性剂分子密度更高所以润湿性更好、铺展面积更大。所以，在使用农药助剂时要注意用量，不仅需要让溶液的表面张力低于叶面的临界表面张力，还需要让助剂浓度显著大于其临界胶束浓度，才能保证药液雾化后还能有较好的铺展性能。

3 讨 论

本文使用不同质量分数的 OP-10 溶液模拟润湿性能不同的农药，通过试验方法研究了液滴粒径、农药润湿性能和叶面倾角对液滴在玉米叶面上铺展面积的影响。液滴在植物叶面上的铺展面积决定了农药有效成分作用范围、蒸发时间和叶面吸收效果。根据 Muntahli 等[29]提出的单液滴杀伤面积理论，单个液滴的作用范围远大于其液滴粒径，液滴在植物叶面上的覆盖范围越大，其杀伤面积也就越大。液滴蒸发时间与铺展面积的关系为同体积的液滴铺展面积越大，蒸发速度越快，蒸发时间越短[30]，当液滴完全蒸发后叶面的吸收效果基本消失[31]。本文探究的液滴粒径、农药润湿性能和叶面倾角及其交互作用均对液滴的铺展面积产生了显著影响。在施药中，叶面倾角为靶标植物固有属性，药液的润湿性能和液滴粒径是人为可控因素。农药的润湿性能可通过添加助剂、表面活性剂来调控；液滴粒径可通过调节压力喷头的压力值、更换喷嘴或改变离心喷头雾化盘转速来控制。在实际应用中应通过农药施用目的来确定适宜的粒径和药液润湿性能。例如，施用植物生长调节剂等内吸性药剂时，应适当调节降低溶液润湿性，降低其在叶面上的铺展面积，控制蒸发速度，保证叶面吸收效果。针对不同虫害的为害部位施药时，可根据靶标叶面倾角来精准控制粒径和药液润湿性能，提高施药效果。例如，玉米螟虫为害玉米心叶，而心叶的叶倾角较大但开口面积较小。小液滴更易进入叶心，更强的药液润湿性能提高小液滴的覆盖面积，增加作用范围。液滴粒径和药液润湿性的交互作用分析显示，二者为协同关系，在不同水平的液滴粒径下，增加药液润湿性均能提高液滴的铺展面积。

4 结 论

本研究探究了 OP-10 表面活性剂浓度、液滴粒径和叶片倾角三种因素对液滴在玉米叶片上铺展面积的影响，得到如下结论：

1）在本文设置的试验参数中，三种因素均对液滴在玉米叶片上的铺展面积有显著影响（P<0.001），且影响大小依次为表面活性剂浓度、液滴粒径、叶面倾角。

2）液滴粒径和铺展面积之间呈现线性关系，拟合系数为 0.969，铺展面积随液滴粒径增加而增加，液滴粒径从 548 μm 增加到 973 μm，铺展面积平均增加了 71.2%；叶面倾角对铺展面积的影响为随叶倾角的增大而增加，叶面倾角为 75° 时平均铺展面积为 1.51 mm^2，相比于 0°、45° 角，铺展面积增大了 18.0%、11.9%；液滴的铺展面积随表面活性剂浓度增加而增加，与去离子水相比，0.1%浓度下的 OP-10 在玉米叶面上的铺展面积平均增加了 572.7%。

3）在不同角度下，增大液滴粒径和溶液的润湿性能均能增加液滴在玉米叶面上的铺展面积，但在不同角度下提高铺展面积的能力有所区别。溶液润湿性能和叶面倾角的交互作用体现在，药液润湿性能差时，铺展面积随叶面倾角的变化不够明显，润湿性能较好，铺展面积呈现出随叶面倾角先上升后下降的趋势。铺展面积最大值在叶面倾角为 45° 左右。在实际应用中应通过施用目的来确定适宜的粒径和药液润湿性能，精准控制液滴在靶标叶面上的铺展面积，来提高农药利用率。

[参 考 文 献]

[1] Zheng L, Cao C, Chen Z, et al. Efficient pesticide formulation and regulation mechanism for improving the deposition of droplets on the leaves of rice (*Oryza sativa L.*)[J]. Pest Management Science, 2021, 77(7): 3198-3207.

[2] 宋玉莹，曹冲，徐博，等. 农药雾滴在植物叶面的弹跳行为及调控技术研究进展[J]. 农药学学报，2019，21(5/6)：895-907.
Song Yuying, Cao Chong, Xu Bo, et al. Research progress on bouncing behavior and control technology of pesticide droplets at plant leaf surface[J]. Chinese Journal of Pesticide Science, 2019, 21(5/6): 895-907. (in Chinese with English abstract)

[3] Zhang Y, Liu B, Huang K, et al. Eco-friendly castor oil-based delivery system with sustained pesticide release and enhanced retention[J]. ACS Applied Materials & Interfaces, 2020, 12(33): 37607-37618.

[4] 袁会珠，王国宾. 雾滴大小和覆盖密度与农药防治效果的关系[J]. 植物保护，2015，41(6)：9-16.
Yuan Huizhu, Wang Guobin. Effects of droplet size and deposition density on field efficacy of pesticides[J]. Plant Protection, 2015, 41(6): 9-16. (in Chinese with English abstract)

[5] Xu L, Zhu H, Ozkan H E, et al. Evaporation rate and development of wetted area of water droplets with and without surfactant at different locations on waxy leaf surfaces[J]. Biosystems Engineering, 2010, 106(1): 58-67.

[6] Cunha J P A R, Lasmar O, Ramos A M P, et al. Evaporation time of droplets containing thiamethoxam and adjuvants sprayed on sugarcane leaves[J]. Pesquisa Agropecuária Tropical, 2016, 46(1): 1-8.

[7] Gao J, Zhu H, Horst L, et al. Determination of foliar uptake of water droplets on waxy leaves in a controlled environmental system[J]. Transactions of the ASABE, 2015, 58(4): 1017-1025.

[8] Ma Y, Hao J, Zhao K, et al. Biobased polymeric surfactant: natural glycyrrhizic acid-appended homopolymer with

multiple pH-responsiveness[J]. Journal of Colloid and Interface Science, 2019, 541: 93-100.

[9] Ma Y, Gao Y, Zhao X, et al. A natural triterpene saponin-based pickering emulsion[J]. Chemistry (Weinheim an der Bergstrasse, Germany), 2018, 24(45): 11703-11710.

[10] Koch K, Bhushan B, Barthlott W. Multifunctional surface structures of plants: An inspiration for biomimetics[J]. Progress in Materials Science, 2009, 54(2): 137-178.

[11] 张晨辉，马悦，杜凤沛. 表面活性剂调控农药药液对靶润湿沉积研究进展[J]. 农药学学报，2019，21(5/6)：883-894.
Zhang Chenhui, Ma Yue, Du Fengpei. Research progress on the wetting and deposition behaviors of pesticide droplet on target surfaces with the addition of surfactants[J]. Chinese Journal of Pesticide Science, 2019, 21(5/6): 883-894. (in Chinese with English abstract)

[12] 康峰，吴潇逸，王亚雄，等. 农药雾滴沉积特性研究进展与展望[J]. 农业工程学报，2021，37(20)：1-14.
Kang Feng, Wu Xiaoyi, Wang Yaxiong, et al. Research progress and prospect of pesticide droplet deposition characteristics[J]. Transactions of the Chinese Society of Agricultural Engineering (Transactions of the CSAE), 2021, 37(20): 1-14. (in Chinese with English abstract)

[13] Xu L, Zhu H, Ozkan H E, et al. Droplet evaporation and spread on waxy and hairy leaves associated with type and concentration of adjuvants[J]. Pest Management Science, 2011, 67(7): 842-851.

[14] Kraemer T, Hunsche M, Noga G. Surfactant-induced deposit structures in relation to the biological efficacy of glyphosate on easy- and difficult-to-wet weed species[J]. Pest Management Science, 2009, 65(8): 844-850.

[15] Oliveira R B, Bonadio P L M, Gandolfo M A, et al. Effect of droplet size and leaf surface on retention of 2, 4-D formulations[J]. Crop Protection, 2019, 119: 97-101.

[16] 徐广春，顾中言，徐德进，等. 稻叶表面特性及雾滴在倾角稻叶上的沉积行为[J]. 中国农业科学，2014，47(21)：4280-4290.
Xu Guangchun, Gu Zhongyan, Xu Dejin, et al. Characteristics of rice leaf surface and droplets deposition behavior on rice leaf surface with different inclination angles[J]. Scientia Agricultura Sinica, 2014, 47(21): 4280-4290. (in Chinese with English abstract)

[17] 朱金文，吴慧明，孙立峰，等. 叶片倾角、雾滴大小与施药液量对毒死蜱在水稻植株沉积的影响[J]. 植物保护学报，2004，31(3)：259-263.
Zhu Jinwen, Wu Huiming, Sun Lifeng, et al. Influence of leaf incline angle, droplet size and spray volume on deposition of chlorpyrifos on rice plants[J]. Journal of Plant Protection, 2004, 31(3): 259-263. (in Chinese with English abstract)

[18] 杨希娃，代美灵，宋坚利，等. 雾滴大小、叶片表面特性与倾角对农药沉积量的影响[J]. 农业工程学报，2012，28(3)：70-73.
Yang Xiwa, Dai Meiling, Song Jianli, et al. Effect of droplet size, leaf characteristics and angle on pesticide deposition[J]. Transactions of the Chinese Society of Agricultural Engineering (Transactions of the CSAE), 2012, 28(3): 70-73. (in Chinese with English abstract)

[19] 李莫飞，王志江，吕明站，等. 影响农药雾滴在烟叶上沉积的关键因子分析[J]. 烟草科技，2022，55(3)：25-30.
Li Mofei, Wang Zhijiang, Lyu Mingzhan, et al. Key factors affecting pesticide droplet deposition on tobacco leaves[J]. Tobacco Science & Technology, 2022, 55(3): 25-30. (in Chinese with English abstract)

[20] 曹军琳，祁力钧，杨知伦，等. 基于图像处理的雾滴沉积分布试验研究[J]. 中国农业大学学报，2019，24(1)：130-137.
Cao Junlin, Qi Lijun, Yang Zhilun, et al. Experimental study of droplet distribution based on image processing[J]. Journal of China Agricultural University, 2019, 24(1): 130-137. (in Chinese with English abstract)

[21] Zisman W A. Relation of the Equilibrium Contact Angle to Liquid and Solid Constitution[M]. Washington, DC: American Chemical Society, 1964.

[22] Young T. An essay on the cohesion of fluids[J]. Philosophical Transactions of the Royal Society of London, 1805, 95: 65-87.

[23] Zhu H, Yu Y, Ozkan H E, et al. Influence of spray additives on droplet evaporation and residual patterns on wax and wax-free surfaces[Z]. St. Joseph, MI: ASABE, 2008.

[24] Lin H, Zhou H, Xu L, et al. Effect of surfactant concentration on the spreading properties of pesticide droplets on Eucalyptus leaves[J]. Biosystems Engineering, 2016, 143: 42-49.

[25] Zhu H, Salyani M, Fox R D. A portable scanning system for evaluation of spray deposit distribution[J]. Computers and Electronics in Agriculture, 2011, 76(1): 38-43.

[26] Gao S, Wang G, Zhou Y, et al. Water‐soluble food dye of Allura Red as a tracer to determine the spray deposition of pesticide on target crops[J]. Pest Management Science, 2019, 75(10): 2592-2597.

[27] 徐广春，顾中言，徐德进，等. 常用农药在水稻叶片上的润湿能力分析[J]. 中国农业科学，2012，45(9)：1731-1740.
Xu Guangchun, Gu Zhongyan, Xu Dejin, et al. Wettability analysis of pesticides on rice Leaf[J]. Scientia Agricultura Sinica, 2012, 45(9): 1731-1740. (in Chinese with English abstract)

[28] 顾中言，许小龙，韩丽娟. 不同表面张力的杀虫单微乳剂药滴在水稻叶面的行为特性[J]. 中国水稻科学，2004，18(2)：90-94.
Gu Zhongyan, Xu Xiaolong, Han Lijuan. Action of drops of monosultap ME with different surface tension on rice leaf[J]. Chinese Journal of Rice Science, 2004, 18(2): 90-94. (in Chinese with English abstract)

[29] Munthali D C, Scopes N E A. A technique for studying the biological efficiency of small droplets of pesticide solutions and a consideration of the implications[J]. Pesticide Science, 1982, 13(1): 60-62.

[30] 周召路，曹冲，曹立冬，等. 不同类型界面液滴蒸发特性与农药利用效果研究进展[J]. 农药学学报，2017，19(1)：9-17.
Zhuo Zhaolu, Cao Chong, Cao Lidong, et al. Reasearch advances of droplet evaporation on different interfaces and the efficiency of pesticide utilization[J]. Chinese Journal of Pesticide Science, 2017, 19(1): 9-17. (in Chinese with English abstract)

[31] 祁力钧，王沛，张建华，等. 杂草叶片表面结构对雾滴铺

展和蒸发的影响[J]. 排灌机械工程学报，2012，30(3)：335-340.
Qi Lijun, Wang Pei, Zhang Jianhua, et al. Influence of weed leaves surface structures on droplet spread and evaporation[J]. Journal of Drainage and Irrigation Machinery Engineering, 2012, 30(3): 335-340. (in Chinese with English abstract)

Factors influencing the spreading areas of pesticide droplets on the surface of maize leaves

Gao Rong[1,2], Huang Lusheng[1,2], Wen Sheng[2], Yin Xuanchun[2], Zhang Jiantao[1,2,3※]

(1. *College of Mathematics and Informatics*, *South China Agricultural University*, *Guangzhou* 510642, *China*; 2. *International Laboratory of Agricultural Aviation Pesticide Spraying Technology*, *Guangzhou* 510642, *China*; 3. *Key Laboratory of Smart Agricultural Technology in Tropical South China*, *Ministry of Agriculture and Rural Affairs*, *Guangzhou* 510642, *China*)

Abstract: Pesticide wastes have caused serious pollution to the air, water, and soil in recent years. It is a high demand to clarify the spreading behavior of pesticide droplets on the plant leaves, particularly for the better utility efficiency of pesticides. Among them, the maximum spreading area of pesticide droplets on the plant leaves can dominate the action range, evaporation time, and foliar absorption of active ingredients in the pesticides. This study aims to explore the influence mechanism of droplet size, surfactant concentration, and leaf inclination on the maximum spreading area of droplets on the corn leaves. The leaf inclination angles were set as 0°, 15°, 30°, 45°, 60°, and 75°. The droplet sizes were 548, 675, 756, 877, and 973 μm. A droplet generator was used to produce the droplets of different sizes, further to reach the plant leaves at the free velocity. The solutions were utilized the 0, 0.1%, 0.01%, and 0.005% of OP-10 surfactant. A full factorial experiment was designed with a total of 120 tests. The results show that there were significant effects of droplet size, surfactant concentration, and leaf inclination on the maximum spreading area (P<0.001). The influencing factors were ranked in the order of the surfactant concentration > droplet size > leaf angle. The partial-eta squares were 0.857, 0.473, and 0.073, respectively. A linear relationship was observed between the droplet size and the spreading area. The spreading area also increased with the increase of the droplet size, leaf angle, and solution surfactant concentration. Once the droplet size increased from 548 to 973 μm, the spreading area increased by 71.2% on average. When the leaf inclination angle was 75°, the average spreading area was 1.512 4 mm^2. The spreading area increased by 18.0%, and 11.9%, compared with the 0°and 45°. The spreading area of 0.1% OP-10 on the maize leaves increased by an average of 572.7%, compared with the deionized water. Therefore, the droplet size increased the maximum spreading area of the droplets on the corn leaf surface with the same increased efficiency under different leaf inclination angles. Furthermore, the relationship between the droplet size and the maximum spreading area was y=0.001 7x+0.022 3, where the goodness of fit R^2 was 0.969. It infers that the maximum spreading area of the droplet increased by 0.17 mm^2 on average, particularly for every 100 μm increase in the droplet size. The highest value of 4.13mm^2 was achieved in the maximum spreading area of 973 μm droplets at 0.1% concentration, when the leaf inclination angle was 75°. By contrast, the average level of the spread area was significantly higher at the 0.1% concentration, compared to the rest groups. The Pearson correlation analysis was carried out between the surface tension, contact angle, adhesion work, and spreading area of the solution. It was found that there was a significant positive correlation between the adhesion work and the spreading area (r=0.995, P=0.009). The adhesion work was well represented by the spreading area trend of the droplets on the leaf. Correspondingly, the surface tension of the liquid medicine was lower than the critical surface tension of the leaves in actual agricultural production. Furthermore, a greater surfactant composition was required for better wetting after atomization in the liquid medicine, compared with the critical micelle concentration. The 0.01%-0.1% OP-10 solution can be expected as a reference surfactant for higher spreading efficiency and better performance at a high level. The findings can provide a strong reference to understanding the spreading mechanism of pesticide droplets on the plant leaves. The particle size of pesticide droplets and the concentration of surfactants can also be adjusted for better spreading performance at the different leaf inclination angles.

Keywords: pesticide droplet; wetting performance; spread area; surfactant; droplet size; adhesion work

《农业工程学报》：对标一流，追求卓越

《农业工程学报》（以下简称《学报》）创刊于1985年，现为半月刊，全年24期，大16开面向国内外公开发行。《学报》是由中国科学技术协会主管、中国农业工程学会主办的全国性专业学术期刊。读者对象为农业工程学科及相关领域的科研、教学及生产科技人员、技术管理及推广人员和高等院校师生。刊载内容涵盖了农业装备工程与机械化、农业航空工程、农业水土工程、农业信息与电气技术、农业生物环境与能源工程、土地保障与生态安全、农产品加工工程等学科专业领域。

《学报》始终坚持“双为”方向和“双百”方针的办刊宗旨及“内容为王，质量为本”的办刊理念。拥有国内外农业工程相关领域各专业的知名专家学者组成的编委会，其中院士10余人。本刊坚持专家办刊，编委在稿件同行评审把关中发挥重要作用。

《学报》是中国农业工程领域的领军期刊，在行业具有较高的学术影响力，被EI Compendex（核心版）、Scopus、CA、CSA、CAB Abstracts、CSCD、《中文核心期刊要目总览》、《中国科技核心期刊目录》、《中国农林核心期刊概览2020》等国内外多个权威数据库收录。中国科学技术信息研究所2020年影响因子2.116，在农业工程类核心期刊中位列第一名。

我们愿与广大农业工程同仁携手并肩，共同奋斗，对标一流，追求卓越，创建国际知名品牌，引领学科发展，培养人才，激励创新，为全面推进乡村振兴，加快农业农村现代化，促进农业农村高质量发展作出新贡献，以优异成绩向建党100周年献礼！



期刊荣誉：多项位列农业工程类期刊榜首

- ✧ 国家新闻出版广电总局“双效期刊”
- ✧ 国家新闻出版广电总局“百强报刊”
- ✧ 中国科技期刊卓越行动计划-梯队期刊
- ✧ 百种中国杰出学术期刊
- ✧ 中国精品科技期刊
- ✧ TOP5%中国最具国际影响力学术期刊
- ✧ RCCSE中国权威学术期刊（A+）
- ✧ 科技期刊数字影响力100强
- ✧ 世界学术影响力指数WAJCI-Q1区期刊（为本学科唯一入选中文刊）
- ✧ Google Scholar学术期刊影响力排名位列高被引中文刊第四名
- ✧ 中国农林领域高质量科技期刊分级目录第一区（T1）
- ✧ 中国科协精品科技期刊工程项目资助期刊

對標一流
追求卓越

ISSN 1002-6819
CN 11-2047/S
国内邮发代号：18-57
海外发行代号：BM3335
国内定价：80元

ISSN 1002-6819
9 771002 681221 20>

3.5 Origami Improved Dielectric Elastomer Actuation for Tunable Lens

Advancing Technology for Humanity

SEARCH 6,260,161 ITEMS

All

ADVANCED SEARCH TOP SEARCHES

IEEE Climate Change Collection

As the world's largest organization of technical professionals, IEEE is uniquely positioned to help organize the world's engineers, scientists, and technical professionals in addressing the causes, mitigating impacts, and adapting to climate change.

Go to the Collection



Featured Authors



Long Cheng
(CHINA)

Passive Model Predictive Impedance Control for Safe Physical Human-Robot Interaction

Follow

MORE FROM LONG CHENG



Mariagrazia Dotoli
(ITALY)

Distributed Noncooperative MPC for Energy Scheduling of Charging and Trading Electric Vehicles in Energy Communities

Follow

MORE FROM MARIAGRAZIA DOTOLI



Mark Anastasio
(UNITED STATES)

A Test Statistic Estimation-based Approach for Establishing Self-interpretable CNN-based Binary Classifiers

Follow

MORE FROM MARK ANASTASIO

Featured Articles







https://ieeexplore.ieee.org/search/searchresult.jsp?topic=climateChange

Feedback

IEEE Transactions on Instrumentation and Measurement

IEEE INSTRUMENTATION & MEASUREMENT SOCIETY

5.6 Impact Factor
0.02974 Eigenfactor
0.882 Article Influence Score
7.4 CiteScore

Author Resources

- Submission Guidelines
- Submit Manuscript
- Author Center
- Become a Reviewer
- Open Access Publishing Options

Meet the Editor

Editor-in-Chief
Ruqiang Yan
School of Mechanical Engineering
Xi'an Jiaotong University
Xi'an, 710049, China
Email:

Popular Articles | Latest Published Articles

Applications Of Unsupervised Deep Transfer Learning To Intelligent Fault Diagnosis: A Survey And Comparative Study
Zhibin Zhao; Qiyang Zhang; Xiaolei Yu; Chuang Sun; Shibin Wang; Ruqiang Yan; Xuefeng Chen

Deep Transfer Learning For Bearing Fault Diagnosis: A Systematic Review Since 2016
Xiaohan Chen; Rui Yang; Yihao Xue; Mengjie Huang; Roberto Ferrero; Zidong Wang

Uncertainty Estimation And Multi-FOV Data Fusion For Star Sensors Based On Directional Statistics
Jisan Yang; Jie Jiang; Jian Li; Yan Ma; Lingfeng Tian; Guangjun Zhang

DS-TransUNet: Dual Swin Transformer U-Net For Medical Image Segmentation
Ailiang Lin; Bingzhi Chen; Jiayu Xu; Zheng Zhang; Guangming Lu;

Feedback

The Fabrication of an Eccentric Three-Core Fiber and Its Application as a Twist Sensor
Pingsheng Xue; Qiang Liu; Qiang Wu; Yongqing Fu
Publication Year: 2022 , Article Sequence Number: 7003806
Cited by: Papers (4)
Abstract HTML

Origami Improved Dielectric Elastomer Actuation for Tunable Lens
Xuanchun Yin; Pengyu Zhou; Sheng Wen; Jiantao Zhang
Publication Year: 2022 , Article Sequence Number: 7502709
Abstract HTML

Intelligent Design of Reconfigurable Microstrip Antenna Based on Adaptive Immune Annealing Algorithm
Xiaoxian Xu; Pengying Xu; Yan Wang; Zhihai Wang; Kunpeng Yu; Haitao Shi; Dongming Ge; Xiaofei Ma; Guojun Leng; Meng Wang; Congsi Wang

Origami Improved Dielectric Elastomer Actuation for Tunable Lens

Xuanchun Yin, *Member, IEEE*, Pengyu Zhou, Sheng Wen, and Jiantao Zhang

***Abstract*— Dielectric elastomer actuators (DEAs) have been applied to the tunable solid lens with the unique characteristics of fast response, low consumption, lightweight, and silent operation. However, the performance of the DEA-based contraction tunable solid lens is limited to the small aperture or tuning range compared to the extension tunable solid lens. In this article, to address this issue, a self-recovery origami mechanism with a modified Yoshimura tessellation structure is presented to improve the contraction-tunable lens driven by the truncated cone-shaped DEA. A model using the virtual work principle and spring in-series theory is established to predict the deformation of the tunable lens, and the experimental result verifies the simulation. The experiment demonstrates that the focal length of the 10-mm-diameter solid lens can vary from 45.4 to 37.7 mm, showing a 17% tunability. Results show that combining origami structure with the unique properties of DEA for a tunable solid lens has the potential to expand its application fields.**

***Index Terms*— Dielectric elastomer actuator (DEA), modeling, origami mechanism, simulation, solid tunable lens.**

I. Introduction

TUNABLE lens technology, including solid lens and fluid lens, has attracted considerable attention due to its applications in various areas, such as optical communication [1], portable consumer electronics [2], medical imaging [3], [4], depth from defocus measurement systems [5], and multispectral iris capture devices [6]. In terms of the fluid lens, modifying the refractive index or surface curvature of the lens is the main strategies to enable the focal length of the fluid lens to be tuned. The liquid crystal (LC) is generally used as the medium of an optical lens because LC changes its optical properties in response to an applied electric field to alter the refractive index of the fluid lens [7]. The lens's surface curvature change can be realized in different ways, such as electrowetting [8], pump actuation [9], electromagnetic actuation [10], dielectric elastomer (DE) [11], [12], piezoelectric actuation [13], and electrothermal actuation [14]. To sum up, whether constant volume or variable volume fluid lens, they are sensitive to gravity and vibrations with the lens's aperture increasing, though it has a larger tuning range than that of a solid lens.

Compared to the liquid lens, the solid lens possesses stronger robustness against gravity and better mechanical stability against vibration and shocks. To change the focal length of a solid lens, modifying the surface curvature is the primary method that can be achieved electrically, electromechanically, and electrothermally. For example, a microlens with 0.75-mm aperture and order of 1-s response time (486.8% tuning range) is actuated by a polyvinyl chloride (PVC)-gel electrically in [15]. For electromechanical actuation, external motors are employed to an 8-mm aperture lens, achieving a 7.4% tuning range in [16]. In addition, both a 0.146-mm lens with a 71.5% tunable range (9.197–2.619 mm) [17] and a 0.15-mm lens with a 45% tunable range (1.852–1.018 mm) [18] are realized by the way of a thermal expansion polymer. These lenses achieve focusing or astigmatism in different ways; however, they have a large tuning range in a relatively small aperture and are limited to low response speed or large consumption.

Dielectric elastomer actuators (DEAs) for the solid lens have the advantages of low consumption, large aperture, and considerable tunable range, compared to those methods mentioned above, such as a 3-mm lens with 65.7% change (14.3–23.7 mm corresponding to 0–4.5 kV) [19] and a 24-mm lens with 209% change (14.8–45.732 mm corresponding to 0–13 kV approximately) [20]. However, when it comes to the solid lens affected by the in-plane contraction induced by the DEA, a larger aperture causing a smaller tunable range is still a challenge. For example, in [21], a 12.5-mm lens that can dynamically deform either radially or along with selectable directions by surrounding DEA segments is presented, achieving a 5.5% focal length change (68–64 mm corresponding to 0–2.7 kV) or astigmatism in the visible range. In addition, a 7.92-mm lens with 27.5% change (120–87 mm corresponding to 0–4 kV) monolithically fabricated with DE membrane is proposed in [22], showing a faster response than the previous lens [19]. To model for the tunable solid lens and improve the performance of contraction-tunable lens driven by DEA, another DEA [23] can be employed instead of the disk-shaped DEA. This will cause the force of DEA acting on the solid lens to be in the axial direction, not the radial direction.

To aid in solving this problem, origami technology [24] is appropriate to improve DE actuation due to its unique characteristics of deployment [25], self-recovery [26], and lightweight [27]. Origami tessellations are mainly categorized as Miura-origami [28], Yoshimura [29], Waterbomb [30],

Manuscript received January 14, 2022; revised March 29, 2022; accepted April 6, 2022. Date of publication April 20, 2022; date of current version May 2, 2022. This work was supported in part by the National Natural Science Foundation of China under Grant 61773171, in part by the Characteristic Innovation Projects of Universities in Guangdong Province under Grant 2019KTSCX016 and Grant 2019KZDZX1002, in part by the Guangdong Province Education Project under Grant 2018KTSCX019, and in part by the Guangdong Natural Science Foundation under Grant 2022A1515011008. The Associate Editor coordinating the review process was Dr. Alessio De Angelis. *(Corresponding authors: Xuanchun Yin; Jiantao Zhang.)*

Xuanchun Yin, Pengyu Zhou, and Sheng Wen are with the College of Engineering, South China Agricultural University, Guangzhou 510642, China (e-mail: xc_yin@scau.edu.cn; pengyu@stu.scau.edu.cn; vincen@scau.edu.cn).

Jiantao Zhang is with the College of Mathematics and Informatics, South China Agricultural University, Guangzhou 510642, China (e-mail: zhangjiantao@yeah.net).

Digital Object Identifier 10.1109/TIM.2022.3168942

1557-9662 © 2022 IEEE. Personal use is permitted, but republication/redistribution requires IEEE permission.
See https://www.ieee.org/publications/rights/index.html for more information.

Authorized licensed use limited to: SHENZHEN UNIVERSITY. Downloaded on July 13,2022 at 09:10:46 UTC from IEEE Xplore. Restrictions apply.

Kresling [31], and Flasher [32] and widely employed in current robotic research. Furthermore, due to the characteristics of compliance, fast response, and compact structure, DEA is proper to actuate origami robot. Besides, commercially miniature high voltage multipliers (e.g., EMCO A series) improve the mobility of the system. Therefore, it is promising to combine origami structure and DE actuation for improving a tunable lens.

In this article, a self-recovery origami mechanism (SOM) is developed to improve the performance of a contraction-tunable lens driven by a DEA, allowing the large aperture solid lens to tune from a large focal length to a small one. The system consists of an optimized truncated cone-shaped DEA, an SOM, and a 10-mm lens. The virtual work principle and spring in-series theory are applied to model the origami structure and predict the focal length change of the lens. A prototype that achieves a focal length modulation from 45.4 to 37.7 mm (17% tunability) under 0–3.5 kV is established for experiment, and the result shows a high degree fit with the theory.

The main contributions of the work can be summarized as follows.

1) An SOM with a modified Yoshimura tessellation is developed to improve the performance of a large aperture tunable lens driven by DEA.

2) A model of the system is established to predict the deformation of the tunable lens, and the experimental result verifies the simulation.

The remainder of this article is organized as follows. In Section II, the design scheme and principles of the tunable lens are presented, followed by the modeling and verification of the origami structure and the DEA. In Section III, experiment and discussion are shown. In Section IV, we conclude this article.

II. Design and Modeling

A. Conceptual Design

Compared to other actuations, the DE actuation for the tunable solid lens with the characteristics of silence, fast response, and lightweight has attracted much attention. However, the performance of contraction-based DEA for the solid lens is limited by a small aperture or tuning range compared to extension-based DEA. Aiming to solve the problem, a truncated cone-shaped DEA is intended for a large aperture solid lens. Therefore, to generate a radial force, the origami mechanism should transform the direction of the force induced by the DEA. In addition, to adapt to the origami mechanism and drive the large aperture solid lens, the design parameters of the selected DEA should be optimized.

As shown in Fig. 1(a), the origami-based tunable lens consists of a DEA, an SOM, and a soft solid (fully elastomeric) lens, enabling the focus of light through the lens to change. When excitation is applied, the axial force of the DEA (the effect of the extension by DE membrane and spring simultaneously) acts on the origami mechanism. Subsequently, the axial force is transformed into a radial force by the SOM, which comprises a laminate of three-layered composites and an origami structure folded by one column and six rows of Yoshimura tessellation, as shown in Fig. 1(b). Also, the SOM can be treated as an amplifier to enhance the geometrical deformation of the DEA. The manufacturing process of the Yoshimura origami-inspired structure (YOS) has three steps, including folded by a Yoshimura tessellation, bending, and installation on the lower layer lamina. With variable voltages applied to the DEA, causing a programmable force acting on the SOM, the SOM controls the change of the solid lens' focal length.

The focus-tuning effect is produced by the locomotion of four origami slices when the DEA activates, as shown in Fig. 1(c). The three-layer laminate guides the locomotion of four origami slices connected to the lens, achieving the axial force F_{DE} transformed into the radial force F_{ori} acting on the lens. The advantage of the method is that the origami slices stiffer than the compliant DE membrane can push the solid lens more effectively, which will improve the performance of the DEA in the tunable lens. The electrode connected to the high voltage is designed inside the origami mechanism, which offers a safer operating environment because the whole origami mechanism makes up of insulation materials. Compared to the integrated lens, another advantage of the design is that the split type offers more convenience to operate the lens, such as altering a new lens when the old lens is burn-in and replacing different apertures lenses.

B. Principle of Tunable Lens

The solid lens, a planoconvex lens, is composed of polydimethylsiloxane (PDMS). Due to the contraction of the four origami slices in the SOM, the surface curvature of the lens decreases, leading to the focal length decreasing synchronously. In this study, the lens is considered a thin planoconvex lens because the thickness of the lens is smaller than the radius. Due to the slight in-plane contraction of the bottom surface, it is assumed that the bottom surface of the lens maintains flat. Hence, the focal length f is computed using the thin lens equation

$$f = \frac{R_1}{n-1} \tag{1}$$

where n is the refractive index of PDMS and R_1 is the radius of the convex surface's curvature. The cross section of the lens is shown in Fig. 1(d), in which two origami slices forces F_{ori} push the solid lens, like Fig. 1(c). Due to the PDMS lens being considered incompressible, the arc length l_{sec} of the lens in the cross section remains constant. The relation of parameters in the geometric model can be written as follows:

$$2R_1 \arcsin\left(\frac{d_r}{R_1}\right) = l_{\mathrm{sec}} \tag{2}$$

where d_r is the radius of the lens. When d_r changes, R_1 and the focal length f change simultaneously, and the resulting focal length in this cross section can represent the entire lens, for the four origami slices that deform equally. Therefore, the focal length of the lens can be calculated by d_r which the SOM of the DE actuation controls.

Authorized licensed use limited to: SHENZHEN UNIVERSITY. Downloaded on July 13,2022 at 09:10:46 UTC from IEEE Xplore. Restrictions apply.

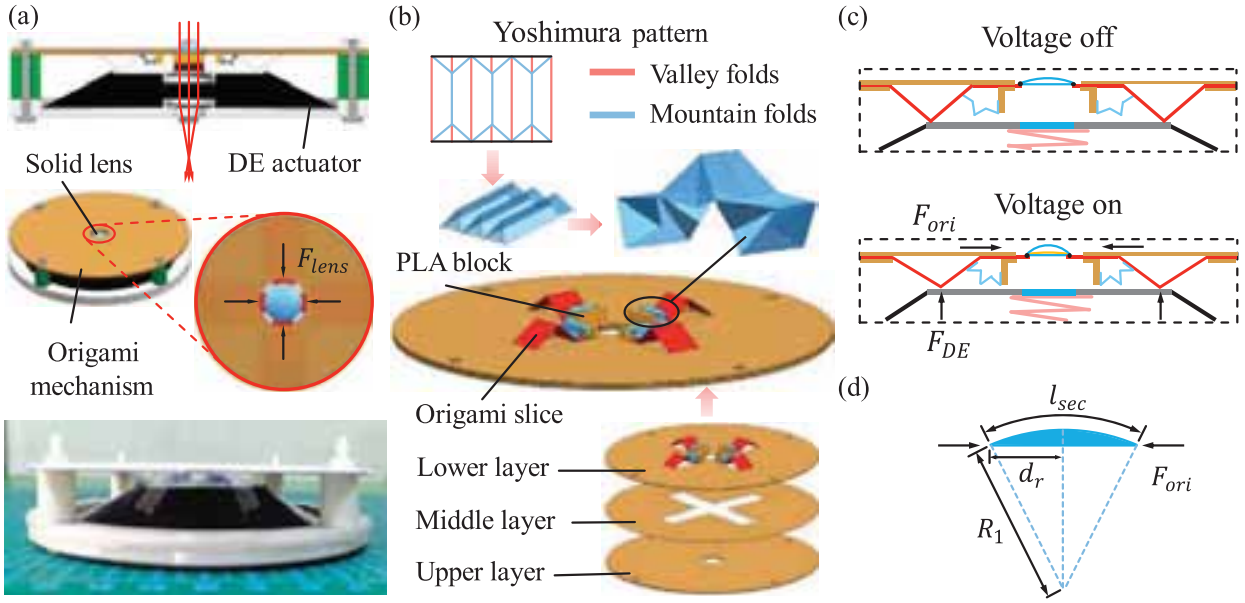


Fig. 1. (a) Conceptual design and the prototype of the origami-based tunable lens. (b) Explosive view of the SOM. (c) Schematic of the focal length modulation. (d) Geometric model of the solid planoconvex lens.

C. Self-Recovery Origami Mechanism

Origami with the characteristics of deployment, self-recovery, lightweight, and compact structure has been widely used to solve engineering problems. In this study, an SOM is proposed to transform the force of the DEA from axial to the radial direction. The SOM can be divided into four segments, and each part consists of a YOS and an origami slice whose shape is similar to a pop-up book. After the voltage is OFF, the four origami slices can restore under the recovery torque and the effect of the YOS. Compared to the integrated DE lens, a split-type tunable DE lens improved by origami can achieve to adjust a large aperture lens in terms of contraction.

For modeling the SOM, one of the origami slices is used to analyze, as the four origami slices have identical motions. Due to the deformation of the solid lens generated by the motion of an origami slice, point M is defined as the point of action between origami slices and the solid lens. Thus, the edge of the lens's motion is consistent with the origami slice. b_0 and s_0 are the geometrical parameters in the undeformed state, while b and s are in the deformed state, as shown in Fig. 2(a). For deriving the motion of an origami slice, the relationship between the displacement of the point $M\Delta s$ and the axial displacement generated by the DEA Δd can be expressed as

$$\Delta s = 2\sqrt{a^2 - (b_0 - \Delta d)^2} - s_0 \tag{3}$$

where a is half the length of an origami slice from the fixed end to point M. The expression indicated that the SOM amplifies the deformation of the DEA.

In order to obtain the force F_{ori} generated by the origami slice, the virtual work principle [33] is used to analyze the force equilibrium. The force F_{lens} induced by the solid lens equals F_{ori} because they are a pair of interacting forces. A Cartesian coordinate system at point A is established, assuming that $\delta\alpha$ is the virtual displacement of segment AB [Fig. 2(b)]. The equation of the whole origami mechanism can be given as

$$2T_1\delta\alpha + T_2\delta\beta - (F_l + F_{\text{lens}})\delta x_M + F_{\text{act}}\delta y_B = 0 \tag{4}$$

where T_1 and T_2 are torque generated in joints A and B, respectively. The torque generated in joint M is equal to T_1 due to the symmetry of the origami mechanism. F_l is the equivalent force of the YOS. F_{act} is the force generated by the DEA. $\delta\beta$ and δy_B are the virtual displacements corresponding to T_2 and F_{act}, respectively, and δx_M corresponding to F_l and F_{lens}. Moreover, $\delta\beta$, δx_M, and δy_B are calculated by the calculus of variations

$$\begin{cases} \delta\beta = -2\delta\alpha \\ \delta x_M = -2a\sin\alpha \cdot \delta\alpha \\ \delta y_B = a\cos\alpha \cdot \delta\alpha. \end{cases} \tag{5}$$

Substituting (5) into (4), F_{lens} can be derived as

$$F_{\text{lens}} = \frac{T_2 - T_1}{b} - F_l + \frac{\sqrt{a^2 - b^2}}{2b}F_{\text{act}}. \tag{6}$$

In this case, the crease is considered a joint area [34], as shown in Fig. 2(c). Hence, we have

$$\begin{cases} \rho_1 = \dfrac{L_{\text{ori}}}{\alpha} \\ \rho_2 = \dfrac{L_{\text{ori}}}{\pi - \beta} \\ L_{\text{ori}} = \dfrac{\pi h_{\text{ori}}}{2} \end{cases} \tag{7}$$

where ρ_1 and ρ_2 are the radii of curvature in joints A and B, respectively, L_{ori} is the arc length in the joint area, and h_{ori} is the thickness of the origami slices. A folded origami in

Authorized licensed use limited to: SHENZHEN UNIVERSITY. Downloaded on July 13,2022 at 09:10:46 UTC from IEEE Xplore. Restrictions apply.

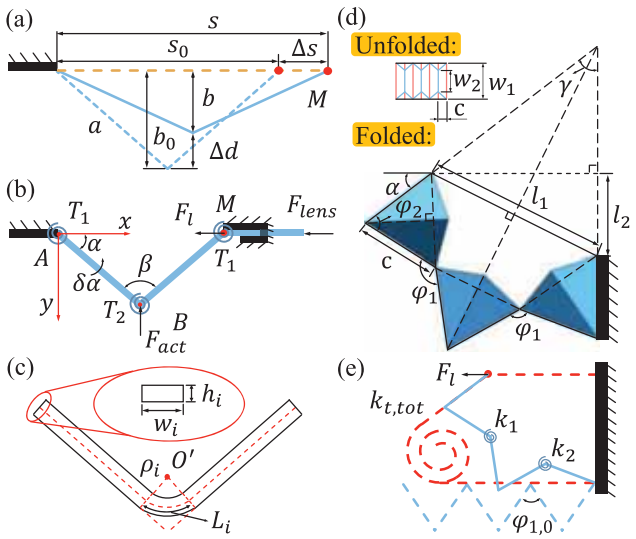


Fig. 2. (a) Geometrical parameters of an origami slice in the undeformed and deformed states. (b) Force analysis diagram of the SOM. (c) Folded origami is regarded as a bending beam in static equilibrium. (d) Yoshimura-inspired origami structure in the unfolded and folded states. (e) Equivalent model of the Yoshimura-inspired origami structure.

static equilibrium is regarded as a pure bending beam. The restoring torque depends on Young's modulus, the moment of inertia of the cross section, and bending curvature. Thus, the relationship between the restoring torque and the bending angle can be expressed as [35]

$$\begin{cases} T_1 = \dfrac{E_{\text{ori}} I_{\text{ori}}}{\rho_1} = \dfrac{E_{\text{ori}} w_{\text{ori}} h_{\text{ori}}^2}{6\pi}\alpha \\ T_2 = \dfrac{E_{\text{ori}} I_{\text{ori}}}{\rho_2} = \dfrac{E_{\text{ori}} w_{\text{ori}} h_{\text{ori}}^2}{6\pi}(\pi - \beta) \end{cases} \tag{8}$$

where E_{ori} and I_{ori} are Young's modulus and the moment of inertia of the origami slices, respectively, w_{ori} is the width of the origami slices, and α and β are bending angles in joints A and B, respectively. Furthermore, α can be inferred by Δd, where $\alpha = \arcsin(b_0 - \Delta d)/a$. Accordingly, the torque of the origami slices can be obtained by the displacement generated by the DEA.

Yoshimura tessellation is generally folded into square or hexagonal bellows for engineering problems, utilizing its self-recovery ability. In this article, one column and six rows of Yoshimura pattern, meaning quarter pattern, are applied to fold into the YOS and bent at an angle. The YOS connects the origami slice and the PLA block bonded to the lower layer lamina so that the moving end can realize a rectilinear motion. The geometrical parameters of the YOS mounted are shown in Fig. 2(d). Each prism-shaped part is deemed equal, and the torque induced by the YOS is relative to the bending angle of φ_1 and φ_2. However, in this article, due to the stiffness in φ_2 being much larger than φ_1, φ_2 is considered static, and the torque of the YOS depends on φ_1. Before finding out the relation of α and φ_1, the equation of φ_2 and γ is

$$c\left[\sin\left(\varphi_2 + \frac{\gamma}{2}\right) + \sin\left(\frac{\varphi_2}{2}\right)\right] - c\sin\frac{\gamma}{2} = \frac{l_1}{2} \tag{9}$$

where c is the length of a trapezoid unit and l_1 is the installation dimension of the YOS. Next, we get

$$\begin{cases} \varphi_1 = (3\varphi_2 + \gamma)/2 \\ \gamma = \dfrac{\pi}{2} - \alpha. \end{cases} \tag{10}$$

The spring model is a suitable way to model a crease of an origami structure so that the model of origami tessellation is usually regarded as the combined action of multiple (extension or torsional) springs [36], [37]. Hence, the YOS is modeled as a torsional spring governed by Hooke's law, and the equivalent model of the YOS is shown in Fig. 2(e). In this article, a torsional spring in-series model is used to analyze the Yoshimura-inspired structure, and the resulting torsional spring is finally equivalent to a horizontal force. The equivalent stiffness of the YOS $k_{t,\text{tot}}$ can be calculated as the following equation:

$$\frac{1}{k_{t,\text{tot}}} = \frac{1}{k_1} + \frac{1}{k_2} \tag{11}$$

where k_1 and k_2 are the equivalent stiffness in two angles φ_1, as shown in Fig. 2(e). Furthermore, $k_1 = k_2$ because of the symmetry of the structure. Eventually, we have

$$k_{t,\text{tot}} = \frac{k_1 k_2}{k_1 + k_2} = \frac{1}{2}k_1. \tag{12}$$

A more considerable spring stiffness indicates that the YOS has larger restoring torque. Thus, it is essential to design a proper stiffness of the YOS that allows the DEA to drive and make the origami slice restore. The bending torque in φ_1 is expressed as follows:

$$T_{k1} = \frac{E_{\text{yos}} w_1 h_{\text{yos}}^2}{6\pi}\Delta\varphi_1 \tag{13}$$

where E_{yos} is Young's modulus of the YOS, w_1 is the length of the trapezoid unit's short base, and h_{yos} is the thickness of the YOS's material. Moreover, $\Delta\varphi_1 = \varphi_1 - \varphi_{1,0}$, where $\varphi_{1,0}$ is the initial angle before bending the YOS. The spring stiffness of the YOS is determined by the property and parameters of the material. From the formula of (13), k_1 can be written as follows:

$$k_1 = \frac{E_{\text{yos}} w_1 h_{\text{yos}}^2}{6\pi}. \tag{14}$$

The torque generated by the YOS is modeled as a horizontal force to simplify the model further because the moving end is the horizontal motion. According to the static analysis, the equivalent force F_l is described as follows:

$$F_l = \frac{k_{t,\text{tot}}}{\left(l_2 + \frac{c}{2}\right)}\Delta\varphi \tag{15}$$

where l_2 is the installation dimension of the YOS, as shown in Fig. 2(d), and $\Delta\varphi = 2\Delta\varphi_1$. Therefore, the simplified model of the YOS is a horizontal force F_l. The force F_{lens} acting on the solid lens can be inferred from F_{act} using the force model of the SOM, which achieves the programmable output from the DEA.

Authorized licensed use limited to: SHENZHEN UNIVERSITY. Downloaded on July 13,2022 at 09:10:46 UTC from IEEE Xplore. Restrictions apply.

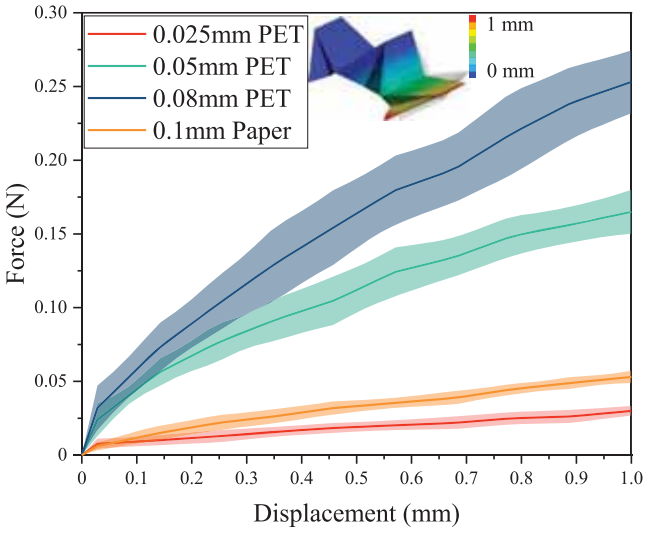


Fig. 3. Relationship between horizontal displacement and force induced by the YOS made up of 0.025-mm-thickness PET, 0.05-mm-thickness PET, 0.08-mm-thickness PET, and 0.1-mm-thickness paper.

D. Design Optimization

1) Materials of the YOS: An experiment of selecting appropriate material for the YOS is conducted to verify and optimize the design of the YOS. Before the experiment, an finite element analysis (FEA)-based simulation about the YOS is performed by ANSYS Workbench 19.2 (ANSYS Inc., Canonsburg, PA, USA) to verify the motion of the YOS, and the result of the simulation verifies the feasibility of the design. Four YOSs are made up of 0.025-mm-thickness PET, 0.05-mm-thickness PET, 0.08-mm-thickness PET, and 0.1-mm-thickness paper. According to the working way of the YOS in the SOM, one end is fixed, and another connects with a load cell. Then, the load cell moves 1 mm horizontally and records the force generated by the YOS. The result of the experiment (see Fig. 3) indicates that smaller thickness has a smaller recovery force, which also confirms the modeling of the YOS. Compared to a typical 0.1-mm paper, the force of 0.08-mm PET is relatively more significant. Therefore, to be effectively driven by the DEA, it is suggested to select 0.025-mm PET or 0.1-mm paper for the YOS.

2) Parameters of the SOM: The performance analysis and experiments of the YOS have verified the motion and guided material selection. In this section, two experiments are designed to optimize the parameter of the SOM. First, 0.1-mm paper is chosen (for a larger force to recovery) to compare with the force generated by the SOM of different origami slice widths, 6, 10, and 12 mm. The result of force as the function of displacement is shown in Fig. 4(a). With the width of origami increasing, the max force generated by the SOM increases. In addition, the growth trend of the line for the 6-mm-width origami slice differs with 10 and 12 mm because the stiffness of the 6-mm-width origami slice is small, causing the origami slice to deform at the noncrease. Hence, a 10-mm-width origami slice is selected to conduct the following experiment. Second, another experiment is conducted for the

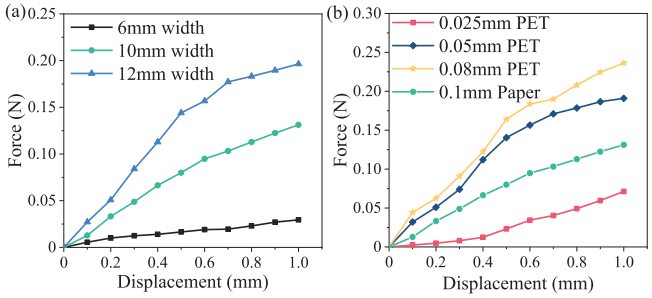


Fig. 4. (a) Relationship between the displacement and the force induced by the SOM made up of a 0.1-mm-thickness YOS and different origami slices, 6, 10, and 12 mm width. (b) Relationship between the displacement and the force induced by the SOM made up of a 10-mm-width origami slice and different YOSs, 0.025-, 0.05-, 0.08-mm-thickness PET, and 0.1-mm-thickness paper.

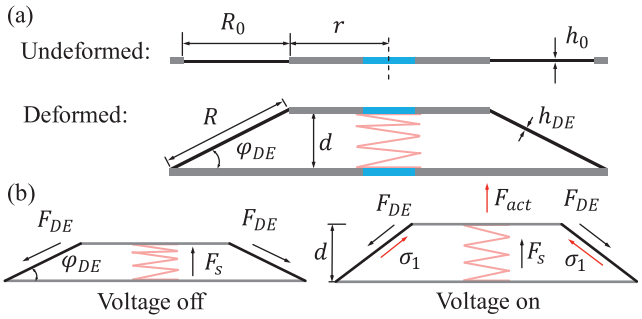


Fig. 5. (a) Parameters of the DEA in the undeformed and deformed states. (b) Force model of the DEA when voltage is OFF and ON.

performance comparison of the 0.025-, 0.05-, and 0.08-mm PET and 0.1-mm paper. The result shows that the force needed to push the SOM made up of 10-mm-width origami slices and 0.025-mm-thickness PET YOSs is the smallest, indicating that it is the optimal solution for the SOM.

E. Dielectric Elastomer Actuation

1) Modeling of DE Actuator: The truncated cone-shaped DEA characterizes its actuation in the out-of-plane direction, as shown in Fig. 5(a) [23]. The DEA will generate an axial force with the extension of spring and DE membrane when a voltage bias is applied to both sides of the DE membrane. In this study, a truncated cone-shaped DEA is optimized for adapting the dimension of the SOM and driving force of the tunable lens. The force generated by the DEA can be expressed as follows [see Fig. 5(b)]:

$$F_{\text{act}} = m\ddot{d} = F_s - F_{\text{DE}} \sin \varphi_{\text{DE}} - mg \tag{16}$$

where m is the mass of the spacer and d is the displacement of spacer. F_s is the force of the spring governed by Hooke's law: $F_s = k(l - d)$, where k is the stiffness of the spring and l is the length of the spring. φ_{DE} is the membrane deflection angle. F_{DE} is the force of the DE membrane, and $F_{\text{DE}} = 2\pi r(R_0 h_0/(d^2 + R_0^2)^{1/2})\sigma_1$, where r, R_0, and h_0 are the parameters of the DEA and σ_1 is the stress in the radial direction.

Authorized licensed use limited to: SHENZHEN UNIVERSITY. Downloaded on July 13,2022 at 09:10:46 UTC from IEEE Xplore. Restrictions apply.

To obtain σ_1, the Helmholtz free energy density function W of the DE membrane takes the form

$$W = -\frac{\mu J_m}{2}\ln\left(1 - \frac{\lambda_1^2 + \lambda_2^2 + \lambda_3^2 - 3}{J_m}\right) + \frac{D^2}{2\varepsilon_0\varepsilon_r} \quad (17)$$

where the first term denotes the elastic strain energy employing a Gent hyperelastic model [38] and the second term denotes the electric energy. μ is the shear modulus of the material and J_m is a material constant representing the limiting stretch. D is the electrical displacement, and λ_1, λ_2, and λ_3 represent the stretch in the radial, circumferential, and thickness directions, respectively. In this case, the DE membrane is prestretched $\lambda_{i,\text{pre}}$ during the manufacturing process and stretched by the spring of the actuator $\lambda_{i,\text{act}}$. Considering the incompressibility of the material, the product of the stretch must be constant and equal to one ($\lambda_1\lambda_2\lambda_3 = \lambda_{1,\text{pre}}\lambda_{2,\text{pre}}\lambda_{3,\text{pre}} = \lambda_{1,\text{act}}\lambda_{2,\text{act}}\lambda_{3,\text{act}} = 1$). It is assumed that the equal biaxial prestretch constant is C, resulting in that

$$\begin{cases} \lambda_1 = \lambda_{1,\text{pre}}\lambda_{1,\text{act}} = C\sqrt{1 + \left(\dfrac{d}{R_0}\right)^2} \\ \lambda_2 = \lambda_{2,\text{pre}}\lambda_{2,\text{act}} = C \\ \lambda_3 = \lambda_{3,\text{pre}}\lambda_{3,\text{act}} = \dfrac{h}{C^2 h_0}. \end{cases} \quad (18)$$

By substituting (18) into (17), W and the partial derivative concerning W can be expressed as

$$\begin{cases} W = -\dfrac{\mu J_m}{2}\ln\left(1 - \dfrac{\lambda_1^2 + C^2 + (C\lambda_1)^{-2} - 3}{J_m}\right) + \dfrac{D^2}{2\varepsilon_0\varepsilon_r} \\ \sigma_1 = \dfrac{\mu J_m\left[\lambda_1^2 - (C\lambda_1)^{-2}\right]}{J_m - \left[\lambda_1^2 + C^2 + (C\lambda_1)^{-2} - 3\right]} - \varepsilon_0\varepsilon_r\left(\dfrac{V}{h}\right)^2. \end{cases} \quad (19)$$

The expression of σ_1 indicates that the applied voltage can control the force generated by the DEA. Furthermore, the prestretch of the DE membrane and the choice of the biasing spring strongly affect the performance of the DEA.

2) Performance Verification of the DEA: To verify the modeling and performance of the DEA, an experiment about the displacement and force generated by the DEA under 0–3.5 kV is conducted. The fitted curves of measured force and the theory are shown in Fig. 6(e). The experimental result shows that the force becomes smaller than that in the model when the voltage exceeds 2.75 kV due to the voltage approaching the breakdown voltage of the DE membrane that causes mechanical instability. However, the max force of 0.27 N under 3.5 kV is enough to permit the DEA to drive the SOM. In general, the optimized actuator is satisfied for the tunable lens.

The deformation of the DE membrane is challenging to model due to its characteristic of a typical hyperelastic elastomer. To predict the displacement generated by the DEA, Ansys APDL is applied to simulate the deformation. Given a displacement boundary condition: fixing the outer ring of the annulus-shaped DE membrane, the inner ring is applied a ramped force for simulating F_s. The DE membrane achieves a 1.3-mm max displacement when the excitation is 0–3.5 kV.

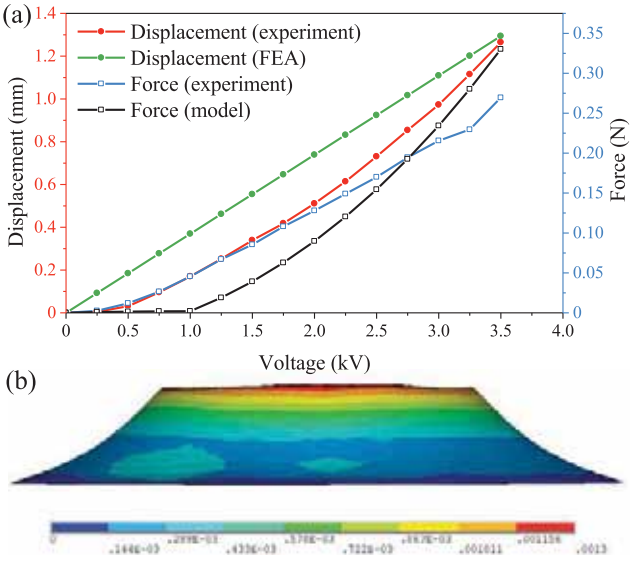


Fig. 6. (a) Force of measurement and modeling generated by the DEA under 0–3.5 kV and the displacement of measurement and FEA under 0–3.5 kV. (b) Deformation of the DEA in the out-of-plane direction in FEA.

TABLE I
PARAMETERS OPTIMIZED FOR THE DE ACTUATOR

Parameters	Symbol	Value	Unit
The stiffness of the spring	k	200	N/m
The length of the spring	l	15	mm
Thickness of the DE membrane	h_0	0.044	mm
The width of the DE ring	R_0	24.5	mm
Radius of the spacer	r	25.5	mm
Initial height of the DE actuator	d_0	11	mm
The ration of stretch	C	500	%

The other parameters of the DEA are shown in Table I. The max displacement of the experiment and simulation shows a good fit, and 1.3 mm is enough for the tunable lens.

III. RESULTS AND DISCUSSION

A. Fabrication of the Tunable Lens

The device consists of the DEA, the SOM, and the solid lens. The solid lens is composed of PDMS (Sylgard 184, Dow Corning, Midland, MI, USA), which is made up of prepolymer and curing agent with a weight ratio of 10:1. A high percentage of the prepolymer will make the lens more durable, though it increases the difficulty of actuation. After mixing for 10 min with an electric mixer, the mixture is poured into a stainless-steel mold whose shape is designed for the lens. Subsequently, the mixture cures at room temperature for 48 h, and an elastomeric lens is then obtained from the mold. For the fabrication of the SOM, the middle layer and the lower layer lamina are made of 0.1-mm paper, and the upper layer is 1-mm-thickness PLA by 3-D printing. A 0.08-mm PET cut by a laser cutting machine is made into four origami slices. As mentioned above, the YOS made of 0.025-mm PET connects the lower layer lamina with origami

Authorized licensed use limited to: SHENZHEN UNIVERSITY. Downloaded on July 13,2022 at 09:10:46 UTC from IEEE Xplore. Restrictions apply.

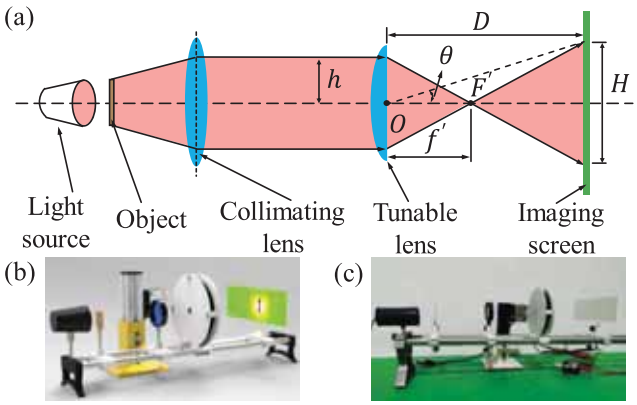


Fig. 7. (a) Schematic of the focal length measurement. (b) CAD model of the experiment platform. (c) Experimental setup for measuring the focal length of the device.

slices. They are then all bonded by solid gum or adhesive tape.

In this study, a common acrylic elastomer (3M VHB4910) is used as the DE membrane, and carbon grease is selected as a compliant electrode. The DE membrane is first prestretched biaxially with a ratio of 500% × 500%, for the equal biaxial stretch that can play to the performance of the DE maximally. Second, the conductive grease is smeared on the surface of the DE through a release paper mark using a soft brush. Third, the DE membrane with the compliant electrode is bonded to an annular PLA and biased by a spring. Finally, the SOM with the solid lens glued on and the DEA is assembled by four nylon bolts.

B. Experiment Setup of Focal Length Measurement

The principle of measuring the focal length applies the paraxial optics for the implementation efficiently and accurately, as shown in Fig. 7(a). Assuming that the lens's nodal point is coincident with its principal points and the angle in the image space equals the angle of incidence in the object space, the measured focal length of the tunable lens f' is

$$f' = \frac{h}{\tan\theta} \tag{20}$$

where h is the height of incident light and θ is the angle in the image space. By measuring the distance between the imaging screen and the tunable lens D and the height of the inverted image H on the imaging screen, the focal length of the tunable lens can be calculated. The computer-aided design (CAD) model and the experiment platform for focal length measurement are shown in Fig. 7(b) and (c), respectively. A light of object is considered a parallel light after a collimating lens. A laser sensor (Banner LM150) is used to record the different distances caused by the tunable lens that is actuated by 0–3.5 kV applied by a dc-HVdc converter (XP power G60).

C. Performance Verification of Tunable Lens

In Fig. 8(a), a curve is fitted through the measured points, which relates the measuring focal length with applied voltage.

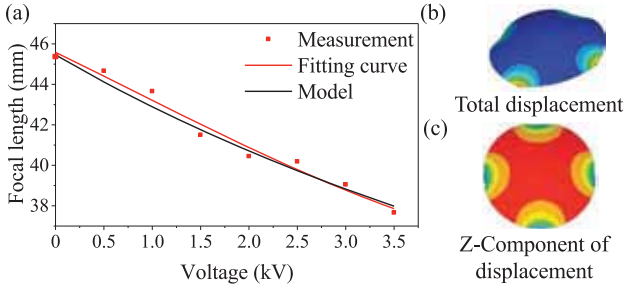


Fig. 8. (a) Focal length of experiment and model as a function of the voltage from 0 to 3.5 kV. (b) and (c) Deformation of the tunable lens in simulation.

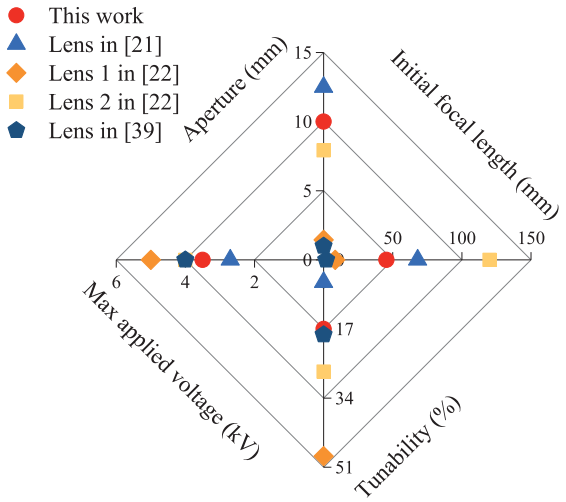


Fig. 9. Parameters of the size of the aperture, initial focal length, tunability, and max applied voltage in [21], [22], [39], and this work.

The experiment result shows a great degree fit compared with the model. In addition, the lens is simulated before the experiment to verify and monitor the surface deformation of the lens. The deformation of the total displacement of the lens mainly focuses on the area of force action, as shown in Fig. 8(b). Moreover, the center part of the lens's upper surface has a more considerable deformation in the Z-component [Fig. 8(c)]. However, only a slight deformation on the area of force action in the Z-component indicates that the bottom surface's deformation is primary in-plane contraction, which verifies the hypothesis in Section II. Compared with the tunable lenses previously proposed [15]–[22], the lens with a mathematic model in this work has the advantage of predictability for designing a suitable tuning range and applying it in different fields.

A comparison with other contraction-tunable lenses driven by the DEA is shown in Fig. 9, which lists four performance parameters, including the size of the aperture, initial focal length, tunability, and max applied voltage. The focal length of the 10-mm lens in this work varies from 45.4 mm at V = 0–37.7 mm at V = 3.5 kV, showing a 17% tunability. In [21], a 12.5-mm lens with 5.5% change (68–64 mm corresponding to 0–2.7 kV) is proposed to achieve variable focal length or astigmatism in the visible range. Besides, a monolithic focus-tunable lens technology enabled by DEA

Authorized licensed use limited to: SHENZHEN UNIVERSITY. Downloaded on July 13,2022 at 09:10:46 UTC from IEEE Xplore. Restrictions apply.

is presented in [22]. A 1.45-mm lens with 48.3% tunability under 0–5 kV and a 7.92-mm lens with 27.5% tunability (120–87 mm corresponding to 0–4 kV) are manufactured. In addition, a 1-mm lens [39] with 18.4% tunability under 0–4 kV is developed, realizing dynamic tunability and a reversible movement response. These lenses are designed for different aims, such as optimizing tunability and response for the previous lens, achieving defocus or astigmatism, and responding reversibly. Although the purpose of this work is not the optimization for a specific performance of the lens, the performance of the 10-mm lens has a large tunability at a relatively low voltage range compared to the lenses mentioned above. With the help of the origami structure model and the optimized DEA model, it is promising to design a suitable lens for different applications. Moreover, this solid lens provides a safer operation environment due to its high-voltage electrode hidden inside the origami structure. Therefore, with the advantage of predictability, safety, durability, and stability, the contraction-tunable lens is highly viable for different kinds of optical zoom systems.

D. Measurement Uncertainty of the Focal Length

For the total error of the laser sensor, the sources of uncertainty mainly include the repeatability of the sensor indications, the resolution of the laser sensor, and the linearity of the sensor.

First, the uncertainty component $u(\epsilon_{f1})$ caused by the repeatability of the sensor indications can be calculated as

$$u(\epsilon_{f1}) = 0.002 \text{ mm}. \tag{21}$$

Second, the uncertainty component $u(\epsilon_{f2})$ caused by the resolution of the laser sensor can be calculated as

$$u(\epsilon_{f2}) = \frac{0.004}{\sqrt{3}} = 0.002 \text{ mm}. \tag{22}$$

Third, the uncertainty component $u(\epsilon_{f3})$ caused by the linearity of the sensor can be calculated as

$$u(\epsilon_{f3}) = \frac{0.06}{\sqrt{3}} = 0.035 \text{ mm}. \tag{23}$$

The parameters are offered by the manufacturer's specification. Hence, the combined standard uncertainty $u(\epsilon_f)$ can be written as

$$u^2(\epsilon_f) = \left(\frac{\partial \epsilon_f}{\partial \epsilon_{f1}}\right)^2 u^2(\epsilon_{f1}) + \left(\frac{\partial \epsilon_f}{\partial \epsilon_{f2}}\right)^2 u^2(\epsilon_{f2}) + \left(\frac{\partial \epsilon_f}{\partial \epsilon_{f3}}\right)^2 u^2(\epsilon_{f3}). \tag{24}$$

The partial derivatives

$$\frac{\partial \epsilon_f}{\partial \epsilon_{f1}} = \frac{\partial \epsilon_f}{\partial \epsilon_{f2}} = \frac{\partial \epsilon_f}{\partial \epsilon_{f3}} = 1. \tag{25}$$

Accordingly, the standard uncertainty $u(\epsilon_f) = 0.035$ mm and the expanded uncertainty u_f (coverage factor, k, of 2) in the measurement can be estimated as follows:

$$u_f = ku(\epsilon_f) = 0.07 \text{ mm}. \tag{26}$$

IV. Conclusion

In this article, an SOM to improve the performance of a contraction-tunable lens driven by a truncated cone-shaped DEA is presented. The SOM consists of a three-layer laminate, four origami slices, and four Yoshimura-inspired origami structures. The functions of the origami slices and the YOSs are transforming the axial force of the DEA to radial force and enabling the mechanism to restore, respectively. A theoretical model is established using the virtual work principle and the spring in-series theory for origami structure to predict the deformation of the solid lens. A truncated cone-shaped DEA is optimized for adapting the SOM. In addition, based on FEA, simulations have proved the feasibility of the origami design, the DEA, and the deformation of the lens. The experiment result demonstrates that the 10-mm lens can tune the focal length from 45.4 to 37.7 mm under 0–3.5-kV voltage, which validates the origami structure and improves the performance of a large aperture contraction-tunable lens. With the characteristic of a mathematic model and a large aperture, the tunable solid lens has the potential to expand its application fields.

Future work will further focus on the miniaturization of the origami structure to adapt to more compact environments. Besides, an improved origami mechanism will enable different aperture lenses for focal length modulation.

References

[1] L. Eldada, "Optical communication components," *Rev. Sci. Instrum.*, vol. 75, no. 3, pp. 575–593, Mar. 2004.

[2] S. Kuiper and B. H. W. Hendriks, "Variable-focus liquid lens for miniature cameras," *Appl. Phys. Lett.*, vol. 85, no. 7, pp. 1128–1130, Aug. 2004.

[3] K. Xiong, S. Yang, X. Li, and D. Xing, "Autofocusing optical-resolution photoacoustic endoscopy," *Opt. Lett.*, vol. 43, no. 8, pp. 1846–1849, Apr. 2018.

[4] J. M. Jabbour *et al.*, "Optical axial scanning in confocal microscopy using an electrically tunable lens," *Biomed. Opt. Exp.*, vol. 5, no. 2, pp. 645–652, Feb. 2014.

[5] S. Pasinetti, I. Bodini, M. Lancini, F. Docchio, and G. Sansoni, "A depth from defocus measurement system using a liquid lens objective for extended depth range," *IEEE Trans. Instrum. Meas.*, vol. 66, no. 3, pp. 441–450, Mar. 2017.

[6] Y. Gong, D. Zhang, P. Shi, and J. Yan, "High-speed multispectral iris capture system design," *IEEE Trans. Instrum. Meas.*, vol. 61, no. 7, pp. 1966–1978, Jul. 2012.

[7] S. Sato, "Liquid-crystal lens-cells with variable focal length," *Jpn. J. Appl. Phys.*, vol. 18, pp. 1679–1684, Sep. 1979.

[8] J. Y. An, J. H. Hur, S. Kim, and J. H. Lee, "Spherically encapsulated variable liquid lens on coplanar electrodes," *IEEE Photon. Technol. Lett.*, vol. 23, no. 22, pp. 1703–1705, Nov. 15, 2011.

[9] D.-Y. Zhang, V. Lien, Y. Berdichevsky, J. Choi, and Y.-H. Lo, "Fluidic adaptive lens with high focal length tunability," *Appl. Phys. Lett.*, vol. 82, no. 19, pp. 3171–3172, May 2003.

[10] H. W. Seo *et al.*, "A tunable optical IRIS based on electromagnetic actuation for a high-performance mini/micro camera," in *Proc. IEEE Int. Conf. Micro Electro Mech. Syst.*, Jan. 2014, pp. 1147–1150.

[11] J. Li *et al.*, "A biomimetic soft lens controlled by electrooculographic signal," *Adv. Funct. Mater.*, vol. 29, no. 36, Sep. 2019, Art. no. 1903762.

[12] F. Carpi, G. Frediani, S. Turco, and D. De Rossi, "Bioinspired tunable lens with muscle-like electroactive elastomers," *Adv. Funct. Mater.*, vol. 21, no. 21, pp. 4152–4158, Nov. 2011.

[13] N. Hasan, A. Banerjee, H. Kim, and C. H. Mastrangelo, "Tunable-focus lens for adaptive eyeglasses," *Opt. Exp.*, vol. 25, no. 2, pp. 1221–1233, Jan. 2017.

[14] A. O. Ashtiani and H. Jiang, "Thermally actuated tunable liquid microlens with sub-second response time," *Appl. Phys. Lett.*, vol. 103, no. 11, Sep. 2013, Art. no. 111101.

Authorized licensed use limited to: SHENZHEN UNIVERSITY. Downloaded on July 13,2022 at 09:10:46 UTC from IEEE Xplore. Restrictions apply.

[15] J. W. Bae *et al.*, "High-performance PVC gel for adaptive micro-lenses with variable focal length," *Sci. Rep.*, vol. 7, no. 1, pp. 1–8, May 2017.
[16] P. Liebetraut, S. Petsch, J. Liebeskind, and H. Zappe, "Elastomeric lenses with tunable astigmatism," *Light, Sci. Appl.*, vol. 2, no. 9, p. e98, Sep. 2013.
[17] W. Wang, J. Fang, and K. Varahramyan, "Compact variable-focusing microlens with integrated thermal actuator and sensor," *IEEE Photon. Technol. Lett.*, vol. 17, no. 12, pp. 2643–2645, Nov. 21, 2005.
[18] S. Y. Lee, H. W. Tung, W. C. Chen, and W. Fang, "Thermal actuated solid tunable lens," *IEEE Photon. Technol. Lett.*, vol. 18, no. 21, pp. 2191–2193, Nov. 1, 2006.
[19] S. Nam *et al.*, "A robust soft lens for tunable camera application using dielectric elastomer actuators," *Soft Robot.*, vol. 5, no. 6, pp. 777–782, Dec. 2018.
[20] Y. Wang, P. Li, U. Gupta, J. Ouyang, and J. Zhu, "Tunable soft lens of large focal length change," *Soft Robot.*, 2021, doi: 10.1089/soro.2021.0036.
[21] M. Ghilardi, H. Boys, P. Török, J. J. C. Busfield, and F. Carpi, "Smart lenses with electrically tuneable astigmatism," *Sci. Rep.*, vol. 9, no. 1, pp. 1–10, Nov. 2019.
[22] B. J. Park *et al.*, "Monolithic focus-tunable lens technology enabled by disk-type dielectric-elastomer actuators," *Sci. Rep.*, vol. 10, no. 1, pp. 1–6, Oct. 2020.
[23] G. Rizzello, M. Hodgins, D. Naso, A. York, and S. Seelecke, "Modeling of the effects of the electrical dynamics on the electromechanical response of a deap circular actuator with a mass-spring load," *Smart Mater. Struct.*, vol. 24, no. 9, Aug. 2015, Art. no. 094003.
[24] D. Rus and M. T. Tolley, "Design, fabrication and control of origami robots," *Nature Rev. Mater.*, vol. 3, no. 6, pp. 101–112, Jun. 2018.
[25] S.-R. Kim, D.-Y. Lee, S.-J. Ahn, J.-S. Koh, and K.-J. Cho, "Morphing origami block for lightweight reconfigurable system," *IEEE Trans. Robot.*, vol. 37, no. 2, pp. 494–505, Apr. 2021.
[26] S. Mintchev, J. Shintake, and D. Floreano, "Bioinspired dual-stiffness origami," *Sci. Robot.*, vol. 3, no. 20, Jul. 2018, Art. no. eaau0275.
[27] H. Suzuki and R. J. Wood, "Origami-inspired miniature manipulator for teleoperated microsurgery," *Nature Mach. Intell.*, vol. 2, no. 8, pp. 437–446, Aug. 2020.
[28] W. Kim *et al.*, "Bioinspired dual-morphing stretchable origami," *Sci. Robot.*, vol. 4, no. 36, Nov. 2019.
[29] S. Seo, W. Park, D. Lee, and J. Bae, "Origami-structured actuating modules for upper limb support," *IEEE Robot. Autom. Lett.*, vol. 6, no. 3, pp. 5239–5246, Apr. 2021.
[30] S. G. Li *et al.*, "A vacuum-driven origami 'magic-ball' soft gripper," in *Proc. IEEE Int. Conf. Robot. Autom.*, May 2019, pp. 7401–7408.
[31] L. S. Novelino, Q. Ze, S. Wu, G. H. Paulino, and R. Zhao, "Untethered control of functional origami microrobots with distributed actuation," *Proc. Nat. Acad. Sci. USA*, vol. 117, no. 39, pp. 24096–24101, Sep. 2020.
[32] S. M. Felton, D. Y. Lee, K. J. Cho, and R. J. Wood, "A passive, origamiinspired, continuously variable transmission," in *Proc. IEEE Int. Conf. Robot. Autom.*, Jun. 2014, pp. 2913–2918.
[33] O. A. Bauchau and J. I. Craig, "Virtual work principles," in *Structural Analyis With Applications to Aerospace Structures*. New York, NY, USA: Springer, 2009, ch. 9.
[34] N. A. Pehrson, S. P. Magleby, L. L. Howell, and R. J. Lang, "Introduction of monolithic origami with thick-sheet materials," in *Proc. IASS Annu. Symp.*, Sep. 2016, pp. 1–10.
[35] J. M. Gere and B. J. Goodno, "Longitudinal strains in beams," in *Mechanics of Materials*, 7th ed. Boston, MA, USA: Cengage Learning, 2020, ch. 5, sec. 4, pp. 356–366.
[36] J. A. Faber, A. F. Arrieta, and A. R. Studart, "Bioinspired spring origami," *Science*, vol. 359, no. 6382, pp. 1381–1391. Mar. 2018.
[37] J. O. Jacobsen, G. Chen, L. L. Howell, and S. P. Magleby, "Lamina emergent torsional (LET) joint," *Mechanism Mach. Theory*, vol. 44, no. 11, pp. 2098–2109, Nov. 2009.
[38] A. N. Gent, "A new constitutive relation for rubber," *Rubber Chem. Technol.*, vol. 69, no. 1, pp. 59–61, Mar. 1996.
[39] S. Yun, S. Park, B. Park, S. Nam, S. K. Park, and K. Kyung, "A thin film active-lens with translational control for dynamically programmable optical zoom," *Appl. Phys. Lett.*, vol. 107, no. 8, Aug. 2015, Art. no. 081907.



Xuanchun Yin (Member, IEEE) received the B.S. degree in mechanical engineering from the Changchun University of Science and Technology, Changchun, China, in 2005, the M.S. degree in mechatronic engineering from South China Agricultural University, Guangzhou, China, in 2012, and the Ph.D. degree in intelligent mechanical systems engineering from Kagawa University, Takamatsu, Japan, in 2016.

He is currently an Associate Professor with the School of Engineering, South China Agricultural University. His research interests include haptics, human–robot interaction, teleoperation systems, artificial intelligence, bioinspired robotics, medical robotics, and agricultural robotics.



Pengyu Zhou received the B.S. degree in Electromechanical Engineering from the Zhongkai University of Agriculture and Engineering, Guangzhou, Guangdong, China, in 2019. He is currently pursuing the M.S. degree with the College of Engineering, South China Agricultural University, Guangzhou.

His research interests include the design and control of the origami robot, dielectric elastomer actuation, and soft grippers.



Sheng Wen received the Ph.D. degree in agricultural electrification and automation from South China Agricultural University, Guangzhou, China, in 2011.

He is currently an Associate Professor with the School of Engineering, South China Agricultural University. His research interests include agricultural artificial intelligence, haptics, human–robot interaction, and teleoperation.



Jiantao Zhang received the B.S., M.S., and Ph.D. degrees from South China Agricultural University, Guangzhou, China, in 2004, 2006, and 2011, respectively, all in agricultural electrification and automation.

He is currently an Associate Professor with the School of Mathematics and Informatics, South China Agricultural University. His research interests include agricultural artificial intelligence, haptics, teleoperated robotics systems, unmanned aerial vehicle (UAV), and precision agriculture.

Authorized licensed use limited to: SHENZHEN UNIVERSITY. Downloaded on July 13,2022 at 09:10:46 UTC from IEEE Xplore. Restrictions apply.

SCAULIB202405438

检索证明

根据委托人提供的论文材料，委托人华南农业大学数学与信息学院 张建桃 3 篇论文收录情况如下表。

序号	论文名称	发表刊物及发表的年月卷期/页码等	作者排名	论文等级	作者文中单位	收录情况	影响因子	中科院大类分区
1	Origami Improved Dielectric Elastomer Actuation for Tunable Lens	IEEE TRANSACTIONS ON INSTRUMENTATION AND MEASUREMENT 出版年：2022 卷期：71 页码：- 文献号：7502709 文献类型：Article	共同通讯作者（倒数第一）	A 类	华南农业大学	SCI	IF2-year=5.6 IF5-year=5.4 （2022）	工程技术 2 区 Top 期刊：否 （2022）
2	Single-rotor UAV flow field simulation using generative adversarial networks	COMPUTERS AND ELECTRONICS IN AGRICULTURE 出版年：2019 卷期：167 页码：- 文献号：105004 文献类型：Article	通讯作者	A 类	华南农业大学	SCI	IF2-year=3.858 IF5-year=4.008 （2019）	农林科学 2 区 Top 期刊：是 （2019）
3	FLUID-SOLID COUPLING AND EXPERIMENTAL REALIZATION OF A PIEZOELECTRIC ATOMIZER UNDER STANDING-WAVE RESONANCE	APPLIED ENGINEERING IN AGRICULTURE 出版年：2016 卷期：32 3 页码：327-340 文献号： 文献类型：Article	通讯作者	B 类	华南农业大学	SCI	IF2-year=0.505 IF5-year=0.667 （2016）	农林科学 4 区 Top 期刊：否 （2016）

华南农业大学图书馆SCAULIB202405438

3.6 Fluid-Solid Coupling and Experimental Realization of a Piezoelectric Atomizer under Standing-Wave Resonance

精选故事



庆祝技术创新：2024 年 AE50 奖项揭晓

週三，03 一月 2024

ASABE 和 Resource 杂志很高兴地宣布 2024 年 AE50 奖获奖者，以表彰公司及其在农业、食品和生物系统方面的技术发展。

查看全文

加入我们的倡议

Alliance for Modernizing African Agrifood Systems
ASABE

加速改善撒哈拉以南非洲粮食作物价值链的整体方法。 ***更多***

Circular Bioeconomy Systems Institute
ASABE

以独特的专业知识引领循环转型，使我们能够跨系统构建。 ***更多***

2024年选举结果

成员投票选举民选职位，修改宪法



雪莉·亨特（Sherry Hunt），2024-2025年当选总统

结果

资源杂志



阅读最新一期

Authors, please use the Guide for Authors when creating your articles.

Public Access Information
= Public Access (PA)
= PA Limited Time
= Open Access
= Contact Us For Purchase

Applied Engineering in Agriculture

Vol. 32 No.3 Return to Issues Return to Publications Included

INFORMATION TECHNOLOGY, SENSORS, & CONTROL SYSTEMS

Modeling and Model Validation of a Chemical Injection Sprayer System

Citation: Applied Engineering in Agriculture. 32(3): 285-297 . (doi: 10.13031/aea.32.10606) @2016
Authors: Kleber Romero Felizardo, Heitor Vinicius Mercaldi, Paulo Estevão Cruvinel, Vilma Alves Oliveira, Brian L Steward
(Free Abstract) (Download PDF) (Export to EndNotes)

MACHINERY SYSTEMS

Review of Robotic Technology for Strawberry Production

Citation: Applied Engineering in Agriculture. 32(3): 301-318. (doi: 10.13031/aea.32.11318) @2016
Authors: Sinem Gozde Defterli, Yeyin - Shi, Yunjun - Xu, Reza - Ehsani
(Free Abstract) (Download PDF) (Export to EndNotes)

Calibration Procedure for Fuel Flow Meters at the Nebraska Tractor Test Lab

Citation: Applied Engineering in Agriculture. 32(3): 319-326. (doi: 10.13031/aea.32.11436) @2016
Authors: Michael F. Kocher, Matthew Thomas Wold, Roger M. Hoy, Austin H. Lammers, Erin E. Blankenship
(Free Abstract) (Download PDF) (Export to EndNotes)

Fluid-Solid Coupling and Experimental Realization of a Piezoelectric Atomizer under Standing-Wave Resonance

Citation: Applied Engineering in Agriculture. 32(3): 327-340. (doi: 10.13031/aea.32.11392) @2016
Authors: Sheng Wen, Jiantao Zhang, Yubin Lan, Zhihua Ning, Shenghua Li, Dingxin Jiang, Hang Xing
(Free Abstract) (Download PDF) (Export to EndNotes)

Effects of Sprayer Boom Height and Operating Pressure on the Spray Uniformity and Distribution Model Development

Citation: Applied Engineering in Agriculture. 32(3): 341-346. (doi: 10.13031/aea.32.11376) @2016
Authors: Vladimir V Vilacki, Aleksandar D Sedlar, Emilio Gil, Rajko M Bugarin, Jan J Turan, Todor V Janic, Patrik Burg
(Free Abstract) (Download PDF) (Export to EndNotes)

Performance of Variable-Orifice Nozzles for Liquid Fertilizer Applications

Citation: Applied Engineering in Agriculture. 32(3): 347-352. (doi: 10.13031/aea.32.11428) @2016
Authors: John P Fulton, Randal K Taylor, Ajay Sharda
(Free Abstract) (Download PDF) (Export to EndNotes)

The Effect of New Wings on Subsoiler Performance

Citation: Applied Engineering in Agriculture. 32(3): 353-362. (doi: 10.13031/aea.32.11500) @2013
Authors: Mohammad Askari, Gholamhossein Shahgholi, Yousef Abbaspour-Gilandeh, Hoseinali Tash-Shamsabadi
(Free Abstract) (Download PDF) (Export to EndNotes)

NATURAL RESOURCES & ENVIRONMENTAL SYSTEMS

Effects of Arkansas Cotton Production Systems on Soil Strength

搜索

FLUID-SOLID COUPLING AND EXPERIMENTAL REALIZATION OF A PIEZOELECTRIC ATOMIZER UNDER STANDING-WAVE RESONANCE

S. Wen, J. Zhang, Y. Lan, Z. Ning, S. Li, D. Jiang, H. Xing

ABSTRACT. *This article introduces the design and analysis of a piezoelectric atomizer based on the principles of standing-wave resonance and a pressure-swirl nozzle. Experiments are conducted to demonstrate that the developed piezoelectric atomizer can produce uniformly sized liquid droplets. The atomizer uses piezoelectric composite plates to acquire a large displacement from the vibration of Pb(Zr, Ti)O_3 (PZT) ceramic and to exert excess pressure on the liquid using standing-wave resonance. The three-dimensional dynamic characteristics of the piezoelectric composite plates, considering the effect of the fluid-solid interface, are determined. An analysis of the fluid-solid coupling between the fluid in the resonance chamber and the vibration of the piezoelectric composite plates is conducted. The Sauter mean diameter (SMD) values of the ejected droplets and the flow rate of the piezoelectric atomizer are measured experimentally as different driving voltages. The experimental results demonstrate that the atomizer is capable of generating droplets with an SMD of 93.5 μm at a flow rate of 18.4 g/s. Relatively uniform droplets are formed below the ligaments, where the cone swirl sheet is fully developed. The piezoelectric atomizer has the potential for use in industrial and agricultural applications.*

Keywords. *Fluid-solid coupling, Piezoelectric atomizer, Pressure-swirl nozzle, Spray characteristics, Standing-wave resonance.*

Spray atomization is a common liquid delivery method used in industrial and agricultural production. The primary objective of liquid atomization is to transform a bulk liquid into drops in a gaseous atmosphere such that the maximum surface-to-volume ratio is achieved. A higher surface-to-volume contact ratio can increase the contact area between the droplets and the ambient air and thereby achieve better atomization. There are many types of atomizers in engineering and agricultural applications, such as pressure atomizers (Basak et al., 2013) and air blast atomizers (Herrero et al., 2007). In recent years, the PZT (Pb(Zr, Ti)O_3)-driven atomizer has received increasing attention because it can provide a mist-like spray with a particularly narrow droplet size distribution and very low spray velocity (Topp et al., 1972; Jeng et al., 2007; Ho et al., 2008).The PZT-driven atomizer can be more energy efficient than conventional atomization because of its lack of moving parts, as it requires only that electrical energy be transmitted to a piezoelectric vibrator. The process of PZT-driven atomization is the ejection of tiny droplets from a liquid film formed on an ultrasonically vibrating surface. There are two major hypotheses that explain the ejection of droplets from a vibrating surface: the capillary wave hypothesis and the cavitation hypothesis (Rajan et al., 2001; Avvaru et al., 2006). The capillary wave hypothesis is the formation of capillary waves composed of crests and troughs on the vibrating surface, with the droplets ejected from the crests when the amplitude of the ultrasound is greater than the threshold value. The cavitation hypothesis is generally applied to liquid disintegration in high-frequency and high-intensity ultrasonic systems. When a liquid film is sonicated, cavitation bubbles are formed. The collapse of these bubbles, especially near the surface, results in the direct ejection of the droplets. PZT-driven atomization is a very effective way of generating small droplets. Donnelly et al. (2004) used PZT-driven atomization to produce a high-density and relatively monodisperse aerosol of water droplets (with an average droplet diameter of approximately 2 μm). These droplets

Submitted for review in June 2015 as manuscript number MS 11392; approved for publication by the Machinery Systems Community of ASABE in November 2015.

The authors are **Sheng Wen,** University Associate Professor, College of Engineering, South China Agricultural University, Guangzhou 510642, China, and International Lab of Agricultural Aviation Pesticide Spraying Technology, Guangzhou 510642, China; **Jiantao Zhang,** University Associate Professor College of Mathematics and Informatics, South China Agricultural University, Guangzhou 510642, China; **Yubin Lan, ASABE Member,** University Professor College of Engineering, South China Agricultural University, Guangzhou 510642, China, and International Lab of Agricultural Aviation Pesticide Spraying Technology, Guangzhou 510642, China; **Zhihua Ning,** University Associate Professor, College of Science and Engineering, Jinan University, Guangzhou 510632, China; **Shenghua Li,** Graduate Student, College of Engineering, South China Agricultural University, Guangzhou 510642, China; **Dingxin Jiang,** University Associate Professor, College of Resources and Environment, South China Agricultural University, Guangzhou 510642, China; **Hang Xing,** University Associate Professor, College of Engineering, South China Agricultural University, Guangzhou 510642, China, and International Lab of Agricultural Aviation Pesticide Spraying Technology, Guangzhou 510642, China. **Corresponding author:** Jiantao Zhang, College of Mathematics and Informatics, South China Agricultural University, Guangzhou 510642, China; phone: 86-130-7675-9646; e-mail: zhangjt@scau.edu.cn.

 © 2016 American Society of Agricultural and Biological Engineers ISSN 0883-8542 DOI 10.13031/aea.32.11392

are generated by driving the fluid harmonically in the MHz frequency range. Jeng et al. (2009) developed a PZT-driven atomizer based on a flexible membrane and a micro-machined trumpet-shaped nozzle array. The atomizer is capable of generating droplets with a Sauter mean diameter (SMD) of 4.6 μm at a flow rate of 2.5 g/min. Although high-frequency PZT-driven atomizers can achieve a small particle size, the use of an air pump to expel the atomized particles increases the power consumption of the device. Especially when used for crops, the smaller droplet diameter makes it prone to spray drift, causing serious environmental problems.

On the fluids side, in addition to the damping effects, the surrounding liquid exerts a reaction force characterized as the added mass, which plays an important role in the dynamic analysis of the piezoelectric structure (Kramer et al., 2013). A number of papers have been published in recent years that investigated the added mass effects of the interacting fluids in macro and micro structures (Jeong et al., 2003; Esmailzadeh et al., 2008; Askari et al., 2010). Although several methods for considering the fluid inertial effect have been developed, the solid structure is mainly considered an isotropic material, such as a metal or metallic alloy. For anisotropic piezoelectric structures, which generally have a lower effective density than metallic structures, the added mass effect of water should be analyzed also. Furthermore, because of the piezoelectric effect, the fluid-solid coupling analysis of the piezoelectric composite structure is more intricate. Therefore, the fluid-solid coupling of the piezoelectric structure, especially the need to consider the piezoelectric effect, should be researched further.

The objectives of this study were:

(1) to design a piezoelectric atomizer based on the principles of standing wave and a pressure-swirl nozzle. In this design scheme, the piezoelectric atomizer can produce uniformly-sized liquid droplets without an additional air pump, which will also be verified by experiments;
(2) to develop a numerical model to investigate the fluid-solid-electric coupling of the piezoelectric atomizer; and
(3) to test the atomization characteristics of the Sauter mean diameter and flow rate by experiments.

In this article, the principle of a piezoelectric atomizer understanding-wave resonance is demonstrated in Section II. The flow-field analysis of the piezoelectric composite plates based on the finite element method, considering the piezoelectric effect, is performed in Section III. The fluid-solid coupling of the standing-wave resonance chamber is developed in Section IV. The analysis of the two-phase flow in the pressure-swirl nozzle is described in Section V. Finally, the continuous spraying experiment using the piezoelectric atomizer is demonstrated.

Design and Fabrication of Atomizer

Design Concepts of Current Atomizer

To generating appropriate droplets with a simplified structure, a novel piezoelectric atomizer is designed based on vibrating piezoelectric composite plates and the principle of standing-wave resonance. Figure 1 presents a schematic illustration of the piezoelectric atomizer. It shows that the device comprises six major components, namely, the piezoelectric composite plates, a standing-wave resonance chamber, a one-way valve as the inlet, a one-way valve as the outlet, and a swirl spool in the swirl chamber.

Principle of Operation

The piezoelectric atomizer shown in figure 1 operates on the direct rectification of a standing pressure wave inside a resonance chamber filled with fluid. The vibration amplitude of the piezoelectric composite plates produces an oscillating flow that may cause the chamber volume to change slightly. As the vibration direction of the piezoelectric composite plates moves outward to increase the chamber volume as shown in figure 2a, the pressure inside the chamber decreases. The inflow enters the chamber based on the pressure difference between the resonance chamber and the outside atmosphere, while the one-way inlet open and the one-way outlet closed. As the vibration direction of the piezoelectric composite plates moves inward, decreasing the chamber volume, as shown in figure 2b, the pressure inside the chamber increases. Partial fluid flows from the outlet close the inlet and open the one-way outlet. With the piezoelectric composite plates at higher frequency, the fluid in the chamber also produces oscillation. Eventually, the motion of the piezoelectric structure causes the fluid to form a standing-wave oscillation into the chamber. According to wave propagation theory (Lighthill, 2001), when the wavelength is a proper divisor of $2L$ (L is the length of the chamber), the fluid oscillation in the chamber will be in the situation of standing-wave resonance. In fluid resonance, the standing pressure wave increases significantly, and pressure fluctuations are obtained as follows (Lighthill, 2001):

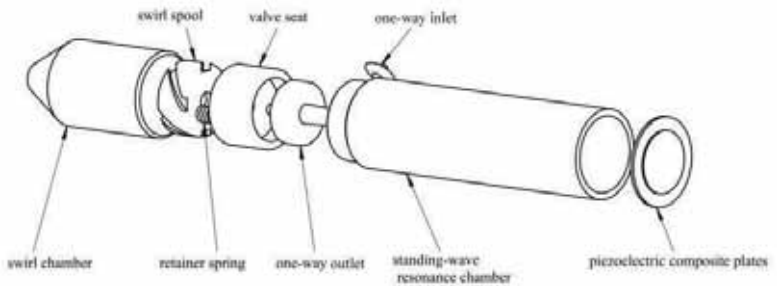


Figure 1. Schematic illustration of piezoelectric atomizer.

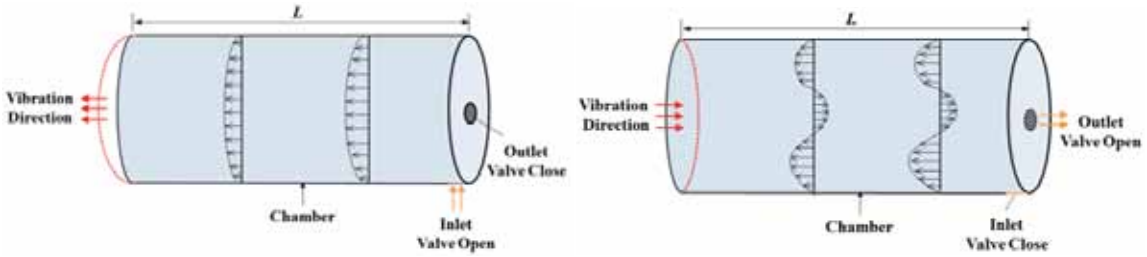


Figure 2. Working principle of resonance chamber.

$$\delta P = \rho_l c u \tag{1}$$

The pressure fluid flows from the outlet and generates a spiral movement through the swirl slots of the pressure-swirl nozzle. Eventually, the pressure fluid forms a rotating flow inside the swirl chamber. The swirling liquid pushes against the walls of the swirl chamber and develops a hollow air core. As this rotating flow exits the axial orifice, an unstable conical swirling sheet is formed that breaks up into ligaments and droplets. The transition from the internal injector flow to a fully developed spray can be divided into three steps: film formation, sheet breakup, and atomization.

Fluid-Solid Coupling of the Piezoelectric Composite Plates

Governing Equations

A piezoelectric structure submerged in a dense fluid changes its natural frequencies in comparison with those in a vacuum due to fluid-structure interaction (FSI). This change is significant when the fluid density is on the order of the structure density. FSI has been the subject of intense research, and various theories have been developed to study the wide array of problems that are of interest. Among these methods, a commonly accepted formulation is outlined in Zienkiewicz (1978). The basic idea is to use a coupled equation that uses the pressure in the fluid domain and the structural displacement as the working variables. According to the theory, when an alternating electric field is exerted on the piezoelectric composite plates, the governing equation of the transverse deflection can be expressed as:

$$\nabla^2\nabla^2 w_c + \frac{\rho_c h}{D_c}\frac{\partial^2 w_c}{\partial t^2} = \frac{f_c - P_l}{D_c} \tag{2}$$

where

$$D_c = Eh^3 / \left[12\left(1-\nu^2\right)\right] \tag{3}$$

In our study, assuming incompressibility and inviscidity, the fluid movement can be described by the Navier-Stokes equations 4 and the mass continuity equation 5:

$$\rho_l \frac{d\vec{V}}{dt} = \rho_l g + \mu\nabla^2\vec{V} - \nabla P_l \tag{4}$$

$$\frac{\partial \rho_l}{\partial t} + (\vec{V}\cdot\nabla)\rho_l = 0 \tag{5}$$

The edge of the piezoelectric composite plates is bonded with the resonance chamber; it can be considered as a clamped boundary condition. Thus the boundary conditions are:

$$w_c\,|_{r=\phi_1} = 0\,,\ \frac{\partial w_c}{\partial r}|_{r=\phi_1} = 0 \tag{6}$$

The movements of the piezoelectric composite plates and the fluid pressure of the working fluid are coupled, which are represented by the dynamic pressure P_l.

The actuating force f_c can be deduced from the coupled electro-mechanical constitutive equation as:

$$T_h = c_{hk}^D S_k - h_{jh} D_j \tag{7}$$

$$h,k = 1,2,\cdots,6 \text{ and } j = 1,2,3$$

Numerical Simulation

It is notably difficult to solve these governing equations analytically. Hence, numerical simulations are commonly used to predict the natural frequencies and mode shapes of a piezoelectric structure (Kozień et al., 2011; Galchev et al., 2012; Pérez et al., 2014). To solve the governing equations numerically, the finite element method (FEM) is applied to predict the performance of the piezoelectric composite plates. In this work, the ANSYS® parametric design language (APDL) is used to determine the dynamic characteristics of the piezoelectric composite plates, e.g., the natural frequencies and the mode shapes in air and in water. The selection of the piezoelectric composite plates is shown in figure 3. A circular PZT-4 piezoelectric element

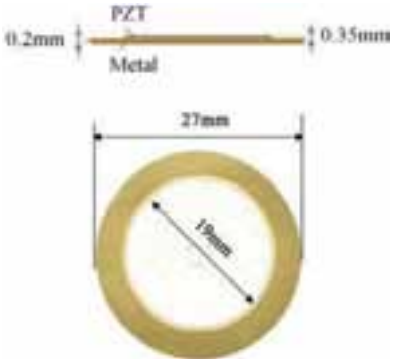
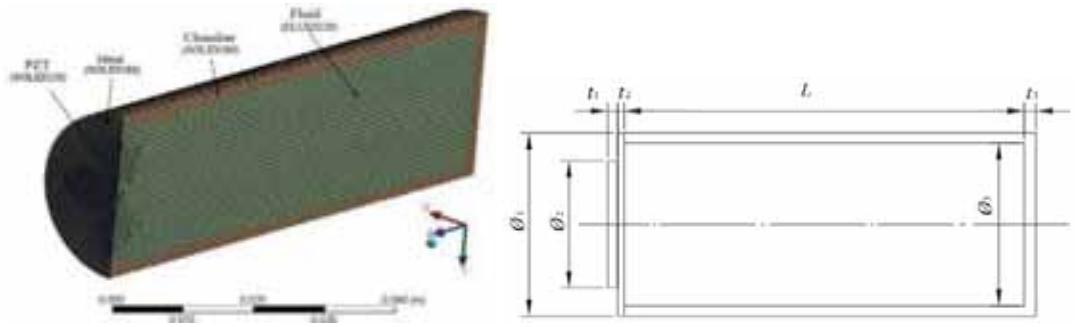


Figure 3. Geometry of the piezoelectric composite plates.



(a) (b)

Figure 4. Finite element mesh and geometry of the three-dimensional model.

is glued on a 0.2 mm thick brass sheet that is attached to the end of the standing-wave resonance chamber (see fig. 1). These piezoelectric elements are light, inexpensive, and convenient to use in experiments.

To evaluate the dynamic characteristics of the piezoelectric composite plates, a symmetrical three-dimensional finite element model, including the piezoelectric composite plates, the standing-wave resonance chamber, and the working fluid, is used for coupled-field analysis. As the one-way outlet is closed in the phase of the inflow, the fluid in the pressure-swirl nozzle has little effect on the inner flow field of the resonance chamber. The pressure-swirl nozzle will be ignored in the subsequent analysis of fluid-solid coupling. In this section, two fluid media are analyzed, air and water, defined as dry and wet configurations. In the dry case, the air is assumed to have a negligible effect that is ignored. Figure 4 illustrates the FE mesh and the geometry, with sizes of $\phi_1 = 27$ mm, $\phi_2 = 19$ mm, $\phi_3 = 23$ mm, $t_1 = 0.35$ mm, $t_2 = 0.2$ mm, $t_3 = 2$ mm, and $L = 75$ mm. The FE mesh consists of two major parts: the solid domain and the fluid domain. The solid domain consists of the piezoelectric composite plates and the resonance chamber, which is made of Plexiglas. The material properties are listed in table 1. In the dry analysis, the fluid domain is not included in the FE mesh.

A flowchart of the fluid-solid coupling between the piezoelectric structure and the working fluid is given in figure 5. The working fluid used in the study is water, and the properties used for the numerical computation are shown in table 2. The commercial finite element (FE) software ANSYS® (ANSYS Inc., Canonsburg, Pa.) is used

Table 1. Material properties for finite element analysis (Daniels et al., 2013).

	PZT	Brass	Plexiglas
Density (kg/m^3)	7500	8300	1200
Young's modulus (GPa)	--	110	20
Poisson's ratio	--	0.34	0.25
Elastic constant (GPa)	c_{11}=119.0 c_{12}=57.9 c_{13}=56.0 c_{33}=110.0 c_{44}=30.5 c_{66}=30.4	--	--
Piezoelectric constant (C/m^2)	e_{31}=5.6 e_{33}=11.3 e_{15}=7.6	--	--
Dielectric constant	ε_{33} =100	--	--

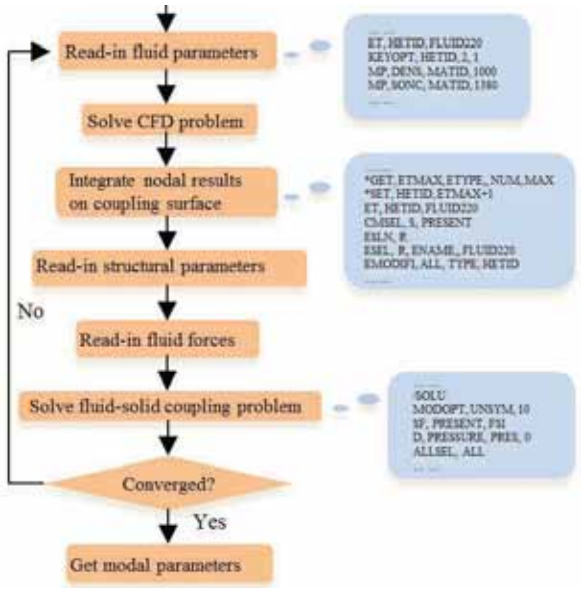


Figure 5. Flow chart of fluid-solid coupling.

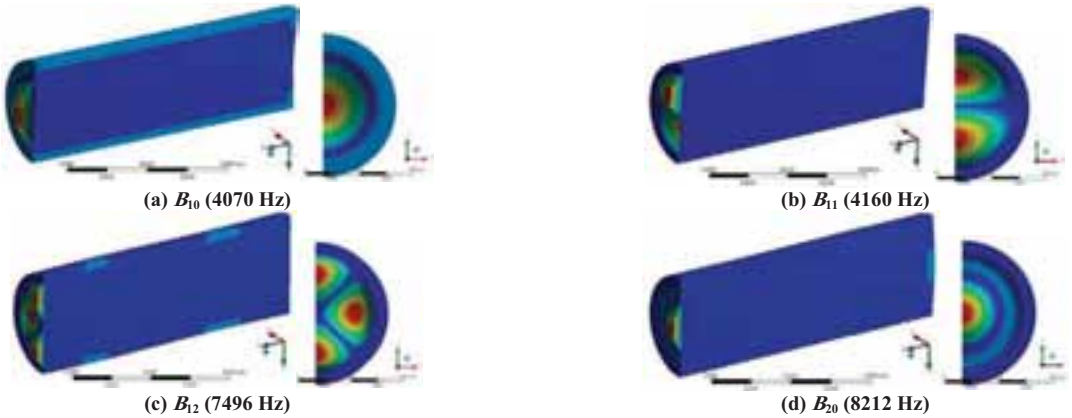
to validate the fluid-solid coupling model in this work. In the process of numerical simulation, the FSI is modeled by coupling an acoustic fluid domain to the fluid-solid coupling surface of the piezoelectric composite plates. 41,108 three-dimensional fluid elements and 16,655 solid elements are used in the ANSYS® FE simulations. The sound pressure (eq. 8) is adopted for the fluid-solid coupling problem, in which the working liquid is treated as an ideal fluid (incompressible and non-viscous):

$$\frac{\partial^2 p_f}{\partial t^2} = c_f{}^2 \nabla^2 p_f \tag{8}$$

The first four in-water (wet) natural frequencies and mode shapes of the piezoelectric composite plates, which are attached to the chamber of the coupled fluid, are shown in figure 6. The natural frequencies of the symmetrical

Table 2. Properties of the working fluid (water).

Properties	Value
Density (ρ_f)	1000 (kg/m^3)
Bulk modulus (B_f)	2.2 (GPa)
Viscosity (μ)	1×10^{-3} (Pa · s)
Sound speed in fluid (c_f)	1380 (m/s)



(a) B_{10} (4070 Hz) (b) B_{11} (4160 Hz)

(c) B_{12} (7496 Hz) (d) B_{20} (8212 Hz)

Figure 6. Mode shapes of the piezoelectric composite plates in water (wet mode).

vibration modes corresponding to the B_{11} and B_{12} modes are found at 4160 and 7496 Hz, while those of asymmetrical vibration modes are at 4070 and 8212 Hz for the B_{10} and B_{20} modes, respectively. In the modal shapes B_{mn}, m is equal to the number of the nodal circle, and n is the number of the nodal diameter. Compared with other mode shapes, the B_{10} mode can provide the volume of the resonance chamber with a greater variation and can obtain better energy conversion efficiency; therefore, it is generally used as the working mode of the piezoelectric atomizer.

By comparison, the in-air (dry) natural frequencies and mode shapes of the piezoelectric composite plates are shown in figure 7. The comparison of the coupled system with the non-coupled system is given in table 3. It is noted that the mode shapes of the diaphragm of the coupled system are almost the same as the counterparts in the non-coupled system. The numerical results also indicate that the natural frequencies of the fluid-solid coupling system are lower than those of the non-coupled system, because of the interaction between the piezoelectric structure and the working fluid.

Flow-Field Analysis of the Resonance Chamber

Background

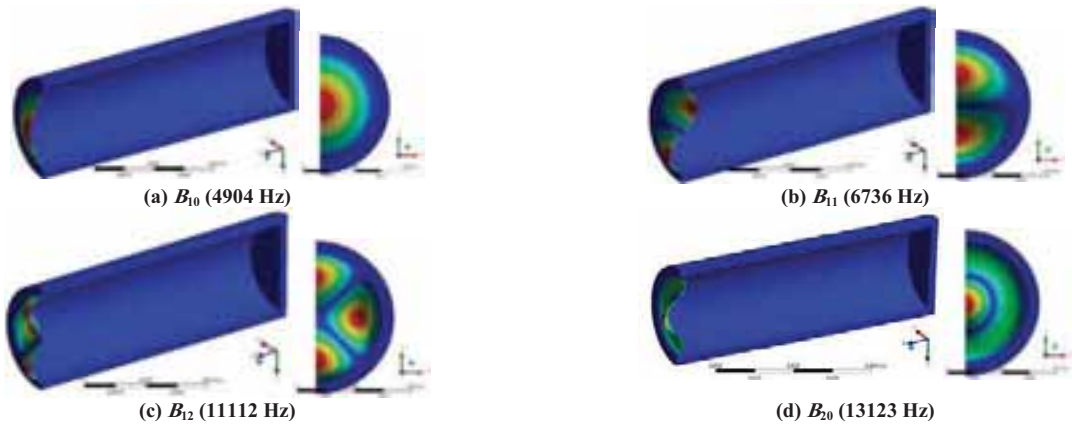
This section is mainly concerned with the unsteady fluid dynamic processes occurring in the resonance chamber and the interactions between the solid and fluid elements. In theory, at standing-wave resonance, the pressure of the fluid inside the chamber can produce a large enhancement. The excess pressure (δP), for undamped pressure waves, is given in equation 1.

According to wave propagation theory (Koveos et al., 2013), the wave celerity in an inviscid fluid is:

$$c = \sqrt{\frac{B}{\rho_l}} \tag{9}$$

Table 3. Comparisons of natural frequencies and mode shapes.

		Natural Frequency /Hz	
Mode	Mode Type	Dry Mode (in air)	Wet Mode (in water)
1	B_{10}	4904	4070
2	B_{11}	6736	4160
3	B_{12}	11112	7496
4	B_{20}	13123	8212



(a) B_{10} (4904 Hz) (b) B_{11} (6736 Hz)

(c) B_{12} (11112 Hz) (d) B_{20} (13123 Hz)

Figure 7. Mode shapes of the piezoelectric composite plates in air (dry mode).

The corresponding wavelength (λ) is:

$$\lambda = \frac{c}{f} \tag{10}$$

To form a standing wave, the condition to hold for a closed chamber of length (L) should be

$$L = k\frac{\lambda}{4} \tag{11}$$

where k = 1, 2,.... from equations 9 to 11, the standing-wave resonance frequency (f_r) is:

$$f_r = \frac{c}{4L} = \frac{1}{4L}\sqrt{\frac{B}{\rho_l}} \tag{12}$$

The fluid oscillation within the chamber is caused by the vibration of the piezoelectric composite plates. Therefore, the vibration frequency of the piezoelectric composite plates should be same as the standing-wave resonance frequency (f_r) in equation 12. Using the wet mode numerical method of piezoelectric composite plates in Section III, combined with equation 12, the length (L) of the standing-wave resonant chamber can be obtained (fig. 8). The dash-dotted curve represents different standing-wave resonant frequencies corresponding to the different lengths (L) of the chamber, based on equation 12. The solid curve with triangles represents different wet mode frequencies of the piezoelectric composite plates corresponding to different lengths (L) of the chamber, as obtained by the FE numerical method in Section III. The wet mode frequency of the piezoelectric composite plates decreases gradually with the increase of chamber length (L), as shown in figure 8. This is because the mass and viscous damping of the fluid increase as the length of the chamber (L) increases, causing the wet mode frequency of the piezoelectric composite plates to decrease (Rodriguez et al., 2012). It can be concluded that the standing-wave resonance frequency of the chamber equal to the wet mode frequency of the piezoelectric composite plates is 1995 Hz, as the resonance chamber has a length of 185 mm. This finding also means that a standing-wave resonance can be produced at the B_{10} mode shape when the length of the resonance chamber (L) is 185 mm. At this time, the vibration frequency of the piezoelectric composite plates coupled with the working fluid is 1995 Hz.

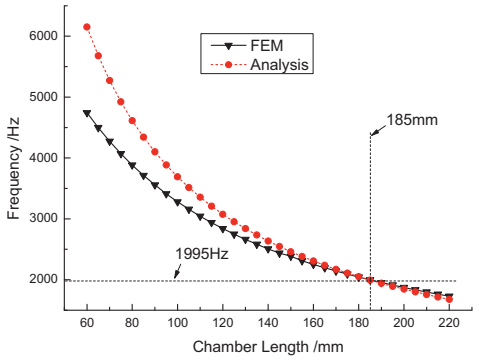


Figure 8. Relation curve between the chamber length and the frequency.

Fluid-Solid Coupling of the Resonance Chamber

In the present work, a numerical model was built using the commercial CFD (computer fluid dynamics) code FLUENT® (ANSYS Inc., Canonsburg, Pa.) to obtain the flow and concentration characteristics. The CFD modeling involves the numerical solution of the unsteady Navier-stokes conservation equations for mass, momentum, and energy based on a finite volume technique (Payri et al., 2005). As explained before, the piezoelectric composite plates were appended to the bottom of the resonance chamber. The transverse vibration of the piezoelectric composite plates, which is excited by an alternating electric field, changes in volume within the resonance chamber. With the periodic vibration of the piezoelectric structure, the fluid in the chamber also produces oscillation. Finally, the fluid motion is turned to form a standing-wave resonance in the chamber. The maximum displacement curve of the piezoelectric composite plates, which is directly obtained from the transient finite element analysis, is shown in figure 9 for the case of a 1995 Hz sinusoidal signal of 200 V peak-to-peak voltage applied on the electrode surface of the piezoelectric ceramics. The fitting curve is drawn according to equation 13:

$$y_1 = y_0 + A\sin(\pi\frac{x - x_c}{w_0}) \tag{13}$$

where

$$\begin{cases} y_0 = 5.77\times10^{-5} \\ A = 6.7\times10^{-5} \\ x_c = 0.00753 \\ w_0 = 0.021 \end{cases} \tag{14}$$

To accurately simulate the periodic vibration of the piezoelectric composite plates, the Spring-Based Smoothing Method among the Dynamic Mesh Methods provided by FLUENT® was used, together with the User-Defined Function (UDF), and the flow chart is given in figure 10. A user-defined function is linked to the main program, and a dynamic mesh is selected to determine the vibration as displacements in the UDF. The equation of movement is defined as:

$$y(x,t) = y_1 \cdot sin\left(2\pi\times f_p \times t\right) \tag{15}$$

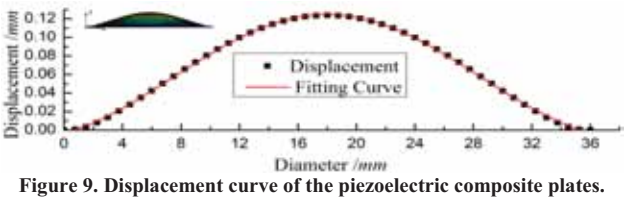


Figure 9. Displacement curve of the piezoelectric composite plates.



Figure 10. Analytical diagram of the resonance chamber.

where f_p=1995 Hz is the vibration frequency of the piezoelectric composite plates. Using the UDF program, FLUENT® can traverse boundary nodes and control the node displacements in the boundary dynamic domain. Finally, the periodic transverse vibration of the piezoelectric composite plates can be simulated, and the effect of the fluid-solid coupling can be realized.

Results of Fluid-Solid Coupling

To research the characteristics of the fluid flow in the resonance chamber, the mesh model used in this numerical analysis is presented in figure 11. In the entire computational domain, approximately 21,082 grids are used for the resonance chamber. Three monitoring points P_1, P_2, and P_3 are arranged to monitor the fluid dynamics of the flow field. The boundary conditions for the import and export are the pressure inlet and pressure outlet, respectively. The convergence criteria are supposed to be 10^{-5} for all predicted parameters. The SIMPLEC pressure-velocity coupling algorithm and the second-order upwind discretization scheme for momentum are utilized.

Figure 12 illustrates the pressure distribution and streamline diagram at the phase of the inflow. As the vibration direction of the piezoelectric composite plates moves outward, the volume of the resonance chamber increases while the pressure inside the chamber decreases. The fluid flows into the resonance chamber through the one-way valve at the inlet. Figure 13 describes the pressure distribution and streamline diagram at the phase of the outflow. When the piezoelectric composite plates move inward, the pressure inside the chamber rises, and then the fluid in the chamber is discharged outside through a one-way valve on the outlet. Hence, continuous fluid output can be achieved by using the periodic vibration of the composite piezoelectric plates.

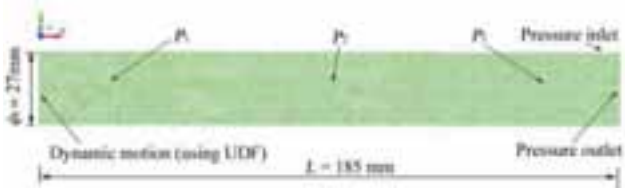


Figure 11. Mesh model of resonance chamber.

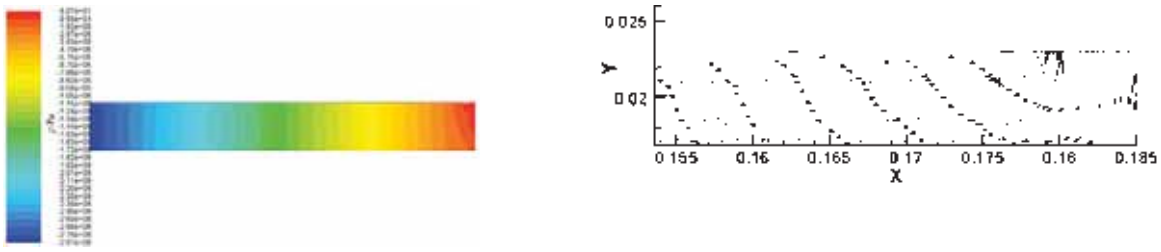
The pressure curves of the monitoring points (P_1, P_2, and P_3) are presented in figure 14a. With the change in volume of the resonance chamber, the flow-field pressure varies periodically. At the phase of the outflow, the flow-field pressure in the chamber is positive-pressure, and the maximum value of P_1 is 2.5 MPa. Pressures P_2 and P_3 decrease gradually, and their maximum values are 1.5 and 0.3 MPa, respectively. Figure 14a also illustrates that, at the phase of the inflow, the entire flow-field pressure in the resonance chamber is negative-pressure. The pressure value is gradually reduced from P_3 to P_1, and the minimum pressure of P_1 is -2.8 MPa. The frequency spectrum of the monitoring points, which is verified by performing a fast Fourier transform (FFT), is illustrated in figure 14b. It is shown that the oscillation frequency of the fluid inside the resonance chamber is 1997 Hz, which accords with the vibration frequency of the piezoelectric composite plates for the B_{10} mode shape.

Figure 15 illustrates the time variations of the static pressure and x-directional velocity at P_1. The flow-field static pressure and the X-directional velocity of the P_1 variation with time are sinusoidal curves, and the phase difference is $\pi/2$. According to the principle of wave interference (Min et al., 2012), a standing wave is produced across the fluid chamber, and the fluid oscillation is a type of standing-wave resonance.

Analysis of Pressure-Swirl Nozzle in Two-Phase Flow

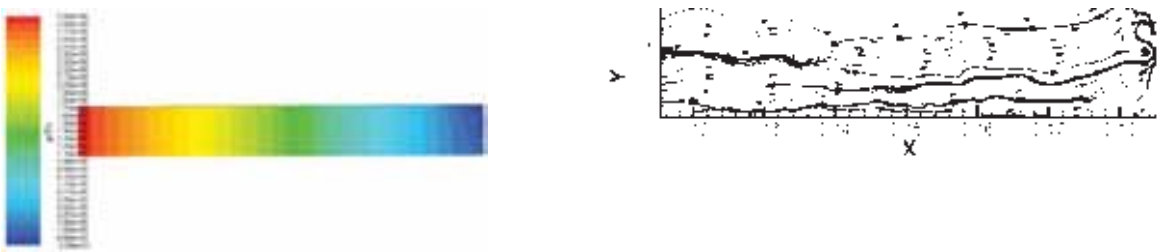
Background

The pressure-swirl nozzle is one of the most commonly used nozzles; it can produce small droplets at low inlet pressures and is used in the industrial and agricultural fields (Laryea et al., 2003). A simplex swirl nozzle always comprises a swirl chamber with several tangential fluid inlets and an axial fluid outlet. The tangential fluid produces a rotating flow inside the swirl chamber. A conical swirling sheet is formed when the rotating flow ejects from the orifice and finally breaks into small droplets. Despite the simple geometry of the pressure-swirl nozzle, its internal flow behavior is complex due to the strong swirling velocity component of the swirl flows. Therefore, the prediction of the fluid dynamics of the pressure-swirl nozzle for design and analysis is critical. In recent years, many experimental and numerical studies have been carried out to determine the internal flow characteristics in a pressure-swirl nozzle. Yang et al. (2012) used a high-speed camera to record detailed information regarding the liquid sheet breakup process and spray development. Experiments were performed with pressure-swirl nozzles of different configurations to test the effect of the nozzle geometry on the spray characteristics. Yule et al. (2000) used laser Doppler anemometry (LDA) to measure a large-scale pressure-swirl nozzle, and information on the air core size and the velocity fields inside the swirl chambers was obtained. However, such studies are difficult to perform on production-scale nozzles. As a complement to the experimental techniques, computational fluid



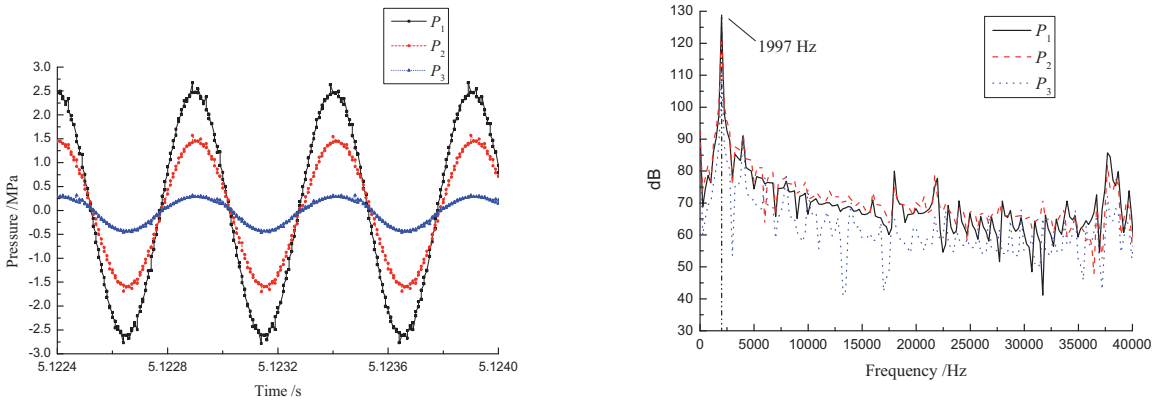
(a) (b)

Figure 12. Pressure distribution and streamline diagram at the phase of the inflow.



(a) (b)

Figure 13. Pressure distribution and streamline diagram at the phase of the outflow.



(a) (b)

Figure 14. Pressure curves and frequency spectra of the monitoring points.

dynamics can provide additional insight into the dynamics of the pressure-swirl nozzles. Zeoli et al. (2011) examined fluids during atomization from different pressure-swirl nozzle designs via the Reynolds stress model (RSM) and the volume of fluid (VOF) method. Mandal et al. (2008) investigated non-Newtonian fluid behavior in a pressure-swirl atomizer. Using the VOF method, they concluded that the spray cone angle and the variation in the film thickness decrease upon increasing the ratio between the orifice length and diameter.

The motivation of this section is to simulate the internal flow field inside the pressure-swirl nozzle of the piezoelectric atomizer. Using the volume of fluid computational fluid dynamics approach, the pressure swirl

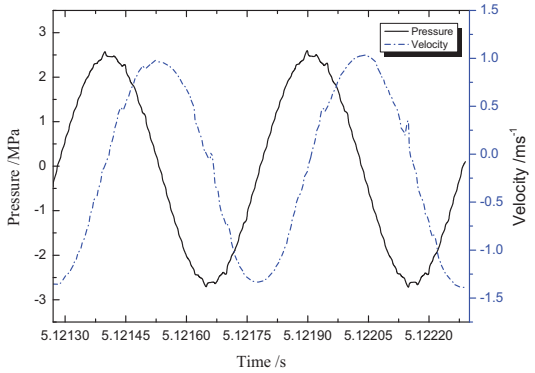


Figure 15. Pressure and velocity curves at P_1.

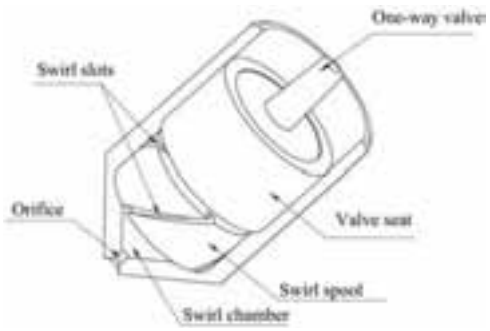


Figure 16. Pressure-swirl nozzle.

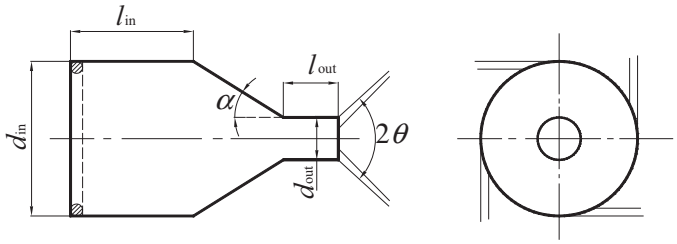
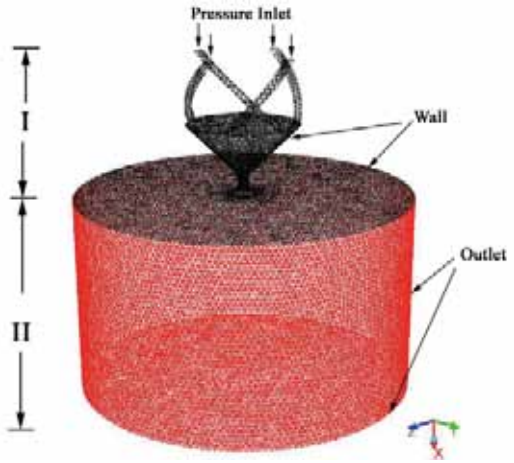


Figure 17. Geometrical characteristics of swirl chamber (d_{in} =22 mm is the swirl spool diameter; l_{in} =12 mm is the swirl spool length; 2α=90° is the cone angle of the swirl chamber; d_{out} =1.5 mm is the orifice diameter; l_{out} =2 mm is the orifice length; 2θ is the spray cone angle).

process of the nozzle is investigated. The axonometric drawing of the pressure-swirl nozzle used for this study is shown in figure 16, in which fluid is fed into the swirl chamber through four swirl slots grooved on the swirl spool. After undergoing rotational acceleration in the swirl chamber, the fluid is finally released from the orifice of the nozzle. The geometrical characteristics of the swirl spool and the swirl chamber are illustrated in figure 17.

NUMERICAL RESULTS OF THE PRESSURE-SWIRL NOZZLE

FLUENT® is used to calculate the governing equations for both the gas and liquid phases. The VOF model is applied in this investigation because it has a conservative formulation and allows for the direct determination of the steady solution of the flow. The second-order centered scheme and the second-order upwind interpolation scheme have been applied to the continuity and momentum equations. The SIMPLE algorithm has been chosen to tackle the pressure-velocity coupling. Because the fluid is injected helically into the swirl chamber, it is not possible to perform two-dimensional simulations on the internal fluid field of the pressure-swirl nozzle. A three-dimensional model is constructed to investigate the flow of water (ρ_1=1000 kg/m^3) into the air (ρ_2=1.225 kg/m^3) from the inside of the nozzle to the external air flow field (see fig. 18). The model is comprised of two parts: Part I represents the internal flow field of the pressure-swirl nozzle, and Part II represents the outlet computational domain attached to the atomizer to calculate the flow at the exit. The fluid is initially injected from the pressure inlet. The outlet boundary conditions are atmospheric pressure, a 5% turbulence intensity and a turbulent viscosity ratio of 10. The wall is a solid wall with a no-slip condition. A non-uniform mesh grid composed of 652,934 tetrahedral elements and 116,980 nodes is used. The VOF method together with the Reynolds-averaged Navier-Stokes (RANS) equations is implemented to capture the turbulent solution of the two-phase flow field.



Part I: Internal flow field of the pressure-swirl nozzle; Part II: Outlet computational domain.

Figure 18. Geometry and boundary conditions, mesh model.

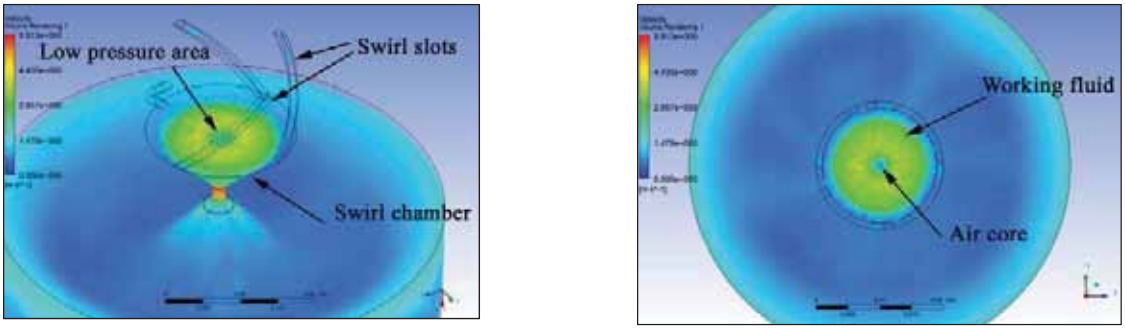
Figure 19 illustrates the velocity contour and streamlined diagram of the nozzle flow field when the fluid pressure at the inlet is 2000 Pa. Passing through the swirl slots, the liquid generates high-speed rotation in the swirl through conical contraction, and a low-pressure area is established at the center of the internal flow field (see fig. 19a). The atmospheric air is sucked into the interior of the nozzle under the action of reverse pressure. An air core is formed around the centerline inside the swirl chamber to balance the static pressure of the working fluid and the ambient pressure, as can be observed in the present simulations (fig. 19b). Consequently, a closed rim sheet is formed near the nozzle orifice. The air core can be developed in the nozzle, resulting in a thin film of liquid exiting the nozzle, as the sheet is fully developed. Belhadef et al. (2012) and Datta et al. (2000) indicate that the liquid sheet exhibits instability linked in particular to the large slip velocity between the liquid sheet and the ambient air that causes the liquid sheet to break up into ligaments and droplets.

The contour of the velocity near the orifice, obtained in the numerical simulations, is shown in figure 20. When the liquid swirls in the chamber, hydrodynamic instabilities develop between the liquid and the gas, and vortices are formed inside the nozzle. These vortices are called Gortler vortices, which accord with the experimental observations of Cooper (1999). Nouri-Borujerdi et al. (2012) considered that these instabilities are produced by Gortler vortices rotating about the air core. An interesting phenomenon is also illustrated in figure 20 in which waves of small amplitude are observed along the interface between the liquid and the gas. The waves originate at the top of the swirl chamber and propagate toward the orifice. One possible explanation is that the wave formation is caused by the recirculating air flow in the swirl chamber.

EXPERIMENT

SWEEP FREQUENCY EXPERIMENT

Frequency measurements of the piezoelectric composite plates in wet mode are taken using a 2-channel Agilent



(a) Three-dimensional velocity contour (b) Top view

Figure 19. Simulation results of the nozzle flow field.

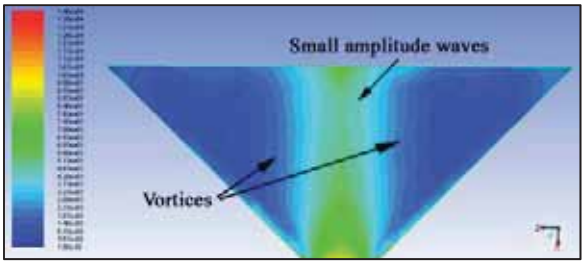
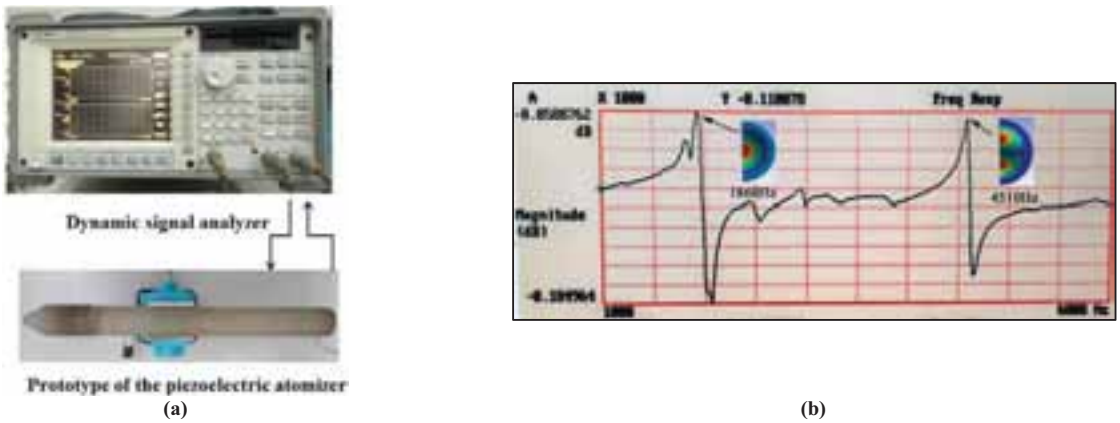


Figure 20. Vorticity map inside the swirl chamber.

35670A (Agilent Technologies Company, Santa Clara, Calif.). The piezoelectric composite plates of the prototype are driven directly by the sweep sine source of the dynamic signal analyzer (fig. 21). This instrument, in the sweep frequency mode, gives rise to a sinusoidal voltage at discrete frequencies over the specified frequency range. The process of sweeping frequencies is that the dynamic signal analyzer supplies a fluctuating periodic chirp. Complying with the oscillograph, an upsurge signal will emerge when the resonant point is experienced. The graph in figure 21b output by the oscillograph demonstrates the resonance frequency of the piezoelectric atomizer coupled with the working fluid. The first two natural frequencies are 1860 Hz and 4510 Hz, which correspond to the B_{10} and B_{11} modes, respectively. The theoretical analysis of fluid-solid coupling in Section III and Section IV shows that the first two wet mode frequencies are 1995 Hz and 4160 Hz when the length of the standing-wave resonance chamber L is 185 mm, and the theoretical and experimental errors are 6.77% and 7.76%, respectively.

SPRAY MEASUREMENT

In assessing the piezoelectric atomizer, two spray parameters, namely, the particle diameter distribution and the flow rate, are experimentally measured. The experimental system for the particle size analysis is presented in figure 22a-b. The experimental setup comprises a signal generator (WF1946A, NF Corporation, Yokohama, Japan), a power amplifier (HSA4052, NF Corporation, Yokohama, Japan), and a laser particle size analyzer (Winner318, WP Corporation, Jinan, China). Using the experimental setup, the effective measurement range of the particle size extends from 15 to 711 μm. A sinusoidal signal of 1860 Hz is generated by the signal generator and is amplified by the power amplifier. Consequently, the piezoelectric atomizer produces droplets in the signal excitation. The laser light is generated by the transmitter of the laser particle size analyzer and passes through the collimating mirror such that it emerges as a parallel light beam with a diameter of 10 mm. When the light beam passes through the spray flow field, a diffraction effect takes place. The diffracted light illuminates the photoelectric detector and is collected by a Fourier lens. The detected light signal is transformed into a digital signal by the A/D converter and analyzed by the computer. The working fluid used to perform the flow rate measurement is



(a) (b)

Figure 21. Sweep test equipment and the resonance response in the wet mode.

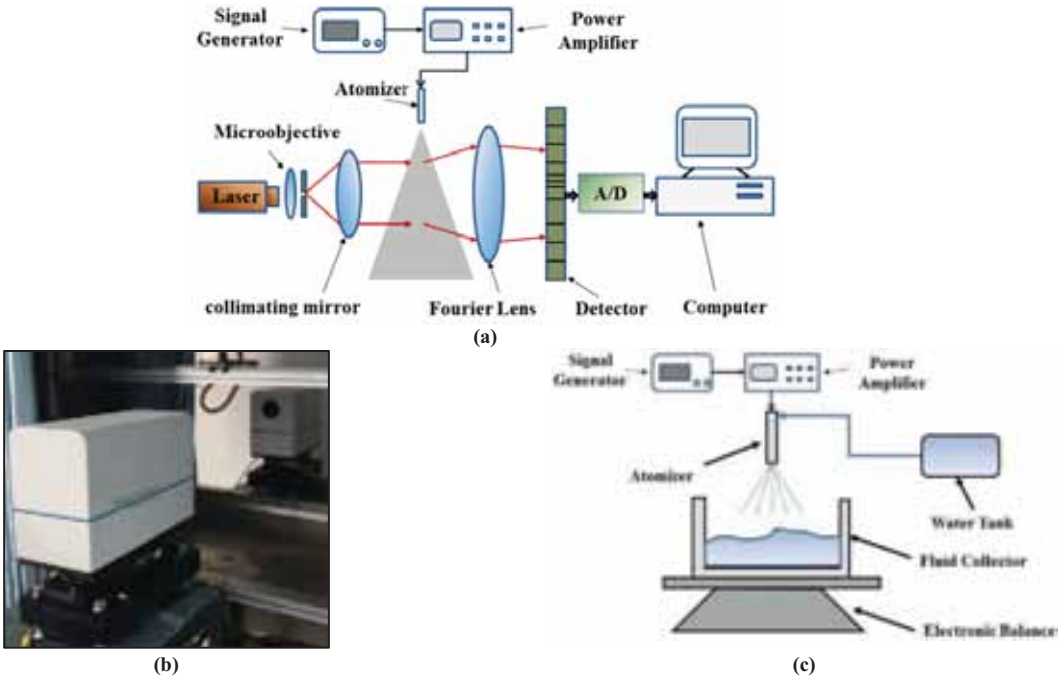


Figure 22. (a) Schematic of particle size measurement; (b) Laser particle size analyzer; (c) Flow rate measurement.

water. The flow rate is surveyed from the weight of the droplets that are ejected from the piezoelectric atomizer. An electronic balance (YP-B 500g/0.01g, SHH Corporation, China) with a resolution of 0.01 g is used in the experiment. A schematic illustration of the experimental setup used to perform the flow rate analysis is shown in figure 22c.

Figure 23 shows the spray patterns of the piezoelectric atomizer for a series of increasing peak-to-peak voltages $V_{pk\text{-}pk}$ from 10 to 150 V. The transition from a swirling jet to the complete atomization of the spray cone can be seen in figure 23. The sheet cone angle increases as the liquid flow rate increases due to the increase of the liquid momentum. When the peak-to-peak operating voltage $V_{pk\text{-}pk}$ reaches 30 V, a jet flow with a circular cross-section is formed near the orifice of the piezoelectric atomizer. A twisted sheet appears below the orifice because of the competition between the swirl strength of the jet flow and the gravity of the fluid (fig. 23a). A low mass flow rate jet is generated by the resonance chamber with a lower driving voltage, and a lower tangential velocity of the swirling sheet results. Consequently, the twisted sheet occurs under gravity, and larger droplets appear in the fog drops.

As the peak-to-peak driving voltage ($V_{pk\text{-}pk}$) increases to 70 V, there still exists a circular jet flow near the orifice (fig. 23b). With the increase of the driving voltage, a rudimentary hollow cone of the swirling sheet near the orifice has been developed because the axial and tangential velocities both increased. The ligaments are formed downstream, and then most of the ligaments break up into droplets. As the peak-to-peak driving voltage ($V_{pk\text{-}pk}$) increases to 120 V, a fully developed hollow cone forms

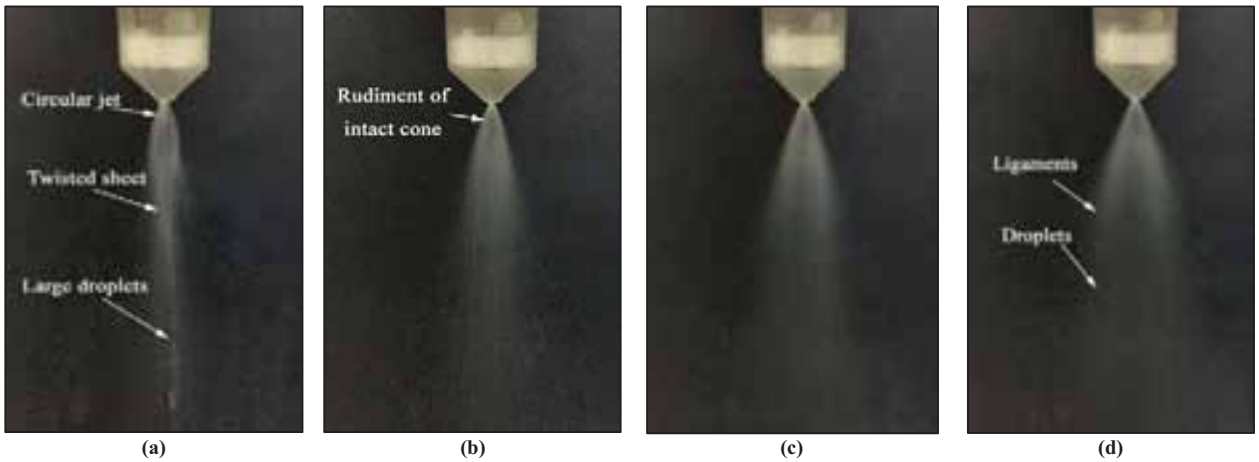


Figure 23. Spray characteristics of the piezoelectric atomizer with different driving voltages. (a) $V_{pk\text{-}pk}$=30 V (flow rate is 7.6g/s), (b) $V_{pk\text{-}pk}$=70 V (flow rate is 12.7g/s), (c) $V_{pk\text{-}pk}$=120 V (flow rate is 15.2g/s), (d) $V_{pk\text{-}pk}$=150 V (flow rate is 18.4g/s).

(fig. 23c-d). Figure 23 also shows that for a given nozzle geometry, the effective spray cone angle increases with an increase in the driving voltage or liquid mass flow rate of the working fluid due to the increase of the liquid momentum. This phenomenon is also consistent with the experiment of Inamura et al. (2003).

The mean diameter with the same ratio of volume to surface area as the entire ensemble is known as the Sauter mean diameter (Wei et al., 2014). It corresponds to values of $p = 3$ and $q = 2$ in equation 16.

$$D_{pq} = \left[\frac{\sum_{i=1}^{\infty} n_i D_i^p}{\sum_{i=1}^{\infty} n_i D_i^q} \right]^{1/(p-q)} \tag{16}$$

The Sauter mean diameter is extensively used in the characterization of liquid/liquid and gas/liquid dispersions.

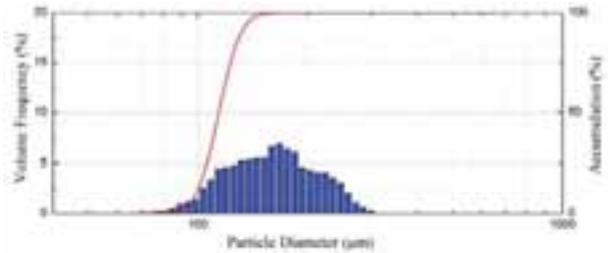
Figure 24 illustrates the dimensions of the sprayed particles at peak-to-peak driving voltages of 30, 70, 120, and 150 V. The particle size distribution for different driving voltages corresponds to the sub-figure shown in figure 23. The figure demonstrates that when operated at a lower driving voltage, the piezoelectric atomizer produces droplets with a less uniform diameter than when operated at a higher driving voltage. When the driving voltage is $V_{pk\text{-}pk}$=30 V, the minimum droplet size produced by the atomizer is 47.7 μm, and the maximum droplet size is 418.2 μm. By comparison, when the driving voltage is increased to $V_{pk\text{-}pk}$=150V, the minimum droplet size is 60.7 μm and the maximum droplet size is 151.9 μm. In addition, more than 76% of the total volume of the droplet diameters is concentrated in the interval from 85.1 to 108.4 μm. This is because a higher driving voltage increases the displacement of the piezoelectric composite plates, which in turn increases the kinetic energy of the ejected liquid, thereby reducing the particle size. It is also deduced that a higher velocity between the spray cone and the ambient gas promotes the centrifugal force of the swirling sheet, and long ligaments are established. Eventually, relatively uniform droplets are formed.

CONCLUSIONS

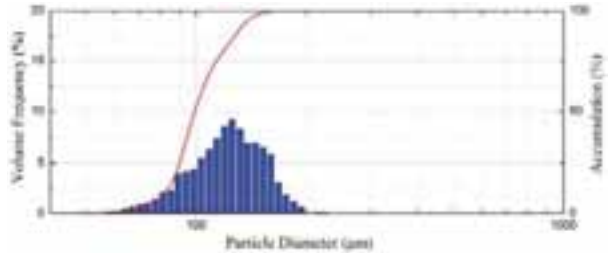
A piezoelectric atomizer based on the principles of standing-wave resonance and a pressure-swirl nozzle was developed, analyzed, and tested. This atomizer uses piezoelectric composite plates to acquire a large displacement from the PZT vibration and exert an excess pressure on the liquid with standing-wave resonance. Utilizing the pressure-swirl nozzle, uniformly-sized liquid droplets can be produced without the use of an additional air pump, which satisfies the need for low-cost mass production for engineering and agricultural applications.

In this study, the three-dimensional dynamic characteristics of the piezoelectric composite plates, considering the effect of the fluid-solid interface, are determined. The natural frequencies and mode shapes of the PZT diaphragm have been simulated using the ANSYS parametric design language in which the FSI is modeled by coupling an acoustic fluid domain to the surface of the fluid-solid coupling.

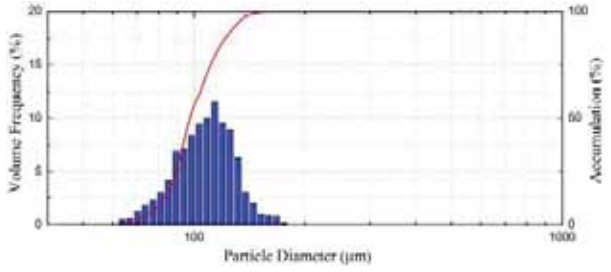
The hydrodynamics inside the standing-wave resonance chamber of the piezoelectric atomizer are determined using the dynamic mesh method and UDF. A subsequent analysis of the fluid-solid coupling between the fluid in the resonance chamber and the vibration of the piezoelectric



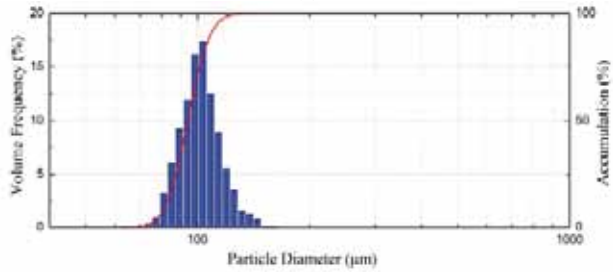
SMD=175.6μm; $V_{pk\text{-}pk}$=30 V; current of 2.7 mA
D(10)=55.9 μm; D(50)= 208.3 μm; D(90)= 376.6 μm
(a)



SMD=131.4 μm; $V_{pk\text{-}pk}$=70 V; current of 7.8 mA
D(10)= 69.3 μm; D(50)= 144.7 μm; D(90)= 212.9 μm
(b)



SMD=115.2 μm; $V_{pk\text{-}pk}$=120 V; current of 13.9 mA
D(10)= 73.2 μm; D(50)= 121.4 μm; D(90)= 163.7 μm
(c)



SMD=93.5 μm; $V_{pk\text{-}pk}$=150 V; current of 18.2 mA
D(10)= 81.9 μm; D(50)= 94.1 μm; D(90)= 108.2 μm
(d)

Figure 24. Variation of particle size distribution for different driving voltages.

composite plates is conducted. It is found that a standing-wave resonance can be achieved in the chamber for the B_{10} mode shape of the PZT diaphragm when the length of the resonance chamber L is 185 mm.

The inner flow and performance characteristics of the pressure-swirl nozzle using the two-phase flow method are investigated. The SMD and flow rate of the piezoelectric atomizer are measured by experiments. We find that a smaller and more uniform SMD could be achieved by operating at a higher amplitude of the driving voltage. The measured flow rate could reach 18.4 g/s with an SMD of 93.5 μm when the device is operated at a 150 V peak-to-peak driving voltage. The atomizer also demonstrates that relatively uniform droplets are formed below the ligaments when the cone swirl sheet is fully developed. This reveals that this atomizer has the potential for applications that require fine droplets.

ACKNOWLEDGMENTS

The authors would like to acknowledge financial support from the Research Fund for the Doctoral Program of High Education of China (Grant No. 20134404120020), the Fund of the Nature Science Foundation of Guangdong Province, China (Grant No. S2013010013747, 2015A030310182), Innovation project of modern agricultural equipment and technology in Jiangsu Province (Grant No. NZXT01201403) and the National Natural Science Foundation of China (Grant No. 11302083).

REFERENCES

Askari, E., & Jeong, K.-H. (2010). Hydroelastic vibration of a cantilever cylindrical shell partially submerged in a liquid. *Ocean Eng., 37*(11-12), 1027-1035. http://dx.doi.org/10.1016/j.oceaneng.2010.03.016

Avvaru, B., Patil, M. N., Gogate, P. R., & Pandit, A. B. (2006). Ultrasonic atomization: Effect of liquid phase properties. *Ultrasonics, 44*(2), 146-158. http://dx.doi.org/10.1016/j.ultras.2005.09.003

Basak, A., Ganguly, R., & Datta, A. (2013). Effect of transesterification of vegetable oil on liquid flow number and spray cone angle for pressure and twin fluid atomizers. *Fuel, 112*, 347-354. http://dx.doi.org/10.1016/j.fuel.2013.05.047

Belhadef, A., Vallet, A., Amielh, M., & Anselmet, F. (2012). Pressure-swirl atomization: Modeling and experimental approaches. *Int. J. Multiphase Flow, 39*, 13-20. http://dx.doi.org/10.1016/j.ijmultiphaseflow.2011.09.009

Daniels, A., Zhu, H., & Tiwari, A. (2013). Evaluation of piezoelectric material properties for a higher power output from energy harvesters with insight into material selection using a coupled piezoelectric-circuit-finite element method. *IEEE Trans. Ultrason. Ferroelectr. Freq. Control, 60*(12), 2626-2633. http://dx.doi.org/10.1109/TUFFC.2013.2861

Datta, A., & Som, S. K. (2000). Numerical prediction of air core diameter, coefficient of discharge and spray cone angle of a swirl spray pressure nozzle. *Int. J. Heat Fluid Flow, 21*(4), 412-419. http://dx.doi.org/10.1016/S0142-727X(00)00003-5

Donnelly, T. D., Hogan, J., Mugler, A., Schommer, N., Schubmehl, M., Bernoff, A. J., & Forrest, B. (2004). An experimental study of micron-scale droplet aerosols produced via ultrasonic atomization. *Phys. Fluids, 16*(8), 2843-2851. http://dx.doi.org/10.1063/1.1759271

Esmailzadeh, M., Lakis, A. A., Thomas, M., & Marcouiller, L. (2008). Three-dimensional modeling of curved structures containing and/or submerged in fluid. *Finite Elem. Anal. Des., 44*(6-7), 334-345. http://dx.doi.org/10.1016/j.finel.2007.11.019

Galchev, T., Aktakka, E. E., & Najafi, K. (2012). A piezoelectric parametric frequency increased generator for harvesting low-frequency vibrations. *J. Microelectromech. Syst., 21*(6), 1311-1320. http://dx.doi.org/10.1109/JMEMS.2012.2205901

Herrero, E., Del Valle, E. M. M., & Galan, M. A. (2007). Instability study of a swirling annular liquid sheet of polymer produced by air-blast atomization. *Chemical Engineering Journal, 133*(1-3), 69-77. http://dx.doi.org/10.1016/j.cej.2007.01.028

Ho, J., Wang, H., & Forde, G. M. (2008). Process considerations related to the microencapsulation of plasmid DNA via ultrasonic atomization. *Biotechnol. Bioeng., 101*(1), 172-181. http://dx.doi.org/10.1002/bit.21876

Inamura, T., Tamura, H., & Sakamoto, H. (2003). Characteristics of liquid film and spray injected from swirl coaxial injector. *J. Propulsion Power, 19*(4), 632-639. http://dx.doi.org/10.2514/2.6151

Jeng, Y. R., Su, C. C., Feng, G. H., Peng, Y. Y., & Chien, G. P. (2009). A PZT-driven atomizer based on a vibrating flexible membrane and a micro-machined trumpet-shaped nozzle array. *Microsyst. Technol., 15*(6), 865-873. http://dx.doi.org/10.1007/s00542-009-0844-z

Jeng, Y. R., Tu, P. Y., Feng, G. H., Su, C. C., & Peng, Y. Y. (2007). PZT bimorph actuated atomizer based on higher order harmonic resonance and reduced operating pressure. *Sens. Actuators, A, 136*(1), 434-440. http://dx.doi.org/10.1016/j.sna.2006.12.004

Jeong, K. H. (2003). Free vibration of two identical circular plates coupled with bounded fluid. *J. Sound Vibration, 260*(4), 653-670. http://dx.doi.org/10.1016/S0022-460X(02)01012-X

Koveos, Y., & Tzes, A. (2013). Resonant fluid actuator: Modeling, identification, and control. *IEEE Trans. Control Syst. Technol., 21*(3), 852-860. http://dx.doi.org/10.1109/TCST.2012.2186964

Kozien, M. S., & Koltowski, B. (2011). Comparison of active and passive damping of plate vibration by piezoelectric actuators-FEM simulation. *Acta Phys. Pol. A, 119*(6A), 1005-1008. http://dx.doi.org/10.12693/APhysPolA.119.1005

Kramer, M. R., Liu, Z., & Young, Y. L. (2013). Free vibration of cantilevered composite plates in air and in water. *Compos. Struct., 95*, 254-263. http://dx.doi.org/10.1016/j.compstruct.2012.07.017

Laryea, G. N., & No, S. Y. (2003). Development of electrostatic pressure-swirl nozzle for agricultural applications. *J. Electrostatics, 57*(2), 129-142. http://dx.doi.org/10.1016/S0304-3886(02)00122-5

Lighthill, J. (2001). *Waves in fluids.* Cambridge, U.K.: University Press.

Mandal, A., Jog, M. A., Xue, J., & Ibrahim, A. A. (2008). Flow of power-law fluids in simplex atomizers. *Intl. J. Heat Fluid Flow, 29*(5), 1494-1503. http://dx.doi.org/10.1016/j.ijheatfluidflow.2008.05.006

Min, Q., Zhang, Q. Y., Tian, J. J., Wang, Q. B., & He, W. Q. (2012). A study on the dissonant standing-wave tube with variable section and its extremely nonlinear standing-wave field. *Phys. Lett. A, 377*(1-2), 99-106. http://dx.doi.org/10.1016/j.physleta.2012.11.020

Nouri-Borujerdi, A., & Kebriaee, A. (2012). Numerical simulation of laminar and turbulent two-phase flow in pressure-swirl atomizers. *AIAA J., 50*(10), 2091-2101. http://dx.doi.org/10.2514/1.J051331

Payri, R., Garcia, J. M., Salvador, F. J., & Gimeno, J. (2005). Using spray momentum flux measurements to understand the influence of diesel nozzle geometry on spray characteristics. *Fuel, 84*(5), 551-561. http://dx.doi.org/10.1016/j.fuel.2004.10.009

Pérez, N., Carbonari, R. C., Andrade, M. A. B., Buiochi, F., & Adamowski, J. C. (2014). A FEM-based method to determine the complex material properties of piezoelectric disks. *Ultrasonics, 54*(6), 1631-1641. http://dx.doi.org/10.1016/j.ultras.2014.03.006

Rajan, R., & Pandit, A. B. (2001). Correlations to predict droplet size in ultrasonic atomisation. *Ultrasonics, 39*(4), 235-255. http://dx.doi.org/10.1016/S0041-624X(01)00054-3

Rodriguez, C. G., Flores, P., Pierart, F. G., Contzen, L. R., & Egusquiza, E. (2012). Capability of structural-acoustical FSI numerical model to predict natural frequencies of submerged structures with nearby rigid surfaces. *Computers Fluids, 64*, 117-126. http://dx.doi.org/10.1016/j.compfluid.2012.05.011

Topp, M. N., & Eisenklam, P. (1972). Industrial and medical uses of ultrasonic atomizers. *Ultrasonics, 10*(3), 127-133. http://dx.doi.org/10.1016/0041-624X(72)90009-1

Wei, X., & Yong, H. (2014). Improved Semiempirical Correlation to Predict Sauter Mean Diameter for Pressure-Swirl Atomizers. *J. Propul. Power, 30*(6), 1628-1635. http://dx.doi.org/10.2514/1.B35238

Yang, L. J., Fu, Q. F., Qu, Y. Y., Zhang, W., Du, M. L., & Xu, B. R. (2012). Spray characteristics of gelled propellants in swirl injectors. *Fuel, 97*, 253-261. http://dx.doi.org/10.1016/j.fuel.2012.02.036

Yule, A. J., & Chinn, J. J. (2000). The internal flow and exit conditions of pressure swirl atomizers. *Atomization Sprays, 10*(2), 121-146. http://dx.doi.org/10.1615/AtomizSpr.v10.i2.20

Zeoli, N., Tabbara, H., & Gu, S. (2011). CFD modeling of primary breakup during metal powder atomization. *Chem. Eng. Sci., 66*(24), 6498-6504. http://dx.doi.org/10.1016/j.ces.2011.09.014

Zienkiewicz, O. C., & Bettess, P. (1978). Fluid-structure dynamic interaction and wave forces. An introduction to numerical treatment. *Intl. J.Numerical Methods Eng., 13*(1), 1-16. http://dx.doi.org/10.1002/nme.1620130102

NOMENCLATURE

B	bulk modulus
c	wave celerity
c_f	sound speed in water
c_{hk}^D	sixth-rank symmetric tensor under a constant electric field, $h,k = 1,2,\cdots,6$
D_i	droplet diameter for size class i
D_j	electric displacement, $j = 1,2,3$
E	elastic modulus
f	wave's frequency
f_c	periodic actuating force generated by the piezoelectric structure
f_p	vibration frequency of the piezoelectric composite plate
f_r	standing-wave resonance frequency
h	thickness of the piezoelectric composite plate
h_{jh}	piezoelectric constant tensor, h = 1, 2, … , 6 and $j = 1,2,3$
L	length of standing-wave resonance chamber
n_i	number of the droplets in size class i
p_f	sound pressure in water
P_l	dynamic pressure imposed on the piezoelectric composite plates by the fluid
S_k	mechanical strain tensor, $k = 1,2,\cdots,6$
t	iteration time
T_h	stress, $h = 1,2,\cdots,6$
u	fluid velocity
$\vec{V}$	velocity vector
w_c	displacement of the piezoelectric composite plate
δP	fluid pressure fluctuation
λ	wavelength
μ	viscosity of the fluid
ρ_c	density of the piezoelectric composite plate
ρ_l	fluid density
ν	Poisson ratio
∇^2	Laplacian operator

SCAULIB202405438

检索证明

根据委托人提供的论文材料，委托人华南农业大学数学与信息学院 张建桃 3 篇论文收录情况如下表。

序号	论文名称	发表刊物及发表的年月卷期/页码等	作者排名	论文等级	作者文中单位	收录情况	影响因子	中科院大类分区
1	Origami Improved Dielectric Elastomer Actuation for Tunable Lens	IEEE TRANSACTIONS ON INSTRUMENTATION AND MEASUREMENT 出版年：2022 卷期：71 页码：- 文献号：7502709 文献类型：Article	共同通讯作者（倒数第一）	A 类	华南农业大学	SCI	IF2-year=5.6 IF5-year=5.4 （2022）	工程技术 2 区 Top 期刊：否 （2022）
2	Single-rotor UAV flow field simulation using generative adversarial networks	COMPUTERS AND ELECTRONICS IN AGRICULTURE 出版年：2019 卷期：167 页码：- 文献号：105004 文献类型：Article	通讯作者	A 类	华南农业大学	SCI	IF2-year=3.858 IF5-year=4.008 （2019）	农林科学 2 区 Top 期刊：是 （2019）
3	FLUID-SOLID COUPLING AND EXPERIMENTAL REALIZATION OF A PIEZOELECTRIC ATOMIZER UNDER STANDING-WAVE RESONANCE	APPLIED ENGINEERING IN AGRICULTURE 出版年：2016 卷期：32 3 页码：327-340 文献号： 文献类型：Article	通讯作者	B 类	华南农业大学	SCI	IF2-year=0.505 IF5-year=0.667 （2016）	农林科学 4 区 Top 期刊：否 （2016）

华南农业大学图书馆SCAULIB202405438

3.7 基于共振声学放大原理的涡激振动自发电装置设计与试验

QK1739385

美国《工程索引》（Ei）收录期刊
美国《化学文摘》（CA）收录期刊
Scopus数据库收录期刊
中文核心期刊　中国科技核心期刊
中国科学引文数据库来源期刊
RCCSE中国权威学术期刊

ISSN 1000-1298
CODEN NUYCA3

农业机械学报

NONGYE JIXIE XUEBAO

Transactions of the Chinese Society for Agricultural Machinery

第48卷

2017 11

中国农业机械学会主办

ISSN 1000-1298

万方数据

农业机械学报
NONGYE JIXIE XUEBAO

2017 年　第 11 期(第 48 卷)

目　次

特约专稿

生物炭吸附水体中重金属机理与工艺研究进展 …… 韩鲁佳　李彦霏　刘　贤　等(1)

农业装备与机械化工程

抓持-旋切式欠驱动双指手葡萄采摘装置设计与试验 …… 尹建军　陈永河　贺　坤　等(12)
机械手不同抓取控制方式对番茄机械损伤的影响分析 …… 周　俊　孟一猛　张　娜　等(21)
夜间自然环境下荔枝采摘机器人识别技术 …… 熊俊涛　林　睿　刘　振　等(28)
利用候选区域的多模型跟踪算法 …… 毕笃彦　张园强　查宇飞　等(35)
基于 EDEM - CFD 耦合的内充气吹式排种器优化与试验 …… 韩丹丹　张东兴　杨　丽　等(43)
秸秆后覆盖小麦播种机设计与试验 …… 牛　琪　王庆杰　陈黎卿　等(52)
轻量化玉米垄作免耕播种机设计与试验 …… 刘艳芬　林　静　李宝筏(60)
油菜纸钵苗移栽机气动取苗机构设计与轨迹分析 …… 廖庆喜　张　照　胡乔磊　等(70)
油菜联合直播机组合式船型开沟器设计与开沟质量试验 …… 刘晓鹏　肖文立　马　磊　等(79)
提土-全膜面覆土装置作业参数优化与试验 …… 戴　飞　赵武云　宋学锋　等(88)
铲齿组合式残膜捡拾装置设计与试验优化 …… 由佳翰　张本华　温浩军　等(97)
地轮中置式高机动性宽幅农具机架平台研究 …… 刘宏新　唐师法　刘俊孝　等(105)
油菜收获机割台螺旋输送器间隙自适应调节机构研究 …… 李海同　万星宇　徐　阳　等(115)
基于 Petri 网模型的收获机轴流式脱分选装置参数化设计 …… 陈　霓　刘正怀　夏劲松　等(123)
立辊式玉米收获机割台间隙夹持输送装置设计与试验 …… 耿端阳　李玉环　何　珂　等(130)
梳割气吸一体式贡菊采摘机设计与试验 …… 姬长英　张　纯　顾宝兴　等(137)
粘重土壤下马铃薯挖掘机分离输送装置改进设计与试验 …… 吕金庆　孙　贺　兑　瀚　等(146)
摆动分离筛薯土分离机理分析与参数优化试验 …… 谢胜仕　王春光　邓伟刚　等(156)
锤片式粉碎机粉碎玉米秸秆机理分析与参数优化 …… 王德福　王　沫　李利桥(165)
基于三维激光点云的靶标叶面积密度计算方法 …… 张美娜　吕晓兰　邱　威　等(172)
基于载荷分布的潜水轴流泵叶轮与导叶水力设计 …… 杨　魏　雷晓宇　张志民　等(179)
小流量工况下旋涡自吸泵流动降噪优化研究 …… 王　洋　胡日新　汤海涛　等(188)
水泵进水池底部压力脉动特性试验 …… 宋希杰　刘　超　杨　帆　等(196)

农业信息化工程

基于共振声学放大原理的涡激振动自发电装置设计与试验 …… 文　晟　李晟华　张建桃　等(204)
基于改进力导向模型的生态节点布局优化 …… 苏　凯　岳德鹏　YANG Di　等(215)
基于物联网和云架构的渠灌闸门智能控制系统 …… 包志炎　王学斌　张海波　等(222)

农业水土工程

不同耕作方式对黄土高原黑垆土有机碳库组成的影响 …… 王旭东　张　霞　王彦丽　等(229)

万方数据

doi:10.6041/j.issn.1000-1298.2017.11.025

基于共振声学放大原理的涡激振动自发电装置设计与试验

文　晟[1,2]　李晟华[2,3]　张建桃[2,4]　兰玉彬[2,3]　张海艳[2,3]　邢　航[2,3]

(1. 华南农业大学工程基础教学与训练中心，广州 510642；2. 国家精准农业航空施药技术国际联合研究中心，广州 510642；
3. 华南农业大学工程学院，广州 510642；4. 华南农业大学数学与信息学院，广州 510642)

摘要：为实现从自然环境中自动获取清洁能源，并给无线传感器和通讯模块供电，基于涡激振动及共振声学放大原理，设计了一种压电自发电装置。首先对位于该自发电装置内的压电悬臂梁复合结构进行力学分析；其次基于计算流体力学数值方法，对绕流圆柱后附加不同板长条件下的流场动力学特性进行分析，以明确悬臂梁长度对脱涡频率和升力、阻力系数的影响规律。利用有限元软件 ANSYS 对压电悬臂梁复合结构的横向往复振动进行数值模拟，确定了复合结构的横向振动频率随板长 L 的变化规律。最后对位于该装置两侧的亥姆霍兹共振器的结构尺寸进行优化设计，以使流场的脱涡频率、压电悬臂梁复合结构的一阶横向振动频率和共振器的谐振频率达到一致，从而使压电发电装置产生共振并输出最大的电能。试验结果表明，涡激振动自发电装置在 5 m/s 的风速下可产生两相峰峰值为 6.0 V 的开路电压，且上述 3 个频率达到一致。4 ~ 6.25 m/s 为该自发电装置的自锁风速区间，在此风速范围内，自发电装置均能产生较大的电压。

关键词：涡激振动；流场分析；压电发电；共振；声学放大

中图分类号：TN384　　文献标识码：A　　文章编号：1000-1298(2017)11-0204-11

Design and Experiment of Vortex-induced Vibration Self-generating Device Based on Principle of Resonant Acoustic Amplification

WEN Sheng[1,2]　LI Shenghua[2,3]　ZHANG Jiantao[2,4]　LAN Yubin[2,3]　ZHANG Haiyan[2,3]　XING Hang[2,3]

(1. *Engineering Fundamental Teaching and Training Center, South China Agricultural University, Guangzhou* 510642, *China*
2. *National Center for International Collaboration Research on Precision Agricultural Aviation Pesticides Spraying Technology, Guangzhou* 510642, *China*
3. *College of Engineering, South China Agricultural University, Guangzhou* 510642, *China*
4. *College of Mathematics and Informatics, South China Agricultural University, Guangzhou* 510642, *China*)

Abstract: In order to acquire clean energy from the natural environment and supply power to the wireless sensors and communication modules, a vortex-induced vibration self-generating device was designed based on the principle of vortex-induced vibration and resonant acoustic amplification. The device mainly consisted of a cavity, a cylinder, a piezoelectric cantilever composite structure, a base and two Helmholtz resonators. Firstly, mechanical analysis of the piezoelectric cantilever composite structure in the self-generating device was carried out. Secondly, based on the computational fluid dynamics method, the dynamic characteristics of the flow field of self-generating device under different plate lengths were analyzed. And the influence of length of cantilever beam on vortex frequency, lift and drag coefficient was clarified. The finite element software ANSYS was used to simulate the transverse reciprocating vibration of piezoelectric cantilever composite structure to finish the structural design. Finally, the structural dimensions of the Helmholtz resonator on both sides of the device were optimized to make the flow field vortex shedding frequency. And the first-order transverse vibration frequency of piezoelectric cantilever composite structure and the resonant frequency of the resonator was consistent. The experimental results demonstrated that the self-generating device can produce an open-circuit voltage with a peak-to-phase voltage of 6.0 V at wind speed of 5 m/s, and the above three frequencies were consistent. The

收稿日期：2017-08-23　修回日期：2017-09-08

基金项目：国家重点研发计划项目(2016YFD0200700)、广东省自然科学基金项目(2015A030310182)和广东省科技计划项目(2016A020210092、2016A020210100)

作者简介：文晟(1974—)，男，副教授，主要从事压电振动和精准农业研究，E-mail：vincen@scau.edu.cn

通信作者：张建桃(1978—)，男，副教授，主要从事精细农业和压电器件研究，E-mail：zhangjiantao@yeah.net

(C)1994-2023 China Academic Journal Electronic Publishing House. All rights reserved.　http://www.cnki.net

experimental results also showed that the speed of 4 ~ 6.25 m/s was the self-locking wind speed range of the self-generating device. Within the wind speed range, the self-generating device can produce the maximum voltage amplitude. The results of the study provided a reference for the structural design of the vortex-induced vibration self-generating device.

Key words: vortex-induced vibration; flow field analysis; piezoelectric power generation; resonance; acoustic amplification

引言

集物联网技术、传感器技术、自动控制技术和通讯技术为一体的农情信息采集系统，可实时采集农田土壤水分肥料信息、农作物生长信息和病虫害杂草信息，是现阶段的研究热点之一[1-2]。传统的化学电池常被用来为数量众多的农情信息采集传感器提供能源[3]，但化学电池的容量有限，能量密度低，使用时间短，且废弃的电池会破坏水体和土壤[4]，因此如何为这些传感器提供持续清洁能量源的研究越来越受到重视[5]。随着微机电系统技术及集成电路的迅速发展，传感器节点能耗进一步减低，这使得直接从自然环境中获取能量并为传感器供能成为可能[6]。风能作为一种清洁能源广泛存在于自然界中，传统的涡轮风力发电机组由于体积较大、造价较高且需定期维护，对于数量众多的传感器网络节点不是理想的能量源[7]。具有压电效应的压电材料能在外力作用下直接产生电荷，易于整合到系统且无电磁干扰，更适合为无线传感器及通讯模块提供电能[8]。

针对目前压电风力发电产生的电压较低、风能利用率不高等问题[9]，本文基于涡激振动及共振声学放大原理，设计一种压电自发电装置。其利用涡激振动原理使位于该自发电装置内的压电悬臂梁复合结构产生横向振动并输出电能，同时将位于该发电装置两侧的亥姆霍兹共振器(Helmholtz resonator)作为风能放大装置。利用流场数值分析和参数优化设计，使脱涡频率、压电悬臂梁复合结构的振动频率和共振器的谐振频率保持一致，且声场放大比率达到最大，最终使该装置产生共振并输出最大的电能。此外，对该发电装置进行流场分析和发电试验，得到外界风速对其自发电能力和振动特性的影响规律，为该装置的工程化应用打下基础。

1　涡激振动自发电装置结构与工作原理

设计的涡激振动自发电装置如图 1 所示，由腔体、绕流圆柱、压电悬臂梁复合结构、基座、亥姆霍兹共振器、支架、导线、整流电路和蓄电池等部件组成。其中，中空腔体的两侧对称布置了 2 个结构相同的亥姆霍兹共振器。压电悬臂梁复合结构包括一块柔性金属基板和 2 片附于该基板两侧的柔性压电材料，其一端固定于腔体内部的基座，另一端与绕流圆柱配合。

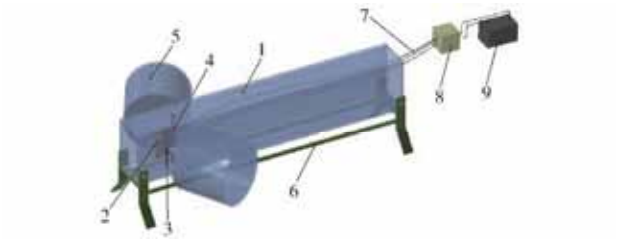


图 1　自发电装置结构示意图

Fig. 1　Schematic diagram of self-generating device

1. 腔体　2. 绕流圆柱　3. 压电悬臂梁复合结构　4. 基座　5. 亥姆霍兹共振器　6. 支架　7. 导线　8. 整流电路　9. 蓄电池

当外部气流从腔体前端流入，并经过绕流圆柱时，在满足一定的条件下(雷诺数 *Re* 大于 150)，气流的边界层在绕流圆柱表面摩擦阻力和压差阻力的共同作用下发生分离，并形成特定频率的交替涡旋，即卡门涡街[10]。同时，涡旋脱落的反作用力又使得绕流圆柱和压电悬臂梁复合结构产生周期性的横向振动，带动柔性压电材料分别产生拉、压应力，从而利用压电效应产生电能。

亥姆霍兹共振器是一种声波加强设备，当卡门涡街的气流扰动波进入共振器时，共振器的剪切层对其进行放大，形成涡环结构并在上游剪切层诱发新的扰动。当这两种扰动匹配时，共振器不断受到周期性激励产生流体自激振荡，并在其出口处形成自激振荡脉冲射流[11]；射流冲击绕流圆柱，进而加大压电悬臂梁复合结构的横向振动幅度。

当卡门涡街的脱涡频率、压电悬臂梁复合结构的横向振动频率以及亥姆霍兹共振器的共振频率一致时，悬臂梁复合结构将达到共振状态，此时其横向振动幅度达到最大，从而使柔性压电体输出最大的电能。电能经整流电路整流后至蓄电池中储存起来。自发电装置的 3 种工作状态如图 2 所示。

2　控制方程

2.1　圆柱绕流

研究表明[12]，流体经过圆柱后的尾流形态与雷诺数 *Re* 直接有关：当 *Re* 较小时，流体流经圆柱时无分离流动；当 *Re* 大于 5 时，流体在圆柱体尾部形成

(C)1994-2023 China Academic Journal Electronic Publishing House. All rights reserved.　http://www.cnki.net

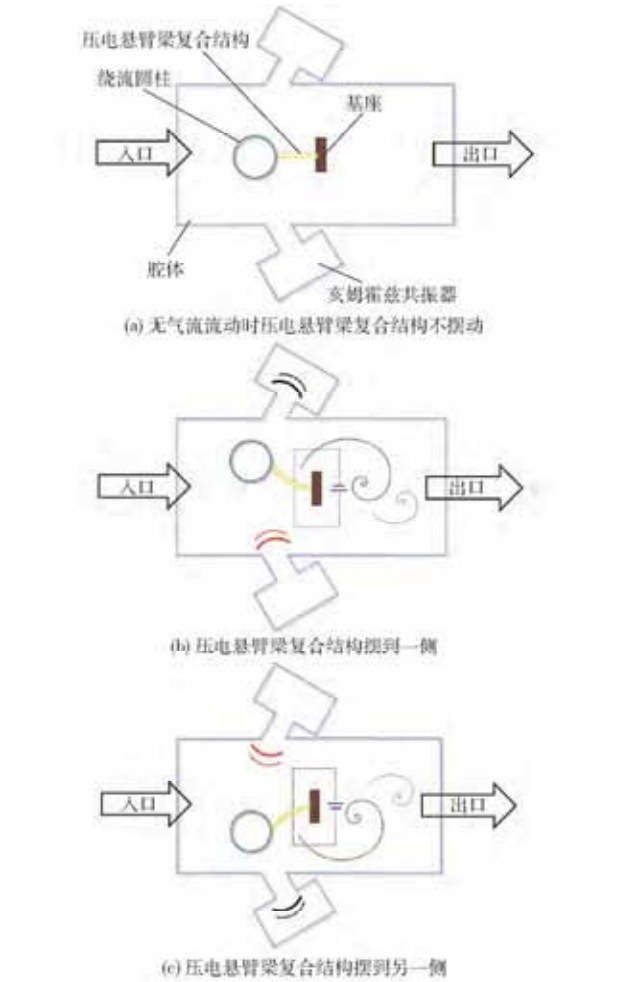


图 2 自发电装置的 3 种工作状态

Fig. 2 Three operating states of self-generating device

一对对称的滞留涡(图 3a);随着 Re 的增大,尾迹开始失稳并出现周期性的振荡,滞留涡则交替脱落而演化成稳定的层流涡街,当 Re 处于 $3\times10^2\sim3\times10^5$ 亚临界区范围内,尾迹已经完全变成湍流涡街(图 3b);当 Re 处于 $3\times10^5\sim3.5\times10^6$ 临界区内,圆柱的边界层受到湍流涡街尾迹的影响从层流分离转变成湍流分离(图 3c)。其中,雷诺数 Re 表达式为[13]

$$Re=\frac{\rho vD}{\mu} \tag{1}$$

式中 ρ——流体密度,kg/m^3

v——流场特征速度,一般取入口处的平均流速,m/s

D——绕流圆柱直径,m

μ——流体动力粘度,Pa·s

当流体经过单圆柱后形成卡门涡街时,在有限流道内涡旋的脱落频率 f 为[14]

$$f=St\frac{v}{\varepsilon D} \tag{2}$$

其中 $$\varepsilon=1-\frac{2}{\pi}\left[\frac{D}{\Phi}\sqrt{1-\left(\frac{D}{\Phi}\right)^2}+\arcsin\frac{D}{\Phi}\right] \tag{3}$$

式中 St——斯特劳哈尔数,表示流体动能与系统固有能的相对关系

ε——圆柱两侧弓形面积与进气道横截面面积之比

Φ——进气道入口处的水力直径,m

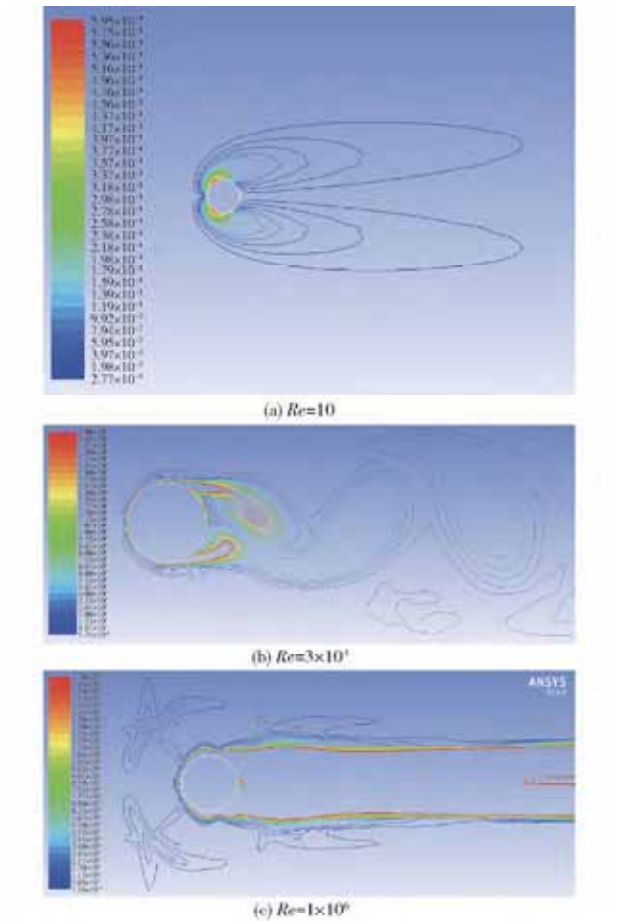


图3 圆柱绕流随 Re 变化的等值线涡量图

Fig. 3 Equivalence vorticity graphs of flow around a circular cylinder with Re

目前较为普遍接受的 St 与 Re 经验关系式为[15]

$$St=0.273\,1-\frac{1.112\,9}{\sqrt{Re}}+\frac{0.482\,1}{Re} \tag{4}$$

2.2 压电悬臂梁复合结构的受迫振动

压电悬臂梁复合结构在来流作用下产生横向振动自发电模型如图 4 所示。该结构包括弹性装载的绕流圆柱、压电悬臂梁和相应的负载电阻电路,由牛顿第二定律对该复合结构进行受力分析得[16]

$$M\ddot{\boldsymbol{Y}}+C\dot{\boldsymbol{Y}}+K\boldsymbol{Y}-\boldsymbol{\Theta}U=\boldsymbol{F}_L(t) \tag{5}$$

$$C_p\dot{U}+\frac{U}{R}+\boldsymbol{\Theta}\dot{\boldsymbol{Y}}=0 \tag{6}$$

其中 $$\boldsymbol{F}_L(t)=\frac{1}{2}\rho v^2AC_L(t) \tag{7}$$

式中 M——圆柱单元长度的质量,kg

$\boldsymbol{Y}$——圆柱轴线沿 Y 轴方向的位移,m

C——结构阻尼常数

(C)1994-2023 China Academic Journal Electronic Publishing House. All rights reserved. http://www.cnki.net

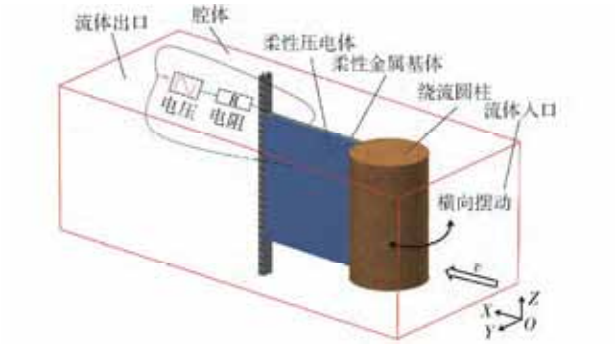


图 4　压电悬臂梁复合结构自发电模型

Fig. 4　Self-generation model of composite structure of piezoelectric cantilever beam

K——结构刚度常数

Θ——系统机电耦合项，N/V

C_p——压电材料的电容，F

R——负载电阻，Ω

U——负载电阻的电压，V

$\boldsymbol{F}_L(t)$——圆柱不同时刻在 Y 轴方向上所受的升力，N

C_L——升力系数

A——圆柱在垂直于来流方向上的迎流投影面积，m^2

为了计算压电悬臂梁复合结构的一阶横向振动频率，选用圆柱直径 D 和流场特征速度 v 作为长度和速度尺度，式(5) ~ (7) 可简写为

$$\ddot{\boldsymbol{Y}}^* + \left(\frac{4\pi\xi}{v^*}\right)\dot{\boldsymbol{Y}}^* + \left(\frac{2\pi}{v^*}\right)^2\boldsymbol{Y}^* - \left(\frac{1}{v^*}\right)U^* = \frac{2}{\pi m^*}\boldsymbol{F} \tag{8}$$

$$\dot{U}^* + \frac{v^* U^*}{RCpf_N} + \frac{\Theta^2\dot{Y}^*}{MCpf_N^2} = 0 \tag{9}$$

其中

$$\boldsymbol{Y}^* = \boldsymbol{Y}/D \tag{10}$$

$$v^* = v/(f_N D) \tag{11}$$

$$\zeta = C/(2\sqrt{KM}) \tag{12}$$

$$m^* = 4m/(\rho\pi D^2) \tag{13}$$

$$U^* = U\Theta/(Mf_N^2 D) \tag{14}$$

$$\boldsymbol{F} = -\int_0^{2\pi}\left(p\sin\theta - \frac{1}{Re}\omega_v\cos\theta\right)\mathrm{d}\theta \tag{15}$$

式中　$\boldsymbol{Y}^*$——圆柱无量纲沿 Y 轴方向的位移

v^*——约化速度，m/s

ξ——结构阻尼比率　　m^*——质量比

U^*——无量纲电压

$\boldsymbol{F}$——流场涡脱力，N

p——流体压力，Pa

ω_v——圆柱表面的翼展涡度分量

θ——面积分量的外法线与流动方向所成的角度，rad

f_N——压电悬臂梁复合结构一阶横向振动频率，Hz

由于固定于压电悬臂梁复合结构末端的圆柱不发生变形，设压电悬臂梁复合结构的绝对横向位移为 $u(x,t)$，根据达朗贝尔原理[17]，视为刚体的圆柱在振动过程中可等效为惯性力 F_g 和惯性力矩 M_g，计算公式为[18]

$$F_g = -M\left[\ddot{u}(L_2,t) + (L-L_2)\frac{\partial\ddot{u}(L_2,t)}{\partial x}\right] \tag{16}$$

$$M_g = -M(L-L_2)\ddot{u}(L_2,t) - \left[J + M(L-L_2)^2\right]\frac{\partial\ddot{u}(L_2,t)}{\partial x} \tag{17}$$

式中　L_2——压电材料长度，m

L——金属基板长度，m

J——圆柱对其重心的转动惯量，$kg\cdot m^2$

由此可得到装载圆柱的压电悬臂梁复合结构的频率特征方程和振动方程分别为

$$1 + \frac{JM\alpha^4}{\Lambda^2} + \cos(\alpha L_2)\cosh(\alpha L_2)\left(1 - \frac{JM\alpha^4}{\Lambda^2}\right) - \frac{M + [J + (L-L_2)M]\alpha^2}{\Lambda}\sin(\alpha L_2)\cosh(\alpha L_2) - \frac{\{[J + (L-L_2)^2 M]\alpha^2 - M\}\alpha}{\Lambda}\cos(\alpha L_2)\sinh(\alpha L_2) - 2\frac{(L-L_2)M\alpha^2}{\Lambda}\sin(\alpha L_2)\sinh(\alpha L_2) = 0 \tag{18}$$

$$\alpha^4 = \frac{\rho_1 A_1}{EJ}\omega^2 \tag{19}$$

其中

$$\omega = 2\pi/f_N \tag{20}$$

式中　ρ_1——压电悬臂梁密度，kg/m^3

A_1——压电悬臂梁横截面积，m^2

E——压电悬臂梁弹性模量，Pa

ω——压电悬臂梁复合结构固有角频率，rad/s

联立式(18) ~ (20)，可求得 f_N。

综上可求得三阶常微分方程耦合系统方程为

$$\dot{\sigma}_1 = \sigma_2 \tag{21}$$

$$\dot{\sigma}_2 = -\left(\frac{2\pi}{v^*}\right)^2\sigma_1 - \frac{4\pi\xi}{v^*}\sigma_2 + \frac{1}{v^{*2}}\sigma^3 + \frac{2}{\pi m^*}C_L \tag{22}$$

$$\dot{\sigma}_3 = -\frac{\Theta^2}{MCp}\sigma^2 - \frac{1}{RCpf_N v^*}\sigma^3 \tag{23}$$

其中

$$\sigma_1 = \boldsymbol{Y}^*\quad \sigma_2 = \dot{\boldsymbol{Y}}^*\quad \sigma_3 = U^*$$

3　流场数值分析

由于流体在绕流圆柱和压电悬臂梁复合结构的共同作用下呈现为湍流，运动形态复杂且难于直接观察，因此本文利用计算流体动力学软件 Fluent 对

(C)1994-2023 China Academic Journal Electronic Publishing House. All rights reserved.　http://www.cnki.net

涡激振动自发电装置的内部流场进行分析，以明确系统的结构参数。

由于亥姆霍兹共振器的共振频率仅与自身结构参数有关[19]，为简化计算过程，本文先使得卡门涡街的脱涡频率、压电悬臂梁复合结构的一阶横向振动频率相等后，再通过设定亥姆霍兹共振器的结构尺寸使 3 个频率达到一致。

3.1 腔体流场设置

赵静等[20]研究表明，当在 $Re=1\,000$ 的条件下，单圆柱尾流侧增设横隔板时，斯特劳哈尔数 St 减小，进而引起脱涡频率发生改变，导致升力幅值增加，并增大压电悬臂梁的摆动幅度。段志强[21]进一步探讨在 $Re=200$ 的条件下，三维圆柱层流模型和不同楔形板长对绕流流场、斯特劳哈尔数 St 和升阻力系数的影响，结果表明，当板长与圆柱直径之比等于 2.5 时，升力系数幅值出现极大值。KWON 等[22]研究结果表明，板长对流场特性的影响与雷诺数有关。梁亮文[23]研究表明，当圆柱的摆动频率与其自身脱涡频率相近时，尾流沿圆柱高度方向的流动会被圆柱抑制，使得流场在较大的雷诺数范围内没有明显的三维特性。由于升力系数均方根在阻流比为 0.2 时达到最大[24]，为使亥姆霍兹共振器的脉冲射流能对圆柱产生作用，以圆柱直径 D 为基准尺度，设置腔体有限流道内流场计算域的范围为 $5D\times45D$，圆柱中心距离流场入口和出口分别为 $5D$ 和 $40D$，两侧壁面距离圆柱中心均为 $2.5D$，最终在计算流体力学软件 Fluent 中所建立的腔体二维流场域模型如图 5 所示。

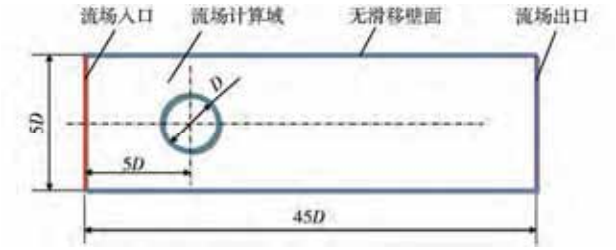


图 5 腔体二维流场域模型

Fig. 5 Two-dimensional flow field model of cavity

3.2 单圆柱绕流数值分析

为验证流场计算结果的准确性，先对 $Re=200$ 时的单圆柱绕流进行数值模拟。数值计算时的边界条件如下：

(1) 模型入口和出口分别设置为速度入口(Velocity inlet)和压力出口(Pressure outlet)，其中入口处的速度为 0.292 m/s，出口绝对压力为 1.01×10^{-5} Pa，环境温度为 25℃，整个流场为等温单相流模型。

(2) 数值计算时工作流体为理想空气，密度为 1.225 kg/m^3，动力粘性系数 μ 为 $1.789\,4\times10^{-5}$ Pa·s。

(3) 整个流场计算域基于纳维-斯托克斯方程(Navier-Stokes equations，N-S 方程)，并使用大涡模拟(Large eddy simulations，LES)湍流模型进行求解。为准确捕捉腔体有限流道内的流场动力学特性，设定流场计算域的基本单元尺寸设置为 1 mm，并对圆柱周面及两侧壁面进行 12 级细化处理，采用混合网格对整个计算域进行划分，最终得到计算域的单元数为 34 554，节点数为 35 071。

(4) 为使卡门涡街的瞬态动力学行为精细化，将流场域求解时间步长设为涡旋脱落周期的 1/20。

图 6 为单圆柱绕流的涡量图。从图 6 可以看出，气体流动在圆柱后面发生分离，并在圆柱尾部附近形成一定频率的卡门涡街。图 7 为单圆柱绕流的升阻力系数随流动时间变化的关系曲线。从图 7 可看出，升阻力系数均呈现周期性的变化，并且阻力系数的变化频率为升力系数的两倍，这一规律与 JIANG 等[25]研究结果一致。

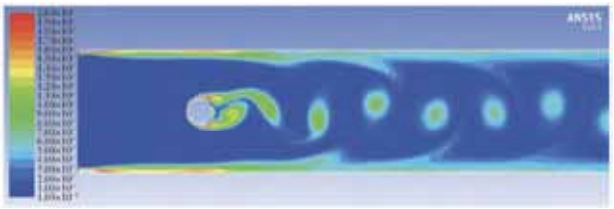


图 6 单圆柱绕流的涡量云图

Fig. 6 Vorticity cloud of single cylinder

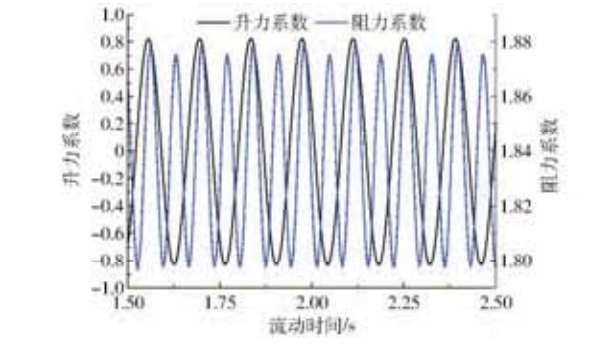


图 7 单圆柱绕流的升阻力系数随时间的变化曲线

Fig. 7 Variation curves of lift-resistance coefficient of single cylinder

通过对图 7 中单圆柱绕流的升力系数曲线进行快速傅里叶变换，得到该条件下单圆柱绕流脱涡频率 $f=7.14$ Hz，利用式(2)和式(3)求得此时的斯特劳哈尔数为 0.183，与经验式(4)的相对误差为 7.1%。

3.3 不同板长对流场特性的影响

为研究流场中压电悬臂梁复合结构柔性金属基板的板长 L 对斯特劳哈尔数 St 和升阻力系数的影响，基于单圆柱绕流流场设置对腔体流场进行仿真

(C)1994-2023 China Academic Journal Electronic Publishing House. All rights reserved. http://www.cnki.net

分析。由于固定和自由边界条件下长短悬臂梁的脱涡频率不变[26]，本文将忽略流体与固体之间的交互作用对脱涡频率的影响。根据江滢等[27]的研究结果，为适应沿海地区夏季近地层自然风速，将流场入口来流速度设为 5 m/s，在此条件下雷诺数 Re 为 3 424。

图 8 为绕流圆柱后方附加不同板长条件下，内流场的涡量云图。从图 8 可以看出，圆柱后附加的压电悬臂梁复合结构明显影响了边界层的气流分离，使得涡旋脱落的起点沿流动方向下移。而且随压电悬臂梁复合结构长度 L 的增加，边界层气流分离的起始点距离圆柱也越远，同时涡间距离变大。

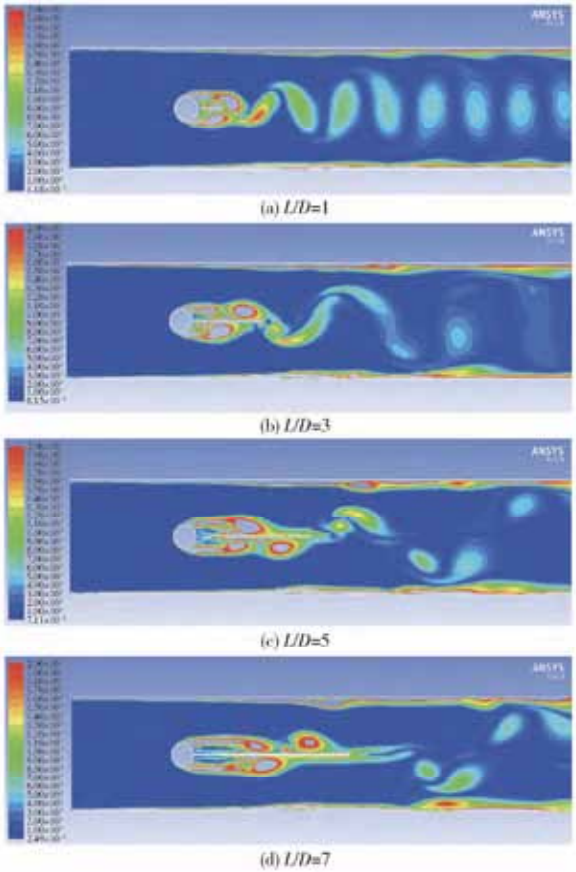


图 8　不同板长条件下流场涡量云图

Fig. 8　Vorticity clouds of flow field under different plate length conditions

图 9 为升力、阻力系数和脱涡频率随板长 L 变化的关系曲线。从图 9 可以看出，当 $L/D=2$ 时，升力系数幅值出现最大值为 1.3。这表明在此条件下，压电悬臂梁复合结构的振幅最大。此后，随着板长 L 的增加，升力、阻力系数均呈减小趋势。此外，图 9 还表明，脱涡频率 f 并非定值，其随板长 L 的增大而减小，在 $L/D=1$ 取得最大值为 130 Hz。显然，带压电悬臂梁复合结构的圆柱体流场的斯特劳哈尔数 St 与板长 L 为非线性的关系。

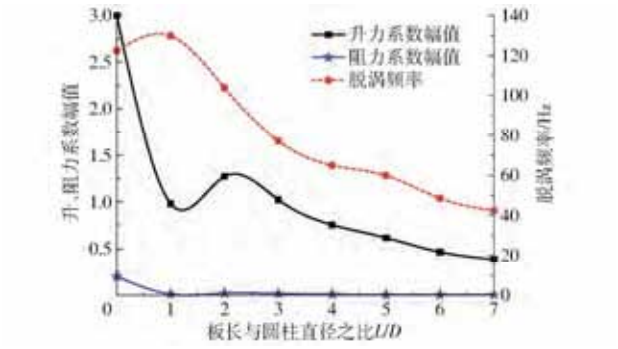


图 9　流场参数随板长的变化曲线

Fig. 9　Variation curves of flow field parameter with board length

4　压电悬臂梁复合结构横向振动频率随板长变化规律

为使压电悬臂梁复合结构的横向振动频率与流场中的脱涡频率一致，利用有限元软件 ANSYS 的动力学和压电分析模块，对压电悬臂梁进行模态分析，以求得到不同板长条件下压电悬臂梁复合结构的一阶横向振动频率。考虑悬臂梁复合结构在工作时须做往复运动[28]，因此分别选用紫铜和聚偏氟乙烯（Polyvinylidene fluoride，PVDF）压电薄膜作为柔性金属基体和柔性压电体的材料；ABS 工程塑料（Acrylonitrile-butadiene-styrene copolymer）作为绕流圆柱的材料。材料参数如表 1 所示。

表 1　材料参数

Tab. 1　Parameters of materials

参数	材料		
	紫铜	ABS 工程塑料	PVDF 压电薄膜
密度 ρ_2/(kg·m^{-3})	8 960	1 050	1 780
弹性模量 E_2/GPa	110	2.5	2.5
泊松比 μ_2	0.320	0.394	
压电常数 d_{33}/(pC·N^{-1})			21
相对压电常数			9.5
机电耦合系数 K_{33}/%			12

图 10 为压电悬臂梁复合结构长度 $L/D=3$ 时一阶横向振动模态振型图。此时，复合结构的一阶横向振动频率为 61.085 Hz。图 11 为压电悬臂梁复合结构一阶横向振动频率和脱涡频率随板长 L 变化的关系曲线。由图 11 可知，复合结构的横向振动频率随板长 L 的增加而减小，当 $L/D=1.8$ 时，压电悬臂梁复合结构的一阶横向振动频率与该条件下流场脱涡频率一致，为 113 Hz。在此条件下，压电悬臂梁复合结构受流场涡激力作用产生共振，使其横向振动的振幅增大。

(C)1994-2023 China Academic Journal Electronic Publishing House. All rights reserved.　http://www.cnki.net

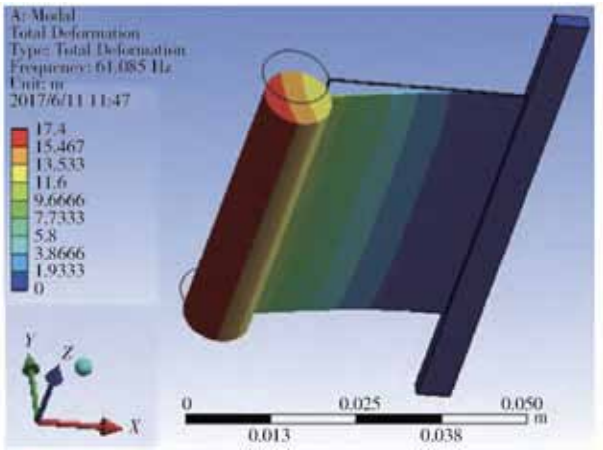


图 10 压电悬臂梁复合结构一阶横向振动模态振型图($L/D=3$)

Fig. 10 First-order transverse vibration mode of composite structure of piezoelectric cantilever beam($L/D=3$)

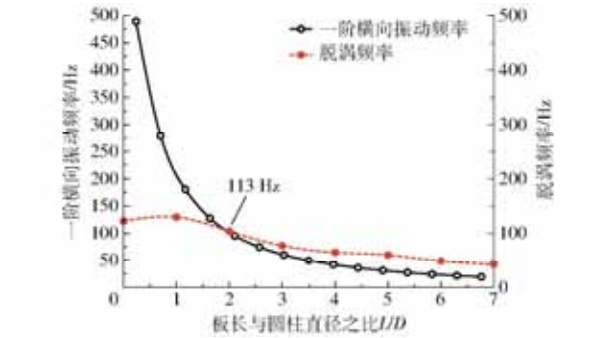


图 11 压电悬臂梁复合结构的一阶横向振动频率和脱涡频率随板长 L 的变化曲线

Fig. 11 Variation curves of first-order transverse vibration and frequency of composite structure of piezoelectric cantilever beam with board length L

5 亥姆霍兹共振器结构优化设计

亥姆霍兹共振器由一个带开口颈部短管的空腔构成。它受外界声场的激发引起空腔气体的振动，同时空腔内的振动又通过短管发出声波加强外界的声场，因此可将其等效为弹簧-质量系统，颈部短管气体体积和空腔气体体积分别等效为质量块和弹簧，其结构示意图如图 12 所示。共振器内气体振动的频率为[29]

$$f_{HR}=\frac{C_1}{2\pi}\sqrt{\frac{S}{VL_1}} \tag{24}$$

其中

$$V=\pi\,(d'/2)^2 l' \tag{25}$$

$$L_1=l+0.85d \tag{26}$$

式中 f_{HR}——亥姆霍兹共振器的谐振频率，Hz

C_1——大气声速，25℃条件下为 346 m/s

S——颈部短管截面面积，m^2

V——容腔容积，m^3

d'——容腔底部直径，m

l'——容腔高度，m

L_1——颈部短管的有效长度，m

l——短管长度，m

d——短管直径，m

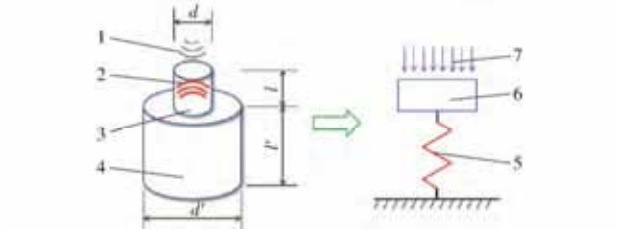


图 12 亥姆霍兹共振器和弹簧-质量系统

Fig. 12 Helmholtz resonator and spring-quality system

1. 外界声场 2. 反射声场 3. 颈部短管 4. 容腔 5. 弹簧 6. 质量块 7. 压力

此外，声场放大比率 G 的表达式为[30-31]

$$G=2\pi\sqrt{V\left(\frac{L_1}{S}\right)^3} \tag{27}$$

高虹[11]研究表明，当外界气流压力扰动的频率是亥姆霍兹共振器的整数倍时，共振器空腔内可以产生自激振荡脉冲射流。因此，本节的优化目标是使声场放大比率 G 达到最大，同时共振器谐振频率与压电悬臂梁复合结构的横向振动频率一致。考虑到压电悬臂梁复合结构的实际尺寸，故共振器优化设计的数学模型可表述为

$$\begin{aligned}&\max G(d',d,l',l)\\ &\text{s. t.}\begin{cases}f_{HR}=113\ \text{Hz}\\ 0.002\ \text{m}\leqslant d'\leqslant 0.1\ \text{m}\\ 0.002\ \text{m}\leqslant d\leqslant 0.1\ \text{m}\\ 0.002\ \text{m}\leqslant l'\leqslant 0.1\ \text{m}\\ 0.002\ \text{m}\leqslant l\leqslant 0.1\ \text{m}\end{cases}\end{aligned} \tag{28}$$

式中：d'、d、l'、l 均为设计变量。利用罚函数法[32]，经优化计算后可得到亥姆霍兹共振器的几何尺寸如表 2 所示，此时声场放大比率 $G=1\,225.82$。

表 2 亥姆霍兹共振器的几何尺寸

Tab. 2 Geometric dimensions of Helmholtz resonator m

参数	数值
容腔底部直径 d'	0.095 3
短管直径 d	0.011 2
容腔高度 l'	0.083 3
短管长度 l	0.029 9

为了提高声场放大功效，本文采用亥姆霍兹共振器组对称布置的方式(图 1)，当脉冲射流从一侧的共振器喷出，推动压电悬臂梁复合结构从中部开始产生向另一侧的横向振动，同时另一侧的共振器处于气体吸入阶段，其出口处产生负压从而拉动压

(C)1994-2023 China Academic Journal Electronic Publishing House. All rights reserved. http://www.cnki.net

电悬臂梁复合结构继续向该侧摆动。当共振器组的脉冲射流进程和吸气进程结束时，压电悬臂梁复合结构达到振幅最大，随后在结构本身弹性力的作用下，向另一侧摆动。由于共振器的谐振频率与压电悬臂梁复合结构的横向振动频率一致，因此，这一过程将循环往复。

图 13 为一个周期内，自发电装置流场在 4 个典型时刻的压力云图。从图 13 可以看出，在圆柱和压电悬臂梁复合结构后部均出现涡旋脱落。其中，在 $T/4$ 和 $3T/4$ 时刻（图 13a），2 个亥姆霍兹共振器内压强相等，此时圆柱处在腔体中部平衡位置；在 $T/2$ 时刻（图 13b），涡旋从压电悬臂梁复合结构的下端部脱落，此时圆柱受到流场升力作用横向振动到腔体下侧，同时 1 号亥姆霍兹共振器的压强变大，处于脉冲射流进程，推动圆柱远离平衡位置，而 2 号亥姆霍兹共振器内为负压，处于吸气进程。同理，在 T 时刻（图 13c），1 号亥姆霍兹共振器处于吸气进程而 2 号亥姆霍兹共振器处于脉冲射流进程。

为明确自发电装置内流场的压强变化规律，在流场内设置了 4 个监测点 A、B、C 和 D（图 13a），图 14 为 4 个监测点的压力随时间变化曲线。由图 14 可知，同一共振器容腔内部的压力始终大于颈部短管处压力。同时，2 个共振器不停在正压—脉冲射流、负压—吸气这 2 个进程之间有规律变换，且同时到达极限值，这种流场压力的变化规律验证了设计的合理性。

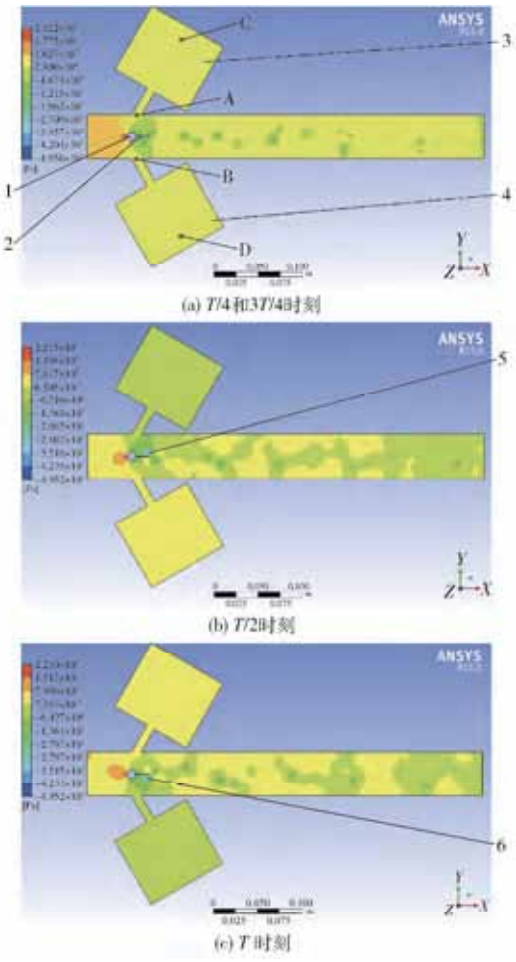


图 13　不同时刻自发电装置流场压力云图

Fig. 13　Flow field pressure clouds of self-generating device at different times

1. 圆柱　2. 压电悬臂梁复合结构　3. 1 号亥姆霍兹共振器　4. 2 号亥姆霍兹共振器　5、6. 涡旋

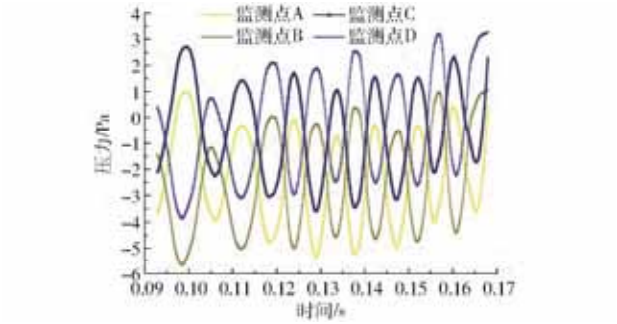


图 14　4 个监测点处压力的时间历程图

Fig. 14　Time history of pressure at four monitoring points

6　试验

为验证涡激振动自发电装置的自发电能力和振动特性，根据上述的理论结果，采用相同材料加工的试验样机如图 15 所示。其中，柔性金属基体和柔性压电体厚度均为 0. 1 mm。



图 15　自发电装置试验样机

Fig. 15　Test prototype of self-generating device

1. 腔体　2. 绕流圆柱　3. 压电悬臂梁复合结构　4. 基座　5. 亥姆霍兹共振器

6. 1　自发电能力试验测试

自发电测试的试验装置如图 16 所示，主要由可调速鼓风机（CZR 型，上海沈业节能设备有限公司）、智能风速风压风量仪（YC-2000A 型，龙岩亚成仪器仪表有限公司）、数字示波器（GDS-2004A 型，苏州固纬电子有限公司）、小型升降台（OMY-200 型，北京柠檬科技有限公司）、压电薄膜（PVDF-100 型，锦州科信电子材料有限公司）等组成。

气流从涡激振动自发电装置的入口处流入，流速可通过鼓风机进行调节，并且由智能风速风压风量仪读取。用风速风压风量仪在入口处测量 3 次，取平均值作为入口风速的测量值。气流通过绕流圆

(C)1994-2023 China Academic Journal Electronic Publishing House. All rights reserved.　http://www.cnki.net

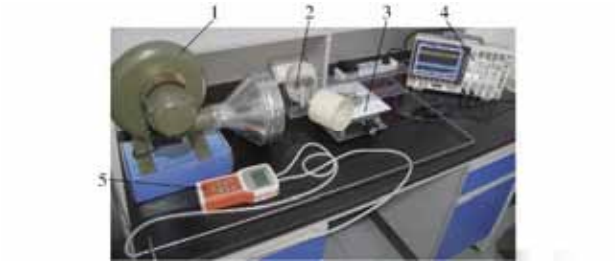


图 16 自发电能力测量试验实物装置

Fig. 16 Physical device of self-generating capacity measurement test

1. 可调速鼓风机 2. 涡激振动自发电装置 3. 小型升降台 4. 数字示波器 5. 智能风速风压风量仪

柱后产生涡旋,而涡旋的脱落又使得绕流圆柱和压电悬臂梁复合结构产生往复式横向振动,由此产生的电压幅值通过数字示波器记录。图 17 为自发电装置在 5 m/s 的风速下产生的理论与试验电压波形,试验测得最大输出电压幅值为 6.0 V。

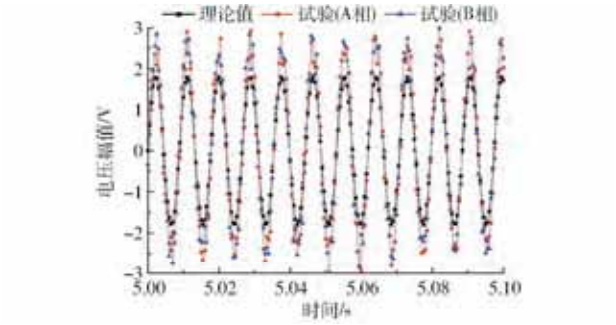


图 17 自发电装置的理论与试验电压幅值

Fig. 17 Theoretical and experimental voltage waveforms of self-generating device

6.2 锁定风速区间测量试验

当圆柱后方涡旋脱落的频率接近于自身横向振动的固有频率时,脱涡频率会被锁定在固有频率上,圆柱振幅会显著增大但振动频率保持不变,当外界风速改变时,脱涡频率不受影响,这就是锁定现象[33]。为了确定该装置的锁定范围,通过测量不同风速条件下样机的发电能力,以求得锁定风速区间。

图 18 为自发电装置在不同入口风速条件下产生的电压幅值。从图 18 可看出,当入口风速在 4 ~ 6.25 m/s 区间内时,自发电装置的脱涡频率被锁定,且能产生输出较大的电压幅值,说明该装置对近地层不同风速的适应能力较强。为获得锁定区间内的脱涡频率,将智能风速风压风量仪的皮托管探头前端置于距离该装置内部的基座 5 cm 处,测量该点实际压力随时间的变化情况,并通过对其进行快速傅里叶变换,得到此时的脱涡频率为 116 Hz。

6.3 振动特性测量试验

为确定绕流圆柱和压电悬臂梁复合结构的横向振动频率,利用激光测振仪(LV-S01 型,舜宇光学科技有限公司)对绕流圆柱的横向振动振幅进行测量,所搭建的测量装置如图 19 所示。

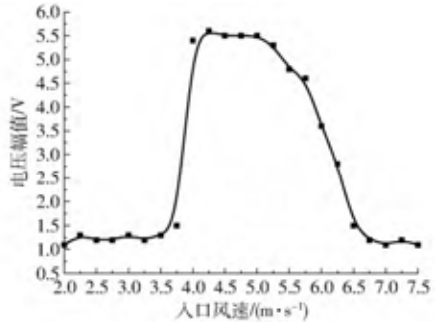


图 18 自发电装置在不同风速下产生的电压幅值

Fig. 18 Voltage magnitude generated by self-generating device at different wind speeds

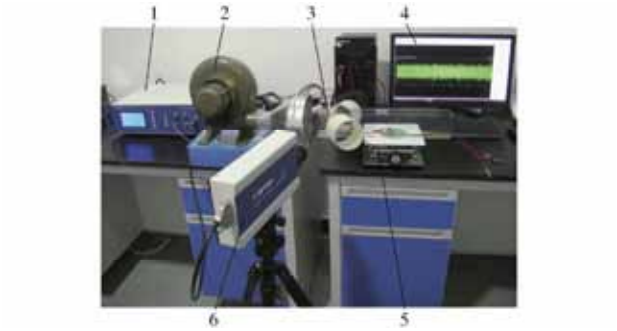


图 19 振幅测量试验实物装置

Fig. 19 Physical device of amplitude measurement test

1. 激光测振仪控制器 2. 可调速鼓风机 3. 涡激振动自发电装置 4. 计算机 5. 小型升降台 6. 激光测振仪光学头

图 20 为绕流圆柱在入口风速为 5 m/s 条件下的理论与试验振幅,由图 20 可以看出,绕流圆柱受涡旋脱落的影响,产生周期性的往复式摆动,其最大振幅可达到 7.6 mm。图 21 为对该曲线进行快速傅里叶变换后的频谱图,可得到绕流圆柱的实际摆动频率为 110 Hz。试验结果表明,在外界气流的冲击下,亥姆霍兹共振器产生谐振,绕流圆柱和压电悬臂梁复合结构发生横向振动,使得柔性压电体产生稳定的电压,且摆动频率与亥姆霍兹共振器的固有频率一致,数值计算结果与试验较为吻合。

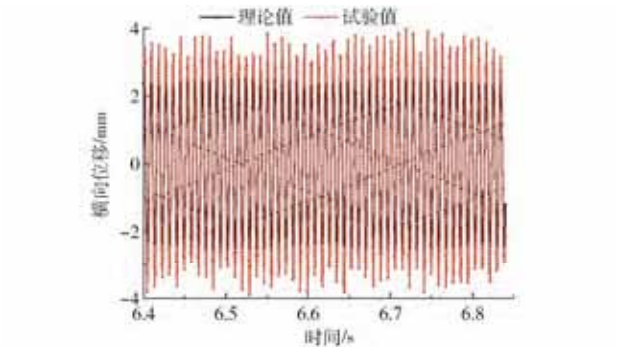


图 20 绕流圆柱在风速为 5 m/s 时的振幅

Fig. 20 Amplitude of cylinder at speed of 5 m/s

(C)1994-2023 China Academic Journal Electronic Publishing House. All rights reserved. http://www.cnki.net

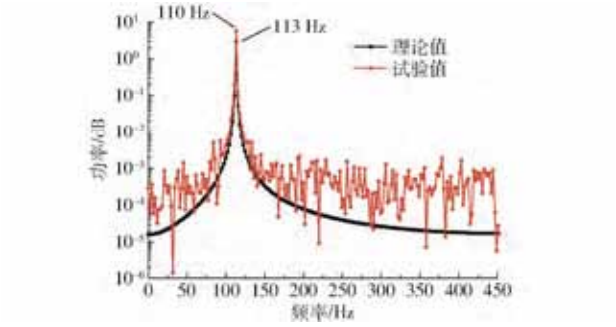


图 21　绕流圆柱振幅的频谱图

Fig. 21　Spectrum of amplitude of cylinder

7　结论

（1）基于 Fluent 的数值分析结果表明，绕流圆柱后方附加的压电悬臂梁复合结构明显影响了边界层的气流分离。在相同风速下，脱涡频率 f 和升力、阻力系数均随板长 L 的变化而改变。其中，随着板长 L 的增加，阻力系数幅值呈减小趋势，而升力系数幅值呈先急剧减小，随后缓慢增加，再逐步减小的趋势。当 $L/D=2$ 时，升力系数幅值出现极大值 1.3，此时压电悬臂梁复合结构的振幅最大。

（2）在 5 m/s 的风速下，绕流圆柱的振动频率为 110 Hz，且流场的涡脱频率、压电悬臂梁复合结构摆动频率与亥姆霍兹共振器的谐振频率一致，数值计算结果与试验较为吻合。

（3）自发电装置在 5 m/s 的风速下可产生两相稳定的开路电压，并且测得最大输出电压幅值为 6.0 V，最大振幅可达到 7.6 mm。当入口处风速范围在 4 ~ 6.25 m/s 时，为该自发电装置的自锁风速区间，在此风速范围内，自发电装置均能产生较大的电压。

参　考　文　献

1　葛文杰，赵春江. 农业物联网研究与应用现状及发展对策研究[J/OL]. 农业机械学报，2014，45(7)：222 - 230. http://www.j-csam.org/jcsam/ch/reader/view_abstract.aspx? flag=1&file_no=20140735&journal_id=jcsam. DOI：10.6041/j.issn.1000-1298.2014.07.035.
GE Wenjie, ZHAO Chunjiang. State-of-the-art and developing strategies of agricultural internet of things [J]. Transactions of the Chinese Society for Agricultural Machinery, 2014, 45(7): 222 - 230. (in Chinese)

2　罗锡文，臧英，周志艳. 精细农业中农情信息采集技术的研究进展[J]. 农业工程学报，2006，22(1)：167 - 173.
LUO Xiwen, ZANG Ying, ZHOU Zhiyan. Research progress in farming information acquisition technique for precision agriculture [J]. Transactions of the CSAE, 2006, 22(1): 167 - 173. (in Chinese)

3　SHAIKH F K, ZEADALLY S. Energy harvesting in wireless sensor networks: a comprehensive review [J]. Renewable and Sustainable Energy Reviews, 2016, 55: 1041 - 1054.

4　YUAN F, JIN S, WONG K K, et al. Wireless information and power transfer design for energy cooperation distributed antenna systems [J]. IEEE Access, 2017, 5: 8094 - 8105.

5　LU X, WANG P, NIYATO D, et al. Wireless networks with RF energy harvesting: a contemporary survey [J]. IEEE Communications Surveys & Tutorials, 2015, 17(2): 757 - 789.

6　MA S, YANG Y, QIAN Y. Energy harvesting for wireless sensor networks: applications and challenges in smart grid [J]. International Journal of Sensor Networks, 2016, 21(4): 226 - 241.

7　赵勇，韩斌，房刚利. 风力发电机状态监测与故障诊断技术综述[J]. 热力发电，2016，45(10)：1 - 5.
ZHAO Yong, HAN Bin, FANG Gangli. A survey of condition monitoring and fault diagnosis for wind power generators [J]. Thermal Power Generation, 2016, 45(10): 1 - 5. (in Chinese)

8　程廷海，王英廷，付贤鹏，等. 定质量分数交变气体载荷激励下压电阵列发电机实验[J/OL]. 农业机械学报，2017，48(2)：407 - 412. http://www.j-csam.org/jcsam/ch/reader/view_abstract.aspx? flag=1&file_no=20170255&journal_id=jcsam. DOI：10.6041/j.issn.1000-1298.2017.02.055.
CHENG Tinghai, WANG Yingting, FU Xianpeng, et al. Experiment on piezoelectric plate array energy harvester excited by alternate high air pressure with constantly gaseous mass [J/OL]. Transactions of the Chinese Society for Agricultural Machinery, 2017, 48(2): 407 - 412. (in Chinese)

9　BOWEN C R, KIM H A, WEAVER P M, et al. Piezoelectric and ferroelectric materials and structures for energy harvesting applications [J]. Energy & Environmental Science, 2014, 7(1): 25 - 44.

10　HEIL M, ROSSO J, HAZEL A. Topological fluid mechanics of the formation of the Kármán-vortex street [J]. Journal of Fluid Mechanics, 2017, 812: 199 - 221.

11　高虹. Helmholtz 共振的机理研究及应用[D]. 重庆：重庆大学，2003.
GAO Hong. Mechanism of Helmholtz oscillator and its application [D]. Chongqing: University of Chongqing, 2003. (in Chinese)

12　白桦，李加武，夏勇. 低雷诺数圆柱绕流数值模拟及控制措施[J]. 建筑科学与工程学报，2010，27(4)：39 - 43.
BAI Hua, LI Jiawu, XIA Yong. Numerical simulation and control measures of flow around circular cylinders at low Reynolds number [J]. Journal of Architecture and Civil Engineering, 2010, 27(4): 39 - 43. (in Chinese)

13　XU F, CHEN W L, BAI W F, et al. Flow control of the wake vortex street of a circular cylinder by using a traveling wave wall at low Reynolds [J]. Computers & Fluids, 2017, 145: 52 - 67.

(C)1994-2023 China Academic Journal Electronic Publishing House. All rights reserved.　http://www.cnki.net

14 文晟，张铁民，杨秀丽，等. 涡致振动型风力压电俘能器流场数值模拟与试验[J/OL]. 农业机械学报，2014，45(2)：269－275. http://www.j-csam.org/jcsam/ch/reader/view_abstract.aspx? flag=1&file_no=20140245&journal_id=jcsam. DOI：10.6041/j.issn.1000-1298.2014.02.045.
WEN Sheng, ZHANG Tiemin, YANG Xiuli, et al. Numerical simulation and experiment of a wind piezoelectric energy harvester based on vortex-induced vibrations[J/OL]. Transactions of the Chinese Society for Agricultural Machinery, 2014, 45(2):269－275. (in Chinese)

15 BOUZARI S, GHAZANFARIAN J. Unsteady forced convection over cylinder with radial fins in cross flow[J]. Applied Thermal Engineering, 2016, 112:214－225.

16 MEHMOOD A, ABDELKEFI A, HAJJ M R, et al. Piezoelectric energy harvesting from vortex-induced vibrations of circular cylinder[J]. Journal of Sound and Vibration, 2013, 332(19):4656－4667.

17 鹿玲，姚建涛，顾伟栋，等. 基于 Kane 方程的冗余驱动 5UPS/PRPU 并联机床动力学分析[J/OL]. 农业机械学报，2016，47(6)：366－372. http://www.j-csam.org/jcsam/ch/reader/view_abstract.aspx? flag=1&file_no=20160648&journal_id=jcsam. DOI：10.6041/j.issn.1000-1298.2016.06.048.
LU Ling, YAO Jiantao, GU Weidong, et al. Dynamics analysis of 5UPS/PRPU parallel machine tool with redundant actuation based on Kane equation[J/OL]. Transactions of the Chinese Society for Agricultural Machinery, 2016, 47(6):366－372. (in Chinese)

18 张淼，孟庆丰，王宏金. 考虑疲劳寿命的压电悬臂梁结构优化设计方法[J]. 压电与声光，2015，37(1)：68－72.
ZHANG Miao, MENG Qingfeng, WANG Hongjin. Structure optimization design method for piezoelectric cantilever beam considering fatigue life[J]. Piezoelectrics & Acoustooptics, 2015, 37(1):68－72. (in Chinese)

19 PILLAI M A, EZHILARASI D. Improved acoustic energy harvester using tapered neck Helmholtz resonator and piezoelectric cantilever undergoing concurrent bending and twisting[J]. Procedia Engineering, 2016, 144:674－681.

20 赵静，潘树春，吕林，等. 带横隔板圆柱绕流的三步有限元大涡模拟[J]. 中国海上油气，2009，21(5)：347－351.
ZHAO Jing, PAN Shuchun, LÜ Lin, et al. Large eddy simulation of flow past a circular cylinder with splitter plate based on three-step finite element method[J]. China Offshore Oil and Gas, 2009, 21(5):347－351. (in Chinese)

21 段志强. 低雷诺数下尾部隔板影响圆柱绕流的数值研究[D]. 重庆：重庆大学，2012.
DUAN Zhiqiang. An numerical investigation on fluid flow past a circular cylinder with splitter plate at low Reynolds number[D]. Chongqing: University of Chongqing, 2012. (in Chinese)

22 KWON K, CHOI H. Control of laminar vortex shedding behind a circular cylinder using splitter plates[J]. Physics of Fluids, 1996, 8(2):479－486.

23 梁亮文. 低雷诺数下圆柱横向受迫振荡和涡激运动的数值分析[D]. 上海：上海交通大学，2009.
LIANG Liangwen. Numerical analysis of forced oscillation and vortex-induced motion of circular cylinder in cross flow with low Reynolds number[D]. Shanghai: Shanghai Jiao Tong University, 2009. (in Chinese)

24 蒋赟. 阻流比与长径比对低雷诺数圆柱绕流尾迹演化的影响研究[D]. 长沙：中南大学，2014.
JIANG Yun. The effect of blockage ratio and aspect ration on the evolution of circular cylinder wake at low Reynolds numbers[D]. Changsha: Central South Univesity, 2014. (in Chinese)

25 JIANG X, ANDREOPOULOS Y, LEE T, et al. Numerical investigations on the vortex-induced vibration of moving square cylinder by using incompressible lattice Boltzmann method[J]. Computers & Fluids, 2016, 124:270－277.

26 EVANGELINOS C, LUCOR D, KARNIADAKIS G. DNS-derived force distribution on flexible cylinders subject to vortex-induced[J]. Journal of Fluids and Structures, 2000, 14(3):429－440.

27 江滢，赵宗慈. 中国沿海地区夏季风速时空变化特征和气候模式结果评估与预估分析[J]. 科技导报，2011，29(6)：21－30.
JIANG Ying, ZHAO Zongci. Characteristics of summer wind speed changes over coastal region of China[J]. Science & Technology Review, 2011, 29(6):21－30. (in Chinese)

28 黄健萌，黄靖. 压电驱动微悬臂梁与基底粗糙面间多次接触分析[J/OL]. 农业机械学报，2015，46(9)：368－372. http://www.j-csam.org/jcsam/ch/reader/view_abstract.aspx? flag=1&file_no=20150954&journal_id=jcsam. DOI：10.6041/j.issn.1000-1298.2015.09.054.
HUANG Jianmeng, HUANG Jing. Multiple-contact analysis between microcantilever and substrate rough surface driven by piezoelectric[J/OL]. Transactions of the Chinese Society for Agricultural Machinery, 2015, 46(9):368－372. (in Chinese)

29 HOUSTON B, WANG J, QIN Q, et al. Experimental and numerical investigation of Helmholtz resonators and perforated liners as attenuation devices in industrial gas turbine combustors[J]. Fuel, 2015, 151:31－39.

30 NOH S, LEE H, CHOI B. A study on the acoustic energy harvesting with Helmholtz resonator and piezoelectric cantilevers[J]. International Journal of Precision Engineering and Manufacturing, 2013, 14(9):1629－1635.

31 NEMATI N, KUMAR A, LAFARGE D, et al. Nonlocal description of sound propagation through an array of Helmholtz resonators[J]. Comptes Rendus Mecanique, 2015, 343(12): 656－669.

32 张建桃，李晟华，文晟，等. 农用超声雾化换能器参数优化设计与试验[J]. 农业工程学报，2015，31(12)：8－15.
ZHANG Jiantao, LI Shenghua, WEN Sheng, et al. Parameter optimization design and experiment of agricultural ultrasonic atomization transducer[J]. Transactions of the CSAE, 2015, 31(12):8－15. (in Chinese)

33 WANG J, WEN S, ZHAO X, et al. Piezoelectric wind energy harvesting from self-excited vibration of square cylinder[J]. Journal of Sensors, 2016:1－13.

(C)1994-2023 China Academic Journal Electronic Publishing House. All rights reserved. http://www.cnki.net

第63期中国科技论坛在武汉隆重举行

以“智能制造引领农业装备创新发展”为主题的“第63期中国科技论坛”于2017年10月24—26日在武汉隆重举行。本次论坛是中国科协主办、中国农业机械学会首次承办的系列性品牌学术交流活动,来自国内农业装备和相关行业的200余位专业人员出席了论坛。

围绕论坛主题,针对“人工智能、智能制造、工业互联网、大数据”与“智能农业装备科研、智能农业装备产品、智能农业装备制造”等方面诸多热点难点问题,李培根院士围绕《智能制造与企业转型》,任露泉院士就《农机装备智能发展的仿生思考》,罗锡文院士聚焦《全程和全面机械化同步推进,农机1.0至4.0并联发展——对我国农业机械化发展的思考》,陈学庚院士针对《科技创新全面提升我国农机装备研究制造与应用水平》,方宪法副院长就《智能农业装备:远景-路径-现状》,汪懋华院士针对《把握信息科技革命新趋势,创新推动农业装备产业发展新未来》,陈立平研究员围绕《农机信息化与农机物联网》,陈志会长就《中国农机工业现状与发展策略》,蔡建国部长针对《e-F@ctory综合解决方案——为了实现智能制造的三菱电机提案》,朱卫江副总经理聚焦《中国一拖智能制造的实践》,王喜恩副总经理围绕《智能农机与智能制造,引领农业现代化发展》,分别作了11个内容丰富、观点新颖、视角开阔、实践特色明显的主旨学术报告,受到了与会者的热烈欢迎。论坛组织全体代表参加了“第六届世界农机峰会”和参观了国内规模最大的“2017中国国际农业机械展览会”。

“智能制造引领农业装备创新发展”科技论坛在搭建的交流平台上,业界学者、专家和各界人士广泛交流了学术思想,充分展现了智能制造领域的创新成就,这对于加快农业装备行业科技创新、提升智能农业装备研发制造水平,进而逐步实现《中国制造2025》的战略目标,必将产生极大的促进作用。

农业机械学报
NONGYE JIXIE XUEBAO
2017年 第48卷 第11期
(月刊,1957年创刊)
2017年11月25日出版

Transactions of the Chinese Society for Agricultural Machinery
No. 11 Vol. 48 2017
(Monthly, started in 1957)
Published on 25, November 2017

主管	中国科学技术协会
主办	中国农业机械学会 中国农业机械化科学研究院
编辑出版	中国农业机械学会 (地址:北京德外北沙滩1号6信箱) 邮政编码 100083
主编	任露泉
印刷	北京富泰印刷有限责任公司
国内发行	中国邮政集团公司北京报刊发行局
订购处	全国各地邮局
国外发行	中国国际图书贸易集团有限公司 (北京399信箱)

Responsible Department: China Association for Science and Technology
Sponsored by: Chinese Society for Agricultural Machinery, Chinese Academy of Agricultural Mechanization Sciences
Published by: Chinese Society for Agricultural Machinery
Editor in Chief: Ren Luquan
Editorial Office: No. 1 Beishatan, Deshengmen Wai, Beijing 100083, China
Tel: 86-10-64882610/64882231
Fax: 86-10-64867367
http://www.j-csam.org
E-mail: njxb@caams.org.cn
Overseas Distributor: China International Book Trading Corporation (P. O. Box 399, Beijing, China)

ISSN 1000-1298
CN 11-1964/S
国内邮发代号 2-363 国外邮发代号 M289 国内定价 70.00元

万方数据

3.8 技术机会发现领域专利挖掘方法研究述评

JOURNAL OF
THE CHINA SOCIETY FOR
SCIENTIFIC AND TECHNICAL INFORMATION

ISSN 1000-0135
CN 11-2257/G3

情报学报

第 42 卷　第 10 期　Volume 42　Number 10　2023

- 技术团队知识多样性及其对创新绩效的影响研究
- 语义增强型全文本共词网络的构建与分析



中国科学技术情报学会
中国科学技术信息研究所　主办

情报学报 JOURNAL OF THE CHINA SOCIETY FOR SCIENTIFIC AND TECHNICAL INFORMATION 第四十二卷 第十期 2023年十月

情报学报

Qingbao Xuebao

第 42 卷　第 10 期　2023 年 10 月

目　　次

情报理论与方法

技术团队知识多样性及其对创新绩效的影响研究 ……石　静，孙建军　（1139）

面向特征挖掘的知识单元学科归属判定方法对比研究 ……操玉杰，向荣荣，毛　进，王施运　（1151）

基于Altmetrics的睡美人文献识别方法研究 ……向　菲，陈华芳，沈　桐，曹　广，刘　艳　（1166）

情报技术与应用

融合语步和文本多特征的科技论文结构化摘要生成 ……习海旭，何　胜，黄纯国　（1176）

语义增强型全文本共词网络的构建与分析 ……赵一鸣，尹嘉颖　（1187）

基于专利文本挖掘的细粒度技术机会分析 ……吴柯烨，孙建军，谢紫悦　（1199）

情报用户与行为

信息行为研究的情报赋能探索解析……

……刘金亚，王馨悦，孟高慧，李雨佳，彭晗琦，宋筱璇，刘　畅，王延飞　（1213）

科研兴趣空间挖掘与多任务推荐研究——基于异质信息网络表示学习 ……崔鸿飞，冯子函，张靖雨　（1224）

情报综述与述评

技术机会发现领域专利挖掘方法研究述评 ……韦婷婷，冯丹钰，宋世领，张建桃　（1238）

专利技术互补性研究综述：概念、测度及应用 ……张金柱，施佳璐，章成志　（1251）

情报学报 2023 年 10 月 第 42 卷 第 10 期
Journal of the China Society for Scientific and Technical Information, Oct. 2023, 42(10): 1238-1250

DOI: 10.3772/j.issn.1000-0135.2023.10.009

技术机会发现领域专利挖掘方法研究述评

韦婷婷，冯丹钰，宋世领，张建桃

（华南农业大学数学与信息学院，广州 510642）

摘 要 在新一轮科技革命背景下，技术机会发现相关研究已受到国内外学界的广泛关注。技术机会发现旨在发现新的技术动向，推测该领域可能出现的技术形态或技术发展点，对于技术创新、产业发展具有重要意义。本文系统梳理了专利挖掘方法在技术机会发现中的应用研究现状，总结了5种底层共性分析方法的代表性研究，厘清分析方法与研究内容的适配关系，为该领域开展后续相关研究和实践的技术选型提供参考依据。研究结果表明，技术机会发现所采用的方法手段虽然一直跟进深度学习的发展，但是尚未针对性地进行方法应用上的创新。最后，本文从数据、方法应用和评价体系3个角度提出了改进思路。

关键词 技术机会发现；专利挖掘；深度学习；自然语言处理

Review of Patent Mining Methods in Technology Opportunity Discovery

Wei Tingting, Feng Danyu, Song Shiling and Zhang Jiantao

(*College of Mathematical Sciences and Information, South China Agricultural University, Guangzhou* 510642)

Abstract: In the context of the ongoing technological revolution, research on technology opportunity discovery has received widespread attention. Technology opportunity discovery aims to discover new technology trends and infer possible technology forms and development points in the field; this is critical for technological innovation and industrial development. This paper presents a systematic review of the current situation of patent mining methods in technology opportunity discovery, summarizes the representative research of five underlying common analysis methods, clarifies the relationship between the analysis methods and research content, and provides a reference basis for the technology selection of subsequent research and practices in this field. It is shown that the methodological tools used for technology opportunity discovery have not yet been targeted for innovations in method application, despite their following of deep learning developments. Finally, ideas for improvement are proposed from three perspectives: the data, method application, and evaluation system.

Keywords: technology opportunities discovery; patent mining; deep learning; natural language processing

0 引 言

随着新一轮科技革命的到来，各国企业面临着急需加大自主创新、提供具有竞争性和差异化的产品、主动适应全球竞争格局等关键问题。技术机会发现（technology opportunities discovery，TOD），又称

收稿日期：2022-09-17；修回日期：2023-02-26

基金项目：教育部人文社会科学研究一般项目“融合知识库与语料库的汉语词义消歧研究”（20YJC740067）；广东省基础与应用基础区域联合基金“基于专利知识图谱的技术创新路径分析研究”（2019A1515110396）。

作者简介：韦婷婷，女，1986年生，博士，讲师，硕士生导师，研究方向为专利挖掘；冯丹钰，女，1997年生，硕士，研究方向为专利挖掘；宋世领，男，1987年生，博士，讲师，硕士生导师，研究方向为管理决策；张建桃，通信作者，男，1978年生，博士，副教授，硕士生导师，研究方向为文本挖掘，E-mail：zhangjiantao@yeah.net。

(C)1994-2023 China Academic Journal Electronic Publishing House. All rights reserved. http://www.cnki.net

为技术机会分析（technology opportunities analysis，TOA），可通过专利挖掘方法发现新的技术动向，推断该领域可能出现的技术形态或技术发展点，从而帮助研究人员识别、推导和评估新技术理念，对于企业技术创新、产业发展具有重要的战略意义[1-2]。

早期的技术机会发现相关研究通常采用德尔菲法、层次分析法和情景规划等定性分析方法，分析结果受专家的经验和领域知识的影响较大[1]。随后的研究将文献计量、专利分析与专家意见相结合进行定量分析，发现可获得更客观的结果，但输出的领域技术机会粒度较大[3]。随着人工智能技术的发展，技术机会发现的方法也经历了一系列变革，近年来的相关研究将自然语言处理与机器学习、复杂网络分析等方法相结合进行定量分析，以期在降低专家依赖的影响的同时得到更具细粒度的分析结果。

图 1 为技术机会发现方法的一般流程。首先，选取数据源并进行数据预处理；其次，根据 IPC（international patent classification）共现关系或专利引用关系构建技术网络，或根据技术功效属性的层次等级（高/低，强/弱）构建技术形态矩阵，建立技术知识的结构化表示；最后，通过挖掘专利技术集群或技术形态矩阵识别潜在的技术机会。

目前技术机会发现研究领域已引起国内外学界的广泛关注，积累了大量研究成果，因此，对其分析方法进行梳理显得十分必要。然而，只有少数学者从特定角度对技术机会发现方法进行综述。例如，伊惠芳等[4]基于技术创新要素，从知识基础以及创新的环境、方式和类型 4 个维度总结相关研究；任海英等[3]根据不同的主体指向性，将技术机会分为领域技术机会和研发机会两大类；苏娜平等[5]总结了目前技术机会分析的主要方法，如基于专利地图的方法、基于形态学分析的方法和基于科技关联的方法等，并指出目前技术机会发现方法的局限性在于数据源相对单一、多为静态分析以及缺

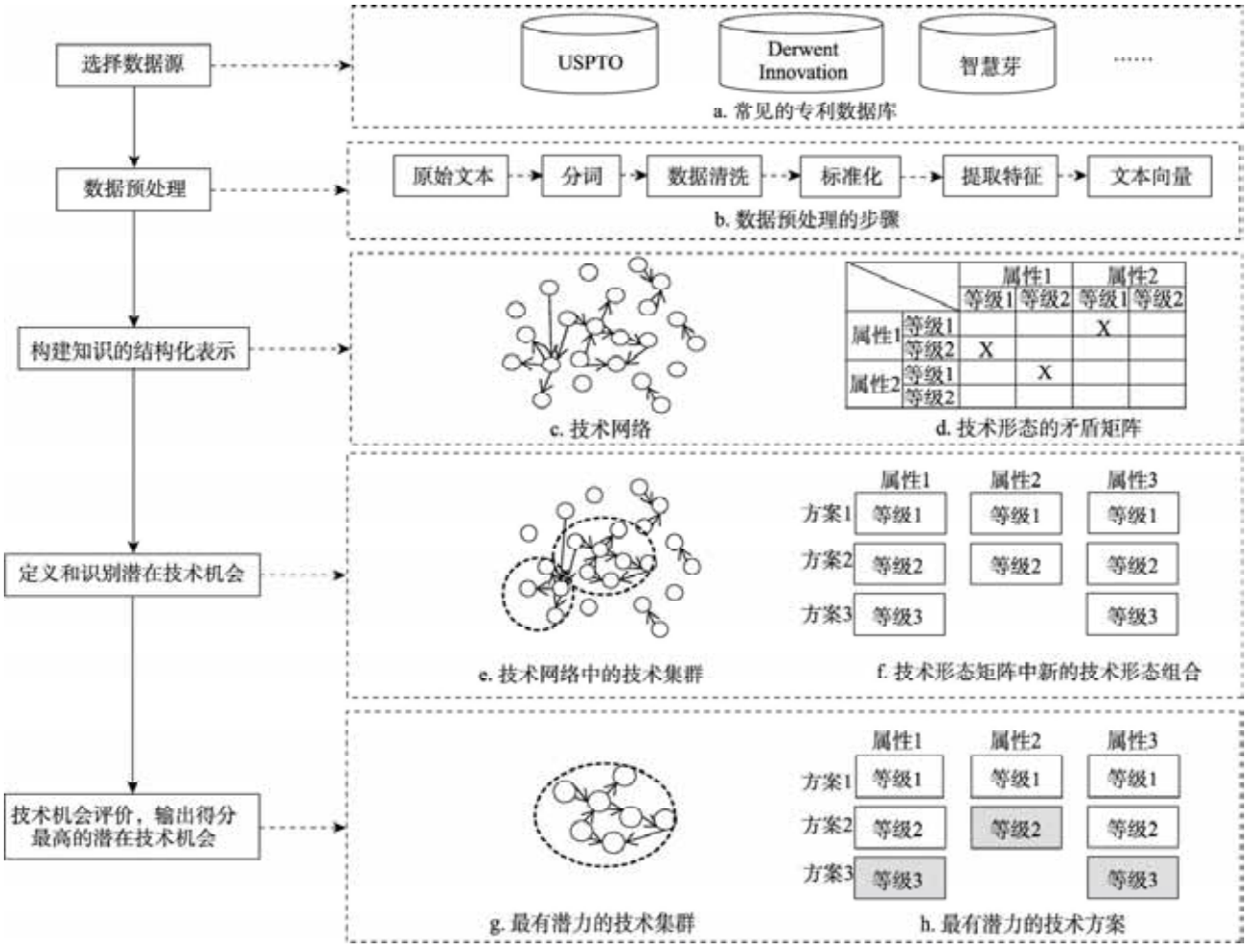


图 1　技术机会发现方法流程图

(C)1994-2023 China Academic Journal Electronic Publishing House. All rights reserved.　http://www.cnki.net

乏完善的技术机会评价体系；Lee[6]指出，目前TOA的研究热点包括从专利文本中提取技术信息、基于TOA寻找新的技术灵感和目标技术领域推荐。

尽管国内外围绕技术机会发现的研究范围、研究对象和研究方法进行了大量的梳理，然而随着人工智能技术的不断发展及其在各个领域的渗透，技术机会发现的方法手段也在发生变化。因此，亟须梳理目前最新的应用进展，尤其是深度学习与自然语言处理相结合的专利挖掘方法在技术机会发现中的重要应用，从技术前沿追踪视角对近年来国内外技术机会发现领域的研究方法进行总结，帮助研究人员厘清分析方法与研究内容的适配关系，为该领域开展后续相关研究和实践的技术选型提供参考依据。

1 技术机会发现中的专利挖掘方法

由于以专利文献作为技术机会发现的数据基石，技术机会发现的相关研究通常采用专利挖掘与分析方法。本文根据技术机会发现领域包含的各子任务所需的底层共性分析方法，将专利挖掘在技术机会发现领域的应用分为5个方面：专利知识表示、专利相似度计算、专利聚类、技术主题识别和链路预测。下文将详细阐述这些方法的应用研究现状。

1.1 专利知识表示

专利知识表示是指将专利知识单元进行编码，以便于计算机的识别与处理。表1总结了现有文献中常见的模型及其代表性研究。

表1 专利知识表示部分代表性模型

专利表示模型	知识分析单元	文本粒度	方法特点	代表性研究
采用LDA(latent Dirichlet allocation)将专利文档向量化，即BOW(bag-of-words)模型	IPC	专利全文	不考虑词汇之间的顺序，通过抽象文本的局部特征，获得专利的“词-主题-文档”分布，基于聚类方法获得专利文档的知识表示。	李慧等[7]
	关键词	技术主题词		Yoon等[8]、Kim等[9]、吴菲菲等[10]
	SAO(subject-action-object)结构	技术关键概念		Ma等[2]
word2vec	关键词	技术主题词	考虑词汇之间的顺序，基于神经网络自动抽取蕴含复杂语义的专利知识表示。	Lee等[11]
	SAO结构	专利全文		饶齐等[12]
	关键词	技术主题词		Hu等[13]
doc2vec	IPC	专利全文	word2vec的衍生形式，可输出整份专利文档的向量表示。	Kim等[14]
SAOvecs	SAO结构	专利全文	doc2vec的衍生形式，通过SAO三元组的TF-IDF(term frequency–inverse document frequency)值构建向量，包含更多的语义信息。	Korobkin等[15]
GloVe(global vectors)	SAO结构	技术关键概念	word2vec的衍生形式，训练周期更短。	Chen等[16]
BERT(bidirectional encoder representations from transformers)	关键词	技术主题词	word2vec的衍生形式，采用双向学习的形式获取更多的专利语义信息。	王秀红等[17]

专利知识表示模型可划分为离散式表示模型和分布式表示模型两类[18]。早期研究通常采用离散式表示模型，即基于专利中术语的出现频率获得专利的知识表示向量。词袋模型（BOW）是一种经典的离散式表示模型，其通常与潜在狄利克雷分布（LDA）算法结合使用，直接输出文本向量表示和主题词概率分布，再进行后续的分析。李慧等[7]采用LDA算法从专利样本中获取技术主题，再结合IPC共现和共类关系构建技术网络，通过将主题词概率分布与IPC分类号的各级含义对比验证，可以更准确地表示领域内的核心技术。Kim等[9]将专利中术语的TF-IDF矩阵输入LDA模型，用输出的每份专利主题分布向量表示其技术类别。Ma等[2]采用LDA获得了各技术主题内关键术语分布，通过分析关键术语之间的SAO结构，将句子结构信息视为技术关联的表示，探索技术主题之间的潜在联系。离散式表示模型是将专利的局部对象（词或短语）作为特征进行抽象以表示专利的含义。

分布式表示模型则是将词的语义分布式地存储在各个维度中，弥补了离散式模型并未考虑上下文单词之间的相互关联关系且不适用于表征长文本的缺点。在自然语言处理领域，代表性的分布式表示模型有word2vec[19]、doc2vec[20]、GloVe[21]和BERT[22]模型，这些模型也都被引入专利文本表示当中。

(C)1994-2023 China Academic Journal Electronic Publishing House. All rights reserved. http://www.cnki.net

在 word2vec 模型的应用方面，Lee 等[11]采用包含输入层、隐藏层和输出层的三层神经网络获得专利的 word2vec 词向量，并基于词向量的相似度建立产品地图，将产品地图视为专利产品的知识表示。Zhu 等[23]采用图卷积网络（graph convolutional network，GCN）获得了专利文本的关键词向量表示，解决了先前基于词向量的方法不能表示专利与技术领域之间语义关系的问题。饶齐等[12]直接采用开源工具获得专利的 word2vec 词向量，比较了 word2vec 词向量与基于词袋模型的词向量在中文专利 SAO 结构抽取任务中的表现，并验证了将词向量用于关系抽取的可行性。

doc2vec 模型在 word2vec 模型的基础上增加一个段落 ID（identifier）特征向量，可用于获得整份专利文档的向量化表示。Kim 等[14]采用 dco2vec 模型获得了每个技术领域的专利文档向量，从专利全文本的视角研究分属不同技术领域的一对 IPC 分类号之间的语义相似性。Kim 等[24]利用专利文本的 SAO 结构和词向量更新，通过 doc2vec 模型得到句向量，此步骤提高了 SAO 结构中单词间的余弦相似度，可以更好地反映专利的技术要素和上下文语义。Korobkin 等[15]基于词频、上下文语义和句子结构信息学习专利的 SAOvecs 向量，提升了后续执行专利聚类、识别核心技术和热点技术的准确性。

GloVe 和 BERT 也属于 word2vec 的衍生模型。GloVe 可获得比传统的 word2vec 模型更充分的全局信息。Chen 等[16]采用 GloVe 模型，基于全局词共现生成专利向量，在语义信息抽取任务中能以更短的训练周期取得比 word2vec 模型更好的效果。BERT 模型则通过双向的学习方式更深度地学习词汇的上下文，仅需采用具体任务的数据集对通用 BERT 模型的最后一层进行微调，就能够被应用于很多实际任务[25]。林原等[26]通过微调使 BERT 模型能够包含更多的领域知识，获得更能精确表达语义的文本表示。王秀红等[17]采用 BERT 模型获得了专利文本的词向量、文本向量和位置向量，再将通过 BERT 训练的向量与采用 LDA 获得的专利主题向量拼接，最终获取了包含丰富语法和语义信息的专利知识表示。

在专利文本表示的对象中，专利的知识单元包括专利的 IPC 分类号、关键词和 SAO 结构。其中，IPC 分类号和关键词所包含的语义信息较弱，无法准确表示专利之间的关系[7,27]；而 SAO 结构是“主语-谓语-宾语”形式的三元组，在专利技术信息的表示上更具细粒度。因此，以 IPC 分类号和关键词作为基础知识单元的通常是那些仅考虑结构化数据和词频概率分布的任务，如基于 LDA 的专利聚类和主题识别[2]；SAO 结构常被应用于考虑语义关系、对深度和精准度有要求的专利文本挖掘任务中[28]。

总体而言，在表示方法层面，分布式表示模型所取得的性能优势使其已逐渐取代离散式模型成为目前主流的专利文本表示方法；在分析对象方面，现有研究很少将整篇专利文档向量化，一般仅提取文档中可以有效表示技术知识的部分，如关键词或专业术语等[8-9]。

1.2　专利相似度计算

基于专利文本进行相似度计算能够获取技术间相似程度，可用于展示技术发展的脉络、现状和趋势，为技术机会发现提供分析基础。该环节的一般流程：先将专利转化为词、短语或句子的表示向量，再采用一些度量指标计算专利之间的相似度。

在专利文本表示方面，如 1.1 节所提方法，专利相似度计算中主要采用了词袋表示法、主题表示法和分布式表示法。其中，基于词袋表示的方法仅利用简单的文本统计信息计算技术之间的相似度；基于主题表示的方法考虑了词共现信息，包含一定的语义；基于分布式表示的方法则是在融合了更多文本语义特征的基础上进行相似度计算[29]。

在相似度的度量方法上，经典的方法是余弦相似度计算法。例如，专利 A 和专利 B 之间余弦相似度的计算公式为

$$\cos\alpha = \frac{\sum_{i=1}^{k} f_{A_i} \cdot f_{B_i}}{\sqrt{\sum_{i=1}^{k} (f_{A_i})^2 \cdot \sum_{i=1}^{k} (f_{B_i})^2}} \tag{1}$$

其中，f_{A_i} 表示专利 A 的向量的第 i 个元素；f_{B_i} 表示专利 B 的向量的第 i 个元素。两个向量之间夹角的余弦值越接近 1，则两份专利的相似度越高。

另一种常用的专利相似度度量指标是 Jaccard 指数，即将两份专利中相同关键词的数量除以两份文本的关键词总和得出的值，计算公式为

$$\text{Jaccard}(A,B) = \frac{N_{A_1B_1}}{N_{A_1B_1} + N_{A_1B_0} + N_{A_0B_1}} \tag{2}$$

其中，$N_{A_1B_1}$ 表示同时存在于向量 $\vec{A}$ 和向量 $\vec{B}$ 中的元素；$N_{A_1B_0}$ 表示存在于向量 $\vec{A}$ 但不存在于向量 $\vec{B}$ 中的元素；$N_{A_0B_1}$ 表示不存在于向量 $\vec{A}$ 但存在于向量 $\vec{B}$ 中

(C)1994-2023 China Academic Journal Electronic Publishing House. All rights reserved.　http://www.cnki.net

的元素。Jaccard指数的取值范围是0~1，值越大，相似度越高[30]。

在实际应用中，Song等[1]利用专利关键词向量之间的余弦值表示对应两项技术的相似度，通过识别出与目标技术专利相似术语最多的其他领域专利文档，找到改进目标技术的解决思路以及潜在的技术融合机会。Arts等[30]通过计算专利关键词之间的Jaccard值测度专利所代表的技术之间的相似性，为从业者评估专利新颖性、寻找技术机会提供帮助。刘俊婉等[31]将Jaccard指数作为相似度指标，用于测度专利技术主题词共现的强度，以发现新兴主题产生关联的机会。Lee等[11]基于具有相似技术基础的产品彼此靠近的假设，根据word2vec词向量之间的余弦距离建立了“专利-产品”网络，基于此确定目前公司有能力进入的新产品领域，即潜在的技术机会。席笑文等[32]将word2vec词向量与LDA主题向量拼接，通过拼接向量之间的余弦相似度测度专利权人之间技术产出的相似性，以帮助技术主体识别潜在的竞争关系或合作机会。Zhang等[33]基于余弦相似度计算寻找关联的LDA主题向量，结合专利发布时间轴获取区块链领域中各项子技术演变的轨迹，发现了当前的热点主题、突破性主题和空白主题，其中热点主题被视为最有前景的技术机会，突破性主题被视为有潜力的技术机会。

总之，现有研究采取的相似度度量指标比较固定，但是在技术挖掘层面根据其具体应用选择不同的方法模型，其中词向量与LDA模型相结合的挖掘方法呈流行趋势。

1.3 专利聚类

专利聚类的核心思想是将高维的原始文本数据投射到低维空间，使相似的数据样本尽可能地集中，而不相似的样本则尽可能地分散。专利聚类的结果常被用于识别该领域的关键技术集群、构建技术网络、识别离群专利等，对于把握技术发展的态势具有重要意义，为技术机会发现提供直观的分析依据。

根据专利知识的使用，专利聚类方法可以分为基于IPC代码的聚类、基于专利主题的聚类以及基于功能信息的聚类[34]等几大类。常用的聚类算法包括主成分分析（principal components analysis，PCA）、k均值聚类算法（k-means clustering algorithm，k-means）和LDA模型。此外，还有LDA的变形模型，如标签化的多重混合狄利克雷模型（labeled Dirichlet multi mixture model，LDMM）的半监督聚类模型。表2总结了现有文献中常用的聚类算法及其应用领域。

表2 常见的聚类算法

方法应用	方法特点	测试领域	性能评估	代表性研究
PCA	无参数限制，但不可通过参数化方式干预计算过程，可能忽略部分重要的数据特征。	发现工业废水处理领域中有潜力的专利	定性分析	Mao等[35]
k-means	需要预先指定k的值，即分类后的簇数，根据数据样本的均值划分类别。	对茶叶领域的专利进行聚类，展示该领域的技术发展现状	定性分析	Shanie等[36]
		对工业机器人领域的专利进行聚类分析	定性分析	田鹏伟等[37]
		从5G领域中发现了7个技术机会	定性分析	Zhang等[38]
		对元数据领域的专利进行聚类分析	定量指标结合定性分析	Anuranjana等[39]
LDA	适用于数据样本主要根据均值进行区分的情况，不适用于数据维度很高但潜在类别很少的情况。	构建冠状病毒领域技术路线图	定性分析	林原等[26]
LDMM	采用半监督学习，只需标注训练集中的一部分数据，模型的输出是句子级的主题描述。	识别3D打印领域的新兴技术	定性分析	Zhou等[40]

各聚类算法中，PCA的特点是不需要输入参数，使用较为简便；k-means需要预先设定集群的类别[38]；LDA则基于主题的分布划分集群，例如，李慧等[7]采用LDA获得特定IPC码类别下的专利主题词聚类，综合专利文本的结构化特征和非结构化特征对该领域中的核心技术演化轨迹和趋势进行分析。LDMM采用半监督方式学习数据特征，Zhou等[40]采用LDMM获得了专利的句子级表示，解决了有监督模型泛化能力不强和无监督学习模型不精确的问题，能够更好地识别新兴技术。除了应用算法，有些研究采取更直接的聚类方式，如Arts等[30]根据专利关键词的共现程度判断技术之间的相似度，以此作为技术聚类的依据。此外，由于聚类结果呈现的是数据集中的专利被划分到不同的技术集群，因此，集群间的空隙、异常专利或离群专利也可被视为技术机会的表示[41]。目前已有一些研究采

(C)1994-2023 China Academic Journal Electronic Publishing House. All rights reserved. http://www.cnki.net

取了通过离群计算的方式进行技术机会分析。例如，Jeon 等[42]计算每份专利的局部离群因子（local outlier factor，LOF）值，从而得到专利的新颖度，识别出有潜力的新专利；Wang 等[43]则通过计算专利的LOF值来寻找相似的专利集合。

目前，基于专利文本的聚类算法其测试领域较为多样化，但由于缺乏统一标准的公开测试集，聚类结果的性能评估通常以定性分析为主。因此，无法公平地对聚类算法进行统一评估，只能根据具体应用领域的需求特点选择更适配的专利聚类算法。未来可以从定量和定性相结合评估的角度针对性地提出技术机会发现中专利聚类的统一模型框架，从而提升技术机会发现领域其分析结果的可靠性。

1.4　技术主题识别

技术主题一般是指某技术领域的关键技术或子领域的关键技术[44]。主题识别旨在获取技术领域中核心或热门的技术主题，进而帮助把握技术发展态势和发掘技术机会。

技术主题识别的经典方法是LDA模型。LDA模型是一种基于概率和统计方法的主题模型，能够从文本中提取出潜在的主题[45]，是由“词-主题-文档”构成的三层贝叶斯概率模型。表3列举了技术机会发现领域中LDA的部分应用实例。

表3　LDA主题模型部分应用实例

方法应用	模型结构	方法特点	测试领域	应用结果
LDA	单一	去除不同主题之间共享的分类码，取得较高精度的主题短语提取结果。	太阳能电池	Ma 等[2]确定了5条核心技术发展路径，通过探索这些路径上的主导或弱技术来预测潜在机会。
		根据词频和语义结构输出潜在的主题。	资环生态	吕璐成等[46]识别出50个动态主题。
LDA+DT（decision tree）	混合	适用于节点之间邻接关系较为稀疏的网络，结果更具可解释性。	医学和材料	陈浩等[47]从广东省和武汉市高校专利库中找出跨地区和跨领域合作关系。
LDA+SVM（support vector machine）	混合	根据主题分布判断专利所属类别，需要预先对训练集进行词性标注等预处理操作。	电力和物理	Yun 等[48]发现电力和物理领域积累了大量专利，且近期增长率很高。
LDA+链路预测	混合	预测技术主题词网络中未来可能出现的链接，侧重对未来技术网络结构的预测。	无人驾驶	Kim 等[49]通过LDA构建了市场层和技术层两类主题网络，采用链路预测识别可能的技术机会。
LDA+BERT	混合	预训练中采用双向的学习模式，结果中包含更多的语义信息。	农业机器人	王秀红等[17]找出了农业机器人领域的三大关键技术。

从方法本身而言，LDA可以根据词频最高的词组得出潜在的主题，但没有考虑语义和词频以外的信息。因此，部分文献采用统计学方法对LDA进行优化。比如，吕璐成等[46]将非负矩阵分解模型与LDA结合，把主题识别任务转换为解决约束最优化的统计学问题，提升了动态识别专利主题的模型性能。此外，考虑到专利的主题词有时并不是独立的词汇，而是由2~3个词汇组成的短语。马建红等[27]通过双向长短时记忆网络-条件随机场模型抽取出专利短语后，采用经广义波利亚瓮模型（generalized Pólya urn）引入先验知识后的LDA模型进行主题短语抽取。该方法既解决了基于短语的主题模型常出现的稀疏性问题，又具备比传统主题模型更高的可读性和判别性。

除了上述两种从LDA的性能上提升主题识别准确度的做法之外，有文献将LDA的结果与其他方法的结果相结合，以期在后续任务中取得更好的效果。例如，王秀红等[17]将通过BERT获得的语义特征向量与采用LDA获得的主题特征向量结合，弥补了单一LDA模型缺乏上下文语义信息的局限性，在后续的专利聚类任务中取得了更具准确性和细粒度的结果。Kim 等[49]将LDA与网络分析方法结合，通过链路预测从主题关键词网络中寻找技术机会。该方法实现了对LDA输出的技术主题之间关系的挖掘，能更好地辅助技术机会发现。

在主题分析对象上，LDA的分析对象通常为专利的部分文本，如摘要或权利声明，或者专利的引用网络。基于纯文本（摘要或权利声明）的主题识别主要利用文本内元素的共现信息；基于所有权人关系网络和引用关系网络的相关研究兼顾了专利文本的内部语义和每份专利文本与外部世界的信息交互。在进行主题识别时，若有多个分析对象，则根据需要对这些对象设置一定的权重比例。例如，Ma 等[2]根据经验将标题和摘要的权重设置为2∶1，其在后续研究中还将探索不同权重比例对识别结果的影响。

在实际应用中，Kim 等[9]将LDA主题词分布与

(C)1994-2023 China Academic Journal Electronic Publishing House. All rights reserved.　http://www.cnki.net

引用网络结合，通过可视化3D打印领域中各技术集群内专利间的继承关系监测技术发展的轨迹，发现技术开发机会。该方法基于LDA主题分布确定专利所属的技术主题集群。Choi等[50]将技术主题的类型设置为主导型、新兴型、饱和型和下降型4类，采用LDA分析物流领域专利的摘要，发现与数据库和传感器子相关的通常为新兴型主题，这意味着数据获取和数据分析可能是物流领域未来的技术热点，即有潜力的技术开发机会。此外，该项研究证明了当无法用某几个美国专利分类（United States patent classification，USPC）中子类的主题词完全覆盖该领域的专利主题时，可用LDA主题模型的结果进行补充，以开展更全面的领域技术发展现状分析。韩芳等[51]采用LDA识别出太阳能光伏领域中12个拥有突破性创新潜力的技术主题，即有前景的技术开发方向。该方法具有比基于共词分析或向量空间模型的主题识别方法更低的算法复杂度。

技术主题识别的结果还可以通过可视化的方式呈现，可视化工具诸如LDAvis[33]、Gephi软件[32]和*t*-SNE算法[7,52]可被用于直观展示技术主题识别的结果。但是，主题模型的可视化往往仅能展示技术的动态演化过程，无法识别和预测技术的突变和融合。

总体而言，技术主题识别容易受所提取的术语和特征选择技术的影响，难以取得较好的性能。改进的方向之一是优化专利文本的向量表示，比如，刘小玲等[53]在构建文本向量时将专利的文本内容、引用关系和分类号信息3个属性进行了融合，提升了专利向量表示的准确性。除了增强专利知识，未来可以从联合模型的层面考虑，利用模型之间相互知识补充的原理将有利于主题的精准识别，这类方法在技术机会发现领域尚处于初始探索阶段，具有很大的改善空间。

1.5 链路预测

在技术机会发现领域，实施链路预测的目的主要是预测技术发展的趋势，找到潜在的技术机会。链路预测的数据基础是技术网络，即先构建一个以节点代表技术、以边代表技术之间关联关系的网络，再通过已知的技术网络拓扑结构如技术节点和链接的特征，预测网络中尚未连接的两个技术节点之间产生链接的可能性[54]。图2为在技术网络中开展静态链路预测的示意图。链路预测的方法可以划分为基于相似度、基于社会网络分析和基于机器学习三大类。表4总结了技术机会发现领域常用的链路预测方法。

基于相似度的链路预测通常采用Jaccard指标、Adamic-Adar（AA）指标、共同邻居算法（common neighbors，CN）、优先依附算法（preferential attachment，PA）等相似度指标或算法预测可能出

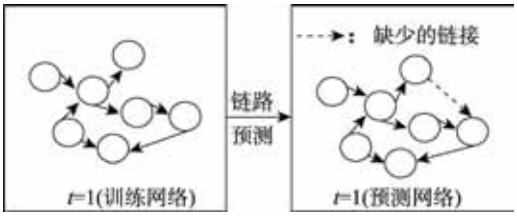


图2 静态链路预测示意图

表4 链路预测部分代表性方法

方法应用	方法特点	候选技术机会的表示形式	测试领域	代表性研究
基于相似度	有基于全局信息和基于局部信息的两大类相似性指标。	技术网络	3D打印	Seo[55]
		SAO网络	医学	Han等[56]
		IPC共现网络	化学和环境	Cho等[57]
		主题网络	深度学习	刘俊婉等[31]
社会网络分析	根据网络结构如节点和边的分布计算节点的重要性。	专利引用网络	BT（biotechnology）和IT（information technology）	Park等[58]
支持向量机（SVM）	将线性不可分的低维数据映射到线性可分的高维度，该方法的难点在于找到效果最好的核函数。	IPC引用网络	云计算	翟东升等[59]
		专利网络	3D打印	Yoon等[54]
		IPC知识流网络	可再生系统	Aaldering等[60]
决策树（DT）	根据特征在不同的决策边界下预测专利所属的类别，其结果具有较好的可解释性。	IPC共现网络	化学和环境	Cho等[57]
随机森林（random forest，RF）	一个采用随机方式建立的、包含多个决策树的分类器。	IPC共现网络	机动车和电信	Kim等[14]
		IPC共现网络	化学和环境	Cho等[57]
图卷积网络（GCN）	图神经网络的变种，通常用于从不规则的图（拓扑）结构中提取特征。	合作网络	丙肝病毒	Qi等[61]

(C)1994-2023 China Academic Journal Electronic Publishing House. All rights reserved. http://www.cnki.net

现的链接。Seo[55]将上述 4 种方法结合用于链路预测，减少了计算过程中的信息丢失。Han 等[56]采用局部随机游走（local random walk，LRW）算法获得技术节点的特征向量，与上述 4 种方法相比，LRW 算法准确度更高。

基于社会网络分析的链路预测通常采用边缘中介中心性、度中心性、接近中心性等指标，根据技术网络的结构特征进行预测。比如，Park 等[58]采用基于边缘中介中心性的方法预测可能出现的跨领域知识流，用经过技术节点的最短路径数量刻画该节点在技术网络中的重要性。

上述两类方法皆是对技术网络的全局或局部特征展开定量分析，不能充分挖掘网络的深层信息。基于机器学习的方法能够更好地获取技术网络中节点和连边的属性和结构信息。涉及机器学习的方法包括基于统计的机器学习模型，如决策树（DT）、随机森林（RF）、支持向量机（SVM）和 *k*-近邻算法（*k*-nearest neighbor，*k*NN）等[62]；还包含基于深度学习的模型，如长短时记忆网络（long short term memory networks，LSTM）、图卷积网络（GCN）。Yoon 等[54]采用基于 SVM 的链路预测模型，预测专利网络中可能出现的新节点；Cho 等[57]采用基于 DT 方法预测可能出现的 IPC 共现；Kim 等[14]采用基于 RF 的方法预测可能出现的技术融合。基于深度学习的方法在获取足够特征信息的同时能够降低对专家领域知识的依赖度[25]。Nakai 等[63]采用 LSTM 预测专利网络中引文规模增长的趋势；Qi 等[61]采用 GCN 将复杂的专家-机构网络简化为图的形式，预测专家合作关系；Zhu 等[23]采用 GCN 获得专利文本的低维知识表示，结合两个能反映专利与技术领域的语义亲密度的指标——技术特征向量和强度坐标，来预测技术融合。

链路预测的应用主要有以下几个拓展方向。首先，需度量技术主体的内在能力是否足以实现该技术机会。例如，Seo[55]通过基于 LDA 的链路预测发现技术主题网络中近期可能出现的新链接，然后采用关联规则分析生成技术主题之间有方向和权重的链接，找到与企业的能力相匹配的技术机会。其次，许多模型仅考虑生成的链路方向，没有保留网络的拓扑结构信息。Chen 等[64]采用 PageRank 计算节点的影响得分，捕捉网络的全局结构信息，然后采用非对称链路聚类计算协同系数得分，获得网络的局部结构信息，最后在非负矩阵分解模型中联合优化这两个参数，使模型同时保留局部和全局信息。此外，除了从技术的角度挖掘有潜力的技术机会，链路预测还可在合作网络中挖掘潜在的合作者关系。比如，Qi 等[61]采用基于 GCN 的链路预测识别论文和专利作者所属机构的合作网络中缺失的链接，以此作为潜在的合作机会。

目前，在链路预测的相关研究中，基于图卷积网络（GCN）的方法能够更全面、更深层次地挖掘技术网络所隐含的信息，极大地提升了预测性能，这将成为一个重要趋势。

2　结果与讨论

本文通过系统性回顾相关文献，总结了专利知识表示、专利相似度计算、专利聚类、技术主题识别和链路预测 5 类技术机会发现中的底层共性分析方法的应用现状。图 3 是上述方法在技术机会发现领域应用的结构图，将 5 类方法与相关业务结合，以期能够从全局的视角展示各类方法与技术机会发现流程中各阶段任务的适配性。

（1）专利知识表示具有关键性作用

在技术机会发现方法的一般流程中，专利知识表示主要应用于数据预处理和构建知识的结构化表示，是后续分析的基础数据。因此，选择何种类型的专利知识以及如何准确地将知识进行表示，对技术机会发现的有效性具有关键性作用。目前沿用的分布式表示模型是通用领域中的文本表示方法，但是针对领域术语较多、语义复杂的专利文本表示尚未发现相关研究。未来研究可以集中于普通文本和专利文本的具体差异和联系，深入探索更好的专利文本表示模型。

（2）技术机会定义决定方法选择

从图 3 可以看出，尽管专利相似度计算方法、专利聚类方法、技术主题识别方法和链路预测方法均可以达到技术机会发现的目的，但是各研究根据技术机会内涵的不同定义而选择不同的底层分析方法。上述 4 种类型挖掘方法的应用场景各自具有相应的侧重点。

专利相似度计算通常用于技术机会发现领域的各个子任务，它在寻找相似技术解决方案上具有一定优势。例如，专利相似度计算通过识别其他领域中与目标专利相似度最大的专利，可以找到改进目标技术的解决方案以及发现目标技术与其他领域的技术发生融合的机会。除了传统的余弦相似度计算之外，目前有些研究利用深度学习模型进行专利之间的自动距离测量，但是需要一定量的标注数据。

(C)1994-2023 China Academic Journal Electronic Publishing House. All rights reserved.　http://www.cnki.net

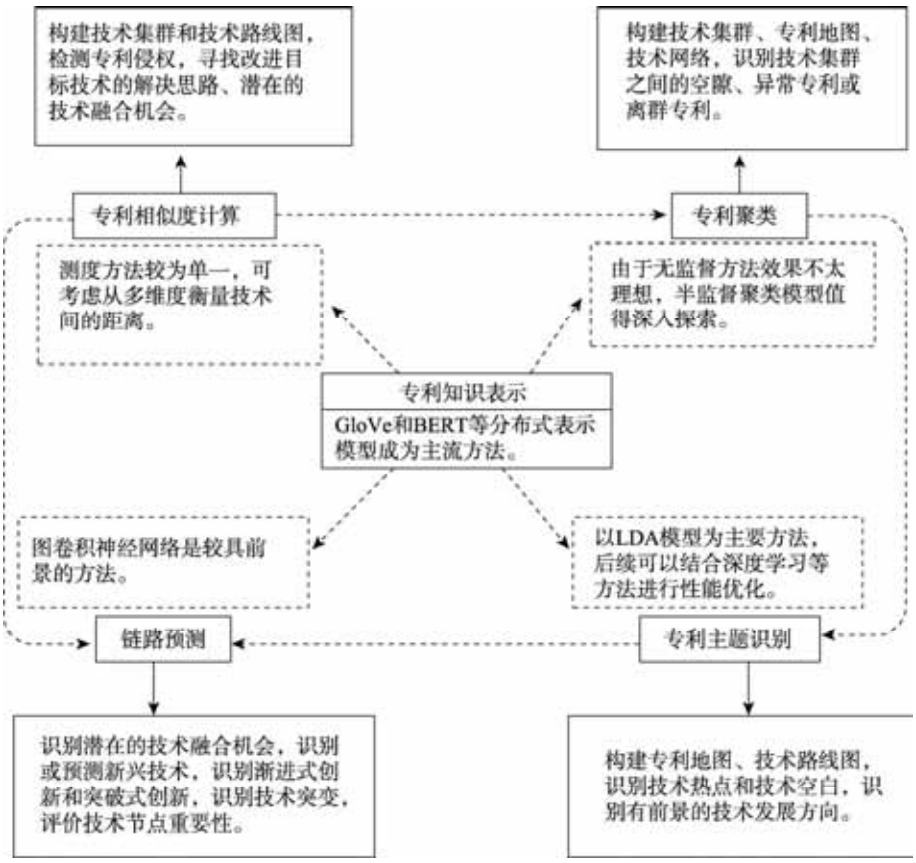


图3 专利挖掘方法在TOD领域的应用结构图

专利聚类方法的主要目的是自动发现技术集群，在大规模数据场景下，该方法相比于专利相似度计算方法更为灵活，但是其效果易受数据样本不均衡的影响。根据聚类输出结果，可以将专利数量庞大的技术集群视为当前的技术热点，将集群之间的空隙视为有待开发的技术空白区域，将明显独立于集群的专利视为可能发生技术突变的异常或离群专利。该方法可用于基于离群点检测的技术机会发现上。但是，目前的聚类手段仍是传统的机器学习方法为主，虽然无监督的方式避免了数据标注的问题，但是技术集群中也包含了大量噪声数据，不利于技术机会的发现。

专利主题识别方法基于专利之间主题的关联度构建技术集群，它将与大量技术主题有关联的目标主题视为技术热点，找寻有前景的技术开发或融合方向。目前的方法以LDA模型为主，该方法的底层思想是从词共现角度识别专利技术主题，对于领域术语多样复杂的专利文本而言，其效果仍有待提升。尽管有将LDA与其他深度学习模型结合使用的相关研究工作，但是目前仍处于探索阶段，在其他子任务的适用性方面还有待考究。

相比于前几类方法，链路预测方法更贴近面向未来的技术预测这个内涵。其通过预测技术网络中缺失或即将出现的链接，识别潜在的技术融合机会，也能识别可通过历史数据预测到的渐进式创新，找到目标技术的改进机会。此类方法也可通过预测技术网络中空白区域新出现的链接和节点，识别可能的技术突变和突破式创新，寻找将在目标技术领域引起重大变革的技术机会。此外，部分文献将通过链路预测获得的边的权重与关联规则分析或综合评价指标结合，评价技术机会的前景和可行性。从现有研究工作来看，图神经网络方法逐渐引起相关研究人员的关注，将成为具前景的热门方法之一。

综上所述，在进行技术机会分析时，往往需要根据通用流程中各个步骤的具体业务，选择合适的方法。其中，预处理阶段的方法最为模式化，通常采用专利知识表示的模型，输出专利文本向量。知识结构化表示的建模方法较为丰富，主要用于构建技术网络或技术路线图，此类方法的输出对技术机会发现的结果影响较大。现有文献对技术机会的定义各不相同，包括但不限于技术热点、技术空白、跨领域的技术融合等，因此，可应用于技术机会识

(C)1994-2023 China Academic Journal Electronic Publishing House. All rights reserved. http://www.cnki.net

别阶段的方法及其应用形式也最为多样。专利相似度计算方法可用于找寻与目标技术相关的改进和融合机会，专利聚类方法和专利主题识别方法可用于找寻技术热点和技术集群之间的空隙，链路预测方法可用于识别和预测技术融合，也有文献选用两种以上的方法构建混合模型，以达到更优的识别效果。目前，适用于技术机会评价阶段的方法主要是基于链路预测的权重计算或评价指标，形式较为单一且未能形成规范的评价体系。有效的评价方法将能够反过来促进专利挖掘方法的进一步改善。未来有前景的研究方向包括优化专利的知识表示、探索效果更好的技术机会识别模型，以及在技术机会的评价阶段应用更多样的方法。

3　面临的挑战

总结现有文献，目前在技术机会发现领域有关专利挖掘方法的应用主要存在以下几个有待解决的问题。

（1）专利全文本分析方法有待挖掘。鲜少文献采用整份专利文本作为研究对象，大部分文献仅采用专利的标题和摘要作为语义分析对象。部分专利挖掘任务相关的研究考虑到了权利要求书中权利要求人之间的关系[65]，但受限于算法效率和硬件算力，对于专利其他部分，如属于长文本的说明书，开展分析的难度依然较大。

（2）用于分析的文本知识结构较单一。现有研究的知识分析单元包括 IPC 分类号、关键词、SAO 结构等。其中，SAO 结构的提取需要预先设置技术关键词，即需要充足的领域知识作为支撑，但仍可能忽略有价值的技术知识。基于 IPC 分类号和关键词的文本分析所包含的技术信息较为宽泛，难以识别出具体的技术机会。目前，大部分文献仅基于专利文本结构的某一类技术要素展开分析，未来的拓展方向之一是基于混合的文本知识结构展开分析。值得注意的是，有时将两类知识分析单元关联起来的做法可能使分析结果变得模糊和不准确[54]。

（3）技术主题识别方法具主观性。技术机会的表征主要由技术主题关键词构成，然而在现有的主流方法中，关键词的提取高度依赖于专业领域词典，并且在提炼技术机会的过程中需要人工定义技术主题的具体名称和内涵，主观成分较大。缺乏客观及普适性的挖掘方法将难以保证结果的可靠性。

（4）检验技术机会的方法有待完善。现有文献对技术机会的检验过程常常是不充分的，模型的输出结果并不一定就是技术机会，因此，需要设计诸如专利被引量、被引量增长率、专利与相关聚类集群相连的节点数等验证指标[66]作为补充。

4　改进思路

基于技术机会发现的流程、各类方法的应用现状及当前研究所面临的挑战，本文提出了一些应用创新方面的切入点，如图 4 所示。



图 4　专利挖掘方法应用创新的思路图

(C)1994-2023 China Academic Journal Electronic Publishing House. All rights reserved.　http://www.cnki.net

（1）数据层面的改进。数据层面的改进主要是选用内涵信息更丰富的专利对象。涉及多源异构专利数据的研究是近年的热点，主要通过集成多个专利数据库并选取不同结构的文本分析对象，从而实现较为全面、深入的分析。此外，鉴于专利主题识别对领域词典的高度依赖，领域词典的自动化或半自动化构建将是未来发展趋势之一。

（2）方法应用层面的改进。方法应用层面的改进主要是对算法本身进行优化，探索组合模型在不同应用场景中的适用性，以及寻找能解决现有问题的新方法。比如，提出可将异构数据向量化的新方法，探索更新颖的文本表示模型，探索BERT、GCN及其衍生模型与传统机器学习模型组合后在专利特征抽取、专利相似度计算、专利主题识别、链路预测等任务中的适用性。此外，可从无监督聚类方法角度，尝试缓解或消除噪声，以实现不需要主题词表的专利聚类，寻找可以快速处理大规模复杂数据的新方法。

（3）评价指标层面的改进。评价指标层面的改进主要是提出具有实践价值的技术机会评价体系。可根据现有研究中常见的社会网络分析指标、文献计量指标、专利质量评价指标等，构建一套较完整的技术机会评价体系；还可采用GCN模型预测技术关系，以被预测边的权重作为技术机会的评价指标[61]。

5 结 语

本文对技术机会发现领域中的专利挖掘方法应用进行了文献综述，总结了该领域底层共性的专利挖掘方法在整个技术机会发现方法流程中的研究现状，构建了研究方法和该领域研究子任务的适配结构图，提出该领域面临的方法上的挑战，并提出了几点改进思路。

在人工智能、大数据技术背景下，未来希望研究者们可以共同丰富专利挖掘对象的内涵，优化专利特征抽取算法，实现大规模领域专利数据集的规范化构建，探索先进的文本表示模型和图卷积网络模型与其他模型组合后在各类专利挖掘任务中的表现，从而能够更好地借鉴目前前沿的深度学习思想，对技术机会发现领域提出针对性的改进方法，并完善技术机会发现定性和定量相结合的统一评价体系，增强技术机会发现结果的有效性和可靠性。

参 考 文 献

[1] Song K, Kim K S, Lee S. Discovering new technology opportunities based on patents: text-mining and *F*-term analysis[J]. Technovation, 2017, 60/61: 1-14.

[2] Ma T T, Zhou X, Liu J, et al. Combining topic modeling and SAO semantic analysis to identify technological opportunities of emerging technologies[J]. Technological Forecasting and Social Change, 2021, 173: 121159.

[3] 任海英, 王倩. 技术机会发现方法的研究现状、趋势和问题[J]. 情报杂志, 2020, 39(4): 51-59.

[4] 伊惠芳, 刘细文, 龙艺璇. 技术创新全视角下技术机会发现研究进展[J]. 图书情报工作, 2021, 65(7): 132-142.

[5] 苏娜平, 谭宗颖. 技术机会分析方法研究综述与展望[J]. 情报理论与实践, 2020, 43(11): 179-186.

[6] Lee C Y. A review of data analytics in technological forecasting [J]. Technological Forecasting and Social Change, 2021, 166: 120646.

[7] 李慧, 孟玮. 专利视角下的美国空军核心技术演化分析[J]. 情报理论与实践, 2021, 44(2): 41-49.

[8] Yoon B, Park Y. A text-mining-based patent network: analytical tool for high-technology trend[J]. The Journal of High Technology Management Research, 2004, 15(1): 37-50.

[9] Kim M, Park Y, Yoon J. Generating patent development maps for technology monitoring using semantic patent-topic analysis[J]. Computers & Industrial Engineering, 2016, 98: 289-299.

[10] 吴菲菲, 陈肖微, 黄鲁成, 等. 基于语义相似度的技术多主题演化路径识别方法研究[J]. 情报杂志, 2018, 37(5): 91-96.

[11] Lee C Y, Jeon D, Ahn J M, et al. Navigating a product landscape for technology opportunity analysis: a word2vec approach using an integrated patent-product database[J]. Technovation, 2020, 96/97: 102140.

[12] 饶齐, 王裴岩, 张桂平. 面向中文专利SAO结构抽取的文本特征比较研究[J]. 北京大学学报(自然科学版), 2015, 51(2): 349-356.

[13] Hu J, Li S B, Yao Y, et al. Patent keyword extraction algorithm based on distributed representation for patent classification[J]. Entropy, 2018, 20(2): 104.

[14] Kim T S, Sohn S Y. Machine-learning-based deep semantic analysis approach for forecasting new technology convergence[J]. Technological Forecasting and Social Change, 2020, 157: 120095.

[15] Korobkin D, Fomenkov S, Kravets A, et al. Methods of statistical and semantic patent analysis[C]// Proceedings of the Conference on Creativity in Intelligent Technologies and Data Science. Cham: Springer, 2017: 48-61.

[16] Chen L, Xu S, Zhu L J, et al. A deep learning based method for extracting semantic information from patent documents[J]. Scientometrics, 2020, 125(1): 289-312.

[17] 王秀红, 高敏. 基于BERT-LDA的关键技术识别方法及其实证研究——以农业机器人为例[J]. 图书情报工作, 2021, 65(22): 114-125.

(C)1994-2023 China Academic Journal Electronic Publishing House. All rights reserved. http://www.cnki.net

[18] 赵京胜, 宋梦雪, 高祥, 等. 自然语言处理中的文本表示研究[J]. 软件学报, 2022, 33(1): 102-128.

[19] Mikolov T, Chen K, Corrado G, et al. Efficient estimation of word representations in vector space[OL]. (2013-09-07). https://arxiv.org/pdf/1301.3781.pdf.

[20] Le Q, Mikolov T. Distributed representations of sentences and documents[C]// Proceedings of the 31st International Conference on International Conference on Machine Learning. JMLR. org, 2014: II-1188-II-1196.

[21] Pennington J, Socher R, Manning C. GloVe: global vectors for word representation[C]// Proceedings of the 2014 Conference on Empirical Methods in Natural Language Processing. Stroudsburg: Association for Computational Linguistics, 2014: 1532-1543.

[22] Devlin J, Chang M W, Lee K, et al. Bert: pre-training of deep bidirectional transformers for language understanding[C]// Proceedings of the 2019 Conference of the North American Chapter of the Association for Computational Linguistics: Human Language Technologies. Stroudsburg: Association for Computational Linguistics, 2018: 4171-4186.

[23] Zhu C, Motohashi K. Identifying the technology convergence using patent text information: a graph convolutional networks (GCN)-based approach[J]. Technological Forecasting and Social Change, 2022, 176: 121477.

[24] Kim S, Park I, Yoon B. SAO2vec: development of an algorithm for embedding the subject-action-object (SAO) structure using doc2vec[J]. PLoS One, 2020, 15(2): e0227930.

[25] Krestel R, Chikkamath R, Hewel C, et al. A survey on deep learning for patent analysis[J]. World Patent Information, 2021, 65: 102035.

[26] 林原, 张乐, 丁堃, 等. 融合专利表示的技术路线图构建研究[J]. 情报杂志, 2021, 40(10): 15-20.

[27] 马建红, 姬帅, 刘硕. 面向专利的主题短语提取[J]. 计算机工程与设计, 2019, 40(5): 1365-1369, 1382.

[28] Kim K, Park K, Lee S. Investigating technology opportunities: the use of SAOx analysis[J]. Scientometrics, 2019, 118(1): 45-70.

[29] 陈泽龙. 基于句法表征的专利文本相似性评估[D]. 北京: 北京交通大学, 2019: 14-18.

[30] Arts S, Cassiman B, Gomez J C. Text matching to measure patent similarity[J]. Strategic Management Journal, 2018, 39(1): 62-84.

[31] 刘俊婉, 龙志昕, 王菲菲. 基于LDA主题模型与链路预测的新兴主题关联机会发现研究[J]. 数据分析与知识发现, 2019, 3(1): 104-117.

[32] 席笑文, 郭颖, 宋欣娜, 等. 基于word2vec与LDA主题模型的技术相似性可视化研究[J]. 情报学报, 2021, 40(9): 974-983.

[33] Zhang H, Daim T, Zhang Y Q. Integrating patent analysis into technology roadmapping: a latent Dirichlet allocation based technology assessment and roadmapping in the field of Blockchain [J]. Technological Forecasting and Social Change, 2021, 167: 120729.

[34] 马建红, 张少光, 曹文斌, 等. 面向功能信息的相似专利动态聚类混合模型[J]. 计算机应用与软件, 2021, 38(5): 201-207.

[35] Mao G Z, Han Y X, Liu X, et al. Technology status and trends of industrial wastewater treatment: a patent analysis[J]. Chemosphere, 2022, 288(Part 2): 132483.

[36] Shanie T, Suprijadi J, Zulhanif. Text grouping in patent analysis using adaptive *k*-means clustering algorithm[J]. AIP Conference Proceedings, 2017, 1827(1): 020041.

[37] 田鹏伟, 张娴. 基于异构信息网络融合的专利技术主题识别研究[J]. 情报杂志, 2021, 40(8): 45-52.

[38] Zhang J Z, Yu W Q. Early detection of technology opportunity based on analogy design and phrase semantic representation[J]. Scientometrics, 2020, 125(1): 551-576.

[39] Anuranjana, Mittas N, Mehrotra D. Clustering the patent data using *k*-means approach[C]// Proceedings of the Conference on Software Engineering. Singapore: Springer, 2019: 639-645.

[40] Zhou Y, Lin H, Liu Y F, et al. A novel method to identify emerging technologies using a semi-supervised topic clustering model: a case of 3D printing industry[J]. Scientometrics, 2019, 120(1): 167-185.

[41] Ren H Y, Zhao Y H. Technology opportunity discovery based on constructing, evaluating, and searching knowledge networks[J]. Technovation, 2021, 101: 102196.

[42] Jeon D, Ahn J M, Kim J, et al. A doc2vec and local outlier factor approach to measuring the novelty of patents[J]. Technological Forecasting and Social Change, 2022, 174: 121294.

[43] Wang H C, Chi Y C, Hsin P L. Constructing patent maps using text mining to sustainably detect potential technological opportunities[J]. Sustainability, 2018, 10(10): 3729.

[44] Kim D H, Lee H, Kwak J. Standards as a driving force that influences emerging technological trajectories in the converging world of the Internet and things: an investigation of the M2M/IoT patent network[J]. Research Policy, 2017, 46(7): 1234-1254.

[45] Blei D M, Ng A Y, Jordan M I. Latent Dirichlet allocation[J]. Journal of Machine Learning Research, 2003, 3: 993-1022.

[46] 吕璐成, 周健, 王学昭, 等. 基于双层主题模型的技术演化分析框架及其应用[J]. 数据分析与知识发现, 2022, 6(2): 18-32.

[47] 陈浩, 张梦毅, 程秀峰. 融合主题模型与决策树的跨地区专利合作关系发现与推荐——以广东省和武汉市高校专利库为例[J]. 数据分析与知识发现, 2021, 5(10): 37-50.

[48] Yun J, Geum Y. Automated classification of patents: a topic modeling approach[J]. Computers & Industrial Engineering, 2020, 147: 106636.

[49] Kim J, Geum Y. How to develop data-driven technology roadmaps: the integration of topic modeling and link prediction[J]. Technological Forecasting and Social Change, 2021, 171:

(C)1994-2023 China Academic Journal Electronic Publishing House. All rights reserved.　http://www.cnki.net

120972.

[50] Choi D, Song B. Exploring technological trends in logistics: topic modeling-based patent analysis[J]. Sustainability, 2018, 10(8): 2810.

[51] 韩芳, 张生太, 冯凌子, 等. 基于专利文献技术融合测度的突破性创新主题识别——以太阳能光伏领域为例[J]. 数据分析与知识发现, 2021, 5(12): 137-147.

[52] 张金柱, 王玥, 胡一鸣. 基于专利科学引文内容表示学习的科学技术主题关联分析研究[J]. 数据分析与知识发现, 2019, 3(12): 52-60.

[53] 刘小玲, 谭宗颖. 基于专利多属性融合的技术主题划分方法研究[J]. 数据分析与知识发现, 2022, 6(2): 45-54.

[54] Yoon B, Magee C L. Exploring technology opportunities by visualizing patent information based on generative topographic mapping and link prediction[J]. Technological Forecasting and Social Change, 2018, 132: 105-117.

[55] Seo W. A patent-based approach to identifying potential technology opportunities realizable from a firm's internal capabilities[J]. Computers & Industrial Engineering, 2022, 171: 108395.

[56] Han X T, Zhu D H, Wang X F, et al. Technology opportunity analysis: combining SAO networks and link prediction[J]. IEEE Transactions on Engineering Management, 2021, 68(5): 1288-1298.

[57] Cho J H, Lee J, Sohn S Y. Predicting future technological convergence patterns based on machine learning using link prediction [J]. Scientometrics, 2021, 126(7): 5413-5429.

[58] Park I, Yoon B. Technological opportunity discovery for technological convergence based on the prediction of technology knowledge flow in a citation network[J]. Journal of Informetrics, 2018, 12(4): 1199-1222.

[59] 翟东升, 刘鹤, 张杰, 等. 一种基于链路预测的技术机会挖掘方法[J]. 情报学报, 2016, 35(10): 1090-1100.

[60] Aaldering L J, Leker J, Song C H. Competition or collaboration? - Analysis of technological knowledge ecosystem within the field of alternative powertrain systems: a patent-based approach[J]. Journal of Cleaner Production, 2019, 212: 362-371.

[61] Qi Y, Zhang X, Hu Z Y, et al. Choosing the right collaboration partner for innovation: a framework based on topic analysis and link prediction[J]. Scientometrics, 2022, 127(9): 5519-5550.

[62] Hong S, Lee C Y. Effective indexes and classification algorithms for supervised link prediction approach to anticipating technology convergence: a comparative study[J]. IEEE Transactions on Engineering Management, 2023, 70(4): 1430-1441.

[63] Nakai K, Nonaka H, Hentona A, et al. Community detection and growth potential prediction using the stochastic block model and the long short-term memory from patent citation networks[C]// Proceedings of the 2018 IEEE International Conference on Industrial Engineering and Engineering Management. Piscataway: IEEE, 2018: 1884-1888.

[64] Chen G F, Xu C, Wang J Y, et al. Nonnegative matrix factorization for link prediction in directed complex networks using PageRank and asymmetric link clustering information[J]. Expert Systems with Applications, 2020, 148: 113290.

[65] Han F, Magee C L. Testing the science/technology relationship by analysis of patent citations of scientific papers after decomposition of both science and technology[J]. Scientometrics, 2018, 116(2): 767-796.

[66] Geum Y, Kim M. How to identify promising chances for technological innovation: keygraph-based patent analysis[J]. Advanced Engineering Informatics, 2020, 46: 101155.

（责任编辑 魏瑞斌）

(C)1994-2023 China Academic Journal Electronic Publishing House. All rights reserved. http://www.cnki.net

邮发代号：82-153　　qbxb.istic.ac.cn





定价：48.00元

3.9 基于 CiteSpace 可视化分析的柑橘黄龙病研究进展

ISSN 1009-9980
CN 41-1308/S

果树学报

GUOSHU XUEBAO

JOURNAL OF FRUIT SCIENCE

第40卷 第4期
Vol.40 No.4
2023

ISSN 1009-9980

中国农业科学院郑州果树研究所 主办

果树学报 JOURNAL OF FRUIT SCIENCE Vol.40 No.4 2023 中国农业科学院郑州果树研究所主办

果 树 学 报

GUOSHU XUEBAO

2023年4月 第40卷 第4期

目 次

种质资源·遗传育种·分子生物学

应用 SSR 荧光标记法构建 22 个柚类品种的分子身份证 …… 吴仕蔓,娄兵海,陈传武,唐 艳,邓崇岭,武晓晓 (605)

自花授粉花柱提取物对澳洲坚果品种间杂交亲和性的影响 …… 孔广红,余文才,柳 觐 (615)

杧果金煌×热农 1 号后代果实糖酸组分遗传分析 …… 李 星,郑 斌,许文天,马小卫,王松标,钱敏杰,武红霞 (630)

刺梨 *CDPK* 基因家族的鉴定及其对供钙水平的表达响应…… 龚丽莎,向芷萱,王 照,鲁 敏,安华明 (639)

基于 WGCNA 的刺葡萄抗白腐病关键基因的发掘 …… 谭西北,李 鹏,孙 磊,樊秀彩,刘崇怀,姜建福,张 颖 (653)

栽培·生理·生态

4 个苹果品种的抗寒性评价 …… 徐功勋,周 佳,吕德国,秦嗣军 (669)

不同矮化中间砧对瑞雪苹果果实品质的影响 … 樊 娟,孙鲁龙,刘振中,杨舜博,朱佳顺,史 涛,赵政阳 (680)

软/硬肉葡萄果实细胞壁结构、组分及降解酶活性的变化 …… 海龙飞,栗温新,李志谦,李 猛,陈超阳,魏红丽,邹东方,何 畅,冯建灿,叶 霞 (690)

外源 γ-氨基丁酸对蛇龙珠葡萄果实糖酸代谢的影响 …… 王宇航,韩爱民,张立梅,李 斗,金 鑫,王春恒,冯丽丹,杨江山 (699)

高温对萨米脱甜樱桃幼苗叶片生理指标的影响 …… 张 琛,刘 辉,郗笃隽,骆慧枫,裴嘉博,黄康康,阮若昕,赖梦霞,樊怀福 (712)

中微量元素钙、镁、硼叶面肥对皱皮木瓜果实产量和品质的影响 …… 陈 珍,曹帮华,耿 颖,刘 炜,曹晓楠,赵钰琪,王可欣,李圣波,诸葛绪钦 (724)

植物保护·果品质量与安全

苹果内生促生真菌筛选及其促生特性 …… 刘娟娟,郑 娇,高成林,刘虹杉,张东华,刘 丽 (735)

嗜果刀孢菌在野杏叶片致病过程中主要酶的种类及活性分析 … 刘楚丽,鲁海龙,陈虹瑾,孙洪涛,马 荣 (747)

专论与综述

梨果肉质地及香气研究进展 … 徐钰清,田路明,曹玉芬,董星光,张 莹,霍宏亮,齐 丹,徐家玉,刘 超 (757)

基于 CiteSpace 可视化分析的柑橘黄龙病研究进展 …… 刘杰帆,林铭佳,张建桃,周腾媛 (771)

技术与方法

Oligo-FISH 涂染揭示柚粗线期 1 号染色体的结构及配对 …… 何 礼,张国艳,陈克玲,何 建,关 斌,李文婷,刘建军 (788)

基于便携式蜜柚光谱仪的金沙柚叶片氮含量监测模型研究 …… 李艳大,曹中盛,潘玉霞,孙滨峰,黄俊宝,杨伟光,彭忻怡,舒时富,叶 春 (797)

新品种选育报告

早熟、优质蟠桃新品种中蟠 101 的选育 …… 牛 良,刘 鑫,潘 磊,曾文芳,崔国朝,鲁振华,王志强 (807)

中熟黄肉桃新品种黄妃的选育 …… 高晓兰,李桂祥,董晓民,李 淼,刘 伟,宫庆涛,刘 进,陈铁牛,张安宁 (811)

大粒早熟葡萄新品种宝光的选育 …… 李敏敏,尹勇刚,韩 斌,刘长江,孙 艳,贾 楠,曾庆明,郭紫娟 (815)

无核柚新品种宝石红柚的选育 …… 唐 娟,望飞勇,高 明,张 兰 (818)

火龙果新品种粉红 1 号的选育 …… 张志珂,马梅冰,胡桂兵,严朝东,叶耀雄,张 荣,秦永华 (822)

《果树学报》投稿须知 …… (827)

《果树学报》参考文献著录格式(828) 征订启事(828)

社 长:张 莉 责任编辑:王 珂,和 静

编辑人员:王 珂,和 静,王小丽,陈新平,樊 辉

果 树 学 报 2023,40(4):771-787
Journal of Fruit Science

DOI:10.13925/j.cnki.gsxb.20220399

基于CiteSpace可视化分析的柑橘黄龙病研究进展

刘杰帆,林铭佳,张建桃*,周腾媛

(华南农业大学数学与信息学院,广州 510642)

摘 要:柑橘黄龙病(Huanglongbing,简称HLB)是柑橘生产中最具毁灭性的病害,给柑橘产业带来巨大的经济损失。为系统了解近年柑橘黄龙病的研究状况,采用CiteSpace,从Web of Science(WOS)和中国知网(CNKI)数据库中分别检索出2108篇英文文献和2359篇中文文献,再以发文量、研究主体(作者、机构及国家)、研究热点及前沿4个角度进行知识图谱分析。由分析可得:(1)国内外正加强对于黄龙病的研究,预计未来仍会保持热度;(2)我国虽已成为黄龙病研究的重要力量,但其科研综合实力与美国相比仍存在巨大差距;(3)中文文献的研究热点主要包括黄龙病综合防治和黄龙病原体,近年关注优势品种的栽培技术及持续重视综合防控;(4)英文文献聚焦于提高柑橘生产力、防治药物、柑橘木虱和黄龙病原体等方面,近年则关注柑橘木虱的生理生化特性和防治手段,并开始重视非洲柑橘木虱对欧洲黄龙病的潜在威胁,然后对黄龙病的分类检测技术进行不断地创新。最后提出缩小我国与美国的黄龙病科研差距的建议。

关键词:柑橘黄龙病;知识图谱;CiteSpace;研究热点

中图分类号:S666 **文献标志码**:A **文章编号**:1009-9980(2023)04-0771-17

Research progress in citrus Huanglongbing based on citespace visual analysis

LIU Jiefan, LIN Mingjia, ZHANG Jiantao*, ZHOU Tengyuan

(College of Mathematics and Informatics, South China Agricultural University, Guangzhou 510642, Guangdong, China)

Abstract: Citrus Huanglongbing (HLB) has brought huge economic losses to the global citrus industry. In order to systematically understand the research status and trend of citrus Huanglongbing in recent years, the CiteSpace was used to select 2359 Chinese journal literature data from CNKI (1956—2021) database with the key words of "Huanglongbing+Yellow shoot disease+Citrus greening+Dieback" in this paper. Besides, A total of 2108 research papers and review papers were selected from the Web of Science (WOS, 2002—2021) database with the key words of "TS=(Huanglongbing) OR TS=(Yellow shoot disease) OR TS=(Citrus greening) OR TS=(Likubing) OR TS=(Vein phloem degradation) OR TS=(Leaf mottle) OR TS=(Dieback) ". The knowledge map of Chinese and English literature data was analyzed from four aspects: the number of published papers, research topics (authors, institutions and countries), research hotspots and frontiers. The results show that: (1) The research on Huanglongbing is being strengthened at home and abroad, and it is expected that it will keep the heat in the future; (2) The number of published articles in the United States is far ahead of other countries with 1062 articles, accounting for 50.38% of WOS-related databases. The intermediary centrality (i.e. influence) of the United States is 0.72, while China is only 0.22, and Australia is 0.23. It can be seen that the research on Huanglongbing in the United States has the strongest influence in the world, followed by Australia and China. Compared with the United States, there is still a huge gap in the comprehensive strength dealt

收稿日期:2022-07-22 **接受日期**:2022-11-28

基金项目:广东省普通高校特色创新类项目(2019KZDZX1002);广东省自然科学基金(2022A1515011008);华南农业大学新农村发展研究院农业科技合作共建项目(2021XNYNYKJHZGJ034);高等学校学科创新引智计划资助(D18019)

作者简介:刘杰帆,男,在读硕士研究生,研究方向为微波处理对柑橘活性的影响。Tel:13380852844,E-mail:710204974@qq.com

*通信作者 Author for correspondence. Tel:13076759646,E-mail:zhangjiantao@yeah.net

(C)1994-2023 China Academic Journal Electronic Publishing House. All rights reserved. http://www.cnki.net

with Huanglongbing research in China; (3) The research hotspots of Chinese literature mainly include comprehensive prevention and control of Huanglongbing as well as Huanglongbing pathogen, among which heat treatment can be effectively applied to control Huanglongbing, but it only stays in the experimental stage. Other treatment methods (using some chemical molecules to induce or stimulate the internal resistance of citrus, using oligosaccharide as plant immune recognition, developing a vaccine targeting nano iodine to kill Huanglongbing pathogen, and using stem tip grafting to detoxify, *etc*.) have problems of high technical threshold. The three-step method summarized by several research groups organized by the Ministry of Agriculture of the PRC is still applicable, which includes killing citrus psyllid, using pathogen-free propagation materials, and eradicating pathogens (trees) in time for comprehensive control. Among them, controlling citrus psyllid is the key measure, which can establish an ecological isolation system and use natural or physical and ecological barriers to block the large-scale spread of psyllid. The chemical control is obvious but unsustainable, and therefore physical and biological control measures can be adopted. In China, there is a phenomenon that the suitable area of citrus psyllids has moved northward, so early warning and prevention measures should be taken. Research frontiers include the following aspects: (1) Some wild disease-resistant citrus varieties have been found in China, which can be used to resist Huanglongbing; (2) From 2015 to 2019, China invested nearly 400 million *yuan* to support the program for prevention and control of Huanglongbing; (3) In 2019, local regulations on prevention and control of Huanglongbing were issued for the first time, and the prevention and control of Huanglongbing in China will continue to be maintained or even strengthened in the future; (4) English literature research focuses on improving citrus productivity, controlling drugs, citrus psyllid control and Huanglongbing pathogen, among which international orchard management focuses on evaluating the optimal dosage of trace elements, improving irrigation system, and applying fertilizer precisely, so as to improve the productivity under the epidemic conditions of Huanglongbing. The research on physiological and biochemical characteristics of Asian citrus psyllid (ACP) has been developed, which is embodied in: (1) It can cross potential geographical obstacles (such as roads and fallow land); (2) After the pathogen can be obtained from infected plants within half an hour, it can be transmitted to healthy plants within less than one hour after an incubation period of 8−12 days; (3) There is a remarkable flight capability. For the control of psyllid, physical stimulation, physiological behavior of ACP destruction and the resistance of host plants to ACP can be explored to improve the comprehensive management of ACP. Research frontiers include the following aspects: The potential threat of African citrus psyllid to European Huanglongbing has been serious, and the classification and detection techniques of Huanglongbing are constantly being innovated. Among them, the hyperspectral remote sensing equipment has a classification accuracy of HLB by no less than 99%, which is expected to be used for early nondestructive detection and classification of citrus diseases. Both of the literature point out that there is no specific chemical to treat Huanglongbing and the isolated culture of Huanglongbing has not been realized. However, some studies have successfully tried co-culture with other bacteria and used Lcr gene to realize the replication and passive growth of CLas. Finally, this paper puts forward some suggestions to narrow the research gap of Huanglongbing between China and the United States, which include the following three aspects: (1) The government continues to invest a lot of money and further improve the prevention and control laws and regulations; (2) Scientific research institutions take the lead in establishing online communication platform to ensure the immediate contact of research institutions in various regions, so as to promote the division of labor and cooperation in Huanglongbing research; (3) Researchers should continue to search for isolation and culture technology of Huanglongbing pathogen or

(C)1994-2023 China Academic Journal Electronic Publishing House. All rights reserved. http://www.cnki.net

other alternative ways, otherwise the research field of biomolecules of Huanglongbing will always be limited.

Key words: Citrus Huanglongbing; Knowledge map; CiteSpace; Research hotspot

柑橘是世界第一大类水果，也是我国南方栽培面积最广的果树，在我国的农业和国民经济中占据十分重要的地位[1]。据统计，从2007年起，我国的柑橘种植面积和产量均已超过巴西，跃居全球第一位，成为世界第一大柑橘生产国[1-2]。然而，柑橘生产过程中会遭受许多病害，这些病害直接威胁着柑橘产业的发展。

柑橘黄龙病（Huanglongbing，简称HLB）是柑橘生产中最具毁灭性的病害，由一种局限于韧皮部筛管细胞的革兰氏阴性细菌引起，该菌归属于原核生物、薄壁菌门、α-变型菌纲（Proteobacteriacea）的候选韧皮部杆菌属（*Candidatus* Liberibacter spp.）[3]，可导致叶片斑驳、发黄、缺锌叶脉枯萎、枝条枯死、生长迟缓、抑制新根生长、变小、变绿等症状[4]。其致病机制为：先引起柑橘韧皮部组织坏死和筛管堵塞，进而导致光合产物从源器官（主要为成熟叶）到库器官（如嫩叶、幼果和根等）的运输受阻，最后造成植株代谢紊乱、衰退直至死亡[5]。目前共发现3个黄龙病菌种：亚洲种（*Candidatus* Liberibacter asiaticus，简称CLas）、非洲种（*Candidatus* Liberibacter africanus，简称CLaf）和美洲种（*Candidatus* Liberibacter americaus，简称CLam），其中亚洲种是目前分布最广的，我国黄龙病菌皆为亚洲种[3,6]。3种病菌都可在22~24 ℃致病，其中非洲种为热敏型，在30 ℃以上症状减轻或消失[7]。美洲种与亚洲种为耐热型，前者在24 ℃滴度很高，在32 ℃以上几乎无法存活，而后者存活温度超过30 ℃，并且在32 ℃和35 ℃有着高滴度，但在38 ℃时滴度不高[8]。黄龙病菌主要通过木虱和带病接穗嫁接传播，具有蔓延速度极快、传播范围广、危害极大、尚无根治措施等特点，给柑橘产业的发展带来极其严重的经济损失[2,9-10]。

目前黄龙病的研究方向大而广，可涉及病原体、寄主抗性评价、防治药剂、基因编辑、检测方法、防控策略等多个方面。面对其海量的文献数据，若想系统、精准地了解该病害的研究现状及发展趋势，最好的方法是利用CiteSpace对其进行统计分析。CiteSpace是陈超美开发的一款引文可视化分析软件，用于分析科学文献中蕴含的潜在知识[11]。该软件的工作原理基于共引分析理论和寻径网络算法，可对特定领域的文献进行信息分析和数据挖掘，从而得到各种科学的知识图谱，进而直观地展示某领域的研究热点及前沿[12]。基于此，笔者在本文中采用信息可视化分析工具CiteSpace（版本号5.8.R3），以CNKI（1956-2021）和Web of Science（WOS）核心合集（2002-2021）为数据源，对中英文黄龙病研究文献进行数据提取、计量分析，归纳两者的热点与前沿，以期了解最新的国际研究动态，为我国黄龙病的研究提供参考。

1　数据来源和研究方法

1.1　中文文献数据

在中国知网数据库中，鉴于以往不同国家和地区对黄龙病的命名不一致的情况[13]，笔者在本文中采用高级检索的方式，以“黄龙病+黄梢病+青果病+梢枯病”为主题词进行检索，设置截止时间为2021年12月31日，取消勾选“中英文扩展”，得到2021年12月31日以前（包含）发表的有关结果共2910条，然后选择“学术期刊”，保留期刊文献2359篇，最后将文献的标题、作者、机构、摘要、关键词等题录信息批量导出为Refworks格式的纯文本文件，即中文文献数据。

1.2　英文文献数据

在Web of Science核心数据库中，笔者在本文中以“TS=(Huanglongbing) OR TS=(Yellow shoot disease) OR TS=(Citrus greening) OR TS=(Likubing) OR TS=(Vein phloem degeneration) OR TS=(Leaf mottle) OR TS=(Dieback)”为检索式进行检索，截止时间设置为2021年12月31日，得到2021年12月31日以前（包含）发表的有关结果2378条。在文献类型中勾选“论文”及“综述论文”进行精炼，保留论文及综述论文共2108篇，选择文献的“全记录与引用的参考文献”，批量导出为纯文本格式文件，即可得到英文文献数据。

1.3　研究方法

笔者在本文中使用Excel及可视化软件CiteSpace软件对从CNKI与WOS检索获得的黄龙病研究相关

(C)1994-2023 China Academic Journal Electronic Publishing House. All rights reserved.　http://www.cnki.net

文献，从发文趋势、研究主体（包括作者、机构、国家）、研究热点、研究前沿等4个角度，进行发文量统计、研究主体共现、关键词共现及聚类、突现词探测，并进行对比分析。

2 研究结果及分析

2.1 发文量统计

笔者在本文中对CNKI和WOS数据库收录的黄龙病相关文献进行检索并筛选，分别以中文发文量和英文发文量进行分析，具体如下。

2.1.1 中文文献发文量 在1956—2021年这66年间，从CNKI数据库筛选出来的黄龙病相关文献共2359篇，年均发文量约35.74篇，年度发文趋势如图1所示。

根据图1可划分为3个阶段。1956—1978年间为起步阶段，该阶段的年度发文量均在10篇以下，

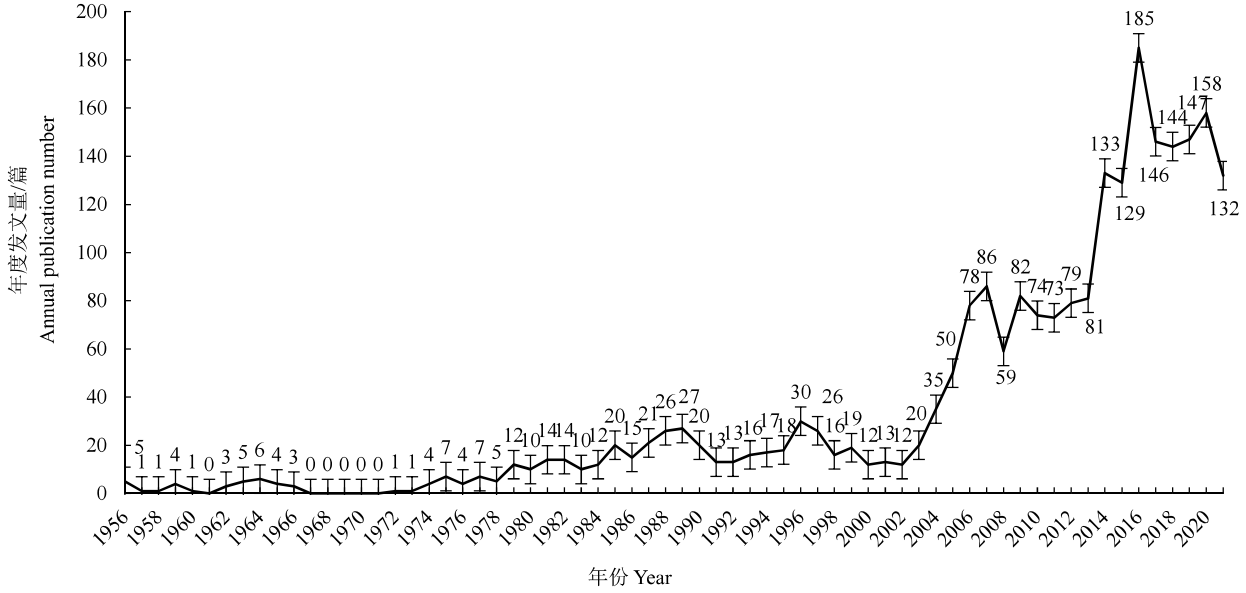


图1 中文文献柑橘黄龙病年度发文趋势

Fig. 1 Trends of annual publications of citrus Huanglongbing from Chinese literature

23年间总发文量为62篇，年均发文量不足2篇，甚至连续5 a（年）（1967—1971）的发文量为0。1979—2001年间为发展阶段，整体呈现稳步增长趋势，少数年份出现回落，年度发文量保持在10篇以上，最高达到30篇（1996年），总发文量为379篇。2002—2021年为快速阶段，年均发文量为95篇，2016年度达到了185篇的峰值。快速阶段的发文量总共为1903篇，占据CNKI总文献数的80.67%，说明近年来，我国比以往更加重视黄龙病的防治工作，预计未来黄龙病的研究热度仍会继续保持。

2.1.2 英文文献发文量 在2002—2021年这20年间，WOS核心数据库收录的黄龙病相关文献共2108篇，年均发文量约106篇，年度发文趋势如图2所示。黄龙病英文文献的发文量整体呈现上升趋势，少数年份出现回落。2021年年度发文量达到了历史峰值，为266篇，说明国际力量正不断加强对黄龙病的研究。

2.2 研究主体分析

2.2.1 作者分析 对从CNKI获得的数据进行作者（Author）分析，绘制得到可视化图谱，如图3（左）所示。图中共出现了1108个节点，1940条连线，其中节点数为对象数，节点越大，表明该对象的文章数量越多；节点之间的连线越粗，表明两个对象之间的合作关系越密切。根据普赖斯定律，核心作者的认证公式为$M\approx0.749\times\sqrt{N_{max}}$，其中$N_{max}$为发文最多的作者发文量，M为核心作者的最低文献数[14]。经计算，$M\approx0.749\times\sqrt{47}\approx5.13$，因此该领域发文数不少于6篇的作者为核心作者。结合图和有关数据可以看出，当前国内黄龙病领域的研究人员呈现出“流线型”，形成了以柯冲（福建省农业科学院，47篇，排名第一）、邱柱石（广西柑橘研究所，43篇，排名第二）、邓晓玲（华南农业大学，37篇，排名第三）等作者为核心的作者群和合作网络，和少数独立的作者。

对从WOS获得的数据进行作者（author）分析，

(C)1994-2023 China Academic Journal Electronic Publishing House. All rights reserved. http://www.cnki.net

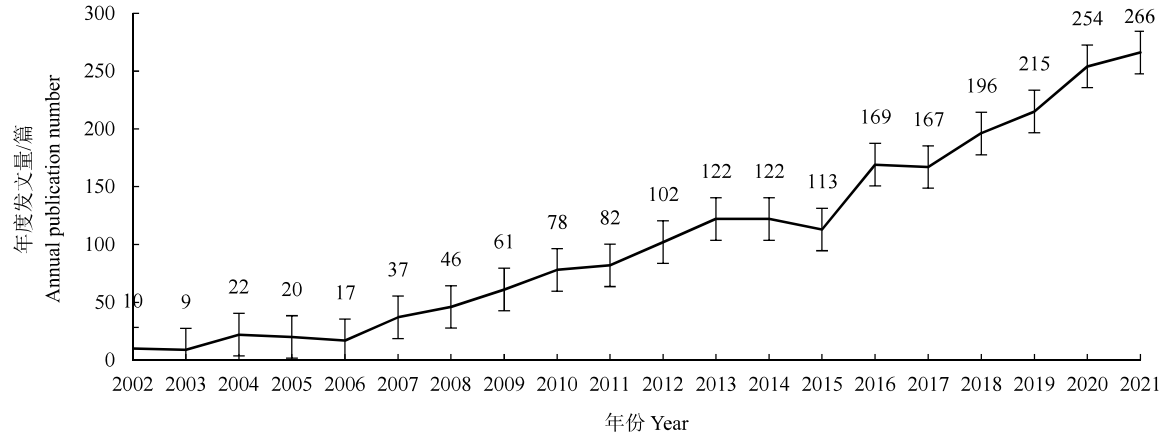


图2　英文文献柑橘黄龙病年度发文趋势

Fig. 2　Trends of annual publications on citrus Huanglongbing from English literature



图3　中、外文作者共现网络

Fig. 3　Co-occurrence network of Chinese and foreign authors

绘制作者合作网络图谱，如图3（右）所示。图中共出现了715个节点，1378条连线。根据普赖斯定律，可计算出发文量7篇及以上的为核心作者。结合图和有关数据，可看出“蛛网型”合作网络密集分布，形成了以DAVID G HALL（美国农业部农业研究局，美国园艺研究实验室，80篇，排名第一）、LUKASZ L STELINSKI（美国佛罗里达大学昆虫学和线虫学教授，77篇，排名第二）、NABIL KILLINY（美国佛罗里达大学植物病理学副教授，63篇，排名第三）等高产作者为核心的作者群及合作网络。

2.2.2　机构分析　对从CNKI获得的数据进行机构（institution）分析，绘制得到可视化图谱，如图4（左）所示。图中共出现了767个节点，282条连线。由图及有关数据可以看出，广西柑橘研究所（广西桂林，94篇，位列第一）、中国农业科学院柑橘研究所（又称“西南大学柑橘研究所”，重庆市，49篇，位列第二）、浙江省台州市黄岩区植物检疫站（浙江台州，26篇，位列第三）、浙江省柑橘研究所（浙江台州，23篇，位列第四）、国家脐橙工程技术研究中心（江西赣州，17篇，位列第五）等机构周围形成了较为密集的合作网络，同省份的地区的机构合作较为紧密，多数机构的关系呈现出独立、两两联系的形式。

对从WOS获得的数据进行机构（institution）分析，绘制得到可视化图谱，如图4（右）所示。图中共出现了617个节点，1215条连线。结合图和有关数据可看出，当前国际黄龙病领域的研究机构较多，整体呈现为密集的蛛网状合作网络，形成了以佛罗里达大学（Univ Florida，美国，580篇，位列第一）、ARS（美国农业科学研究院，美国，201篇，位列第二）、美国农业部农业研究局（USDA-ARS，美国，195篇，位列第三）、圣保罗大学（Univ Sao Paulo，巴西，94篇，位列第四）、华南农业大学（South China Agr Univ，中

(C)1994-2023 China Academic Journal Electronic Publishing House. All rights reserved.　http://www.cnki.net



图4 国内(左)与国际(右)柑橘黄龙病研究机构合作网络

Fig. 4 Cooperation network of domestic (left) and international (right) citrus Huanglongbing research institutions

国,75篇,位列第五)、西南大学(Southwest Univ,中国,73篇,位列第六)等机构为主要核心的合作关系,并向四周延展开。

进一步获取CiteSpace中机构分析的有关数据,截取发文量30篇以上的高产机构共12个。其中有6个机构属于美国,4个机构属于中国,2个机构属于巴西。12个机构中,中国机构的总发文量为225篇,巴西机构的总发文量为133篇,而美国机构的总发文量为1129篇,是中国机构和巴西机构的发文量总和的2.15倍,占据WOS数据库总发文量(2108条)的53.56%。可以初步判断出,我国机构虽已成为国际黄龙病研究领域的重要力量,但其科研实力与美国相比,仍存在较大差距。

2.2.3 国家分析 对从WOS获得的数据进行国家(country)分析,绘制得到可视化图谱,如图5所示。图中共出现了83个节点,386条连线。根据在CiteSpace中获取国家分析的有关数据,截取发文量排名前10位的国家发文信息,然后汇总并制作成表格,如表1所示。

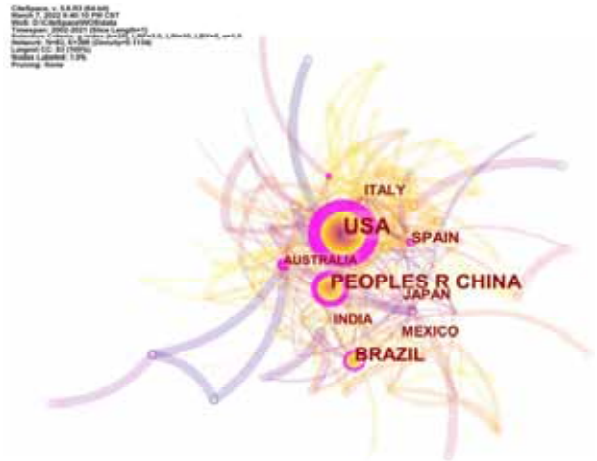


图5 国际柑橘黄龙病研究国家合作网络

Fig. 5 National cooperation network of international citrus Huanglongbing research

表1 国际柑橘黄龙病研究发文量排名前10的国家

Table 1 Top 10 countries in terms of the number of articles published on international citrus Huanglongbing research

国家 Country	发文量/篇 Articles No.	首次发文年份 Year of first publication	中介中心性 Betweeness centrality
美国 USA	1062	2002	0.72
中国 China	475	2004	0.22
巴西 Brazil	255	2003	0.16
西班牙 Spain	122	2002	0.16
墨西哥 Mexico	84	2011	0.05
印度 India	68	2004	0.03
意大利 Italy	67	2002	0.09
日本 Japan	58	2002	0.03
澳大利亚 Australia	53	2003	0.23
巴基斯坦 Pakistan	49	2003	0.03

由表1可以看出,当前国际上已有较多国家在黄龙病领域展开了相关研究,呈现出以美国(USA)、中国(China)、巴西(Brazil)等国家为核心的较为密集的合作网络,可见国家之间存在深度的合作关系。此外,美国以1062篇的发文量遥遥领先于其他国家,占据WOS数据库总发文量的50.38%,比第二名(中国,475篇)和第三名(巴西,255篇)的总和还多出332篇,可见美国的黄龙病科研实力强劲。

具有高中介中心性的文献通常是连接两个不同领域的关键枢纽[11],当某节点的中介中心性≥0.1时,该节点为关键节点。一个节点的中介中心性越高,表明其在网络中的连接程度越强,科研影响力越大[15]。美国的中介中心性以0.72排名第一,比中国

(C)1994-2023 China Academic Journal Electronic Publishing House. All rights reserved. http://www.cnki.net

（第三名，0.22）还多0.5。澳大利亚（Austraila）的发文量虽只有53篇，排名第九，其中介中心性却以0.23排名第二。综上，美国的黄龙病研究的影响力在全球最强，澳大利亚与中国次之。

美国相关科研成果的全球影响力虽然大，但实际防控效果很差。据统计，佛罗里达州的甜橙产量由2005—2006年的1.5亿箱下降至2019年的7200万箱[9]。2021年2月，美国批准使用涕灭威防控柑橘黄龙病，但早在2003年，涕灭威就因对人类造成健康问题而被欧盟禁用，中国自2020年10月1日起禁止含涕灭威的产品在境内销售和使用[16]。澳大利亚并无黄龙病的困扰，其研究角度是仅从检疫角度加以重视的，也难以说明该国的相关研究水平比中国高。虽然中国的发文量及质量不如美国，中介中心性稍差于澳大利亚，但应用下三项基本措施的实际防控效果是喜人的，全国的柑橘产量由2000年的878.31万t持续增长至2021年的5 121.9万t[17-18]，与美国形成了鲜明的对比，是生产防控和科研攻关相协调的体现。

2.3　研究热点

2.3.1　中文文献研究热点　关键词能够反映一篇文章的内容，凝练了最核心、最关键的信息，能协助了解到该领域的研究热点。对从CNKI获得的数据进行关键词（keyword）分析，然后选择Pathfinder算法，对同义词进行合并，生成关键词共现图谱。根据图谱截取频次大于25的高频关键词信息，再选择LLR（Log-likelihood Ratio）算法，对关键词进行聚类，得到15个有效聚类标签，最后将聚类结果可视化展示，如图6（左）所示。

15个聚类标签有：栽培技术（#0）、柑橘木虱（#1）、黄龙病（#2）、柑橘（#3）、黄化病（#4）、初步研究（#5）、青果病（#6）、温州蜜柑（#7）、柑橘生产（#8）、植物检疫（#9）、吸果夜蛾（#10）、种群动态（#11）、红江橙（#12）、墨西哥（#13）、早结丰产（#14）。根据关键词聚类图，进一步剔除与黄龙病无关的关键词，再将中文文献的黄龙病研究热点归纳为以下两个方面：

（1）黄龙病综合防治的相关研究。1）目前我国的综合防控按照20世纪80年代初我国农业部组织多个研究小组所总结出来的三项必要措施，具体为：灭杀柑橘木虱、使用无毒繁殖材料、及时铲除病原（树）进行综合防治，其中防控柑橘木虱是关键措施，对此可建立生态隔离系统：种植乔木、灌木、杉木等树种作为防护隔离林带（切忌种植木虱寄主植物），以及利用天然或物理生态屏障来阻断木虱大规模扩散[19-20]；在气候变暖的影响下，木虱适生区正在北移，预计在2081—2100年，其生活北界将由北纬30° N转移至32°~37° N，应加强早期预警和检疫防控措施[21-22]；目前防控柑橘木虱的方法以化学防治（杀虫剂）为主，也有研究提出采用绿色环保的生物防治，即通过投放捕食性天敌和寄生性天敌昆虫和微生物，如跳小蜂、啮小蜂、六斑月瓢虫等，以及其他物理防治措施，如杀虫灯、黄色粘虫板、性诱剂、糖醋液和诱蝇球等，这些物理措施在我国湖南部分地区已投入使用，可尝试用于其他地区[23-25]。2）治疗药剂：现今的药剂以防治为主，暂无特效药；土霉素可有效抑制黄龙病菌亚洲种，可减少柑橘叶片内的淀粉含量，增加柑橘产量，也未对果实品质产生显著影响[26]；磺胺二甲氧嘧啶钠盐（sulfadimethoxine sodium salt，SDM）对黄龙病（以纽荷尔脐橙为对象）有一定的抑制效果[27]；对柑橘树干注射1 g·L^{-1}的盐酸四环素能够显著降低黄龙病菌浓度，但经叶面喷施和根际浇灌盐酸四环素的方式防治效果不明显[28]。3）其他治疗手段：在研究早期，以林孔湘为代表的科研人员对黄龙病的治疗开展了一系列的初步研究，发现湿热空气热处理可致使病菌钝化甚至死亡，且植物活力不受影响，之后热处理的方式发展成：温控箱、热空气、热水蒸汽、可透太阳光的田间移动温室（国外）、远红外、微波等，但上述实验尚无田间规模应用的条件，而多用于无毒幼苗的培育[29-33]。除了热处理，还有：a. 利用一些化学分子诱导或激发柑橘内部抗病；b. 以寡糖为植物免疫识别、以纳米碘为靶向消杀黄龙病菌的疫苗研制思路，对病树处理后可达到PCR转阴率50%的效果，但仅停留在试验阶段[10]；c. 利用茎尖嫁接脱毒：依据病毒在植物体内分布不均匀性原理，将顶端分生组织不带毒区域切下并嫁接到健康砧木上进行培育获得无病毒植株[34]，是20世纪80年代以来应用最广，也是迄今最为有用的技术。

（2）黄龙病原体的相关研究：1）病原体分布：CLas在病枝中分布不均匀，在果实处（橘络、果中轴或种皮）富集[35]；柑橘花器中的花瓣、雄蕊、雌蕊和花粉以及种子中的种皮和胚乳组织均可检测到CLas，但未发现播种和授粉可传播HLB[36]；广东黄龙病菌以Type-2原噬菌体类型和Type-1+3混合原噬菌体类型为主，前者比后者更容易在柑橘木虱成虫体内

(C)1994-2023 China Academic Journal Electronic Publishing House. All rights reserved.　http://www.cnki.net

增殖，对柑橘也具有更强的致病力[37]。2）黄龙病原体的检测技术：掌上纳米孔测序仪MinION：可弥补因柑橘木虱虫体过小或损坏难以进行光学识别的不足；可视化LAMP快速检测技术：具有成本低、30 min即可观察到检测结果、操作简便、准确性高等优点，有望替代qPCR在田间进行黄龙病的快速鉴定；基于串联重复序列的柑橘黄龙病菌聚合酶链式置换反应（TR-PCDR）检测技术，该技术的检测灵敏度比基于SYBR Green的实时荧光定量PCR高10倍，已大规模应用于广西全区柑橘样品的黄龙病菌检测[36,38-39]。3）离体培养：国内外均有黄龙病菌成功分离纯培养的报道，但未完成科赫氏法则检验，也无法被他人重复，有待进一步验证[40-41]；有研究将黄龙病菌与有益及有害的伴生菌在培养基内进行共培养，并发现黄龙病菌的增殖量高达50倍，实现了黄龙病菌与伴生菌的共培养，有望推动病原学及生物学的基础研究[42]。4）病原分泌蛋白：黄龙病菌亚洲种Psy62基因组共有57个可能的Sec依赖分泌蛋白（HLB侵染过程中重要的毒力因子），其中分泌蛋白m3875和m4405具有抑制寄主PCD的功能，并且能影响寄主正常生长[43]；CLas Sec6为韧皮部杆菌属亚洲种特异性分泌蛋白，可作为黄龙病感病指示分子标志物[44]；分泌蛋白Clsp33不具有跨膜结构域，但具有典型的信号肽，长度为20 aa，具有分泌能力，对本氏烟具有致病性，可推测其为潜在的毒力因子[45]。5）寄主抗性评价：CLas侵染柑橘寄主后，会引起大多数寄主防御相关蛋白或转录因子的上调表达，如过氧化氢酶、Cu/Zn超氧化物歧化酶、几丁质酶、植物凝集素相关蛋白及神秘果素样蛋白等[46]；在黄龙病菌与柑橘互作早期，寄主叶脉和根分别调控糖代谢和次生代谢相关通路以响应CLas侵染，而CLas通过调控物质跨膜运输和能量代谢来维持病原细胞在柑橘中的增殖和扩散[47]；SA（水杨酸）与MeSA（水杨酸甲酯）信号转导的关键酶基因*CsSABP2-1*和*CsSABP2-4*在柑橘SAR响应CLas侵染中起着重要作用，其高水平表达与柑橘HLB抗性紧密相关[48]；染HLB的椪柑，萜类化合物中相对含量显著增加的有大根香叶烯D和大根香叶烯B（柑橘类植物次生化合物中半萜及倍半萜含量与病原真菌的抑制效果呈正相关）[49]。6）基因：目前针对黄龙病菌序列拼接策略更多的是结合从头拼接和基于参考基因组的拼接方法进行互补，从而得到最终的基因组序列；黄龙病菌基因组由保守的染色体区域序列和高变异的原噬菌体序列组成；原噬菌体区域的变异主要表现为噬菌体类型的差异，其基因组大小约为1.26 Mb，GC含量约为36.5%；黄龙病菌缺乏编码毒素或特殊分泌系统的基因，含有一套完整的三羧酸循环（TCA）所需的酶，但是缺乏用于直接形成丙酮酸的酶，如丝氨酸脱水酶、丙氨酸消旋酶和丙氨酸脱氢酶[13]；黄龙病菌涉及DNA复制和细胞分裂功能的管家基因表达较稳定，在CLas的基因表达研究中可选择ftsZ+gyrA的基因组合作为内参基因[50]。

2.3.2 英文文献研究热点 对从WOS获得的数据进行关键词（keyword）分析，生成关键词共现图谱。根据图谱截取频次大于100的高频关键词信息，再选择LLR（Log-likelihood Ratio）算法，对关键词进行聚类，形成11个有效聚类标签，最后将聚类结果可视化展示，如图6（右）。

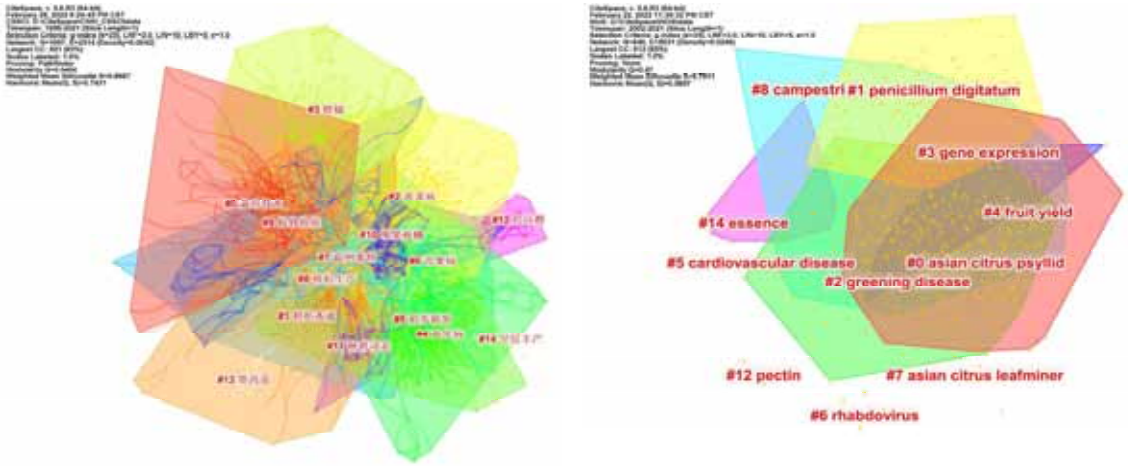


图6 国内（左）与国际（右）柑橘黄龙病研究关键词聚类图

Fig. 6 Cluster diagram of key words in domestic (left) and international (right) citrus Huanglongbing research

(C)1994-2023 China Academic Journal Electronic Publishing House. All rights reserved. http://www.cnki.net

11个聚类标签有：Asian citrus psyllid（#0亚洲柑橘木虱）、*Penicillium digitatum*（#1柑橘绿霉病）、greening disease（#2青果病）、gene expression（#3基因表达）、fruit yield（#4果实产量）、cardiovascular disease（#5心血管疾病）、rhabdovirus（#6棒状病毒）、asian citrus leafminer（#7亚洲柑橘潜叶蛾）、campestris（#8野生的）、pectin（#12果胶）、essence（#14本质）。根据关键词聚类图，进一步剔除与黄龙病无关的关键词，再将英文文献的黄龙病研究热点归纳为以下3个方面：

（1）提高柑橘生产力、防治药物的相关研究：1）黄龙病流行的情况下，为提高柑橘生产力，近年国际果园管理成果有：评估微量元素的最佳用量，如在佛罗里达，受HLB影响的的幼树的最佳Mn用量是8.9~11.5 kg·hm^{-2}；改善灌溉系统：珍珠岩基质的土壤可节约用水；潜灌长凳比传统滴灌节省98%的水，且潜灌长凳所栽砧木的生长速度比滴灌快4周；对不同类型的柑橘树精准施肥：受HLB影响的柑橘树中，Mg肥对土壤和养分浓度的影响比N或Ca的影响大；施用生物农药和化学农药[51-54]。2）药物方面，用赤霉素或抗氧化剂（尿酸、芸香苷）对受HLB影响的柑橘进行叶面喷雾，可减少韧皮部组织中的细胞死亡和过氧化氢浓度，并减轻HLB症状[55]；噻唑磷（FOS）和铜铵复合物（CAC）组成根浸液，对染病植株处理90 d后，可有效控制HLB[56]；含有活性成分土霉素(OTC)的杀菌剂用于叶面喷雾，已用来控制美国佛罗里达州的HLB，其抑制植物中CLas种群的最低含量（w）为0.68和0.86 μg·g^{-1} [57]；除了药物，也有研究对染HLB的柑橘树引入从健康柑橘树中分离的本地内生枯草芽孢杆菌$L_{1\text{-}21}$，经过2 a的时间，病树的CLas发病率降低到不高于3%，因此有望利用本地内生菌重组柑橘内生微生物群，进而建立可持续的HLB控制策略[58]。

（2）柑橘木虱的相关研究：1）能穿越潜在的地理障碍（如道路和休耕地）；可在15~30 min内从受感染的植物中获得病原体，并在8~12 d的潜伏期后，在不到1 h内将病原体传播给健康的植物；具有显著的飞行能力：没有风的辅助下，3 h内分散320 m，最远2.4 km，有风的影响下，ACP会顺风而分散，并随柑橘产区发生的高风速而移动；没有恶劣天气的影响下，12 d内ACP的传播路径至少2 km[59-61]；在−4 ℃的寒冷环境下，ACP可在两周内逐渐适应并在短时间内继续存活[62]。2）化学防治：其合成杀虫剂丙溴磷+氯氰菊酯对ACP毒性更大，但杀虫剂不可持续且成本高，可探究物理刺激（植物挥发物、光、色）、破坏ACP的生理行为（喂养和消化）及寄主植物对ACP的抗性，来改进对ACP的综合管理[63-64]。3）物理防治：用单个保护罩（IPC）可有效隔离木虱与柑橘幼树，IPC引起的树冠内的微气候变化也促进植物生长，适合于HLB流行地区的新柑橘种植园；3D打印的黄色圆筒诱捕器的捕获率与黄色粘虫板接近，并且可重复利用和收集完好的ACP[65-67]。4）CLas与ACP的部分互作如下：CLas能在木虱体内持续存在12周，且木虱雌性产生的卵或后代未检测到该菌[68]；CLas对ACP的繁殖力（产卵、发育、交配）有着积极影响，可使成虫的饥饿程度更高，并使其更频繁地觅食和更倾向于长途飞行（可增加ACP的概率分布），以及降低对大多数商业杀虫剂的敏感性和提升对昆虫病原真菌的易感性；CLas阳性植物释放的水杨酸甲酯明显多于CLas阴性植物，前者的枝条、成熟叶及着色对ACP更具有吸引力[4]。

（3）黄龙病原体的相关研究：1）离体培养：目前所有用CLas实现无源生长和完成科赫法则的尝试都失败了，有研究尝试通过添加缺失的与可培养性相关的*Lcr*（*Liberibacter crescens*，新月自由杆菌）基因来实现CLas的复制无源生长，成功创造了初步的实验条件，为将大量“必要”的*Lcr*基因转移到CLas提供了一种实用方法[69]；目前新月体乳杆菌菌株BT-1在遗传上易受标准分子操作技术的控制，已被开发为一种替代模型，用于基因、调控元件、启动子和来源于未培养的致病性Liberibacters的分泌效应子的功能研究[70]。2）病原分泌蛋白：CLas基因组中，原噬菌体编码蛋白AGH17470为非经典分泌蛋白，是第一个前噬菌体编码的分泌蛋白，能引发过敏反应（HR）并诱导强的植物免疫反应，可对本氏烟草进行瞬时表达，导致整个植物矮化[71]；CLas的分泌蛋白SDE1可用作检测标记，用于各种血清学平台以鉴定受感染的树木，优势有：a. 监测不同类型的标记（即蛋白质对DNA）；b. 潜在地增加了识别被感染的树木，尤其是在无症状阶段；c. 允许支持大规模现场调查的成本可控的测定，有望替代qPCR检测[72]。CLas的蛋白LasP235和效应子3参与HLB的发病机制为：a. 两者的显著植物柑橘靶标包括柑橘先天免疫蛋白；b. 能与多种柑橘蛋白质互作并抑制其功能，

(C)1994-2023 China Academic Journal Electronic Publishing House. All rights reserved.　http://www.cnki.net

然后导致高水平的活性氧、杀菌脂质转移蛋白(LTP)的阻断和过早程序性细胞死亡(PCD)的诱导[73]。3)寄主抗性评价:SA(水杨酸)介导的SAR(植物获得性抗性)信号的实现需要活性SA的阈值水平,当SA水平升至某阈值以上时,SAR和其他防御反应被触发以防御病原体攻击,而HLB感染则通过干扰SA信号传导抑制柑橘免疫力[74];寄主植物中与HLB相关的潜在脂肪酸标志物:POA、OA、ALA和ARA,可见CLas感染可能导致长链脂肪酸代谢的改变,也可能导致宿主对脂肪酸防御的操纵[75]。4)基因:遗传工程技术,如遗传转化和基因组编辑,是开发抗病作物的有效方法,目前有广谱抗病基因AtNPR1(一种修饰的植物硫素基因)和抗菌肽基因Cecropin B和attacin A已分别引入柑橘,均有效提高了植株对HLB的抗性;近年来,基于簇状规则间隔短回文重复序列(CRISPR)的系统使基因组编辑成为一种不可或缺的遗传操作工具,已应用于包括柑橘在内的许多作物;在木虱的基因编辑方面也有创新突破,如BAPC辅助的CRISPR/Cas9系统,能够在成年雌性卵巢附近注射,并产生可遗传的种系基因编辑,不仅绕过了卵子显微注射的需要,也能抑制ACP的内共生体和Liberibacter病原体,不过仍面临着监管审批时间长和成本高的问题[76];有研究已成功实现纳米粒子介导的体外被动给药和体内被动给药,有着高效低毒被动给药的潜力,其原理为:纳米颗粒可用作载体系统,将质粒DNA、RNA和寡核苷酸等遗传物质高效、快速地传递到细胞中,从而减少当前农杆菌介导的转基因传递系统的缺点和限制[77]。

2.4 研究前沿

关键词突现是指在某一时期内与研究主题相关的词的频次显著增加,它能够挖掘研究热点,反映研究趋势[78]。与关键词分析相比,突现词分析可以捕捉到研究领域拐点和热点的出现时段,从而推断该领域的研究前沿。

2.4.1 *中文文献研究前沿* 笔者在本文中基于关键词(keyword)分析的基础,对黄龙病领域的突现词进行探测,得到突变强度最高的25个关键词,如图7(左)所示。图中突现词列表按照起始年份的先后顺序进行排序,“Strength”表示关键词的突变强度,值越大表示突变强度越强,红色部分表示该突现词持续的时间长度,其起止年份分别与“Begin”和“End”列下的年份相对应。

图7(左)反映出中文文献的黄龙病研究领域于1956—2021年间的研究趋势及研究前沿。根据该图可划分为3个时间段:1956—1978年、1979—2001年、2002—2021年,剔除与黄龙病无关的突现词,然后进行如下具体分析:

1956—1978年,涌现出“黄梢病”(黄龙病的旧称)、“柑橘树”、“林孔湘”、“病毒病”、“病原体”、“类菌原体”等突现词,其中“病毒病”的突现强度最高,持续时间最长,表明这一阶段内,以林孔湘为主力的研究人员就黄龙病的致病原因展开了大量研究。黄龙病的致病因子在1956年首次被证明为病毒,在未更正为韧皮部杆菌之前得到学界的广泛认可。林孔湘尝试用湿热空气处理柑橘芽条,发现能短时间内有效破坏黄龙病的致病力且不损伤柑橘芽条的生活力,表明柑橘芽条的致死温度与黄龙病菌受破坏的温度有明显差距,为热治疗奠定了基础。1964年,广西柳州园艺场的病树分布并非向原来病树区的四周扩散,而是沿边缘线扩展,病害田间发病中心不明显,是最早确认黄龙病害在田间存在着边界效应的事例[7]。1974—1975年,赵学源等[79]用四环素浸泡染病柑橘芽条2 h,然后将其嫁接在健康的柑橘树上,并发现柑橘树在未来5年都没有发病,并首次确定出黄龙病原体对抗生素敏感的事实。

1979—2001年,“柑橘生产”的突现强度最高,持续时间最长。说明在这一阶段,由于改革开放及进入WTO(世界贸易组织)后,在水果消费市场的冲击及黄龙病的影响下,我国开始重视柑橘的生产及布局优化工作,如扩大出口、根据适宜的生态区发展名特优新品种、建立规模化柑橘生产基地、提高果农福利、柑橘产业化及建立市场营销策略等[80]。这一时期,柑橘木虱的栖息地逐渐北移,其防治及预警势在必行,并总结出防控措施:控制人为传播(如引种)、及时挖除病树及药剂防治、通过种植适合天敌的栖息地进行生物防治[81],在争取提高柑橘产量的同时做好防护工作。

2002—2021年,“栽培技术”突现强度最高,持续时间最长,证明近年来,我国就柑橘的栽培技术持续展开研究,如栽培生草(百喜草、白三叶)来提高果实产量及提高土壤矿质养分(氮、钾、铁和锌等)含量[82-83],以及广西的姑婆山野生元橘等16种野生柑橘种质资源表现出更强的耐病性,可尝试用于培育抗病品种[84]。“防控”“综合防控”持续时间分别从

(C)1994-2023 China Academic Journal Electronic Publishing House. All rights reserved. http://www.cnki.net

2009—2017年、2015—2019年，持续时间较长，足以看出我国持续重视黄龙病的防控。这一期间，我国制定了HLB的诊断标准、防控规范、发放救灾基金和设立国家重点研究项目等。2015—2019年，中国农业（农村）部安排近4亿元农业生产救灾资金用于支持防控黄龙病[85]。2017年，“国家柑橘优势带HLB综合防控协同创新联盟”成立，加强全国协同联动[2]。2019年，广西壮族自治区人大常委会通过了《广西壮族自治区柑橘黄龙病防控规定》，这是我国首部黄龙病防控地方性法规[86]。相信黄龙病的防控工作以及柑橘优质品种的培育仍将是研究的主要趋势。

2.4.2　英文文献研究前沿　在关键词（keyword）分析的基础上，笔者对该领域的突现词进行探测，得到突变强度较高的25个关键词，如图7（右）所示。该图反映出英文文献的黄龙病研究领域在2002—2021年间的研究趋势及前沿。将年段细分为2002—2004年、2005—2011年、2012—2021年3个时间段，剔除与黄龙病无关的突现词，然后分别探讨各个阶段的研究状况。

2002—2004年间，该阶段出现了“strain（菌株）”，可见当时研究前沿侧重于对病菌的探索。此时多数研究已采用聚合酶链式反应（PCR）快速且灵敏的检测方法，其中的实时荧光PCR（RT-PCR，也叫定量PCR（qPCR））自1996年开始商用以来，已成为迄今为止用于检测和定量HLB病原体最准确和最灵敏的方法[87]。在PCR检测技术的应用下，巴西作为仅次于中国的柑橘生产大国，于2004年首次报告由CLas引起的HLB[88]。HLB在亚非拉地区也相继被发现，但只有成本高昂且耗时长的PCR技术可以确认病原体的存在，为了及早控制病情，最好通过综合疾病管理来管控，包括使用健康的苗圃材料、清除受感染的树木或树枝以及综合病媒控制，同时在无HLB的柑橘产区做好消杀传播媒介的预警工作[89]。

2005—2011年间，“DNA（脱氧核糖核酸）”的持续时间最长，“PCR（聚合酶链式反应）”的突现强度最大，表明在该阶段，分子生物学为研究前沿。美国于2005年9月在佛罗里达州首次发现到由黄龙病菌亚洲种CLas引起的HLB[61]。CLas的全基因序列通过测序及PCR等多种手段被获取并注释[90]。利用PCR也可确定病原体在寄主中的分布，如：柑橘

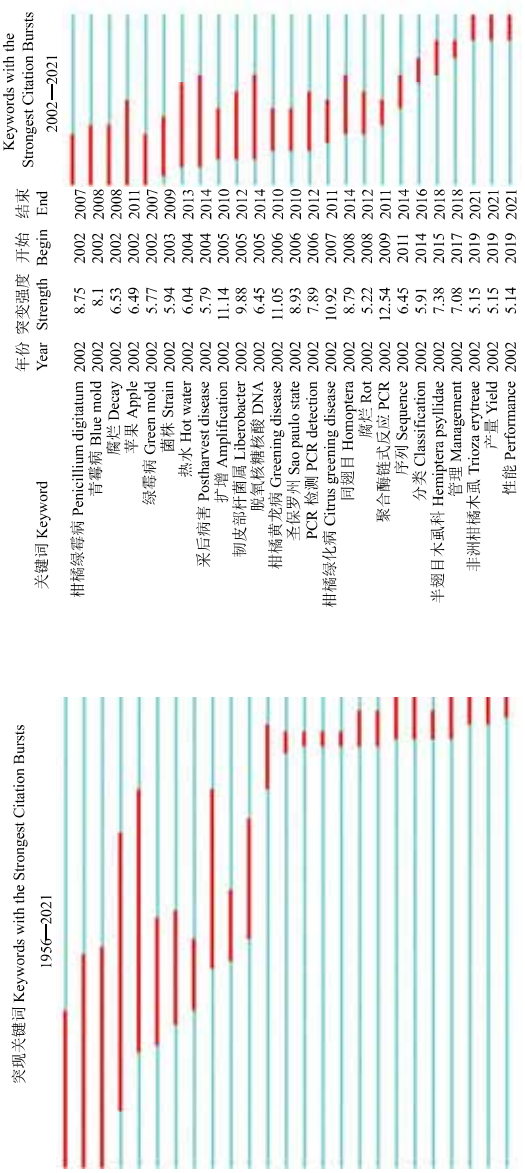


图7　国内（左）与国际（右）柑橘黄龙病研究突现词

Fig. 7　Emergent words in domestic (left) and international (right) research on citrus Huanglongbing

(C)1994-2023 China Academic Journal Electronic Publishing House. All rights reserved.　http://www.cnki.net

木虱的唾液腺是CLas的重要传播屏障，以及CLas可能在木虱的消化道和唾液腺中复制或积累[91]；CLas分布在柑橘树的树皮组织、叶中脉、根部以及不同的花果部分，但不存在于胚乳和胚芽中，分布也不均匀，可从感染部位传播到植物全身的不同部位[92]。此外，CLas可影响寄主植物中的基因表达变化，包括细胞防御、运输、细胞组织、光合作用和碳水化合物代谢等，尤其可诱导韧皮部中特异性凝集素PP2样蛋白的转录物积累[93]。足以看出在此阶段，黄龙病的分子研究领域正处在蓬勃发展中。

2012—2021年间，突现词有“classification（分类）”、“hemiptera psyllidae（半翅目木虱科）”、“trioza erytreae（非洲柑橘木虱）”、“performance（性能）”，持续时间都较短，其中“hemiptera psyllidae（半翅目木虱科）”突现强度最大，可看出此时国际研究开始关注非洲柑橘木虱（简称AfCP）。AfCP在欧洲持续蔓延，对欧洲的柑橘产业造成潜在风险，目前有研究者主张对未检测到HLB的地方实行生物防治，对检测到HLB的地方进行严格的化学防治[94]。黄龙病的分类检测技术也在不断创新，具体为：(1)使用环介导等温扩增：简称LAMP，可在单一温度下进行特异性扩增DNA模板，比传统PCR需要更少的专业设备；(2)LAMP侧向流动试纸：具有qPCR的功效，并且经济、方便、响应迅速，尚未商用；(3)重组酶聚合酶扩增：简称RPA，使用对象为粗提物和便携式加热块，可在大约30 min内完成整个测试过程，灵敏度与qPCR相当，但距离替代qPCR还需长期的验证；(4)基于生物标志物和植物挥发物（病原体分泌物）和感染宿主释放的挥发性有机化合物（VOC））的气相色谱-质谱 (GC-MS)、气相色谱/差示迁移谱或者犬科动物进行HLB识别检测的技术[87]；(5)解吸电喷雾电离与质谱成像：简称DESI-MSI，可快速、有效地检测甜橙中的生物标志物，有望开发成实时、快速的诊断技术[95]；(6)高光谱遥感设备：将高光谱相机安装于无人机，基于像素级识别HLB，分类准确率不低于99%，有望用于柑橘病害的早期无损检测和分级[96]。

3 结论与展望

3.1 结论

笔者在本文中基于知识图谱技术，通过检索CNKI、Web of Science数据库，收集与黄龙病研究相关的文献，再采用CiteSpace软件构建知识图谱并进行可视化分析，可总结出4条结论：(1)国内外正加强对黄龙病的研究，预计未来仍会保持热度；(2)美国的发文量全球最多，国际影响力最强。我国机构虽已成为国际黄龙病研究领域的重要力量，但其科研实力与美国相比，仍存在巨大差距；(3)中文文献的研究热点主要包括黄龙病综合防治和黄龙病病原体，英文文献的研究热点聚焦于提高柑橘生产力、防治药物、柑橘木虱和黄龙病病原体方面等；(4)中文文献近年关注优势品种的栽培技术以及持续重视综合防控，英文文献近年则关注柑橘木虱的生理生化特性及防治手段，开始重视非洲柑橘木虱对欧洲黄龙病的潜在威胁，并对黄龙病的分类检测技术进行不断创新。

进一步讨论，美国的主体研究形式是小单元开展，发表文章时甚至有国际合作人员（大多为海外进修人员）。我国通常以大合作为主，只是考虑到知识产权的归属问题，成果大多为分开发表的形式，攻关起始时间也比美国早几十年。正常来说，我国在黄龙病领域的影响力应高于美国，但根据图谱分析，我国在黄龙病的科研影响力远低于美国。究其原因，除了历史因素外，主要与经费限制有关。我国黄龙病的研究经费远低于美国的研发投入[97]，美国自2005年发现该病后，所投入的研究经费是中国的40余倍，因此客观上我国黄龙病科研综合实力不如美国。

本文也存在不足之处，在于：(1)选用的WOS数据库的收录年限只有2002—2021年，原因是所属机构所订购的WOS数据库只收录进20 a的文献，故无法系统分析发表时间更早的文献数据；(2)部分英文作者有很大可能性来自同一国家，尤其是我国，因此我国与国际的热点与前沿部分有难以避免的交叉重合之处，同时也存在着导致小部分数据漏检的问题：我国部分作者发表基于其他语种的文献及使用不同英文名字写法发表英文文章，种种因素致使本次研究无法完美地统计数据，也难以详细区分出我国与国际一流水平的科研差异，只能通过中英文发文量及研究主体对我国相关研究进行计量分析，并得出“我国黄龙病的综合科研实力落后于美国”的初步结论。

3.2 展望

为了缩小我国与美国的黄龙病的科研差距，除了政府持续投入大量资金及进一步完善防控法规外，还需科研机构牵头建立线上沟通平台，以便即时

(C)1994-2023 China Academic Journal Electronic Publishing House. All rights reserved. http://www.cnki.net

答疑，同时也要定期举行全国性的会议，以便确定各大机构接下来的具体攻关方向和更为细致的分工合作，从而更加从容地应对黄龙病广且深的攻关难题。此外，由于黄龙病菌暂时无法进行离体培养，科研人员难以从形态学、生物学、病原学等方面对病原体进行深入研究[3]，应需坚持寻找黄龙病菌离体培养的技术，或者另寻其他可替代的方式。

参考文献 References：

[1] 郭文武，叶俊丽，邓秀新 . 新中国果树科学研究 70 年：柑橘[J]. 果树学报，2019，36(10)：1264-1272.
GUO Wenwu，YE Junli，DENG Xiuxin. Fruit scientific research in new China in the past 70 years：Citrus[J]. Journal of Fruit Science，2019，36(10)：1264-1272.

[2] ZHOU C Y. The status of citrus Huanglongbing in China[J]. Tropical Plant Pathology，2020，45(3)：279-284.

[3] 郑正 . 柑橘黄龙病菌的全基因组测序及分析[D]. 广州：华南农业大学，2017.
ZHENG Zheng. Whole genome sequencing and analysis of ‘*Candidatus* Liberibacter asiaticus’，the associated pathogen of citrus Huanglongbing[D]. Guangzhou：South China Agricultural University，2017.

[4] GALDEANO D M，PACHECO I D S，ALVES G R，GRANATO L M，RASHIDI M，TURNER D，LEVY A，MACHADO M A. Friend or foe? Relationship between ‘*Candidatus* Liberibacter asiaticus’ and *Diaphorina citri*[J]. Tropical Plant Pathology，2020，45(6)：559-571.

[5] 邱志燏，黄红兰，舒畅，邱俊洁 . 柑橘黄龙病发病机理、症状及防控措施[J]. 生物灾害科学，2015，38(3)：193-200.
QIU Zhiyu，HUANG Honglan，SHU Chang，QIU Junjue. Citrus yellow dragon disease pathogenesis，symptoms and prevention measures[J]. Biological Disaster Science，2015，38(3)：193-200.

[6] 范国成，刘波，吴如健，李韬，蔡子坚，柯冲 . 中国柑橘黄龙病研究 30 年[J]. 福建农业学报，2009，24(2)：183-190.
FAN Guocheng，LIU Bo，WU Rujian，LI Tao，CAI Zijian，KE Chong. Thirty years of research on citrus Huanglongbing in China[J]. Fujian Journal of Agricultural Sciences，2009，24(2)：183-190.

[7] 柏自琴，周常勇 . 柑橘黄龙病病原分化及发生规律研究进展[J]. 中国农学通报，2012，28(1)：133-137.
BAI Ziqin，ZHOU Changyong. The research progress of citrus Huanglongbing on pathogen diversity and epidemiology[J]. Chinese Agricultural Science Bulletin，2012，28(1)：133-137.

[8] LOPES S A，FRARE G F，BERTOLINI E，CAMBRA M，FERNANDES N G，AYRES A J，MARIN D R，BOVÉ J M. Liberibacters associated with citrus Huanglongbing in Brazil：‘*Candidatus* Liberibacter asiaticus’ is heat tolerant，‘*Ca.* L. americanus’ is heat sensitive[J]. Plant Disease，2009，93(3)：257-262.

[9] GRAHAM J，GOTTWALD T，SETAMOU M. Status of Huanglongbing (HLB) outbreaks in florida，california and texas[J]. Tropical Plant Pathology，2020，45(3)：265-278.

[10] 胡雪芳，田志清 . 柑橘黄龙病防治技术研究进展[J]. 中国植保导刊，2021，41(7)：32-38.
HU Xuefang，TIAN Zhiqing. Research progress on control technology of citrus Huanglongbing[J]. China Plant Protection，2021，41(7)：32-38.

[11] 李杰，陈超美 . CiteSpace：科技文本挖掘及可视化[M]. 北京：首都经济贸易大学出版社，2016：138-177.
LI Jie，CHEN Chaomei. CiteSpace：Text mining and visualization in scientific literature[M]. Beijing：Capital University of Economics and Business Press，2016：138-177.

[12] 陈悦，陈超美，刘则渊，胡志刚，王贤文 . CiteSpace 知识图谱的方法论功能[J]. 科学学研究，2015，33(2)：242-253.
CHEN Yue，CHEN Chaomei，LIU Zeyuan，HU Zhigang，WANG Xianwen. The methodology function of CiteSpace mapping knowledge domains[J]. Studies in Science of Science，2015，33(2)：242-253.

[13] 邓晓玲，郑永钦，郑正，许美容 . 柑橘黄龙病菌基因组学的研究进展[J]. 华南农业大学学报，2019，40(5)：137-148.
DENG Xiaoling，ZHENG Yongqin，ZHENG Zheng，XU Meirong. Current research on genomic analysis of ‘*Candidatus* Liberibacter spp.’[J]. Journal of South China Agricultural University，2019，40(5)：137-148.

[14] 宗淑萍 . 基于普赖斯定律和综合指数法的核心著者测评：以《中国科技期刊研究》为例[J]. 中国科技期刊研究，2016，27(12)：1310-1314.
ZONG Shuping. Evaluation of core authors based on price law and the comprehensive index method：A case study of Chinese Journal of Scientific And Technical Periodicals[J]. Chinese Journal of Scientific and Technical Periodicals. 2016，27(12)：1310-1314.

[15] 林德明，陈超美，刘则渊 . 共被引网络中介中心性的 Zipf：Pareto 分布研究[J]. 情报学报，2011，30(1)：76-82.
LIN Deming，CHEN Chaomei，LIU Zeyuan. Study on Zipf：Pareto distribution of the betweenness centrality of a co-citrtion network[J]. Journal of the China Society for Scientific and Technical Information，2011，30(1)：76-82.

[16] SUNSA. 2020/2021 年度佛罗里达州柑橘产量缩水 7%[EB/OL]. [2022-11-09]. https://guojiguoshu.com/article/6609. html.
SUNSA. Citrus production in Florida shrank by 7% in 2020/21[EB/OL]. [2022-11-09]. https://guojiguoshu.com/article/6609. html.

[17] 奎国秀，祁春节 . 我国柑橘产业生产贸易的变化及机遇与挑战[J]. 中国果树，2021(6)：93-97.
KUI Guoxiu，QI Chunjie. Changes，opportunities and challenges of citrus production and trade in China[J]. China Fruits，2021(6)：93-97.

[18] 国家统计局 . 茶叶、水果产量年度数据[EB/OL]. [2022-11-22]. https://data.stats.gov.cn/easyquery.htm?cn=C01&zb=A0D0K&sj=2021.
National Bureau of Statistics. Annual data of tea and fruit output[EB/OL]. [2022-11-22]. https://data.stats.gov.cn/easyquery.htm?cn=C01&zb=A0D0K&sj=2021.

[19] 杨德荣，曾志伟，周龙 . 柚树高产栽培技术（系列）V：黄龙病的识别与防治[J]. 南方农业，2019，13(1)：47-51.
YANG Derong，ZENG Zhiwei，ZHOU Long. High-yield cultivation techniques of citrus maxima (series) V：Identification and prevention of Citrus greening disease[J]. South China Agricul-

(C)1994-2023 China Academic Journal Electronic Publishing House. All rights reserved.　http://www.cnki.net

ture，2019，13(1)：47-51.

[20] 胡文娟，张宇平，祁春节，尤有利，郑丽真．永春芦柑生产成本与收益的比较研究：基于柑橘黄龙病防控新栽培模式[J]. 中国果树，2022(2)：60-64.
HU Wenjuan，ZHANG Yuping，QI Chunjie，YOU Youli，ZHENG Lizhen. Comparative study on production cost and benefit of ‘Yongchun pokan’：Based on new cultivation mode for prevention and control of citrus Huanglongbing[J]. China Fruits，2022(2)：60-64.

[21] 汪善勤，肖云丽，张宏宇．我国柑橘木虱潜在适生区分布及趋势分析[J]. 应用昆虫学报，2015，52(5)：1140-1148.
WANG Shanqin，XIAO Yunli，ZHANG Hongyu. Studies of the past，current and future potential distributions of *Diaphorina citri* Kuwayama (Homoptera: Psyllidae) in China[J]. Chinese Journal of Applied Entomology，2015，52(5)：1140-1148.

[22] 姚俊萌，刘丹，段里成，蔡哲．CMIP6气候变化情景下中国区域柑橘木虱潜在影响范围预估[J]. 中国农业气象，2021，42(12)：1031-1041.
YAO Junmeng，LIU Dan，DUAN Licheng，CAI Zhe. Prediction of potential distribution of *Diaphorina citri* Kuwayama in China under future climate change scenarios of CMIP6[J]. Chinese Journal of Agrometeorology，2021，42(12)：1031-1041.

[23] 廖勇军．柑橘木虱的发生及防治[J]. 农村经济与科技，2020，31(18)：40-41.
LIAO Yongjun. Occurrence and control of citrus psyllid[J]. Rural Economy and Science-Technology，2020，31(18)：40-41.

[24] 周军辉，徐腾，李鹏雷，黄建，王竹红．基于两性生命表评价取食柑橘木虱对六斑月瓢虫和龟纹瓢虫生长发育及种群的影响[J]. 植物保护学报，2022，49(2)：629-636.
ZHOU Junhui，XU Teng，LI Penglei，HUANG Jian，WANG Zhuhong. Effects of *Diaphorina citri* feeding on the growth and development and population parameters of *Cheilomenes sexmaculata* and *Propylea japonica* based on two-sex life tables[J]. Journal of Plant Protection，2022，49(2)：629-636.

[25] 张阳，戴素明，龙桂友，周敏，孙太安，李大志．湖南省柑橘主要病虫发生情况及防控现状[J]. 湖南农业科学，2021(12)：61-64.
ZHANG Yang，DAI Suming，LONG Guiyou，ZHOU Min，SUN Taian，LI Dazhi. Investigation on the occurrence and control status of main citrus diseases and pests in Hunan[J]. Hunan Agricultural Sciences，2021(12)：61-64.

[26] 姚廷山，周彦，ACHOR D，LI J Y，WANG N，周常勇．土霉素对柑橘黄龙病的防治效果及对柑橘产量和品质的影响[J]. 植物保护学报，2020，47(6)：1353-1361.
YAO Tingshan，ZHOU Yan，ACHOR D，LI J Y，WANG N，ZHOU Changyong. Inhibition effect of oxytetracycline on citrus Huanglongbing and its effect on citrus yield and quality[J]. Journal of Plant Protection，2020，47(6)：1353-1361.

[27] 黄洋，关巍，王铁霖，晏建红，田二渊，刘堰凤，刘博，杨玉文，赵廷昌．两类抗生素药剂对‘纽荷尔’脐橙黄龙病菌的抑制作用及根际细菌群落结构的影响[J]. 植物保护，2021，47(6)：83-92.
HUANG Yang，GUAN Wei，WANG Tielin，YAN Jianhong，TIAN Eryuan，LIU Yanfeng，LIU bo，YANG Yuwen，ZHAO Tingchang. Effects of two antibiotics on pathogen causing Huanglongbing of ‘Newhall’ navel orange and the community structure of rhizosphere bacteria[J]. Plant Protection，2021，47(6)：83-92.

[28] 王圣通．黄龙病对柑橘果实品质的影响及其防治药剂的初步筛选[D]. 广州：华南农业大学，2016.
WANG Shengtong. Effects of citrus fruit quality by citrus Huanglongbing and preliminary screening of agents against Huanglongbing in the field[D]. Guangzhou：South China Agricultural University，2016.

[29] 张建桃，陈鸿，文晟，李晟华，邓小玲，兰玉彬．柑橘黄龙病热空气快速处理温度场分布特性试验研究[J]. 农业工程学报，2017，33(8)：267-277.
ZHANG Jiantao，CHEN Hong，WEN Sheng，LI Shenghua，DENG Xiaoling，LAN Yubin. Experiment on temperature field distribution characteristics of citrus Huanglongbing hot air rapid treatment[J]. Transactions of the Chinese Society of Agricultural Engineering，2017，33(8)：267-277.

[30] 张建桃，叶剑云，曾莉，杨曦，罗永强，张武标．柑橘黄龙病苗木微波加热试验研究[J]. 江苏农业科学，2020，48(12)：75-79.
ZHANG Jiantao，YE Jianyun，ZENG Li，YANG Xi，LUO Yongqiang，ZHANG Wubiao. Experimental study on microwave heating of citrus Huanglong disease seedlings[J]. Jiangsu Agricultural Sciences，2020，48(12)：75-79.

[31] 陈燕玲．砂糖橘响应黄龙病菌及热处理胁迫的生理生化特征[D]. 广州：华南农业大学，2019.
CHEN Yanling. The characteristics of physiological and biochemical in Shatangju following thermotherapy and infection by ‘*Candidatus* Liberibacter asiaticus’[D]. Guangzhou：South China Agricultural University，2019.

[32] 张建桃，林耿纯，陈鸿，文晟，尹选春，邓小玲．柑橘黄龙病远红外热处理温度场分布特性试验研究[J]. 农业机械学报，2019，50(10)：175-188.
ZHANG Jiantao，LIN Gengchun，CHEN Hong，WEN Sheng，YIN Xuanchun，DENG Xiaoling. Experiment on temperature field distribution characteristics of citrus HLB far infrared heat treatment[J]. Transactions of the Chinese Society for Agricultural Machinery，2019，50(10)：175-188.

[33] 贾志成，郑加强，黄雅杰，周宏平，REZA E. 柑橘黄龙病热处理防治技术研究进展[J]. 农业工程学报，2015，31(23)：1-9.
JIA Zhicheng，ZHENG Jiaqiang，HUANG Yajie，ZHOU Hongping，REZA E. Review and prospect of thermotherapy for citrus Huanglongbing[J]. Transactions of the Chinese Society of Agricultural Engineering，2015，31(23)：1-9.

[34] 黄秀，徐建国，聂振朋，王平，孙立方，孙建华，柯甫志．柑橘黄龙病脱毒技术研究进展[J]. 浙江柑橘，2021，38(3)：7-11.
HUANG Xiu，XU Jianguo，NIE Zhenpeng，WANG Ping，SUN Lifang，SUN Jianhua，KE Fuzhi. Research progress on virus-free technology of citrus Huanglongbing[J]. Zhejiang Ganju，2021，38(3)：7-11.

[35] 黄桢辉，王娟，高洁，郑正，邓晓玲，许美容．黄龙病菌在4个品种柑橘果枝内的时空分布[J]. 华南农业大学学报，2022，43(5)：35-42.
HUANG Zhenhui，WANG Juan，GAO Jie，ZHENG Zheng，DENG Xiaoling，XU Meirong. Distribution of ‘*Candidatus* Liberibacter asiaticus’ in the fruit branch of four citrus cultivars[J]. Journal of South China Agricultural University，2022，43(5)：35-42.

[36] 白先进，赵小龙，娄兵海，邓崇岭，付慧敏．回顾广西柑橘黄龙病防控(1982—2020)[J]. 南方园艺，2020，31(6)：5-16.
BAI Xianjin，ZHAO Xiaolong，LOU Binghai，DENG Chongling，

(C)1994-2023 China Academic Journal Electronic Publishing House. All rights reserved. http://www.cnki.net

FU Huimin. A review of citrus Huanglongbing control in Guangxi from 1982 to 2020[J]. Southern Horticulture，2020，31(6)：5-16.

[37] 黄家权，李莉，吴丰年，郑正，邓晓玲．携带不同原噬菌体的黄龙病菌在柑橘木虱体内的增殖及致病力[J]. 中国农业科学，2022，55(4)：719-728.
HUANG Jiaquan，LI Li，WU Fengnian，ZHENG Zheng，DENG Xiaoling. Proliferation of two types prophage of ‘*Candidatus* Liberibacter asiaticus’ in *Diaphorina citri* and their pathogenicity[J]. Scientia Agricultura Sinica，2022，55(4)：719-728.

[38] 卢慧林，陈大嵩，陈逢浩，叶静文，欧阳革成．基于纳米孔测序技术的柑橘黄龙病检测方法建立[J]. 环境昆虫学报，2021，43(6)：1596-1600.
LU Huilin，CHEN Dasong，CHEN Fenghao，YE Jingwen，OUYANG Gecheng. Establishment of detection method of Huanglongbing based on nanopore sequencing technology[J]. Journal of Environmental Entomology，2021，43(6)：1596-1600.

[39] 李镇希，李文婷，黄家权，郑正，许美容，邓晓玲．膜吸附法结合可视化环介导等温扩增技术检测柑橘黄龙病菌[J]. 中国农业科学，2022，55(1)：74-84.
LI Zhenxi，LI Wenting，HUANG Jiaquan，ZHENG Zheng，XU Meirong，DENG Xiaoling. Detection of ‘*Candidatus* Liberibacter asiaticus’ by membrane adsorption method combined with visual loop-mediated isothermal amplification[J]. Scientia Agricultura Sinica，2022，55(1)：74-84.

[40] 胡文召，周常勇．柑橘黄龙病病原研究进展[J]. 植物保护，2010，36(3)：30-33.
HU Wenzhao，ZHOU Changyong. Advances in the pathogen of citrus Huanglongbing[J]. Plant Protection，2010，36(3)：30-33.

[41] 宋晓兵，彭埃天，陈霞，程保平，凌金锋．柑橘黄龙病病原培养及分子检测技术研究进展[J]. 广东农业科学，2013，40(23)：65-69.
SONG Xiaobing，PENG Aitian，CHEN Xia，CHENG Baoping，LING Jinfeng. Research advances of citrus Huanglongbing pathogen culture and detection technology[J]. Guangdong Agricultural Sciences，2013，40(23)：65-69.

[42] 谢攀．柑橘黄龙病病原菌共培养体系的构建[D]. 重庆：重庆大学，2015.
XIE Pan. Construction of the co-culture system of *Candidatus* Liberibacter asiaticus[D]. Chongqing：Chongqing University，2015.

[43] 张超．柑橘黄龙病病菌亚洲种 Sec 依赖分泌蛋白的预测、鉴定及功能研究[D]. 北京：中国农业科学院，2020.
ZHANG Chao. Prediction，validation and functional study of *Candidatus* Liberibacter asiaticus Sec dependent secretary proteins[D]. Beijing：Chinese Academy of Agricultural Sciences，2020.

[44] 王春庆．柑橘黄龙病菌分泌蛋白鉴定分析和检测技术开发[D]. 赣州：赣南师范大学，2020.
WANG Chunqing. Characterisation of secretory proteins in ‘*Candidatus* Liberibacter asiaticus’ and the application for developing citrus Huanglongbing detection technology[D]. Ganzhou：Gannan Normal University，2020.

[45] 刘雪禄．柑橘黄龙病菌分泌蛋白 Clsp33 致病机理初步研究[D]. 重庆：西南大学，2019.
LIU Xuelu. Preliminary study on the pathogenic mechanism of the secreted protein Clsp33 of ‘*Candidatus* Liberibacter asiaticus’[D]. Chongqing：Southwest University，2019.

[46] 胡燕，王雪峰，周常勇．柑橘黄龙病菌亚洲种、虫媒及植物寄主互作研究进展[J]. 园艺学报，2016，43(9)：1688-1698.
HU Yan，WANG Xuefeng，ZHOU Changyong. Recent advances in interactions among ‘*Candidatus* Liberibacter asiaticus’，insect vector and plant host[J]. Acta Horticulturae Sinica，2016，43(9)：1688-1698.

[47] 谢竹．柑橘黄龙病菌在根和叶中与寄主互作的比较分析[D]. 重庆：西南大学，2020.
XIE Zhu. Comparative analysis of the interaction of *Candidatus* Liberibacter asiaticus with root and leaf of host[D]. Chongqing：Southwest University，2020.

[48] 赵珂，郑林，杜美霞，龙俊宏，何永睿，陈善春，邹修平．柑橘 SAR 及其信号转导基因 *CsSABP2* 在黄龙病菌侵染中的响应特征[J]. 中国农业科学，2021，54(8)：1638-1652.
ZHAO Ke，ZHENG Lin，DU Meixia，LONG Junhong，HE Yongrui，CHEN Shanchun，ZOU Xiuping. Response characteristics of plant SAR and its signaling gene *CsSABP2* to Huanglongbing infection in citrus[J]. Scientia Agricultura Sinica，2021，54(8)：1638-1652.

[49] 卢慧林，梁广文，李周文婷，欧阳革成．寄主抗性与黄龙病寄主植物次生化合物相关性初步探讨[J]. 环境昆虫学报，2019，41(5)：1099-1106.
LU Huilin，LIANG Guangwen，LI Zhouwenting，OUYANG Gecheng. Preliminary discussion the correlation between host resistance and plant secondary compounds of Huanglongbing disease[J]. Journal of Environmental Entomology，2019，41(5)：1099-1106.

[50] 郑永钦，郑正，陈燕玲，黄洪霞，许美容．柑橘黄龙病菌内参基因的筛选与评估[J]. 微生物学通报，2019，46(11)：2985-2995.
ZHENG Yongqin，ZHENG Zheng，CHEN Yanling，HUANG Hongxia，XU Meirong. Screening and evaluation of reference genes for *Candidatus* Liberibacter asiaticus[J]. Microbiology China，2019，46(11)：2985-2995.

[51] KWAKYE S，KADYAMPAKENI D M，VAN SANTEN E，VASHISTH T，WRIGHT A. Variable manganese rates influence the performance of Huanglongbing-affected citrus trees in Florida[J]. HortScience，2022，57(3)：360-366.

[52] ESTEVES E，KADYAMPAKENI D M，ZAMBON F，FERRAREZI R S，MALTAIS-LANDRY G. Magnesium fertilization has a greater impact on soil and leaf nutrient concentrations than nitrogen or calcium fertilization in Florida orange production[J]. Nutrient Cycling in Agroecosystems，2022，122(1)：73-87.

[53] ZAMBON F T，MEADOWS T D，ECKMAN M A，RODRIGUEZ K M R，FERRAREZI R S. Automated ebb-and-flow subirrigation accelerates citrus liner production in treepots[J]. Agricultural Water Management，2022，262：107387.

[54] DORJI K，LAKEY L，CHOPHEL S，DORJI S D，TAMANG B. Adoption of improved citrus orchard management practices：A micro study from Drujegang growers，Dagana，Bhutan[J]. Agriculture & Food Security，2016，5(1)：3-8.

[55] MA W X，PANG Z Q，HUANG X E，XU J，PANDEY S S，LI J Y，ACHOR D S，VASCONCELOS F N，HENDRICH C，HUANG Y X，WANG W T，LEE D，DANIEL S，WANG N. Cit-

(C)1994-2023 China Academic Journal Electronic Publishing House. All rights reserved.　http://www.cnki.net

rus Huanglongbing is a pathogen-triggered immune disease that can be mitigated with antioxidants and gibberellin[J]. Nature Communications,2022,13(1):529.

[56] DUAN J W,LI X,ZHANG J Z,CHENG B P,LIU S H,LI H M,ZHOU Q,CHEN W L. Cocktail therapy of fosthiazate and cupric-ammoniun complex for citrus Huanglongbing[J]. Frontiers in Plant Science,2021,12:643971.

[57] LI J Y,PANG Z Q,DUAN S,LEE D,KOLBASOV V G,WANG N. The in planta effective concentration of oxytetracycline against '*Candidatus* Liberibacter asiaticus' for suppression of citrus Huanglongbing[J]. Phytopathology,2019,109(12):2046-2054.

[58] MUNIR S,LI Y M,HE P B,HE P F,HE P J,CUI W Y,WU Y X,LI X Y,LI Q,ZHANG S X,XIONG Y S,LU Z J,WANG W B,ZONG K X,YANG Y C,YANG S C,MU C,WEN H M,WANG Y H,GUO J,KARUNARATHNA S C,HE Y Q. Defeating Huanglongbing pathogen *Candidatus* Liberibacter asiaticus with indigenous citrus endophyte *bacillus subtilis* L_{1-21}[J]. Frontiers in Plant Science,2022(12):789065.

[59] LEWIS-ROSENBLUM H,MARTINI X,TIWARI S,STELINSKI L L. Seasonal movement patterns and long-range dispersal of Asian citrus psyllid in Florida citrus[J]. Journal of Economic Entomology,2015,108(1):3-10.

[60] ANTOLÍNEZ C A,MARTINI X,STELINSKI L L,RIVERA M J. Wind speed and direction drive assisted dispersal of Asian citrus psyllid[J]. Environmental Entomology,2022,51(2):305-312.

[61] LI W B,HARTUNG J S,LEVY L. Quantitative real-time PCR for detection and identification of *Candidatus* Liberibacter species associated with citrus huanglongbing[J]. Journal of Microbiological Methods,2006,66(1):104-115.

[62] MARTINI X,MALFA K,STOCKTON D,RIVERA M J. Cold acclimation increases Asian citrus psyllid *Diaphorina citri* (Hemiptera:Liviidae) survival during exposure to freezing temperatures[J]. Insect Science,2022,29(2):531-538.

[63] GRAFTON-CARDWELL E E,STELINSKI L L,STANSLY P A. Biology and management of Asian citrus psyllid,vector of the Huanglongbing pathogens[J]. Annual Review of Entomology,2013,58(1):413-432.

[64] IQBAL M,AHMAD S,GOGI M,ATTA B,NISAR M J. Comparative efficacy of synthetic insecticids against citrus psylla,*diaphorina citri* Kuwayama (Homoptera: Psyllidae) under laboratory and field conditions[J]. Plant Protection,2022,6(1):43-50.

[65] HALL D G,RICHARDSON M L,AMMAR E D,HALBERT S E. Asian citrus psyllid,*Diaphorina citri*,vector of citrus Huanglongbing disease[J]. Entomologia Experimentalis et Applicata,2013,146(2):207-223.

[66] GAIRE S,ALBRECHT U,BATUMAN O,QURESHI J,ZEKRI M,ALFEREZ F. Individual protective covers (IPCs) to prevent Asian citrus psyllid and *Candidatus* Liberibacter asiaticus from establishing in newly planted citrus trees[J]. Crop Protection,2022,152:105862.

[67] SNYDER J,DICKENS K L,HALBERT S E,DOWLING S,RUSSELL D,HENDERSON R,ROHRIG E,RAMADUGU C. The development and evaluation of insect traps for the Asian citrus psyllid,*Diaphorina citri* (Hemiptera: Psyllidae),vector of citrus Huanglongbing[J]. Insects,2022,13(3):295.

[68] HUNG T H,HUNG S C,CHEN C N,HSU M H,SU H J. Detection by PCR of *Candidatus* Liberibacter asiaticus,the bacterium causing citrus huanglongbing in vector psyllids:Application to the study of vector-pathogen relationships[J]. Plant Pathology,2004,53(1):96-102.

[69] CAI L L,JAIN M,MUNOZ-BODNAR A,HUGUET-TAPIA J C,GABRIEL D W. A synthetic '*essentialome*' for axenic culturing of '*Candidatus* Liberibacter asiaticus'[J]. BMC Research Notes,2022,15(1):125.

[70] JAIN M,CAI L,FLEITES L A,MUNOZ-BODNAR A,DAVIS M J,GABRIEL D W. *Liberibacter crescens* is a cultured surrogate for functional genomics of uncultured pathogenic '*Candidatus* Liberibacter' spp. and is naturally competent for transformation[J]. Phytopathology,2019,109(10):1811-1819.

[71] DU J,WANG Q Y,ZENG C H,ZHOU C Y,WANG X F. A prophage-encoded nonclassical secretory protein of '*Candidatus* Liberibacter asiaticus' induces a strong immune response in *Nicotiana benthamiana* and citrus[J]. Molecular Plant Pathology,2022,23(7):1022-1034.

[72] PAGLIACCIA D,SHI J,PANG Z,HAWARA E,CLARK K,THAPA S P,DE FRANCESCO A D,LIU J F,TRAN T,BODAGHI S,FOLIMONOVA S Y,ANCONA V,MULCHANDANI A,COAKER G,WANG N,VIDALAKIS G,MA W B. A pathogen secreted protein as a detection marker for citrus Huanglongbing[J]. Frontiers in Microbiology,2017,8:2041.

[73] BASU S,HUYNH L,ZHANG S J,RABARA R,NGUYEN H,GUZMÁN J V,HAO G X,MILES G,SHI Q C,STOVER E,GUPTA G. Two liberibacter proteins combine to suppress critical innate immune defenses in citrus[J]. Frontiers in Plant Science,2022,13:869178.

[74] ZOU X P,BAI X J,WEN Q L,XIE Z,WU L,PENG A H,HE Y R,XU L Z,CHEN S C. Comparative analysis of tolerant and susceptible citrus reveals the role of methyl salicylate signaling in the response to Huanglongbing[J]. Journal of Plant Growth Regulation,2019,38(4):1516-1528.

[75] SUH J H,NIU Y S,WANG Z B,GMITTER JR F G,WANG Y. Metabolic analysis reveals altered long-chain fatty acid metabolism in the host by Huanglongbing disease[J]. Journal of Agricultural and Food Chemistry,2018,66(5):1296-1304.

[76] HUNTER W B,CLARKE S V,MOJICA A F S,PARIS T M,MILES G,METZ J L,HOLLAND C S,MCCOLLUM G,QURESHI J A,TOMICH J M,TOMICH J M,BOYLE M J,CANO L,ALTMAN S,PELZSTELINSKI K S. Advances in RNA suppression of the Asian citrus psyllid vector and bacteria (Huanglongbing pathosystem)[M]//Asian citrus psyllid:Biology,Ecology and Management of the Huanglongbing Vector,UK:CABI International,2020:258-284.

[77] SUN L F,NASRULLAH,KE F Z,NIE Z P,WANG P,XU J G. Citrus genetic engineering for disease resistance: past,present and future[J]. International Journal of Molecular Sciences,2019,20(21):5256.

[78] 张增可,王齐,吴雅华,刘兴诏,黄柳菁. 基于 CiteSpace 植物功能性状的研究进展[J]. 生态学报,2020,40(3):1101-1112.
ZHANG Zengke,WANG Qi,WU Yahua,LIU Xingzhao,

(C)1994-2023 China Academic Journal Electronic Publishing House. All rights reserved. http://www.cnki.net

HUANG Liujing. Research progress of plant functional traits based on CiteSpace[J]. Acta Ecologica Sinica，2020，40(3)：1101-1112.

[79] 赵学源，邱柱石，苏维芳，蒋元晖 . 四环素浸泡芽条消除柑橘黄龙病的持续效果[J]. 植物保护学报，1982，9(1)：67-68.
ZHAO Xueyuan，QIU Zhushi，SU Weifang，JIANG Yuanhui. Continued effect of tetracycline on the elimination of Citrus yellow shoot by budwood immersion[J]. Journal of Plant Protection，1982，9(1)：67-68.

[80] 祁春节 . 中国柑橘产业的经济分析与政策研究[D]. 武汉：华中农业大学，2001.
QI Chunjie. The citrus industry in China：An economic analysis and policy studies[D]. Wuhan：Huazhong Agricultural University，2001.

[81] 马骁，王祖泽 . 柑橘木虱的发生消长规律及防治措施[J]. 浙江柑橘，2001(1)：26-28.
MA Xiao，WANG Zuze. Occurrence，decline and control of citrus psyllid[J]. Zhejiang Ganju，2001(1)：26-28.

[82] 李国怀，伊华林 . 生草栽培对柑橘园土壤水分与有效养分及果实产量、品质的影响[J]. 中国生态农业学报，2005，13(2)：161-163.
LI Guohuai，YI Hualin. Influences of sod culture on the soil water content，effect of soil nutrients，fruit yield and quality in citrus orchard[J]. Chinese Journal of Eco-Agriculture，2005，13(2)：161-163.

[83] 章慧璇，武晓晓，娄兵海，陈传武，刘萍，唐艳，门友均，黄俊源，吴仕蔓，邓崇岭 . 广西特有柑橘种质资源响应黄龙病菌侵染后的动态含量变化[J/OL]. 分子植物育种，2022：1-12[2022-02-07]. http://kns.cnki.net/kcms/detail/46.1068.S.20220207.1143.004.html.
ZHANG Huixuan，WU Xiaoxiao，LOU Binghai，CHEN Chuanwu，LIU Ping，TANG Yan，MEN Youjun，HUANG Junyuan，WU Shiman，DENG Chongling. The dynamic content changes of endemic citrus germplasm resources infected with citrus Huanglongbing in Guangxi[J/OL]. Molecular Plant Breeding，2022：1-12[2022-02-07]. http://kns.cnki.net/kcms/detail/46.1068.S.20220207.1143.004.html.

[84] 武晓晓，娄兵海，唐艳，陈传武，刘萍，章慧璇，范七君，黄俊源，门友均，邓崇岭 . 耐(抗)柑橘黄龙病种质材料的评价研究[J]. 中国果树，2021(11)：44-49.
WU Xiaoxiao，LOU Binghai，TANG Yan，CHEN Chuanwu，LIU Ping，ZHANG Huixuan，FAN Qijun，HUANG Junyuan，MEN Youjun，DENG Chongling. Study on the evaluation of resistance to citrus Huanglongbing of citrus germplasm materials[J]. China Fruits，2021(11)：44-49.

[85] 农业农村部 . 对十三届全国人大四次会议第 8590 号建议的答复[EB/OL]. [2022-06-15]. http://www.moa.gov.cn/govpublic/ZZYGLS/202108/t20210824_6374804.htm.
Ministry of Agriculture and Rural Affairs of the People's Republic of China. Reply to proposal No. 8590 of the fourth session of the 13th national people's congress[EB/OL]. [2022-06-15]. http://www.moa.gov.cn/govpublic/ZZYGLS/202108/t20210824637480 4.htm.

[86] 刘刚 . 我国第一部柑橘黄龙病防控地方性法规出台[J]. 农药市场信息，2019(20)：1.
LIU Gang. China's first local regulation on prevention and control of citrus Huanglongbing was issued[J]. Pesticide Market News，2019(20)：1.

[87] DAS A K，SHARMA S K，THAKRE N. Diagnostics for citrus greening disease (Huanglongbing)：Current and emerging technologies[J]. Plant Biotechnology：Progress in Genomic Era，2019：597-630.

[88] COLETTA-FILHO H D，TARGON M，TAKITA M A，DE NEGRI J D，POMPEU JR J，MACHADO M A，DO AMARAL A M，MULLER G W. First report of the causal agent of Huanglongbing (‘*Candidatus* Liberibacter asiaticus’) in Brazil[J]. Plant Disease，2004，88(12)：1382.

[89] DA GRAÇA J V，KORSTEN L. Citrus Huanglongbing：Review，present status and future strategies[M]//NAQVI S A M H. Diseases of Fruits and Vegetables Volume I：Diagnosis and Management，Netherlands：Springer Dordrecht，2004：229-245.

[90] DUAN Y P，ZHOU L J，HALL D G，LI W B，DODDAPANENI H，LIN H，LIU L，VAHLING C M，GABRIEL D W，WILLIAMS K P，DICKERMAN A，SUN Y J，GOTTWALD T. Complete genome sequence of citrus huanglongbing bacterium，‘*Candidatus* Liberibacter asiaticus’ obtained through metagenomics[J]. Molecular Plant-Microbe Interactions，2009，22(8)：1011-1020.

[91] AMMAR E，SHATTERS JR R G，LYNCH C，HALL D G. Detection and relative titer of *Candidatus* Liberibacter asiaticus in the salivary glands and alimentary canal of *Diaphorina citri* (Hemiptera：Psyllidae) vector of citrus Huanglongbing disease[J]. Annals of the Entomological Society of America，2011，104(3)：526-533.

[92] TATINENI S，SAGARAM U S，GOWDA S，ROBERTSON C J，DAWSON W O，IWANAMI T，WANG N. In planta distribution of ‘*Candidatus* Liberibacter asiaticus’ as revealed by polymerase chain reaction (PCR) and real-time PCR[J]. Phytopathology，2008，98(5)：592-599.

[93] ALBRECHT U，BOWMAN K D. Gene expression in *Citrus sinensis* (L.) osbeck following infection with the bacterial pathogen *Candidatus* Liberibacter asiaticus causing Huanglongbing in Florida[J]. Plant Science，2008，175(3)：291-306.

[94] COCUZZA G E M，ALBERTO U，HERNÁNDEZ-SUÁREZ E，SIVERIO F，DI SILVESTRO S，TENA A，CARMELO R. A review on *Trioza erytreae* (African citrus psyllid)，now in mainland Europe，and its potential risk as vector of Huanglongbing (HLB) in citrus[J]. Journal of Pest Science，2017，90(1)：1-17.

[95] DE MORAES P J G，VENDRAMINI P H，FERNANDES L S，DE SOUZA F H，PILAU E J，EBERLIN M N，MAGNANI R F，WULFF N A，FILL T P. Mass spectrometry imaging as a potential technique for diagnostic of Huanglongbing disease using fast and simple sample preparation[J]. Scientific reports，2020，10(1)：13457.

[96] TERENTEV A，DOLZHENKO V，FEDOTOV A，EREMENKO D. Current state of hyperspectral remote sensing for early plant disease detection: A review[J]. Sensors，2022，22(3)：757.

[97] 周常勇 . 对柑橘黄龙病防控对策的再思考[J]. 植物保护，2018，44(5)：30-33.
ZHOU Changyong. Reconsideration on the control strategy of citrus Huanglongbing[J]. Plant Protection，2018，44(5)：30-33.

(C)1994-2023 China Academic Journal Electronic Publishing House. All rights reserved.　http://www.cnki.net

《果树学报》第八届编辑委员会成员名单

（2022.01—2024.12）

顾　问　束怀瑞　张上隆　张光伦　马宝焜　林顺权　李绍华　陈学森　戴洪义　王志强

主　编　方金豹

副主编　韩振海　陈昆松　马锋旺　谢江辉　王力荣　刘崇怀　陈新平　王　珂

委　员　（按姓氏笔画排序）

王玉柱　王世平　王国平　王贵禧　王爱德　王海波　方从兵　古勤生　叶正文

冯建灿　刘凤之　刘文革　刘庆忠　刘孟军　刘威生　齐秀娟　关军锋　汤浩茹

孙崇德　李天红　李亚东　李明军　杨国顺　吴　俊　吴巨友　汪良驹　沈元月

张开春　张玉星　张运涛　张志宏　张绍铃　陈佰鸿　陈厚彬　陈清西　陈锦永

易干军　罗正荣　周永锋　周志钦　周厚成　周常勇　郑少泉　郑先波　胡桂兵

钟彩虹　段长青　俞明亮　夏　瑞　徐　强　徐小彪　徐永阳　郭文武　黄旭明

曹　珂　曹尚银　戚行江　阎振立　梁振昌　彭福田　程运江　焦中高　曾文芳

曾黎辉　詹儒林　滕元文　姚家龙（新西兰）　Desmond R. Layne（USA）

著作权使用声明：本刊已许可中国知网以数字化方式复制、汇编、发行、信息网络传播本刊全文。本刊支付的稿酬已包含中国知网著作权使用费，所有署名作者向本刊提交文章发表之行为视为同意上述声明。如有异议，请在投稿时说明，本刊将按作者说明处理。

果　树　学　报

（1984年8月创刊，月刊，公开发行）

2023年4月10日　第40卷　第4期

Journal of Fruit Science

（Published since August 1984, Monthly）

2023-04-10　Vol. 40　No. 4

主　　管　中华人民共和国农业农村部

主　　办　中国农业科学院郑州果树研究所

支　　持　浙江省农业科学院园艺研究所

上海市农业科学院林木果树研究所

中国热带农业科学院南亚热带作物研究所

辽宁省果树科学研究所

主　　编　方金豹

编辑出版　《果树学报》编辑部

E-mail：guoshuxuebao@caas.cn

450009 河南省郑州市未来路南端

中国农业科学院郑州果树研究所

电　　话　编辑部：(0371)63387308，65330928

发行部：65330982

印　　刷　河南瑞之光印刷股份有限公司

国内发行　郑州市邮政局

订 购 处　全国各地邮局（所）

国外发行　中国国际图书贸易总公司

（北京399信箱，100044）

Responsible Institution: Ministry of Agriculture and Rural Affairs of the People's Republic of China

Sponsored by: Zhengzhou Fruit Research Institute, CAAS

Jointly Sponsored by: Institute of Horticulture, Zhejiang Academy of Agricultural Sciences

Research Institute of Forestry & Pomology, Shanghai Academy of Agricultural Sciences

South Subtropical Crops Research Institute, Chinese Academy of Tropical Agricultural Sciences

Liaoning Institute of Pomology

Editor-in-chief: Fang Jinbao

Edited and Published by: Office of Journal of Fruit Science

E-mail: guoshuxuebao@caas.cn

Zhengzhou Fruit Research Institute, CAAS

450009 South Weilai Road, Zhengzhou, Henan

Tel: Editing Office: (0371)63387308, 65330928

Distribution Office: 65330982

Printed by: Henan Ruizhiguang Printing Co., LTD.

Domestic Distribution: Zhengzhou Post Office

Domestic Subscription: All Local Post Offices in China

Foreign Distribution:

China International Book Trading Corporation

(P. O. Box 399, Beijing, 100044 China)

公开发行　ISSN 1009-9980　CN 41-1308/S　国外代号：M1107　国内邮发代号：36-93　准予广告发布登记号：郑管市监广发登字（2019）1号　国内定价：30.00元

3.10 An improved YOLO model for detecting trees suffering from pine wilt disease at different stages of infection

Taylor & Francis Online

Access provided by South China Agricultural University

Log in | Register | Cart

Home ► All Journals ► Remote Sensing Letters ► List of Issues ► Volume 14, Issue 2

Remote Sensing Letters

Enter keywords, authors, DOI, etc

This Journal

Advanced search Citation search

Submit an article | About this journal | Browse all articles & issues | Alerts & RSS feed | Buy a subscription



Remote Sensing Letters, Volume 14, Issue 2 (2023)

Volume 14, 2023 | Vol 13, 2022 | Vol 12, 2021 | Vol 11, 2020 | Vol ›

See all volumes and issues

‹ Issue 5 | Issue 4 | Issue 3 | Issue 2 | Issue 1 ›

Browse this journal

- Latest articles
- Current issue
- List of issues
- Open access articles
- Most read articles
- Most cited articles

Download citations | Download PDFs | Download issue

Browse by section (All) | Display order (Default)

Research Article

Article

High-boost-based local Weber contrast method for infrared small target detection ›

Shun He, Yongni Xie & Zhiwei Yang

Pages: 103-113

Published online: 01 Jan 2023

Abstract | Full Text | References | PDF (2.4 MB) | EPUB

205 Views | 1 CrossRef citations | 0 Altmetric

Article

An improved YOLO model for detecting trees suffering from pine wilt disease at different stages of infection ›

Kunjie Wu, Jiantao Zhang, Xuanchun Yin, Sheng Wen & Yubin Lan

Pages: 114-123

Published online: 02 Jan 2023

Abstract | Full Text | References | PDF (3.5 MB) | EPUB

304 Views | 1 CrossRef citations | 0 Altmetric

Article

Improving power transmission tower state recognition in remote sensing images using cooperative Adaboost-MobileNet ›

Hemeng Yang, Sen Wang, Yanfang Chen, Zhengliang Yan, Yansheng Cheng, Tong Wang & Ruizeng Wei

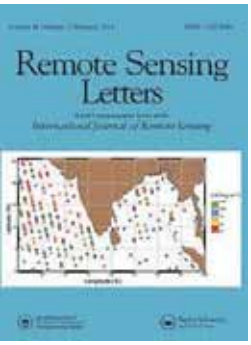
Pages: 124-134

Published online: 09 Jan 2023

Abstract | Full Text | References | PDF (1.3 MB) | EPUB

1100 Views | 0 CrossRef citations | 0 Altmetric

Article



Remote Sensing Letters

ISSN: (Print) (Online) Journal homepage: https://www.tandfonline.com/loi/trsl20

An improved YOLO model for detecting trees suffering from pine wilt disease at different stages of infection

Kunjie Wu, Jiantao Zhang, Xuanchun Yin, Sheng Wen & Yubin Lan

To cite this article: Kunjie Wu, Jiantao Zhang, Xuanchun Yin, Sheng Wen & Yubin Lan (2023) An improved YOLO model for detecting trees suffering from pine wilt disease at different stages of infection, Remote Sensing Letters, 14:2, 114-123, DOI: 10.1080/2150704X.2022.2161843

To link to this article: https://doi.org/10.1080/2150704X.2022.2161843

Published online: 02 Jan 2023.

Submit your article to this journal

Article views: 116

View related articles

View Crossmark data

Full Terms & Conditions of access and use can be found at
https://www.tandfonline.com/action/journalInformation?journalCode=trsl20

REMOTE SENSING LETTERS
2023, VOL. 14, NO. 2, 114–123
https://doi.org/10.1080/2150704X.2022.2161843

Taylor & Francis
Taylor & Francis Group

Check for updates

An improved YOLO model for detecting trees suffering from pine wilt disease at different stages of infection

Kunjie Wu[a,b], Jiantao Zhang[a,b,c], Xuanchun Yin[b,d], Sheng Wen[b,d] and Yubin Lan[b,e]

[a]College of Mathematics and Informatics, South China Agricultural University, Guangzhou, China; [b]National Center for International Collaboration Research on Precision Agricultural Aviation Pesticide Spraying Technology, South China Agricultural University, Guangzhou, China; [c]Key Laboratory of Smart Agricultural Technology in Tropical South China, Ministry of Agriculture and Rural Affairs, Guangzhou, China; [d]College of Engineering, South China Agricultural University, Guangzhou, China; [e]College of Electronic Engineering (College of Artificial Intelligence), South China Agricultural University, Guangzhou, China

ABSTRACT

Pine wilt disease (PWD) is one of the most destructive forest diseases in the world. Therefore, timely monitoring of PWD is essential to the preservation of the ecological environment. However, the complex topography of PWD-outbreak locations affords many limitations in the manual detection of the disease. The use of unmanned aerial vehicles (UAVs) and deep learning technology to detect PWD-infected trees has gained popularity in recent years. In this study, we configured the You Only Look Once version 3 (YOLOv3) model according to the characteristics of the three disease stages of PWD and proposed an improved model called Effi_YOLO_v3. The results revealed that the improved model achieved good detection performance. The proposed model yielded a mean average precision (mAP) of 94.39%, and the classification of the different infection stages was relatively accurate. The recall values for the classifications of trees in the early-infection, late-infection, and death stages were 89.15%, 86.13%, and 86.77%, respectively. This indicates that the model offers good applicability in detecting different stages of PWD in trees.

ARTICLE HISTORY
Received 18 May 2022
Accepted 7 December 2022

1. Introduction

The pine wood nematode (PWN, *Bursaphelenchus xylophilus*) is a common plant parasitic nematode (Jones et al. 2013) that can cause PWD, which is a devastating epidemic disease affecting pine trees. If a pine tree is infected with PWD and the infection is not detected at the early stage, the entire pine forest in its vicinity can be infected in turn, which can subsequently be managed only by, for example, cutting down or burning the whole forest. PWD is common in North America (Knowels et al. 1983; Dwinell 1993); however, the pine trees in these regions are not affected severely because of resistance to PWN (Dropkin and Foudin 1979). However, the PWD epidemic in Asia, especially in China, has exhibited a trend of continuous spread since the disease was first detected in Nanjing, Jiangsu Province, in 1982 (Sun 1982), causing economic losses approximating hundreds of

CONTACT Jiantao Zhang zhangjiantao@yeah.net College of Mathematics and Informatics, South China Agricultural University, Guangzhou, China

© 2023 Informa UK Limited, trading as Taylor & Francis Group

billions in Chinese yuan (Li et al. 2021). Worldwide, PWD has led to the destruction of many pine forests, thereby causing considerable economic and ecological losses (Sun et al. 2021; Ye 2019). The impact of PWD on forest resources will lead to a series of adverse events, such as climate change (Allen et al. 2010; Wong and Daniels 2017), and the global warming problem caused by the weakening of the climate-regulation ability of forests will, in turn, promote the spread of PWD (Kärvemo et al. 2016). Therefore, there is an urgent need for a rapid and effective method to monitor PWD for treating diseased trees.

Currently, most PWD monitoring methods are relatively simple. Many foresters regularly inspect forests or parks to assess the condition of pine trees. However, this traditional method has many limitations for PWD prevention. Sites with PWD outbreaks may exhibit complex topography, thereby making them inaccessible to many foresters. In recent years, the use of unmanned aerial vehicle (UAV)-based remote-sensing technology to detect pests has gained the attention of many researchers (Banu, Borlea, and Banu 2016). Compared to traditional methods, UAVs are adaptable, low-cost, and efficient (Tang and Shao 2015), which is a breakthrough for PWD control. However, many foresters only detect diseased trees manually via visual inspection of UAV images, which requires considerable manpower and is not a reliable solution to stop the spread of PWD.

Owing to the rapid development of computing power, various new algorithms have been applied in the field of detecting pest-induced diseases in forests. Syifa, Park, and Lee (2020) used various classifier methods, artificial neural networks, and support vector machines to classify healthy and PWD-infected pine trees. Iordache et al. (2020) utilized multispectral and hyperspectral data and designed two different algorithms based on the random forest (RF) approach to distinguish between healthy trees and those infected with PWD. Lee et al. (2021) analysed the geographical and meteorological characteristics of PWD in South Korea and developed RF and maximum entropy machine-learning algorithms to obtain a potential risk map for the occurrence of PWD. In these studies, different types of machine-learning algorithms were used for PWD detection. However, traditional machine learning requires complex feature engineering, and the best features must be carefully selected for the machine learning algorithm. In addition to the techniques mentioned above, a new technology which has become popular in agriculture recently is deep learning (Kamilaris and Prenafeta-Boldú 2018). Deng et al. (2020) combined the ideas of region proposal network and ResNet, optimized the loss function, and improved a model based on faster region-based convolutional neural network (Faster R-CNN) for detecting trees that died owing to PWD. Tao et al. (2020) collected images of dead pine trees from UAV to train the AlexNet and GoogLeNet CNNs to compare the accuracies of different classification methods. Both Wu et al. (2021) and Yu et al. (2021) employed various models, such as Faster R-CNN and YOLO, to diagnose the early-infection stage of PWD. Qin et al. (2021) and Xia et al. (2021) used different segmentation algorithms to segment PWD-infected trees and found that the improved network of Xia et al. (2021) was 17.67% more accurate than the other proposed network. Li et al. (2021) designed a system based on edge-computing and lightweight YOLOv4-tiny with an AP of 84.88% for the detection of PWD-infected trees. In conclusion, PWD detection using deep learning is an effective method that requires fewer resources and offers great potential for application. However, the above-mentioned studies involving deep learning have certain shortcomings, some of them do not detect for all stages of the disease, and some of them have low

detection accuracy, so further improvement of the algorithms is needed to make them as applicable as possible.

Timely detection of PWD can prevent the spread of the disease and reduce losses. In this regard, the aims of this study are as follows.

- We propose a dedicated deep learning model dedicated for detecting different stages of PWD in trees.
- Different stages of PWD infection were compared using different detection models to determine whether the proposed model has actual application.

2. Materials and methods

2.1. Study area

The study area is in the northeast of Guangzhou City, Guangdong Province, China (23°4629″–23°4659″N, 113°4659″–113°4753″E) and has a subtropical monsoon climate. The average annual temperature of the study site ranges from 19.5°C to 21.4°C, and the mean annual precipitation is approximately 1800–2200 ml. The plants in the study area mainly consisted of *Pinus massoniana*, camphor trees, and bamboo cypresses.

2.2. Data acquisition and data processing

Remote sensing images of the study area were acquired using a DJI Phantom 4 Pro V2.0 drone. Remote sensing images were collected between 11:10 and 12:30 on October 20–23, 2021. The UAV was configured to fly at an altitude of 400 m, with a spatial resolution of 0.1 m, a heading overlap rate of 75% and a side overlap rate of 65%. A total of 318 remote sensing images were acquired during the three days of shooting, and some of the images that were not useful for network training were discarded because they did not contain PWD-infected trees. Finally, 242 remote sensing images were suitable and used as the initial dataset for this study.

The original remote sensing images were segmented using the sliding-window method. The size of the segmented image was set to 768 × 768 pixels, and 2070 segmented images containing PWD-infected trees were obtained. The classification of the PWD-infected trees is shown in Figure 1. We used the dark channel defogging algorithm (He, Sun, and Tang 2010) to solve the problem of blurred sharpness. Subsequently, additional data augmentation was performed on the images with a total of 6210 images to improve the training of the neural network. Finally, we used LabelIMG to label the images after enhancement. The labelled samples are randomly divided into train, validation and test set in the ratio of 7:1:2, in which there are 4347 images in the train set, 621 images in the validation set, and 1242 image in the test set.

2.3. Proposed Effi_YOLO_v3 model

In this study, the backbone and neck of the YOLOv3 model were improved for the characteristics of PWD-infected trees. The architecture of the proposed PWD detection model is depicted in Figure 2. We used the *k*-means++ algorithm (Arthur and Vassilvitskii



Figure 1. The classification of the three infection stages.
Note: Photo (a) shows a tree in the early stage of infection, when the pine needles begin to change color and the pine transpiration decreases; Photo (b) shows a tree in the late stage of infection, when the pine needles turn reddish brown and appear wilted; Photo (c) shows a dead tree due to pine wilt disease, when the tree has wilted and appears greyish white.

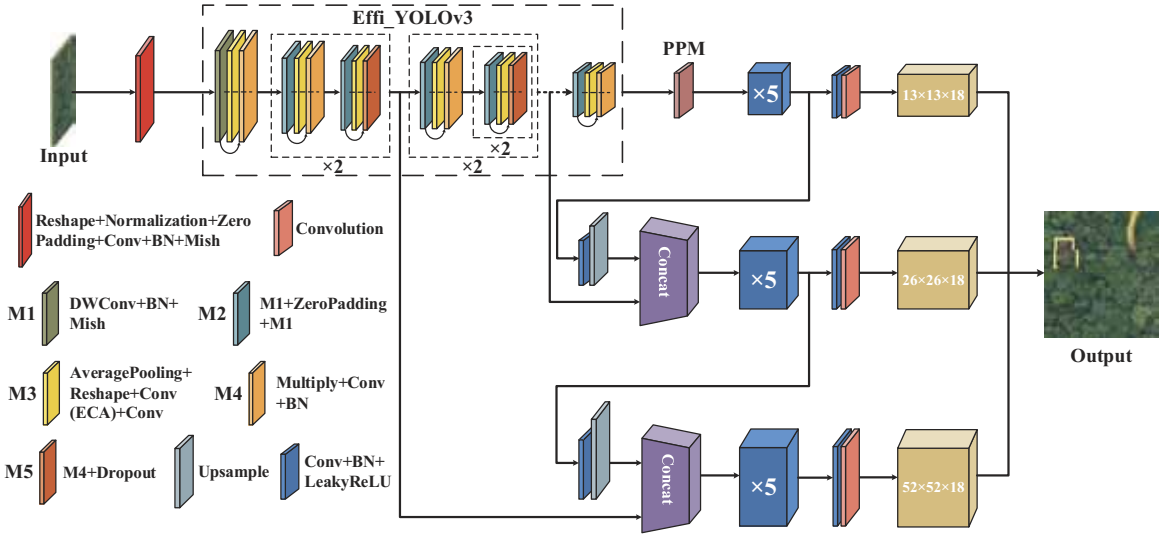


Figure 2. Architecture of the Effi_YOLO_v3 model.
Note: Module (M)1, M2, M3, M4, M5 are the internal modules of the Effi_YOLO_v3 model. 'Conv' and 'BN' are for Convolution and Batch Normalization respectively.

2006) to cluster anchor boxes before the network training. In the backbone feature extraction network, the original backbone DarkNet53 was replaced with the better-performing EfficientNet-B1, which achieved high accuracy and significant savings in computational resources through the extension of the standardized convolutional network (Tan and Le 2019). Subsequently, a more efficient activation function, Mish, was used in EfficientNet-B1, and its accuracy was improved by 0.494% over Swish. This activation function still maintains good performance, especially when applied to very deep networks (Misra 2019). In contrast, we used an efficient channel attention (ECA) module (Wang et al. 2020) to replace the squeeze-and-excitation(SE) module in the backbone. A set of weight parameters is learned autonomously by the network, and the dynamic weighting method is used to emphasize the diseased regions of the PWD-infected trees while suppressing

irrelevant background regions, which avoids dimensionality reduction and thus feature loss. The number of parameters in this module is equal to the size of a convolutional kernel, reducing model complexity while maintaining considerable performance and effectively capturing information about cross-channel interactions. Finally, we use the pyramid pooling module(PPM) in the neck, which was proposed by PSPNet (Zhao et al. 2017). The feature map extracted by PPM from the previous convolution is divided into two branches. One of the branches was divided into multiple sub-regions for global average pooling using a 1×1 convolution to resize the channel, and bilinear interpolation was performed to obtain the size before pooling. The processed branch was concatenated with the other branch. The receptive field was expanded and the context of different regions was aggregated to obtain the global context. The improved model can better fuse deep and shallow feature information, while saving computational costs and improving the accuracy and efficiency of PWD detection.

2.4. Experimental environment settings

A computer with an Intel Xeon E5–2620 v3 64-bit 2.40 GHz CPU, a 32 GB RAM, an NVIDIA GTX 1080 GPU, CUDA v10.1, and OpenCV v4.5.4 was used for model training and testing. The size of the input image was set to 416×416 pixels. The parameters were updated with an initial learning rate of 0.001 and a momentum of 0.94 over 400 epochs.

2.5. Evaluation indicators and comparison model

In this study, average precision (AP), mean AP (mAP), and number of floating point operations (FLOPs) are used as evaluation indicators for detecting accuracy and calculating the computational cost of the model. AP is the area under the accuracy and recall curves, mAP is the average of AP for all categories, and FLOPs can be understood as the computational volume, which can be used to measure the complexity of the model.

The improved YOLO model is compared with commonly used target detection models such as Faster R-CNN, SSD, YOLOv3, YOLOv4, etc., while controlling for the same training platform, configuration information and dataset. Different models are used to train and detect the same images respectively, and the mAP, size, parameters, and FLOPs of the different models are compared.

3. Results

3.1. Comparative analysis of model performances

The results of the comparison are shown in Table 1. Except for the Faster R-CNN and single shot multibox detector (SSD) models, the mAP of all other models exceeds 85%, but their weight sizes, number of parameters, and FLOPs vary significantly. Compared to other models, Faster R-CNN and SSD have a larger number of parameters, lower detection accuracy, and larger values of FLOPs, which means that these two models have limited practical use. In contrast, the original YOLOv3 and YOLOv4 series models exhibit good detection performance. But their weight size and FLOPs are relatively large, which means a high level of hardware is required. The Effi_YOLO_v3 model proposed herein has the

Table 1. Performance comparison of different detection models.

Model	Backbone	mAP (%)	Size (MB)	No. of Parameters	No. of GFLOPs[b]
Faster R-CNN	ResNet-50	63.84	315.0	28,469,983	134.57
SSD	VGG	79.67	91.6	26,151,824	30.50
YOLOv4	CSPDarkNet-53	95.96	244.0	64,363,101	29.89
	MobileNet v2	88.31	149.0	39,062,013	27.23
	CSPDarkNet-53-tiny	89.10	22.4	6,056,606	34.12
YOLOv3	DarkNet-53	89.23	234.7	61,534,504	32.77
	Improved EfficientNet-B1[a]	94.39	47.6	12,570,818	1.94

[a]The improved model proposed in this paper; [b]1×10^9 FLOPs = 1 GFLOPs.

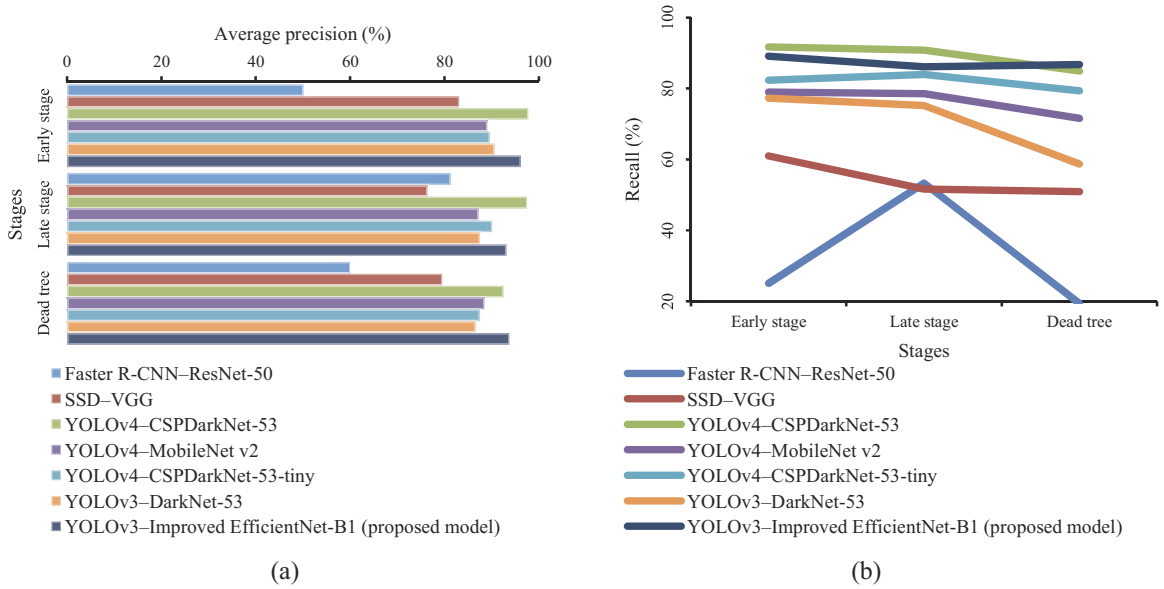


Figure 3. The comparisons of AP (a) and Recall (b) among different detection models.

best overall performance with a second-ranked mAP of 94.39% despite the low number of parameters and FLOPs value.

To further confirm the detection results of each model for different categories, the recall and AP values of each model corresponding to the different categories were compared, as shown in Figure 3. The comparison shows that, similar to the previous evaluation results, the Faster R-CNN and SSD models suffer from low precision and recall in different categories. In contrast, the AP values of the original YOLOv3 and YOLOv4 series models are at a relatively high level. However, the original YOLOv4 model has a large number of parameters and a large weight, which consumes considerable computational resources. The proposed model achieved an average detection accuracy exceeding 93% for different categories, and the recall of different categories was close to 90%. The improved model outperforms almost all the indicators except the comparison with the original YOLOv4. Combining the above results with the parameters, FLOPs, recall, and other indicators, it can be seen that the model proposed in this study achieves the best performance in the detection of PWD.

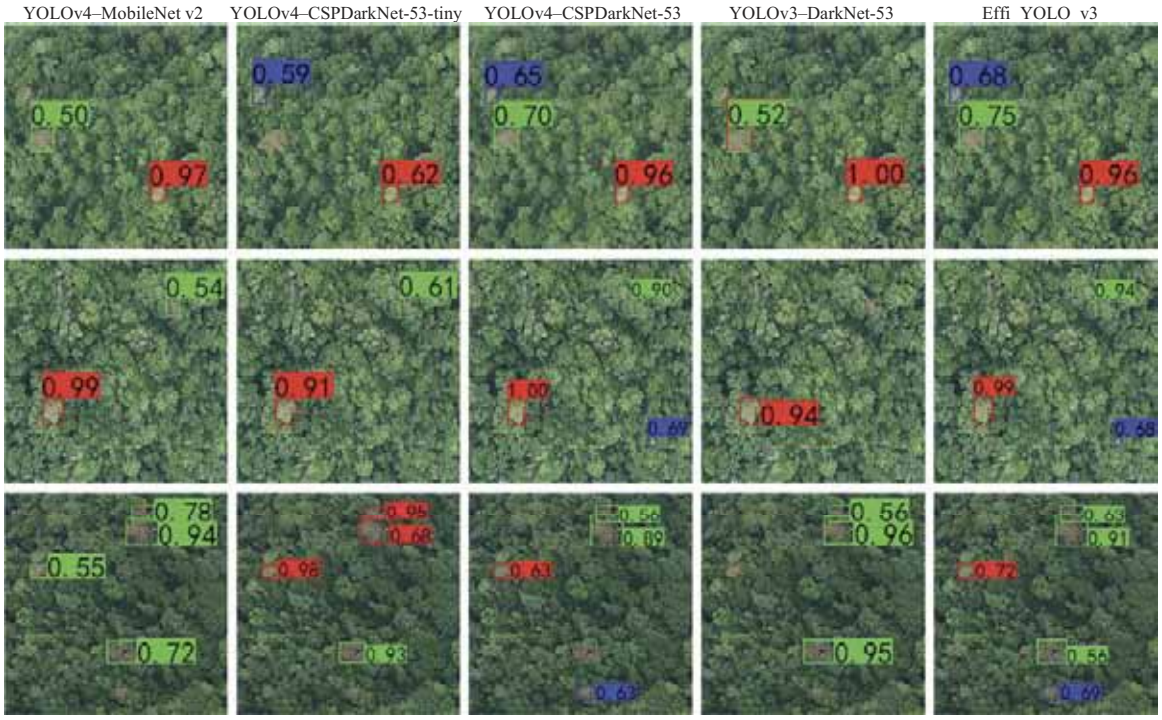


Figure 4. The detection results of the chosen models on diseased trees at different stages of infection. Note: Red, green, and blue boxes represent the early infection stage, late infection stage, and dead trees, respectively. Numbers indicate their confidence.

3.2. Comparative analysis of detection results

For further comparison and discussion of the detection capabilities of different models, we compared the detection results of all models in the YOLO series. We randomly screened images containing different infection stages of PWD, including adjacent and detached trees. The prediction results are shown in Figure 4.

By comparing the prediction results of these models, we can observe that there are large differences in the detection results of the different models. The YOLOv3 model suffers from duplicate detection and, like YOLO v4 (MobileNet v2 and tiny), has problems with inaccurate classification and missed detections. The YOLOv4 model, on the other hand, can detect more accurately, but there will also be some missed detections. The Effi_YOLO_v3 model proposed in this paper can detect all disease trees basically, which is sufficient for small targets and dense diseased trees. Therefore, the Effi_YOLO_v3 model has the best detection performance among these models.

4. Discussion

Nowadays, the combination of UAV remote sensing and deep learning techniques is increasingly applied to PWD detection. In this study, the improved YOLOv3 model was used for automatic detection of PWD-infected trees with an mAP of 94.35%. Compared with Yu et al. (2021), Qin et al. (2021), Iordache et al. (2020), and Wu et al. (2021), the proposed model can detect diseased trees with different stages of disease, and the accuracy is basically improved over them. Although Yu et al. (2021) may have better

generality as the research object includes other trees, the accuracy of its deep learning model is only 66.7% at the highest.

In this study, the proposed model significantly reduces the number of parameters and computational resources required for PWD detection, which means that the improved model reduces the computational burden and lowers the level of computer hardware required by the model. The improved model achieves a higher detection accuracy and recall for detecting PWD-infected trees at different infection stages. It should be noted that the learning ability of this model must be improved by expanding the dataset to accommodate the impact of a more complex and wider range of environments. The coordinates of the PWD-infected trees in the model will also be subsequently targeted based on the geographic coordinates of the orthophotos in order to support forest management more effectively.

5. Conclusion

After pine trees are affected by PWD, the colour of pine needles gradually appears as yellowish-brown in the early stage, reddish-brown in the late stage and to the final dead greyish-white due to the proliferation of PWN in pine trees, which led to a significant decrease in resin secretion, attenuation of photosynthesis, and decrease in transpiration. In this study, the YOLOv3 model was improved based on the manifestation of the disease characteristics of PWD. The mAP of the improved model in detecting PWD-infected trees at different stages of infection increased from 89.23% to 94.39% before the improvement, and the number of parameters were reduced by about 80%, and the evaluation indicator of model complexity FLOPs was reduced from 32.77 to 1.94 GFLOPs (gigaFLOPs). These results prove that the improved model proposed herein is capable of detecting PWD-infected trees efficiently.

Acknowledgments

The authors would like to acknowledge the funding from the National Natural Science Foundation of China. The authors would like to acknowledge the funding from the Characteristic Innovation Projects of Universities in Guangdong Province. The authors would also like to thank the developers in the ArcGIS and Pytorch developer communities for their open source projects.

Disclosure statement

No potential conflict of interest was reported by the author(s).

Funding

This work was supported in part by the National Natural Science Foundation of China [grant number 32271985] and in part by the Special Project in key Areas of Artificial Intelligence in Guangdong Universities [grant number 2019KZDZX1002].

ORCID

Kunjie Wu http://orcid.org/0000-0002-5895-3483

Data availability statement

The datasets generated and analysed during the current study are not publicly available due to the need for further research, but are available from the corresponding author on reasonable request.

Geolocation information

483 Wushan Road, Tianhe District, Guangzhou, 510642, China.

References

Allen, C. D., A. K. Macalady, H. Chenchouni, D. Bachelet, N. McDowell, M. Vennetier, T. Kitzberger, et al. 2010. "A Global Overview of Drought and Heat-Induced Tree Mortality Reveals Emerging Climate Change Risks for Forests." *Forest Ecology and Management* 259 (4): 660–684. doi:10.1016/j.foreco.2009.09.001.

Arthur, D., and S. Vassilvitskii. 2006. *K-Means++: The Advantages of Careful Seeding*. In: Stanford.

Banu, T. P., G. F. Borlea, and C. Banu. 2016. "The Use of Drones in Forestry." *Journal of Environmental Science and Engineering B* 5 (11): 557–562. doi:10.17265/2162-5263/2016.11.007.

Deng, X., Z. Tong, Y. Lan, and Z. Huang. 2020. "Detection and Location of Dead Trees with Pine Wilt Disease Based on Deep Learning and UAV Remote Sensing." *AgriEngineering* 2 (2): 294–307. doi:10.3390/agriengineering2020019.

Dropkin, V., and A. Foudin. 1979. "Report of the Occurrence of Bursaphelenchus Lignicolus-Induced Pine Wilt Disease in Missouri." *Plant Disease Reporter* 63: 904–905.

Dwinell, L. 1993. "First Report of Pinewood Nematode (Bursaphelenchus Xylophilus) in Mexico." *Plant Disease* 77 (8): 846. doi:10.1094/pd-77-0846a.

He, K., J. Sun, and X. Tang. 2010. "Single Image Haze Removal Using Dark Channel Prior." *IEEE Transactions on Pattern Analysis and Machine Intelligence* 33 (12): 2341–2353. doi:10.1109/TPAMI.2010.168.

Iordache, M. -D., V. Mantas, E. Baltazar, K. Pauly, and N. Lewyckyj. 2020. "A Machine Learning Approach to Detecting Pine Wilt Disease Using Airborne Spectral Imagery." *Remote Sensing* 12 (14): 2280. doi:10.3390/rs12142280.

Jones, J. T., A. Haegeman, E. G. J. Danchin, H. S. Gaur, J. Helder, M. G. K. Jones, T. Kikuchi, et al. 2013. "Top 10 Plant-Parasitic Nematodes in Molecular Plant Pathology." *Molecular Plant Pathology* 14 (9): 946–961. doi:10.1111/mpp.12057.

Kamilaris, A., and F. X. Prenafeta-Boldú. 2018. "Deep Learning in Agriculture: A Survey." *Computers and Electronics in Agriculture* 147: 70–90. doi:10.1016/j.compag.2018.02.016.

Kärvemo, S., V. Johansson, M. Schroeder, T. Ranius, and K. Haynes. 2016. "Local Colonization-extinction Dynamics of a Tree-killing Bark Beetle During a Large-scale Outbreak." *Ecosphere* 7 (3): e01257. doi:10.1002/ecs2.1257.

Knowels, K., Y. Beaubien, M. Wingfield, F. Baker, and D. French. 1983. "The Pinewood Nematode New in Canada." *Forestry Chronicle* 59: 40.

Lee, D. -S., W. I. Choi, Y. Nam, and Y. -S. Park. 2021. "Predicting Potential Occurrence of Pine Wilt Disease Based on Environmental Factors in South Korea Using Machine Learning Algorithms." *Ecological informatics* 64: 101378. doi:10.1016/j.ecoinf.2021.101378.

Li, M., Y. Dai, Y. Wang, L. Wang, S. Sun, and F. Chen. 2021. "New Insights into the Life History of Monochamus Saltuarius (Cerambycidae: Coleoptera) Can Enhance Surveillance Strategies for Pine Wilt Disease." *Journal of Forestry Research* 32 (6): 2699–2707. doi:10.1007/s11676-021-01296-x.

Li, F., Z. Liu, W. Shen, Y. Wang, Y. Wang, C. Ge, F. Sun, and P. Lan. 2021. "A Remote Sensing and Airborne Edge-Computing Based Detection System for Pine Wilt Disease." *IEEE Access* 9: 66346–66360. doi:10.1109/ACCESS.2021.3073929.

Misra, D. 2019. "Mish: A Self Regularized Non-Monotonic Activation Function." *arXiv preprint*. doi:10.48550/arXiv.1908.08681.

Qin, J., B. Wang, Y. Wu, Q. Lu, and H. Zhu. 2021. "Identifying Pine Wood Nematode Disease Using UAV Images and Deep Learning Algorithms." *Remote Sensing* 13 (2): 162. doi:10.3390/rs13020162.

Sun, Y. 1982. "First Report of Pine Wilt Disease from Pinus Thunbergii Parl in Sun Yat-Sen Mausoleum." *Journal of Jiangsu Forestry Science and Technology* 2: 27.

Sun, H., Y. Zhou, X. Li, Y. Zhang, and Y. Wang. 2021. "Occurrence of Major Forest Pests in 2020 and Prediction of Occurrence Trend in 2021 in China." *Forest Pest Disease* 40 (02): 45–48. doi:10.19688/j.cnki.issn1671-0886.20210004.

Syifa, M., S. -J. Park, and C. -W. Lee. 2020. "Detection of the Pine Wilt Disease Tree Candidates for Drone Remote Sensing Using Artificial Intelligence Techniques." *Engineering* 6 (8): 919–926. doi:10.1016/j.eng.2020.07.001.

Tang, L., and G. Shao. 2015. "Drone Remote Sensing for Forestry Research and Practices." *Journal of Forestry Research* 26 (4): 791–797. doi:10.1007/s11676-015-0088-y.

Tan, M., and Q. Le. 2019. Efficientnet: Rethinking Model Scaling for Convolutional Neural Networks. Paper presented at the International conference on machine learning, Long Beach, United State.

Tao, H., C. Li, D. Zhao, S. Deng, H. Hu, X. Xu, and W. Jing. 2020. "Deep Learning-Based Dead Pine Tree Detection from Unmanned Aerial Vehicle Images." *International Journal of Remote Sensing* 41 (21): 8238–8255. doi:10.1080/01431161.2020.1766145.

Wang, Q., B. Wu, P. Zhu, P. Li, and Q. Hu. 2020. ECA-Net: Efficient Channel Attention for Deep Convolutional Neural Networks. Paper presented at the 2020 IEEE/CVF Conference on Computer Vision and Pattern Recognition (CVPR), Seattle, United State.

Wong, C. M., and L. D. Daniels. 2017. "Novel Forest Decline Triggered by Multiple Interactions Among Climate, an Introduced Pathogen and Bark Beetles." *Global Change Biology* 23 (5): 1926–1941. doi:10.1111/gcb.13554.

Wu, B., A. Liang, H. Zhang, T. Zhu, Z. Zou, D. Yang, W. Tang, J. Li, and J. Su. 2021. "Application of Conventional UAV-Based High-Throughput Object Detection to the Early Diagnosis of Pine Wilt Disease by Deep Learning." *Forest Ecology and Management* 486: 118986. doi:10.1016/j.foreco.2021.118986.

Xia, L., R. Zhang, L. Chen, L. Li, T. Yi, Y. Wen, C. Ding, and C. Xie. 2021. "Evaluation of Deep Learning Segmentation Models for Detection of Pine Wilt Disease in Unmanned Aerial Vehicle Images." *Remote Sensing* 13 (18): 3594. doi:10.3390/rs13183594.

Ye, J. 2019. "Epidemic Status of Pine Wilt Disease in China and Its Prevention and Control Techniques and Counter Measures." *Scientia Silvae Sinicae* 55 (9): 1–10. doi:10.11707/j.1001-7488.20190901.

Yu, R., Y. Luo, Q. Zhou, X. Zhang, D. Wu, and L. Ren. 2021. "Early Detection of Pine Wilt Disease Using Deep Learning Algorithms and UAV-Based Multispectral Imagery." *Forest Ecology and Management* 497: 119493. doi:10.1016/j.foreco.2021.119493.

Zhao, H., J. Shi, X. Qi, X. Wang, and J. Jia. 2017. "Pyramid Scene Parsing Network." *Proceedings of the IEEE conference on computer vision and pattern recognition*:2881–2890. doi: 10.1109/CVPR.2017.660.

SCAULIB202405679

检索证明

根据委托人提供的论文材料，委托人华南农业大学数学与信息学院 张建桃 1 篇论文收录情况如下表。

序号	论文名称	发表刊物及发表的年月卷期/页码等	作者排名	论文等级	作者文中单位	收录情况	影响因子	中科院大类分区
1	An improved YOLO model for detecting trees suffering from pine wilt disease at different stages of infection	REMOTE SENSING LETTERS 出版年：2023 卷期：14 2 页码：114-123 文献号： 文献类型：Article	通讯作者	B 类	华南农业大学	SCI	IF2-year=2.3 IF5-year=2.4 （2022）	地球科学 4 区 Top 期刊：否 （2023）

说明：论文等级和中科院大类分区按《华南农业大学学术论文评价方案（试行）》划分。

报告免责声明:如未盖章,报告无效

检索员：张进

华南农业大学图书馆

2024-03-13

华南农业大学图书馆SCAULIB202405679

四、科研成果

1. 知识产权

1.1 专利授权证书：一种柑橘黄龙病的热空气处理装置及其使用方法

证书号第3646600号

发明专利证书

发明名称：一种柑橘黄龙病的热空气处理装置及其使用方法

发明人：张建桃;李晟华;文晟;陈鸿;兰玉彬;陈建国;陈嘉豪

专利号：ZL 2016 1 0566664.3

专利申请日：2016年07月15日

专利权人：华南农业大学

地址：510642 广东省广州市天河区五山路483号

授权公告日：2019年12月27日　　授权公告号：CN 106416854 B

国家知识产权局依照中华人民共和国专利法进行审查，决定授予专利权，颁发发明专利证书并在专利登记簿上予以登记。专利权自授权公告之日起生效。专利权期限为二十年，自申请日起算。

专利证书记载专利权登记时的法律状况。专利权的转移、质押、无效、终止、恢复和专利权人的姓名或名称、国籍、地址变更等事项记载在专利登记簿上。

局长
申长雨

国家知识产权局

2019年12月27日

其他事项参见背面

1.2 专利授权证书：一种柑橘幼苗微波加热杀菌装置

证书号第5185612号

发明专利证书

发明名称：一种柑橘幼苗微波加热杀菌装置

发 明 人：张建桃;宋庆奎;周腾媛;吴金泳;文晟;尹选春;王立浩

专 利 号：ZL 2020 1 0778637.9

专利申请日：2020年08月05日

专利权人：华南农业大学

地 址：510642 广东省广州市天河区五山路483号

授权公告日：2022年05月27日　　授权公告号：CN 111903373 B

国家知识产权局依照中华人民共和国专利法进行审查，决定授予专利权，颁发发明专利证书并在专利登记簿上予以登记。专利权自授权公告之日起生效。专利权期限为二十年，自申请日起算。

专利证书记载专利权登记时的法律状况。专利权的转移、质押、无效、终止、恢复和专利权人的姓名或名称、国籍、地址变更等事项记载在专利登记簿上。

局长
申长雨

国家知识产权局

2022年05月27日

其他事项参见续页

1.3 专利授权证书：基于胜任力的招聘文本专业知识点分类方法及装置

证书号第8298146号

专利公告信息

发明专利证书

发明名称：基于胜任力的招聘文本专业知识点分类方法及装置

专利权人：华南农业大学

地　　址：510642 广东省广州市天河区五山路483号

发 明 人：张建桃;林筱芸;韦婷婷;姜可欣;陈霖琳;张叶

专　利　号：ZL 2023 1 1534648.2　　授权公告号：CN 117556045 B

专利申请日：2023年11月17日　　授权公告日：2025年09月23日

申请日时申请人：华南农业大学

申请日时发明人：张建桃;林筱芸;韦婷婷;姜可欣;陈霖琳;张叶

国家知识产权局依照中华人民共和国专利法进行审查，决定授予专利权，并予以公告。

专利权自授权公告之日起生效。专利权有效性及专利权人变更等法律信息以专利登记簿记载为准。

局长
申长雨

2025年09月23日

1.4 专利授权证书：一种基于改进 Yolo v3 网络模型的松材线虫病疫木检测方法

证书号第8181206号

专利公告信息

发明专利证书

发明名称：一种基于改进Yolo v3网络模型的松材线虫病疫木检测方法

专利权人：华南农业大学

地　　址：510642 广东省广州市天河区五山路483号

发 明 人：张建桃;吴锟杰;尹选春;文晟;林筱芸

专　利　号：ZL 2022 1 1172167.7　　授权公告号：CN 115619719 B

专利申请日：2022年09月26日　　授权公告日：2025年08月22日

申请日时申请人：华南农业大学

申请日时发明人：张建桃;吴锟杰;尹选春;文晟;林筱芸

国家知识产权局依照中华人民共和国专利法进行审查，决定授予专利权，并予以公告。

专利权自授权公告之日起生效。专利权有效性及专利权人变更等法律信息以专利登记簿记载为准。

局长
申长雨

2025年08月22日

1.5 专利授权证书：一种微孔压电超声雾化器

证书号第7190906号

实用新型专利证书

实用新型名称：一种微孔压电超声雾化器

发　明　人：张建桃;胡慧卿;文晟;尹选春;梁玉燕;汤镇安

专　利　号：ZL 2017 2 1021855.8

专利申请日：2017年08月15日

专利权人：华南农业大学

授权公告日：2018年04月10日

本实用新型经过本局依照中华人民共和国专利法进行初步审查，决定授予专利权，颁发本证书并在专利登记簿上予以登记。专利权自授权公告之日起生效。

本专利的专利权期限为十年，自申请日起算。专利权人应当依照专利法及其实施细则规定缴纳年费。本专利的年费应当在每年08月15日前缴纳。未按照规定缴纳年费的，专利权自应当缴纳年费期满之日起终止。

专利证书记载专利权登记时的法律状况。专利权的转移、质押、无效、终止、恢复和专利权人的姓名或名称、国籍、地址变更等事项记载在专利登记簿上。

局长
申长雨

中华人民共和国国家知识产权局

2018年04月10日

1.6 软著授权证书：植保无人机喷雾雾滴在水稻叶片表面润湿展布性能预测系统

中华人民共和国国家版权局

计算机软件著作权登记证书

证书号：软著登字第3622900号

软件名称：植保无人机喷雾雾滴在水稻叶片表面润湿展布性能预测系统
[简称：PSOWSPOPPDSDORLS]
V1.0

著作权人：华南农业大学

开发完成日期：2018年12月02日

首次发表日期：2018年12月02日

权利取得方式：原始取得

权利范围：全部权利

登记号：2019SR0102143

根据《计算机软件保护条例》和《计算机软件著作权登记办法》的规定，经中国版权保护中心审核，对以上事项予以登记。

中华人民共和国国家版权局
计算机软件著作权
登记专用章

2019年01月29日

No. 03562739

五、其他业绩

1. 指导学生学科竞赛

1.1 第五届广东省暨粤港澳大湾区工业工程创新大赛三等奖

“基于线性回归模型的气象预测系统”

荣誉证书

HONORARY CREDENTIAL

第五届广东省暨粤港澳大湾区工业工程创新大赛

三等奖

作品名称：基于线性回归模型的气象预测系统

参赛组别：研究生组　　指导教师：张建桃

参赛人员：梁嘉文、吴逢秋、姜可欣

参赛单位：华南农业大学

广东省机械工程学会

二〇二三年十二月

证书编号：2023-GDMES-IE-Y3-13

1.2 第三届广东省暨粤港澳大湾区工业工程创新大赛三等奖

“基于 SLP 的胶粘剂生产车间布置优化”

证书编号 Certificate Number

2021-GDCIE-Y001-T

第三届广东省暨粤港澳大湾区工业工程创新大赛

The 3rd Guangdong Province and Guangdong-Hong Kong-Macao Greater Bay Area Innovation Competition of Industrial Engineering

获奖证书

Certificate

作品名称 Name of the Work

基于 SLP 的胶粘剂生产车间布置优化

Layout optimization of adhesive production workshop based on SLP

获奖等级 Level of Award

三等奖

Third Prize

团队成员 Team Members

曾莉

Zeng Li

指导老师 Instructor

张建桃

Zhang Jiantao

所在学校 Affiliation

华南农业大学

South China Agricultural University

广东省机械工程学会

二〇二一年 十二月

1.3 第五届广东省暨粤港澳大湾区工业工程创新大赛二等奖

“Amazon kindle 保护壳精密注塑成型仿真及工艺参数多目标优化”

荣誉证书

HONORARY CREDENTIAL

第五届广东省暨粤港澳大湾区工业工程创新大赛

二等奖

作品名称：Amazon kindle 保护壳精密注塑成型仿真及工艺参数多目标优化

参赛组别：研究生组　　指导教师：张建桃

参赛人员：刘广彬、曾慧娟、陈霖琳、黄路生

参赛单位：华南农业大学

广东省机械工程学会

二〇二三年十二月

证书编号：2023-GDMES-IE-Y2-7

1.4 第六届广东省暨粤港澳大湾区工业工程创新大赛三等奖

“基于 IE 的现代办公家具设计研究”

荣誉证书

HONORARY CREDENTIAL

第六届广东省暨粤港澳大湾区工业工程创新大赛

三等奖

作品名称：基于 IE 的现代办公家具设计研究

参赛组别：研究生组　　指导教师：张建桃

参赛人员：唐宝华/陈霖琳/曾慧娟/刘广彬/张宇煦

参赛单位：华南农业大学

广东省机械工程学会

二〇二四年十二月

证书编号：2024-GDMES-IE-Y3-3

1.5 第六届广东省暨粤港澳大湾区工业工程创新大赛三等奖

“基于 Anylogic 的 H 医院急诊中心仿真与优化”

荣誉证书

HONORARY CREDENTIAL

第六届广东省暨粤港澳大湾区工业工程创新大赛

三等奖

作品名称：基于 Anylogic 的 H 医院急诊中心仿真与优化

参赛组别：研究生组　　指导教师：张建桃

参赛人员：何建明/张宇煦/余重庆

参赛单位：华南农业大学

广东省机械工程学会

二〇二四年十二月

证书编号：2024-GDMES-IE-Y3-5

1.6 第七届广东省暨粤港澳大湾区工业工程创新大赛二等奖“无人机蝶旋桨注塑参数优化”


荣誉证书

HONORARY CREDENTIAL

第七届广东省暨粤港澳大湾区工业工程创新大赛

二等奖

作品名称：无人机螺旋桨注塑参数优化

参赛组别：研究生组　　指导教师：张建桃

参赛人员：刘伟俊/李俊杰/刘玉博/谢春光/李开隽

参赛单位：华南农业大学

广东省机械工程学会

二零二五年十一月

证书编号：2025-GDMES-IE-Y2-1

1.7 第七届广东省暨粤港澳大湾区工业工程创新大赛三等奖

“基于供应商交付的物料齐套方法研究”



2. 个人荣誉

2.1 华南农业大学十佳创新创业导师证书

华南农业大学创新创业学院文件

关于表彰2018年华南农业大学十佳创新创业导师的决定

为推进我校创新创业工作发展，强化创新人才培养机制，按照《印发<华南农业大学关于进一步推动大学生创新创业工作的实施意见>的通知》（华南农办〔2015〕161号）和《华南农业大学大学生创新创业导师管理办法（暂行）》（华南农办〔2016〕号）的规定，学校于2019年4月启动了华南农业大学十佳创新创业导师评奖工作程序。经过学院推荐、个人自荐、专家考评、评奖领导小组讨论、结果公示等环节，现决定对在2018年创新创业教育指导工作中表现突出的10位校内导师、10位校外导师进行表彰。

希望受表彰的个人珍惜荣誉，谦虚谨慎，再接再厉，不断取得更大更好的新成绩。希望全校教职工、全体校外创新创业导师向先进学习，进一步做好创新创业教育指导工作。

附件：2018年华南农业大学十佳创新创业导师

华南农业大学创新创业学院

2019年4月28日

附件：2018年华南农业大学十佳创新创业导师

一、校内十佳创新创业导师（按拼音字母顺序）

曹　帅　李继宇　林钻辉　刘秀琴　陆　星　巫光宏　吴　琪

吴珍芳　张建桃　左两军

二、校外十佳创新创业导师（按拼音字母顺序）

朗恒教育事业部总经理　陈少强

广州火花传媒有限公司执行董事总经理　黄栩槟

广州星唯信息科技有限公司总经理　李　明

广州大智汇创业服务有限公司董事长　施开亮

广州亿账柜信息科技有限公司总经理　王海云

慧科教育集团总经理　曾　憨

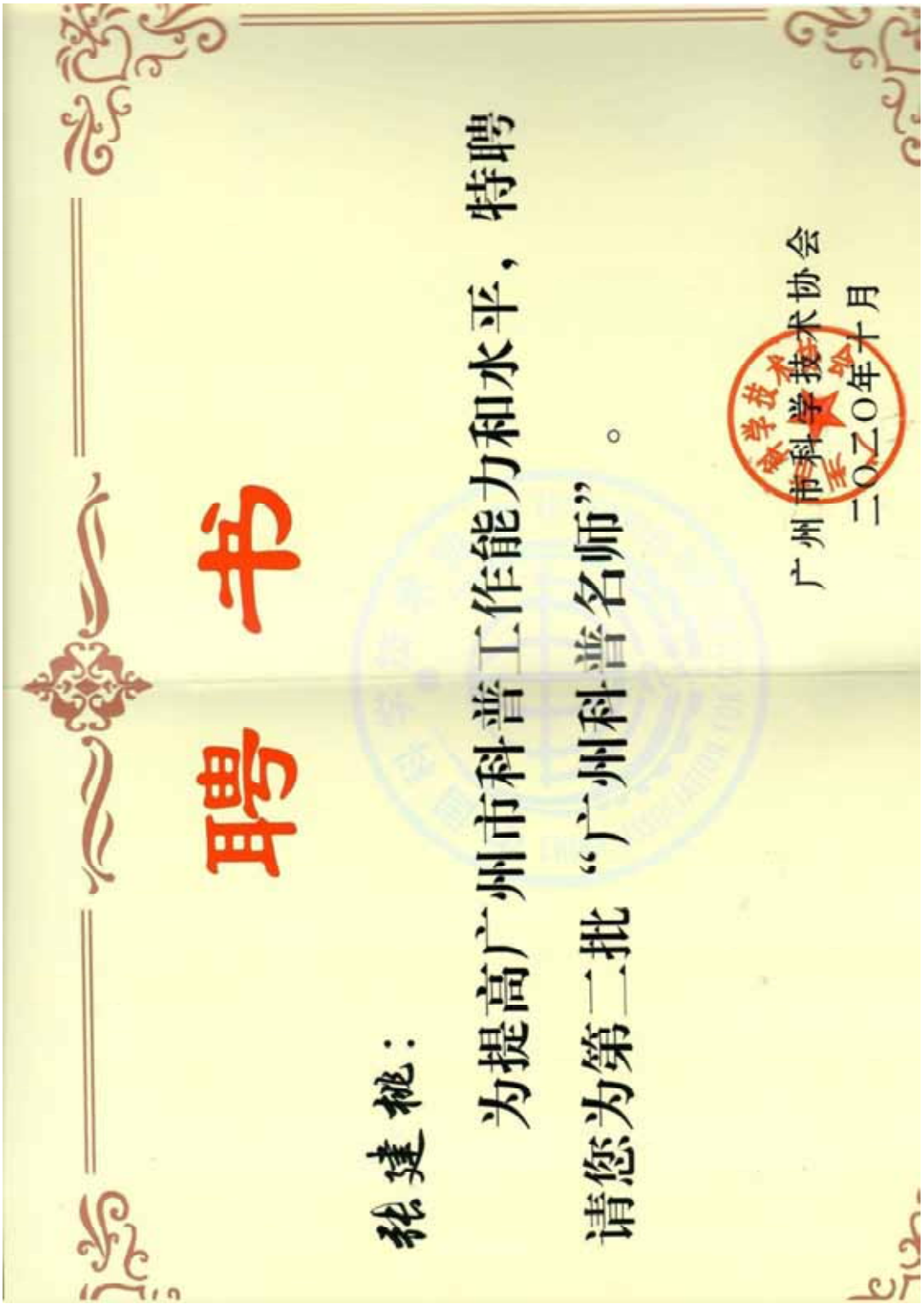
广州灵聚信息科技有限公司首席执行官　张　胜

广州南菱汽车股份有限公司副总经理　郑建群

广州飞瑞敖电子科技股份有限公司双创事业部总监　衷诚武

广州创龙电子科技有限公司首席执行官　朱　雅

2.2 广州市科普名师



聘书

张建桃：

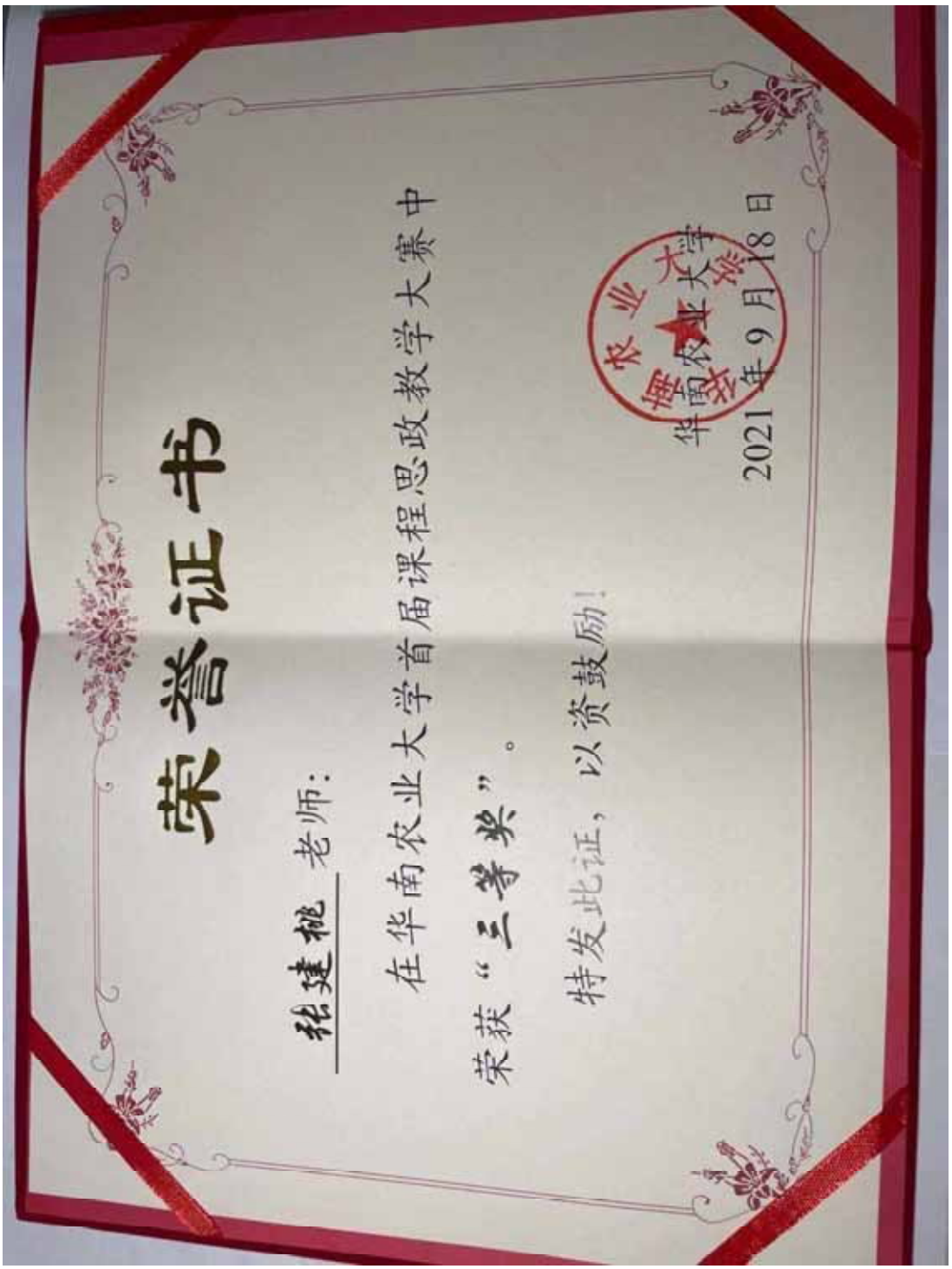
为提高广州市科普工作能力和水平，特聘

请您为第二批“广州科普名师”。

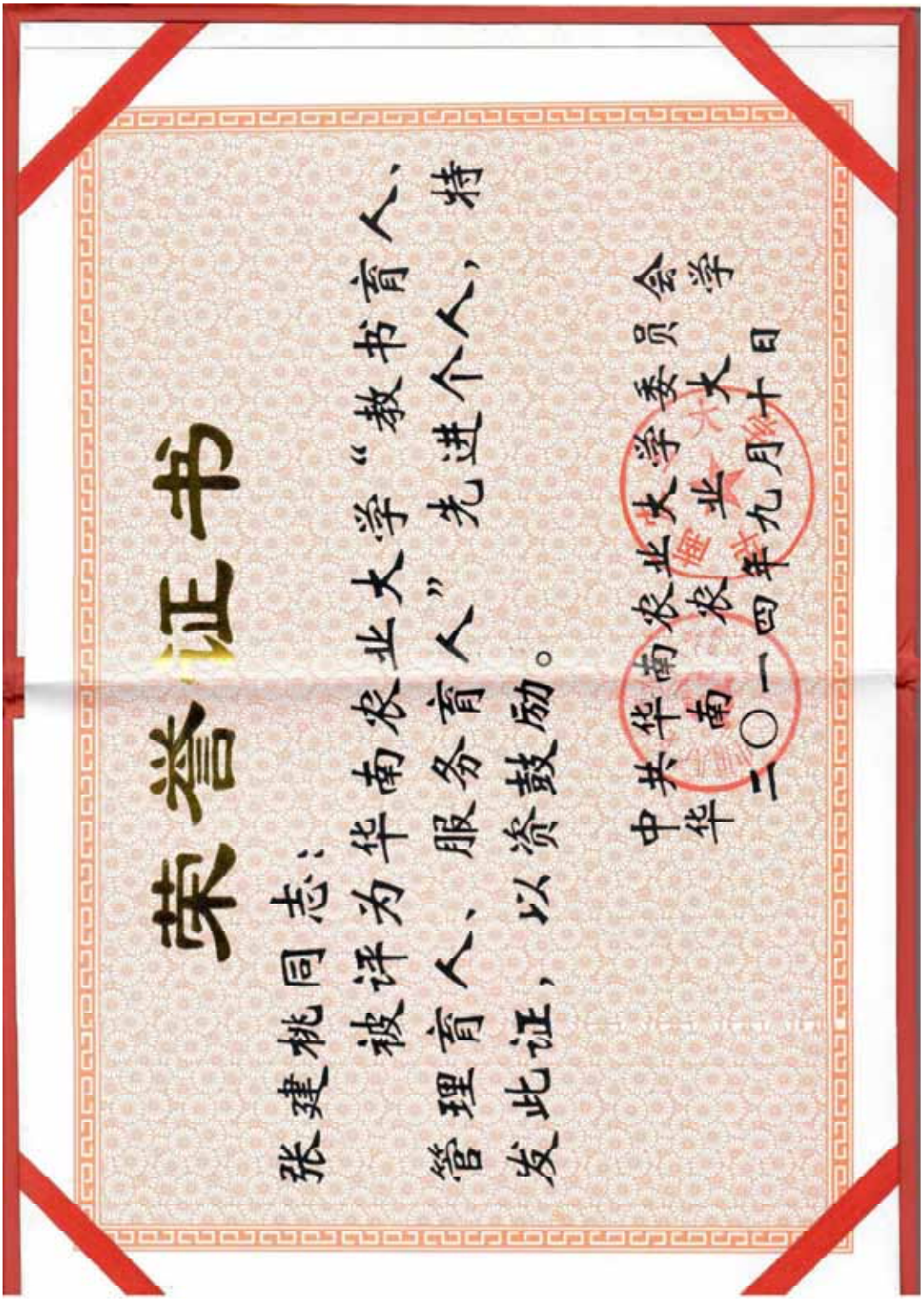
广州市科学技术协会

二〇二〇年十月

2.3 华南农业大学首届课程思政教学大赛三等奖



2.4 华南农业大学 “教书育人、管理育人、服务育人” 校级先进个人


荣誉证书

张建桃同志：

被评为华南农业大学“教书育人、管理育人、服务育人”先进个人，特发此证，以资鼓励。

中共华南农业大学委员会学生工作部
华南农业大学
二〇一四年九月十日

2.5 华南农业大学 研究生教学成果奖一等奖（排第二）：真场景，实应用:面向农业数智化转型的信息管理类硕士培养模式创新与实践


华南农业大学

研究生教学成果奖

获奖证书

获奖成果：真场景，实应用：面向农业数智化转型的信息管理类硕士培养模式创新与实践

获 奖 者：熊俊涛、张建锐、韦婷婷、宋 歌、余平祥、张勇威、黄丽清、黄文玲、邓 金、古万荣

获奖等级：一等奖

证书编号：YJSJXCG25016

2.6 广东省高等学校教学管理学会“高校学生实习实践典型案例”二等奖（排第四）：真场景.实应用.双师型、共育知农爱农数智新农人



荣誉证书

HONORARY CERTIFICATE

华南农业大学 黄文玲：

您主持的案例《真场景·实应用·双师型、共育知农爱农数智新农人》在我会2025年学术年会“高校学生实习实践典型案例”评选活动中，荣获二等奖。

特发此证，以资鼓励。

团队成员名单：熊俊涛、余平祥、张建锐、韦婷婷、古万荣、陈炜颖

广东省高等学校教学管理学会

2025年12月

3. 社会服务

3.1 2022 年社会服务工作量：58



3.2 2023 年社会服务工作量：114



3.3 2024 年社会服务工作量：133



3.4 2025 年社会服务工作量：94

